



# Kent Academic Repository

**Whitewood, Austin (2019) *New insights into integrin-mediated adhesion formation*. Doctor of Philosophy (PhD) thesis, University of Kent,.**

## Downloaded from

<https://kar.kent.ac.uk/82201/> The University of Kent's Academic Repository KAR

## The version of record is available from

## This document version

UNSPECIFIED

## DOI for this version

## Licence for this version

UNSPECIFIED

## Additional information

## Versions of research works

### Versions of Record

If this version is the version of record, it is the same as the published version available on the publisher's web site. Cite as the published version.

### Author Accepted Manuscripts

If this document is identified as the Author Accepted Manuscript it is the version after peer review but before type setting, copy editing or publisher branding. Cite as Surname, Initial. (Year) 'Title of article'. To be published in *Title of Journal*, Volume and issue numbers [peer-reviewed accepted version]. Available at: DOI or URL (Accessed: date).

## Enquiries

If you have questions about this document contact [ResearchSupport@kent.ac.uk](mailto:ResearchSupport@kent.ac.uk). Please include the URL of the record in KAR. If you believe that your, or a third party's rights have been compromised through this document please see our [Take Down policy](https://www.kent.ac.uk/guides/kar-the-kent-academic-repository#policies) (available from <https://www.kent.ac.uk/guides/kar-the-kent-academic-repository#policies>).

# New insights into integrin-mediated adhesion formation

**Austin James Whitewood**

A thesis submitted for degree of doctor of philosophy

Department of Biosciences

The University of Kent

2019

## Declaration

Crystals for the talin-2 head crystal structure (Chapter 5) were grown and optimised by the previous Goult lab member Marie D. Anderson. The crystal structures reported in this thesis have also been solved with the assistance of Professor Dave Brown and Dr. Abhimanyu K. Singh.

No part of this thesis has been submitted in support of an application for any degree or qualification of the University of Kent or any other University or Institute of learning.

Austin Whitewood

October 2019

## Acknowledgements

I would firstly like to thank my supervisor Dr. Ben Goult for all his guidance, support and inspiration throughout my PhD, he has made my PhD a truly fascinating adventure. I would also like to say a big thank you to all the members of the Goult lab past and present, Rejina Khan, Gabriella Laker, Alana Cowell, Karen Baker, Rosemarie Gough, Abhi Singh, Marie Anderson, Tom Paige and Lorena Varela-Alvarez, who have all provided me with support, smiles and plenty of cake a coffee breaks, making my PhD a fully enjoyable experience. Additionally, all those from the Toseland, Geeves and Mulvihill labs who put up with all my shenanigans in our shared labs.

I would also like to thank all of my friends at University of Kent who drunk, played sport and laughed with me. A special note to my old house mates Alex Cook and Elliot Piper-Brown and honouree house mate Diego Cantoni for sharing the highs and lows of our PhDs together.

I am truly grateful for all the help and support Dave Brown and Abhi Singh provided me in x-ray crystallography, a discipline I have learnt to love. Additionally, for the help and guidance provided by Gary Thompson who helped me understand the enigma of NMR through a series of arm movements.

A big thank you to my family and my partner's family for providing me with a bed, a place to write, food, coffee and wine during the writing of this thesis, without which I would not have survived.

And last but not least, I am forever grateful to my loving partner Harriet, who has listened to me prattle on about every aspect and idea of my PhD. Without her support I would most probably be a totally mad scientist instead of the quite mad scientist I am today.

## Contents

<b>DECLARATION .....</b>	<b>2</b>
<b>ACKNOWLEDGEMENTS .....</b>	<b>3</b>
<b>CHAPTER 1: FOREWORD .....</b>	<b>11</b>
<b>1.1 Research contributions.....</b>	<b>11</b>
1.1.1 Publications .....	11
1.1.2 Posters.....	11
<b>1.2 Abstract.....</b>	<b>12</b>
<b>1.2 Abbreviations.....</b>	<b>13</b>
<b>CHAPTER 2: INTRODUCTION .....</b>	<b>15</b>
<b>2.1 Integrin-mediated adhesions.....</b>	<b>15</b>
2.1.1 Cell migration.....	15
2.1.2 Types of integrin adhesions.....	17
<b>2.2 Integrin.....</b>	<b>19</b>
2.2.1 Integrin structure .....	20
2.2.2 Extracellular matrix .....	21
2.2.3 Integrin ligand recognition .....	22
<b>2.3 Talin .....</b>	<b>22</b>
2.3.1 Isoforms.....	22
2.3.2 Structure.....	23
2.3.3 Talin autoinhibition and mechanosensing.....	25
2.3.4 Talin actin binding.....	26
2.3.5 Leucine-Aspartic acid motif binding.....	26
2.3.6 Talin rod interactions .....	27
2.3.7 Talin head interactions.....	28
<b>2.4 Kindlins.....</b>	<b>29</b>

2.4.1	Isoforms.....	29
2.4.2	Structure.....	29
2.4.3	Interactions within the adhesome .....	30
2.4.4	Disease .....	31
<b>2.5</b>	<b>Integrin activation .....</b>	<b>31</b>
2.5.1	Integrin activation states.....	32
2.5.2	Kindlin and talin mediated integrin activation.....	33
2.5.3	Talin recruitment in integrin activation.....	35
<b>2.6</b>	<b>Vinculin .....</b>	<b>35</b>
2.6.1	Structure.....	36
2.6.2	Interactions within the adhesome .....	37
<b>2.7</b>	<b>Additional core adhesome proteins.....</b>	<b>38</b>
2.7.1	Rap1 .....	38
2.7.2	Paxillin .....	39
2.7.3	Focal Adhesion Kinase.....	39
<b>2.8</b>	<b>Objectives of work.....</b>	<b>39</b>
<b>CHAPTER 3:</b>	<b>METHODS .....</b>	<b>42</b>
<b>3.1</b>	<b>Materials .....</b>	<b>42</b>
3.1.1	Buffers.....	42
3.1.2	Plasmids.....	43
3.1.3	Peptides.....	44
<b>3.2</b>	<b>Recombinant Protein Expression .....</b>	<b>45</b>
3.2.1	Expression in E.coli.....	45
3.2.2	Protein Purification .....	45
3.2.3	Ni-affinity purification using FPLC AKTA system .....	46
3.2.4	Ni-affinity purification by batch method.....	46
3.2.5	TEV protease cleavage .....	46

3.2.6	Anion/Cation Exchange Chromatography .....	47
3.2.7	Mouse Rap1 expression and purification from CK600K cells.....	47
3.2.8	Protein concentration estimation .....	48
3.2.9	SDS-PAGE gels.....	48
<b>3.3</b>	<b>Biochemical methods .....</b>	<b>49</b>
3.3.1	Circular Dichroism (CD) .....	49
3.3.2	Fluorescence Polarisation (FP).....	50
3.3.3	Microscale Thermophoresis (MST) .....	52
3.3.4	Analytical size exclusion chromatography – multi-angle light scattering (SEC-MALS) .....	53
3.3.5	Multi-lamellar vesicle co-sedimentation assay.....	53
3.3.6	Peptide conjugated lipid co-sedimentation assay.....	54
<b>3.4</b>	<b>Structural methods.....</b>	<b>55</b>
3.4.1	X-ray Crystallography .....	55
3.4.2	Nuclear Magnetic Resonance (NMR) .....	58
<b>4.</b>	<b>METHOD DEVELOPMENT TO GAIN BIOCHEMICAL INSIGHT INTO INTERACTIONS AT INTEGRIN-MEDIATED ADHESIONS.....</b>	<b>60</b>
<b>4.1</b>	<b>Investigating protein:protein interactions using microscale thermophoresis (MST) .....</b>	<b>60</b>
4.1.1	Difficulty expressing recombinant proteins.....	60
4.1.2	Recombinant expression of full length talin .....	61
4.1.3	Recombinant expression of kindlin-1.....	62
4.1.2	MST experiment.....	63
4.1.3	Coupling to RED-tris-NTA dye .....	65
4.1.4	Test 1: Talin autoinhibition interaction between F2F3 and R9R10 .....	66
4.1.5	Test 2: Full-length talin and KANK peptide.....	67
4.1.6	Test 3: interaction between kindlin-1 and integrin.....	69
<b>4.2</b>	<b>Application of the MST assay: Kindlin-1 regulates epidermal growth factor receptor (EGFR) signalling.....</b>	<b>71</b>
4.2.1	Biochemical characterisation of the novel interaction between kindlin-1 and the EGFR .....	71

<b>4.3</b>	<b>Peptide-conjugated lipid co-sedimentation assay.....</b>	<b>73</b>
4.3.1	Cell membrane mediation of protein:protein interactions .....	73
4.3.2	Lipid co-sedimentation assays .....	74
4.3.3	Incorporating membrane proteins into lipid coseds. ....	74
4.3.4	Experiment design .....	75
4.3.5	Optimisation: peptide conjugation .....	77
4.3.5	Optimisation: Co-sedimentation assay setup.....	79
<b>4.4</b>	<b>Discussion.....</b>	<b>81</b>
4.4.1	Using MST to provide quantitative data on protein-protein interactions. ....	82
4.4.2	Peptide-conjugated lipid coseds as an adaptable method for investigating the influence of membranes on molecular interactions.....	83
4.4.3	Use of the newly developed assays .....	84
<b>CHAPTER 5:</b>	<b>REGULATION OF THE TALIN FERM DOMAIN.....</b>	<b>85</b>
<b>5.1</b>	<b>Biochemical characterisation of talin autoinhibition mutant E1770A .....</b>	<b>85</b>
5.1.1	Introduction.....	85
5.1.2	E1770A mutant design .....	86
5.1.3	Recombinant expression of the E1770A full-length talin mutant and analysis .....	87
5.1.4	Investigating the propensity of the E1770A mutant to bind integrin.....	88
5.1.5	Conclusions from the mouse study.....	90
<b>5.2</b>	<b>Talin FERM domain is regulated through a rotational axis.....</b>	<b>92</b>
5.2.1	Crystal structure of talin-2 FERM reveals novel conformation .....	92
5.2.2	The F1-F2 rotational axis alludes to conformational regulation of the talin head .....	98
5.2.3	Involvement of the F1-loop in conformational regulation .....	100
<b>5.3</b>	<b>Investigating the effects of lipid composition on the talin head membrane binding.....</b>	<b>100</b>
<b>5.4</b>	<b>Novel interaction between kindlin and the talin FERM domain .....</b>	<b>103</b>
5.4.1	Introduction.....	103
5.4.2	The talin FERM domain binds to kindlin-1.....	103
5.4.3	The talin F1-loop is involved in kindlin binding.....	105



5.4.4	Phosphorylation of the F1-loop affects kindlin binding.....	107
5.4.5	Kindler syndrome mutant has reduced affinity to integrin and talin .....	108
<b>5.5</b>	<b>Discussion.....</b>	<b>112</b>
5.5.1	Conformational regulation of the talin head .....	113
5.5.2	Understanding the talin:kindlin interaction .....	114
<b>CHAPTER 6: INVESTIGATING THE ROLE OF THE ALPHA-INTEGRIN SUBUNIT IN TALIN-MEDIATED INTEGRIN ACTIVATION .....</b>		<b>117</b>
<b>6.1</b>	<b>Introduction .....</b>	<b>117</b>
6.1.1	Talin mediated integrin activation .....	117
6.1.2	The current understanding of the $\alpha$ -subunit cytoplasmic domain in integrin regulation .....	118
6.1.3	Aim: investigate talin binding to the $\alpha$ -subunit of integrin .....	119
<b>6.2</b>	<b>The talin head binds to the <math>\alpha</math>-tail.....</b>	<b>119</b>
<b>6.3</b>	<b>Investigating talin F3 binding to <math>\alpha</math>-integrin .....</b>	<b>120</b>
6.3.1	NMR data reveals talin F3 binds to the $\alpha$ -tail .....	120
6.3.2	NMR peak shift mapping reveals the $\alpha$ -tail binds to a similar site as the $\beta$ -tail on F3. ....	123
6.3.3	X-ray crystallography.....	124
6.3.4	Peptide-conjugated lipid co-sedimentation assay suggests talin F3 interaction with the $\alpha$ -tail is membrane dependent.....	127
<b>6.4</b>	<b>Investigating talin F1 binding to <math>\alpha</math>-integrin .....</b>	<b>128</b>
6.4.1	NMR investigation into talin F1 interacting with the $\alpha$ -tail .....	129
6.4.2	Peak shift mapping of the $\alpha$ -tail binding to F1.....	133
<b>6.5</b>	<b>The alpha binding site sits between talin and Rap1 .....</b>	<b>134</b>
6.5.1	Molecular modelling suggests a tripartite interaction between F1, Rap1 and the $\alpha$ -tail .....	135
6.5.2	NMR investigation into Rap1b interacting with the $\alpha$ -tail.....	136
<b>6.6</b>	<b>Discussion .....</b>	<b>138</b>
6.6.1	Talin as an integrin 'inactivator'.....	139
6.6.2	Talin as an integrin 'inactivator' further work .....	141
6.6.3	Talin-Rap1-mediated integrin activation.....	142

6.6.4 Talin-Rap1-mediated integrin activation further work .....	143
6.6.5 Talin mediates integrin activation through both integrin subunits.....	144
<b>CHAPTER 7: BIOCHEMICAL CHARACTERISATION OF NOVEL INTERACTIONS OF TALIN AND VINCULIN.....</b>	<b>146</b>
<b>7.1 Introduction .....</b>	<b>146</b>
7.1.1 Talin and Vinculin at adhesions .....	146
7.1.2 Talin vinculin binding sites.....	146
7.1.2 Aims .....	148
<b>7.2 Force-independent VBS in talin R8 determines nascent adhesion maturation.....</b>	<b>148</b>
7.2.1 Talin and vinculin dependent nascent adhesion maturation.....	148
7.2.2 Force independent talin-vinculin pre-complex in nascent adhesion assembly .....	149
7.2.3 Talin R8 contains a threonine belt .....	150
7.2.4 Stabilising R8 using a 'VVV' mutant.....	152
7.2.5 R7R8vvv mutant stabilises the R8 domain .....	152
7.2.6 R7R8vvv mutation has no major effect on LD-motif containing ligand binding.....	153
7.2.7 The VVV mutation reduces the propensity of the R8 domain to bind vinculin.....	155
7.2.8 Biochemical conclusions.....	156
7.2.9 R7R8vvv mutation impairs nascent adhesion maturation.....	157
<b>7.2 Discussion: Force-independent VBS in talin R8 determines nascent adhesion maturation .....</b>	<b>157</b>
7.3.1 Conclusions.....	157
7.3.2 Fine tuning of talin rod domain plasticity mediates adhesions .....	158
7.3.3 The roll of the talin-vinculin pre-complex in NA maturation.....	160
<b>7.4 Chlamydial virulence factor TarP mimics talin to disrupt the talin-vinculin complex. ....</b>	<b>161</b>
7.4.1 Pathogens target intracellular adhesion proteins for cell entry .....	161
7.4.2 Chlamydial virulence factor TarP .....	161
7.4.3 TarP reported to contain both a VBS and LD-motif.....	162
7.4.4 Sequence analysis of TarP LD motif .....	162
7.4.5 TarP LD does not bind to FAK-FAT or talin R7R8.....	163

7.4.6	Sequence analysis of TarP VBS region.....	167
7.4.7	TarP VBS1 binds to vinculin with a high affinity.....	168
7.4.8	TarP VBS are constitutively active.....	169
7.4.9	Crystal Structure reveals TarP VBS1 mimics talin VBS.....	170
7.4.10	The TarP VBS1 competes with talin, disrupting talin:vinculin complexes.....	173
7.4.11	Investigating TarP VBS3.....	176
7.4.12	Crystal Structure of Vd1 bound to TarP VBS3 reveals strong hydrophobic interaction .....	177
<b>7.5</b>	<b>Discussion: Chlamydial virulence factor TarP mimics talin to disrupt the talin-vinculin complex.</b>	<b>180</b>
7.5.1	TarP hijacks the host adhesion machinery .....	180
7.5.2	Disruption of talin-vinculin complexes by constitutively active VBS.....	181
7.5.3	Lack of observable binding of TarP LD.....	182
7.5.3	Future work .....	183
<b>CHAPTER 8: DISCUSSION .....</b>		<b>184</b>
<b>8.1</b>	<b>The not so simple core of cell-matrix adhesions .....</b>	<b>184</b>
<b>8.2</b>	<b>Fine tuning of the talin domains .....</b>	<b>185</b>
<b>8.3</b>	<b>Potential limitations .....</b>	<b>187</b>
<b>CHAPTER 9: REFERENCES.....</b>		<b>187</b>
<b>CHAPTER 10: APPENDIX .....</b>		<b>206</b>

## Chapter 1: Foreword

### 1.1 Research contributions

#### 1.1.1 Publications

Han, S.J., K.M. Dean, A.J. Whitewood, A. Bachir, E. Guttierrez, A. Groisman, A.R. Horwitz, B.T.

Goult, and G. Danuser. 2019. Formation of talin-vinculin pre-complexes dictates maturation of nascent adhesions by accelerated force transmission and vinculin recruitment. *bioRxiv*. 735183. doi:10.1101/735183.

Michael, M., R. Begum, G.K. Chan, A.J. Whitewood, D.R. Matthews, B.T. Goult, J.A. McGrath, and M. Parsons. 2019. Kindlin-1 Regulates Epidermal Growth Factor Receptor Signaling. *J. Invest. Dermatol.* 139:369–379. doi:10.1016/j.jid.2018.08.020.

Whitewood, A.J., A.K. Singh, D.G. Brown, and B.T. Goult. 2018. Chlamydial virulence factor TarP mimics talin to disrupt the talin-vinculin complex. *FEBS Lett.* 592:1751–1760. doi:10.1002/1873-3468.13074.

Haage, A., K. Goodwin, A. Whitewood, D. Camp, A. Bogutz, C.T. Turner, D.J. Granville, L. Lefebvre, S. Plotnikov, B.T. Goult, and G. Tanentzapf. 2018. Talin Autoinhibition Regulates Cell-ECM Adhesion Dynamics and Wound Healing In Vivo. *Cell Rep.* 25:2401-2416.e5. doi:10.1016/j.celrep.2018.10.098.

#### 1.1.2 Posters

**Gordon Research Conference: Fibronectin, integrins and related molecules (2018) in Lucca, Italy**

“Biochemical insight into protein:protein interactions at integrin-mediated cell adhesions”

A.J. Whitewood and B.T. Goult

**UK Cell Adhesion Society Meeting (2018) in University College London**

“Chlamydial virulence factor TarP mimics talin to disrupt the talin-vinculin complex.”

A.J. Whitewood, A.K. Singh, D.G. Brown, and B.T. Goult

## 1.2 Abstract

Integrin-mediated cell adhesions are highly regulated structures forming between the cell and the extracellular matrix (ECM). These structures form a bidirectional signalling platform between the cell and its environment with important functions in cell migration, shape, wound repair and tissue development. These adhesions are regulated by a complex network of proteins and lipids, allowing for an ever-expanding diversity in adhesion type and function. This network forms on a core consisting of integrin linked to actin via the large adapter protein talin. Integrins are dimeric transmembrane receptors with a large ECM binding ectodomain and two cytoplasmic tails. Talin is comprised of a FERM domain consisting of four subdomains in an atypical linear form linked to a long mechanosensitive rod domain containing thirteen helical bundle subdomains. A major pathway to activate integrin is for talin, via its F3 FERM subdomain, to bind to the  $\beta$ -integrin cytoplasmic tail and separate the two cytoplasmic tails. For talin-mediated integrin activation to occur, the FERM-domain containing adapter protein kindlin and the small GTPase Rap1, have both been demonstrated to be necessary.

We have combined biochemical and structural approaches to elucidate novel regulatory mechanisms, which may be controlling talin-mediated integrin activation. Solving of a novel crystal structure of the talin-2 FERM domain revealed conformational plasticity in the talin FERM that alludes to a novel way of regulating the integrin activating ability of talin. Additionally, identification and characterisation of an interaction between talin and kindlin has provided a new insight into the role of kindlin in integrin activation. Furthermore, elucidation of an interaction between talin, Rap1 and the  $\alpha$ -integrin cytoplasmic tail hints at a new twist in the integrin tail separation story and the essential function of Rap1 in adhesions, with both tails being simultaneously bound to talin.

Vinculin is an important adhesion adapter protein consisting of a talin-binding head region linked to an actin binding tail domain. The talin rod contains 11 vinculin binding sites (VBS), 10 of which

are cryptic, which are revealed in response to mechanical force. Vinculin binding reinforces force transmission across talin, a process that is crucial for adhesion maturation. We identify a “threonine-belt” in the talin rod subdomain R8 that destabilises the domain, enabling vinculin binding in the absence of force. The accessibility of the VBS in the R8 subdomain proved essential for talin-vinculin pre-complexes to form prior to force onset, an important process in adhesion maturation. Additionally, we have identified a mechanism by which pathogenic bacteria mimic talin VBS to disrupt the talin-vinculin interaction, aiding cell entry.

This multidisciplinary approach employed in this thesis has provided new insights into the complex mechanisms at play in the formation and maturation of integrin-mediated adhesions.

## 1.2 Abbreviations

ABS	Actin Binding Site
Amp	Ampicillin antibiotic
BSA	Bovine Serum Albumin
CD	Circular dichroism
cosed	co-sedimentary assay
DD	Dimerization Domain
dH <sub>2</sub> O	distilled water
DLC1	Deleted Liver Cancer 1
DTT	Dithiothreitol
ECM	Extracellular Matrix
F...	FERM subdomain
FA	Focal Adhesions
FAK	Focal Adhesion Kinase
FERM	4.1 protein

FPLC	fast protein liquid chromatography
HSQC	Heteronuclear single quantum spectroscopy
IBS	Integrin Binding Site
IPTG	Isopropyl- $\beta$ -D- thiogalactopyronoside
KANK	Kidney Ankyrin Repeat-containing protein
$K_d$	Dissociation constant
LD	Leucine Aspartate
MST	Microscale thermophoresis
NA	Nascent adhesion
NaCl	Sodium Chloride
NMR	Nuclear Magnetic Resonance
NT-647	Nanotemper RED-tris-NTA dye
PBS	Phosphate Buffered Saline
PC	L- $\alpha$ -Phosphatidylcholine
PE-MCC	2-dioleoyl-sn-glycero-3-phosphoethanolamine-N-[4-(p- maleimidomethyl)cyclohexane-carboxamide]
PI	Isoelectric Point
PIP2	Phosphatidylinositol 4
PS	L- $\alpha$ -phosphatidylserine
R...	Talin rod subdomain...
RIAM	Rap1-interacting adapter molecule
RPM	Rotations per minute
SDS-PAGE	sodium docecylsulfate polyacrylamide gel electrophoresis
TarP	translocated actin recruiting protein
TCEP	tris(2-carboxyethyl)phosphine

TLN1	Talin1 gene
TLN2	Talin2 gene
TM	Transmembrane
VBS	Vinculin Binding Site
Vd1	vinculin domain 1
$\alpha$ -tail	Alpha-integrin cytoplasmic tail
$\beta$ -tail	Beta-Integrin cytoplasmic tail

## Chapter 2: Introduction

### 2.1 Integrin-mediated adhesions

Integrin-mediated adhesions are well-conserved multi-component structures that link the extracellular matrix (ECM) via integrin transmembrane receptors, to the actin cytoskeleton. These structures are capable of sensing and transmitting force, and are critical for cell morphogenesis, mechanosensation and cell migration (Parsons et al., 2010).

#### 2.1.1 Cell migration

Cell migration is a vital function in all multicellular organisms and is essential for development, tissue formation, immune response and wound healing (Case and Waterman, 2015). When regulation of cell migration is lost, organisms can develop severe diseases including cancer metastasis, chronic inflammatory diseases and vascular diseases. Directed cell movement is dictated by cell polarity with a defined leading edge and rear end. This allows organisation of cellular components, shape, structure and function (Case and Waterman, 2015).

Cell migration requires traction force generation against the immediate surroundings. The main force comes from the actin cytoskeleton, generated through actin polymerisation and actomyosin contraction, coordinating to generate an actin retrograde flow (Theriot and Mitchison, 1991).



This retrograde flow is translated into traction force through cell adhesion molecules (CAMs), such as integrins, through a mechanism defined as 'the molecular clutch' in which the CAMs adhere to the ECM anchoring the position of the actin and enabling it to push against the leading edge of the cell membrane (Elosegui-Artola et al., 2016) (fig. 2.1).

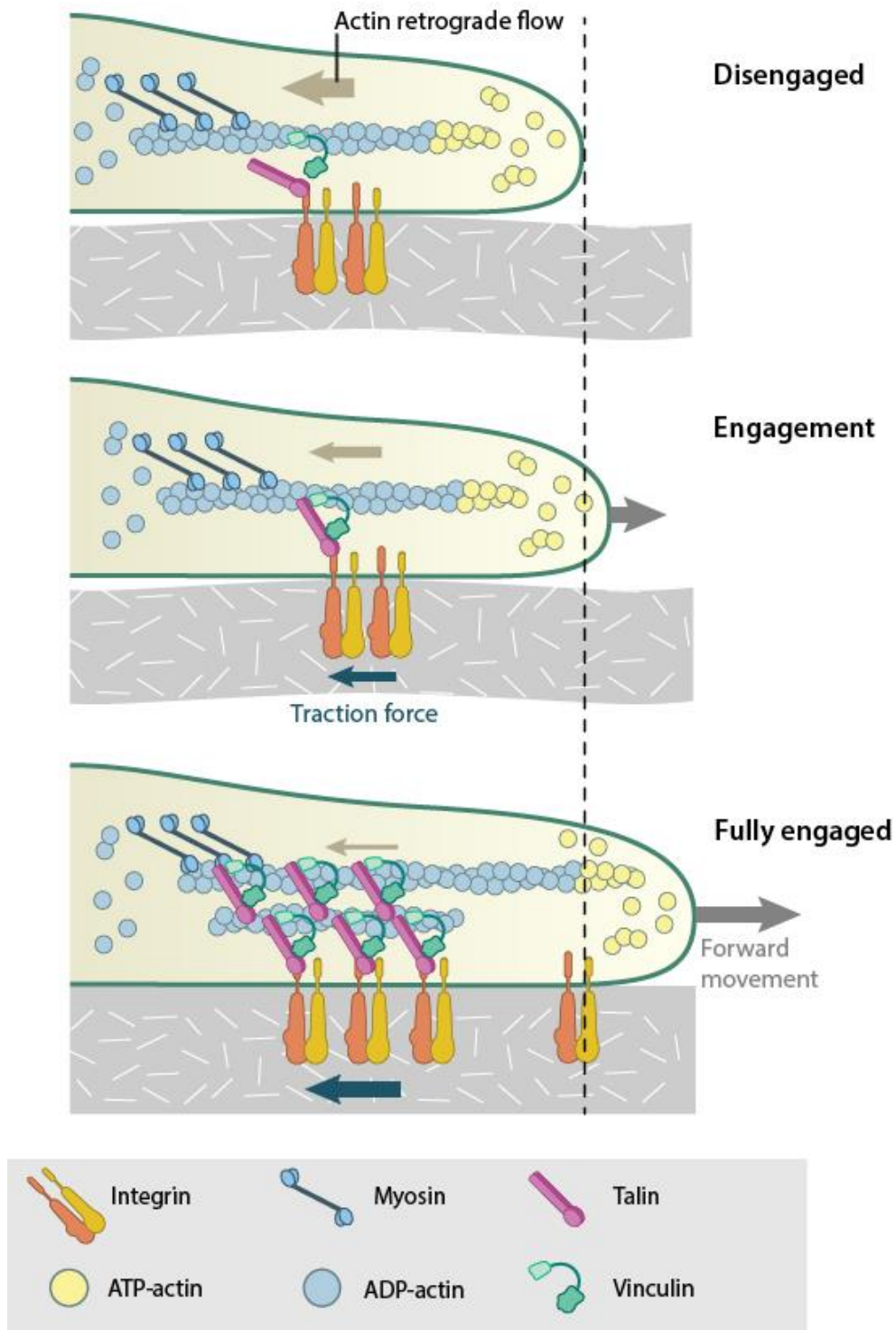


Figure 2.1: **The molecular clutch.** Schematic demonstrating how actin retrograde flow combines with adhesion molecules to generate traction force and enabling the cell to spread, through a mechanism termed the molecular clutch. taken from (MBInfo).

### 2.1.2 Types of integrin adhesions

Cell-matrix adhesion complexes are diverse structures that can be broken down into different sub-types of adhesions based on size, maturity and function. At the leading edge of a migrating

cell there is an actin projection termed the lamellipodium, in the lamellipodium there are numerous small short-lived adhesions termed nascent adhesions (NAs) (more detail in section 7.2.1), most of these structures are rapidly turned over. Some NAs mature to larger dot-like structures referred to as focal complexes (FCs); these are located just behind the leading edge and are approximately 1  $\mu\text{m}$  in diameter, persisting for several minutes. As the cell migrates FCs can further mature into the much larger focal adhesions (FAs) that are about 2  $\mu\text{m}$  wide and 3-10  $\mu\text{m}$  long, residing at the end of large actin bundles or stress fibres (Zimerman et al., 2004) (fig. 2.2).

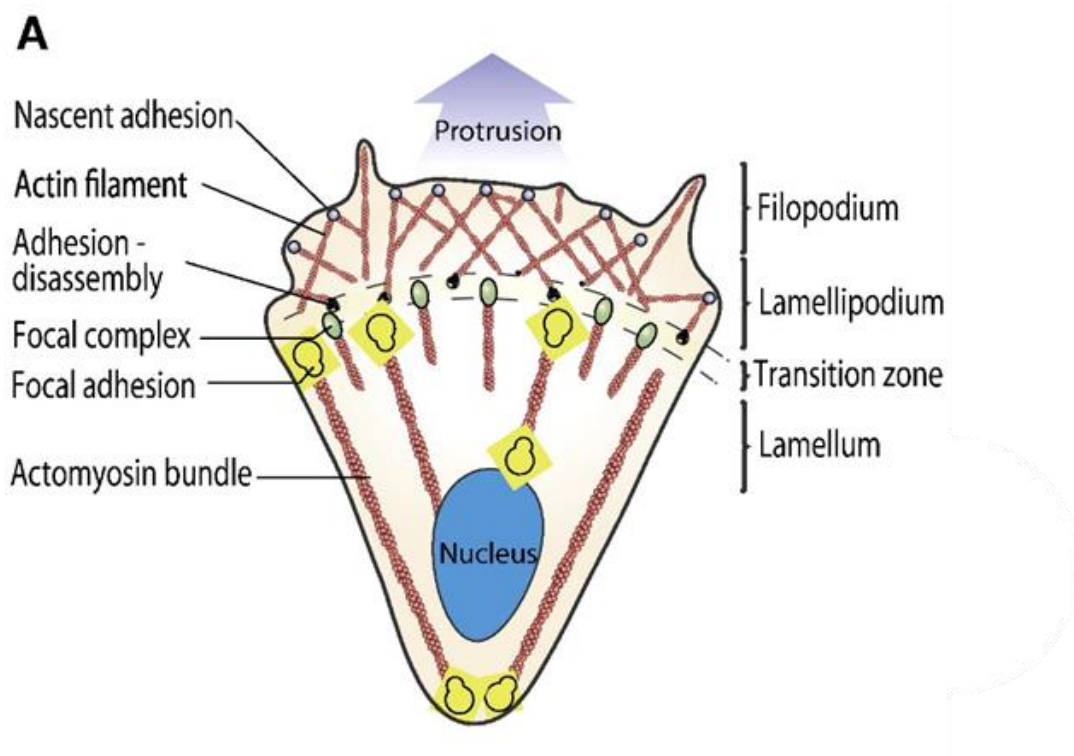


Figure 1.2: Maturation of Cell-Matrix adhesion. Schematic demonstrating the evolution of the cell-matrix adhesion at the lamellipodium. Adapted from (Klotzsch et al., 2015).

Other classes of adhesions include podosomes and invadopodia; these are typically found in leukocytes, endothelial, smooth muscle and tumour cells (Linder, 2007). Podosomes comprise of a central actin core with adhesion molecules arranged in a ring forming small circular adhesions that turn over in 2-10 minutes (Luxenburg et al., 2006). Invadopodia resemble podosomes but do not arrange into ring structures, they are more stable and can protrude slightly further into the

ECM (Weaver, 2006). Both structures contact the substratum where they function as sites of localised protease secretion and ECM degradation (Albiges-Rizo et al., 2009).

## 2.2 Integrin

Integrins are heterodimeric transmembrane proteins expressed in all metazoan species. First discovered in 1986 they were named for their ability to integrate the intracellular and extracellular environments of a cell (Tamkun et al., 1986). Composed of  $\alpha$  and  $\beta$  integrin subunits, humans have 18  $\alpha$  and 8  $\beta$  that form a total of 24 heterodimeric pairs (fig. 2.3) (Campbell and Humphries, 2011).

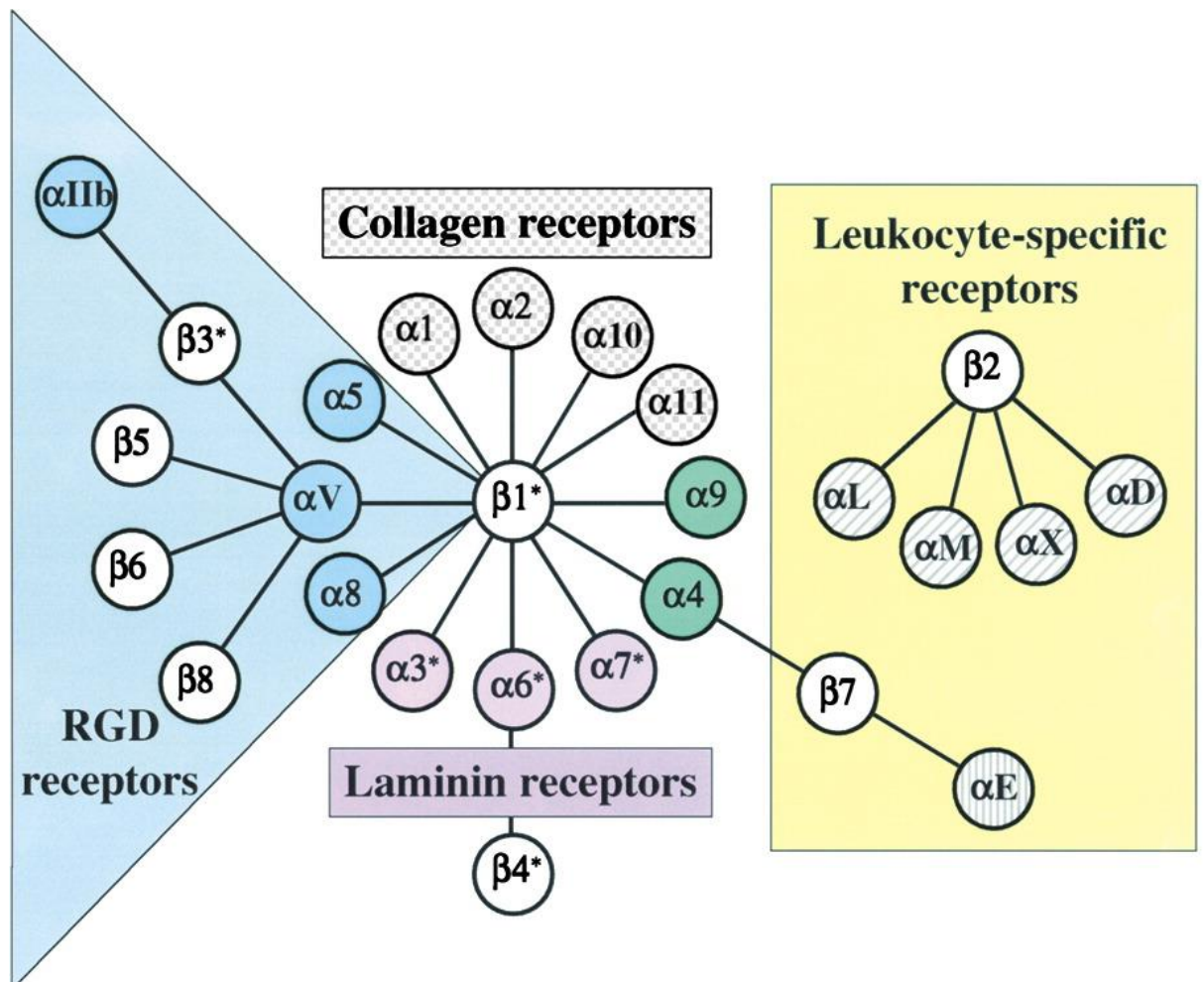


Figure 2.3: **Integrin receptor family.** Diagram showing the possible combinations of integrin subunits and their ECM ligands. Taken from (Hynes, 2002)

### 2.2.1 Integrin structure

Both integrin subunits consist of a large ectodomain, a well-conserved single transmembrane (TM) region and relatively short cytoplasmic domains termed the tails. The  $\alpha$ -subunit is slightly larger than the  $\beta$ -subunit comprising of around 1000aa and 750aa respectively (Luo et al., 2007).

$\alpha$ -integrins ectodomains are composed of four or five domains, depending on the presence of an  $\alpha$ -I domain, a seven-bladed  $\beta$ -propeller, a thigh and two calf domains. Conversely,  $\beta$ -integrin ectodomains are composed of several domains forming more complex and flexible interconnections; including a hybrid domain, a plexin-semaphorin-integrin (PSI), followed by four epidermal growth factor (EGF) modules and a  $\beta$ -tail domain. (Xia et al., 2004) (fig. 2.4).

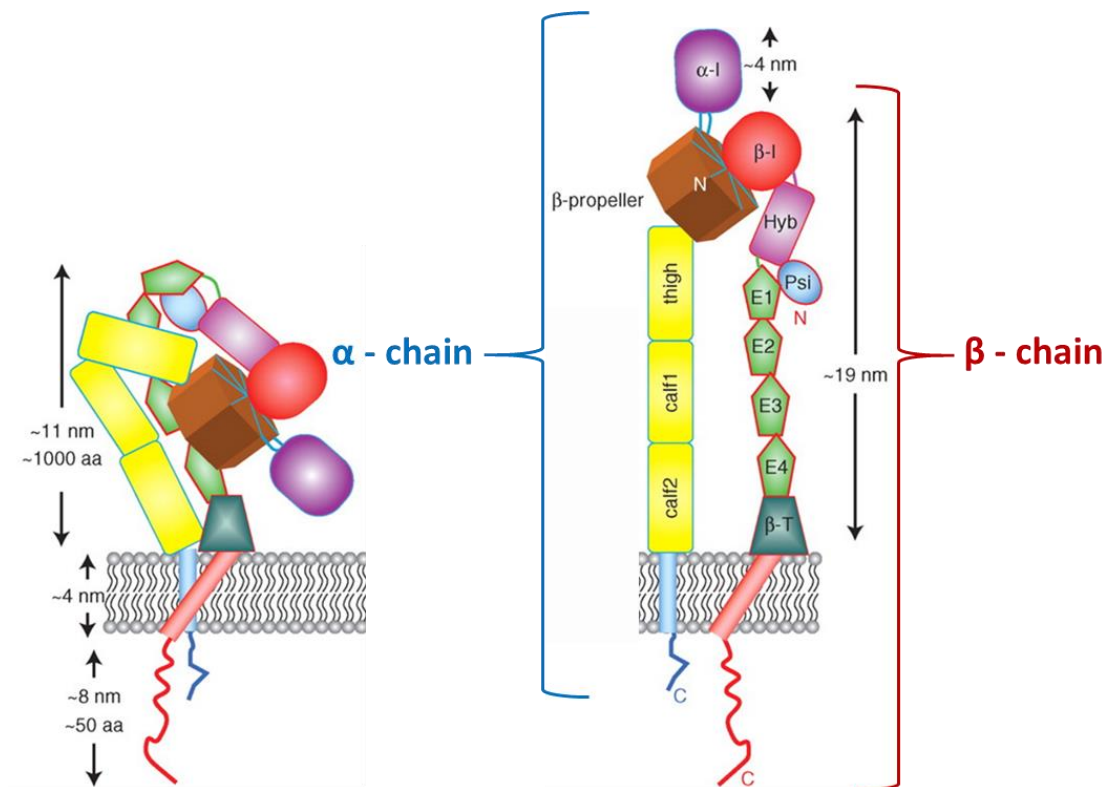


Figure 2.4: **Structure of integrins.** Schematic diagram of integrin domain structure in the inactive (left) and active (right) conformations. Adapted from (Campbell and Humphries, 2011)

The cytoplasmic tails of  $\beta$ -integrin have a well conserved membrane proximal Asp-Pro-x-Tyr (NPxY) motif and membrane distal Asp-x-x-Tyr (NxxY) motif, important for binding to particular PTB-domain containing proteins, including talin and kindlin (Wegener and Campbell, 2008).  $\alpha$ -

integrin tails also contain a conserved region, consisting of a GFFKR motif conserved in all isoforms, which has proved vital for binding to both sharnin and mammary-derived growth factor (Li et al., 2014). These interactions are necessary for inhibition of integrin activation (Rantala et al., 2011).

### 2.2.2 Extracellular matrix

The extracellular matrix (ECM) is a 3D meshwork composed of proteoglycans (PGs), and fibrous proteins. ECM is present within all tissues and organs providing a platform onto which cells and tissues can morph (Frantz et al., 2010). The physical and biochemical properties of the ECM are highly regulated through biophysical and biochemical dialogue between various cellular components (e.g. fibroblasts, epithelial and adipocytes). These properties are very variable according to tissue type; physiological states, for example ageing and tissue repair; or pathological conditions, such as cancer and fibrosis (Lu et al., 2012).

PGs consist of a protein core covalently linked to glycosaminoglycan chains. They are currently classified into three major categories: leucine-rich proteoglycans, modular proteoglycans, and cell-surface proteoglycans (Schaefer and Schaefer, 2010). Proteoglycans are extremely hydrophilic enabling them to form a hydrogel that supports the ECM structure. Proteoglycans have also been demonstrated to assist adhesion, migration and proliferation (Schaefer and Schaefer, 2010).

ECM proteins mostly consist of collagens, fibronectins, elastins and laminins. Collagen is the most abundant of these proteins, providing tensile strength to tissues; collagens are the main protein constituent of bones (Kadler et al., 2008). In contrast, elastins provide elasticity to tissues, allowing them to stretch; elastins are enriched in the blood vessels, lungs and skin (Frantz et al., 2010). Fibronectins are glycoproteins that crosslink cells to collagen fibres, thereby having a major role in cell adhesion (Pankov and Yamada, 2002). Laminins are also glycoproteins, they are predominantly found in basement membranes, providing a meshwork for cells to adhere to (Durbeej, 2010).

### 2.2.3 Integrin ligand recognition

The integrin ligand binding site sits between the intersection of the integrin  $\alpha$ -chain  $\beta$ -propeller and the  $\beta$ I domain, with the alpha chain determining the ligand specificity (Luo et al., 2007). Typically,  $\alpha$ V,  $\alpha$ 5 and  $\alpha$ 8 containing heterodimers bind to an “RGD” motif present in the ECM glycoproteins: fibronectin, vitronectin, fibrinogen and many other ECM constituents (Humphries et al., 2006).  $\alpha$ 9 and  $\alpha$ 4 integrins also bind to fibronectins but through an “LDV” motif. Collagen binding integrins contain either  $\alpha$ 1,  $\alpha$ 2,  $\alpha$ 10 or  $\alpha$ 11 chains; these integrins recognise a triple helical conformation with a “GFPGER” motif (Humphries et al., 2006). Integrins containing  $\alpha$ 3,  $\alpha$ 6 or  $\alpha$ 7 bind specifically to laminin’s  $\alpha$ LG domains 1-3 and  $\alpha$ LN domains (Durbeej, 2010). Finally, integrins containing  $\alpha$ L,  $\alpha$ M,  $\alpha$ X,  $\alpha$ D, and  $\alpha$ E are specific to different leukocyte populations (Harris et al., 2000). (Summarised in fig 2.3)

## 2.3 Talin

Talin is large mechanosensitive adapter protein, with a critical role in linking integrin receptors to the actin cytoskeleton in cell-matrix adhesions.

### 2.3.1 Isoforms

There are two isoforms of talin, talin-1 and talin-2 (Monkley et al., 2001). The two proteins have an identical domain structure and have a high (74%) sequence identity. The two isoforms are encoded by the *TLN1* and *TLN2* genes located on different chromosomes (Monkley et al., 2001). Talin-1 is ubiquitously expressed; in contrast, talin-2 expression is more variable, being entirely absent in some cell types, such as endothelial cells. Talin-2 appears to have higher expression levels in the cerebral cortex of the brain, heart muscle and the kidney (Gough and Goult, 2018; Debrand et al., 2009). The regulation between the two is not fully understood, however in *TLN1*-knockout cells talin-2 expression is upregulated, rescuing many consequences of loss of talin-1,

indicating they both have a similar role (Kopp et al., 2010) at least as far as rescuing adhesion is concerned.

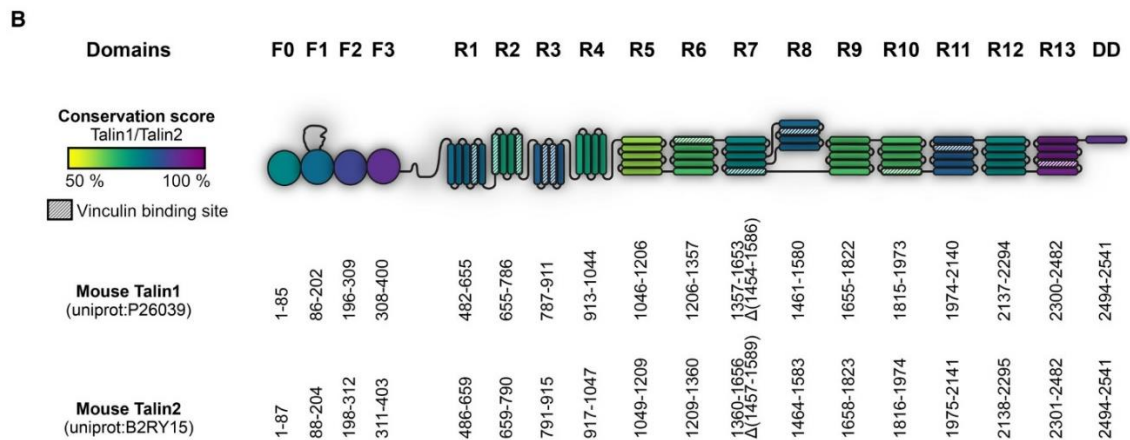


Figure 2.5: **Conservation of talin between isoforms.** Schematic diagram showing the domain structure of talin molecules, coloured by conservation between the two isoforms and labelled with the individual domain boundaries of the two isoforms. Adapted from (Gough and Goult, 2018)

### 2.3.2 Structure

Talin is a 270 kDa homodimer, consisting of an N-terminal FERM region, termed the talin head, attached through an 82 amino acid (aa) flexible linker to a large C-terminal rod domain.

The talin head is a 47 kDa atypical FERM domain (4.1 protein, ezrin, radixin, moesin). FERM domains are typically found in cytoskeletal adapter proteins, localising them to the plasma membrane. They usually consist of three domains arranged in a compact cloverleaf like shape. Unlike other FERM domains, the talin head consists of four domains; both F0 and F1 have ubiquitin-like folds, F1 contains an additional large disordered loop region in its centre (Goult et al., 2010a), the F2 domain contains a 4-helix bundle and the F3 domain has a phosphotyrosine binding domain (PTB) fold. The four domains form an atypical linear shape as opposed to the typical FERM domain cloverleaf like shape (Elliott et al., 2010). However, this 4 domain arrangement of F0-F3 has also been shown to be in kindlin proteins (see section 2.3.2) (Goult et al., 2009b).



At the C-terminus of talin is a large mechanosensitive rod region (220 kDa) consisting of 62  $\alpha$ -helices, grouped into 13 helical bundle domains, four 4-helix (R2, R3, R4 and R8) and nine 5-helix (R1, R5, R6, R7, R9-R13), and a single helix forming a C-terminal dimerization domain (Goult et al., 2013b). The rod contains an integrin binding site in R11 (Rodius et al., 2008; Gingras et al., 2009) and two actin binding sites, ABS2 (Hemmings et al., 1996; Atherton et al., 2015; Kumar et al., 2016) between R4-R8 and ABS3 consisting of R13 and the dimerization domain (McCann and Craig, 1997; Gingras et al., 2008). Furthermore, the rod contains 11 cryptic vinculin binding sites buried amongst the helical bundles (Gingras et al., 2005) (fig. 2.6) and at least five LD-motif binding sites, on R2, R3, R7, R8 and R11 (Goult et al., 2013b; Zacharchenko et al., 2016b; Bouchet et al., 2016).

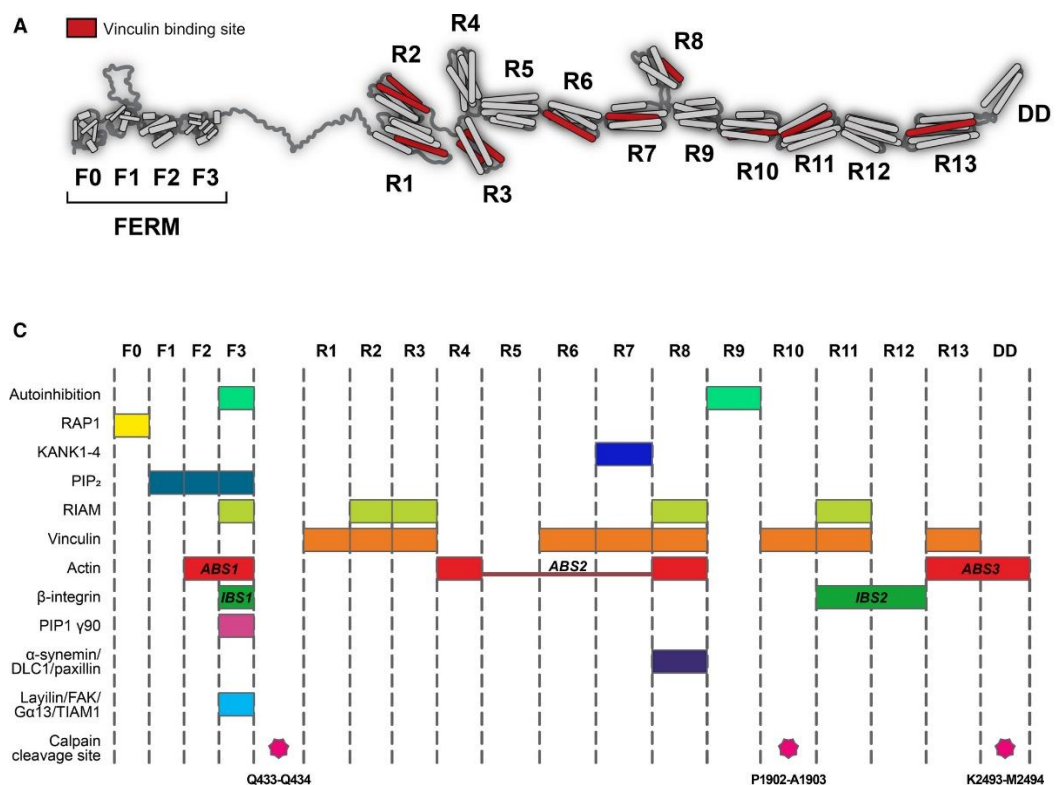


Figure 2.6: **Talin structure and binding sites.** A) Cartoon structure of talin, cryptic vinculin binding sites located on helices coloured red. C) Table summarising known talin ligands and their binding sites. Adapted from (Gough and Goult, 2018)

### 2.3.3 Talin autoinhibition and mechanosensing

A key feature of talin is the multiple layers of folding which cover up numerous binding sites, these become exposed under certain stimulus such as ligand binding and force. This feature of talin allows masking of specific binding sites at certain times enabling talin to respond to different signals within the cell; the feature is termed 'layers of autoinhibition' (Gough and Goult, 2018).

In the cytosol, talin adopts a globular conformation through an interaction between the F3 and R9 domains. This conformation masks the critical integrin binding site found on the F3 domain (Goult et al., 2009a), without this interaction the talin FERM domain can constitutively activate integrin (Goksoy et al., 2008; Goult et al., 2009a; Banno et al., 2012). It is not fully understood what relieves this conformation into the more active elongated structure. However, it has been suggested that it is relieved through interactions with  $G\alpha_{13}$  (Schiemer et al., 2016), RIAM and PIP2 (Goksoy et al., 2008).

Once in the elongated conformation talin still has multiple cryptic vinculin binding sites in the helical bundles. Upon force transduction these domains have been demonstrated to reversibly unfold (Yao et al., 2016; del Rio et al., 2009) unveiling the vinculin binding sites. However, the process simultaneously disrupts the binding sites on the surface of the helical bundles such as that for RIAM TBS1 on talin R3, an important interaction in the recruitment of talin, no longer necessary (Yao et al., 2014b; Goult et al., 2018).

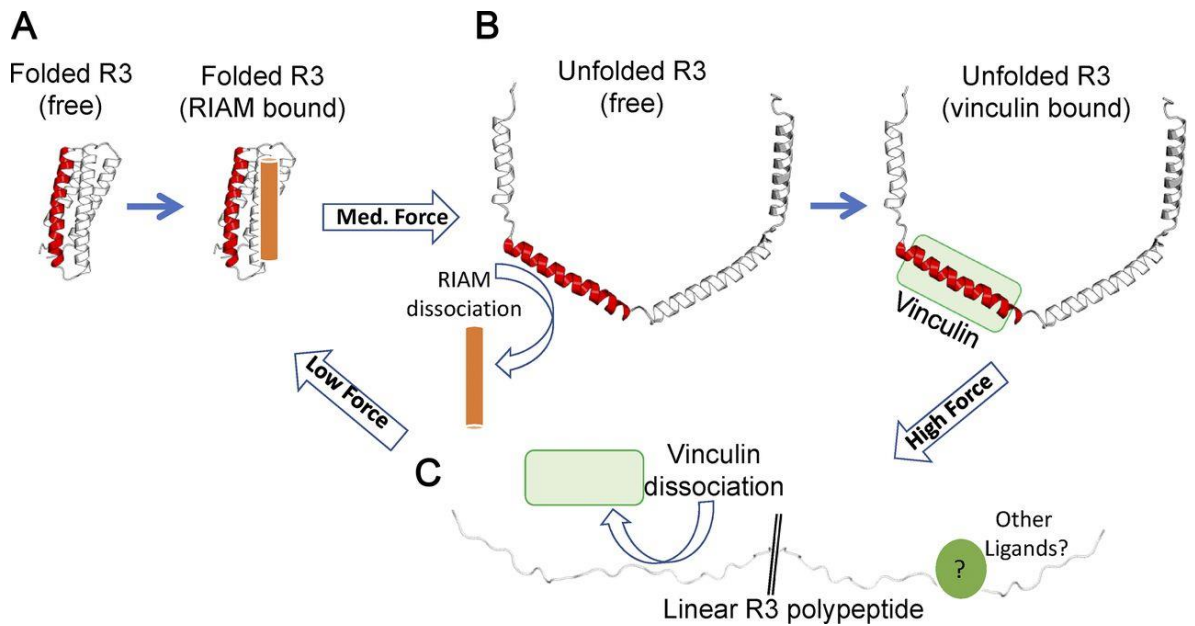


Figure 2.7: **Talin rod domains as mechanical switches.** A) shows folded talin R3 bound to RIAM (orange); B) as force is exerted on talin R3 the bundle unfolds revealing cryptic vinculin binding site (red) and dissociating from RIAM; C) as force increases the helices unfurl leading to vinculin dissociation. Figure taken from (Goult et al., 2018).

### 2.3.4 Talin actin binding

Talin contains three actin-binding sites, ABS1 in the head region consisting of F2 and F3, and ABS2 and ABS3 located on the talin rod (Hemmings et al., 1996; Atherton et al., 2015; Kumar et al., 2016; Lee et al., 2004). These actin-binding sites have a positively charged surface at physiological pH enabling electrostatic interactions with the negatively charged actin.

The C-terminus ABS3 is essential for adhesion assembly. The current model suggests initial engagement of actin to ABS3 enables force transmission across the whole rod necessary for the unfolding of vital vinculin binding sites in R3 (Yao et al., 2014b). Once R3 has unfolded and is bound to vinculin, ABS2 is activated locking talin in a high tension bearing connection, leading to FA maturation (Atherton et al., 2015; Klapholz and Brown, 2017; Kumar et al., 2016).

### 2.3.5 Leucine-Aspartic acid motif binding

LD-motif interactions are prevalent interactions in and around focal adhesions first identified in paxillin (Alam et al., 2014; Brown et al., 1996). LD-motifs are named due to their consensus sequence (LDxLLxxL) (Brown et al., 1996). They bind to helical bundles through a helix addition

mechanism in which the LD-motif forms an amphipathic  $\alpha$ -helix orientated by a salt bridge formed between the aspartate in position 2 to an adjacent helix in the binding site, the  $\alpha$ -helix then packs tightly against the domain (Zacharchenko et al., 2016b; Hoellerer et al., 2003).

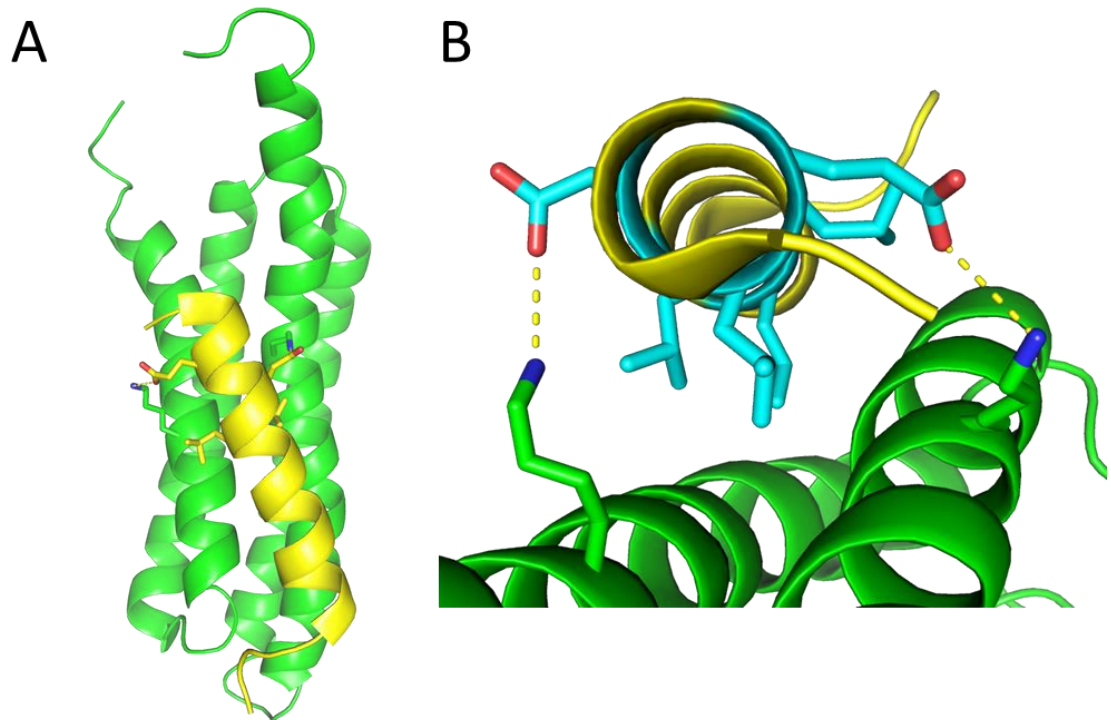


*Figure 2.8: LD motif binding. A) Atomic structure of paxillin LD2 (yellow) bound to FAK-FAT domain (green) (pdb: 2L6F) as an example of LD-motif binding by helix addition. B) View down the  $\alpha$ -helix of LD motif showing consensus residues (cyan) and the orientating salt bridges that orientate the LD-motif binding.*

### 2.3.6 Talin rod interactions

The function of talin as an integrin-associated adapted protein can be defined by the interactions with integrin, actin and vinculin; however, there is an ever-increasing number of additional ligands that contribute to talin being a mechanosensitive signalling hub (Goult et al., 2018). Talin has been shown to bind a series of proteins through a helix addition mechanism, whereby an  $\alpha$ -helix from the ligand packs against the side of a helical bundle domain in the talin rod. A number of these ligands contain an 'LD' motif that enables this to occur (Alam et al., 2014). This mode of binding has been demonstrated in interactions with deleted in liver cancer 1 (DLC1), a RhoGAP and tumour suppressor (Zacharchenko et al., 2016b); Rap1-GTP-interacting adapter molecule (RIAM) (Goult et al., 2013b; Chang et al., 2014); and kidney ankyrin repeat containing (KANK)

protein, linking talin to the cortical microtubule stabilising complex (Bouchet et al., 2016). Talin has also been demonstrated to be linked with alpha-synemin, an intermediate filament protein expressed in skeletal muscle (Sun et al., 2008). Together with the KANK and actin interactions, this places talin as a coordinator of actin, microtubule and intermediate filaments altogether. Furthermore, it has been demonstrated that a direct interaction between the C-terminus of the talin rod and the FERM domain of moesin is required to recruit the sodium/hydrogen exchanger (NHE-1) to adhesion sites (Beatty et al., 2014). Directly linking talin to alterations in the local intracellular environment, this has the potential for greater regulation on adhesion dynamics.

### 2.3.7 Talin head interactions

The talin head harbours binding sites for multiple proteins, the most important of which is the integrin binding site located on the F3 domain (Anthis et al., 2009; Bouaouina et al., 2008; Calderwood et al., 1999; Wegener et al., 2007). In addition, essential contacts between basic residues in the talin head F1-F3 domains and Phosphatidylinositol 4,5-bisphosphate (PIP2) are necessary for talin head orientation and membrane anchoring (Elliott et al., 2010; Goult et al., 2010a; Legate et al., 2011; Raucher et al., 2000; Saltel et al., 2009). Moreover, the talin head has two binding sites for the membrane bound small GTPase Rap1, in F0 and F1, with essential roles in integrin activation (Gingras et al., 2019; Goult et al., 2010a; Han et al., 2006; Lagarrigue et al., 2018; Bromberger et al., 2019). In addition to essential contacts with integrin, PIP2 and Rap1, the talin head has been linked with multiple other ligands. Specifically the talin F3 demonstrates extraordinary plasticity interacting with PIP kinase gamma (Pereda et al., 2005), layilin (Wegener et al., 2008), FAK (Lawson et al., 2012), RIAM (Yang et al., 2014) and G-protein subunit G $\alpha$ 13 (Schiemer et al., 2016) all on the same binding site; in exactly what order and the effect they have on integrin binding is not fully understood. The head also contains one of three talin actin binding sites (ABS1) between F2 and F3; with a recently revealed role in capping actin filaments (Ciobanasu et al., 2018; Lee et al., 2004).

## 2.4 Kindlins

Kindlins, like talin, are cell-matrix adhesion adapter proteins, with important functions in integrin activation and adhesion dynamics.

### 2.4.1 Isoforms

The kindlin family consists of three evolutionary conserved proteins, kindlin-1, -2 and -3, aptly named after a rare congenital disease - Kindler syndrome – which results from mutations in the kindin-1 gene (Jobard et al., 2003; Siegel et al., 2003). Kindlin-1 and -2 share a high sequence identity as they diverged from kindlin-3 during evolution (Siegel et al., 2003).

Kindlin-1 is predominantly expressed in epithelial cells, including keratinocytes and intestinal epithelial cells. Conversely, kindlin-2 is ubiquitously expressed and kindlin-3 expression is restricted to the hematopoietic system (Meves et al., 2009; Ussar et al., 2006). This profound difference in tissue expression indicates kindlins acquired specific roles during evolution.

### 2.4.2 Structure

The kindlin family are all FERM-domain containing proteins. Compared to typical FERM domains that consist of three lobes, kindlins contain four lobes like talin (Goult et al., 2009b). Similarly to talin, kindlin F0 and F1 form ubiquitin-like folds with a loop present in F1, and F3 consists of an integrin binding PTB fold. However, unlike talin they are arranged in a typical cloverleaf-like structure (Li et al., 2017a). Moreover, they also differ from talins as the kindlin F2 domain contains an inserted pleckstrin homology domain (PH domain) consisting of around 131aa (Liu et al., 2011). The PH-domain is necessary for recruitment to the cell membrane through direct interactions with multiple phosphoinositides, especially phosphatidylinositol (3,4,5)-trisphosphate (PIP3) and phosphatidylinositol (4,5)-bisphosphate (PIP2) (Qu et al., 2011). It is possible that kindlins may form homo-dimers, albeit this was shown with a kindlin-2 missing the PH-domain and had very slow dynamics (Li et al., 2017a).

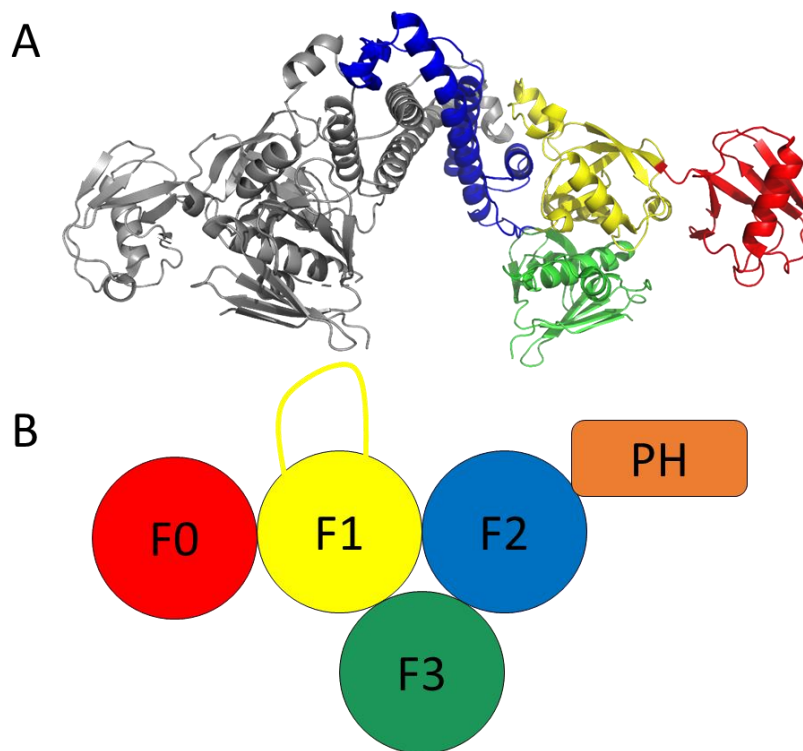


Figure 2.9: **Structure of Kindlin.** A) crystal structure of kindlin-2 dimer bound to integrin (5XQ0) (Li et al., 2017a) coloured by domain (F0 red, F1 yellow, F2 blue, F3 green); B) schematic diagram representing the domain structure of kindlins.

### 2.4.3 Interactions within the adhesome

Like talin, kindlins have an essential role in integrin activation and adhesion dynamics through multiple interactions. The most important of which is a direct interaction between the kindlin F3 domain and the membrane distal NxxY motif of  $\beta$ -integrin tail that is necessary for integrin activation (Bledzka et al., 2012). Additionally, Kindlin-2 has been demonstrated to directly interact with the integrin linked kinase (ILK) through the F2 domain (Fukuda et al., 2014). This interaction links kindlin-2 to the ILK-PINCH-parvin complex, and the actin cytoskeleton. Kindlin-2 is also involved in paxillin recruitment to sites of adhesions through an interaction with the paxillin-LIM3 domain (Theodosiou et al., 2016). The kindlin interaction with paxillin has been linked with an interaction with the ARP2/3 complex, promoting FAK-mediated cell spreading, and RAC1-mediated membrane protrusions (Böttcher et al., 2017).

#### 2.4.4 Disease

A significant hallmark of kindlins is their role in disease (Rognoni et al., 2016). The most apparent of which is Kindler syndrome, first described by Theresa Kindler in 1954. Kindler syndrome is a subtype of bullous skin disease that is characterised by skin blistering, hyperkeratosis, skin atrophy, photosensitivity and poikiloderma in sun-exposed areas (Kindler, 1954). The disease is caused from mutations in the *FERMT-1* (kindlin-1) gene that leads to loss of expression of functional kindlin-1 in epithelial tissues (Kloeker et al., 2004; Jobard et al., 2003; Has et al., 2011). Additionally, kindlin-1 has been implicated in cancer, with *FERMT-1* mRNA upregulated in most lung, breast and colon cancers. It appears to intervene in TGF $\beta$  signalling leading to constitutively active cell motility and invasion (Sin et al., 2011).

Due to kindlin-2 ubiquitous expression, loss of the protein leads to peri-implantation lethality in mice (Dowling et al., 2008). However, dysregulation of kindlin-2 expression has been observed in multiple diseases such as tubular intestinal fibrosis of the kidney (Bielesz et al., 2010). Like kindlin-1, upregulation of kindlin-2 has also been implemented in a series of cancers, increasing invasiveness, metastasis and poor disease outcome (Mahawithitwong et al., 2013; An et al., 2010; Talaat et al., 2011).

Kindlin-3 is highly expressed in hematopoietic cells (Ussar et al., 2006). Kindlin-3 deficient mice die shortly after birth, suffering from severe haemorrhages, anaemia, leucocytosis and loss of hematopoietic stem cells (Moser et al., 2008; Ruppert et al., 2015). These symptoms are all hallmarks of leukocyte adhesion deficiency type III (LAD III), which is caused by the loss of kindlin-3 expression (Kuijpers et al., 2009; Svensson et al., 2009; Mory et al., 2008). This disease is primarily caused by loss of integrin function.

#### 2.5 Integrin activation

Integrin receptors act as bidirectional signalling molecules, having two conventional methods of activation. One is inside-out activation, by this mechanism the ectodomain of integrin adopts the



extended high affinity state for the ECM via signalling from cytoplasmic domain, most commonly associated with talin-mediated integrin activation (Ginsberg, 2014). The alternative mechanism is outside-in activation, whereby ECM ligand binding to the integrin extracellular head domain leads to a partial extension of the integrin ectodomain, separating the integrin tails and stimulating the adhesion machinery formation on the intracellular face (Mehrbod et al., 2013). In this thesis I will focus on inside-out integrin activation.

### 2.5.1 Integrin activation states

The current model suggests integrin goes through three affinity states in the conventional inside-out activation process. In the lowest energy-state, integrins are in an inactive bent-closed conformation in-which the transmembrane domains closely associate and the cytoplasmic tails are clasped. In this conformation, integrins have low affinity for their ligand (Li and Springer, 2018). The second state is the extended closed state. This is induced by talin and kindlin binding to the  $\beta$ -integrin tail; this disrupts the transmembrane association reorienting the integrin ectodomain into an extended conformation. Once in the extended closed, integrin shifts to the extended open conformation because of the slightly lower free energy state; in this state integrin has a ligand-binding affinity 5000-fold higher than the bent closed conformation or extended closed conformation (Li et al., 2017b; Li and Springer, 2018) (fig. 2.10).

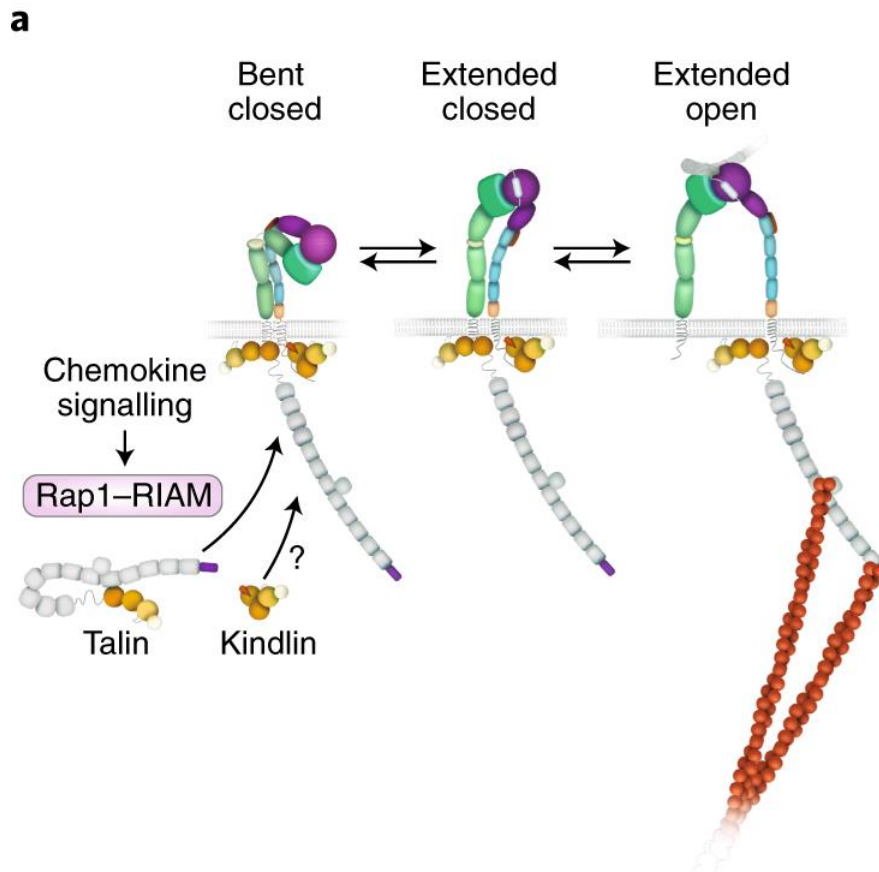


Figure 2.10: **Integrin activation states.** Schematic describing the events of inside-out integrin activation. Talin and kindlin are recruited to the integrin tails via RAP1 and RIAM; talin and kindlin bind to the beta integrin tail separating the tails and leading to the extension of the integrin ectodomains into the extended closed conformation; talin binds links actin to integrin and the ECM, force transmission across this axis leads to integrin adapting the extended open conformation. Adapted from (Sun et al., 2019)

### 2.5.2 Kindlin and talin mediated integrin activation

Integrin activation has major consequences on cell shape, proliferation and motility, therefore this crucial step has to be tightly regulated. There is a complex system of proteins and signalling molecules which can regulate integrin activity, so called the 'integrin adhesome' (Horton et al., 2015). However, at the core of this complex network is a simple interaction between the  $\beta$ -integrin tail, talin and kindlin. Biochemical (Calderwood et al., 1999) and structural studies (Anthis et al., 2009; Wegener et al., 2008) have elucidated an interaction between talin F3 domain and the membrane proximal NPXY motif in  $\beta$ -integrin tails that is necessary for inside-out integrin activation (Ye et al., 2010). Later it was demonstrated that talin was not capable of activating integrin alone, requiring kindlin as a co-activator (Meves et al., 2009; Calderwood et al., 2013; Theodosiou et al., 2016). Kindlins like talin bind to the  $\beta$ -integrin tail through an interaction with

the kindlin F3 domain; however, they exclusively bind to the membrane distal NxxY motif (Li et al., 2017a; Bledzka et al., 2012).

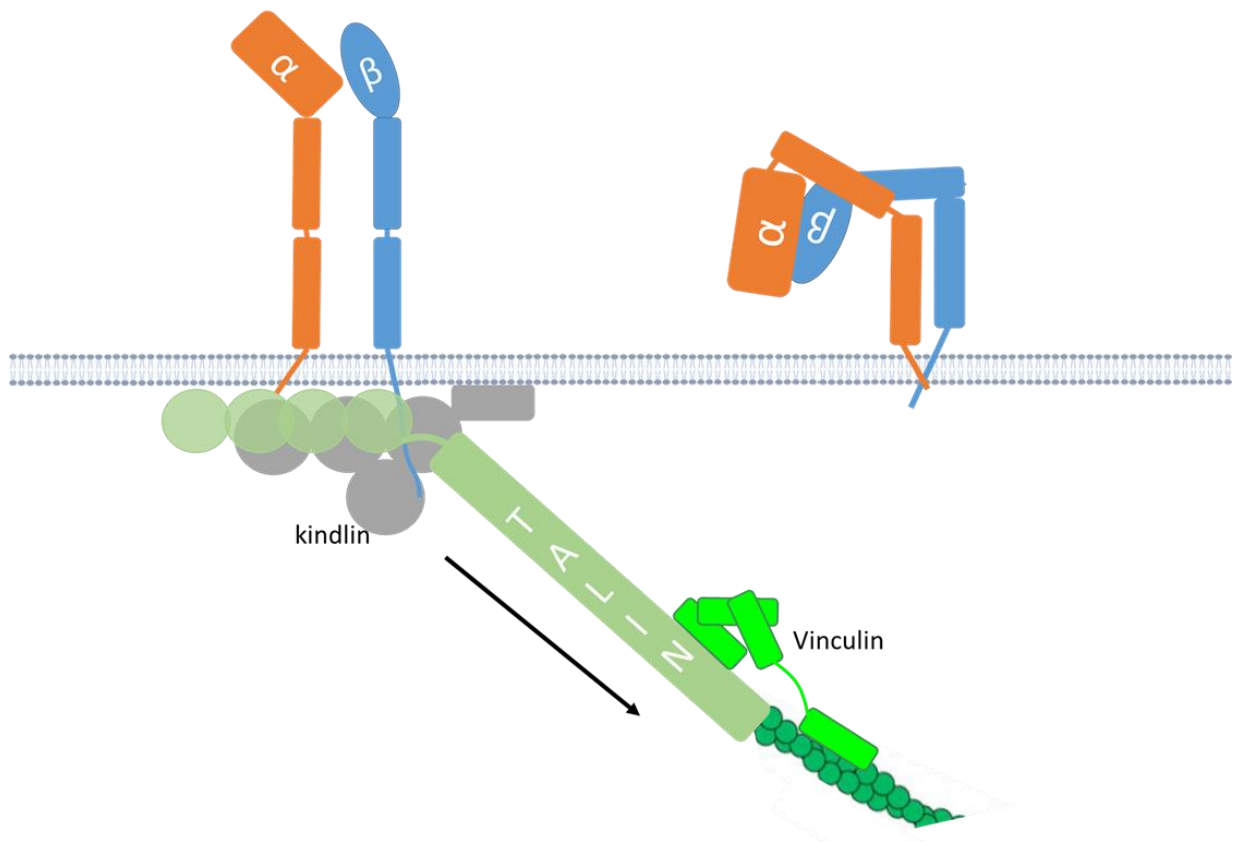


Figure 2.11: **Talin and kindlin activate integrin.** Schematic demonstrating talin and kindlin F3 domains binding to the  $\beta$ -integrin tail to activate integrin.

As to how kindlin and talin cooperative binding activates integrin is up for much debate (Theodosiou et al., 2016; Bachir et al., 2014; Sun et al., 2019; Calderwood et al., 2013). Structural studies indicate talin binding to integrin disrupts the transmembrane helix association in the bent-closed conformation. The  $\beta$ -TM is usually tilted and  $\alpha$ -TM perpendicular to the membrane in the bent-closed conformation; binding of talin to the  $\beta$ -tail extends the TM helix and rotates the complex; this increases the tilt and separates the  $\alpha$ - and  $\beta$ - TM regions, thereby opening the conformation (Anthis et al., 2009; Kalli et al., 2010, 2011; Lau et al., 2009) (fig. 2.12).

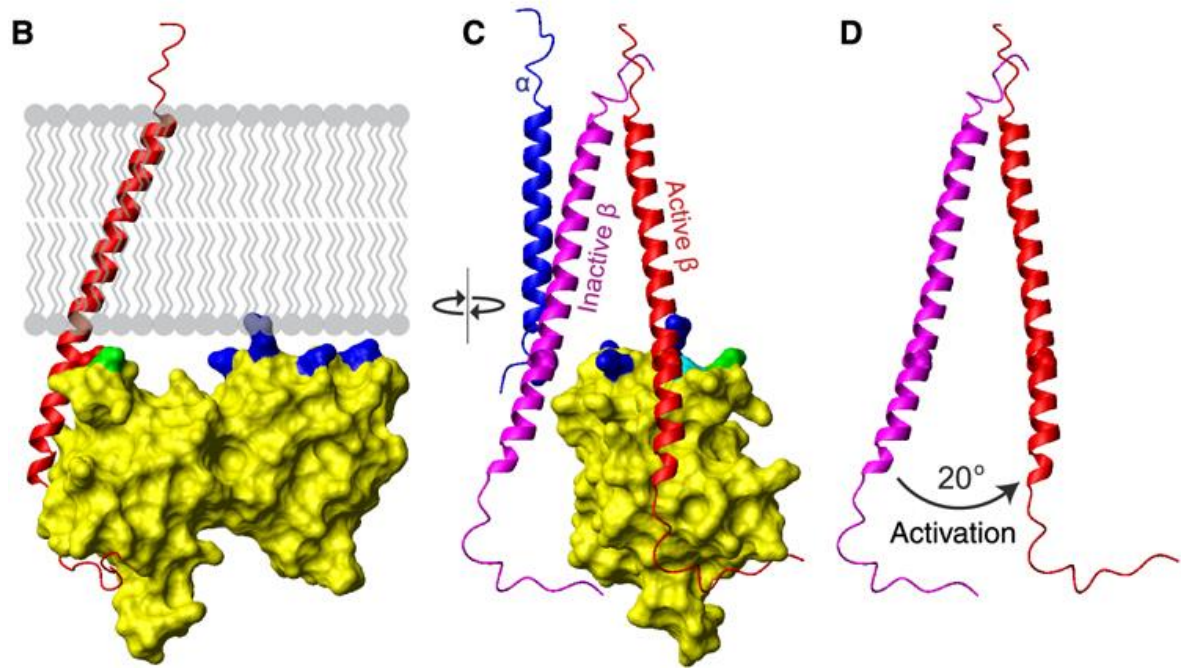


Figure 2.12: **Disruption of the  $\alpha/\beta$  integrin dimer by talin.** Binding of talin F3 (yellow) to the  $\beta$ -tail (magenta/red) induces a twist and tilt that disrupts the  $\alpha/\beta$  dimer, thereby separating the tails and leading to the activation state. Adapted from (Anthis et al., 2009).

### 2.5.3 Talin recruitment in integrin activation

An important regulatory step in integrin activation is the recruitment of talin from the cytosol to sites of integrin adhesions. Recruitment of talin could be through a number of mechanisms (Klapholz and Brown, 2017). One of the best studied pathways is talin recruitment through the Rap1 effector protein RIAM and other members of the MRL (Mig-10/RIAM/Lamellipodin) family of proteins (Lee et al., 2009). RIAM has two LD-motifs in the N-terminus which have been demonstrated to bind to the talin rod (Yang et al., 2014; Chang et al., 2014; Goult et al., 2013b). Rap1 is activated by protein kinase C, this leads to the recruitment of RIAM to the membrane via the Ras association (RA) domain (Lafuente et al., 2004). During recruitment to activated Rap1, RIAM acts as a scaffold pulling talin with it to the sites of adhesion.

## 2.6 Vinculin

Vinculin is an important adhesion complex scaffolding protein involved in cell-matrix and cell-cell junctions. Vinculin has essential roles in adhesion maturation (Humphries et al., 2007),

mechanosensing (Plotnikov et al., 2012; Yao et al., 2014a), regulation of actin dynamics (Thievensen et al., 2013) and cell proliferation (Subauste et al., 2004).

### 2.6.1 Structure

Vinculin is a 117 kDa protein consisting of a large globular head attached to a tail region. The head comprises of three tandem pairs of 4-helix bundles termed 'vinculin/ $\alpha$ -catenin repeats' (Vd1-3) and an additional 4-helix bundle (Vd4). The vinculin head is attached via a proline-rich linker to the C-terminal tail region (Vt) that resembles a 5 helix bundle. The vinculin head forms a 'pincer'-like structure which holds the vinculin tail, maintaining vinculin in an autoinhibited state (Bakolitsa et al., 2004). The high affinity interaction between the vinculin head and tail domains obscures ligand binding sites on the proline-rich linker region as well as F-actin and PIP2 on the Vt (Ziegler et al., 2006). To relieve the autoinhibited conformation, vinculin activation requires simultaneous binding of both F-actin to the Vt and talin (or likewise) VBS to Vd1 (Chen et al., 2006).

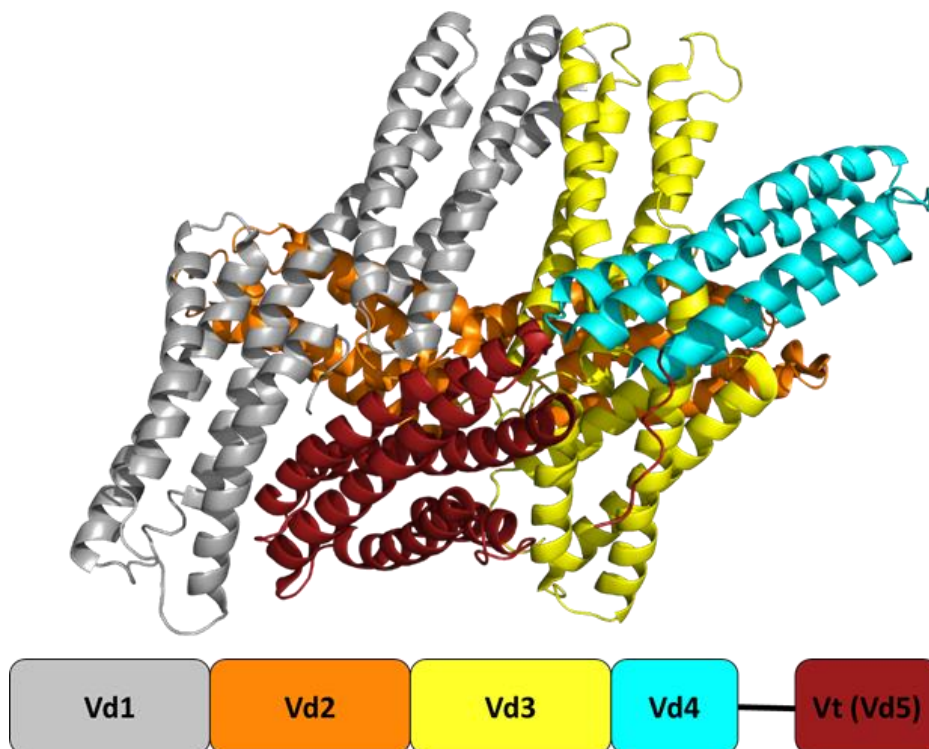


Figure 2.13. **Structure of vinculin.** Crystal structure of vinculin in the autoinhibited conformation (pdb: 1TR2); coloured by domain as indicated in the schematic diagram (bottom).

### 2.6.2 Interactions within the adhesome

Vinculin has many essential roles in both integrin and cadherin mediated adhesions, this multitude of roles is regulated through multiple distinct binding partners. Indeed, it has been demonstrated vinculin can interact with 19 binding partners (fig. 2.14) (Carisey and Ballestrem, 2011).

Vinculin is critical in mediating the link between the adhesion molecules integrin and cadherin and the actin cytoskeleton. This is achieved through force dependent interactions between the VBS found in the scaffolding proteins talin (Burrige et al. 1984),  $\alpha$ -actinin (Bois et al., 2006a) and  $\alpha/\beta$ -catenin (Rangarajan and Izard, 2012), and Vd1. The scaffold protein bound vinculin then reinforces the interactions with the actin cytoskeleton by itself binding to actin through the Vt region (Hüttelmaier et al., 1997; Janssen et al., 2006).

Activated vinculin also regulates actin dynamics through interactions between the proline rich region and SH3 domains found on potent actin regulators, ARP2/3 complex - an actin nucleator with a unique ability to organise actin filaments into branched networks (DeMali et al., 2002), VASP – an actin polymerisation promotor (Reinhard et al., 1992), and members of the vinexin family – a family of actin regulators with roles in capping the actin cytoskeleton (Mandai et al., 1999; Kawabe et al., 1999; Kioka et al., 1999).

In addition to the roles already stipulated, vinculin has also been demonstrated to bind with paxillin, an important interaction for recruitment of the two proteins to FAs (Wood et al., 1994). Furthermore, vinculin appears to be involved in mRNA processing through an interaction with the splicing mediator raver1 (Hüttelmaier et al., 2001).

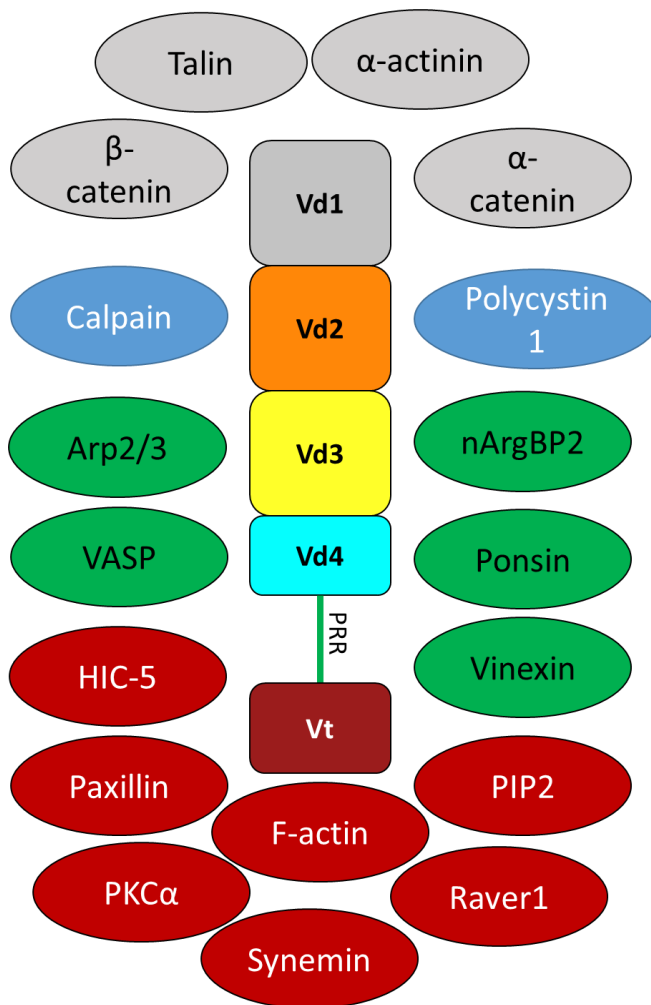


Figure 2.14: **Interactions of vinculin.** Schematic showing previously reported vinculin binders at adhesion sites, coloured by region of vinculin in which they bind, grey = Vd1; green = proline rich region; red = vinculin tail; blue = unknown.

## 2.7 Additional core adhesome proteins

### 2.7.1 Rap1

Rap1 is a member of the Ras associated small GTPase superfamily consisting of two homologs Rap1a and Rap1b. Rap1 is best known for its function as an integrin activator (Boettner and Van Aelst, 2009). Currently, this process is thought to be regulated via its interactions with RIAM (Lee et al., 2009); however, it has also been demonstrated to weakly interact with the talin FERM domains F0 and F1 suggesting a possibility for coordination of talin at the cell membrane (Goult et al., 2010a; Zhu et al., 2017; Gingras et al., 2019; Bromberger et al., 2019) (see section 6.5).

### 2.7.2 Paxillin

Paxillin is an important scaffolding protein in focal adhesions, recruiting both structural and signalling proteins. Paxillin is a 65 kDa protein consisting of five N-terminus LD motifs (LD1 to LD5) containing the consensus (LDxLLxxLL). The LD motifs have been identified as sites for FAK, talin and vinculin binding (Thomas et al., 1999; Vanarotti et al., 2016; Hoellerer et al., 2003; Zacharchenko et al., 2016b). Additionally paxillin contains four LIM-domains at the C-terminus that have an important role in protein:protein interactions anchoring paxillin at the cell membrane (Brown et al., 1996). Paxillin also contains a proline-rich sequence enabling binding of SH3-containing proteins and numerous serine and tyrosine residues for SH2 domain binding (Schaller, 2001). Together, paxillin is a large docking molecule tightly regulated by multiple phosphorylation sites (López-Colomé et al., 2017; Webb et al., 2005).

### 2.7.3 Focal Adhesion Kinase

FAK is a protein tyrosine kinase that plays an essential role in regulation of focal adhesions. FAK is a ubiquitously expressed and highly conserved protein vital for normal tissue development (Schaller, 2010). FAK is a 110 kDa protein consisting of an N-terminus FERM domain, a central catalytic tyrosine kinase domain and a C-terminus focal adhesion targeting domain (FAT). The FERM domain complexes with the catalytic domain to autoinhibit FAK kinase activity. The FAT domain is an LD-motif binding domain essential for FAK localisation and downstream signalling.

## 2.8 Objectives of work

Integrin-mediated adhesions are essential biological structures involved in tissue development, wound repair, cell shape and cell migration. These structures are formed of a complex web of proteins and signalling molecules that form a bidirectional signalling platform between the cell and its environment. The complex nature of integrin-mediated adhesions allows them to form diverse structures with multiple different roles. The formation and maturation of integrin-



mediated adhesions occur through integrin receptor activation and force transmission. However, whilst our knowledge of the many mechanisms by which integrin activation and force transmission is quickly improving, there is still much to be learnt.

In this thesis I will be focusing on interactions between the essential cell-matrix adhesion proteins: integrin, talin, kindlin, and vinculin. Using a combination of biochemical and structural techniques and in collaboration with other research groups, we sought to provide insight into the intricacies of known and novel mechanisms involved in the initial stages of adhesion formation.

The aims of the thesis were as follows:

1. To develop new biochemical assays to study the interactions that occur at integrin mediated adhesions, which are otherwise difficult/not possible to study. (i) The first method was a microscale thermophoresis (MST) assay that could provide quantitative information on interactions that were previously not measurable using more conventional biochemical assays, due to limitations on size and protein expression.  
(ii) Integrin-mediated adhesion complexes form at the cell membrane, to further understand the influence of the membrane on adhesion formation we wanted to develop a relatively accessible high throughput assay to investigate the role of lipid environment on protein-integrin cytoplasmic tail interactions. An important factor in this experiment design was to bypass the need for transmembrane domains to attach ligands to the membrane. To this purpose we developed a peptide-conjugated lipid co-sedimentation assay.
2. Using the biochemical suite from Aim 1 we wanted to elucidate the mechanisms that may regulate the integrin activating ability of the talin head. First, we investigated talin autoinhibition as a primary way of inhibiting talin head activity by characterising a mutant which leads to constitutively active talin. Next, following determining the atomic structure of the talin-2 head we investigated how the conformational plasticity of the talin head

may regulate integrin adhesions, and avenues which may control the conformation.

Finally, we investigated a direct interaction between kindlin and talin, to further understand how kindlin may assist/control talin-mediated integrin activation.

3. In the 3<sup>rd</sup> aim we investigated the role of the  $\alpha$ -integrin tail in talin-mediated integrin activation by following up on two reports from the mid-90s that identified a direct interaction between talin and the  $\alpha$ -integrin tail (Knezevic et al., 1996; Pavalko and Otey, 1994). Using a biochemical and structural approach we confirmed and characterised an interaction between talin and  $\alpha$ -tail, which may provide a new insight into talin-mediated integrin activation.
4. The final aim of my thesis was to improve our understanding of the interactions between talin and vinculin. We were first interested in understanding how the talin-vinculin interaction can determine nascent adhesion maturation, by investigating the possibility of a talin-vinculin pre-complex. Following this, we were keen to understand how pathogens can hijack the talin-vinculin interaction to aid infection, specifically investigating the Chlamydial virulence factor TarP.

## Chapter 3: Methods

### 3.1 Materials

#### 3.1.1 Buffers

Table 3.1: *Buffer table*

Buffer	Components
<b>Ni buffer A</b>	500 mM NaCl, 20 mM Imidazole, 20 mM Tris pH 8
<b>Ni buffer B</b>	500 mM NaCl, 1 M Imidazole, 20 mM Tris pH 8
<b>Q buffer A</b>	50 mM NaCl, 20 mM Tris pH 8
<b>Q buffer B</b>	1 M NaCl 20 mM Tris pH 8
<b>S buffer A</b>	50 mM NaCl, 20 mM Phosphate buffer (NaH <sub>2</sub> PO <sub>4</sub> , Na <sub>2</sub> HPO <sub>4</sub> ) pH 6.5
<b>S buffer B</b>	1M NaCl, 20 mM Phosphate buffer (NaH <sub>2</sub> PO <sub>4</sub> , Na <sub>2</sub> HPO <sub>4</sub> ) pH 6.5
<b>NMR Buffer</b>	50 mM NaCl, 20 mM Phosphate buffer (NaH <sub>2</sub> PO <sub>4</sub> , Na <sub>2</sub> HPO <sub>4</sub> ) pH 6.5, 2 mM DTT
<b>PBS</b>	137 mM NaCl, 2.7 mM KCl, 8 mM Na <sub>2</sub> HPO <sub>4</sub> , and 2 mM KH <sub>2</sub> PO <sub>4</sub> pH 7.4
<b>NMR Solution A</b>	12.5 g Na <sub>2</sub> HPO <sub>4</sub> (88 mM) , 7.5 g KH <sub>2</sub> PO <sub>4</sub> (55 mM) Make to 1 L
<b>NMR Solution B</b>	4.0 g D-glucose, 10.0 mL H <sub>2</sub> O, 10.0 mL BME Vitamins, 2.0 mL MgSO <sub>4</sub> (1 M), 0.1 mL CaCl <sub>2</sub> (1 M), 1.0 mL Antibiotic (1000x), 1.0 g <sup>15</sup> NH <sub>4</sub> Cl (for 1 L culture)

<b>SDS running buffer</b>	50 mM MOPS, 50 mM Tris, 0.1% SDS, 1 mM EDTA, pH 7.7
<b>5x Sample Buffer</b>	0.625 M Tris, 40% Glycerol, 10% SDS, 10% $\beta$ -mercaptoethanol, 0.005% Bromophenol Blue
<b>Lipid buffer</b>	20 mM HEPES pH 7.4, 0.2 mM EGTA
<b>MLV pull down buffer</b>	20 mM Tris pH 7.4, 0.1 mM EDTA, 15 mM $\beta$ -mercaptoethanol

### 3.1.2 Plasmids

Table 3.2: *Plasmid table*

Protein	Plasmid Vector	Resistance	Gene	Species	Domain/s	Residues	Source
Talin1_R7R8	pET151TOPO	ampicillin	TLN1	mouse	R7-R8	1357-1659	Dr. Ben Goult
Talin1_R11R12	pET151TOPO	ampicillin	TLN1	mouse	R12-R13	2137-2294	Dr. Ben Goult
Talin1_R9R10	pET151TOPO	ampicillin	TLN1	mouse	R9-R10	1655-1973	Dr. Ben Goult
Talin1_F2F3	pET151TOPO	ampicillin	TLN1	mouse	F2-F3	196-405	Dr. Ben Goult
Talin1_head	pET151TOPO	ampicillin	TLN1	mouse	F0-F3	1-405	Dr. Ben Goult
Talin2_head	pET151TOPO	ampicillin	TLN2	mouse	F0-F3	1-403	GeneArt
Talin1_F3	pET151TOPO	ampicillin	TLN1	mouse	F3	308-400	Dr. Ben Goult
Talin1_F0-F2	pET151TOPO	ampicillin	TLN1	mouse	F0-F2	1-309	Dr. Ben Goult
Talin1_F1	pET151TOPO	ampicillin	TLN1	mouse	F1	86-202	Dr. Ben Goult
Talin1_F1_loop_deletion	pET151TOPO	ampicillin	TLN1	mouse	F1	86-202 ( $\Delta$ 139-168)	Dr. Ben Goult

Talin1_head_loop_deletion	pET151TOPO	ampicillin	TLN1	mouse	F0-F3	1-405 ( $\Delta$ 139-168)	Dr. Ben Goult
Talin1_head_phosphomimetic	pET151TOPO	ampicillin	TLN1	mouse	F0-F3	1-405 (T144E, T150E)	Dr. Ben Goult
Talin1_F1_phosphomimetic	pET151TOPO	ampicillin	TLN1	mouse	F1	86-202 (T144E, T150E)	Dr. Ben Goult
Talin1_F0	pET151TOPO	ampicillin	TLN1	mouse	F0	1-85	Dr. Ben Goult
FL_talin1	pEt21a	ampicillin	TLN1	mouse	F0-DD	1-2541	Dr. Ben Goult
FL_talin1_autoinhibitor	pEt21a	ampicillin	TLN1	mouse	F0-DD	1-2542 (E1770A)	Dr. Ben Goult
FL_kindlin1	pET151TOPO	ampicillin	FERMT 1	mouse	F0-F3	1-677	Dr. Ben Goult
FL_kindlin1_kindler	pET151TOPO	ampicillin	FERMT 1	mouse	F0-F3	1-678 ( $\Delta$ 623-625)	Prof. Maddy Parsons
Kindlin_F0F1	pET151TOPO	ampicillin	FERMT 1	mouse	F0-F1	1-275	Dr. Ben Goult
Vinculin_Vd1	pET151TOPO	ampicillin	VCL	mouse	Vd1	1-258	Dr. Ben Goult
FAK_FAT	pOPINB	kanamycin	PTK2	mouse	FAT	902-1050	Dr. Igor Barsukov
Rap1b	pTAC	kanamycin + ampicillin	Rap1b	mouse	G-domain	1-166	Dr. Igor Barsukov
Talin_F2F3_β3	pET151TOPO	Ampicillin	TLN1/ ITGB3	Mouse/ chicken	F2-F3	196-405 + 765-775	Dr. Ben Goult

### 3.1.3 Peptides

Table 3.3: *Peptide table*

Peptide	Protein	Gene	Species	Residues
α2-tail_short	Integrin	ITGA2	human	C-1154-1173
α2-tail	Integrin	ITGA2	human	C-1154-1181
β1a-tail	Integrin	ITGB1	human	C-752-798

TarP_VBS1	TarP	TARP	C. caviae	850-868-C
TarP_VBS3	TarP	TARP	C. caviae	745-769-C
TarP_LD	TarP	TARP	C. caviae	655-680-C
Pax_LD1	paxillin	PXN	mouse	3-22-C
Pax_LD2	paxillin	PXN	mouse	C-141-153
Pax_LD4	paxillin	PXN	mouse	C-262-274
mTalin_VBS33	talin 1	TLN1	mouse	C-1512-1546
mTalin_VBS36	talin 1	TLN1	mouse	C-1622-1656
RIAM_TBS1	RIAM	APBB1IP	mouse	4-30-C
KANK1_KN	KANK1	KANK1	human	30-60-C
EGFR_CD	EGFR	EGFR	human	C-668-711

## 3.2 Recombinant Protein Expression

### 3.2.1 Expression in E.coli

All proteins were expressed in E.coli BL21(DE3) unless stated otherwise. Plasmids containing the recombinant protein gene of interest and ampicillin resistance, were transformed into chemically competent cells, then spread onto LB agar plates containing 100 µg/mL ampicillin for selection then incubated overnight at 37°C. A single colony was picked and transferred to a 10 mL starter culture of LB broth containing 100 µg/mL ampicillin. The starter culture was incubated at 37°C in a shaking incubator overnight. 4 mL of starter culture was added to a 1 l volume of LB broth supplemented with 100 µg/mL ampicillin and incubated at 37°C in a shaking incubator. Cultures were grown to an OD600 of 0.5-0.8 then cooled to 18°C and inoculated with 100 µg/mL IPTG to induce protein production, then incubated at 18°C overnight unless stated otherwise. The cells were pelleted at 4200 rpm for 20 minutes, resuspended in Ni buffer A and frozen at -20°C.

### 3.2.2 Protein Purification

Cell pellets were defrosted then lysed by sonication, using 6 cycles of 20 seconds on 40 seconds off at 20,000 kHz. The resulting lysates were centrifuged at 18,000 rpm for 20 minutes to separate the soluble fraction. The soluble fraction was subjected to further purification.

### 3.2.3 Ni-affinity purification using FPLC AKTA system

Unless stated otherwise, all proteins used had a polyhistidine-tag attached to aid purification. These proteins were purified using a 5 mL HisTrap HP column (GE healthcare) connected to either an AKTastart or AKTApure900 system. The column was equilibrated with Ni buffer A. The supernatant from cell lysate was loaded onto the primed column, then washed with Ni buffer A to remove non-specific binders. Proteins were eluted from the column by titrating an increasing gradient of imidazole. The flow through from the increasing imidazole gradient was collected in fractions. Chromatograms were produced by the AKTA system measuring the A280 allowing for analysis of the elution profile. Fractions were selected based on peaks at A280 then analysed using SDS-PAGE to confirm the correct sized protein has been purified. Selected fractions were pooled together then dialysed at 4°C overnight into buffer of choice.

### 3.2.4 Ni-affinity purification by batch method

Kindlin and full length talin both give low yields of protein, making them difficult to observe at A280 on an AKTA system. Therefore they were purified on Ni-NTA beads using the batch method. Ni-NTA beads were primed in Ni buffer A then added to the supernatant from the cell lysate and incubated for 30 minutes at room temperature. The beads were then pelleted at 4000 rpm for 5 minutes. The supernatant was carefully removed and the beads resuspended in 30 mL of Ni buffer A. This process was repeated 5 times to wash off non-specific binders. The beads were then collected in a gravity column and allowed to stack. The proteins were eluted from the beads by the addition of 5 mL of Ni buffer B, 1 mL at a time, and collected in 1 mL fractions. Fractions were analysed by SDS-PAGE, selected fractions were then buffer exchanged using a desalting column into PBS.

### 3.2.5 TEV protease cleavage

Protein constructs expressed from the PET-151 plasmids had the His-tag cleaved off by TEV (Tobacco Etch Virus) nuclear-inclusion-a endopeptidase, a cysteine protease that cleaves between the Q\S of the ENLYFQ\S recognition site) unless needed for labelling in MST. Cleavage was

carried out after Ni-affinity purification, by incubation of recombinant TEV with the purified protein during the dialysis step.

### 3.2.6 Anion/Cation Exchange Chromatography

Proteins were subjected to further purification by anion/cation exchange based upon their respective isoelectric point (pI), calculated from ProtParam (Gasteiger et al., 2005). Proteins with a pI <7 were dialysed into Q buffer A then loaded onto a 5 mL HiTrap Q HP (GE healthcare) anion exchange column using an AKTA system. Proteins with a pI >7 were dialysed into S buffer A and loaded onto a 5mL HiTrap S HP (GE healthcare) cation exchange column using an AKTA system. The proteins were eluted with an increasing gradient of NaCl concentration and fractions collected. The elution was monitored using A280 and selected fractions were analysed by SDS-PAGE. Samples were then buffer exchanged by either dialysis or desalting column into the desired buffer.

### 3.2.7 Mouse Rap1 expression and purification from CK600K cells

The Rap1 construct came in a pre-transformed glycerol stock donated from Dr Igor Barsukov. Due to being in a different vector and cell type to our usual proteins, the Rap1 expression required a different expression and purification strategy.

#### *Rap1 expression in CK600K cells*

A 10 mL starter culture was prepared from a stab of the glycerol stock, this was grown overnight at 37°C in LB media containing both ampicillin and kanamycin. Cultures were treated as described previously (section 3.2.1), however after induction the cultures were left at 30°C overnight.

For <sup>15</sup>N-minimal media preparations solution B was supplemented with 100 mg of leucine, threonine and thiamine.

#### *Rap1 purification*

The Rap1 construct has no purification tag attached, therefore it was not possible to purify by Ni-NTA methods. Due to the acidic pI we first used anion exchange on a Q column to purify the



protein, as described previously (section 3.2.6). As the Q column was overloaded, the flow through was loaded again and run for an extra cycle. Following the Q column the fractions were analysed by SDS-page. Selected fractions were then run on a HiPrep 26/60 size exclusion chromatography column (GE Healthcare); 13 mL of the sample was loaded and run at a flow rate of 1.3 mL/min. Fractions of the corresponding peaks were analysed on SDS-PAGE and correct fractions collected.

The selected bands from the gel were sent for mass spectrometry to confirm the right protein has been purified. The gel pieces were treated with DTT to reduce disulphides, treated with chloroacetamide to alkylate the cysteines and then subjected to overnight cleavage with trypsin. The peptides generated were extracted and analysed by MALDI-TOF mass spec to give a peptide mass fingerprint that was used to search the Swiss-Prot database (UniProt) using the MASCOT search engine. The 15 most intense peptide masses were subject to further analysis by MS/MS and this data searched against the same database. With proteins expressed in prokaryotes the MS/MS search result typically confirms the identification from the peptide mass fingerprint.

### 3.2.8 Protein concentration estimation

The concentration of purified proteins was estimated by measuring the relative  $A_{280}$  using a NanoPhotometer N60/N50 (Implen). The molecular weight and extinction coefficient were calculated using ProtParam (Gasteiger et al., 2005). Protein concentration was calculated in mg/mL according to Beer-Lamberts Law.

### 3.2.9 SDS-PAGE gels

Samples were prepared for SDS-PAGE by boiling with 5x sample buffer at 95°C for 5 minutes. Gels were prepared in gel cassettes (Novex) with a 12% separating component and a 4% stacking component.

Table 3.3: SDS-PAGE gel content

Separating Gel - 12%		Stacking Gel - 4%	
40 % Acrylamide	7.5 mL	40 % Acrylamide	1.25 mL
Separating Gel Buffer (1 M Tris pH 8.8)	9.4 mL	Stacking Gel Buffer (0.375 M Tris pH 6.8)	4.2 mL
10% SDS	250 $\mu$ L	10% SDS	125 $\mu$ L
50% Sucrose	4 mL	Water	6 mL
Water	3.3 mL	TEMED	5 $\mu$ L
TEMED	6.25 $\mu$ L	Ammonium Persulphate	1 mL
Ammonium Persulphate	625 $\mu$ L		

### 3.3 Biochemical methods

#### 3.3.1 Circular Dichroism (CD)

Circular Dichroism is the difference in the absorption of left-handed circularly-polarised light and right handed circularly-polarised light. The difference results from circularly-polarised light rays travelling through a medium at different velocities. This phenomenon occurs when a molecule contains one or more chiral chromophores (light-absorbing groups). It is used as a powerful tool for investigating the folded nature of a protein, providing information on the secondary structure of a protein due to the ordered alignments of the polypeptide backbone (Greenfield, 2007).

Spectra were recorded using a JASCO J-715 spectropolarimeter equipped with a JASCO PTC-423S temperature control unit. Spectra were measured at 25°C with the wavelength changing from 260nm to 190nm. Denaturation profiles, followed the unfolding of  $\alpha$ -helices at 208 nm, from 20-80°C at 0.2°C intervals. 0.1 mg/mL of protein was dissolved in phosphate buffered saline (PBS). Measurements were made in a quartz cell of 0.1 cm path length.

### 3.3.2 Fluorescence Polarisation (FP)

Fluorescence polarisation is a method used to determine the affinity of a binding interaction between two molecules. This method requires a smaller molecule (peptide <10 kDa) coupled to a fluorophore. This small molecule will tumble rapidly in solution, however when bound to a larger molecule (our target protein) the tumbling will slow down. Therefore when the fluorophore is excited with polarised light, naturally it will scatter the light in all directions, but when bound to the target protein the emitted light will depolarise more slowly, resulting in increased polarised light being detected. The change in polarised light can be plotted against the target protein concentration, enabling a dissociation constant to be calculated (Moerke, 2009).

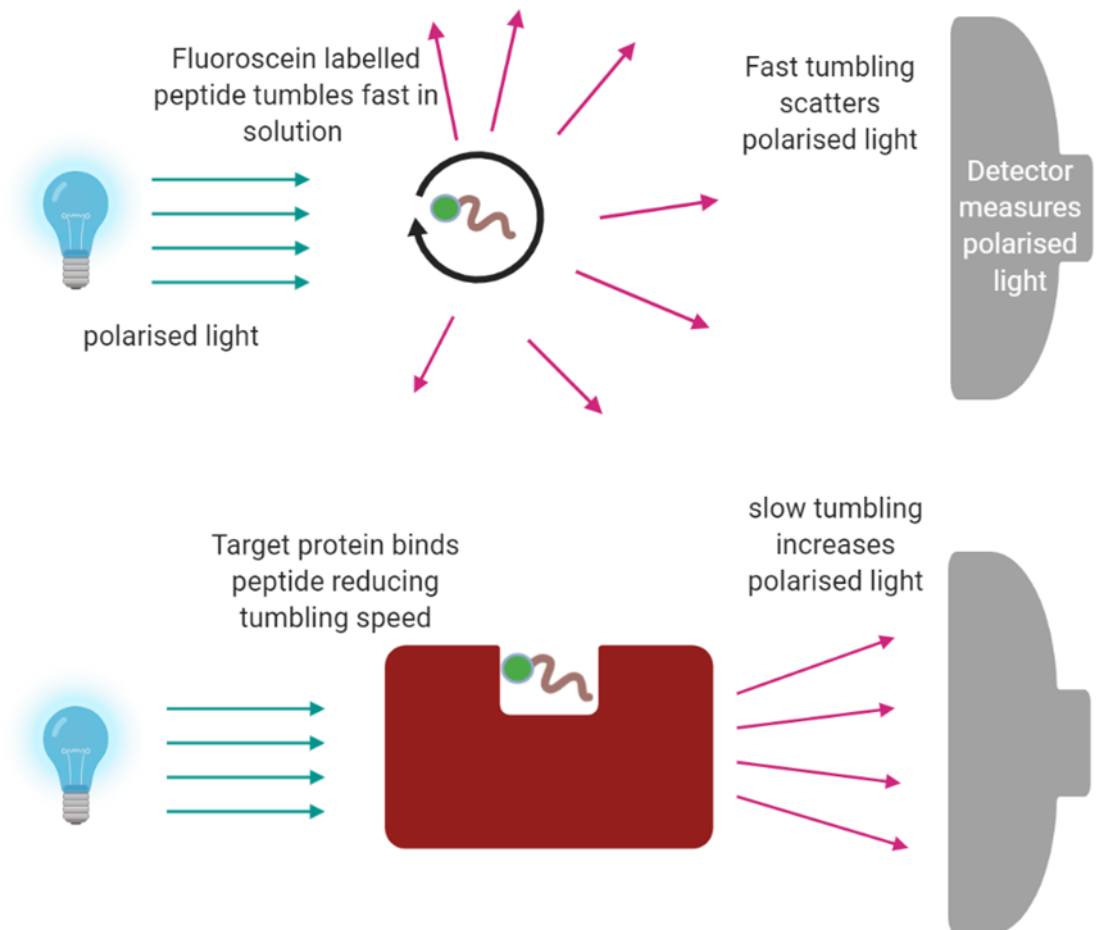


Figure 3.1: *Fluorescence polarisation assay.*

### *Fluorescently labelling peptides*

Synthetic peptides were designed with a cysteine on either the N-terminal or C-terminal, this allowed for coupling to Fluorescein-5-Maleimide via a stable thioether bond. Peptides were coupled to the fluorophore in a reaction consisting of: 300 µM peptide, 25 µL Fluorescein-5-Maleimide, 5 mM TCEP, 0.05% v/v Triton X-100 and final volume made up to 1 mL using PBS to ensure the reaction is carried out at pH 7.4. The coupling reaction was left for 2 hours at room temperature, stirring in the dark. The reaction is stopped and the excess fluorescein is removed using a PD-10 desalting column (GE healthcare) to exchange the coupled peptide into PBS, separating it from the free fluorescein.

### *Fluorescence polarisation assay*

A 50 µL serial dilution of target protein is set up in PBS in the first 11 wells of a black 96 well plate (Nunc), with 50 µL of PBS in well 12 (considered the blank). To each well 50 µL of 200 nM fluorescent peptide solution was added and mixed by pipette. The plate was then inserted into the plate reader (BMG LABTECH, CLARIOstar) at 25°C, which took the polarisation measurements, the run settings were optimised for fluorescein dye.

### *Calculation of dissociation constant ( $K_d$ )*

The dissociation constant is defined as an equilibrium constant that measures the propensity of a complex to dissociate reversibly into smaller components. To determine the  $K_d$  of the interaction, the fluorescence polarisation data was entered into GraphPad Prism v7.00 software and data fitted to the non-linear binding equation 'one site total binding'. Equation shown below:

$$Y = \frac{BMAX * X}{KD + X} + NS * X + Background$$

Y = protein concentration

X = ligand concentration

NS = Slope of non-specific binding in Y units/X units

Background = nonspecific binding with no ligand added.

### 3.3.3 Microscale Thermophoresis (MST)

MST, like fluorescence polarisation, is used to measure the binding affinities between two molecules. However, unlike FP there are no restrictions on the size of the molecules. MST works on the basis of using fluorescent labelled molecules to track the small movements made in response to a microscopic temperature gradient, called thermophoresis. Any alteration in the local environment of the target fluorescent molecule (e.g. binding) will have an effect on the thermophoresis of the target molecule. Therefore, it is possible to plot the change in thermophoresis in response to change in ligand concentration to calculate a binding affinity. (See section 4.1 for more detail)

#### *Coupling of target proteins to NT-647 dye*

Recombinantly expressed proteins are coupled to equimolar amount of NT-647 dye (RED-tris-NTA NanoTemper) via their 6xHis-tag, in a one-step coupling reaction. The dye was mixed with the target protein in a coupling reaction at a 1:1 ratio at a concentration of 100 nM in PBS, then left at room temperature for 30 minutes. The solution was then centrifuged at 13,000 rpm for 10 minutes at 4°C to remove any aggregated protein.

#### *MST assay*

A serial dilution of the ligand was performed in 10 µL PBS. Next, 10 µL of 100 nM labelled-target-protein was added to each well. There was a final volume of 20 µL in each well with a final target concentration of 50 nM. Prepared samples were filled into Monolith NT.115 capillaries (NanoTemper). Measurements were recorded on a Monolith NT.115 at 25°C, excited under red light, medium MST power and 40% excitation power. The data was analysed using MO.Affinity Analysis software and fitted using the  $K_d$  fit model. Dissociation constants and errors were calculated using the MO.Affinity Analysis software.

### 3.3.4 Analytical size exclusion chromatography – multi-angle light scattering (SEC-MALS)

SEC-MALS provides information on the size of a molecule/molecular complex in solution. Using SEC-MALS under native conditions it is possible to visualise and estimate the size of the molecule. An accurate estimate of the molecules size is determined by combining the retention time of the SEC with the light scattering generated by the MALS (Wen et al., 1996).

#### *SEC-MALS assay*

100  $\mu$ L of sample was injected onto a superdex-75 size exclusion chromatography column (GE healthcare) at a flow rate of 0.7 mL/min at room temperature in 50 mM Tris pH 7.5 150 mM NaCl, 2 mM DTT. The elution was monitored by a Malvern Viscotek SEC-MALS-9 (Malvern Panalytical, Malvern, UK).

#### *SEC-MALS analysis*

Data was analysed using OmniSEC software (Malvern Panalytical). The analysis methods were calibrated to the retention time and MALS signal of a BSA monomer, according to the manufacturer's instructions. Estimates for the molar mass and percentage weight fraction of the proteins/complexes were determined by selection of the respective refractive index and MALS peaks according to the manufacturer's instructions.

### 3.3.5 Multi-lamellar vesicle co-sedimentation assay

This assay enables assessment of a proteins interaction with a lipid membrane. By altering the lipid composition of the vesicles it is possible to assess the influence of different membrane compositions on a proteins ability to bind the membrane.

#### *Multi-lamellar vesicle (MLV) preparation*

L- $\alpha$ -phosphatidylserine (16:0-18:1 1-palmitoyl-2-oleoyl-*sn*-glycero-3-phospho-L-serine, PS) and L- $\alpha$ -Phosphatidylcholine (16:0-18:1 1-palmitoyl-2-oleoyl-*sn*-glycero-3-phosphocholine, PC) were weighed and dissolved in chloroform at 5 mg/mL. compositions of 100% PC, 20% PS, 50% PS and 100% PS were made by mixing the appropriate ratios of chloroform dissolved lipids in a round bottom flask. The resulting mixture was dried on a rotary-evaporator, then left on a vacuum

pump for 2 hours to remove any leftover chloroform. The dried lipid film was resuspended in Lipid buffer at a concentration of 5 mg/mL. The lipids were then swollen at 50°C for 3 hours.

#### *Protein preparation*

Recombinantly expressed proteins were diluted to 40 µM in MLV pull down buffer and centrifuged at 13,000 rpm for 20 minutes at 4°C to remove aggregates.

#### *Multi-lamellar vesicle pull down assay*

Assays were prepared using 0.5 mg/mL of lipids and 12 µM protein in MLV pull down buffer with a final 200 µL volume. The reaction was left for 30 minutes at room temperature on a roller, then pelleted at 13,000 rpm for 20 minutes.

The supernatant (SN) was taken off the top, 10 µL of 5x sample buffer was added to 40 µL of the SN; the pellet was resuspended in 120 µL of 2x sample buffer. The samples were boiled for 5 minutes at 95°C then 10 µL pellet to 20 µL SN were loaded and run on SDS-PAGE. The gels were stained in Coomassie Blue, then scanned.

Band intensity was measured using ImageJ (Abràmoff et al., 2004). To calculate percentage bound we used the equation below:

$$B = \frac{P}{SN + P} * 100$$

B = percentage bound

P = band intensity of pellet

SN = band intensity of SN

#### 3.3.6 Peptide conjugated lipid co-sedimentation assay

To investigate the effects of a lipid environment on protein binding we designed a method in which we attach our cysteine-modified peptides to vesicles. This method utilises a maleimide modified phospholipid 1,2-dioleoyl-sn-glycero-3-phosphoethanolamine-N-[4-(p-maleimidomethyl)cyclohexane-carboxamide] (PEMCC) (AVANTI). When proteins are bound to the

peptide-conjugated LUVs we would expect an increased amount of protein in the pellet fraction when compared to the controls. (More detail in section 4.2)

#### *Conjugated large unilamellar vesicle (LUV) preparation*

The LUVs consisted of 20% PS, 16% PEMCC and 64% PC. Vesicles were prepared the same way as the MLV preparation, however, after resuspension the lipids were subjected to 30 minutes in a sonicating water bath, to make the vesicles unilamellar. Following this they were subjected to 9 freeze thaw cycles, in order to make LUVs that were uniform in size. Following the freeze thaw cycles the LUVs were left to swell at the lipid transition temperature of 50°C for 30 minutes. The lipids were then centrifuged at 70,000 rpm for 30 minutes, the SN removed and pellet resuspended in the lipid buffer.

The lipid suspension was divided into equal aliquots. Each aliquot of vesicles was coupled to the desired peptide in a reaction consisting of 200 µM peptide, 5 µL/mL TCEP, 5 mg/mL lipid in the lipid buffer. The mixture was left on a roller at 4°C overnight. The reaction was stopped by pelleting the LUVs then resuspending them in fresh lipid buffer.

#### *Conjugated-LUV pull down assay*

Assays were prepared using a 0.325 mg/mL lipid concentration with 6 µM concentration of target protein (prepared the same way as MLV pull downs) in the lipid buffer, at a final volume of 200 µL. The mixture was incubated at 25°C for 30 mins on a roller. Following incubation the lipids were pelleted at 70,000 rpm. The samples were then prepared and analysed as described in the MLV pull down assay.

### 3.4 Structural methods

#### 3.4.1 X-ray Crystallography

##### *Hanging drop vapour diffusion crystallisation*

Crystals were obtained by hanging drop vapour diffusion technique at either 21°C or 4°C. Protein and complex solutions were produced with various concentrations, ratios and buffers. These



solutions were screened using Hampton crystal screen 1 +2 (Hampton) and the JCSGplus crystal screen (Molecular Dimensions) in a 96 well plate. A Mosquito crystallography robot (TTP Labtech) was used to pipette 0.2  $\mu$ l drops containing a 1:1 ratio of protein to well solution. The drops were suspended over 100  $\mu$ l of well solution, sealed and incubated. Screens were checked every 24 hours for a week, then once a week.

If a successful screening condition was identified, either by small crystals or a promising looking precipitate, the condition was optimised to gain larger higher quality crystals. The conditions were varied slightly by adjusting the pH and precipitant concentration. 2  $\mu$ l drops were prepared manually at a 1:1 ratio, then suspended over 500  $\mu$ l of well solution, and checked as before.

Successfully grown crystals were cryoprotected in the well solution supplemented with 20% v/v glycerol prior to vitrification in liquid nitrogen. Details about individual crystals are given in (table 3.4).

Table 3.4: *Crystallography conditions*

Data name	Protein conc. $\mu\text{M}$	Ligand conc. $\mu\text{M}$	Buffer	Precip.	Salt	Phaser search	Ligand bound
<b>Vd1 + TarP VBS1</b>	310	310	0.1 M sodium citrate tribasic dehydrate pH 5.6	20% v/v 2- propanol	-	3ZDL	yes
<b>Vd1 + TarP VBS3</b>	350	1050	0.1 M BIS- TRIS pH 5.5	27% w/v PEG 3350	-	6FQ4	yes
<b>Talin 2 head</b>	-	-	0.1 M Sodium Citrate pH 5.6	20-30% PEG 4000 5 $\mu\text{M}$ TFE	0.1 M $\text{NH}_4\text{CH}_3\text{CO}_2$	3IVF	-
<b>F2F3<math>\beta</math> + <math>\alpha</math>2</b>	400	3200	0.1 M BIS- TRIS pH 5.9	39% w/v PEG 3350	0.2M $\text{MgCl}_2$	3G9W	no

*X-ray crystallography data collection and processing.*

Diffraction datasets were collected at 100 K on beamLine I03/104-1 at Diamond Light Source (Didcot, UK) using a Pilatus3 6M detector (Dectris, Baden, Switzerland). Crystallographic data was processed by autoPROC (Vonrhein et al., 2011), which incorporates XDS (Kabsch, 2010), AIMLESS (Evans and Murshudov, 2013) and TRUNCATE (Evans, 2011) for data integration, scaling and merging. All structures were solved by a molecular replacement search carried out with PHASER (McCoy et al., 2007). Manual model adjustment and refinement was performed with COOT (Emsley et al., 2010) and REFMAC (Murshudov et al., 2011) respectively. Models were validated with MOLPROBITY (Chen et al., 2010) and interaction properties were determined by PISA

(Krissinel and Henrick, 2007). Figure preparation was done using PYMOL (Schrödinger LLC, Cambridge MA, USA).

### 3.4.2 Nuclear Magnetic Resonance (NMR)

#### *<sup>15</sup>N Protein preparation*

Picked colonies were grown overnight in a starter culture consisting of 10 mL Solution A and 270 µL solution B at 37°C. 500 mL of <sup>15</sup>N-minimal media (500 mL solution A, 13 mL solution B) were inoculated with 4 mL of starter culture. The cultures were incubated at 37°C in a shaking incubator. Cultures were grown to an OD<sub>600</sub> of 0.5-0.8 then cooled to 18°C and inoculated with 100 µg/mL IPTG to induce protein production, then incubated at 18°C overnight as described in the section 3.2.1. Proteins were purified as described previously (section 3.2.2) and exchanged into NMR buffer.

#### *1D NMR experiments*

All NMR experiments were performed on a Bruker Avance III 600 MHz NMR spectrometer equipped with QCI-P CryoProbe at 298K. All samples were prepared with a concentration between 50-100 µM, supplemented with 5% v/v D<sub>2</sub>O, and transferred to a Shigemi tube (Sigma-Aldrich), with a final sample volume of 450 µL.

1D NMR experiments allowed us to check the quality of the NMR sample, by providing information on the concentration, signal/noise and water suppression.

#### *2D <sup>1</sup>H - <sup>15</sup>N HSQC experiments*

A <sup>1</sup>H - <sup>15</sup>N heteronuclear single quantum correlation (HSQC) experiment was used for all 2D NMR experiments (Mori et al., 1995). In every protein residue, barring proline, there is an amide proton bonded to a nitrogen in a peptide bond. The HSQC experiments correlate these amide protons with the corresponding nitrogen atom to produce a peak in a 2D spectrum, providing a peak for every amino acid except for proline. These experiments are a powerful tool for investigating protein-ligand interactions as changes in the local environment of a residue can lead to the

corresponding peak shifting location; identification of peak shifts in a spectrum in response to titration of ligand is thus indicative of an interaction.

2D Spectra were acquired using a HSQC pulse sequence at 600 MHz; the data was acquired with 1024 points in the  $^1\text{H}$  dimension over a sweep width of 10,484 Hz and 124 increments in the indirect  $^{15}\text{N}$  dimension over a sweep width of 4600 Hz.

### Spectra Analysis

Spectra were displayed and analysed using CCPNMR analysis version 2.5.2 (Skinner et al., 2015; Vranken et al., 2005). Previously assigned protein assignments could be read into CCPN from the Biological Magnetic Resonance Bank (BMRB), this allowed identification of each peak in the spectra (fig. 3.2). Assignment of the peaks enabled mapping of the peak shifts in response to ligand addition, providing a binding surface on the target protein.

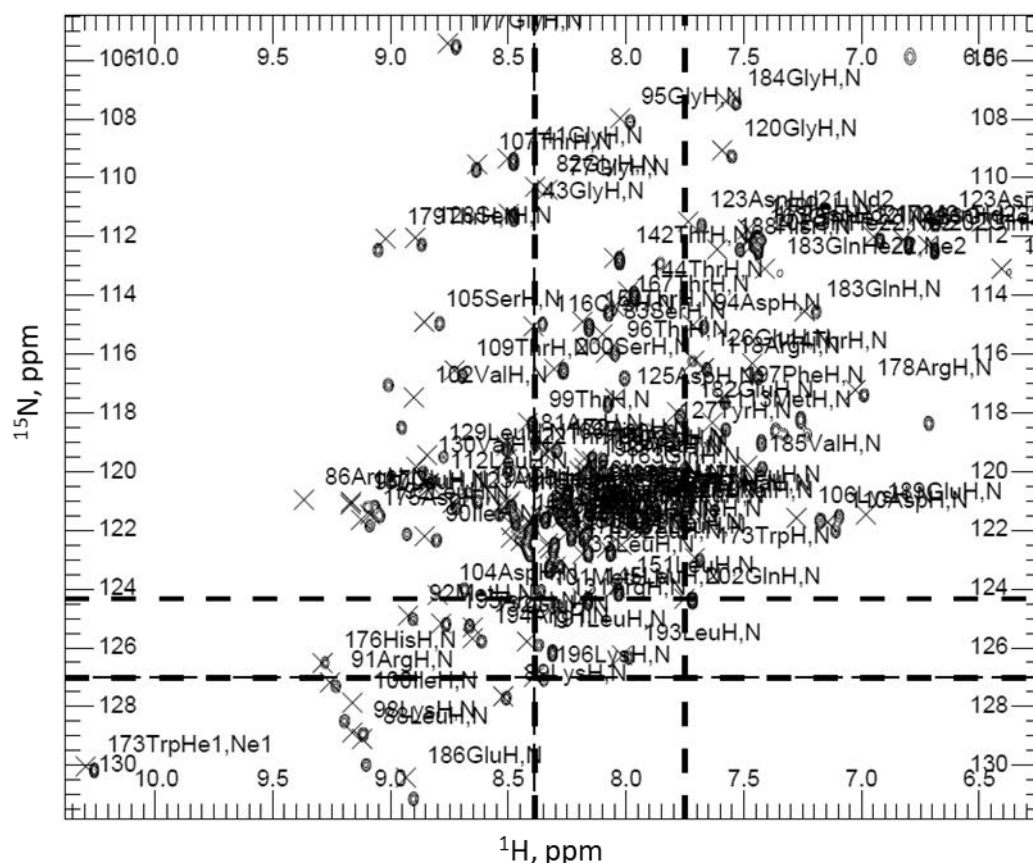


Figure 3.2: Example NMR peak assignment of talin F1. Map imported from BMRB entry 15616 shown in analysis.

## 4. Method development to gain biochemical insight into interactions at integrin-mediated adhesions.

Integrin-mediated adhesions are a complex network of proteins and signalling molecules, in which mechanical force and regulatory signals can be passed between the cell and the extracellular matrix (Horton et al., 2015). Understanding this vast network requires breaking down of the intricacies of each individual interaction. The most comprehensive way of investigating these interactions is through a combination of *in vivo* and biochemical techniques. Whilst there is a vast array of methods available for studying interactions biochemically, many of these methods have limitations on materials and equipment (Hayes et al., 2016). These limitations can lead to a loss of important biochemical insight into interactions.

In this chapter we report on the development of two novel biochemical assays for investigating molecular interactions involved in integrin-mediated adhesions, which were otherwise difficult to study. The first is the use a microscale thermophoresis assay to overcome difficulties in protein expression and size (section 4.1). The second is a peptide conjugated lipid co-sedimentation assay as an accessible way of investigating membrane-mediated protein interactions (section 4.3).

### 4.1 Investigating protein:protein interactions using microscale thermophoresis (MST)

#### 4.1.1 Difficulty expressing recombinant proteins

A significant problem in biochemistry is working with difficult proteins where gaining high yields (>5mg/l) of purified proteins is not possible. A lot of time and effort can be exhausted to overcome these issues without any results. Using recombinant *E.coli* systems, this is a regular issue affecting large proteins, proteins with complex folds, aggregation prone regions and disordered loops (Rosano and Ceccarelli, 2014; Makrides, 1996). Whilst, a lot of these problems can be overcome by expressing recombinant proteins in baculovirus-infected insect cells and

mammalian cell lines, these systems require specialist equipment and cloning strategies a lot of labs do not have access to (Hacker and Balasubramanian, 2016; Unger and Peleg, 2012).

Therefore, a lack of recombinant protein production has led to a loss of biochemical characterisation and validation within many systems in biology. Here we will talk about two example adhesion protein systems, full-length talin (FL-talin) and full-length kindlin-1.

#### 4.1.2 Recombinant expression of full length talin

The core adhesion protein talin is a well characterised protein biochemically (Gough and Goult, 2018). This is because the individual domains of talin have been optimised for recombinant expression; producing high yields of purified protein, on average >20mg/l, from recombinant *E.coli* systems. However, biochemical characterisation of the FL-talin system is considerably limited by protein expression. FL-talin forms an antiparallel dimer consisting of two 270 kDa monomers formed of 17 distinct domains (Goult et al., 2013b). In addition to its size, FL-talin contains multiple aggregation prone regions (unpublished data); a large disordered lipid-binding loop in the head domain (Goult et al., 2010a); a long 82 aa flexible linker region between the talin head and rod domain (Bate et al., 2012); and adopts multiple conformations (Goult et al., 2013a; Molony et al., 1987). Altogether, this culminates in FL-talin being a complex system to work with recombinantly. Indeed, we only achieve maximum yields of 10 mg/l (fig. 4.1).

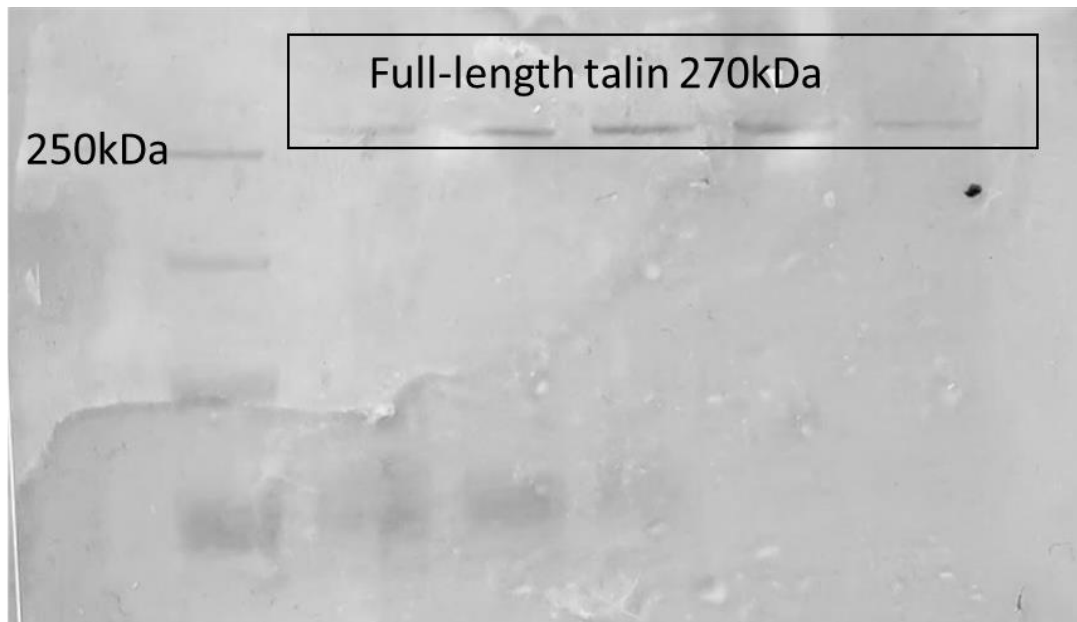


Figure 4.1: **Low yields of full-length talin.** Full-length talin purification elution profile from 2 L culture observed on SDS-PAGE stained with Coomassie blue, FL-talin bands are within labelled box.

#### 4.1.3 Recombinant expression of kindlin-1

Kindlin-1, is a vital partner to talin in integrin activation and an important player all round in adhesions (Calderwood et al., 2013), mutations in which lead to the dermatological disorder kindler syndrome (KS) (Siegel et al., 2003). Kindlin-1 is a 77 kDa FERM domain protein, consisting of four domains (F0-F3) (Goult et al., 2009b). Kindlin F1 contains a 109 aa disordered loop and F2 contains a 131 aa membrane binding PH domain (D'Souza et al., 2010; Li et al., 2017a; Goult et al., 2009b). Until recently (Li et al., 2017a; Michael et al., 2019) little quantitative biochemistry was completed on the full-length wild-type kindlin-1. This is due to extremely low recombinant expression; we achieve maximum yields of 0.3 mg/l with a low purity (fig. 4.2).

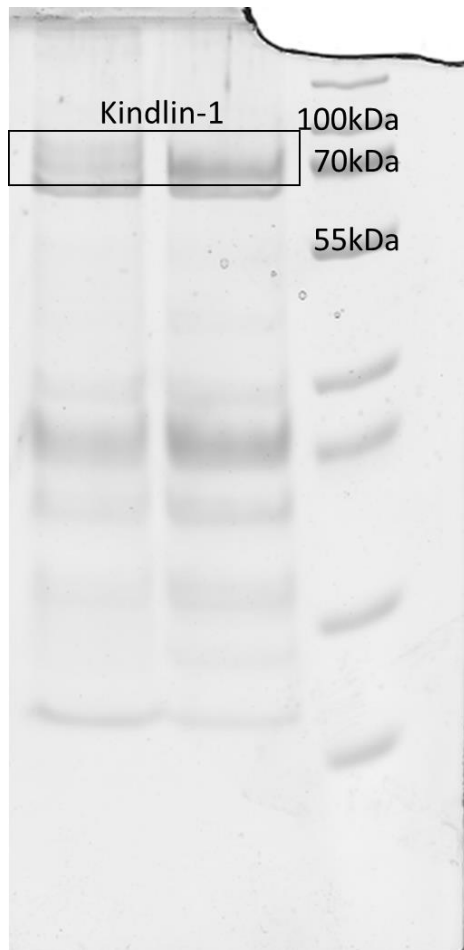


Figure 4.2: **Kindlin-1 has low yields of purified recombinant protein.** Full-length kindlin-1 purification from 2 l culture observed on SDS-PAGE stained with Coomassie blue, kindlin-1 bands are within labelled box.

#### 4.1.2 MST experiment

MST is a sensitive biophysical method that is used to measure binding affinities between biomolecules. MST measures the thermophoresis effect; the dispersion of molecules in response to a temperature gradient. The thermophoresis effect is strongly influenced by a variety of molecular properties including size, charge, hydration shell and conformation. The thermophoresis effect occurs when an increase in temperature ( $\Delta T$ ) in space depletes the solvated biomolecules in the region of elevated temperature, and can be quantified by the Soret coefficient  $S_T$ :  $C_{\text{hot}}/C_{\text{cold}} = \exp(-S_T \Delta T)$  (Ludwig, 1856; Duhr and Braun, 2006). Thus, this technique is extremely sensitive to almost any change in molecular properties. Utilising this process, it is possible to detect binding by titrating your ligand against a fluorescently labelled target molecule. The diffusion of the target molecule can then be tracked in response to the temperature gradient;



if the ligand binds to the target molecule this will alter the rate of diffusion (Zillner et al., 2012) (fig. 4.3).

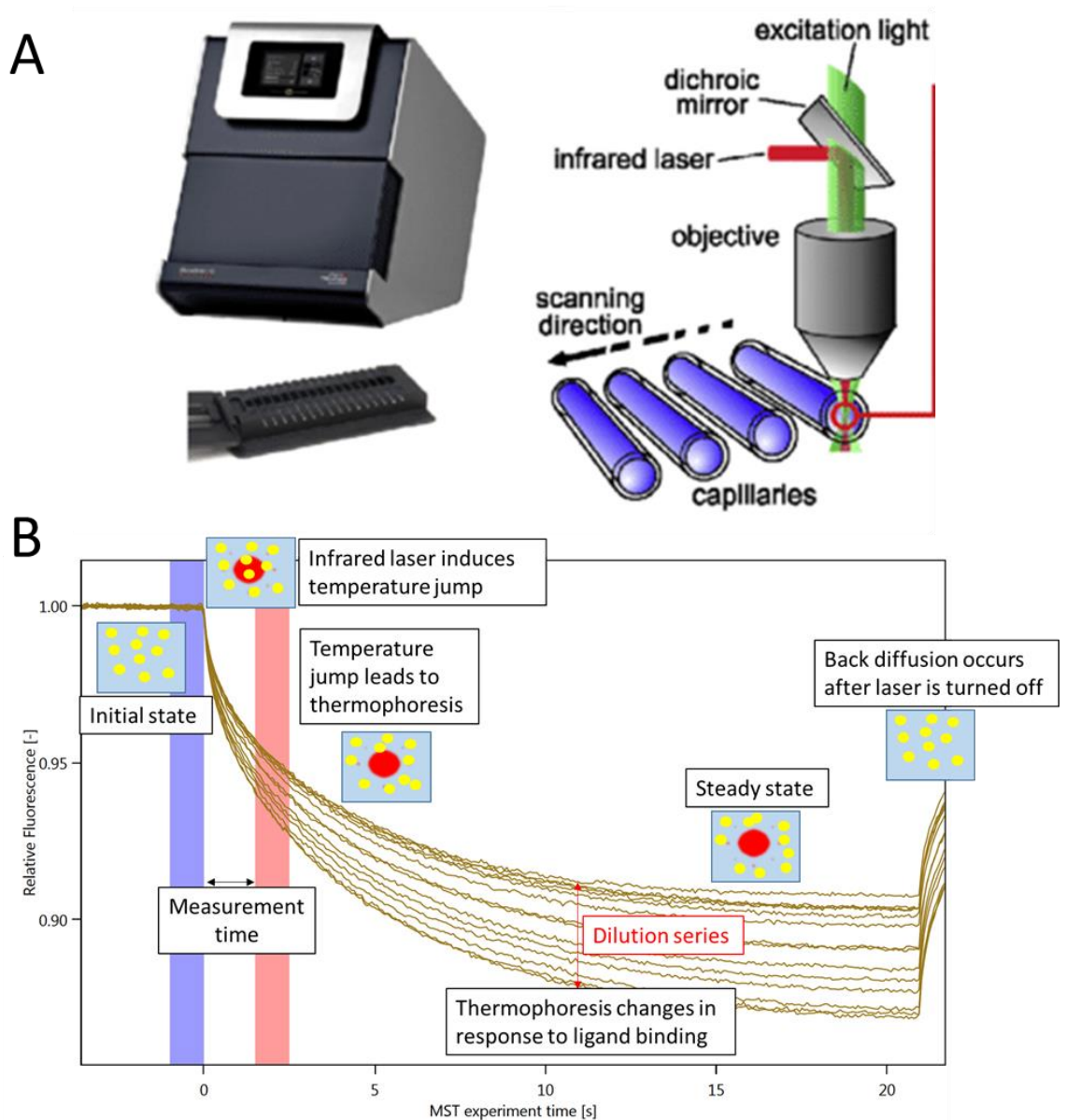


Figure 4.3: **MST**. (A) MST setup of monolith NT.115: titrations are prepared and transferred into glass capillaries, which are then placed onto the stage in order, the stage is inserted into the MST machine; a temperature gradient is triggered by an infrared laser, then the thermophoresis effect is tracked by measuring fluorescence intensity at the point of heating. Adapted from (Jerabek-Willemsen et al., 2014). (B) Diagram of how MST functions to measure molecular interactions. MST traces (mustard) shows the tracing of the fluorescence intensity over time after a temperature gradient is induced. Blue and red lines represent the measurement window that is used to calculate the change in fluorescence intensity from the normal ( $\Delta F_{norm}$ ) through the dilution series. Illustrations of the molecular movements in response to the IR-laser show the various states the molecules are in within the system.

In our lab we have previously used fluorescence polarisation and NMR assays to investigate molecular interactions (Bouchet et al., 2016; Whitewood et al., 2018); whilst both are powerful

and useful in their own right, they are both limited by the size of the target molecule (Jameson and Sawyer, 1995). In contrast, due to the sensitive nature of MST it can detect interactions of almost any size. This allows for the measurement of binding of large target proteins against all sizes of ligands, e.g. two large proteins (>20 kDa) interacting directly. Furthermore, MST has advantages over other more common binding techniques such as isothermal titration calorimetry (ITC) and surface plasmon resonance (SPR), by avoiding surface immobilization and significantly reducing the sample consumption (Wienken et al., 2010).

#### 4.1.3 Coupling to RED-tris-NTA dye

To use the macromolecules as targets we require a way in which to fluorescently label them. When using peptides as the target, they are engineered to have a single terminal cysteine for covalent attachment to maleimide conjugate dyes. Unlike the engineered peptides, this maleimide approach is not suitable for labelling large proteins, as talin contains 38 cysteine residues. Moreover, kindlin-1 does not yield 100% purity, therefore the dye needs to be specific to the target protein as to reduce noise and false results. Most of the protein constructs we use contain a cleavable 6×His-tag for purification. Looking for a specific fluorescent label we identified NanoTemper RED-tris-NTA (NT647) dye as suitable candidate (fig. 4.4). NT647 binds specifically to a 6×His-tag with a high affinity of  $K_d = 2.7$  nM through the tris-NTA group. The high specificity of the NT647 dye enables it to be used on whole cell cytosol, making it more than suitable for purified proteins with a few contaminants, such as kindlin-1. The NT647 dye is also extremely versatile in multiple buffers, giving a high signal-to-noise ratio (Bartoschik et al., 2018). Proteins of interest are coupled to the dye following the manufacturer's instructions in a one-step coupling reaction (NanoTemper; Bartoschik et al., 2018).

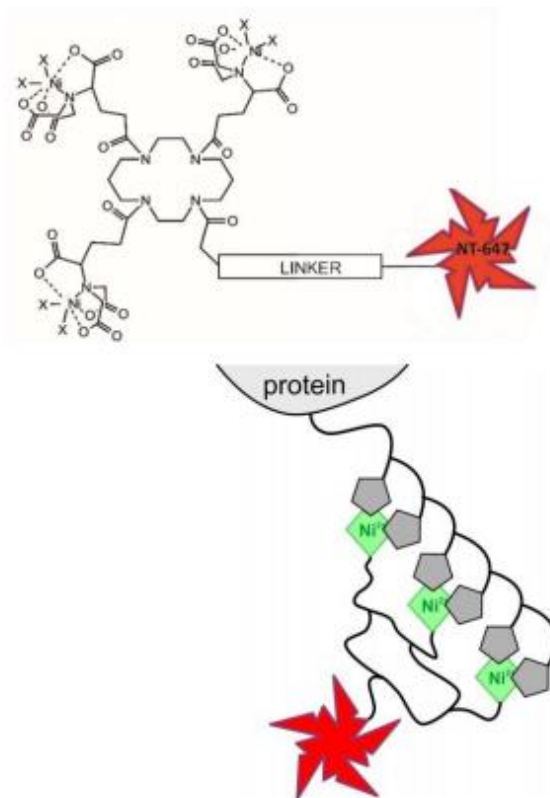


Figure 4.4: **RED-tris-NTA dye.** (top) Schematic of RED-tris-NTA (NT647) dye, (bottom) NT647 bound to polyhistidine tag via the NTA group; pentagons represent histidine residues. adapted from (Bartoschik et al., 2018)

#### 4.1.4 Test 1: Talin autoinhibition interaction between F2F3 and R9R10

The well characterised talin autoinhibition interaction between R9 in the rod domain and F3 in the talin head (Goult et al., 2013a, 2009a; Goksoy et al., 2008) provided an excellent model system to develop the new method. Both R9R10 and F2F3 constructs produce high yields of purified protein enabling us to be confident in the proteins we were working with. With R9R10 being 33 kDa and F2F3 being 24 kDa, the interaction between the two constructs is too large to measure using more conventional methods. In this experiment, His-tagged R9R10 was coupled to the NT647 dye with a final target concentration of 50 nM. F2F3 and R7R8 (control) were titrated against the labelled R9R10 (fig. 4.5). Analysis of the results revealed F2F3 bound to R9R10 with an affinity of  $K_d = 15.25 \mu\text{M}$  and R7R8 gave a flat line indicating no binding. These results demonstrated the ability of the

technique to accurately measure specific interactions between two large protein constructs.

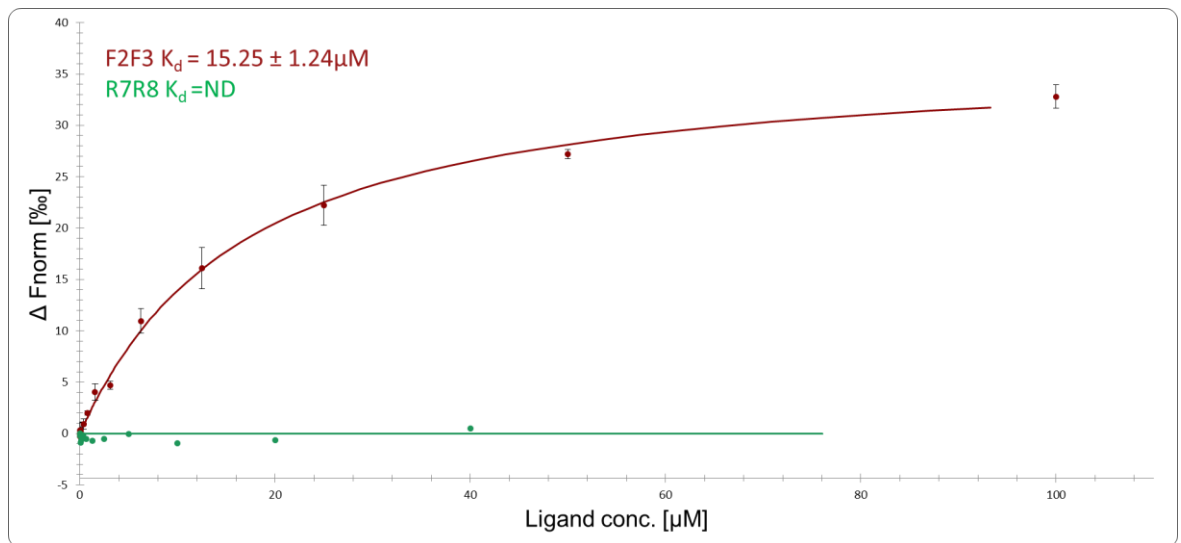


Figure 4.5: **Biochemical characterization of talin autoinhibition complex.** Binding of 50 nm RED-tris-NTA labelled R9R10 to F2F3 (red,  $n=3$ ) and R7R8 (green  $n=1$ ) measured using an MST assay. Data was analysed by nanotemper analysis software to a  $K_d$  fit model. Dissociation constants  $\pm K_d$  confidence for the interactions are indicated in the legend. ND = not determined.

#### 4.1.5 Test 2: Full-length talin and KANK peptide

The next important test was on a challenging system, FL-talin. We aimed to test the ability of the assay to measure binding between a very large protein as the target and a small peptide as the titrant. Measuring binding of a 4.5 kDa peptides against a 540 kDa protein is challenging, and was used to test the applicability of the assay to challenging systems. In this test we used the interaction between KANK and talin (Bouchet et al., 2016) as the model system. In this experiment the synthetic KANK peptide (4.5 kDa) and TarP LD peptide (control) were titrated against NT647-labelled FL-talin (270 kDa dimer). The KANK peptide bound to FL-talin with a binding constant of  $K_d = 13.1 \mu\text{M}$ , whilst the TarP LD showed no binding (fig. 4.6).

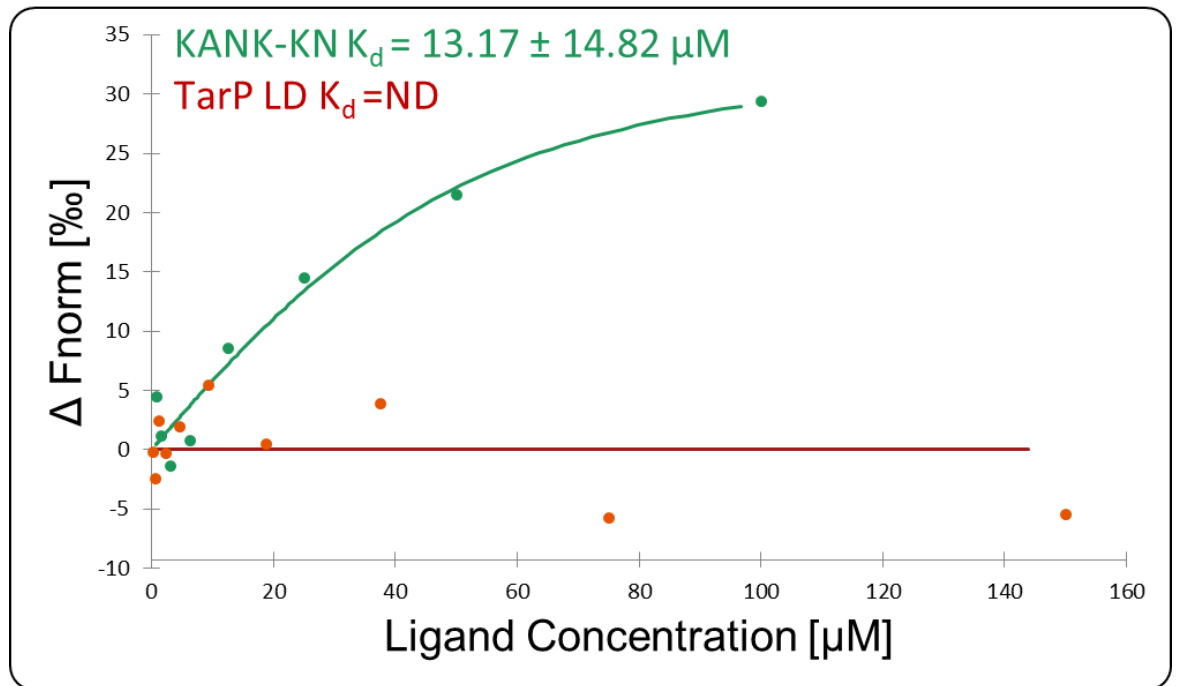


Figure 4.6: **Biochemical characterization of the FL-talin-KANK interaction.** Binding of 50 nm RED-tris-NTA labelled FL-talin to TarP LD (red,  $n=1$ ) and KANK-KN (green  $n=1$ ) measured using an MST assay. Data was analysed by nanotemper analysis software to a  $K_d$  fit model. Dissociation constants  $\pm K_d$  confidence for the interactions are indicated in the legend. ND = not determined.

Curiously, the binding detected has a lower affinity than that previously measured directly between talin R7 and KANK (Bouchet et al., 2016). However, the  $K_d$  measurement has a very low significance as indicated from the error, so does not accurately reflect the affinity of the interaction. In solution, we are not fully confident in what conformation FL-talin is adopting, it is possible the low significance of the affinity measurement is because the KANK binding site on R7 is partially inaccessible in the conformation that talin was adopting. It has previously been demonstrated KANK binding to R7 is associated with talin activation (Sun et al., 2016), if FL-talin is already unfolded in the active conformation, this may interfere with KANK interaction. To get a more accurate measurement of affinity for this interaction would require more repeats and a higher starting ligand concentration to fully saturate the system. However, despite the low significance of the binding affinity measurement, we were still able to observe a binding event which previously had been unquantifiable; demonstrating the potential of the MST assay to quantify binding events between small molecules as the titrant and macromolecules as the target.

#### 4.1.6 Test 3: interaction between kindlin-1 and integrin

Another important test for this assay was whether we could employ it to investigate kindlins. As mentioned earlier, kindlins express poorly. We were only able to purify kindlin-1 by batch method, as the small amount of pure protein we yielded could not be identified at A280 on the AKTA system. Whilst this provided a suitable amount of protein for the assay it was not of a high purity, thus we were relying on the specificity of the NT647 dye. Whilst little quantitative biochemistry has been done on kindlin-1, there is a well-characterised interaction between kindlins and the cytoplasmic tails of  $\beta$ -integrin (Rognoni et al., 2016; Bledzka et al., 2012; Calderwood et al., 2013; Harburger et al., 2009). Thus, to test the assay on this system, recombinant integrin  $\beta$ 1a cytoplasmic tail peptide was titrated against His-tagged kindlin-1 coupled to the NT647 dye.

The first experiment on this system showed binding with a relatively high affinity with a  $K_d = 1.15 \mu\text{M}$ . However, an initial quality control check done by the Monolith NT-115 machine is to measure the initial fluorescence intensity of each capillary as a difference in fluorescence intensity can significantly alter the result; upon the addition of the  $\beta$ 1a peptide to kindlin there was significant ligand induced fluorescence (fig. 4.7 A). After trouble shooting, we established this was because our  $\beta$ 1a peptide did not have the His-tag fully cleaved, causing the dye to disassociate from the target protein and bind to the titrated ligand, giving a false positive result. Having identified this as a potential source of error, the initial capillary-scan became a vital test for data quality control.

Repeating the assay using a fully cleaved integrin  $\beta$ 1a peptide markedly improved the experiment, with a consistent capillary scan showing no significant differences ( $\pm 10\%$ ) in initial fluorescence (fig. 4.7 B). Using cleaved integrin gave an affinity of  $K_d = 6.8 \mu\text{M}$ , which was in agreement with previous SPR measurements using kindlin-2 (Bledzka et al., 2012), demonstrating the MST assay can be used to investigate kindlin-1. Interestingly, the curve generated from the cleaved integrin showed the opposite effect on diffusion as most other interactions, demonstrating a negative

$\Delta F_{norm}$ , in which binding of the peptide to kindlin led to reduced diffusion in response to the temperature gradient, the opposite of the false positive (fig. 4.7 C).

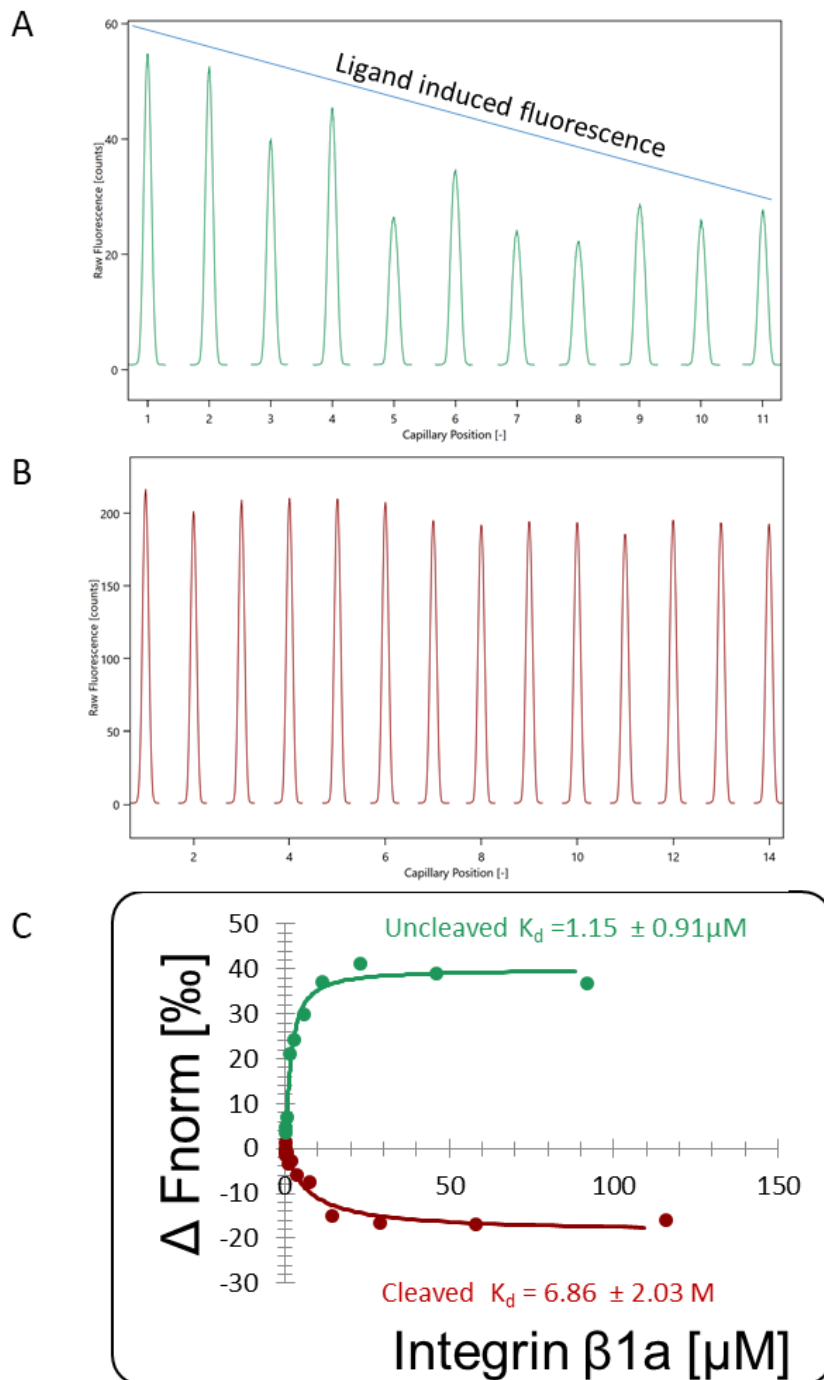


Figure 4.7: **Biochemical characterization of the kindlin-1: integrin  $\beta 1a$  interaction.** A) Capillary scan of uncleaved integrin  $\beta 1a$  (752-798) titrated against 50 nM NT647-labelled kindlin-1, demonstrating ligand induced fluorescence. B) Capillary scan of cleaved integrin  $\beta 1a$  (752-798) titrated against NT647-labelled kindlin-1, demonstrating even fluorescence distribution. C) Binding of 50 nM RED-tris-NTA labelled kindlin-1 to fully cleaved integrin  $\beta 1a$  (red,  $n=1$ ) and partially cleaved integrin  $\beta 1a$  (green,  $n=1$ ) measured using an MST assay. Data was analysed by nanotemper analysis software to a  $K_d$  fit model. Dissociation constants  $\pm K_d$  confidence for the interactions are indicated in the legend.

## 4.2 Application of the MST assay: Kindlin-1 regulates epidermal growth factor receptor (EGFR) signalling

The first application of the MST assay was to provide important biochemical validation to a collaborative project with the Parsons lab at Kings College London, investigating a direct interaction between kindlin-1 and the EGFR (Michael et al., 2019).

Patients who suffer from Kindler syndrome (KS) have a significant reduction, or absence, of kindlin-1 in keratinocytes (Siegel et al., 2003). This has been linked to loss of integrin signalling, cell adhesion and migration in these cells (Has et al., 2011; Lai-Cheong et al., 2009). Apart from the role of kindlin-1 in adhesion (Rognoni et al., 2016), less is known about the non-adhesion functions of kindlin-1. To investigate these functions our collaborators in the Parsons lab used mass spectrometry analysis of keratinocytes from healthy vs KS patients. They identified a significant reduction in the levels of the EGFR in the KS keratinocytes. The EGFR is a transmembrane receptor for members of the epidermal growth factor family, upon activation the EGFR dimerises, stimulating intracellular signalling pathways important in cell migration, adhesion and proliferation (Wee and Wang, 2017). By rescuing KS keratinocytes with exogenous expression of kindlin-1 the Parsons lab restored EGFR levels, thereby attributing this phenotype directly to kindlin-1 expression.

### 4.2.1 Biochemical characterisation of the novel interaction between kindlin-1 and the EGFR

It has been previously demonstrated kindlin-2 directly interacts with the EGFR kinase domain (Guo et al., 2015), thus we hypothesised the KS effect on EGFR expression was through a direct interaction between kindlin-1 and the EGFR. Using cell lysate pulldowns, our collaborators mapped the interaction between the EGFR and kindlin-1 to the kindlin-1 FOF1 domain and the EGFR juxta membrane segment A (JMA). To further validate and quantify their observations we used our MST assay to assess the binding between kindlin-1 and a peptide of the EGFR-JMA. In



this assay a synthetic peptide of the EGFR-JMA was titrated against NT647-labelled kindlin-1, kindlin-1 FOF1, and talin R9R10 (control) (fig. 4.8). The FL-kindlin-1 bound to the EGFR with an affinity of  $K_d = 7.17 \mu\text{M}$ , demonstrating a robust interaction between the two proteins. Furthermore, kindlin-1 FOF1 domains bound with a comparable affinity of  $K_d = 10.98 \mu\text{M}$ , localising this interaction to a specific region of kindlin-1. This data was confirmed by our collaborators GST pull down experiments in solution, from which they were able to deduce the binding between the EGFR cytoplasmic tail and kindlin-1 and locate the interaction to the kindlin-1 F1-loop (Michael et al., 2019).

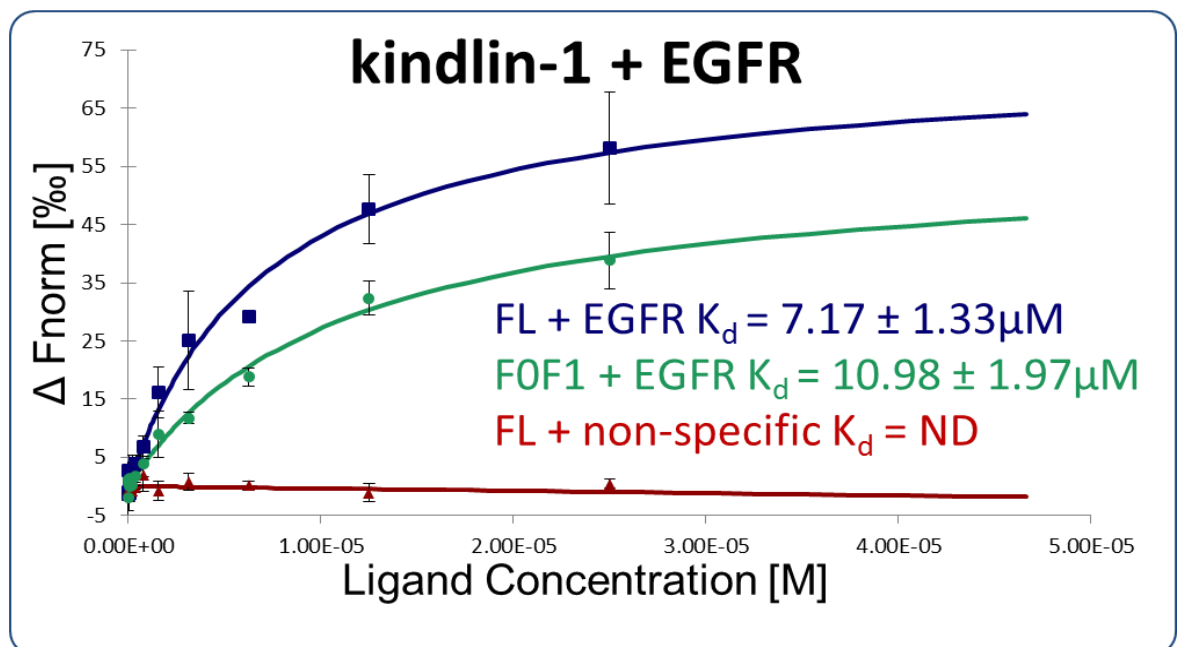


Figure 4.8: **Biochemical characterisation of the kindlin-1:EGFR interaction.** Binding of 50 nm EGFR membrane proximal region peptide to RED-tris-NTA labelled talin R9R10 (red, n=3), kindlin-1 FOF1 (green, n=3) and FL-kindlin-1 (blue, n=3) measured using an MST assay. Data was analysed by nanotemper analysis software to a  $K_d$  fit model. Dissociation constants  $\pm K_d$  confidence for the interactions are indicated in the legend

The EGFR-kindlin-1 interaction was shown to be important in EGF-dependent migration.

Altogether, we showed this novel interaction was necessary to protect the EGFR from lysosomal degradation. Moreover, we demonstrated a role for kindlin-1 independent of adhesions, and found a new pathway in which it might be possible to target treatment of KS-patients (Michael et al., 2019).

## 4.3 Peptide-conjugated lipid co-sedimentation assay

### 4.3.1 Cell membrane mediation of protein:protein interactions

Focal-adhesions form around the cytoplasmic-tail of the integrin receptor at the cell membrane, connecting the cell cytoskeleton to extra cellular matrix (Winograd-Katz et al., 2014). Integrin-mediated adhesions are very diverse and highly regulated structures. One such way that integrin-mediated adhesions are heavily regulated is through the lipid composition of the cell membrane, with a number of core protein interactions being mediated by the lipid environment (Son et al., 2017; Liu et al., 2011; Bouaouina et al., 2008). An example of lipid regulation is in the core adhesion protein talin, required to activate integrins and link them to the actin cytoskeleton (Klapholz and Brown, 2017). The activity of talin is heavily mediated by the cell membrane as basic residues in the talin FERM directly interact with the net negative charge from phosphatidylinositol-4,5-biphosphate (PIP2) (Goult et al., 2010a; Kalli et al., 2010). The presence of PIP2 in the cell membrane is vital for integrin activation, as it orientates the talin FERM to bind to the  $\beta$ -integrin cytoplasmic tail (Bouaouina et al., 2008; Kalli et al., 2010; Goult et al., 2010a; Elliott et al., 2010). Biochemical assays demonstrate the binding affinity between the  $\beta$ -integrin cytoplasmic tail and talin F3 is relatively weak in aqueous environments (Tadokoro et al., 2003; Anthis et al., 2009), however at a membrane this affinity is increased 100-fold (Moore et al., 2012).

It is clear that accounting for the influence of lipids is important when investigating interactions that natively occur at the cell membrane. The lipid environment of biological membranes mediates many important protein interactions and biochemical reactions. To study these interactions there are multiple techniques available (Zhao and Lappalainen, 2012). However, many of these techniques require specialised equipment and have complex protocols, e.g. SPR and ITC assays (Besenicar et al., 2006; Ananthanarayanan et al., 2003), restricting usage. Furthermore, most of these methods require the complicated step of inserting proteins into

membranes using transmembrane domains (TMDs) (Bond and Sansom, 2006; De Franceschi et al., 2019). Therefore, we sought to design a more accessible assay to investigate how the membrane influences interactions between talin and its ligands that is relatively quick, cheap and easy.

#### 4.3.2 Lipid co-sedimentation assays

One of the more common and accessible assays to investigate interactions between proteins and lipids are co-sedimentation assays (coseds) (Zhao and Lappalainen, 2012; Anthis et al., 2009). Lipid co-sedimentation assays are based on the sedimentation of large-unilamellar-vesicles (LUVs) or multilamellar-vesicles (MLVs) and interacting proteins by high-speed centrifugation. These assays are quick, very accessible (most labs have access to a centrifuge) and by measuring relative band intensities using Image-J (Abràmoff et al., 2004) one can assess the relative strength of the interaction.

#### 4.3.3 Incorporating membrane proteins into lipid coseds.

Next, we needed a way in which we could incorporate our ligands with the lipid vesicles to measure the effect of ligand binding on the cosed assays. Most conventional methods make use of transmembrane domains (fig. 4.9 A), however, these can be particularly difficult to purify and handle due their high hydrophobicity (De Franceschi et al., 2019). Therefore, instead of using transmembrane helices we were after a more versatile way of anchoring our ligands. Most the synthetic peptides we use have been modified with a cysteine on either the C/N-terminus for coupling to fluorescent labels through a maleimide bond; we sought to utilise this feature to anchor our peptides to lipid vesicles. To do this we prepared maleimide-functionalised vesicles using N-[4-(p-maleimidomethyl)cyclohexane-carboxamide] (PE-MCC) (AVANTI lipids), a lipid with maleimide modified head group that can form a covalent thiol bond with cysteine residues (fig. 4.9 C)(Gureasko et al., 2010).

#### 4.3.4 Experiment design

For the final experiment design it was more economic to incorporate PE-MCC into LUVs instead of MLVs as it increases the surface area for maleimide head groups to conjugate the peptides. For ease and economy, we used phosphatidylserine (PS) to mimic the net charge of PIP<sub>2</sub>, as PS has been shown before to be a good PIP<sub>2</sub> mimetic (Anthis et al., 2009). Together with the PE-MCC and phosphatidylcholine (PC) a 20% w/w PS concentration was used for initial experiments as this was effective at pulling down most of the talin head domains in the MLV assays (section 5.3; fig. 5.8) (Anthis et al., 2009). A 16% w/w concentration of PE-MCC was used for a 4:1 ratio of the desired target peptide concentration of 20  $\mu$ M. Conjugated LUVs were incubated with the target protein for 30 minutes at room temperature as previously done using MLVs (Anthis et al., 2009). Following incubation the LUVs were pelleted at 70,000 rpm, a greater spin speed than previously used on MLVS was necessary as the LUVs are much smaller.

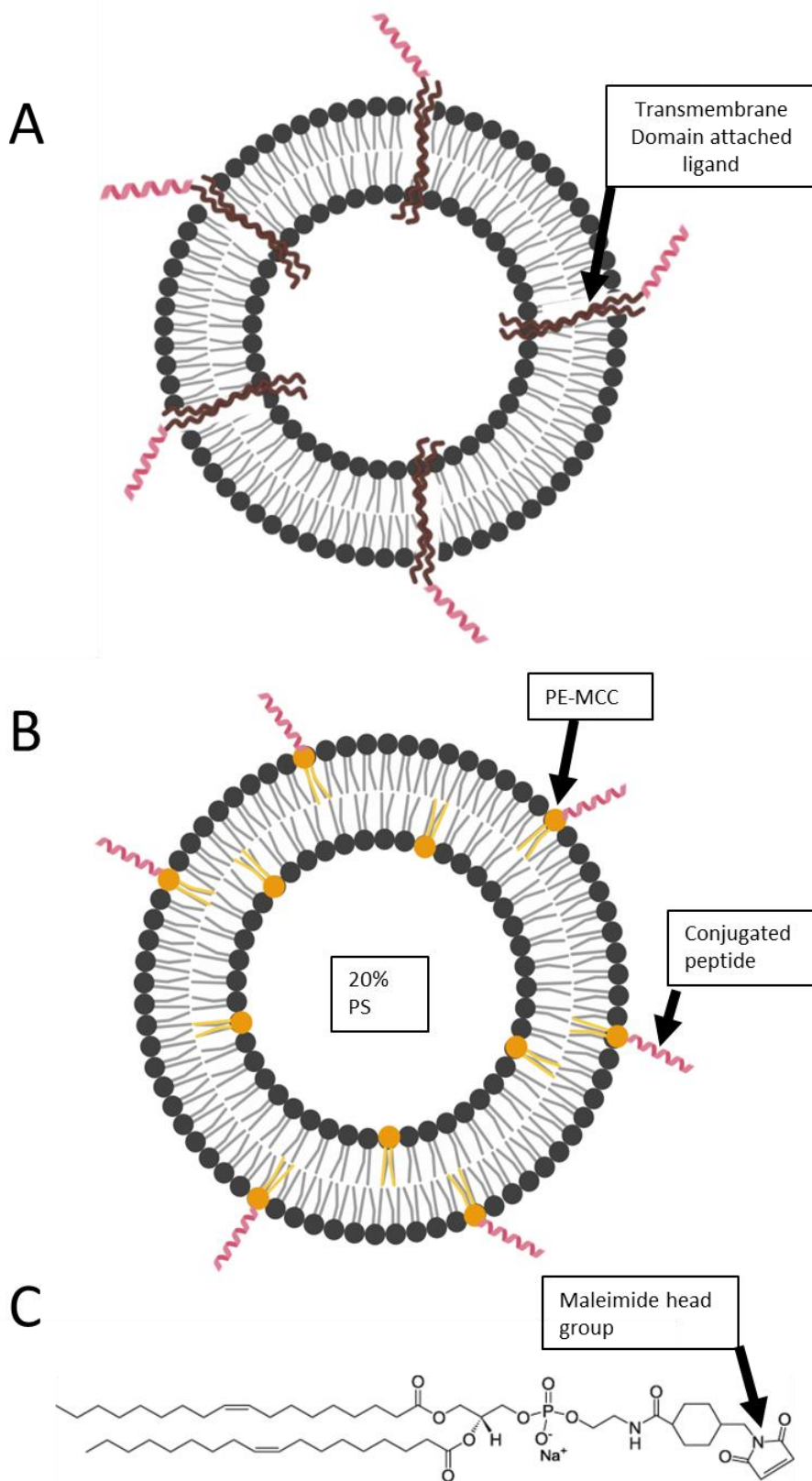


Figure 4.9 **Design of peptide-conjugated large unilamellar vesicles.** A) Illustration of LUVs featuring TMD attached ligands. B) Illustration of final design of peptide conjugated LUVs. C) Diagram of maleimide functionalised lipid PEMCC (taken from AVANTI).

#### 4.3.5 Optimisation: peptide conjugation

As the peptide-conjugated lipid cosed experiment is the first of its kind it was important to go through a series of method optimisation steps to ensure the experiment was functional and accurate. The LUVs were initially prepared using a standard protocol (section 3.3.6) (Akbarzadeh et al., 2013). Following the LUV preparation it was important to optimise the peptide coupling to the maleimide-active LUVs. For the experiment to be accurate, there needed to be a high peptide coupling efficiency together with a high purity of constituents in the assay. The peptides were coupled to the LUVs using similar conditions to those used to couple the peptides to maleimide conjugate dyes (section 3.3.2) as we were trying to induce the same disulphide bond formation. To measure the peptide coupling efficiency, the LUVs were pelleted by centrifugation then run on SDS-PAGE to visualise the peptides in the pellet and the supernatant (SN) fractions. Conjugation tests were carried out using three different peptides; integrin  $\beta$ 1a-tail, integrin  $\alpha$ 2-tail, TarP VBS1 and a blank, prepared under the same conditions (section 3.3.6).

In the first attempt, the peptides were directly coupled to the lipid mixture following the LUV freeze thaw cycle. At this point we assumed all the lipids in the mixture formed LUVs. The peptides were added to the lipids in a coupling reaction. Following the coupling reaction the lipids were pelleted, all the SN was removed and the remaining pellet was resuspended in sample buffer. SDS-page analysis revealed only around 10% of the peptide was in the pellet (fig. 4.10 A). Investigating the low peptide coupling efficiency we discovered it was normal practice to leave a small proportion of liquid surrounding the pellet by carefully taking off the top and treating it as the 'pellet', as a large proportion of lipids are concentrated into this small amount of liquid instead of sedimenting on the centrifuge tube (Blin et al., 2008). To investigate whether the lipids were concentrating but not sedimenting, left-over SN from the first experiment was subject to an additional high speed centrifugation cycle, and the analysis process repeated, carefully taking off the top of the SN and leaving a residual 20  $\mu$ L of solution around the pellet. Analysis of this

process revealed a significant increase in the amount of peptide in the pellet fraction (fig. 4.10 B). However, whilst leaving a residual 20  $\mu$ L increased the yield of peptide in the pellet, there was still a large amount of peptide in the SN fraction.

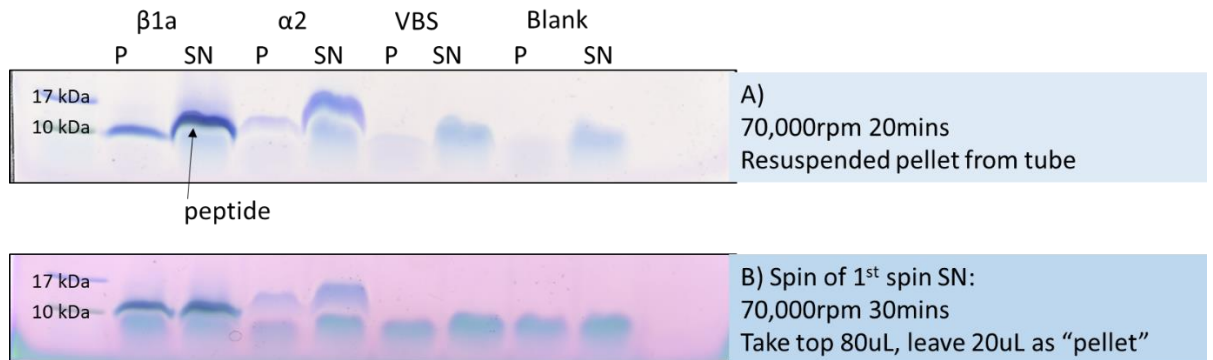


Figure 4.10: **First peptide LUV conjugation test** SDS-PAGE analysis of first attempt of making LUVs conjugated to integrin  $\beta$ 1a-tail (752-798), integrin  $\alpha$ 2-tail (1154-1181), TarP VBS1 (850-868) and no peptide (blank). A) Analysis after first spin cycle, P = pellet and SN = supernatant. B) Analysis of second spin of SN from (A) plus extra 20  $\mu$ L at the bottom of tube treated as ‘pellet’.

In an attempt to improve the efficiency of coupling the peptides to the LUVs we added an additional centrifuge cycle before the peptides were coupled to the lipids. This step was added to purify the vesicles from any contaminants, such as chloroform that may have remained from the vesicle formation steps. Following the coupling reaction the lipids were pelleted and analysed. Analysis revealed >50% of the peptide was in the pellet (fig. 4.11). Whilst the coupling efficiency was not the 100%, we expected the loss of peptide coupling resulted from the loss of lipids with ‘contaminants’ or loss of availability of the PEMCC maleimide head group due to formation of MLVs as opposed to LUVs. Despite the losses we decided the resultant peptide-conjugated LUVs would be suitable to carry on our investigation.

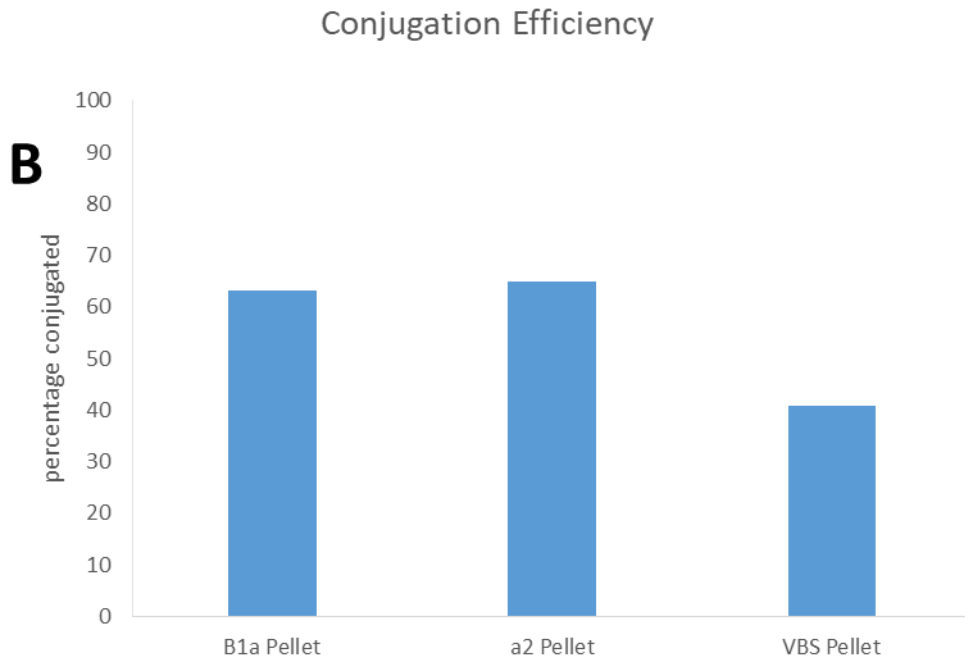
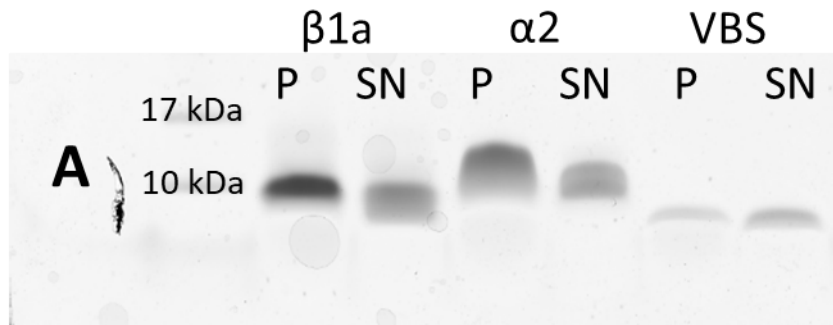


Figure 4.11: **Second peptide LUV conjugation test.** SDS-PAGE analysis of optimised attempt of making LUVs conjugated to integrin  $\beta$ 1a-tail (752-798), integrin  $\alpha$ 2-tail (1154-1181), TarP VBS1 (850-868) and no peptide (blank). A) SDS-PAGE analysis of peptides conjugated in pellet (P) and non-conjugated in supernatant (SN). B) Quantification of conjugation efficiency calculated as a percentage proportion of total peptide intensity on the gel, measured using ImageJ ( $n=1$ ).

#### 4.3.5 Optimisation: Co-sedimentation assay setup

Following preparation and purification of the peptide-conjugated LUVs, it was important to determine if they were suitable for measuring protein-peptide interactions at a membrane. To test the ability of the assay we used the well characterised interaction between talin F2F3 and the  $\beta$ -integrin tail as the model system (Calderwood et al., 1999). We hypothesised that every condition would pull down the protein, due to the basic membrane interacting residues on talin



F2F3 (Raucher et al., 2000), but we would expect to see a larger amount of protein in the pellet of the  $\beta$ 1a condition. In this assay 6  $\mu$ M of talin F2F3 was incubated for 30 mins at room temperature with 0.25 mg/mL lipids conjugated to integrin  $\beta$ 1a-tail, TarP VBS1 and no peptide (blank); following incubation the lipids were pelleted and analysed by SDS-page. SDS-page analysis showed a more intense band in the pellet fraction of integrin  $\beta$ 1a compared to the blank and TarP VBS1 (non-specific), suggesting the specific interaction between integrin  $\beta$ 1a and F2F3 led to an increase in pelleted protein (fig. 4.12 A-B). The experiment was then repeated with an increased lipid concentration from 0.25 mg/mL to 5 mg/mL, in an attempt to exacerbate the effect of the specific interaction between F2F3 and integrin. The higher lipid concentration led to a greater proportion F2F3 in the pellet of all conditions with a larger proportion of F2F3 in  $\beta$ 1a pellet condition than the other peptide conditions, consistent with the lower lipid concentration (fig. 4.12 C-D). Both lipid concentrations demonstrated an increase in F2F3 in the pellet of the  $\beta$ 1a condition, however to get the clearest difference we decided to do follow up experiments using a compromise lipid concentration of 0.325 mg/mL.

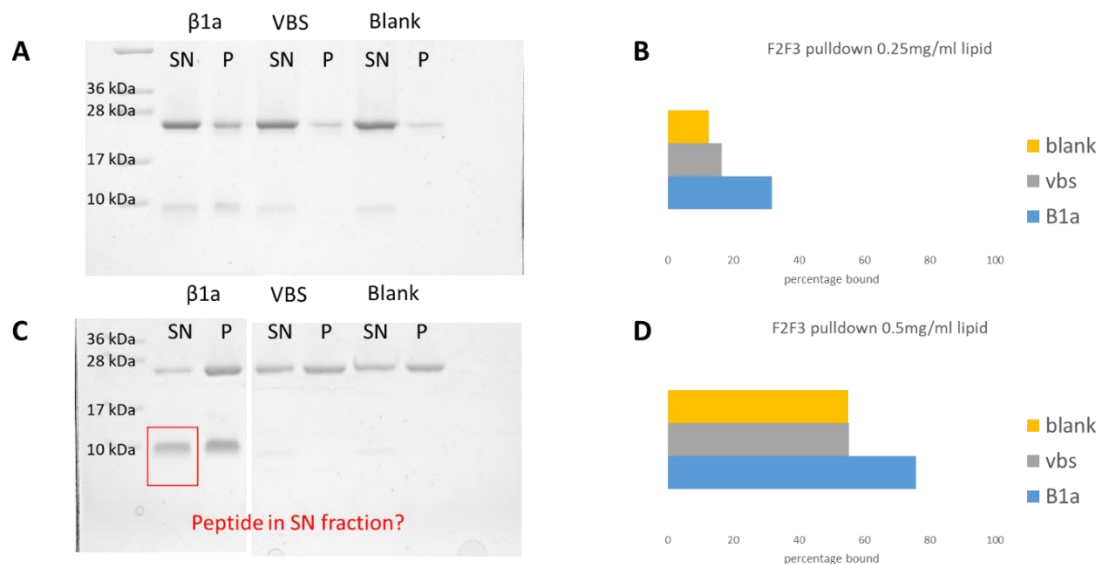


Figure 4.12: **Binding of F2F3 to lipid conjugated integrin.** Analysis of 6  $\mu$ M F2F3 binding to LUVs conjugated to integrin  $\beta$ 1a-tail (752-798), TarP VBS1 (850-868) and no peptide (blank). A) SDS-PAGE showing pull down assay using a target LUV concentration of 0.25 mg/mL. B) quantification of percentage bound from (A) based on band intensity, measured using image J. C) SDS-PAGE showing pull down assay using a target LUV concentration of 0.5 mg/mL. D) quantification of percentage bound from (C) based on band intensity, measured using image J (n=1). Peptide in SN fraction indicated in red box.

The F2F3-integrin model-cosed assay appeared relatively successful, with the desired result of increased F2F3 in the integrin  $\beta$ 1a condition; however, we were baffled by the presence of peptide in the SN band of the gel (fig. 4.12 C). After troubleshooting we hypothesised this was due to the 15 mM  $\beta$ -mercaptoethanol in the reaction buffer dissociating the maleimide bond. The  $\beta$ -mercaptoethanol was in the reaction buffer to prevent non-specific disulphide bonds occurring between free maleimide head groups and the target protein. To investigate whether we could abrogate the peptide dissociation the F2F3-integrin cosed assay was repeated with 2 mM  $\beta$ -mercaptoethanol, to maintain the reducing conditions without dissociating pre-formed maleimide bonds. Analysis of the resultant cosed assay demonstrated almost no peptide dissociation (fig. 4.13). Following this final optimisation we had a method for a basic setup of peptide-conjugated lipid coseds for investigating membrane-mediated interactions (section 3.3.6).

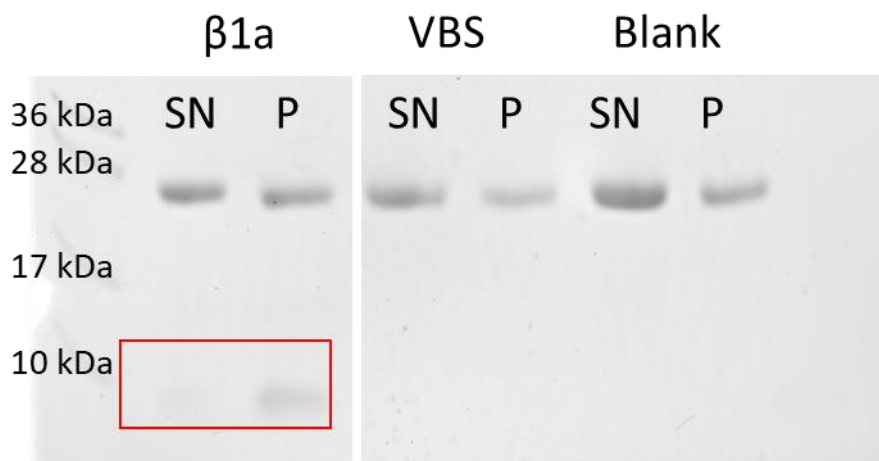


Figure 4.13: **Binding of F2F3 to lipid conjugated integrin  $\beta$ 1a optimisation.** SDS-PAGE analysis of 6  $\mu$ m F2F3 binding to LUVs conjugated to integrin  $\beta$ 1a-tail (752-798), TarP VBS1 (850-868) and no peptide (blank) in the presence of 2mM  $\beta$ -mercaptoethanol. Red box indicates the peptide bands.

#### 4.4 Discussion

Biochemistry can provide vital information on molecular interactions within complex systems, such as integrin mediated adhesions. However, important details of an interaction can be missed due to the difficulty of using biochemistry on certain systems. Integrin-mediated adhesions are a complex web of protein interactions (Horton et al., 2015). To unravel the web requires important

biochemical characterisation which can prove to be difficult. Here I have reported the development of an MST assay and a peptide-conjugated lipid coated assay that have increased the accessibility of previously difficult systems to work with.

#### 4.4.1 Using MST to provide quantitative data on protein-protein interactions.

We have designed a versatile MST assay that enables us to characterise interactions on different scales. We demonstrated the assays ability to characterise interactions between two large protein constructs using the talin-autoinhibition complex as a model; this has the potential to add an extra dimension to studies of protein:protein interactions and allows quick qualitative and quantitative information on novel protein-protein interactions. Furthermore, we were able to measure the binding between the very large FL-talin (540 kDa) as the target and the small KANK-KN peptide (5 kDa), demonstrating there is little restriction in size of the target molecule and its ligands, allowing use on all different sizes of proteins. Using MST to investigate interactions on different scales also enables the assessment of interactions in whole protein systems, taking into account the conformational state and steric hindrance as contributing factors for an interaction.

Additionally, we have demonstrated we can employ the MST assay to bypass difficulties of recombinant systems. We were able to biochemically characterise kindlin-1, an important adhesion protein complicated by a series of loops, which expresses <0.3 mg/l recombinantly. We were able to provide important quantitative data on the interaction between kindlin-1 and  $\beta$ -integrin, a well-studied interaction that has previously been difficult to quantify. Furthermore, we employed MST to provide key biochemical validation on the novel interaction between kindlin-1 and the EGFR, an interaction with high importance in keratinocyte proliferation (Michael et al., 2019).

The high sensitivity of MST makes it an ideal system for investigating difficult protein systems such as FL-talin and kindlin-1. As there is no size limit for target or the titrant protein, it is now possible to use the low expressing large proteins as the target molecule. Treating the difficult proteins as

the target molecule enables us to use them at low concentrations of around 50 nM; using the proteins at such a low concentration means the very low yields of recombinant protein we acquire is more than enough for multiple experiments. This feature of MST is advantageous over FP experiments in which the target has to be a small peptide and then the much larger proteins need an average titrant concentration of >100  $\mu$ M for most experiments.

#### 4.4.2 Peptide-conjugated lipid vesicles as an adaptable method for investigating the influence of membranes on molecular interactions

In addition to the MST assay, we have been developing a novel peptide-conjugated lipid co-sedimentation assay. Integrin-mediated adhesions form across the cell membrane, therefore, the membrane composition heavily influences interactions in and around these structures. Indeed, this has been demonstrated to be vital in talin-mediated integrin activation (Moore et al., 2012; Bouaouina et al., 2008). Therefore, we sought to develop an assay to investigate the membranes influence on interactions that occur at the membrane, which is accessible, relatively cheap and easy to carry out. Using the maleimide active lipid PE-MCC we have developed a method to covalently attach peptides to LUVs. Employing the peptide conjugated LUVs in a standard co-sedimentation assay, we have demonstrated how it is possible to assess the influence of the membrane on ligand binding, using the interaction between integrin  $\beta$ 1a and talin F2F3 as an example. Through multiple optimisation steps, we have weaned out complications in making the peptide-conjugated LUVs to produce a systematic method for their preparation.

The lipid composition of a cell membrane, and the large number of interactions that can occur at the membrane has a great diversity, we have therefore developed an assay which is highly adaptable. The obvious benefit of the assay is the ease with which the target peptides can be changed. This allows a relatively high throughput way of assessing the membranes influence on multiple interactions. Furthermore, an important use of this assay is to assess the effect of

different lipid environments on interactions; by changing the lipid composition of the vesicles, it is possible to investigate the influence of charge and presence of particular lipids. Membrane composition is an important driver of integrin-mediated adhesions (Thapa et al., 2012; Thapa and Anderson, 2012); using peptide-conjugated lipid vesicles to understand how different lipid compositions influence interactions could provide vital information on the formation and breakdown of adhesions.

Taking into consideration both assays we have developed, it is possible to combine the MST and peptide-conjugated LUVs together to gain a quantitative understanding of interactions at the membrane. MST has previously been used for investigating the influence of LUVs on binding interactions (Van Bogaart et al., 2012). By conjugating the LUVs with fluorescently labelled peptides it would be possible to treat the peptide-conjugated LUVs as the target and titrate the proteins of interest against them to calculate accurate binding affinities.

#### 4.4.3 Use of the newly developed assays

In summary, we have designed and demonstrated the values of two novel biochemical assays. Together these assays are providing vital new data for my projects, which was previously difficult/impossible to obtain. Indeed, throughout my PhD MST has enabled me to characterise a talin autoinhibition mutant in the FL-talin system, a novel interaction between the talin head and kindlin, and assess the effect of a talin R8 stability mutation on vinculin binding (Chapters 5 and 7). Additionally, the peptide-conjugated lipid vesicles have assisted with the characterisation of novel interaction between talin and  $\alpha$ -integrin tail (Chapter 6). These new assays are also contributing valuable data to other projects within our lab having been added to our biochemical suite of assays that is enabling us to provide novel biochemical characterisation within the adhesion field.

## Chapter 5: Regulation of the talin FERM domain

The N-terminal FERM domain of talin (talin head) is of vital importance for integrin control, due to the integrin activating interaction between talin F3 PTB region and the NPxY motif of the  $\beta$ -integrin cytoplasmic tail (Calderwood et al., 1999). The talin FERM domain consists of four domains (F0-F3) arranged in an atypical linear conformation (Elliott et al., 2010). Each individual domain of the talin head has a unique function providing tight regulation on the talin head and its interacting molecules (Gough and Goult, 2018). This regulation of the talin head provides another layer of control of talin-mediated integrin activation. In this chapter we utilise biochemical and structural techniques to investigate molecular interactions and conformational states of the talin FERM to provide intricate detail on regulatory events that may occur to the talin FERM domain.

### 5.1 Biochemical characterisation of talin autoinhibition mutant E1770A

In collaboration with the Tanentzapf lab from the University of British Columbia we aimed to investigate ubiquitously increased adhesion *in vivo* by disrupting talin autoinhibition. To do this we designed and tested a talin autoinhibition mutant (E1770A) that abrogates autoinhibition without effecting other important functions of talin. The effects of the E1770A mutation were studied using a mouse model. Details of the study can be found in (Haage et al., 2018).

#### 5.1.1 Introduction

The talin FERM domain is critical for inside-out integrin activation (Calderwood et al., 1999). This occurs through a direct interaction between talin F3 and the NPxY motif on the  $\beta$ -integrin cytoplasmic tail (Ginsberg, 2014; Calderwood, 2004). Talin then connects integrin to the rest of the adhesome through various protein:protein interactions along the rod and head domains (Gough and Goult, 2018). Talin activity, like many other adhesion proteins, is regulated by

autoinhibition. This autoinhibition state occurs through an intramolecular interaction between the FERM domain and the rod domain R9 (Goult et al., 2009a). Previous cell culture experiments have used targeted mutations to block this interaction, leading to an increase in integrin activity. (Goksoy et al., 2008; Kopp et al., 2010). Furthermore, *in vivo* studies using fly models with talin autoinhibition mutants (Ellis et al., 2014), revealed a gain-of-function phenotype, with morphogenetic defects occurring from too much, as opposed to too little, adhesion. Together these studies demonstrate abrogating talin autoinhibition provides an excellent method to increase cell-ECM adhesion.

### 5.1.2 E1770A mutant design

Structural investigations revealed autoinhibited talin has an overall compact doughnut-shaped conformation (Goult et al., 2013a), in which many intramolecular interactions stabilise the conformation. Critical to the closed conformation is a direct interaction between the integrin binding site on F3 and the rod domain R9. The F3:R9 autoinhibition interaction is mutually exclusive to the F3:integrin interaction (Goult et al., 2009a). Multiple point mutations in R9 and F3 have been identified that can block the interaction between the two domains *in vitro* (Goult et al., 2009a). One of the major intramolecular interactions identified is a salt bridge formed between a conserved glutamate residue on R9 (E1770) with lysine 318 (K318) on F3 (fig. 5.1); by mutating E1770 to an alanine (E1770A) we aimed to disrupt this salt-bridge relieving talin autoinhibition. Whilst the E1770A mutation has been demonstrated to directly disrupt the interaction between the individual R9 and F3 domains (Goult et al., 2009a), it hasn't been biochemically characterised in the context of full-length talin. To ensure viability for *in vivo* studies we wanted to confirm the mutation was first viable in the full-length protein.

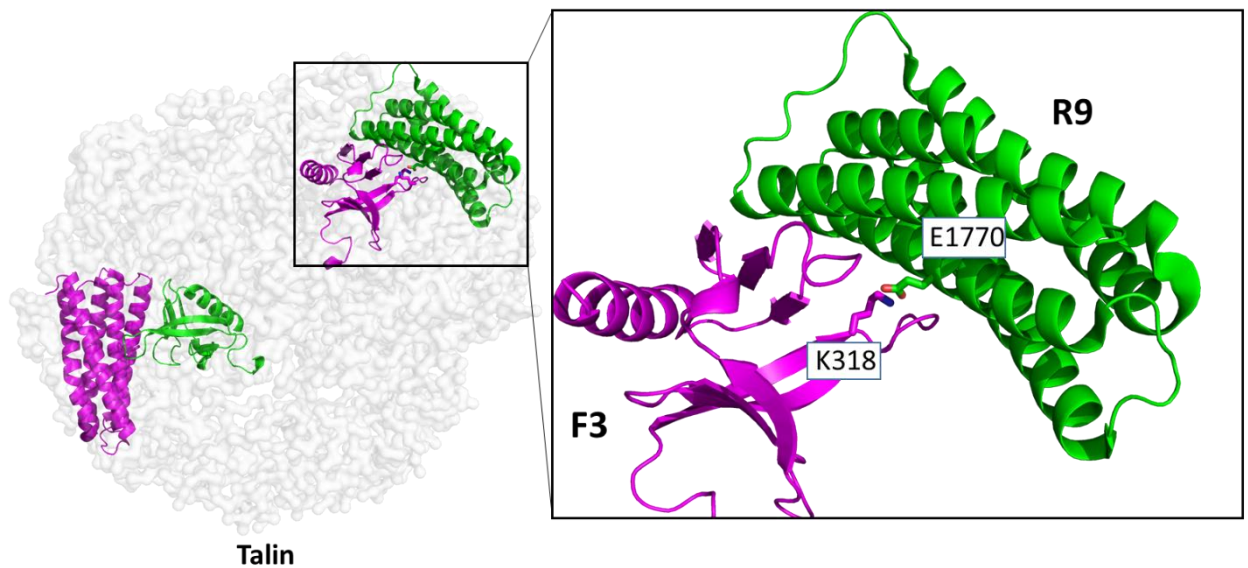


**Figure 5.1: Talin autoinhibition.** (A) Structural Model of the autoinhibited talin dimer. The grey envelope represents the autoinhibited dimer as visualised by Electron Microscopy. The two monomers are shown in green and purple. The two autoinhibitory intra-molecular interactions between F3 and R9 are shown. Inset: The structure of the F3:R9 complex (pdb: 4F7G) with the key buried salt bridge between R9 E1770 and F3 K318 highlighted. adapted from (Haage et al., 2018)

### 5.1.3 Recombinant expression of the E1770A full-length talin mutant and analysis

Due to the size (270 kDa) and complexity of full-length talin it was important to optimise the expression and purification conditions. To minimise proteolytic degradation we used a short induction protocol to express the FL-talin constructs, in this case 3 hours at 37°C following the addition of IPTG. To purify the proteins we used a batch purification method (section 3.2.4) that we found to be a more effective approach than FPLC purification for FL-talin constructs as it provided a higher yield of purified protein. The resulting ‘purified’ protein was analysed by SDS-PAGE (fig. 5.2a). SDS-PAGE revealed both the WT and E1770A FL-talin constructs were expressed and purified. The purified protein was then further analysed and purified by size exclusion chromatography. The chromatograms revealed both proteins had a similar retention time confirming they were full length and homogenous (fig. 5.2b). Unfortunately, the SEC-column used (HiLoad Superdex 200pg) was not able to clearly separate the folded and unfolded conformations so there was no observable difference in conformational state between the WT and mutant using this method.



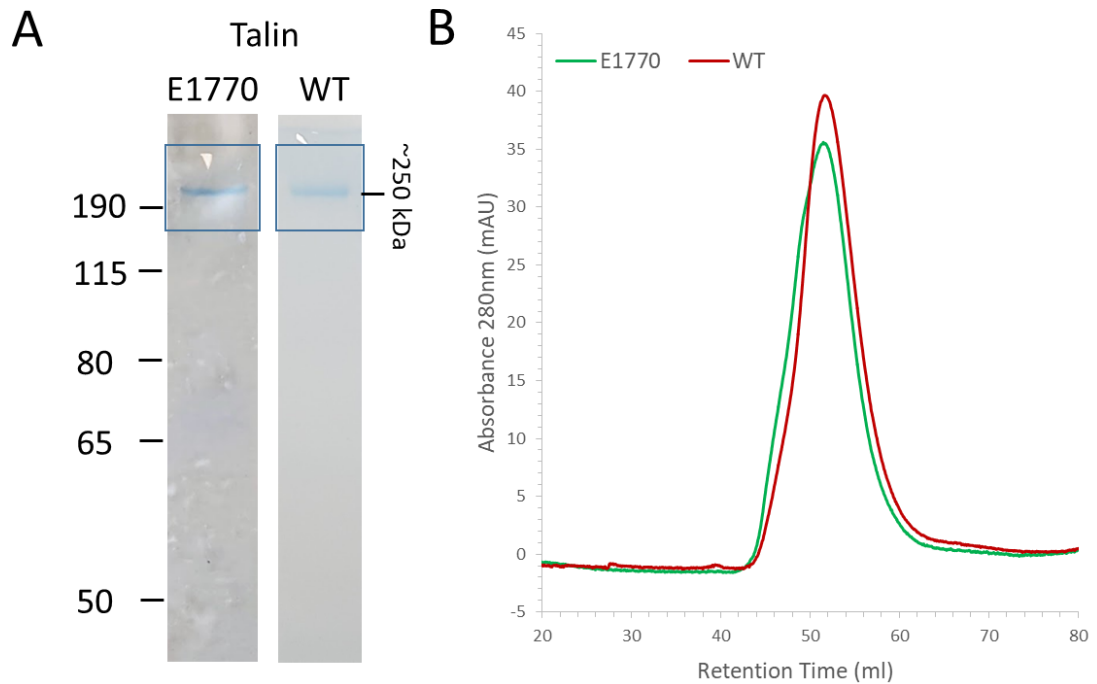


Figure 5.2: **Expression of E1770A mutant** A) Coomassie-stained SDS-PAGE gel of purified recombinant wild-type and E1770A Tln1. B) Gel filtration (Superdex 200) elution profiles of purified recombinant wild-type (red) and E1770A Tln1 (green).

#### 5.1.4 Investigating the propensity of the E1770A mutant to bind integrin

The E1770A mutant was designed to make a constitutively active talin. Active talin has a high propensity to activate integrin as the integrin binding site on talin F3 becomes exposed (Goksoy et al., 2008; Goult et al., 2009a). To ensure the E1770A mutant adopted the active conformation it was important to investigate the ability of the mutant to bind to integrin. Using the MST assay we have developed (section 4.1), it was now possible to gain quantitative measurement of integrin binding to the FL-talin constructs. In this assay recombinant integrin  $\beta$ 1a cytoplasmic tail (752-798) was titrated against 50 nM NT647-labelled FL-talin WT and E1770A. We observed that under the same conditions both the WT and E1770A bound to integrin (fig. 5.3A). E1770A bound to integrin with a slightly higher affinity ( $K_d = 10.96 \mu\text{M}$ ) than the WT ( $K_d = 14.8 \mu\text{M}$ ); suggesting the mutant had a greater propensity to bind to integrin, although the difference in affinity were only subtle and could be due to changes in protein concentration. Initial experiments were done in PBS buffer with 150 mM salt; this salt concentration has been demonstrated to unfold talin from its autoinhibited form before (Molony et al., 1987; Goult et al., 2009a), making it difficult to observe

differences between folded and unfolded talin as it is likely the majority of talin molecules in both the WT and mutant samples were in the open conformation. In an attempt to maintain WT talin in the autoinhibited state we repeated the experiment using a 50 mM salt concentration. Despite the lower salt concentration, both proteins bound to integrin with similar affinities, E1770A mutant bound with an affinity of  $K_d = 21.39 \mu\text{M}$  and the WT bound with an affinity of  $K_d = 14.4 \mu\text{M}$  (fig. 5.3B); the similar affinities we observed suggests that both proteins were still in the open conformation as in the higher salt conditions previously. Moreover, the low salt conditions led to increased aggregation in both the WT and mutant, making it difficult to attain an accurate result. Together, our results demonstrate the mutant is still able to bind to integrin at a similar affinity to the WT. However, we were unable to determine a difference in integrin binding ability between the mutant and the WT as we were limited by the sensitivity of the FL-talin system *in vitro*. Despite us not being able to observe a significant difference *in vitro* between the mutant and WT FL-talin constructs, mice containing the E1770A mutation were then generated for *in vivo* studies and demonstrated a significantly different phenotype.

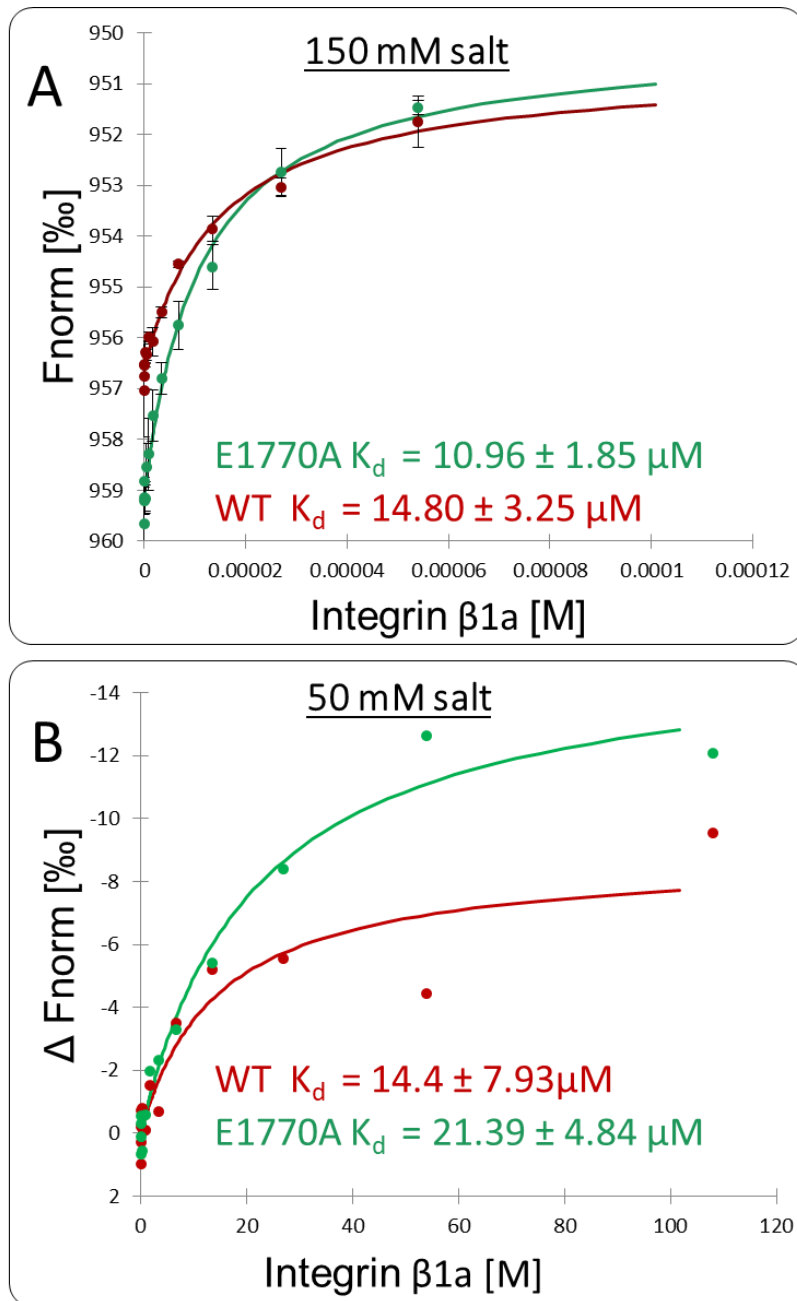


Figure 5.3: **Integrin binding to E1770A.** MST binding curves showing integrin  $\beta$ 1a binding to 50 nm NT647-labelled FL-talin WT (red) and E1770A (green) in (A) 150 mM salt ( $n=3$ ) and in (B) 50 mM salt phosphate buffer ( $n=1$ ). Data was analysed by nanotemper analysis software to a  $K_d$  fit model. Dissociation constants  $K_d$  +/- confidence are indicated in the legend (ND = not determined)

### 5.1.5 Conclusions from the mouse study

Mice containing the mutation were viable, although analysis of the mouse embryonic fibroblasts (MEFs) revealed multiple defects associated with increased FA maturation and stability, in addition to increased integrin activation. Moreover, the MEFs containing the mutation had stronger adhesion to substrate, cell spreading and migration defects, and abnormal morphology.

These defects led to wound healing delays in the mice, revealed from *in vivo* wound healing assays. Lastly, the mutant containing MEFs had reduced traction force generation and dysfunctional actin dynamics (fig. 5.4).

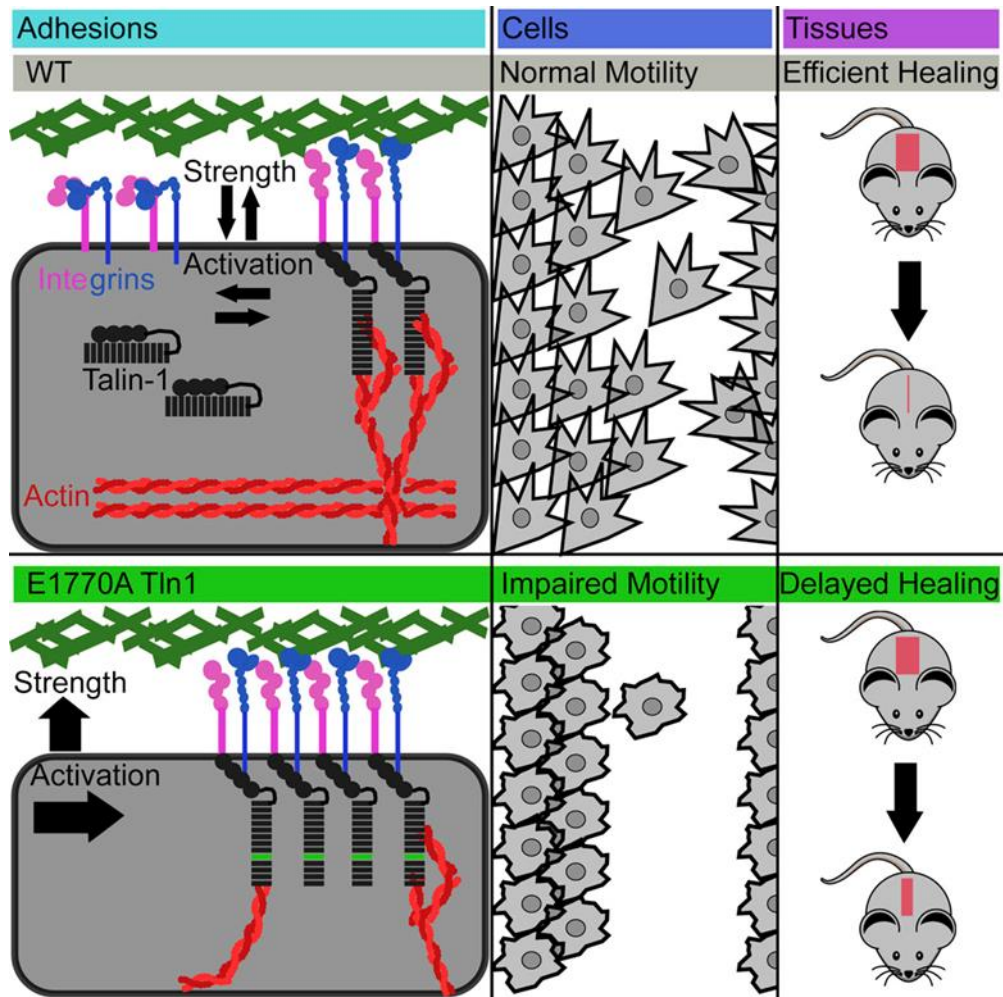


Figure 5.4: Summary of E1770A *in vivo* findings. Taken from (Haage et al., 2018)

Together, these results demonstrate the importance of the layers of regulatory mechanisms involved in integrin activation by talin. They exhibit the importance of talin autoinhibition as a function to control integrin regulation via the talin FERM domain. However, there were no major morphological defects from the mutation. It could have been presumed that a constitutively active talin IBS1 leads to constitutively active integrin which would lead to major defects throughout the mouse; indeed, the same E1770A mutation and other talin autoinhibition mutants led to defects in dorsal closure in flies and disruption of mechanical forces (Ellis et al., 2014;

Goodwin et al., 2016). The lack of adverse defects from the constitutively active talin demonstrates there are more regulatory mechanisms involved in integrin activation than just talin autoinhibition. By using mutations that effect single regulatory steps we have the means to unravel the complex nature of integrin activation.

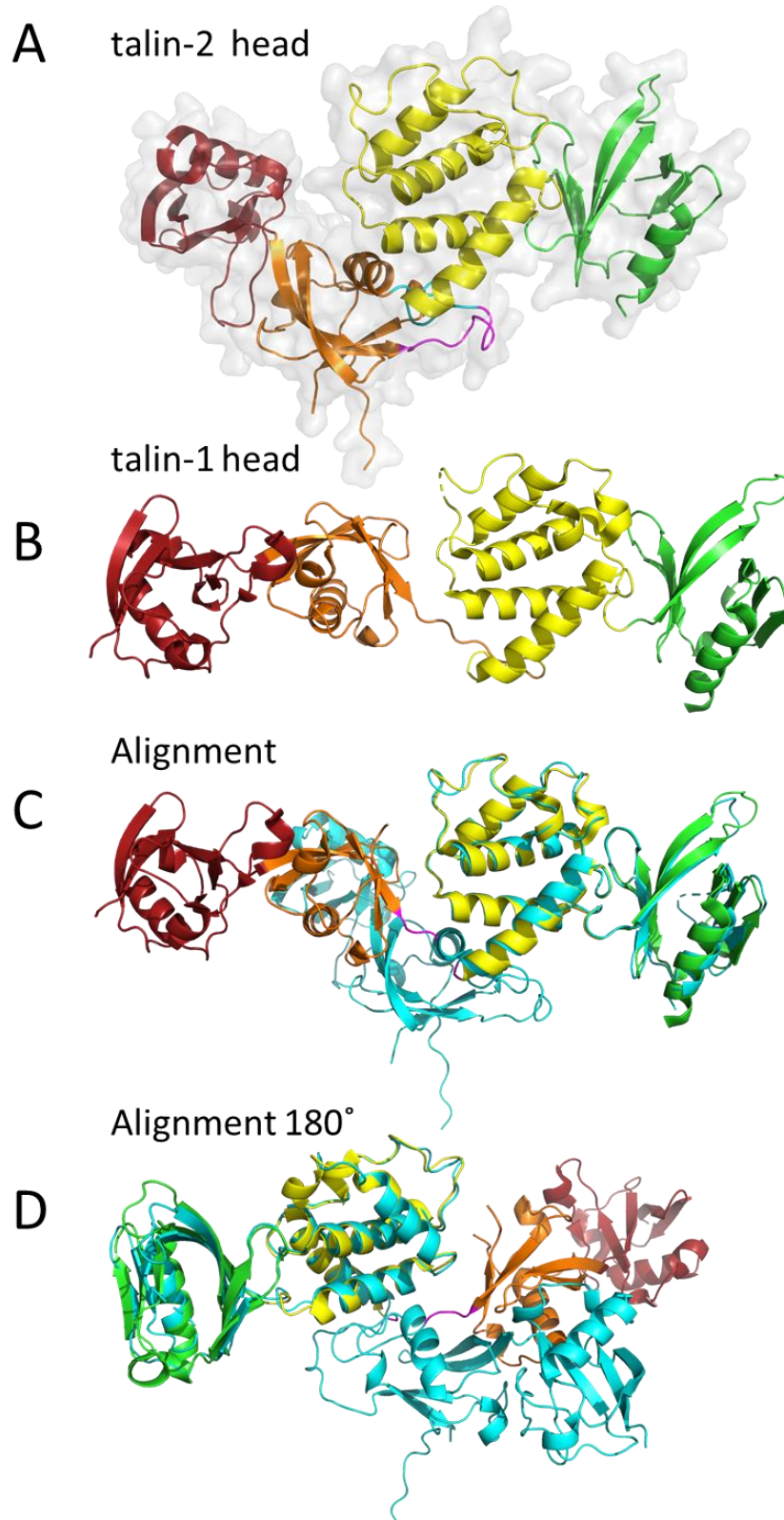
## 5.2 Talin FERM domain is regulated through a rotational axis

In this section we report on the structural characterisation of the talin-2 FERM domain. The atomic structure of the talin-2 head revealed a novel 'twisted conformation' as opposed the previously solved linear structure of talin-1 head (Elliott et al., 2010). We provide evidence that both talin isoforms can adopt the twisted and linear conformations; suggesting that the difference in the two structures is due to conformational plasticity of the talin head, which may be a form of regulation on the ability of talin to activate integrin.

### 5.2.1 Crystal structure of talin-2 FERM reveals novel conformation

The atomic structure of the talin-1 head demonstrated all four lobes of the FERM domain adopted an atypical linear conformation (Elliott et al., 2010), much different to other FERM domains which typically form a more cloverleaf like shape. The F2 and F3 domains of talin contain a series of basic residues that enables the region to interact with the negatively charged, PIP2 enriched membrane (Calderwood et al., 2002). Additionally, talin F1 contains a large disordered loop that forms a basic helix upon interaction with the negatively charged membrane (Goult et al., 2010a). This open structure of the talin FERM allows simultaneous binding of integrin to F3 and the basic surfaces on F1-F3 to the PIP2 enriched membrane. The talin-1 structure is the only linear FERM domain to be solved so far. The talin-1 head and talin-2 head have high sequence similarity, with only subtle differences in the sequence of the two (fig. 5.7). Thus, we hypothesised that the talin-2 FERM domain would adopt a similar conformation, helping us to further structurally understand linear FERM domains. To test this hypothesis, crystal trials were set up to gain an atomic structure of the talin-2 FERM domain. Suitably sized crystals were grown (conditions in table 3.3) and

picked for data collection. The crystal diffracted to 2.26 Å in the hexagonal space group P6<sub>3</sub>, containing one molecule of the protein within the asymmetric unit. The structure was solved by molecular replacement using the talin-1 head structure (PDB 3IVF) (fig. 5.5; table 5.1).



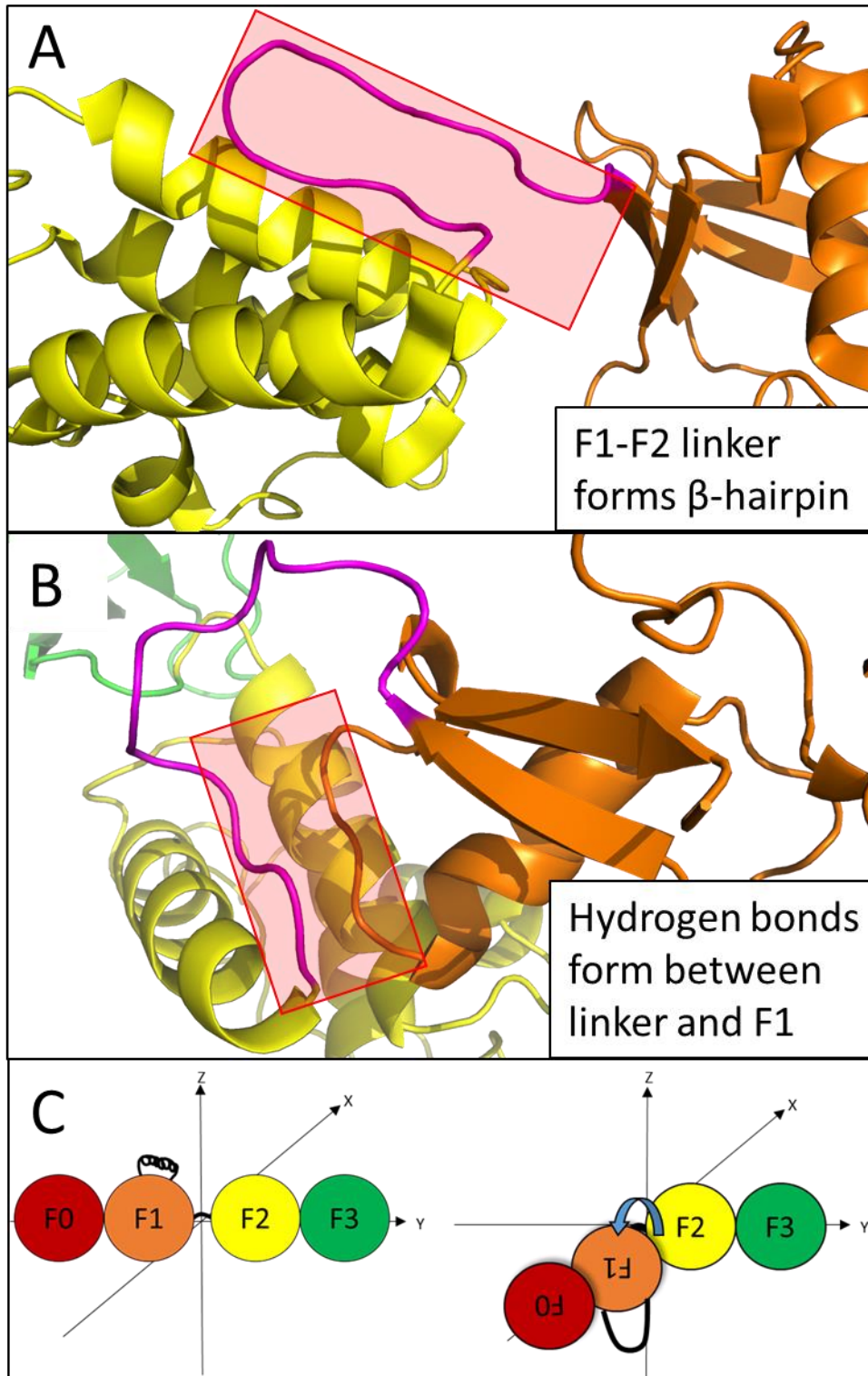
*Figure 5.5: Crystal structure of the talin-2 head. (A) Crystal structure of talin-2 head Cartoon representation within transparent surface (grey); coloured by domain: F0 (red), F1 (orange), F2 (yellow) F3 (green). (B) crystal structure of talin-1 head (3IVF), coloured as in A. (C) Alignment of talin-2 structure (cyan) with talin-1 structure (coloured by domain); (D) reverse view of alignment (C).*

Table 5.1: **Statistics from crystal structure of the talin 2 head.** Data collected from a single crystal. *A* Values in parentheses are for highest-resolution shell. *B* Values in parentheses indicate percentile scores as determined by Molprobit.

<b>Data collection</b>	
Synchrotron and BeamLine	Diamond Light source; I03
Space group	P65
Molecule/a.s.u	1
<b>Cell dimensions</b>	
<i>a</i> , <i>b</i> , <i>c</i> (Å)	58.420, 58.420, 161.921
$\alpha$ , $\beta$ , $\gamma$ (°)	90, 90, 120
Resolution (Å)	2.39 – 48.29
<i>CC</i> (1/2)	0.997 (0.999)
Completeness (%)	95.9 (99.7)
<b>Refinement</b>	
Resolution (Å)	2.39
No. reflections	11245
<i>R</i> <sub>work</sub> / <i>R</i> <sub>free</sub>	0.18/0.27
No. atoms	
Protein	2924
Water	56
<b>B-factors (Å<sup>2</sup>)</b>	
Protein	59.55
Water	55.58
R.m.s. deviations	
Bond lengths (Å)	0.014
Bond angles (°)	1.87
<b>Ramachandran plot</b>	
Favoured/allowed/outlier (%)	95.48/ 4.24/ 0.28
Rotamer outliers (%)	10.22
<b>Molprobit scores</b>	
Protein geometry	2.84
Clash score all atoms	15.75
PDB accession no.	Pending submission



Strikingly, the final structure revealed a novel alternative 'twisted' conformation. In this conformation the ubiquitin like domains F0 and F1 are inverted 180° relative to F2-F3 when compared to the talin-1 head structure. However, the talin-2 head still adopts a more linear conformation than the standard cloverleaf-like FERM domain structure. The structure shows good agreement between each individual domain to equivalent talin-1 domains, with both F2F3 and F0F1, aligning almost perfectly between the two isoforms, supporting the idea the FERM domains exist as double domain modules. Despite the talin-2 construct crystallised contained the F1-loop, the loop was not visible in the density, suggesting it is still flexible in this conformation and does not form the membrane binding helix. However, it is apparent from the start and finish of the loop that it is located on the complete opposite side of the talin head to that of talin-1. Interestingly, the main difference between the talin-1 and talin-2 head structures is the large linker region between F1 and F2. In talin-1 the linker forms a  $\beta$ -hairpin leading to a separation distance between the two domains of around 28 Å, whereas in talin-2 the linker is more loop like and the F1 and F2 domains brought into a much closer proximity of around 7 Å of each other. The structure demonstrates the talin-2 F1-F2 linker does not form the  $\beta$ -hairpin like that in the talin-1 structure (fig. 5.6 A); instead the C-terminus of the linker forms hydrogen bonds with the F1 domain, such as between asparagine-125 and aspartic acid-206, holding the F1 domain in close proximity to F2 (fig. 5.6 B). This linker rearrangement in the talin-2 structure leads to a rotation of F0-F1 180° on the Z-axis and 90° on the XY axis relative to that of the talin-1 structure (fig. 5.6C). It is this rotation that gives the structure the 'twisted' appearance.



*Figure 5.6: The F1-F2 linker controls the conformational state of the talin head. A) Zoom in on the F1-F2 linker from talin-1 head (PDB: 3IVF) showing the F1-F2 linker (purple) forming a beta-hairpin (red box). B) Zoom in on talin-2 head structure, showing hydrogen bonds (red box) form between residues on the C-terminus of the F1-F2 linker and the F1 domain (orange). (C) Schematic diagram demonstrating the rotation of the talin head domains due to the linker rearrangement.*

### 5.2.2 The F1-F2 rotational axis alludes to conformational regulation of the talin head

As previously stated, both talin-1 and talin-2 heads have a high sequence similarity of 92.3% (fig. 5.7A). Moreover, the F1-F2 linker region is completely conserved between both talin isoforms. This suggests that both isoforms can adopt the 'twisted' and linear conformation. Indeed, the small angle x-ray scattering data from (Elliott et al., 2010) demonstrates talin-1 has already been observed in a compact conformation, consistent with the twisted conformation (fig 5.7B). Together, this alludes to a novel form of conformational regulation on the talin head, present in both isoforms. The conformational state of the talin head may dictate its ligand binding properties much like that observed previously in the talin rod domain R3, switching ligand binding between RIAM in the folded and vinculin binding in the unfolded conformation (Goult et al., 2013b). What regulates the rotational conformation is not fully understood although it most likely comes from external stimuli.

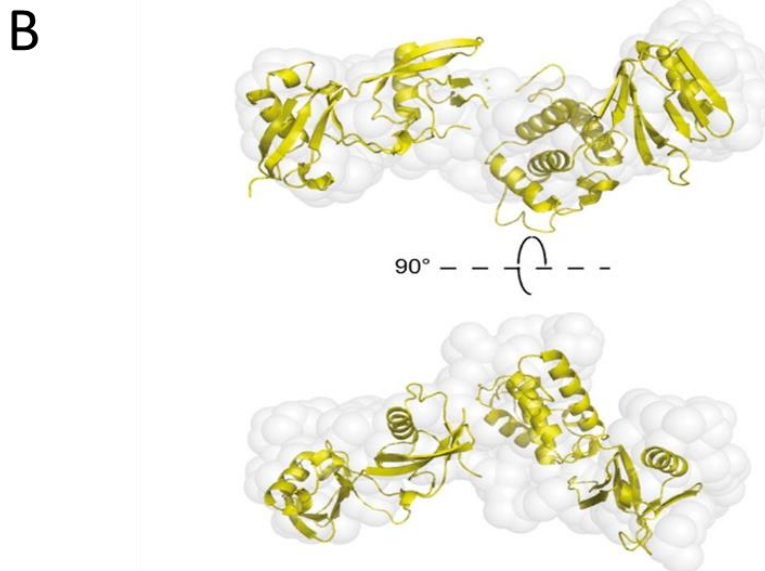
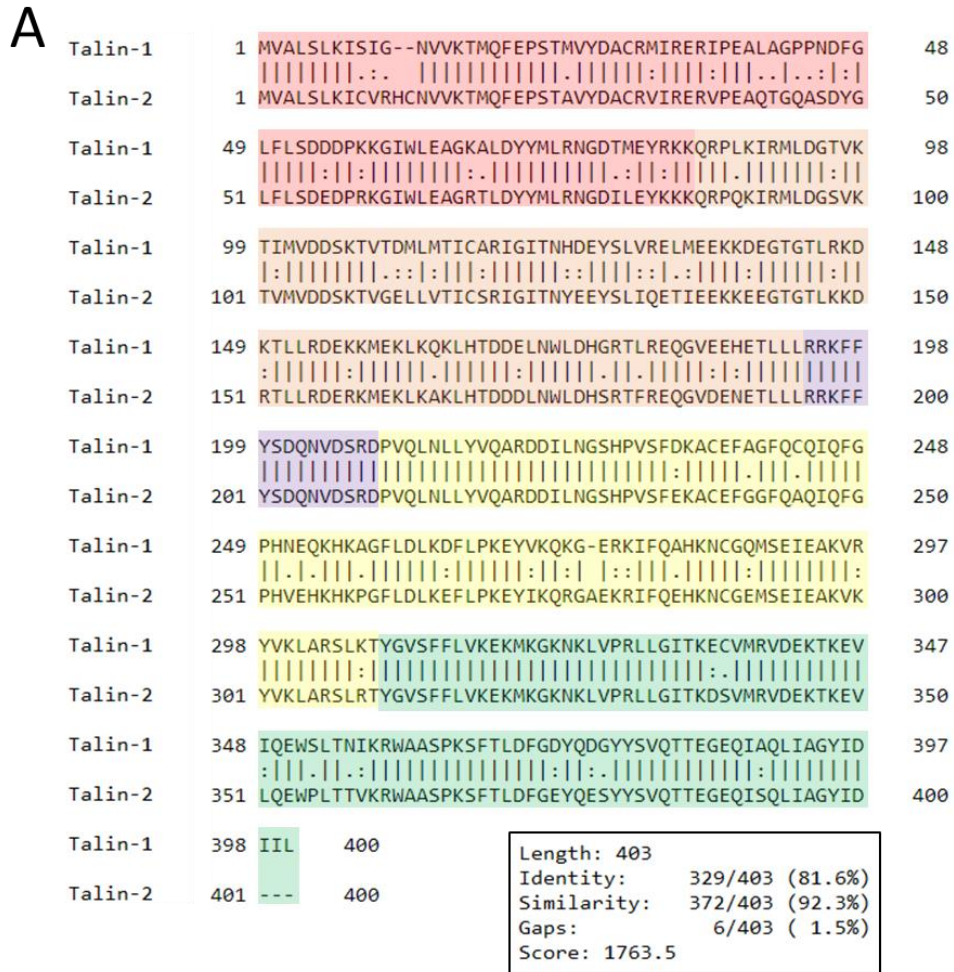


**Figure 5.7: Talin-1 can also adapt the ‘twisted’ conformation.** (A) Pairwise sequence alignment of mouse talin-1 (1-400) aligned to mouse talin-2 (1-400) generated using EMBOSS Needle (Madeira et al., 2019). F0 (red), F1 (orange), F1-F2 linker (purple) F2 (yellow) F3 (green) (B) SAXS data taken from (Elliot et al., 2010) demonstrating talin 1 in a compact’ conformation similar to the ‘twisted’ conformation. GASBOR shape envelope (transparent gray surface) superimposed with the BUNCH model (yellow). The two orientations shown are related by a 90° rotation around the horizontal axis.

### 5.2.3 Involvement of the F1-loop in conformational regulation

It has previously been demonstrated the F1-loop can form an  $\alpha$ -helix that binds to the cell membrane, an interaction critical for talin-mediated integrin activation (Goult et al., 2010a). The F1-loop is positioned in opposite directions in both structures, suggesting it may have a critical role in the conformational state of the talin head. In the 'twisted' conformation the loop is facing the opposite direction to that of the positively charged PIP2 binding surface located on F2-F3, suggesting the 'twisted' conformation would prevent the F1 loop from engaging the membrane, thereby disrupting talin-mediated integrin activation. The F1-loop has previously been demonstrated to contain two phosphorylation sites T144 and T150 (Ratnikov et al., 2005). Phosphorylation of the loop would lead to a negatively charged loop which could repel from a negatively charged membrane or destabilise the helix that binds to the membrane. Indeed, previous studies have demonstrated a phosphomimetic mutant, in which the T144 and T150 residues are substituted with negatively charged glutamate residues, blocks the interaction between F1 and the membrane (Goult et al., 2010a).

### 5.3 Investigating the effects of lipid composition on the talin head membrane binding

The presence of PIP2 in the cell membrane is crucial for talin-mediated integrin activation, providing a net negative charge to which the talin head is oriented (Moore et al., 2012; Bouaouina et al., 2008). Furthermore, talin translocation to the membrane and focal adhesion assembly are regulated by the PIP-kinase type1y maintaining membrane PIP2 enrichment (Ling et al., 2002; Thapa et al., 2012; Di Paolo et al., 2002). As aforementioned, the talin head interacts with a PIP2 enriched membrane through the F1-F3 domains, it is possible that a varying level of net negative charge at the membrane can effect these interactions, which may in-turn influence the conformational state of the talin head. To assess the influence of membrane charge on the talin

head domains we used a multilamellar-vesicle (MLV) co-sedimentation experiment similar to that described in (Anthis et al., 2009).

In this assay, talin constructs F0-F3, F2-F3 and F0-F2 were pre-incubated with MLVs composed with a combination of the neutral charged POPC and the negatively charged POPS: 0% PS, 20% PS, 50% PS and 100% PS. (Anthis et al., 2009) previously demonstrated PS can be used to replicate the negative charge carried by PIP2. Thereby, increasing PS concentration mimics an increase in membrane PIP2 enrichment. Following incubation with the talin constructs the MLVs were pelleted, along with any protein bound to the MLVs. The pelleted fraction was compared to the supernatant (SN) fraction using SDS-PAGE and results processed using ImageJ as described in section 3.3.5 (fig. 5.8A). As expected, there was very little protein from any of the constructs bound to the 0% PS MLVs as there was no net negative charge for the talin head to interact with. Both F2F3 and F0-F3 demonstrated a similar trend; increased lipid binding from 0-20% PS and then a further increase from 20-50% PS; following the rise there was then a slight drop from 50-100% PS, suggesting the constructs do not bind as tightly to a heavily charged membrane; alternatively, the 100% PS MLVs were altered in some way without the presence of PC that disrupted the ability of talin to bind. Interestingly, F0-F2 bound tightest to 20% PS MLVs and demonstrated almost no binding to 100% PS. The significant drop in F0-F2 lipid binding from 50% PS to 100% PS suggests the lipid binding surfaces on F2 and the F1-loop are disrupted by the heavily charged membrane.

These lipid binding results suggest each lipid binding domain in the talin head responds to the membrane charge individually, a property that might facilitate different conformations of the talin head. At a low charge, represented by 20% PS, F1 and F2 bind to the membrane with the strongest affinity; as polarisation increases to the equivalent of 50% PS, all domains bind to the membrane with a high affinity; as polarisation increases further to the equivalent of 50% to 100% PS there appears to be loss of F1 and F2 binding, however F3 may remain bound (fig. 5.8C). It is

possible the loss of F1-F2 membrane binding is due to the increase in negative charge

destabilising or repelling the helix of the F1-loop, possibly leading to conformational change.

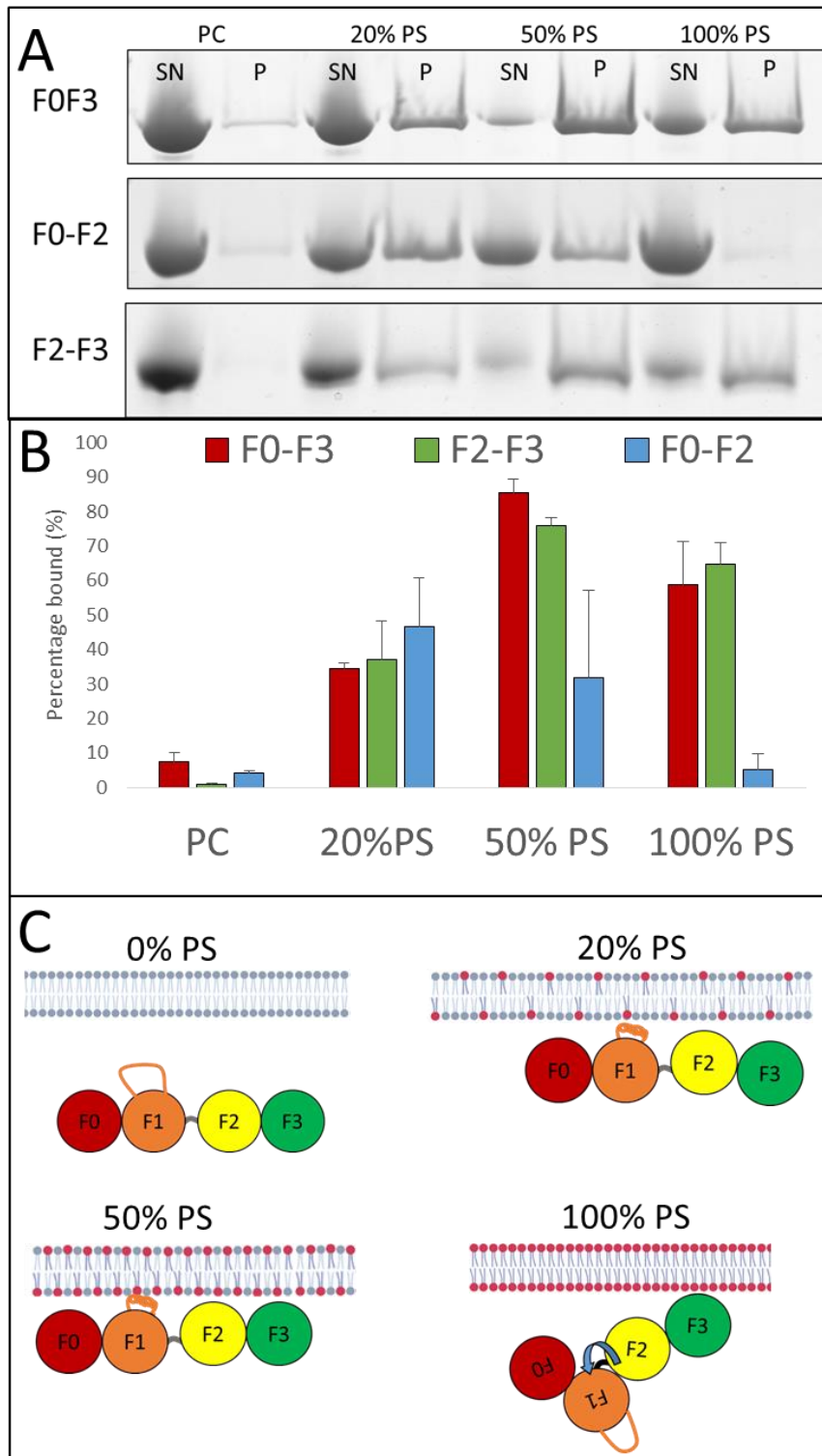


Figure 5.8: **Effect of membrane polarisation on talin conformation.** (A) Coomassie-blue stained SDS-PAGE analysis of MLV co-sedimentation assay of 12  $\mu$ M talin F0-F3, F0-F2 and F2F3 binding to 0%, 20%, 50% and 100% PS MLVs. [P] = pellet fraction, [SN] = supernatant. (B) Quantitative analysis of co-sedimentation assay using ImageJ; F0-F3 (red), F2-F3 (green) and F0-F2 (blue); error bars represent SEM (n=3). (C) schematic diagram describing polarisation effect on talin head conformation theory. At 0% PS the head does not bind to the membrane; at 20% PS F1-loop and F2 fully bind to the membrane; at 50% all lipid binding surfaces in the talin head are fully bound to the membrane; at 100% PS membrane repels F1-loop and/or F2 but F3 remains bound.

## 5.4 Novel interaction between kindlin and the talin FERM domain

### 5.4.1 Introduction

Kindlin, like talin, is a FERM domain containing protein, consisting of four lobes (F0-F3) (Goult et al., 2009b). Additionally, kindlin binds to the  $\beta$ -integrin cytoplasmic tail, like talin via the PTB like fold in the F3 domain (Montanez et al., 2008). However, kindlin binds to the membrane distal NxxY motif as opposed to the membrane proximal NPxY that talin binds to (Fukuda et al., 2014; Li et al., 2017a), enabling both talin and kindlin to bind to integrin simultaneously (Bledzka et al., 2012; Theodosiou et al., 2016). This coordinated binding event has proved vital for integrin activation (Calderwood et al., 2013). Remarkably, whilst the role of talin binding in activating integrin is relatively well understood (Anthis et al., 2009; Kalli et al., 2010, 2011; Lau et al., 2009), the necessity of kindlin binding is yet to be fully elucidated (Sun et al., 2019; Rognoni et al., 2016).

The coordinated integrin binding event that occurs between talin and kindlin places the two proteins into close proximity of each other; indeed, there are only eight residues separating the membrane proximal NPxY motif and the membrane distal NxxY motif. We hypothesised that for talin and kindlin to be in such a close proximity it is likely that the two proteins interact. As previously discussed in section 4.2, using MST we now have a biochemical assay that we can use to probe kindlin interactions. Through this assay we aim to gain biochemical insight into a novel interaction between talin and kindlin.

### 5.4.2 The talin FERM domain binds to kindlin-1

To confirm there was a direct interaction between the talin head and kindlin-1 we used an MST assay, in which recombinant talin-1 FERM (1-400) was titrated against NT647-labelled kindlin-1. The talin head bound with a relatively tight affinity,  $K_d = 8.65 \mu\text{M}$  (fig 5.9).



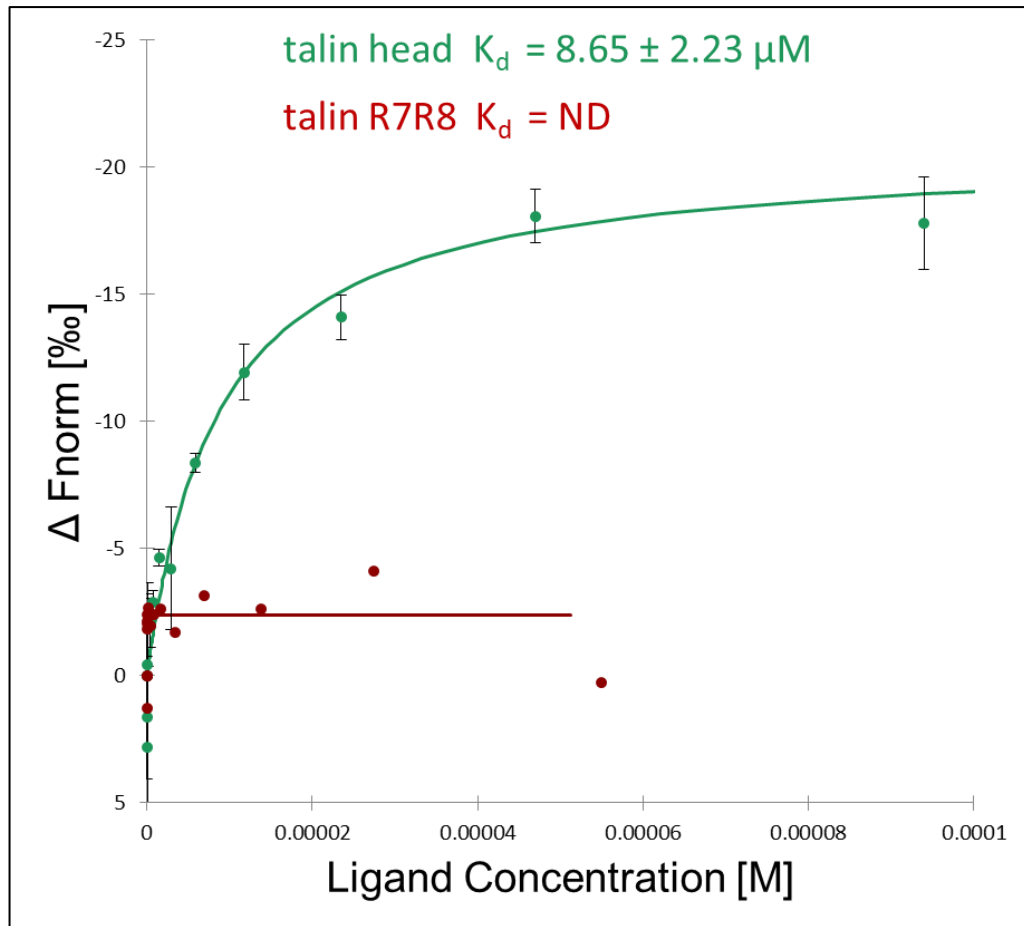


Figure 5.9: **Talin-1 head binds kindlin-1.** Binding of 50 nm NT 647-labelled kindlin-1 to talin head (green,  $n=3$ ) and talin R7R8 (non-specific) (red,  $n=1$ ). Data was analysed by nanotemper analysis software to a  $K_d$  fit model. Dissociation constants +/-  $K_d$  confidence are indicated in the legend (ND = not determined).

After confirming there was a direct interaction between talin and kindlin-1, we wanted to establish contact areas in the interaction. To do this we needed to test the separate domains of the two proteins. Separating talin into individual domains proved much easier than separating kindlin domains, as the kindlin-1 F2F3 construct was not obtainable from recombinant expression and purification. Therefore, we sought to establish the talin binding sites involved first. In this experiment talin F1 and F2F3 were titrated against NT647-labelled kindlin-1. Interestingly, we found both talin F1, and F2F3 constructs bound to kindlin-1 (fig. 5.10). Talin F1 had a binding affinity of  $K_d = 13.83 \mu\text{M}$  and F2F3 an affinity of  $K_d = 4.06 \mu\text{M}$ ; similar to that of the whole head  $K_d = 6.09 \mu\text{M}$ . This data suggests that multiple domains are involved in the interaction between the two proteins, as opposed to the interaction being specific to one single domain. Identification of multiple domains being involved in the interaction between talin and kindlin raises the possibility

of the interaction being conformation specific. However, it is also possible that the talin-kindlin interaction may be domain specific, enabling a stoichiometry of 1:2; in this case our one site total  $K_d$  fit model of kindlin binding to the whole talin head does not measure the affinities of the each binding site independently but rather the affinity of the two interactions together.

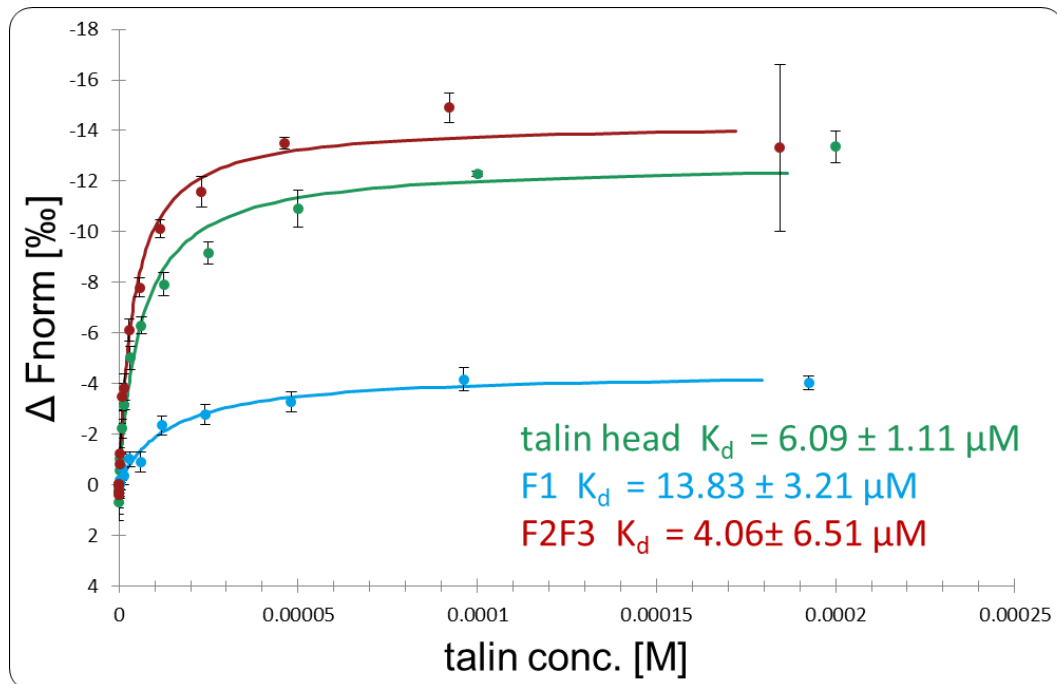


Figure 5.10: **Multiple talin domains bind to kindlin.** Binding of 50 nm NT647- labelled kindlin-1 to talin head (green), talin F2F3 (red) and talin F1 (blue). Data was analysed by nanotemper analysis software to a  $K_d$  fit model. Dissociation constants +/-  $K_d$  confidence are indicated in the legend ( $n=3$ ).

#### 5.4.3 The talin F1-loop is involved in kindlin binding

After demonstrating that talin F1 binds to kindlin, we wanted to investigate whether the F1-loop was involved in direct binding. As aforementioned, the F1-loop is vital for integrin activation (Goult et al., 2010a), we also hypothesised the F1-loop is involved in coordinating the conformation state of the talin head at the cell membrane. We were interested to determine whether the F1-loop was also involved in the talin-kindlin interaction. To investigate the role of the F1-loop on the interaction we used a talin head construct with the F1-loop deleted ( $\Delta 139-168$ ). Using the MST assay, talin head ( $\Delta 139-168$ ) was titrated against NT647-labelled kindlin-1. The mutant bound with a  $K_d$  of  $27.3 \mu\text{M}$ , four times weaker than the WT which bound with a  $K_d$  of

6.69  $\mu\text{M}$  (fig. 5.11A). To confirm the lower affinity was as a result of a direct interaction between the F1-loop and kindlin and not due to adverse effects of deleting the loop, such as a conformational switch, we repeated the experiment using the individual F1 domain with the loop deletion ( $\Delta 139-168$ ). The F1 mutant bound with a  $K_d$  of 35.93  $\mu\text{M}$ , three times weaker than the WT that bound with a  $K_d$  of 12.99  $\mu\text{M}$  (fig. 5.11B).

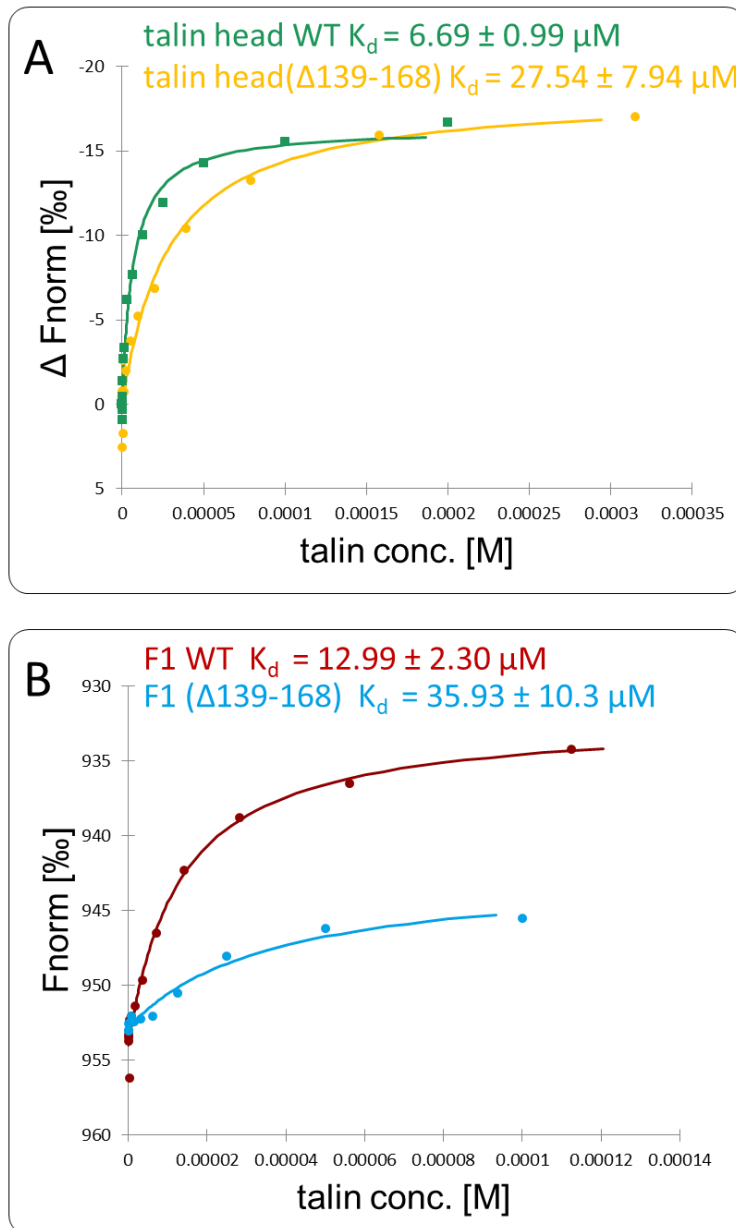


Figure 5.11: **Talin F1-loop binds to kindlin.** Binding of 50 nm NT647-labelled kindlin-1 to (A) talin head (green), talin head ( $\Delta 139-168$ )(yellow), (B) talin F1 (red) and F1 ( $\Delta 139-168$ )(blue). Data was analysed by nanotemper analysis software to a  $K_d$  fit model. Dissociation constants +/-  $K_d$  confidence are indicated in the legend (n=1).

The loop-deletion results suggest there is a direct interaction between the talin F1-loop and kindlin-1. Whether this interaction holds the talin F1-loop away from the membrane or stabilises the F1-loop at the membrane, requires further investigation. If kindlin holds the F1-loop away from the membrane the complex may function as a negative regulator of talin mediated integrin activation, as the loop binding to the membrane is necessary for integrin activation (Goult et al., 2010a). However, if kindlin is in fact stabilising the F1-loop at the membrane, the talin-kindlin complex may behave as an integrin activating complex. It is also possible, kindlin may have a role in both these scenarios and regulates the talin head conformation.

#### 5.4.4 Phosphorylation of the F1-loop affects kindlin binding

We have demonstrated talin and kindlin interact across multiple domains and the interaction involves the F1-loop. Next we wanted to consider how this interaction is regulated. Taking into consideration the phosphorylation sites on the F1-loop (Ratnikov et al., 2005), we hypothesised phosphorylation may have a role in the interaction. To investigate this we used a phosphomimetic talin head construct and F1 construct, where the threonine-144 and threonine-150 phosphorylation sites were mutated to glutamate residues (T144E/T150E), providing the residues with a net negative charge representative of phosphorylation (Goult et al., 2010a). In this experiment talin head (T144E/T150E) and talin F1 (T144E/T150E) were titrated against NT647-labelled kindlin-1. The phosphomimetic talin head bound with a weak affinity  $K_d = 55.6 \mu\text{M}$ , almost ten times weaker than the WT  $K_d = 6.69 \mu\text{M}$  (fig. 5.12A). Furthermore, the F1 (T144E/T150E) mutant also bound kindlin with a weaker affinity,  $K_d = 22.69 \mu\text{M}$ , than the WT F1,  $K_d = 12.99 \mu\text{M}$  (fig. 5.12B). These results suggest that talin head phosphorylation prevents kindlin binding. If this is the case then phosphorylation of the F1-loop could be a way of negatively regulating the kindlin-talin interaction.

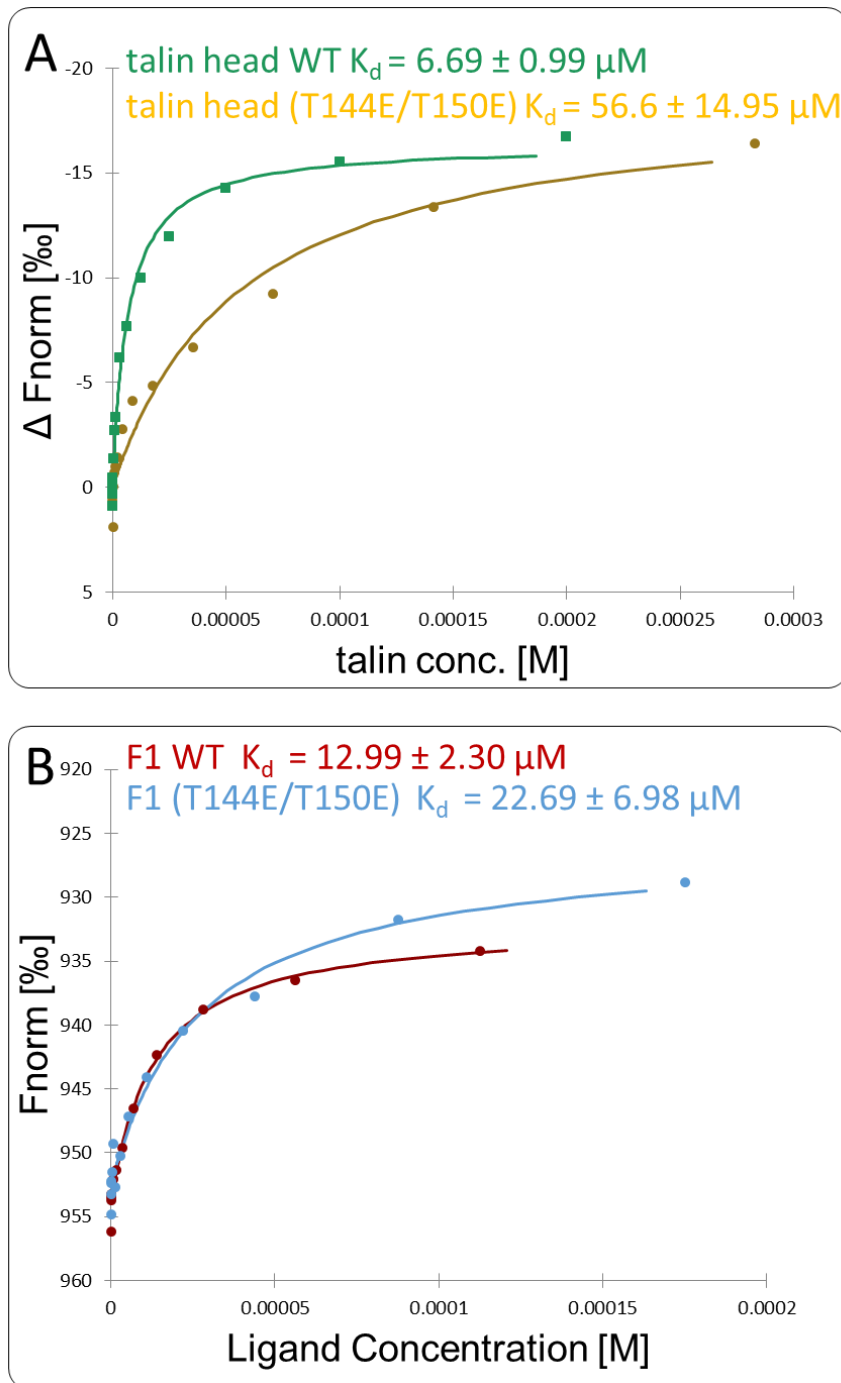


Figure 5.12: **Phosphorylation of talin reduces kindlin binding.** Binding of 50 nm NT647-labelled kindlin-1 to (A) talin head (green), talin head (T144E/T150E)(mustard), (B) talin F1 (red) and F1 (T144E/T150E)(blue). Data was analysed by nanotemper analysis software to a  $K_d$  fit model. Dissociation constants +/-  $K_d$  confidence are indicated in the legend ( $n=1$ ).

#### 5.4.5 Kindler syndrome mutant has reduced affinity to integrin and talin

Kindler syndrome is bullous skin disease arising from mutations in the FERM1 (kindlin-1 gene).

These mutations usually lead to premature termination of translation (Jobard et al., 2003).

However, courtesy of Professor Maddie Parsons from King College London, we have a kindlin-1 mutant derived from a patient who suffered all the symptoms of Kindler syndrome, but has normal kindlin-1 protein expression levels. The mutation is a 9 bp deletion culminating in the loss of three residues located in the kindlin F3 domain ( $\Delta 3aa$ ), adjacent to the integrin binding site (fig. 5.13A). One could postulate this mutation could affect the folding of the domain. Thus we hypothesised the mutation would reduce integrin binding. Using MST to investigate this, integrin  $\beta 1a$  cytoplasmic tail (752-798) was titrated against NT647-labelled kindlin-1 WT and kindlin-1 ( $\Delta 3aa$ ). The WT bound with a  $K_d = 19.56 \mu M$ , the ( $\Delta 3aa$ ) mutant also bound, although with a weaker affinity,  $K_d = 76.09 \mu M$  (fig. 5.13B). Whilst integrin bound to the mutant kindlin weaker than the WT, we were surprised to measure any binding as our prediction was that the integrin binding site in kindlin F3 might be misfolded due to the location and nature of the mutation.

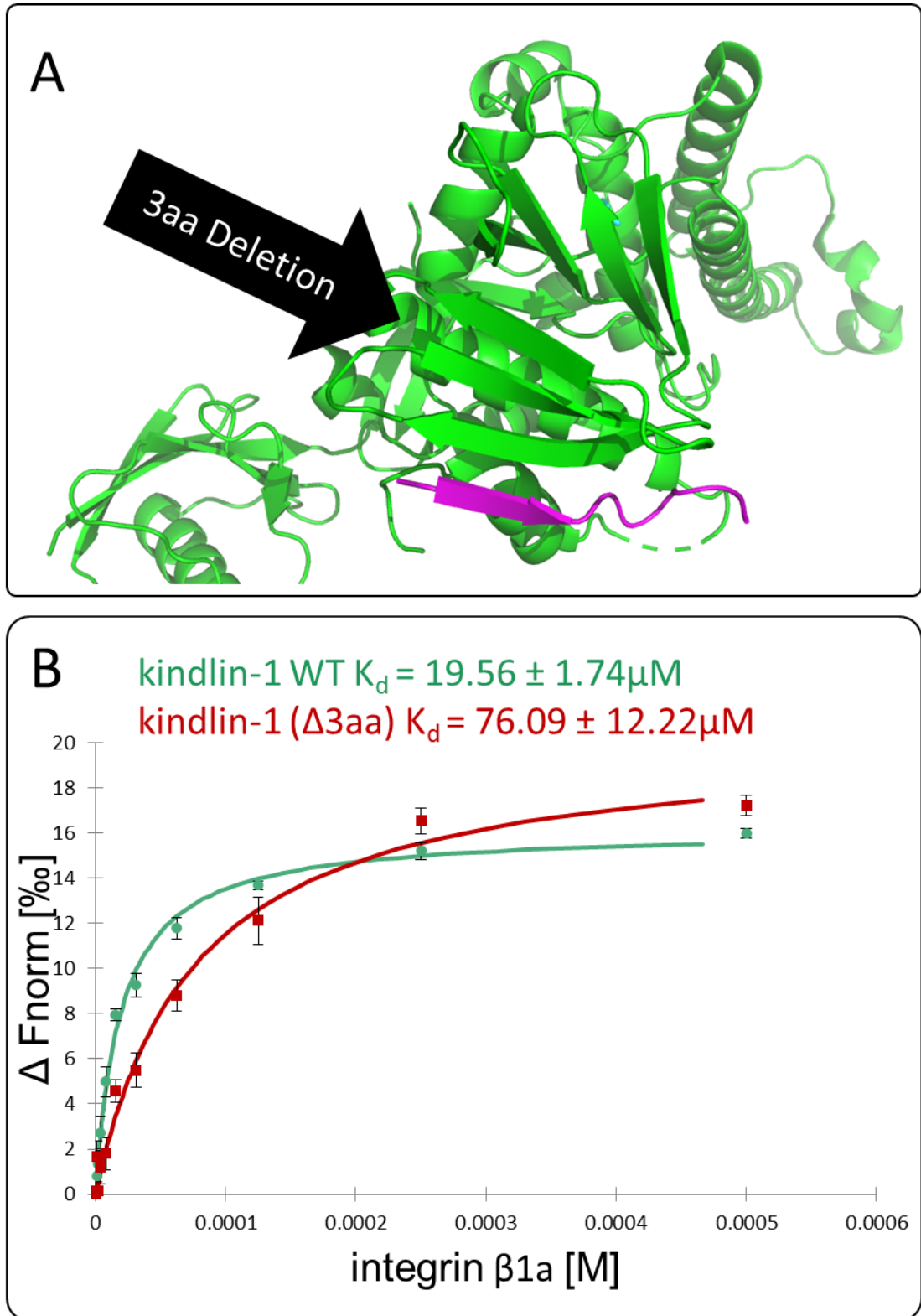


Figure 5.13: **Kindler mutant binding integrin.** (A) Crystal structure of kindlin-2 bound to integrin  $\beta 1$  (5XQ0); integrin peptide in magenta; location of three amino acid deletion from kindler mutant indicated by arrow. (B) Binding of 50 nm NT647-labelled kindlin-1 WT (green) and kindlin-1 ( $\Delta 3\text{aa}$ ) to integrin  $\beta 1\text{a}$  (752-798). Data was analysed by nanotemper analysis software to a  $K_d$  fit model. Dissociation constants  $\pm K_d$  confidence are indicated in the legend ( $n=3$ ).

Interestingly, the interaction between the kindler mutant and integrin was only four times weaker than the WT suggesting the mutant still has the capacity to bind integrin *in vivo*. This led us to question how else the kindler mutant might be leading the Kindler syndrome symptoms. We decided to test the kindler mutant against talin to see if the mutation influenced the interaction. Using an MST assay, talin head was titrated against NT647-labelled WT and kindlin-1 ( $\Delta 3aa$ ). The WT bound with  $K_d = 6.69$ ; strikingly the  $\Delta 3aa$  mutant bound over ten times weaker,  $K_d = 79.44$ . The effect of the kindler mutant on talin binding was greater than on integrin binding, suggesting that the effect of the mutation in patients might be due to the interaction with talin rather than, or in conjunction with, integrin. Moreover, the mutant provides us with a talin binding location; it confirms talin binds to kindlin F3. Whether or not the talin-kindlin interaction is mutually exclusive to integrin binding remains to be determined.

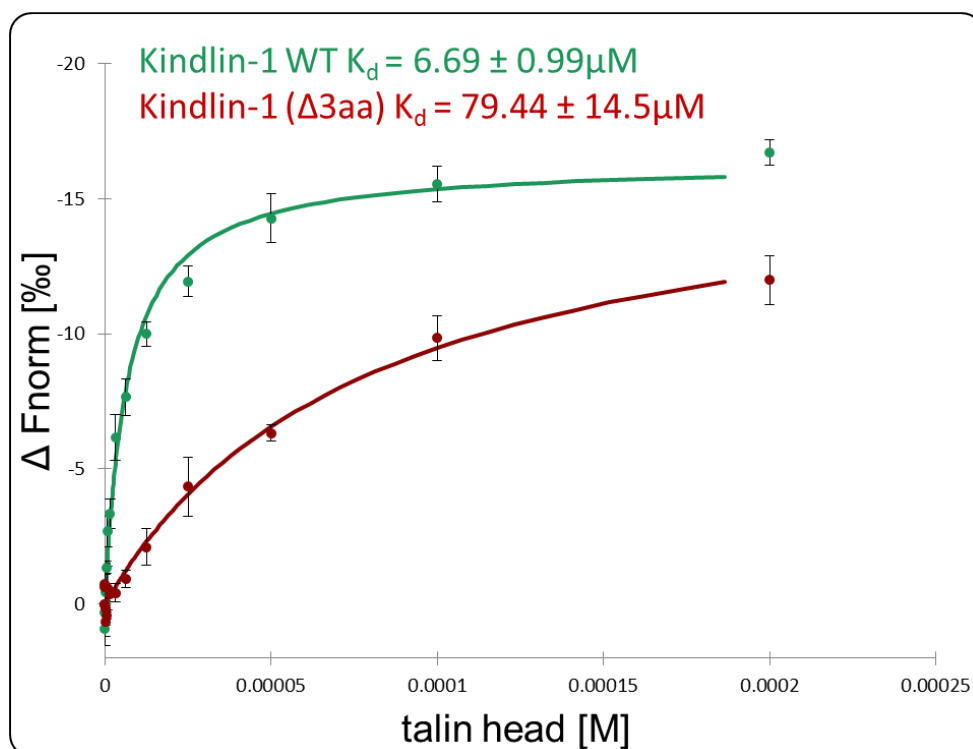


Figure 5.14: **Kindler mutant reduces talin binding.** Binding of 50 nm NT647-labelled kindlin-1 WT (green) and kindlin-1 ( $\Delta 3aa$ ) to talin-1 head. Data was analysed by nanotemper analysis software to a  $K_d$  fit model. Dissociation constants +/-  $K_d$  confidence are indicated in the legend ( $n=3$ ).



## 5.5 Discussion

It is evident there is more complex regulation of integrin activation than the basic model of 'active' talin (elongated as opposed to autoinhibited) binding to the  $\beta$ -integrin tail separating the integrin  $\alpha$ - and  $\beta$ -transmembrane cytoplasmic domains leading to the open high affinity conformational state of the integrin ectodomains (Iwamoto and Calderwood, 2015). This was demonstrated through our work with the E1770A autoinhibition mutant. Here we observed overactive talin leading to a gain of function phenotype of increased adhesion. However, the mice containing the mutation did not exhibit any dramatic morphological defects, one might expect with constitutively active integrin (Winograd-Katz et al., 2014). Whilst it is clear talin has a major function in integrin activation (Klapholz and Brown, 2017), how talin is regulated in doing so needs to be further elucidated. Using a combination of structural and biochemical techniques we have looked specifically at mechanisms that may influence the integrin binding ability of the talin head.

Through this chapter I have reported multiple ways in which the talin head may be regulated. The first is talin autoinhibition, whereby important integrin binding sites in the talin head are masked through an interaction with the tail. The second is through conformational regulation, whereby the F1-F2 linker acts as a rotational axis, with which talin can adopt either a linear conformation or a 'twisted' conformation potentially affecting the ligand binding properties of the talin head. The third is through membrane composition, we suggest each talin head lipid binding domain is finely tuned to the overall charge and composition of the membrane, with the talin head requiring an optimum lipid composition to be in a preferential conformation for integrin activation. The final mechanism is through a direct interaction with kindlin, a vital integrin co-activator. Whilst I have reported the mechanisms of regulation separately it is possible they are all interlinked with one another, contributing to a tightly controlled talin FERM domain.

### 5.5.1 Conformational regulation of the talin head

Conformational control of talin is not a new idea, it has been evident for some time that the complex structure of talin provides layers of autoinhibition (Gough and Goult, 2018), however apart from the autoinhibited globular form (Goult et al., 2013a), much of the focus has been on the conformational plasticity of the rod domain (Yao et al., 2016; Yan et al., 2015; Goult et al., 2018). Here we report the atomic structure of the talin 2 FERM domain, revealing a novel ‘twisted’ conformation. A similar compact conformation has previously been observed in talin-1 SAXS data (Elliott et al., 2010). Comparison of the atomic structures of the linear (PDB: 3IVf) and twisted (talin-2 head structure) conformations, has identified the F1-F2 linker as a rotational axis that enables the talin FERM to adopt at least two conformational states. In the linear conformation the F0F1 domains face in the same direction as F2F3 and in the ‘twisted’ the F0F1 domains face the opposite direction to F2F3. We suggest the ‘twisted’ conformation is less able to activate integrin, and might represent a lower activity conformation. This is because the F1-loop is directed in the opposite direction, towards the cytoplasm, relative to the lipid binding residues on F2F3, thereby preventing the F1-loop from binding to the cell membrane, an interaction that has proved vital for integrin activation (Goult et al., 2010a; Gingras et al., 2019) (fig. 5.15). How the rotational axis is controlled remains to be determined, however we have provided insight into how membrane composition may finely tune the conformational state by influencing the lipid binding domains individually. Using a lipid co-sedimentation assay we have demonstrated F1F2 lipid binding surfaces appear to have a higher affinity for relatively low charged membranes and are repelled from a highly charged membrane. In contrast, our data suggests talin F3 lipid binding surfaces is not repelled by the more negatively charged lipid membrane.

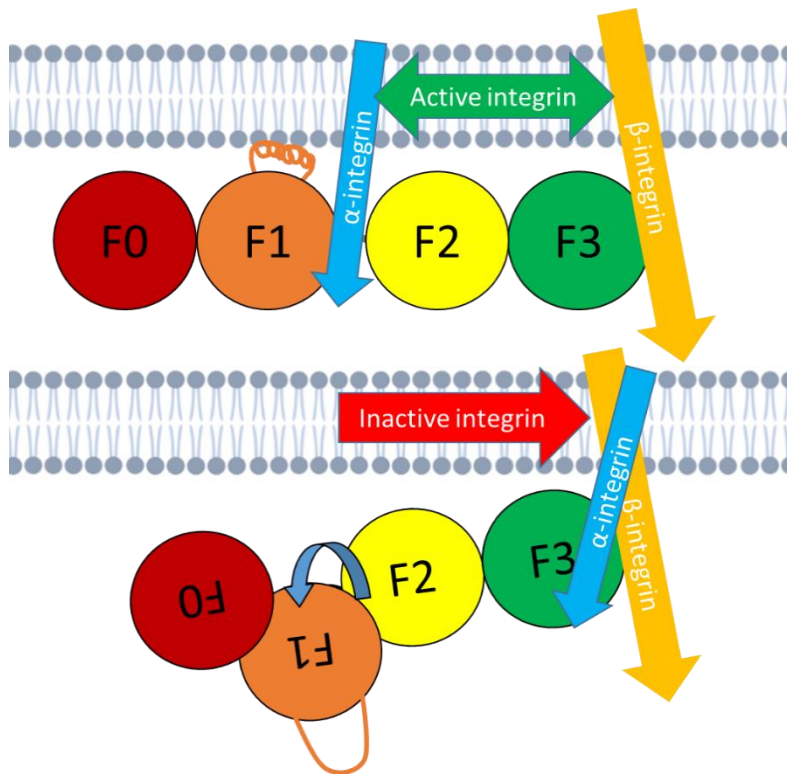


Figure 5.15: **Conformational regulation of the talin head.** Schematic diagram showing talin in linear (top) and twisted (bottom) conformations and demonstrating our proposed effect on integrin activation.

Further investigations into the conformational control of the talin head are needed to confirm the function of the different conformations and how they are controlled. To do this we would need a way in which to lock the FERM domain in either the linear or twisted conformations which would enable us to test the conformational effect on integrin binding/activation, lipid binding and additional talin head binders, such as Rap1 (Zhu et al., 2017). Moreover, it would be desirable to find a marker that can determine the conformation state of the head *in vivo* and *in vitro*, enabling us to derive what controls the conformational state of the talin head and confirm the membrane composition theory.

### 5.5.2 Understanding the talin:kindlin interaction

Simultaneous binding of kindlin and talin to integrin is believed to be necessary for integrin activation, however the need for kindlin is not fully understood in this interaction (Rognoni et al., 2016). Here we have demonstrated there is a relatively strong interaction between the talin-1 head and kindlin-1. It is likely this interaction is not isoform specific due to the high conservation

between the different isoforms of talin and kindlin (Monkley et al., 2001; Siegel et al., 2003). We investigated the effect of a kindlin-1 mutant ( $\Delta 3aa$ ) acquired from a Kindler syndrome patient with normal kindlin-1 expression levels. We observed significantly reduced affinity between talin and the kindler mutant, elucidating the functional importance of the talin-kindlin interaction.

When determining the binding site of the talin-kindlin interaction we demonstrated kindlin binds to multiple domains of the talin head, including F1-F3. Exactly how kindlin and talin interact, and in what conformation we do not know, and it is something that will need further investigating. However, we have deduced the importance of the talin F1-loop for the complex; by deleting it we significantly reduce binding of kindlin to both the whole talin head and the F1 domain. How kindlin binds to the F1-loop may allude to the function of the complex; if kindlin holds the talin F1-loop away from the membrane then the talin head would be unable to activate integrin, alluding to the talin-kindlin complex negatively regulating integrin activation. Conversely, kindlin may stabilise the talin F1-loop at the cell membrane providing a means of talin mediated integrin activation. To further elucidate the function of the talin-kindlin complex we used the Kindler mutant ( $\Delta 3aa$ ); the location of the mutation is on the kindlin F3 domain adjacent to the integrin binding site. The significantly reduced binding affinity of the mutant to talin, hints at the talin binding site being located on kindlin F3. This has the potential to put the integrin binding sites of talin and kindlin in close proximity, providing a high affinity binding site for the  $\beta$ -integrin cytoplasmic tail. Alternatively, talin binding to kindlin F3 may block the integrin binding site preventing integrin activation.

To further understand the regulation of the talin-kindlin complex we tested phosphomimetic talin constructs against kindlin; strikingly, phosphorylation significantly reduced the talin-kindlin binding affinity. Whether or not this is due to conformational changes induced by phosphorylation is unclear; however, phosphorylation of the F1-loop could be a way in which the complex is negatively regulated.

Through our work it is clear the talin:kindlin interaction has an important role in the regulation of integrin activation; either as a negative or positive regulator. Further investigations into this interaction could improve our understanding of the role of kindlin in integrin activation (Sun et al., 2019) and integrin clustering (Ye et al., 2013). Whilst the MST assay has provided us with vital information on the talin-kindlin complex we otherwise would have had difficulty to acquire, we are only able to speculate on the mechanisms involved with the information we have so far. To validate our data and further our understanding of the function of this interaction we would need an atomic structure of the complex. Unfortunately, we have been limited by kindlin-1 expression. It might be useful to adopt a recombinant protein expression system like that used in (Li et al., 2017a), to increase protein yield. With an atomic structure of the complex one can deduce the conformation of kindlin bound talin and the binding sites involved in the interactions; enabling us to design mutants that disrupt the interaction and can be used in further *in vivo* studies.

## Chapter 6: Investigating the role of the $\alpha$ -integrin subunit in talin-mediated integrin activation

### 6.1 Introduction

#### 6.1.1 Talin mediated integrin activation

Integrin activation can be defined as the change from the low affinity folded conformation of the integrin ectodomain to the high affinity extended conformation (Ye et al., 2011). This conformational change can occur as a result of intracellular signalling, termed 'inside-out' signalling. When integrin is in the inactive conformation the cytoplasmic domains of the  $\alpha$ - and  $\beta$ -subunits are held together through electrostatic interactions (Hughes et al., 1996) and thereby holding the TM-regions together. In the active conformation the integrin cytoplasmic domains and TM-domains become separated (Partridge et al., 2005). Talin has been demonstrated to activate integrin by inducing this conformational change through a direct interaction with the membrane proximal NPxY motif of the  $\beta$ -integrin cytoplasmic tail (Calderwood, 2004; Anthis et al., 2009; Wegener et al., 2007). The exact mechanism as to how talin causes the spreading of the integrin TM- and cytoplasmic domains is not fully understood, however there are a few theories (Ye et al., 2011). The first of which is by talin binding causing a motion, such as tilting or lateral movement, leading to the disruption of the  $\alpha$  and  $\beta$  subunit interactions (Kalli et al., 2010). A different hypothesis suggests the interaction of talin with the NPxY motif disrupts an important salt-bridge between Asn995 and Arg723 that holds the  $\alpha$  and  $\beta$  tails together; through breaking this interaction the integrin conformation favours the active state (Anthis et al., 2009). Another hypothesis is the talin head binding to the  $\beta$ -tail leads to steric hindrance between the  $\alpha$ -tail and talin head thereby separating the two integrin tails (Wegener et al., 2007). It is quite possible talin

mediated-integrin activation occurs through a combination of these theories; indeed, there is evidence for each of them. What is clear, is the exact nature of talin-mediated integrin activation is yet to be fully elucidated.

### 6.1.2 The current understanding of the $\alpha$ -subunit cytoplasmic domain in integrin regulation

The integrin  $\alpha$ -subunit cytoplasmic domains consists of a completely conserved membrane proximal GFFKR motif, with a highly variable region distal of the GFFKR motif (Li et al., 2014). The GFFKR motif of the  $\alpha$ -tail has been established as a crucial component in integrin inactivation. Association of the GFFKR motif with the  $\beta$ -tail membrane proximal motif holds the integrin-tails in the resting state and dissociation results in integrin activation (Kim et al., 2003). The 'FF' region of the motif has been demonstrated to provide important hydrophobic contacts between the  $\alpha$ - and  $\beta$ - membrane proximal  $\alpha$ -helices (Vinogradova et al., 2002; Weljie et al., 2002). In fact, deletion or mutation of this motif leads to constitutively active integrin (Hughes et al., 1996). The role of the region distal to the GFFKR motif has remained elusive, although with the high variability between isoforms it is easy to imagine the region has isoform specific roles. However, the distal region has been demonstrated to be crucial for talin-mediated integrin activation in  $\alpha$ IIb $\beta$ 3, by providing steric hindrance with the talin head (Li et al., 2014).

There is some evidence that the  $\alpha$ -tail may be involved in a direct interaction with talin. Indeed, direct interactions between talin and the cytoplasmic tails of  $\alpha$ IIb,  $\alpha$ 4 and  $\alpha$ 5 have been previously reported (Pavalko and Otey, 1994; Knezevic et al., 1996). Moreover, a closer look at some of the studies over the years reveal clues of an interaction between talin and the  $\alpha$ -tail. A recent study using palmitoylated peptides corresponding to various parts of the  $\alpha$ IIb-tail, demonstrated the peptides inhibited platelet aggregation by inhibiting talin-mediated integrin activation (Gkourogianni et al., 2014); the authors suggested this was due to the peptides inhibiting talin binding to  $\alpha$ IIb $\beta$ 3 by competing talin off the  $\beta$ -membrane proximal region; however, it is possible

the peptide was actively binding to talin thereby inhibiting an interaction between talin and  $\alpha$ -tail. Moreover,  $\alpha$ -tail binding proteins, such as sharpin (Rantala et al., 2011) and CIBP (calcium and integrin binding protein) (Naik et al., 1997), have been demonstrated to block the talin-integrin interaction (Yuan et al., 2006).  $\alpha$ -tail binding proteins blocking the talin-integrin interaction may be due to steric hindrance preventing talin binding to the  $\beta$ -tail, alternatively these proteins are actively competing with talin to bind to the  $\alpha$ -tail.

### 6.1.3 Aim: investigate talin binding to the $\alpha$ -subunit of integrin

The talin interaction with the  $\beta$ -tail is critical for inside-out activation. For this reason much impetus has been put into studying this interaction. However, direct interactions between talin and the  $\alpha$ -tail have previously been reported but not followed up (Pavalko and Otey, 1994; Knezevic et al., 1996). An interaction between talin and both integrin subunits may provide a further theory as to how talin induces the conformational activation of integrin. In this chapter we sought to test whether the  $\alpha$ -tail directly binds to talin, providing a new role for the  $\alpha$ -tail in talin mediated integrin activation.

## 6.2 The talin head binds to the $\alpha$ -tail

A direct interaction between the  $\alpha$ -cytoplasmic domain and talin was observed in 1996 but never followed up (Knezevic et al., 1996), therefore to investigate whether the talin head interacts with  $\alpha$ -integrin a fluorescence polarisation assay was used to assess the relative binding. This assay provides fast quantitative data on interactions between proteins and fluorescently labelled peptides (see section 3.3.2). In this assay talin-1 head was titrated against fluorescein labelled  $\alpha$ 2-tail peptide. We observed a significant increase in polarisation when the talin head was titrated against the  $\alpha$ 2-tail compared to the titration against the control peptide (paxillin LD1), indicative of a binding event as previously observed (Pavalko and Otey, 1994; Knezevic et al., 1996). However, over the talin head concentration range used in the titration the system was not fully



saturated, demonstrating a relatively low affinity, we were therefore unable to derive an accurate binding affinity for the interaction (fig. 6.1). Whilst the talin: $\alpha$ -tail interaction has a relatively low affinity, low affinities are also observed in talin  $\beta$ -integrin interactions without the presence of the membrane to orientate the talin head (Bouaouina et al., 2008; Moore et al., 2012).

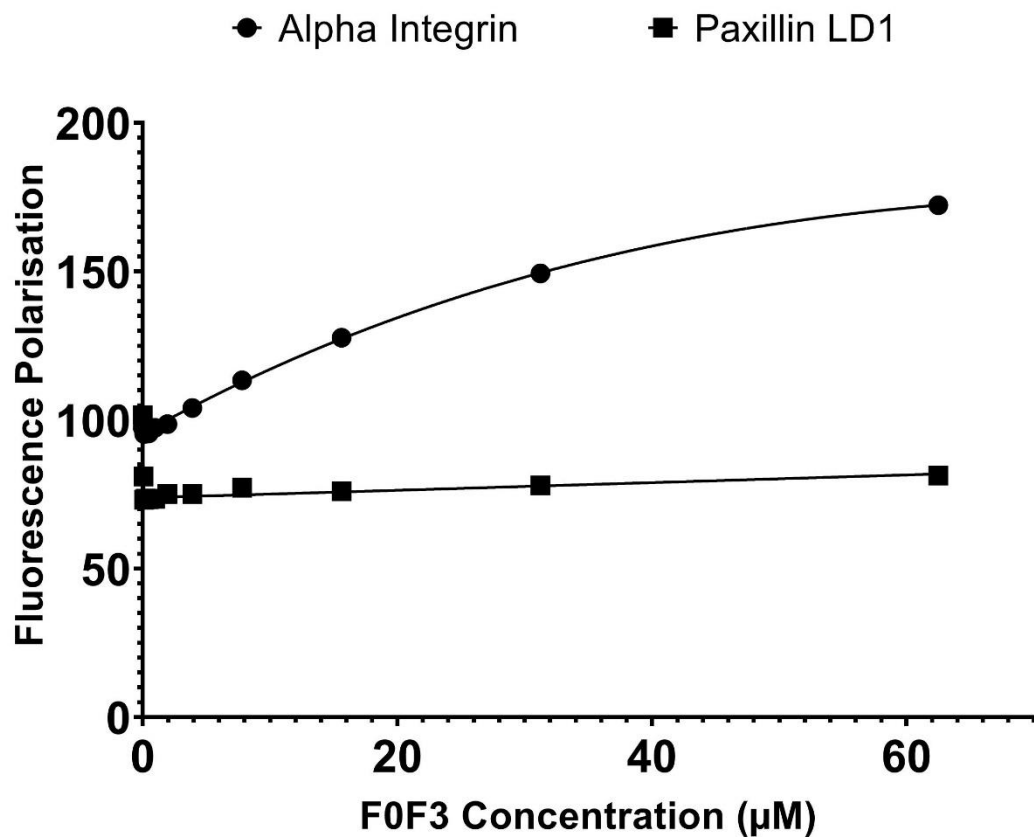


Figure 6.2: **The talin head binds the  $\alpha$ 2-tail.** Binding of talin F0-F3 to fluorescein labelled  $\alpha$ 2-tail (1154-1181), and paxillin LD1 (3-22) peptides measured using a fluorescence polarisation assay. Dissociation constants were not determined over the concentration range used ( $n=1$ ).

### 6.3 Investigating talin F3 binding to $\alpha$ -integrin

#### 6.3.1 NMR data reveals talin F3 binds to the $\alpha$ -tail

After establishing the talin head binds to the  $\alpha$ -tail we were interested in identifying the specific binding site between the two proteins as this may provide insight on the function of the interaction. It is now well established talin F3 binds to the  $\beta$ -tail (Calderwood et al., 2002; Anthis

et al., 2009), for this to occur talin F3 must come into close proximity of the  $\alpha$ -tail that is bound to the  $\beta$ -tail. This led to the hypothesis that the  $\alpha$ -tail was binding to talin F3. As the fluorescence polarisation detected weak binding to the whole head we wanted to use a more sensitive technique for weaker interactions; therefore, a HSQC NMR experiment was used to investigate the  $\alpha$ -tail:talin F3 interaction. NMR is powerful method for investigating protein:protein interactions, as it is able to measure minute changes to the localised environment of each individual amino acid, providing crucial information on an interaction (section 3.4.2). A HSQC spectrum of  $^{15}\text{N}$ -labelled talin F3 was collected with and without the addition of a 1:8 ratio of  $\alpha$ -tail peptide. The addition of the  $\alpha$ -tail peptide to F3 caused multiple peaks to shift indicative of a direct interaction between talin F3 and the  $\alpha$ -tail (fig. 6.2).

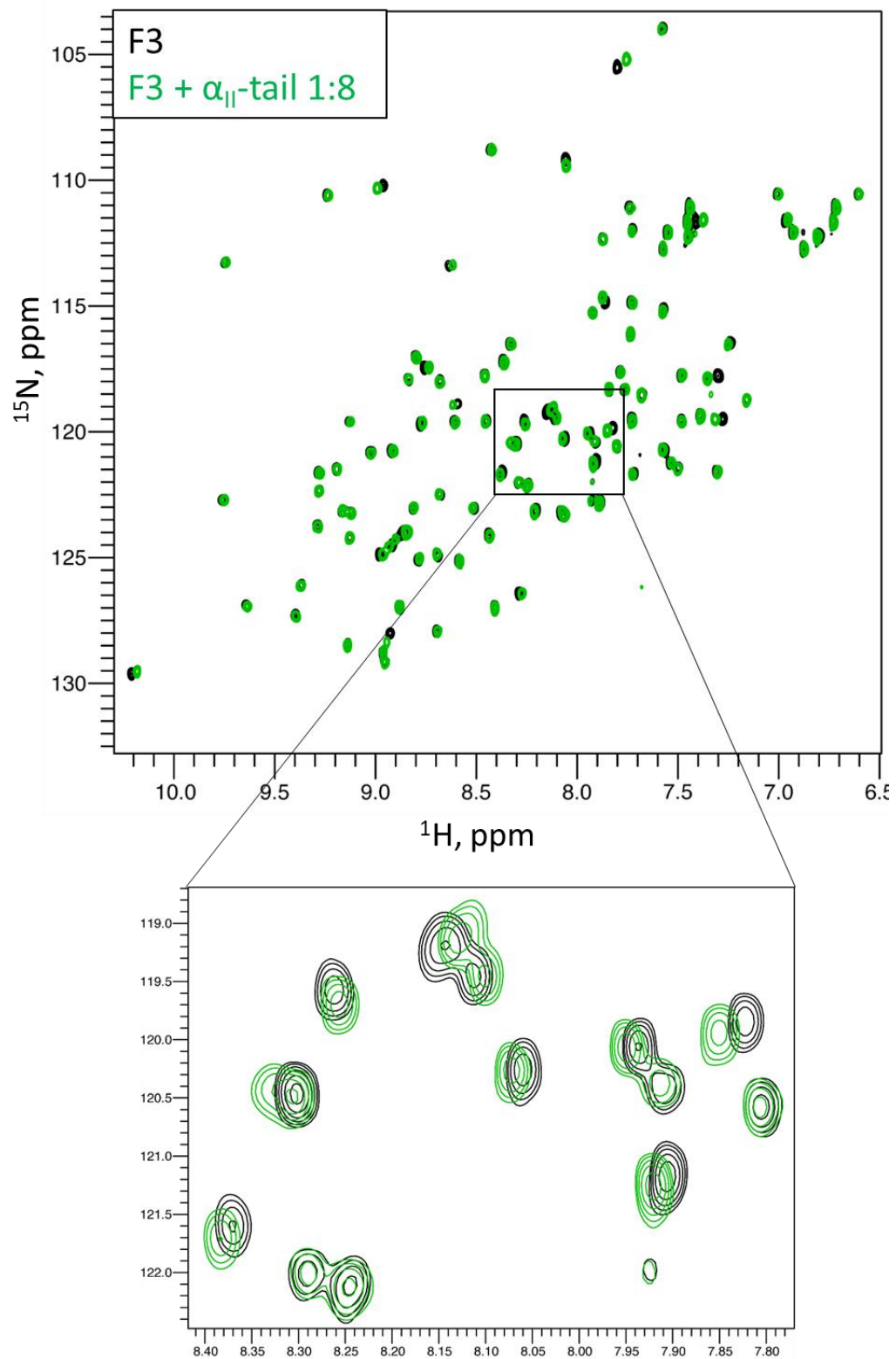


Figure 6.2: **Talin F3 binds the  $\alpha 2$ -tail.** NMR HSQC spectra of  $^{15}\text{N}$ -labelled F3 (black) with the addition of a 1:8 ratio of  $\alpha 2$ -tail peptide (1154-1173) (green); box represents zoomed in area.

### 6.3.2 NMR peak shift mapping reveals the $\alpha$ -tail binds to a similar site as the $\beta$ -tail on F3.

To map the binding surface of the  $\alpha$ 2-tail on F3, the peak shifts identified from the  $\alpha$ -tail:F3 interaction were compared to a pre-assigned HSQC spectrum of talin F3 (unpublished), this enabled identification of the specific amino acids involved in the interaction. The interacting amino acids were then mapped onto the atomic structure of talin F3 (PDB: 3G9W) (Anthis et al., 2009) (fig. 6.3A). Strikingly, the NMR chemical shift mapping revealed the  $\alpha$ 2-tail peptide interacts on a similar surface on F3 to the  $\beta$ -tail. Interestingly, when we mapped the shifts onto our own talin F2F3- $\beta$ 3 chimera structure (section 6.3.3) we noticed the beta-sheet surface that is involved in the binding contains a hydrophobic pocket, in which Trp-735 and a Phe-737 from the  $\beta$ 3-tail bury into – this hydrophobic interaction appears to be an artefact of our chimera system, as Phe-737 is an artefact residue from the vector used; moreover, the  $\beta$ 3-talin (PDB: 1MK7) and  $\beta$ 1d-talin (PDB: 3G9W) structures that do not contain the artefact residue also do not show the hydrophobic interaction. However, we speculated that this hydrophobic surface may accommodate the two phenylalanine residues of the GFFKR (fig. 6.3B). Strikingly, modelling of the  $\alpha$ -tail GFFKR into the hydrophobic pocket on the atomic structure of F3 orientates the peptide along the mapped surface with the possibility of a salt bridge forming between the lysine of the GFFKR motif and Asn-372 on the F3 face (fig. 6.3C,D). The proximity of the integrin tail binding sites in F3 proposes two theories. The first, talin may be holding the  $\alpha$ - and  $\beta$ -tails together in an inactive state. If talin is holding the two tails together, they would be in much closer proximity than previously seen in the autoinhibited state (Lau et al., 2009). Alternatively, the interactions between the individual tails and talin F3 may be mutually exclusive, which begs to question the purpose of an interaction between the  $\alpha$ -tail and talin F3.

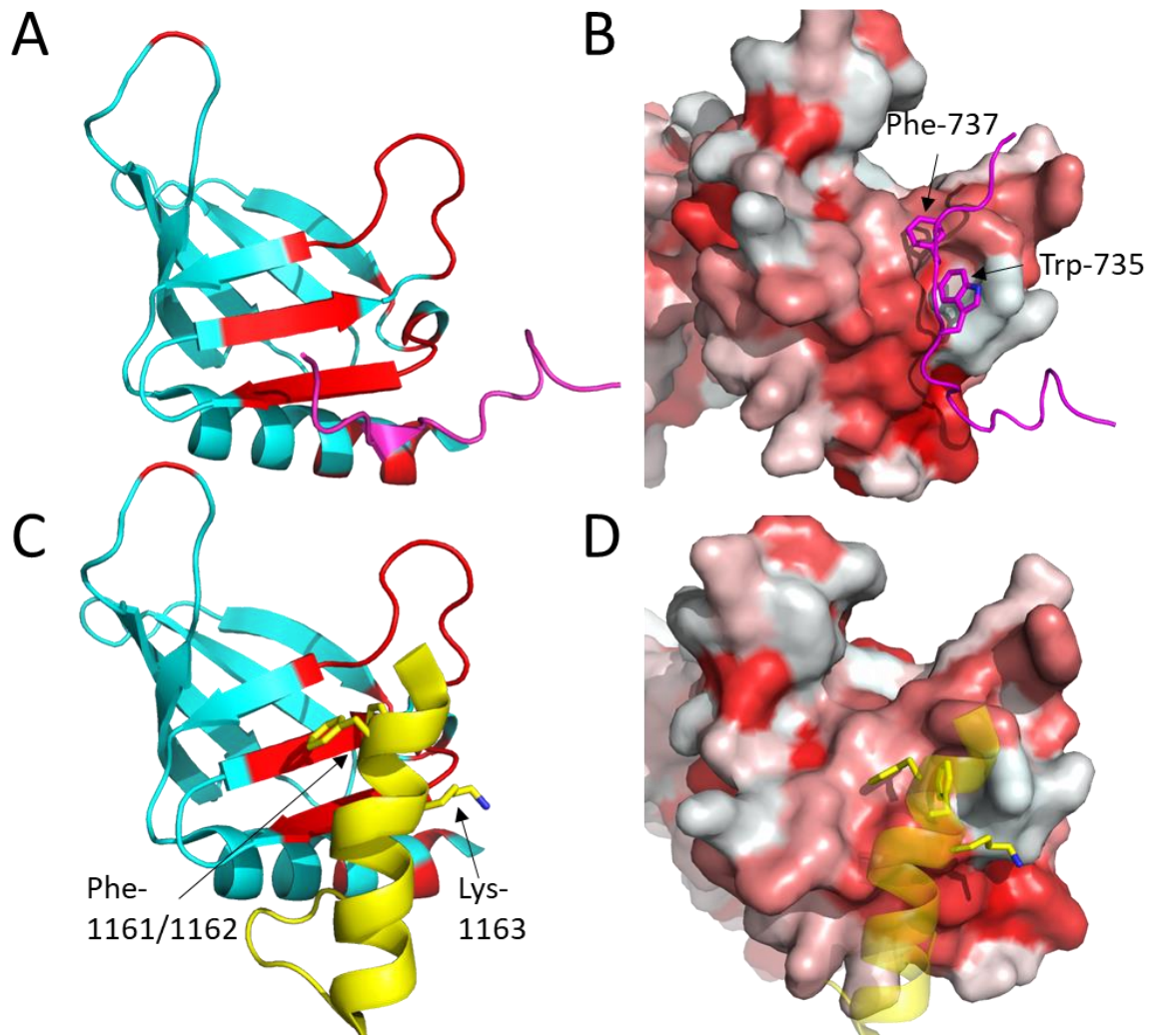


Figure 6.3:  **$\alpha$ -integrin binds to a similar place on F3 as the  $\beta$ -tail.** A) structural mapping of NMR peak shifts from  $\alpha$ 2-tail binding to talin F3 (red), onto  $\beta$ 1D (purple) bound F3 structure (pdb: 3G9W). B) Our structure of  $\beta$ 3-talin F2F3 chimera (6.3.3), showing  $\beta$ 3 (purple) residues Trp-735 and Phe-737 buried into hydrophobic surface on F3. Surface coloured by hydrophobicity (hydrophilic = white, hydrophobic = red). C)  $\alpha$ -tail (yellow; pdb: 2lke) modelled onto peak shifts (red) and D) hydrophobicity surface, ‘FFK’ residues shown as sticks buried into hydrophobic pocket and in the direction of talin Asn-372.

### 6.3.3 X-ray crystallography

To further elucidate if both integrin tails bind to talin F3 we aimed to gain an atomic structure of the talin F3: $\beta$ -tail: $\alpha$ -tail complex. To achieve this we grew crystals of a talin F2F3- $\beta$ 3 chimera, similar to that used in (García-Alvarez et al., 2003), in which a integrin  $\beta$ 3-tail peptide is added to the N-terminus of an F2F3 construct, with the aim of bringing the integrin peptide and F3 binding site into close proximity. Initially, we tried to co-crystallise the chimera with a 1:8 ratio of the  $\alpha$ -tail peptide; these attempts proved unsuccessful as we were unable to grow the crystals.

Following this we tried a soaking technique in which the peptide is soaked through solvent channels of a preformed crystal. The chimera crystals were successfully screened and optimised in a condition consisting of: 0.2 M MgCl<sub>2</sub>, 0.1 M Bis-Tris pH 5.5 and 25% w/v PEG-3350. The fully grown crystals were then transferred into mother liquor containing 3.6 mM of  $\alpha$ 2-tail peptide (1154-1173), in which they were soaked for 24 hours prior to harvesting and vitrification. Multiple crystals were chosen for data collection from two different conditions, all of which diffracted well. The highest resolution data of 1.5 Å was chosen for data processing. The structure was solved by molecular replacement based off the F2F3- $\beta$ 1d chimera 3G9W (Anthis et al., 2009). Processing of the crystal structure revealed the  $\alpha$ -tail was not present in the structure. However, there were subtle differences between our structure and the previous  $\beta$ 3-chimeric structure, 1MK7, demonstrating some limited flexibility of the talin F2 and F3 domains much like that seen in Chapter 5.

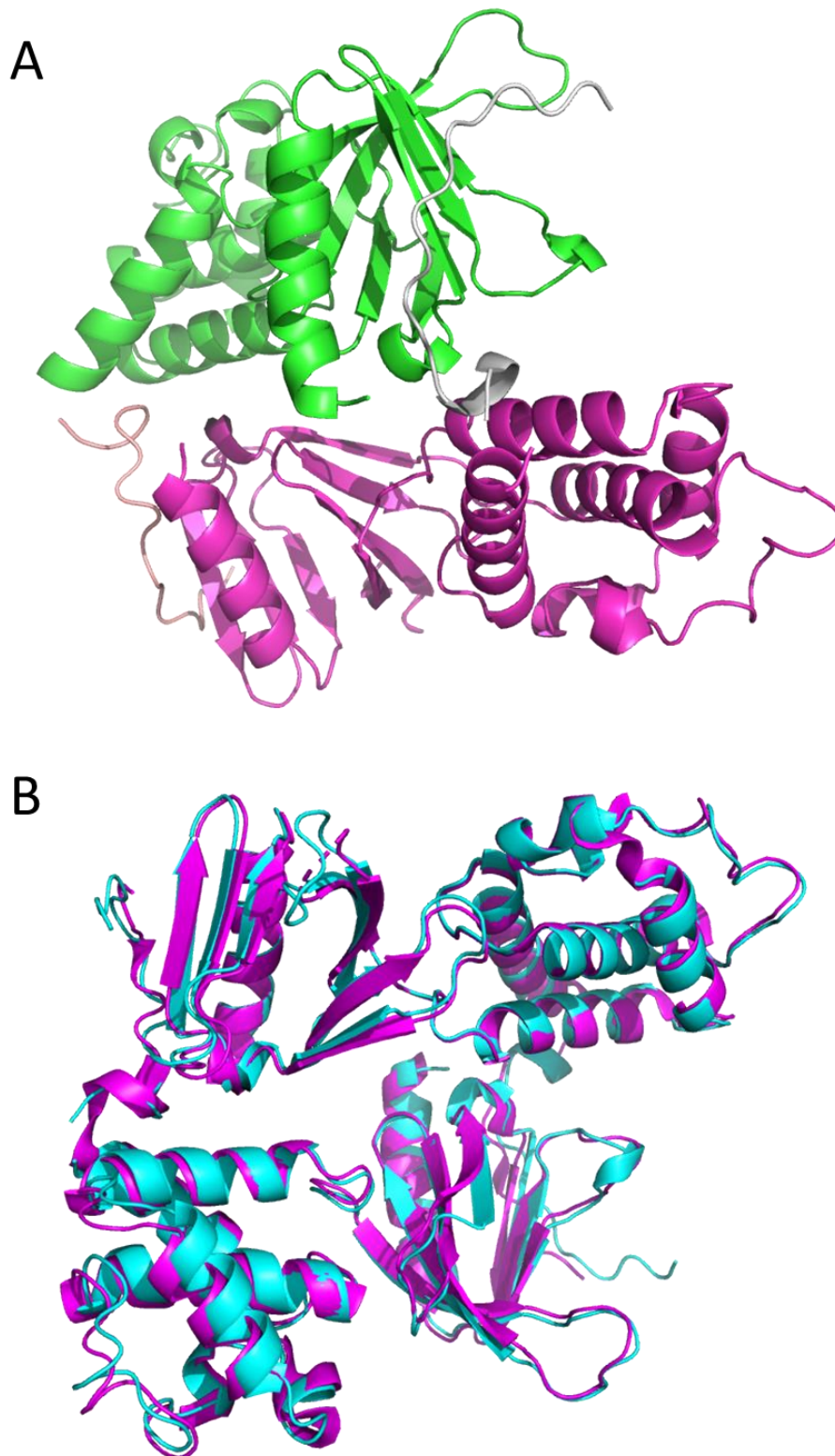


Figure 6.4: **Crystal structure of talin F2F3 B3 chimera.** A) Our high resolution crystal structure of F2F3 B3 chimera showing dimerization of the chimera through  $\beta$ -tail interaction, coloured by chain. B) Alignment of our structure (cyan) vs. 3G9W (green); subtle differences can be seen in the orientation of the F3 domain

#### 6.3.4 Peptide-conjugated lipid co-sedimentation assay suggests talin F3 interaction with the $\alpha$ -tail is membrane dependent

In the fluorescence polarisation assay we detected a very weak interaction for the talin head: $\alpha$ 2-tail interaction. Moreover, despite the 8-fold excess of the  $\alpha$ -tail peptide we added to F3 in the HSQC NMR experiment, the peak shifts were relatively small which may be due to the weak interaction. As aforementioned, the F3: $\beta$ -tail interaction also has a low affinity in the absence of a membrane; as for integrin tail binding to occur, the talin head needs to be correctly orientated through interactions with the PIP2 enriched membrane (Bouaouina et al., 2008; Elliott et al., 2010; Goult et al., 2010a; Saltel et al., 2009; Moore et al., 2012). We therefore hypothesised that the F3: $\alpha$ -tail interaction is also modulated by the membrane. To test this hypothesis we made use of the peptide-conjugated lipid cosed assay we developed (section 4.3). In this assay the LUVs, consisting of 20% PS to provide a negative charge representative of PIP2, were conjugated to integrin  $\beta$ 1a-tail peptide,  $\alpha$ 2-tail peptide or a VBS peptide as a control. The LUVs were incubated with talin F2F3 and R7R8 as a control, then pelleted and analysed by SDS-PAGE. Analysis of the pellets revealed both the  $\beta$ -tail and  $\alpha$ -tail enhanced the amount of talin F2F3 pulled down into the pellet compared to the control and blank conditions (fig. 6.5). Interestingly, the  $\alpha$ -tail conjugated LUVs pulled down a similar amount of F2F3 as the  $\beta$ -tail LUVs; suggesting both peptides bind in a membrane dependent manner to talin F2F3 with a similar affinity. However, despite optimisation it was apparent we were getting dissociation of the peptide from the LUVs during the experiment, as is visible in the SDS-PAGE analysis. With greater optimisation of the assay conditions we may get a more significant result.



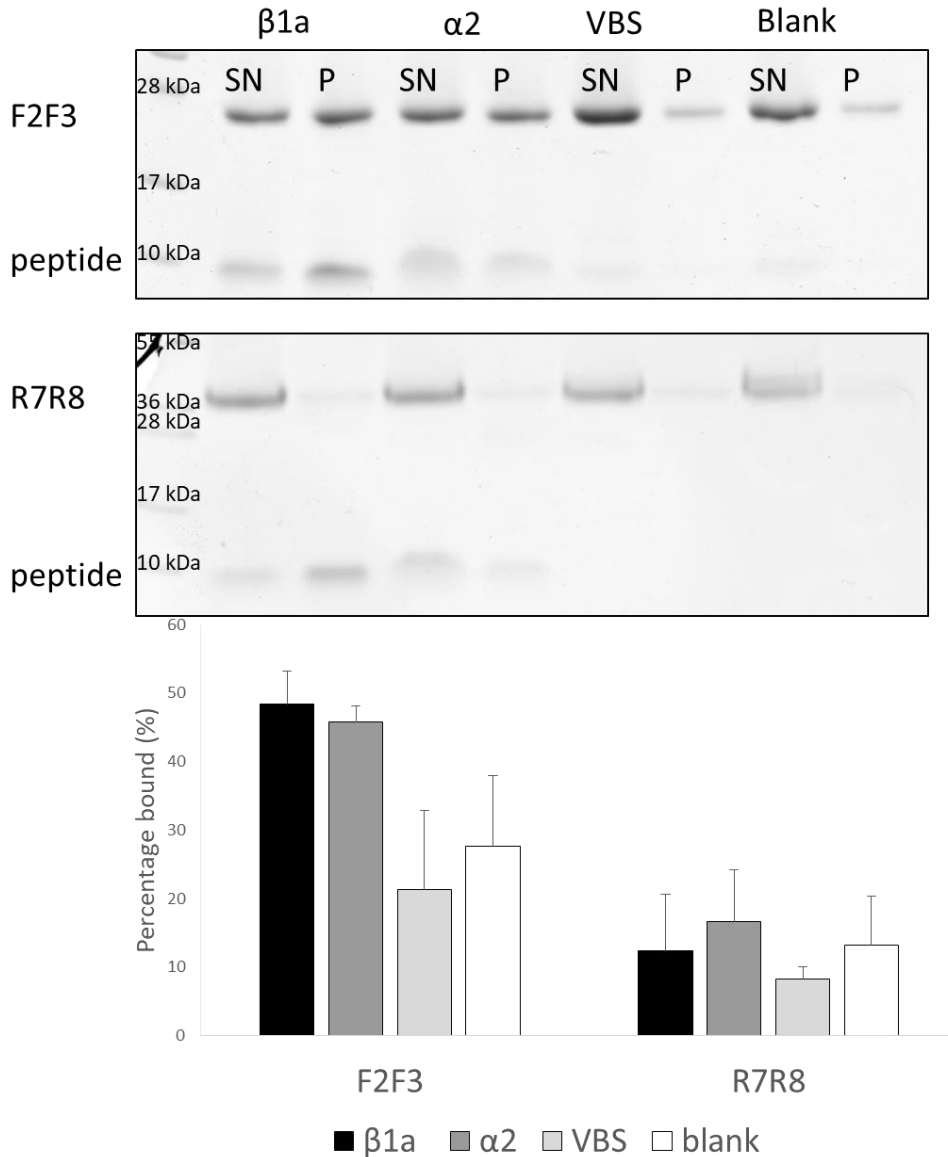


Figure 6.5: **Talin F2F3 binds the  $\alpha$ -tail in a membrane dependent manner.** (top) SDS-PAGE analysis of integrin  $\alpha$ 2-tail (1154-1181), integrin  $\beta$ 1 $\alpha$ -tail (752-798), talin VBS1 (607-636) peptide conjugated and blank (no peptide) LUV pull downs of 6  $\mu$ M talin F2F3 and R7R8, P = pellet fraction, SN = supernatant fraction. (bottom) Triplicate analysis of the pull downs measured as percentage of total protein in pellet fraction (percentage bound); error bars represent SEM (n=3).

#### 6.4 Investigating talin F1 binding to $\alpha$ -integrin

Whilst there are multiple credible theories on how the two integrin tails are separated (Ye et al., 2011), the exact mechanism is yet to be fully elucidated. Throughout my thesis I have emphasised the importance of the orientation of the talin head at the cell membrane in integrin activation, with a particular focus on the talin F1 loop interacting with the membrane (Goult et al., 2010a). It is not clear as to why the talin head orientation is important for integrin activation. In particular

the importance of the F0 and F1 domains orientation, which are separated from F2 and F3 through a large linker (section 5.2), is not understood. Indeed, we and others have demonstrated that talin F2-F3 is capable of binding to the  $\beta$ -tail without the presence of F0-F1 (Calderwood et al., 2002; Anthis et al., 2009; Wegener et al., 2007). Despite no clear role in integrin activation being established for talin F0-F1, it is apparent these domains are not redundant in the process (Bouaouina et al., 2008). Therefore, understanding the role of F0-F1 in integrin activation may provide insight into the exact mechanism of talin-mediated integrin activation.

After establishing an interaction between the talin head and the  $\alpha$ -integrin cytoplasmic tail, we were keen to deduce whether this interaction may play a part in integrin activation through separation of  $\alpha$ - and  $\beta$ -tails (Wegener et al., 2007). Moreover, we wanted to explore how F0F1 were involved in separating of the tails.

#### 6.4.1 NMR investigation into talin F1 interacting with the $\alpha$ -tail

To investigate whether the talin head has a second  $\alpha$ -integrin binding site besides that on F3, an NMR HSQC experiment was used to investigate whether F1 might bind to integrin peptides. The same approach was employed as previously used to investigate talin F3  $\alpha$ -integrin binding. In this experiment a 2D HSQC spectrum of  $^{15}\text{N}$ -labelled talin F1 alone and with a 1:8 ratio of  $\alpha$ 2-tail peptide were collected. Initial addition of the  $\alpha$ -tail peptide to the labelled F1 led to slight precipitation of the peptide, as analysis of the 1D spectra revealed a final 1:5 ratio of alpha integrin (fig. 6.6A). The amount of F1 looked similar with and without the peptide. Despite the slight loss of the peptide, there was still a 5 fold excess of peptide, and multiple small shifts across the HSQC spectra were observed indicative of an interaction between talin F1 and the  $\alpha$ -tail (fig. 6.6).

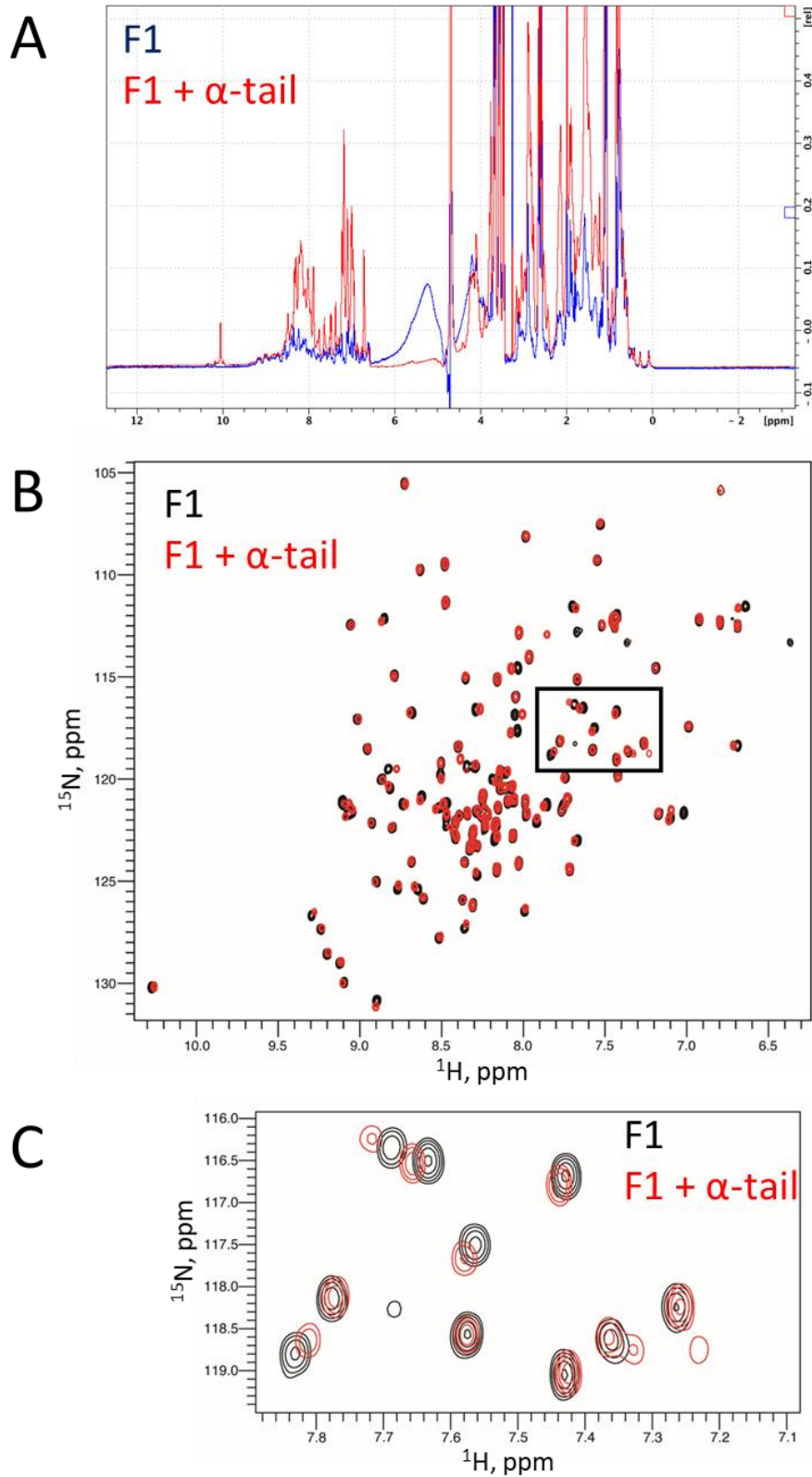


Figure 6.6: **Talin F1 binds the integrin  $\alpha$ -tail.** A) 1D  $^1\text{H}$ -spectra of talin F1 alone (blue) and with the  $\alpha$ -tail peptide (1154-1181) added, demonstrating a  $\sim 5$  fold excess of the  $\alpha$ -tail peptide. B) 2D HSQC spectra of  $^{15}\text{N}$ -labelled talin F1 alone (black) and with a 5 fold addition of the  $\alpha$ -tail peptide (red). C) Zoomed in region of HSQC spectra in B from within the black box.

The alpha tail contains a highly conserved “GFFKR” motif and so we next sought to test whether this motif might be involved in the interaction with talin. To investigate the involvement of the GFFKR motif the HSQC NMR experiment was repeated this time with the addition of an  $\alpha$ 2-tail GFFKR deletion mutant ( $\Delta$ GFFKR) at an 8:1 ratio. The addition of the peptide did not cause any obvious peak shifts, indicative of the mutant peptide not binding to F1 (fig. 6.7). The GFFKR motif is conserved in all alpha-integrin tails so this data suggests the  $\alpha$ 2-tail is binding to talin F1 in a GFFKR-dependent manner and therefore maybe a ubiquitous across all  $\alpha$ -integrin isoforms. It is possible that the GFFKR is a conserved talin-binding site.

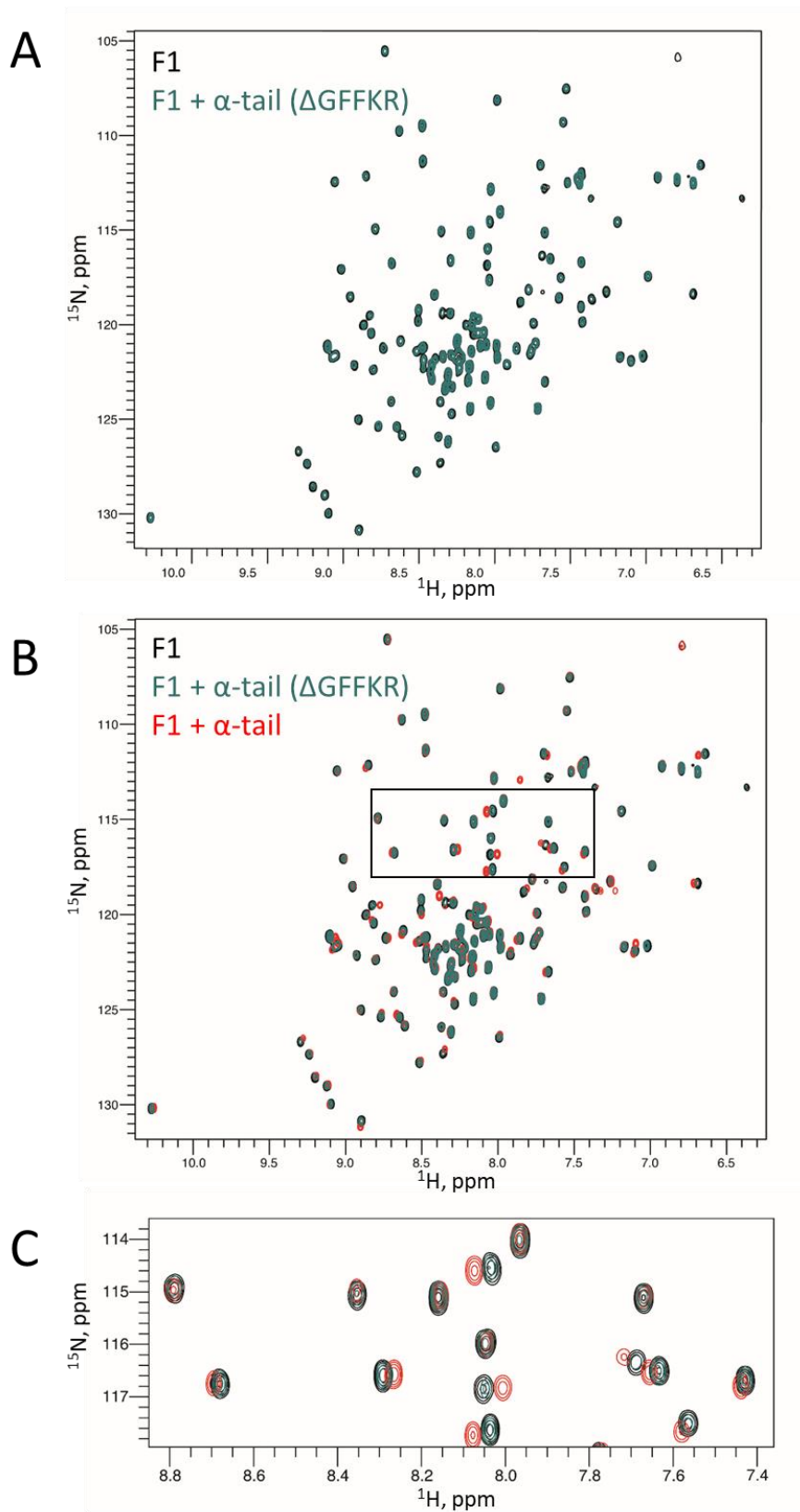


Figure 6.7: The GFFKR motif is necessary for  $\alpha$ -tail binding to talin F1. A) HSQC spectra of  $^{15}\text{N}$ -labelled talin F1 alone (black) and with the  $\alpha$ -tail ( $\Delta\text{GFFKR}$ ) peptide (green). B) Comparison of HSQC spectra of F1 with the WT- $\alpha$ -tail (1154-1181) (red) and the  $\Delta\text{GFFKR}$ -peptide (green). C) Zoomed in region of HSQC spectra in B from within the black box.

#### 6.4.2 Peak shift mapping of the $\alpha$ -tail binding to F1

Comparison of the peak shifts from the interaction between the  $\alpha$ -tail and talin F1 to a pre-assigned HSQC spectrum of F1 (BMRB Entry 15616) enabled identification of the residues involved in the interaction. The identified residues were then mapped onto the atomic structure of F1 (PDB: 2KC2). At first look the map suggested multiple regions of F1 were involved in the binding. However, upon closer inspection a lot of the shifts were in or around four of five histidine residues found in F1 (fig. 6.8). Histidine residues are very sensitive to changes in pH as the histidine side chain has a pKa around 6; our HSQC NMR experiments are buffered to pH 6.5. Despite our best efforts to regulate the pH in these experiments it is likely some of the shifts observed are due to subtle changes in pH after the addition of the peptide.

Interestingly, the peak shift mapping did raise the possibility of talin F1 being a pH-sensitive domain of the talin head. Talin has previously been described as a pH-sensitive protein, with pH affecting actin binding to the talin rod and adhesion dynamics (Srivastava et al., 2008; Goldmann et al., 2001). Moreover, talin also directly interacts with moesin-NHE-1 (sodium hydrogen exchanger 1) complex, an interaction that leads to a local increase in cytoplasmic pH within invadopodia (Beaty et al., 2014). Numerous peak shifts were mapped to an area around His-124 and His-176; it is possible with a local change in cytoplasmic pH, His-124 and His-176 could lead to conformational/surface charge changes within talin F1 that accommodate binding of different ligands, including the  $\alpha$ -tail and Rap1 (Gingras et al., 2019).

Due to this pH sensitivity of the F1 domain it is difficult to separate the shifts that are due to pH change and/or  $\alpha$  tail binding as we cannot determine what effects the pH is having on the structure of the domain. Therefore, it is important to repeat the experiment in a tightly pH-controlled system. This could be achieved by dialysing prepared samples together, ensuring a consistent pH across all samples.

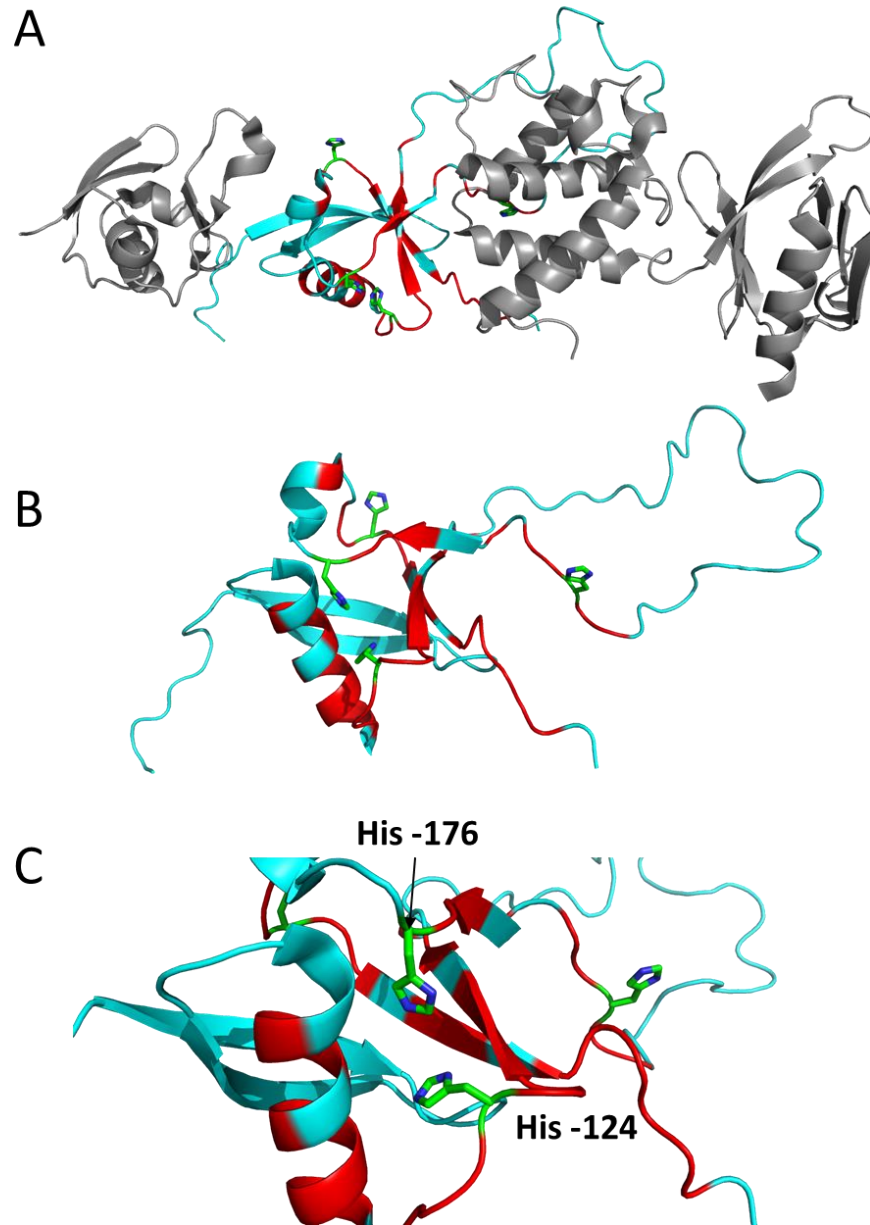


*Figure 6.8: Talin F1 is a pH sensitive domain. A) Atomic structure of talin head (3IVF) (grey) with the addition of F1 structure (2KC2; cyan), peak shifts coloured red; shifted histidines coloured green and shown as sticks. B) Atomic model showing just the shifts in talin F1 (2KC2). C) pH sensitive pocket in talin F1 due the presence of His-176 and His-124 (labelled).*

## 6.5 The alpha binding site sits between talin and Rap1

Rap1 is a Ras associated GTPase, with an essential function as an integrin activator (Boettner and Van Aelst, 2009; Stefanini et al., 2018). Currently, the reason why Rap1 is essential in talin-mediated integrin activation has not been fully elucidated. There are established roles for Rap1 as a talin recruiter through the Rap1 effector protein RIAM (Lee et al., 2009; Yang et al., 2014; Boettner and Van Aelst, 2009; Zhu et al., 2017). However, despite Rap1 being vital for platelet

integrin activation and function, RIAM is not necessary (Lagarrigue et al., 2018; Stefanini et al., 2018). Rap1 has also been demonstrated to bind to talin F0 coordinating the talin head at the cell membrane (Goult et al., 2010a; Zhu et al., 2017; Camp et al., 2018). However, as with RIAM, the F0:Rap1 interaction hasn't proved vital for integrin activity as mutants which disrupt the interaction did not greatly affect integrin activation (Bromberger et al., 2018), or have severe defects in mice (Lagarrigue et al., 2018). Interestingly, it has recently been demonstrated there is a very weak interaction between talin F1 and Rap1b (Gingras et al., 2019); mutants that disrupt this interaction prevent talin-mediated integrin activation.

#### 6.5.1 Molecular modelling suggests a tripartite interaction between F1, Rap1 and the $\alpha$ -tail

We were keen to deduce whether the Rap1-F1 interaction is involved in the  $\alpha$ -tail binding site on talin F1. To do this we initially made a molecular model of Rap1 binding to talin F1 using PyMOL. As both talin F0 and F1 form ubiquitin like folds (Goult et al., 2010a), it was possible to make an alignment between the previously solved talin F0:Rap1b structure (PDB: 6BA6) and talin F1 domain. The interacting residues between F1 and Rap1 identified from (Gingras et al., 2019) were used to validate the model (fig. 6.9 A). Onto the model we mapped the F1: $\alpha$ -tail NMR peak shifts; this revealed a cleft between Rap1, talin F1 and F2 into which the alpha tail could bind (fig. 6.9 B). In the cleft there are multiple hydrophobic pockets and charged residues in both talin and Rap1 which could accommodate the GFFKR motif of the  $\alpha$ -tail, forming a high affinity tripartite interaction (fig. 6.9 C).

The essential Rap1:F1 interaction has a very low affinity (Gingras et al., 2019); the talin F1: $\alpha$ -tail interaction also appears to have a very low affinity. Moreover, modelling of the Rap1-F1 interaction revealed a cleft in the  $\alpha$ -tail might sit between the two proteins. Therefore we hypothesised that Rap1 and talin F1 form a tripartite interaction with the  $\alpha$ -tail; in forming the tripartite complex each component could then form higher affinity complex as there will be a greater interacting surface.



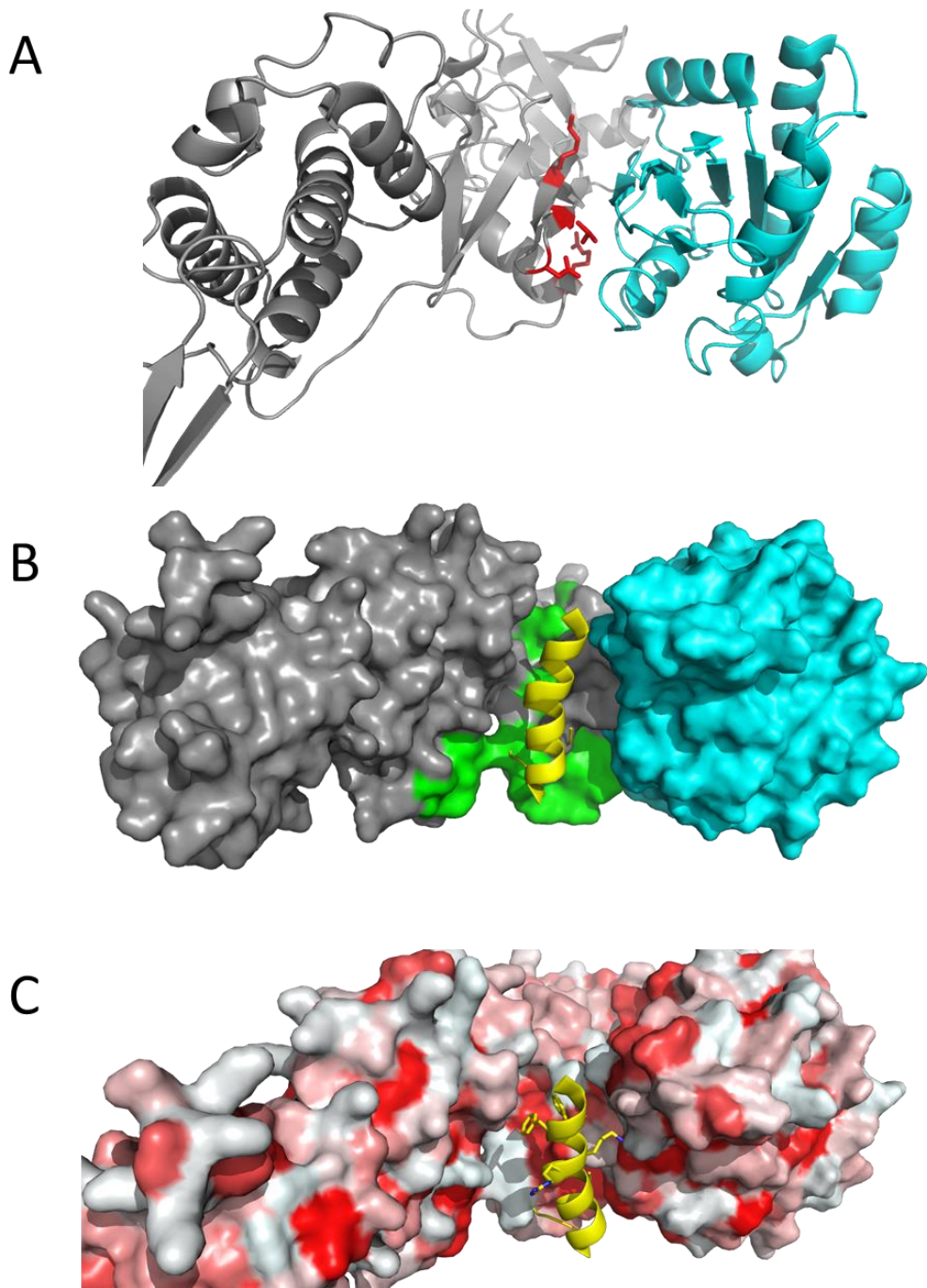


Figure 6.9: **Model of tripartite interaction between Rap1, talin and the  $\alpha$ -tail.** Atomic structure of the talin head (grey; 3IVF) with Rap1 (cyan; 6BA6) modelled onto talin F1. A) Cartoon format showing Rap1 modelled onto F1 with key talin residues for the interaction shown as red sticks. B) Surface representation of Rap1 bound talin head with talin: $\alpha$ -tail peak shifts coloured green and the  $\alpha$ -tail (yellow; 2LKE) modelled into groove between Rap1 and talin. C) Surface representation of Rap1 bound talin coloured by hydrophobicity (hydrophilic = white, hydrophobic = red), with the  $\alpha$ -tail modelled in showing the FFKR residues as sticks.

### 6.5.2 NMR investigation into Rap1b interacting with the $\alpha$ -tail

To test our hypothesis of a tripartite interaction between talin, Rap1 and the  $\alpha$ -tail, we used a HSQC NMR experiment, like those used previously on talin F3 and F1. In this experiment a 2D

spectrum of  $^{15}\text{N}$ -labelled Rap1b was measured with and without the addition of a 1:8 ratio of the FL- $\alpha$ -tail peptide. The addition of the  $\alpha$ -tail peptide caused multiple small peak shifts in the spectrum; these shifts are indicative of an interaction (fig. 6.10), like that observed between Rap1b and talin F1 (Gingras et al., 2019) and between talin F1 and the  $\alpha$ -tail. Moreover, there are no histidine residues in the Rap1b (1-166) construct used, so we can rule out pH-induced peak shifts like those observed by the addition of  $\alpha$ -tail peptide to talin F1. This data suggests there is a novel interaction directly between Rap1b and the  $\alpha$ -tail. Moreover, it supports our theory of a tripartite interaction between Rap1, talin and the  $\alpha$ -tail, which may strengthen the interaction between each protein.

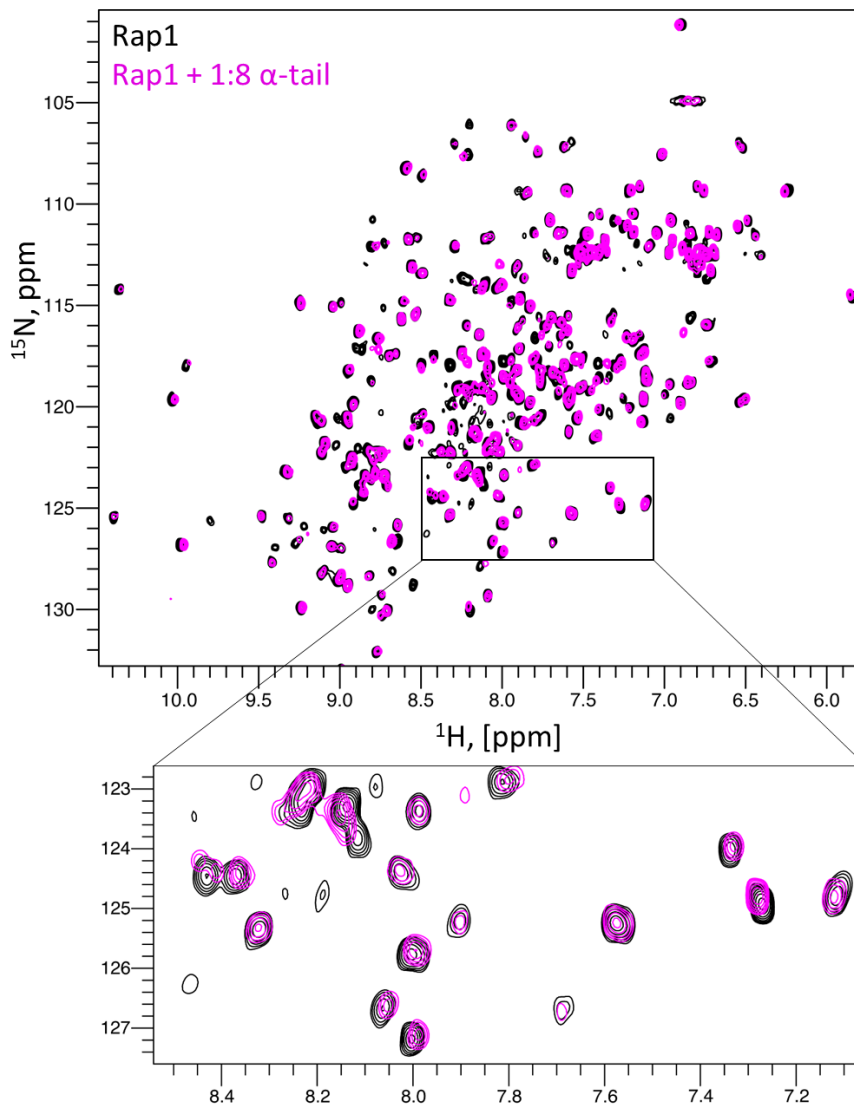


Figure 6.10: **Rap1 binds to the  $\alpha$ -tail.** 2D HSQC spectra of  $^{15}\text{N}$ -labelled Rap1 alone (black) and with the addition of a 1:8 ratio of the  $\alpha$ -tail peptide (magenta). (bottom) Zoomed in region of HSQC spectra from within the black box.

## 6.6 Discussion

Talin has a well-established and fundamental role as an integrin activator through an interaction between talin F3 and the  $\beta$ -cytoplasmic tail (Calderwood et al., 1999, 2002). Since the discovery of this interaction much focus has been put onto the talin: $\beta$ -tail interaction, whilst the  $\alpha$ -tail has been mostly overlooked. Indeed, there have been previously reported interactions between talin and the  $\alpha$ -tail that hadn't been followed up (Knezevic et al., 1996; Pavalko and Otey, 1994). Here we follow up on those initial studies confirming a direct interaction between the talin head and

the  $\alpha$ -tail. Moreover, we report on two novel  $\alpha$ -tail binding sites in talin on FERM domains F1 and F3, and a novel interaction between Rap1 and the  $\alpha$ -tail. Together, these results suggest there is an important new role for the  $\alpha$ -tail in talin-mediated integrin activation and control. Additionally, these results suggest talin has a more complex function in coordinating the activation state of integrin than previously thought.

#### 6.6.1 Talin as an integrin 'inactivator'

Talin has many established roles within integrin adhesions (Klapholz and Brown, 2017), one of the most established of which is as an integrin activator (Calderwood, 2004; Sun et al., 2019). Here we report a novel interaction between the  $\alpha$ -integrin cytoplasmic tail and talin F3; the same talin domain that interacts with the  $\beta$ -integrin cytoplasmic tail, as was previously observed (Knezevic et al., 1996). Moreover, NMR mapping reveals both integrin subunit tails bind in a similar region upon talin F3. These results raise the possibility that talin F3 can coordinate both the  $\alpha$ - and  $\beta$ -tails in close proximity to each other. The close proximity of the two tails causes integrin to remain in a bent closed low affinity state/inactive state (Wegener et al., 2007; Li et al., 2017b). If talin is holding the two tails in close proximity to one another it raises the possibility of a new role for talin holding integrin inactive. In this scenario talin might bind to inactive integrin and be poised to activate integrin upon a certain stimuli (fig. 6.11).

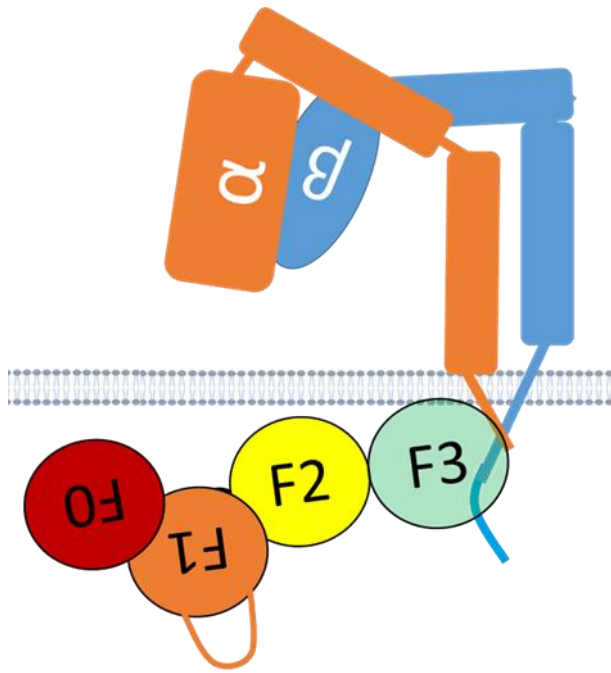


Figure 6.11: **Could Talin hold integrin in an inactive conformation.** Schematic diagram showing the talin head holding both integrin tails together on the F3 domain, thereby holding integrin in an inactive conformation.

Alternatively, binding of the  $\alpha$ - and  $\beta$ -tails to talin F3 could be a mutually exclusive event with unknown function. It may be possible that upon talin-mediated integrin activation the released  $\alpha$ -tail binds to a free talin molecule, leading to the reinforcement of the integrin:talin:actin complex (fig. 6.12). However, this would not be in agreement with stoichiometry measurements of 2:1 integrin receptors to talin molecules that have been previously observed (Calderwood et al., 1999; Bachir et al., 2014).

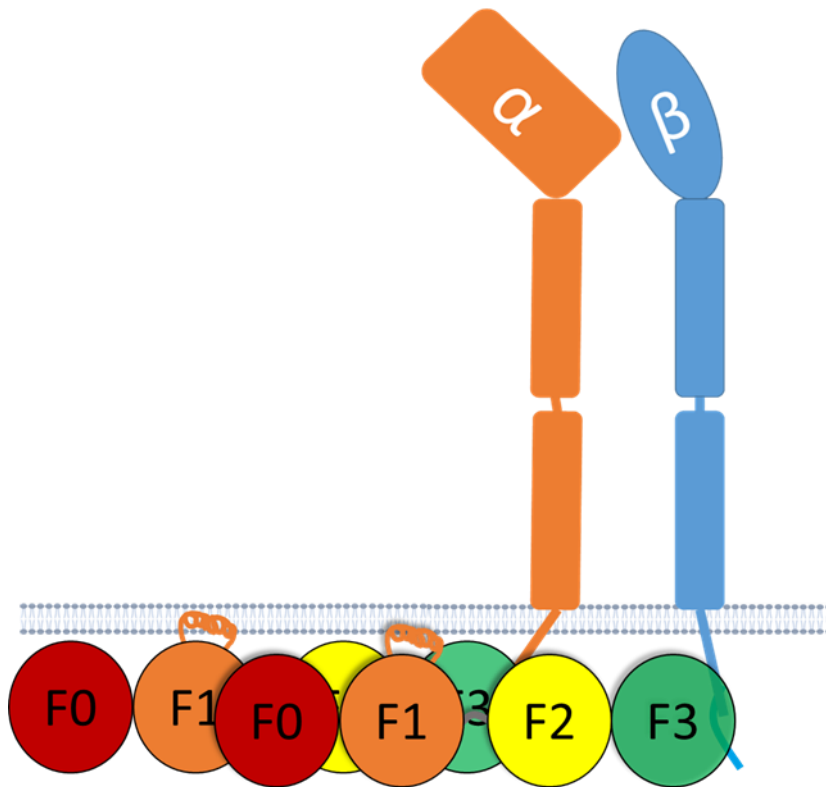


Figure 6.12: *Talin could reinforce active integrin via the F3 domain.* Schematic showing second model of talin F3 binding to the  $\alpha$ -tail exclusive to the  $\beta$ -tail which would allow reinforcement of active integrin.

#### 6.6.2 Talin as an integrin 'inactivator' further work

To fully elucidate whether the interactions between the  $\alpha$ - and  $\beta$ -tails and talin F3 are mutually exclusive requires further work. I would suggest to make use of a HSQC NMR experiment of  $^{15}\text{N}$ -labelled F3 in which a comparison in peaks is made through the addition of a  $\beta$ -tail peptide, an  $\alpha$ -tail peptide and then the two peptides together; if the addition of the two peptides leads to peaks shifting differently to the two individual tail spectra, then it suggests the two integrin subunits can bind at the same time. To understand the function of the interaction between talin F3 and the  $\alpha$ -tail it would be useful to design a mutant that can disrupt the interaction. Designing a mutant for this interaction would prove particularly difficult due to proximity of the  $\beta$ -integrin binding site on F3 and the multiple functions of the GFFKR motif found on the  $\alpha$ -tail in holding integrin inactive. However, if it were possible to obtain a crystal structure of the  $\alpha$ -tail bound to talin F3, then it would enable design of a very specific talin mutant that may disrupt the interaction.

### 6.6.3 Talin-Rap1-mediated integrin activation

Integrin activation requires the separation of the  $\alpha$ - and  $\beta$ - integrin cytoplasmic tails. Since the discovery of talin F3 binding to the  $\beta$ -tail (Calderwood et al., 1999) the interaction has defined the separation of the two integrin subunits (Wegener et al., 2007; Anthis et al., 2009). However, despite multiple theories there is not a decided mechanism by which the two tails are separated (Ye et al., 2011). Here we have evidence of a novel interaction between talin F1, Rap1b and the  $\alpha$ 2-tail. We believe these interactions may form a tripartite interaction between talin, Rap1 and  $\alpha$ -tail. Modelling of the tripartite interaction suggests there is a cleft between talin and F1-bound Rap1 which we speculate may create a high affinity site for the  $\alpha$ -tail. Based on these results we propose a new theory for separation of the integrin tails, in which Rap1 binding to talin F1 forms a high affinity binding site for the  $\alpha$ -tail holding it separated from the F3 bound  $\beta$ -tail (fig. 6.13). This theory is backed up by the recent discovery of an interaction between talin F1 and Rap1 being essential for talin mediated integrin activation (Gingras et al., 2019). Moreover, the necessity of the Rap1-F1 interaction and the F1 loop binding to the cell membrane for integrin activation (Goult et al., 2010a; Gingras et al., 2019) is difficult to contextualise, due to the large linker between F1 and F2. The large linker may prevent mechanical signals from ligand binding crossing between the F0F1 and F2F3 modules. Thus, an interaction on F0F1 would be unlikely to directly impact the integrin binding/activating capacity of talin F3. If the tail separation theory were to prove correct it would provide a rationale for the essential role of the Rap1-F1 interaction and conformational regulation of the F1 domain in integrin activation.

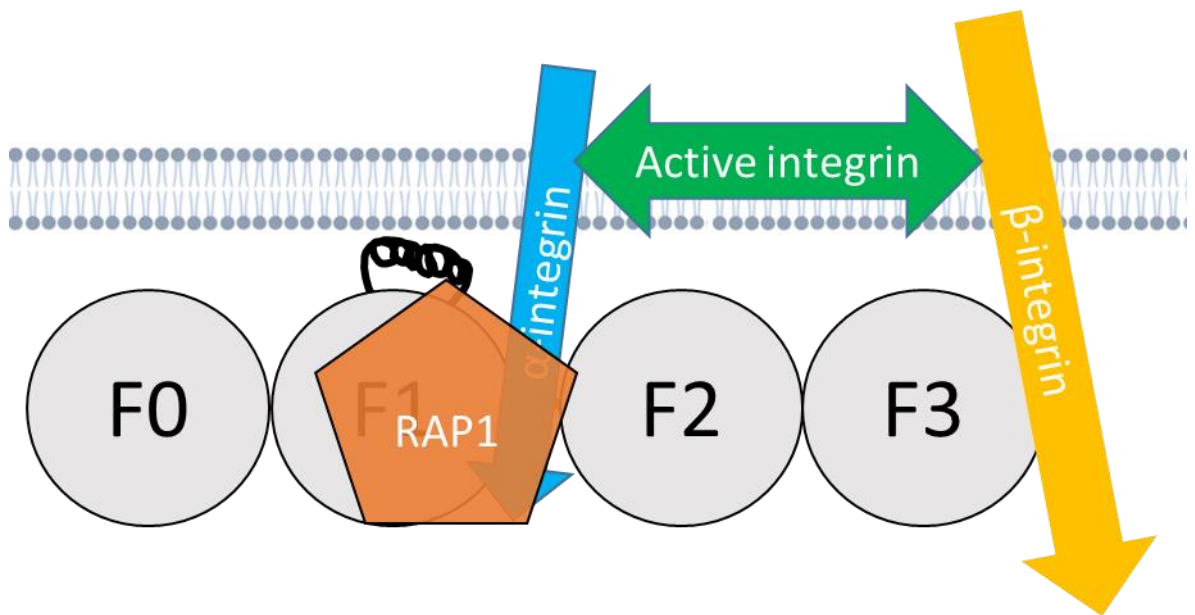


Figure 6.13: **Model for Talin-Rap1-mediated integrin activation.** Schematic diagram showing the talin head and holding the two integrin tails separated through a tripartite interaction involving talin F1, Rap1 and  $\alpha$ -tail and the  $\beta$ -tail:F3 interaction, thereby activating integrin.

#### 6.6.4 Talin-Rap1-mediated integrin activation further work

In this chapter, we have reported evidence of novel interactions between talin F1, Rap1 and the  $\alpha$ 2-tail, allowing us to propose a new theory for talin-mediated integrin activation. However, there has been a limitation to the F1: $\alpha$ -tail data, due to the pH-sensitivity of the F1 domain. Despite our best efforts to regulate the pH of the F1 experiments it is not possible to conclusively attribute peak shifts to alpha binding and not to pH effects. These changes in pH are very small but NMR titrations are particularly sensitive to them as the titration of histidines occurs within a fraction of a pH unit of our buffer. To account for the pH sensitivity in the future, the NMR experiments should be repeated after all prepared samples of the titration are dialysed into the same buffer, this would rule out the pH effect and allow identification of interacting residues. Moreover, an MST assay, like that described in section 4.1, could be used to reinforce the findings of the NMR experiments and provide a binding affinity for the interaction.

To further investigate the talin:Rap1: $\alpha$ -tail tripartite model it would be interesting to investigate the binding of the  $\alpha$ -tail to talin F2 as our model puts the talin domain and the  $\alpha$ -tail in close proximity. Furthermore, if the tripartite theory is correct we would expect to observe increased

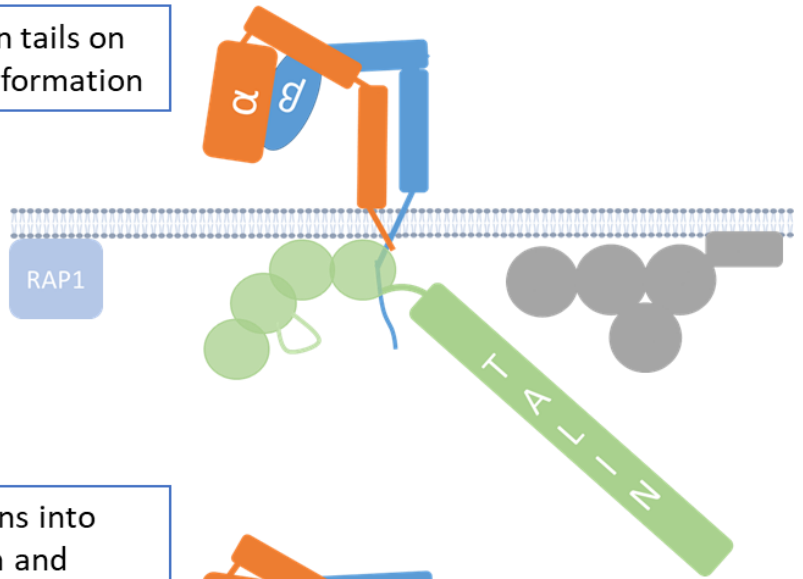


affinity between all three components; to test this you could use an NMR experiment in which all three components are involved, if there is an increase in affinity there would be an enhancement of the peak shifts observed compared to the two component experiments we have previously done. Further, the enhanced affinity of the tripartite interaction may facilitate the crystallisation of the complex; an atomic model of the complex would further our understanding of the interaction and enable accurate mutant design for *in vivo* studies.

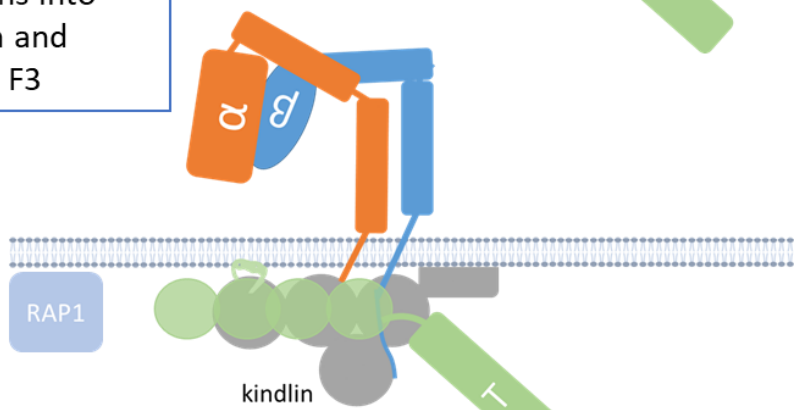
#### 6.6.5 Talin mediates integrin activation through both integrin subunits

Throughout my thesis so far it is clear there are multiple complex mechanisms regulating talin-mediated integrin activation. Whilst I have reported these mechanisms separately, they are almost certainly interlinked, providing important context to each other. By coordinating the individual mechanisms I have described, here I propose a model that encompasses all of the mechanisms involved in talin-mediated integrin activation. 1) The talin head holds both integrin tails on F3 when in the 'twisted' conformation holding integrin inactive. 2 i) Upon a certain stimuli the talin head is altered into the linear conformation with the F1 loop bound to the membrane. 2 ii) In the transition from twisted to linear conformation the  $\alpha$ -tail is released from talin F3. 3) The linear conformation is stabilised by kindlin binding to the talin head. 4) The membrane bound talin F1 recruits Rap1 and the  $\alpha$ -tail simultaneously; the tripartite interaction then holds the  $\alpha$ -tail separated from the  $\beta$ -tail thereby activating integrin (fig. 6.14).

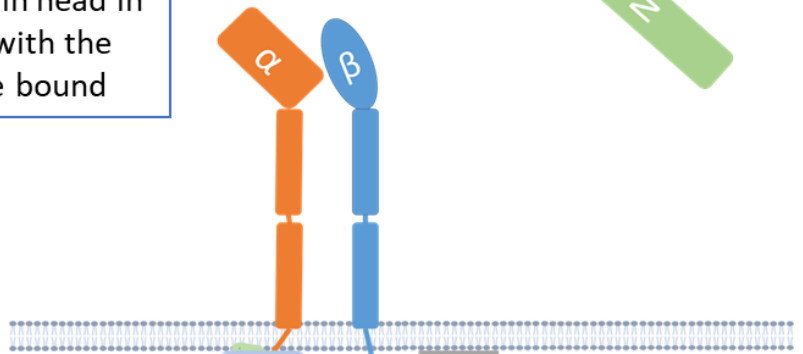
1. Talin holds both integrin tails on F3 whilst in twisted conformation



2. The talin head transitions into the linear conformation and releases the  $\alpha$ -tail from F3



3. kindlin stabilises the talin head in a linear conformation, with the talin F1 loop membrane bound



4. Tripartite interaction forms between RAP1, the  $\alpha$ -tail and talin F1, holding the integrin tails separated, thereby activating integrin

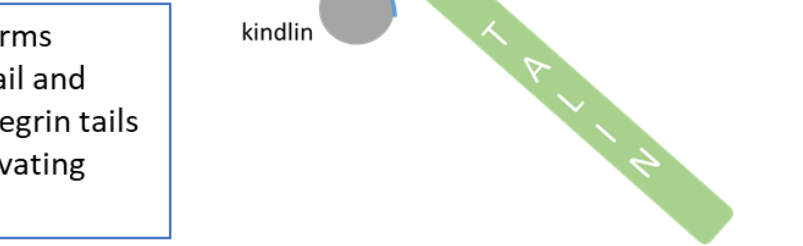


Figure 6.14: Talin mediated integrin activation. Schematic describing the steps in proposed integrin activation theory.

## Chapter 7: Biochemical characterisation of novel interactions of talin and vinculin.

### 7.1 Introduction

#### 7.1.1 Talin and Vinculin at adhesions

Talin and vinculin provide a critical mechanical link between integrins and the actin cytoskeleton. Talin is a large scaffolding protein consisting of an integrin binding head region attached to a large actin binding mechanosensitive rod, made up of 13 helical bundle domains, four 4-helix (R2, R3, R4 and R8) and nine 5-helix (R1, R5, R6, R7, R9-R13), and a single helix forming a C-terminal dimerization domain (Goult et al., 2013b). Locked inside the talin rod helical bundles are at least 11 cryptic vinculin binding sites (VBS) (Gingras et al., 2005; Papagrigoriou et al., 2004) (fig. 7.1 A). As actomyosin machinery increases the tension across the integrin-talin-actin complex, the rod bundles unfold incrementally in the force transduction pathway between forces of 5 to 25 pN (Yao et al., 2016, 2014a). Once the cryptic VBS are exposed they can recruit and bind vinculin (del Rio et al., 2009). Binding of exposed VBS to Vd1 in coordination with actin binding of the Vt activates autoinhibited vinculin (Chen et al., 2006). The simultaneous binding of vinculin to talin and actin reinforces the engagement of talin with the actomyosin machinery allowing greater force transduction (Humphries et al., 2007; Thievensen et al., 2013; Goult et al., 2013b; Atherton et al., 2015).

#### 7.1.2 Talin vinculin binding sites

Talin contains 11 VBS inside the talin rod. Each VBS is a single amphipathic  $\alpha$ -helix which are locked inside 4/5 helix bundles with a consensus sequence of LxxAAxxVAxxVxxLxxA (Gingras et al., 2005; Papagrigoriou et al., 2004). To expose the cryptic VBS force is required to overcome the hydrophobic core that holds the bundle together, thereby unfolding the domains (fig. 7.1 B) (Goult et al., 2013b). Each talin helical bundle in the force transduction pathway unfolds in a step-

wise manner in response to increasing force, with R3 unfolding first under the lowest force ~5 pN (Yao et al., 2014a, 2016).

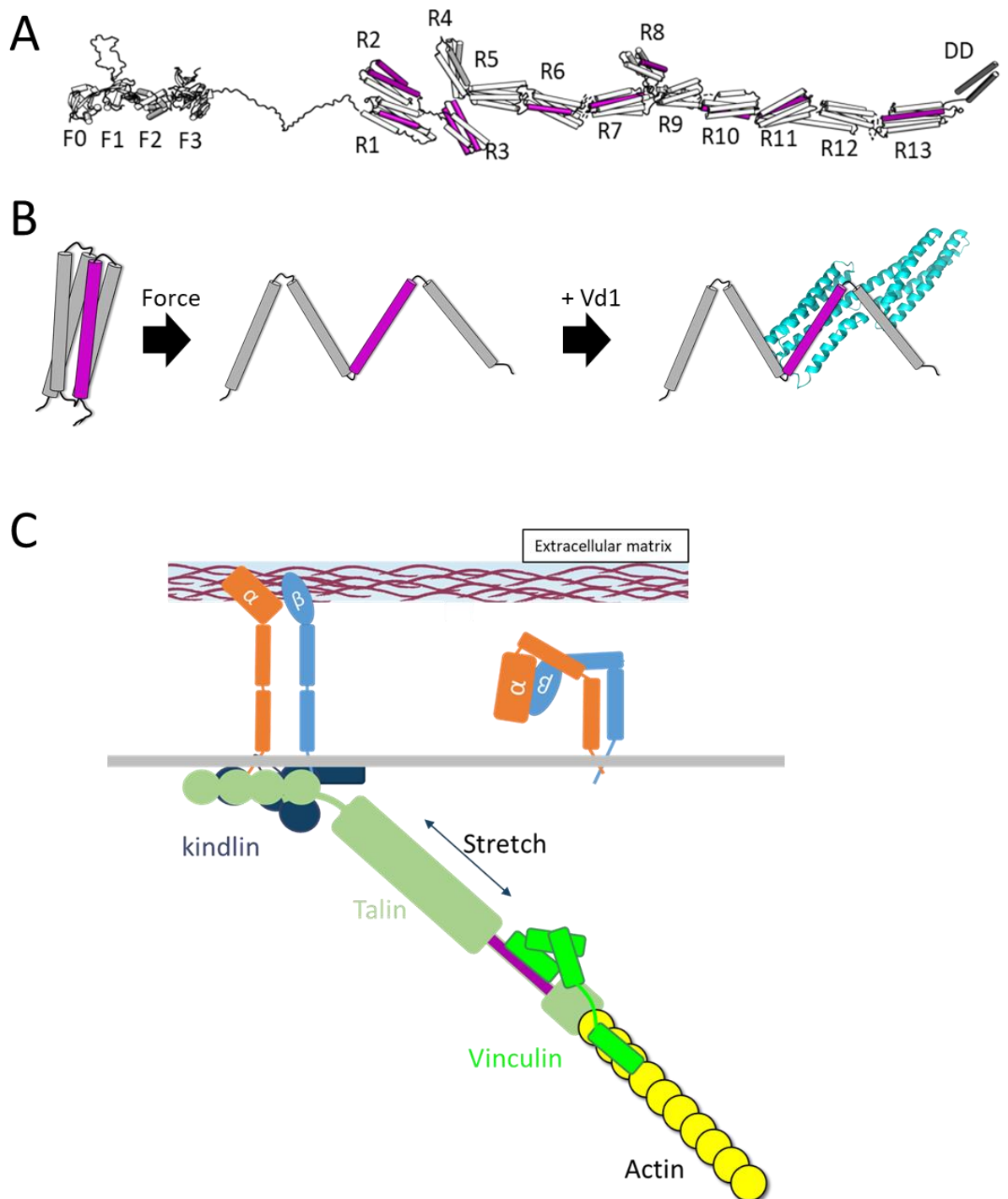


Figure 7.3: **Vinculin binding to talin.** A) structure of full length talin showing the VBS (purple) locked inside helical bundles. B) Schematic showing the unfolding of a four helix domain under force exposing the VBS (purple) and binding of Vd1 (cyan). C) schematic showing vinculin (green) reinforcing the talin binding to actin.

### 7.1.2 Aims

The talin-vinculin interaction is a crucial axis within adhesions for translating the mechanical forces exerted on adhesions into downstream signalling pathways (Goult et al., 2018; Carisey and Ballestrem, 2011). Through understanding the intricacies of this interaction we aim to elucidate the mechanisms by which the talin-vinculin axis determines the fate of a cell in response to mechanical signals. In this chapter we investigate how the talin-vinculin axis dictates nascent adhesion maturation through an interaction with a force-independent talin VBS found in talin R8 (section 7.2). Additionally, we elucidate how the talin-vinculin axis can be hijacked by pathogenic virulence factors, specifically the chlamydial virulence factor TarP, to aid host cell entry (section 7.3).

## 7.2 Force-independent VBS in talin R8 determines nascent adhesion maturation

### 7.2.1 Talin and vinculin dependent nascent adhesion maturation

Nascent adhesions (NAs) are small adhesion structures that form in the cell lamellipodium. NAs are rapidly turned over at the protruding edge of the cell during the early maturation stages (Parsons et al., 2010). However, some NAs mature into larger focal complexes ( $>0.5\mu\text{M}$  in length) and focal adhesions ( $>2\mu\text{M}$  in length)(Gardel et al., 2010). For NAs to mature a series of events must occur regarding the stoichiometry of core adhesion proteins before and after force onset. In particular, the recruitment of talin and vinculin play a critical role due the mechanical sensitivity of the interaction (Bachir et al., 2014). The cryptic nature of vinculin binding sites within talin correlates with a force-assisted adhesion maturation model (Vogel and Sheetz, 2006), whereby activated talin engages integrin and captures the actin retrograde flow; under force the talin rod domains then unfold in response to different forces exposing the cryptic VBS (Yao et al., 2014a); vinculin binding to the exposed VBS stabilises the integrin-talin-actin complex; vinculin engagement also enables cross linking to multiple actin filaments; as force increases more vinculin

is recruited and more cross linking occurs enabling focal complexes and adhesions to eventually form (Yan et al., 2015; Atherton et al., 2015; Yao et al., 2016; Case et al., 2015) (fig. 7.2).

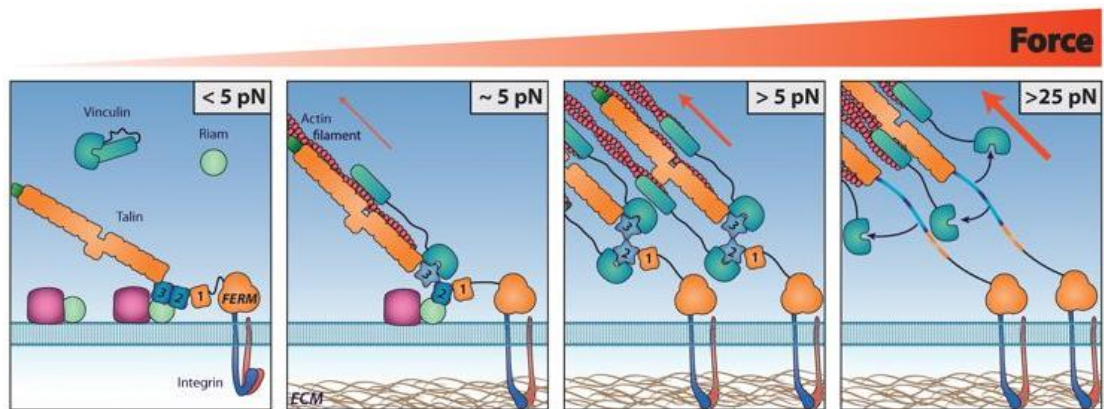


*Figure 7.4: Force dependent model adhesion maturation. <5 pN activated talin engages integrin. ~5 pN the talin rod catches the actin retrograde flow; the forces lead to talin R3 unfolding exposing VBS; vinculin binds and reinforces talin and actin. >5 pN more rod domains unfold revealing more VBS leading to cross-linking of adhesion complexes. >25pN the talin rod helices unfold and lose vinculin binding. Adapted from (Yao et al., 2014a)*

### 7.2.2 Force independent talin-vinculin pre-complex in nascent adhesion assembly

Most nascent adhesions are rapidly turned over at the protruding edge of the lamellipodium but some of these adhesions mature into the much larger FCs and FAs (Parsons et al., 2010; Gardel et al., 2010). For NAs to mature into the larger FCs and FAs they undergo many decision processes regarding their fate and morphology. However, compared to FAs of which size, composition and signalling has been relatively well studied (Horton et al., 2015; Winograd-Katz et al., 2014), very little is known about the formation, mechano-regulation and maturation of NAs. Recent technological advances in traction force microscopy (Gutierrez et al., 2011) have enabled the determination of force transmission as a vital factor for NA stabilisation and maturation (Han et al., 2015). However, the factors that determine whether a NA begins to bear forces enabling maturation, are still unknown. It has been hypothesised that the stoichiometry of the earliest components recruited to NAs could play an important role in NA fate (Digman et al., 2009; Zaidel-Bar et al., 2004). In particular, the recruitment of talin, vinculin and paxillin could have a critical role due to their mechanosensitive nature (Carisey et al., 2013; Kumar et al., 2016; Humphries et al., 2007).

To investigate the effects of stoichiometry on force transmission and NA maturation, our collaborators from the Danuser lab combined high-resolution traction force microscopy with single-particle-tracking of fluorescently labelled molecules and fluorescence fluctuation time-series analysis. This enabled them to track the recruitment of the core adhesion proteins: talin, vinculin and paxillin in relation to traction force onset; then by applying machine learning approaches to the data set, they were able to separate NAs into nine different subsets based on their size, force transmission and lifetime.

A particular focus was put on two subclasses: non-maturing NAs (G1) and maturing NAs (G2). Nascent adhesions classified into G2 formed at the protruding edge of the lamellipodium but slide rearward relative to the substrate and mature to form larger FCs and FAs, with a high fluorescence intensity; they also had the longest lifetime of all the subtypes. G1 adhesions also formed at the protruding edge, however they stay relatively stationary, have weak fluorescence intensity and a short lifetime. In the non-maturing NAs talin and vinculin were recruited sequentially before the onset of force transmission; and paxillin recruitment coincided with force transmission. Whereas, in maturing NAs all three component's recruitment coincided with the onset of force transmission. The contrast in stoichiometry between the two subtypes of NAs suggests the speed in which the adhesion forms determines its ability to mature. Our collaborators hypothesised this speed of assembly was determined by talin forming a pre-complex with vinculin in the absence of force, as has previously been suggested (Bachir et al., 2014), prior to force transmission.

### 7.2.3 Talin R8 contains a threonine belt

It is well established the talin R3 domain is the first domain to unfold following force transduction (Yao et al., 2014a). Structural studies of the R3 domain revealed it was destabilised due to the presence of a 'threonine belt' consisting of four threonine residues protruding into the hydrophobic core of the domain (Goult et al., 2013b). The R3 domain has been stabilised by

mutating the suspect threonine residues into hydrophobic residues in an 'IVVI mutant'. The IVVI mutant prevented R3 from unfolding and significantly reduced the activity of the two VBS found inside the domain (Yao et al., 2014b; Elosegui-Artola et al., 2016; Goult et al., 2013b) (fig. 7.3).

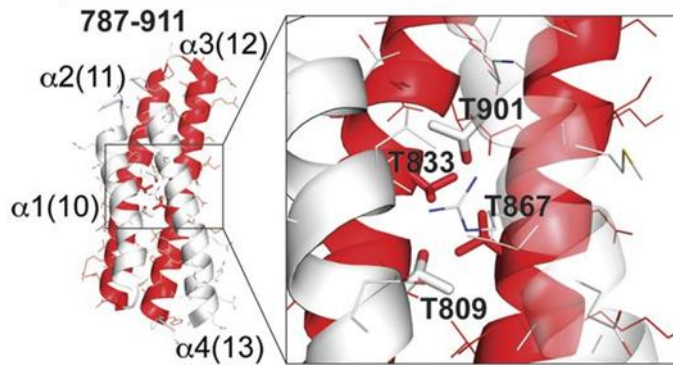


Figure 7.5: **talin R3 contains a threonine belt.** Atomic structure of R3, with VBS11, and VBS12 coloured red; zoomed in on threonine residues T809, T833, T867 and T901 destabilising the hydrophobic core. Adapted from (Goult et al., 2013b)

As aforementioned, the talin-vinculin interaction is usually force dependent. However, the formation of a talin-vinculin pre-complex suggests talin contains a VBS that is exposed spontaneously in the absence of force. The spontaneous exposure of a talin VBS suggests there is another destabilised talin domain like R3 that is outside the force transmission pathway.

It is believed the talin R8 domain is situated outside the force transmission pathway due to the protection provided by the adjacent R7 domain (Gingras et al., 2010; Yao et al., 2016); however, on its own R8 unfolds at ~5 pN, a similar force to R3 (Yao et al., 2016), suggesting the domain is also destabilised. Moreover, it has been demonstrated that the VBS (helix-33) within R8 is readily able to bind vinculin without force (Gingras et al., 2010). Through investigating the atomic structure of the R8 domain (pdb: 2X0C), we have identified the R8 domain is indeed destabilised through a threonine belt, consisting of T1502, T1542 and T1562 (fig. 7.4).



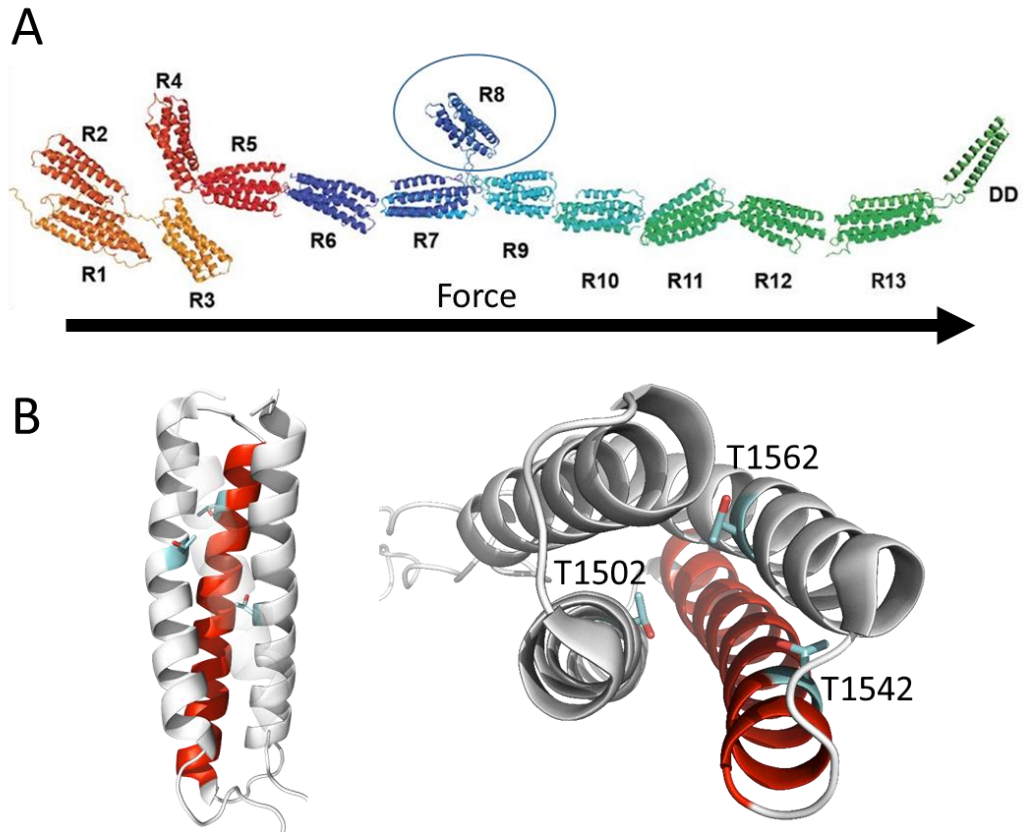


Figure 7.6: **Talin R8 contains a threonine belt.** A) domain structure of talin showing talin R8 adjacent to R7 outside the force transmission pathway (adapted from (Goult et al., 2013b)). B) Atomic structure of R8 (pdb: 2X0C) showing VBS33 (red) and the threonine belt – residues T1502, T1542 and T1562 (cyan) – destabilising the hydrophobic core.

#### 7.2.4 Stabilising R8 using a ‘VVV’ mutant

To stabilise the R8 domain we used similar approach to that used to stabilise R3 using the IVVI mutant (Goult et al., 2013b). In this case we designed an R8 ‘VVV’ mutant in which the threonine residues identified in the threonine belt (T1502, T1542 and T1562) were mutated to valine residues. In theory, the hydrophobic valine residues should stabilise the hydrophobic core that holds the R8 domain together.

#### 7.2.5 R7R8vvv mutant stabilises the R8 domain

To investigate the biochemical properties of the ‘VVV’ mutation we used a talin R7R8 construct containing the ‘VVV’ mutation (R7R8vvv). Initially it was important to confirm the mutation stabilised the hydrophobic core of the R8 domain. To test the stability of the R7R8vvv mutant, circular dichroism (CD) was used to measure the unfolding characteristics of the mutant in

comparison to the wild-type R7R8 construct (R7R8wt) (fig. 7.5). In the R7R8wt the two domains unfolded cooperatively with a single unfolding step, at a melting temperature of ( $T_m$ ) of 55°C as has been previously observed (Gingras et al., 2010). In contrast, the R7R8vvv mutant resulted in the two domains unfolding independently, with R7 unfolding at a similar temperature to the R7R8wt ( $T_m = 56^\circ\text{C}$ ) and the stabilised R8 domain increased from a melting temperature of 55°C to 82°C. The two unfolding steps demonstrate that as opposed to the R7R8wt, in the R7R8vvv mutant R7 and R8 behave independently with regard to thermal stability, demonstrating the 'VVV' mutation has stabilised the R8 domain.

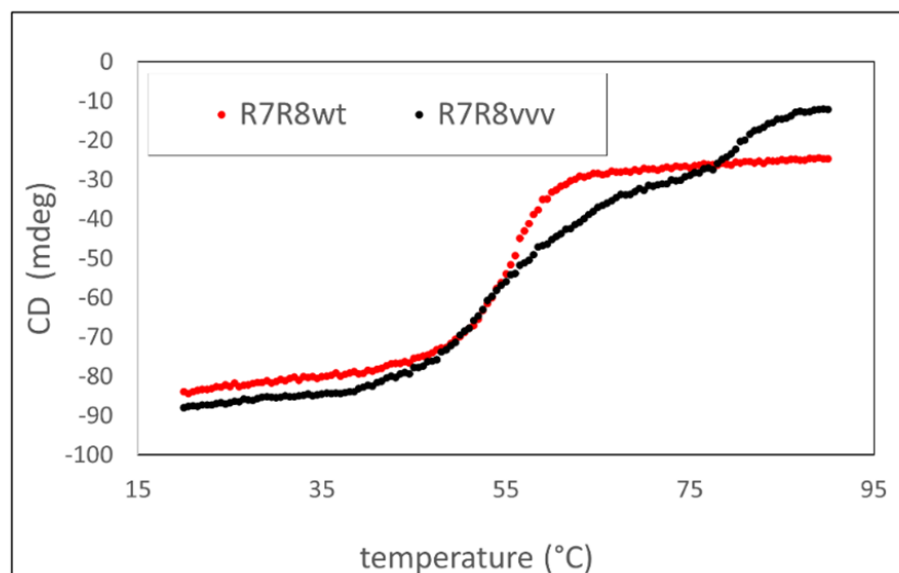


Figure 7.7: **The 'VVV' mutation stabilises the R8 domain.** Denaturation profiles for wildtype R7R8wt (red) and R7R8vvv (black) measured by monitoring the change in circular dichroism at 208 nm with increasing temperature. R7R8wt has a melting temperature of 55°C, whereas R7R8vvv unfolds in two steps, one (R7) with a melting temperature of 56°C and R8 unfolding at 82°C.

#### 7.2.6 R7R8vvv mutation has no major effect on LD-motif containing ligand binding

The R8 domain not only contains a VBS but also has an important role in talin signalling, as it serves as an LD-motif binding domain. The domain has been demonstrated to bind both DLC1 and RIAM (Goult et al., 2013b; Zacharchenko et al., 2016a). Whilst the VVV mutations are located in the core of the domain, it was important to test that the mutations were not altering the R8 surface, in particular the LD-motif binding site. To test whether the R7R8vvv mutation has an

effect on the LD-motif binding properties of R8, we used a fluorescence polarisation assay to measure the binding affinities between fluorescein labelled RIAM TBS1 and DLC1 peptides and the R7R8vvv compared to the R7R8wt. The R7R8wt bound to DLC1 with a  $K_d = 15.24 \mu\text{M}$ , the R7R8vvv mutant bound with a comparable affinity of  $K_d = 13.85 \mu\text{M}$  (fig. 7.6). Additionally, R7R8wt and R7R8vvv bound to RIAM with comparable affinities of  $K_d = 5.94 \mu\text{M}$  and  $K_d = 3.62 \mu\text{M}$  respectively. Together these results demonstrate the mutation does not dramatically affect the LD-binding ability of the domain.

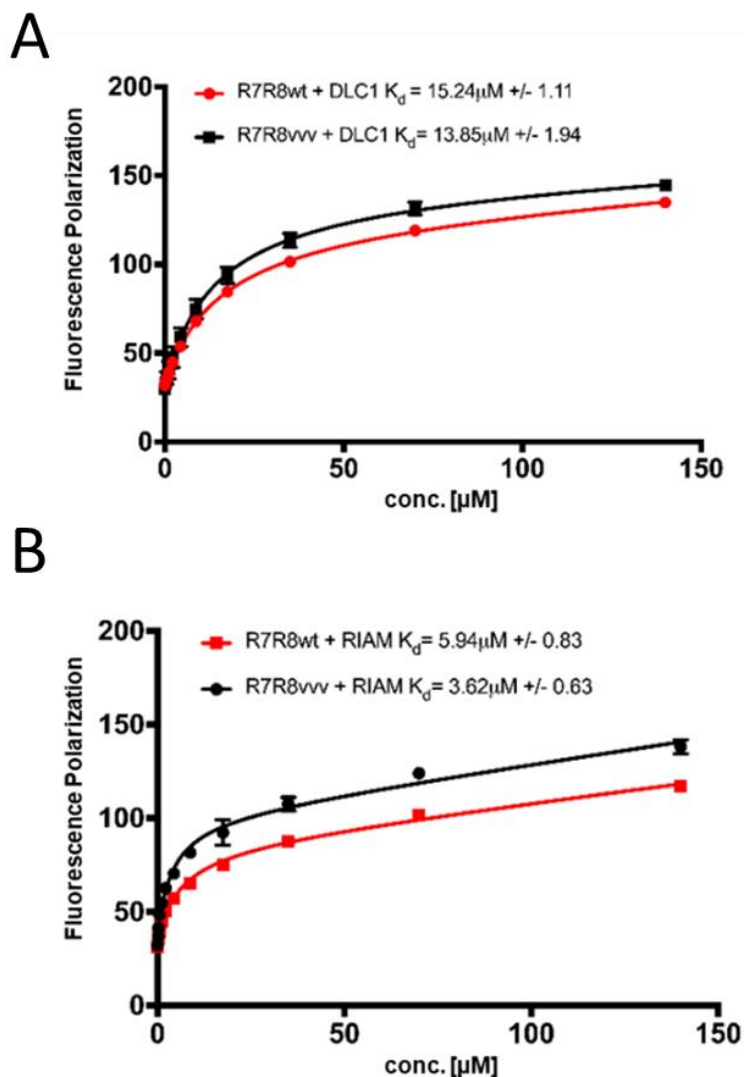


Figure 7.8: The VVV mutation has no dramatic effect on LD-motif binding ability of R8. Binding of Fluorescein-labelled DLC1 peptide (465-489) (A) and RIAM TBS1 peptide (4-30) (B) to talin R7R8wt (red) and R7R8vvv (black), was measured using a Fluorescence polarization assay. Dissociation constants for the interactions are indicated in the legend +/- SEM ( $n=3$ ).

### 7.2.7 The VVV mutation reduces the propensity of the R8 domain to bind vinculin

It has previously been demonstrated that VBS33 in R8 can spontaneously bind to vinculin in the absence of force, or raise in temperature (Gingras et al., 2010). By stabilising the R8 domain with the VVV mutation, we hypothesised the mutation would reduce the availability of VBS33 to bind to vinculin, thereby reduce the overall ability of the domain to bind vinculin. To test this hypothesis we used an analytical size exclusion chromatography (SEC) assay to look at complex formation. In this assay R7R8wt and R7R8vvv were pre-incubated with an equimolar amount of vinculin Vd1 at room temperature, the resulting mixture was then run on SEC-column. The resulting analysis of the chromatograms revealed that 71.4 % of R7R8wt complexed with Vd1, in contrast only 42.4% of R7R8vvv complexed with Vd1. The lower proportion of R7R8vvv-Vd1 complex compared to the R7R8wt-Vd1 suggests the VVV mutation reduces the ability of R8 VBS33 to bind to vinculin (fig. 7.7).

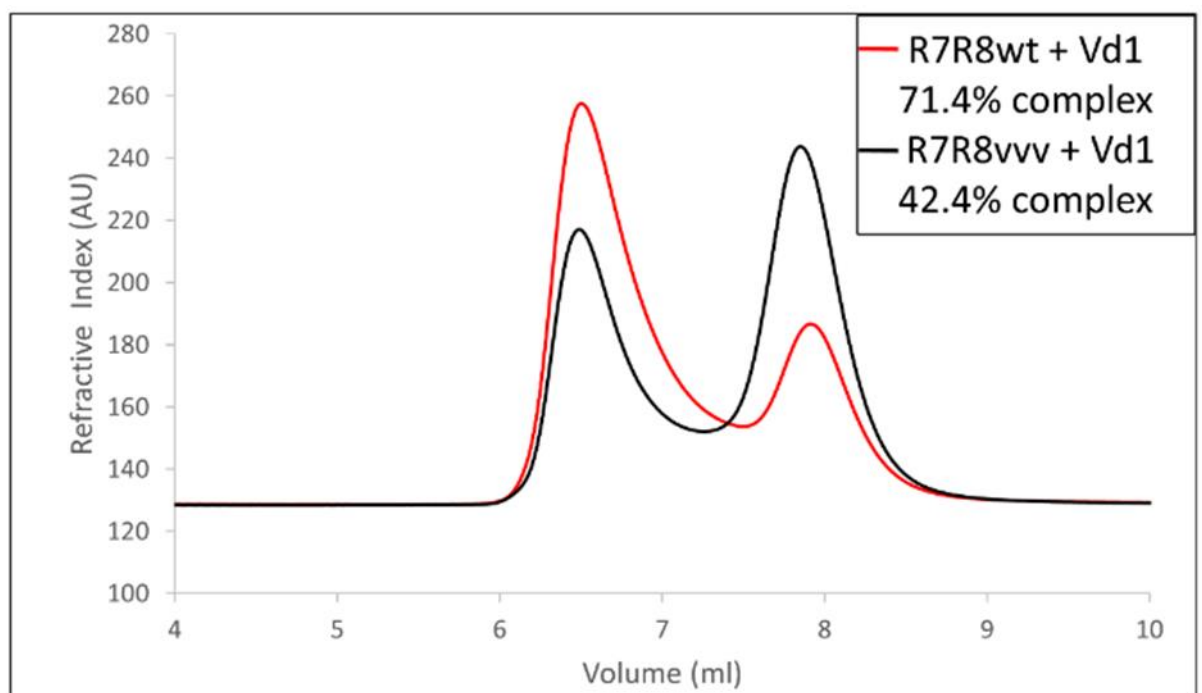


Figure 7.9: **Size exclusion chromatography demonstrates the VVV mutation reduces the ability of R8 to bind to vinculin.** Chromatograms showing binding of Talin R7R8 to Vd1. WT R7R8 (red) and R7R8vvv (black) binding to Vd1. Complex peaks and unbound peaks are indicated.

To further quantitate the effect of the VVV mutation on vinculin binding we used an MST assay, titrating the talin proteins against RED-tris-NTA labelled Vd1. R7R8wt bound to Vd1 with a relatively high affinity of 2.07  $\mu\text{M}$ , whereas under the same conditions, we were not able to detect any binding of the R7R8vvv mutant to Vd1 (fig. 7.8). Together with the SEC data, these results confirmed the stabilising effect of the VVV mutation also reduces the ability of the R8 domain to bind vinculin.

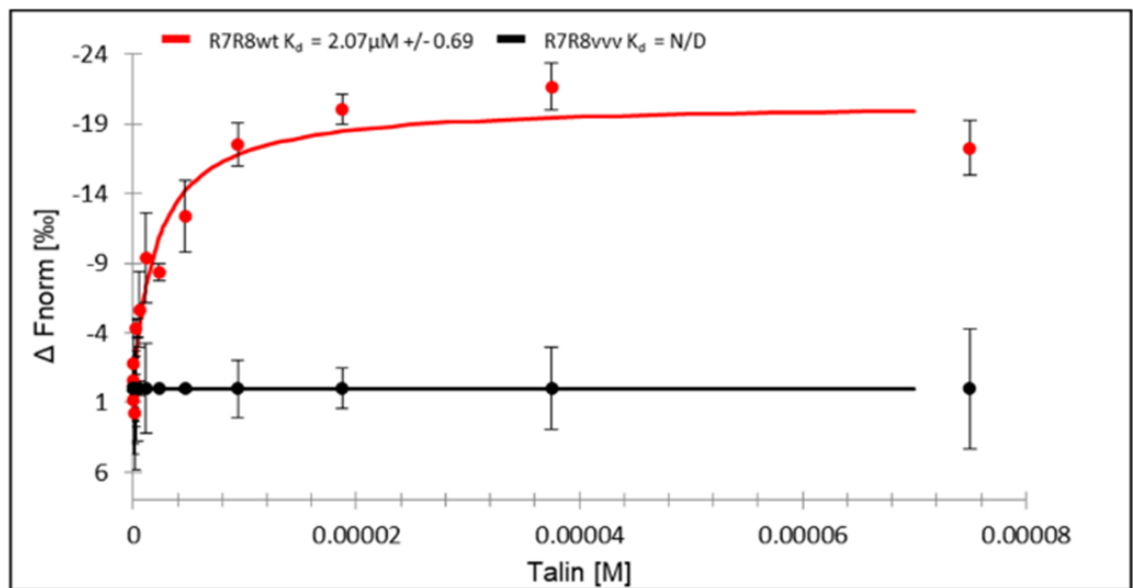


Figure 7.10: **MST demonstrates the VVV mutation reduces the ability of R8 to bind to vinculin.** MST analysis of wild type talin R7R8 (red) and R7R8vvv (black) interaction with the vinculin head (Vd1). Experiments were done in triplicate and analysed using the  $K_d$  fit model on NanoTemper analysis software. Dissociation constants  $\pm K_d$  confidence for the interactions are indicated in the legend ( $n=3$ ). ND not determined.

### 7.2.8 Biochemical conclusions

In conclusion, we believe VBS33 situated in the R8 domain is responsible for the formation of talin-vinculin pre-complexes due to the domain being outside the force transmission pathway, having a low stability (Yao et al., 2016) and having the ability to spontaneously bind to vinculin (Gingras et al., 2010). We have identified a ‘threonine belt’ within R8, like that previously identified in R3 (Goult et al., 2013b), that destabilises the R8 domain, enabling increased availability to VBS33. By mutating the suspect threonine residues of the belt into valines in a VVV mutation we increased the thermo-stability of R8. The stabilising mutation reduced the

availability of VBS33 thereby reducing the ability of R8 to bind to vinculin in the absence of force, whilst not affecting the LD-motif binding site on the surface of the domain. Together, this confirms the VVV mutation is a useful tool for investigating the effect of inhibiting talin-vinculin pre-complex formation on adhesion maturation *in vivo*.

### 7.2.9 R7R8vvv mutation impairs nascent adhesion maturation

To investigate whether talin-vinculin pre-complex formation promotes adhesion maturation our collaborators in the Danuser lab prepared cells expressing talin with the VVV mutation in R8, and utilised their NA tracking and classification system to observe the effects of the mutation.

Markedly, the cells expressing the talin mutant contained many more NAs, but less and smaller FCs and FAs compared to the wildtype cells. Moreover, in the mutant cells a lower fraction of the NAs and FCs grew to FAs compared to the wildtype. These results suggest the VVV mutation is leading to enhanced NA formation. However, the mutation significantly impairs NA maturation. Strikingly, both maturing and non-maturing NAs had a significantly lower traction force development rate in the R7R8vvv mutant cells than the wildtype cells. A lower rate in traction force development alludes to a slow rate of adhesion formation. As previously observed, the slow rate of adhesion development correlates with the sequential adhesion complex formation observed in G1 NAs, as opposed the pre-complex formation observed in G2; this suggests the VVV mutation is indeed inhibiting the pre-complex formation. Together, these results demonstrate talin-vinculin pre-complex is essential for NAs to mature through the development of traction force across the adhesion complex.

## 7.2 Discussion: Force-independent VBS in talin R8 determines nascent adhesion maturation

### 7.3.1 Conclusions

The Danuser lab demonstrated that a sub-class of maturing NAs required fast assembly of the talin-vinculin complex, upon force transduction. It has previously been suggested this was due to

the formation of talin-vinculin pre-complex (Bachir et al., 2014). Together with our collaborators, to further investigate pre-complex formation we sought to design a talin mutant that would inhibit their formation. We identified VBS33 in the R8 domain as the most likely candidate for pre-complex formation, due to being outside the force transduction pathway (Yao et al., 2016) and being readily available to bind to vinculin in the absence of force (Gingras et al., 2010). We identified the R8 domain was destabilised by a 'threonine belt' within its core and so stabilised the domain by designing a VVV mutant like that used on R3 previously (Goult et al., 2013b). We demonstrated in vitro that the VVV mutation indeed stabilised the domain and thereby reduced the propensity of R8 to bind to vinculin. Our collaborators then investigated the effects of the VVV mutation in vivo. There was a reduced rate of traction force development, suggesting the R8vvv mutation was disrupting pre-complex formation. Strikingly, the mutant led to a significant reduction in NA maturation, and an increase in non-maturing NAs. This data confirmed that talin R8 mediated pre-complex formation is necessary for NA maturation.

### 7.3.2 Fine tuning of talin rod domain plasticity mediates adhesions

The talin rod consists of series of mechanosensitive domains containing multiple VBS, LD-motif binding sites, actin binding sites and many possible unknown sites (Gough and Goult, 2018). These sites provide a platform in which the complex adhesome (Horton et al., 2015) can assemble, dictating the fate and diversity of the adhesions (Goult et al., 2018). This unique ability of talin is due to the rod domains being able to adopt different states under different stimuli, due to the fine tuning of the domain's molecular makeup. The most apparent example of this domain plasticity is in talin R3; R3 forms part of a high affinity LD-motif binding site for the interaction with the RAP1 adapter protein RIAM, an interaction necessary for talin recruitment to adhesion sites (Goult et al., 2013b; Chang et al., 2014). However, upon the onset of traction force talin R3 is the first rod domain in the force transduction pathway to unfold, exposing two VBS but breaking the interaction with RIAM (Goult et al., 2013b; Yan et al., 2015; Yao et al., 2014a). Upon force

transduction RIAM is no longer necessary for talin recruitment, however vinculin is necessary to reinforce the talin-actomyosin interaction (Atherton et al., 2015).

Here we report a force-independent interaction between the R8 domain and vinculin, necessary for pre-complex formation and NA maturation. R8 has been finely tuned for this role through the presence of a threonine belt destabilising the hydrophobic core of the domain. Interestingly, the R8 domain also demonstrates extraordinary plasticity; in the folded conformation, R8 provides a high affinity binding site for LD-motifs such as those in DLC1 and RIAM (Zacharchenko et al., 2016a; Chang et al., 2014); moreover, R8 forms a major part of ABS2 (Hemmings et al., 1996; Atherton et al., 2015; Kumar et al., 2016; Lee et al., 2004); and when unfolded R8 binds to vinculin (fig. 7.9). The exact order of these interactions and how they are mediated is yet to be elucidated. It could be speculated the LD-motif protein DLC1, a tumour suppressor protein (Zacharchenko et al., 2016a; Liu et al., 2017), may stabilise the R8 domain, preventing pre-complex formation and adhesion maturation, thereby reducing invasiveness and motility. However, unlike R3, our results demonstrate the R8 plasticity is not regulated through mechanosensing as R8 is outside the force transduction pathway, it is clear further investigation is necessary to understand the regulation of these interactions.



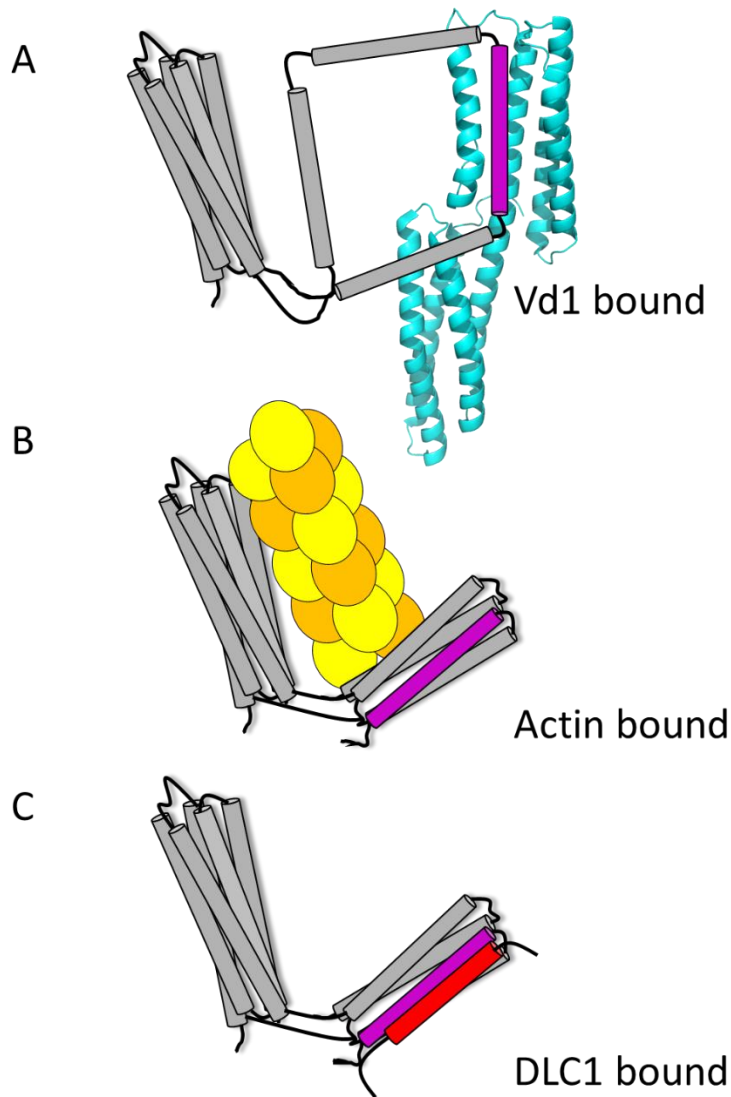


Figure 7.11: **Ligand plasticity of the R8 domain.** Model of talin R7-R8 (grey; VBS33 coloured purple) bound to Vd1 (A; Cyan), F-actin (B; yellow) and DLC1 (C; red).

### 7.3.3 The roll of the talin-vinculin pre-complex in NA maturation

We report the talin-vinculin pre-complex is necessary for NA maturation by enabling a greater rate of traction force development, exactly how the pre-complex does this is not known. We speculate that the pre-complex formation of talin R8 enables a faster rate of force development by linking talin to additional actin filaments. With another link to the actomyosin machinery there will be greater force exerted on talin, necessary to unfold talin R3, then R1 and R2 exposing further VBS (Atherton et al., 2015; Yao et al., 2016). Furthermore, vinculin binding to R8 could disrupt ABS2, leading to primary actin binding on ABS3, at the C-terminus of talin. Binding to ABS3

instead of ABS2 would extend the force transduction pathway, down the whole talin rod and enabling greater talin mechanosignalling (Goult et al., 2018; Yao et al., 2014a, 2016).

*Details of this study can be found in: Han, S.J., K.M. Dean, A.J. Whitewood, A. Bachir, E. Gutierrez, A. Groisman, A.R. Horwitz, B.T. Goult, and G. Danuser. 2019. Formation of talin-vinculin pre-complexes dictates maturation of nascent adhesions by accelerated force transmission and vinculin recruitment. bioRxiv. 735183. doi:10.1101/735183.*

## 7.4 Chlamydial virulence factor TarP mimics talin to disrupt the talin-vinculin complex.

### 7.4.1 Pathogens target intracellular adhesion proteins for cell entry

Focal adhesions are highly conserved attachment points that have become a common recognition site for numerous infectious agents (Reis and Horn, 2010; Grove and Marsh, 2011) with some bacteria specifically targeting intracellular adhesion proteins for cell entry. It has previously been demonstrated that the *Shigella flexneri* effector protein IpaA (Izard et al., 2006) and the *Rickettsia* cell surface antigen Sca4 interact with vinculin (Park et al., 2011a). Atomic structures of Sca4 and IpaA bound Vd1 reveal both these virulence factors mimic talin VBS by forming amphipathic  $\alpha$ -helices that bind Vd1. It has been suggested that by mimicking talin VBS these pathogenic virulence factors can activate vinculin, through a binding mechanism that displaces the vinculin tail from Vd1 (Izard et al., 2006; Park et al., 2011b; Lee et al., 2013a).

### 7.4.2 Chlamydial virulence factor TarP

Chlamydiae are obligate intracellular pathogens that infect and cause disease in humans and animals. *Chlamydia trachomatis* is the cause of the most prevalent bacterial sexually transmitted disease in the world (Rowley et al., 2016). Chlamydia cell invasion has been shown to require the effector protein 'translocated actin recruitment protein' (TarP), a type-III secreted protein that recruits and remodels the actin cytoskeleton (Carabeo et al., 2002; Clifton et al., 2004). This

remodelling is thought to aid a phagocytosis-like internalisation of the chlamydial elementary bodies (Carabeo et al., 2002). Every chlamydial species expresses an orthologue of TarP, whilst there is variation in the domain multiplicity; most variants contain actin binding sites (Jiwani et al., 2013) and a proline rich oligomerisation domain (Clifton et al., 2004).

#### 7.4.3 TarP reported to contain both a VBS and LD-motif

Much like Sca4 and IpaA (Park et al., 2011b; Izard et al., 2006) TarP has been reported to contain a vinculin binding region (Thwaites et al., 2015). Whilst there are varying number of VBS amongst species, most species contained at least one VBS, with *C. caviae* reported to contain three VBS, with VBS1 reported at the time being the most important for the actin recruiting effects of TarP (Thwaites et al., 2015).

Leucine-Aspartic acid motifs (LD-motifs) are well-recognised protein:protein interaction motifs (Alam et al., 2014), first identified in the FA protein paxillin, and shown to be required for paxillin to interact with Focal Adhesion Kinase (FAK) (Thomas et al., 1999). The FAK-paxillin interaction was subsequently mapped to the Focal Adhesion Targeting (FAT) domain of FAK (Hoellerer et al., 2003). In addition to the TarP VBS, it was reported previously that TarP contains an LD-motif (residues 655-680; TarP LD) with sequence homology to paxillin LD2 (Thwaites et al., 2014), and that this LD-motif interacts with the FAK-FAT domain and plays a role in actin recruitment (Schaller, 2010).

#### 7.4.4 Sequence analysis of TarP LD motif

Using Clustal Omega (Sievers and Higgins, 2014) we generated a multiple sequence alignment of the TarP LD-motif with the LD domains in KANK1 (Bouchet et al., 2016), RIAM (Goult et al., 2013b), DLC1 (Zacharchenko et al., 2016a) and the paxillin LD1 and LD2 motifs (Brown et al., 1996) (fig. 7.10). The sequence alignment revealed the TarP LD has a high sequence homology to known FAK-FAT and talin R8 ligands, suggesting the TarP LD would bind to FAK and/or talin R8.

KANK1   38–60	GFQLDLDFVKYVDDIQKGNTIKK–
RIAM   5–28	NEDIDQMFSTLLGEMDLLTQSLGV
DLC1   467–490	FPELDDILYHVKGMQRIVNQWSEK
PAX_LD2   142–165	LSELDRLLELNAVQHNPPGFPAD
PAX_LD1   1–24	MDDL DALLADLESTTSHISKRPVF
TARP_LD   657–680	AEGLEHLLPQLRSHLDDAFDQQGN
Consensus seq.	LDxLLxxL

Figure 7.12: **TarP LD-motif alignment.** Multiple sequence alignment of known LD-motifs and TarP, generated using Clustal Omega (Sievers and Higgins, 2014); the consensus binding residues are highlighted in blue.

#### 7.4.5 TarP LD does not bind to FAK-FAT or talin R7R8

To investigate the binding of the TarP LD to FAK-FAT a fluorescence polarisation assay was used. In this assay FAK-FAT was titrated against fluorescein-labelled TarP LD and Paxillin LD2 peptides. As expected, paxillin LD2 bound well to the FAK-FAT domain,  $K_d = 9.01$ , in line with previous reports (Hoellerer et al., 2003). However, there was no increase in polarisation with the TarP LD-motif, suggesting that any interaction between TarP and FAK is too weak to be detected by the FP assay (fig. 7.11).

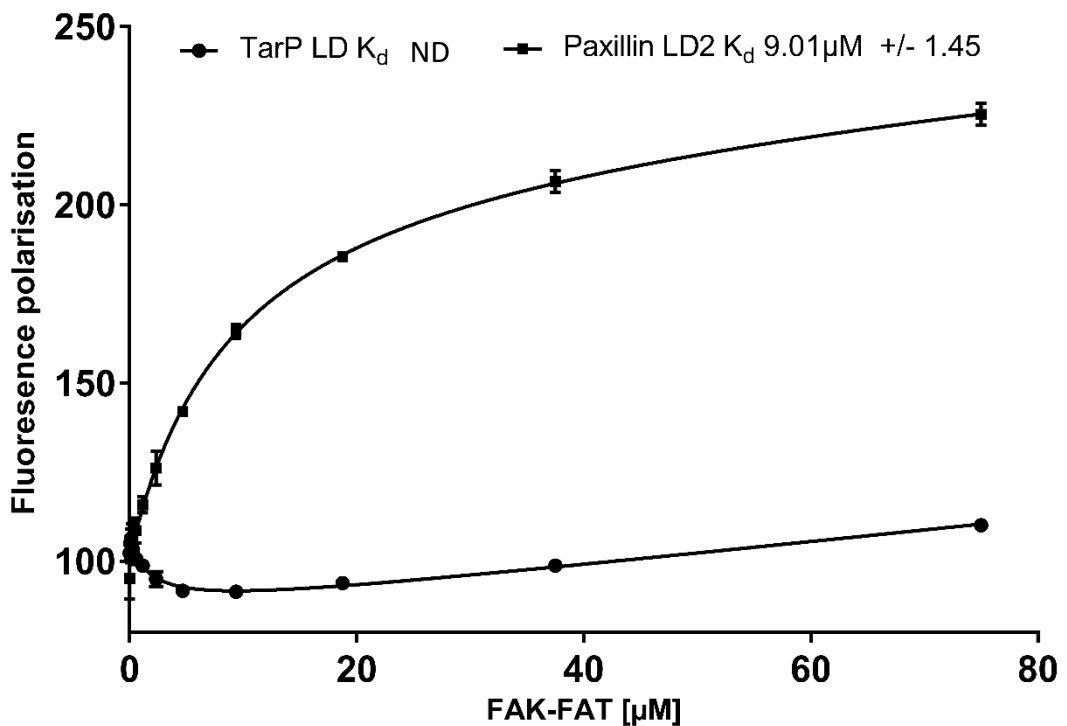


Figure 7.13: **FP shows TarP LD motif does not bind to FAK-FAT.** Binding of fluorescein-labelled TarP LD (655–680)<sub>C</sub> and Paxillin LD2 (141–153)<sub>C</sub> peptides to FAK-FAT, measured using a fluorescence polarisation assay. Dissociation constants  $\pm$  SE ( $\mu$ m) for the interactions are indicated in the legend ( $n=3$ ). ND, not determined.

To confirm there was no weak interaction we may have missed with the FP experiment, we used 2D HSQC NMR experiments in which spectra were collected of <sup>15</sup>N-labelled FAK-FAT with and without the addition of a 3-fold excess of TarP LD and paxillin LD2 peptides. Analysis of the spectra revealed the addition of the paxillin LD2 peptide resulted in multiple large peak shifts indicative of a strong interaction (fig 7.12 A). In stark contrast, the addition of TarP LD peptide led to very few small peak shifts (fig. 7.12 B). The lack of large shifts suggests the peptide might interact, however, it does so very weakly. This weak interaction clarifies why we were unable to observe binding in our FP experiments.

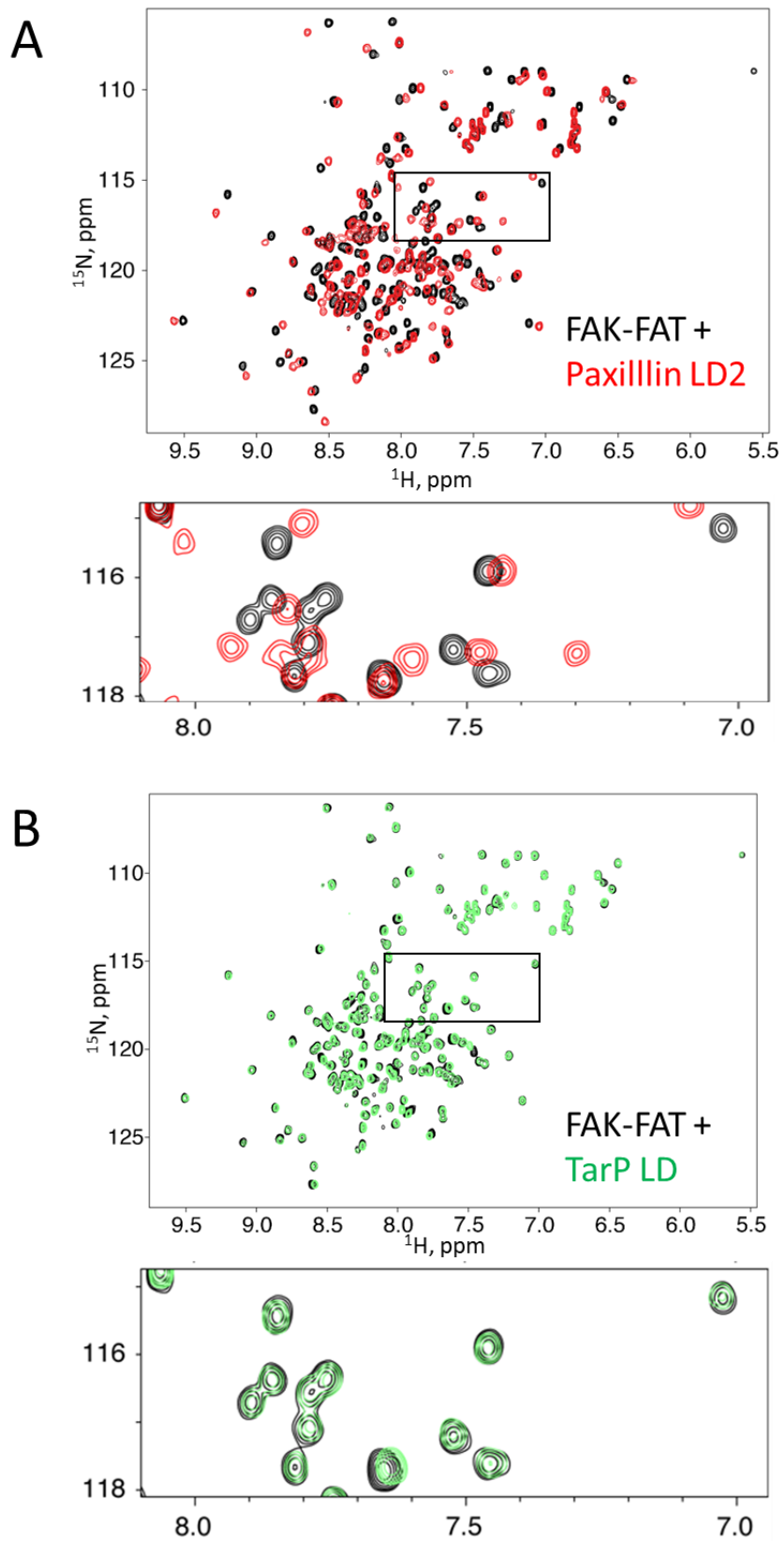


Figure 7.14: **NMR demonstrates the TarP LD does not bind FAK-FAT.**  $^1\text{H},^{15}\text{N}$ -HSQC spectra of  $130\ \mu\text{m}$   $^{15}\text{N}$ -labelled FAK-FAT in the absence (black) or presence of paxillin LD2 (141–153) peptide (A; red) or TarP LD (655–680) (B; green) at a ratio of 1 : 3.

It was possible that the TarP LD may be a specific binder of talin instead of the FAK-FAT as other LD motifs, such as those in KANK, are specific for talin (Bouchet et al., 2016). To investigate this, we repeated the FP experiment using talin R7R8. However, when compared to RIAM – a known talin R8 ligand (Goult et al., 2013b) – which showed a relatively strong interaction with a binding affinity of  $K_d$  5.03  $\mu$ M, the TarP LD again had no observable increase in polarisation and therefore demonstrated no obvious binding (fig. 7.13 A). To confirm there was no interaction between the talin rod and the TarP LD motif, we used the FP experiment on the rest of the rod domains, using R4-R8, R9-R12 and R13-DD. Again, we saw no observable increase in polarisation (fig. 7.13 B), therefore we concluded that the TarP LD does not bind to talin, at least not strong enough to be detectable by the FP assay.

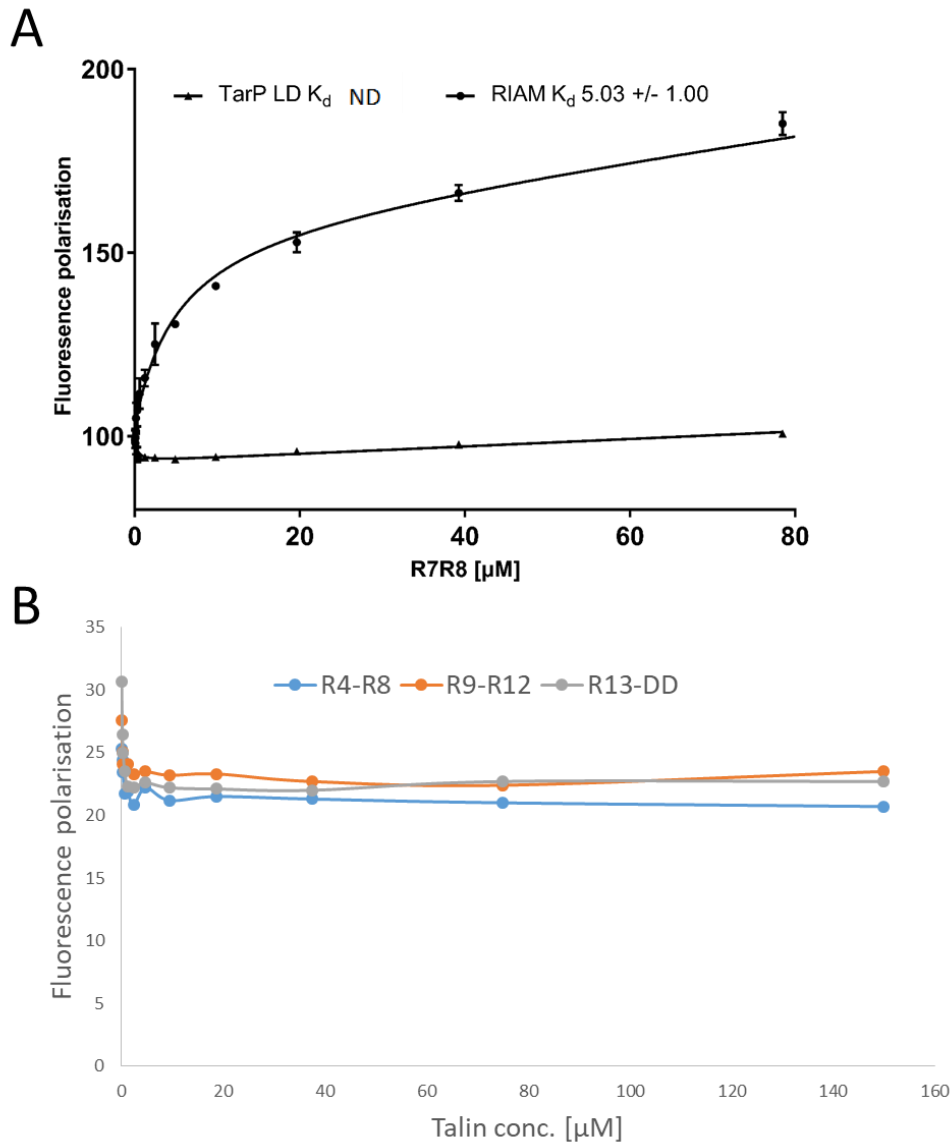


Figure 7.15: **TarP LD does not bind to talin.** A) Binding of fluorescein-labelled TarP LD (655–680)C and Paxillin LD2 (141–153)C peptides to talin R7R8, measured using a fluorescence polarisation assay. Dissociation constants  $\pm$  SE ( $\mu\text{M}$ ) for the interactions are indicated in the legend ( $n=3$ ). ND, not determined. B) binding of fluorescein-labelled TarP LD to talin R4-R8 (blue), R9-R12 (orange) and R13-DD (grey); there was no observable increase in polarisation in any talin construct so no binding constant could be determined ( $n=1$ ).

#### 7.4.6 Sequence analysis of TarP VBS region.

It was demonstrated previously that the interaction between TarP and vinculin is critical for Chlamydial infection (Thwaites et al., 2015). All Chlamydia species have been shown to contain at least one VBS, with *C. caviae*, our species of study, containing three. It was reported that only TarP VBS1 was vital for the role of TarP (Thwaites et al., 2015), we therefore selected this site as the main focus of our initial investigation. Using Clustal Omega (Sievers and Higgins, 2014) we



generated a multiple sequence alignment of the TarP VBS1, VBS2 and VBS3 with talin VBS36, VBS33, VBS1, VBS2 and those of *Shigella* IpaA and *Rickettsia* Sca4 (fig. 7.14). The alignment confirmed all three TarP VBS contained the VBS consensus motif LxxAAxxVxxVxxLIxxA (Gingras et al., 2005) as reported previously (Thwaites et al., 2015).

```

Talin_VBS36|1628-1652      --VNPRDPPRWSVLAGHSRTVSDSIKKLITSMRDKA--PGQ-
Talin_VBS33|1512-1546     ASARTANPTAKRQFVQSAKEVANSTANLVKTIKAL-----
Talin_VBS1|607-636        -----PILQAAKGLAGAVSELLRSAQPASAEPRQN
Talin_VBS3|1944-1969     -----AYTKKELIECARRVSEKVVSHVLAALQ-----
Sca4_VBS|814-832         -----IYNKAREVINAVNPVIEAL-----
IpaA_VBS2|566-584        -----IYEKAKEVSSALSKVLSKI-----
TarP_VBS3|745-769        -----DLHGAAKGVADSLSNLLQAATPSTT-----
TarP_VBS2|805-829        -----GIPGAAANVTATLSSVANKIALFEK-----
TarP_VBS1|850-868        -----LLEAARNITTTMLSKTLSKV-----
consensus seq.           L--AA--VA--V--LI--A

```

Figure 7.16: **Sequence alignment of TarP VBS.** Multiple sequence alignment of vinculin binding sites, aligned using Clustal Omega (Sievers and Higgins, 2014). The consensus residues are highlighted in green.

#### 7.4.7 TarP VBS1 binds to vinculin with a high affinity

To investigate whether TarP VBS1 binds to Vd1 we used a fluorescence polarisation assay. In this assay Vd1 was titrated against fluorescein-labelled TarP VBS1 peptide. The TarP VBS1 peptide bound to Vd1 with a relatively high affinity,  $K_d = 1.28 \mu\text{M}$ . To investigate how this compared to various talin VBS we repeated the FP assay using the talin VBS located on helices 33 and 36 (VBS33 and VBS36). These bound with comparable affinities to the TarP VBS of  $K_d = 0.34 \mu\text{M}$  and  $1.03 \mu\text{M}$  respectively (fig. 7.15). This data combined with the sequence homology suggests the TarP VBS binds in a similar manner to the talin VBS.

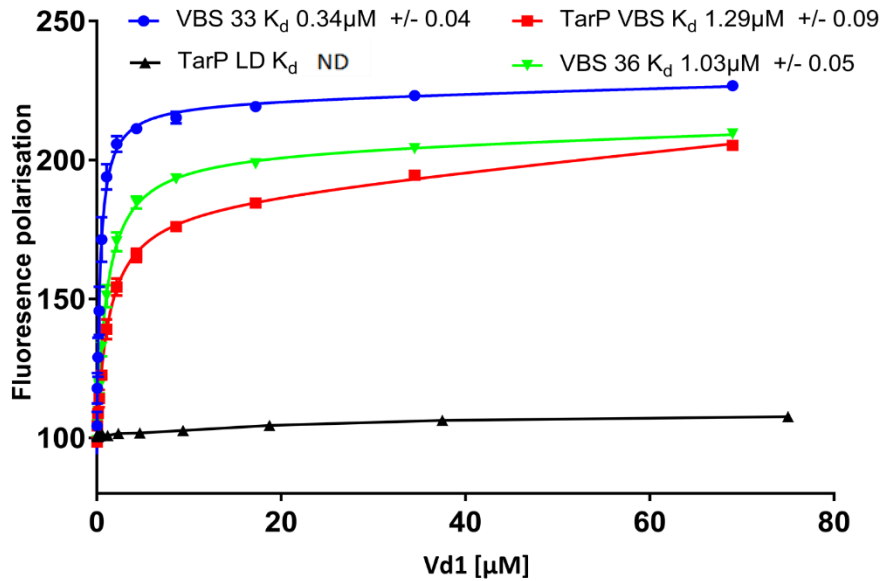


Figure 7.17: **Comparison of the Vd1:TarP and Vd1:talın interactions.** Binding of fluorescein labelled talin VBS33, VBS36, TarP VBS (850–868)C and LD (655–680)C peptides to Vd1, measured using a fluorescence polarisation assay. Dissociation constants  $\pm$  SE ( $\mu\text{M}$ ) for the interactions are indicated in the legend ( $n=3$ ). ND, not determined.

#### 7.4.8 TarP VBS are constitutively active

Interestingly, the TarP VBS were predicted by DISOPRED3 (Jones and Cozzetto, 2015) to be found within a disordered region of the protein (fig. 7.16), they are therefore likely to be constitutively active. This is in stark contrast to those of talin which are buried inside the hydrophobic core of the talin rod domain bundles. With the exception of VBS33 situated in talin R8 (section 7.2), talin VBS activation requires mechanical force transduction across talin to expose the VBS. Therefore, whilst talin VBS have comparable affinity in their active form to TarP VBS1, the overall affinity for Vd1 would be considerably lower once the energy needed to unfold the domains is taken into account (Wang et al., 2019). Thus, with the talin:vinculin interaction being almost exclusively force dependent, in the absence of force TarP has the potential to outcompete folded talin to bind vinculin.

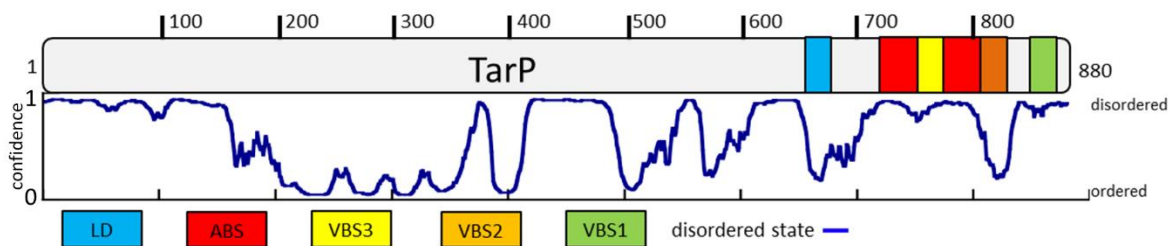


Figure 7.18: **TarP VBS are constitutively active.** Schematic of TarP, indicating locations of VBS1 (green), VBS2 (orange), VBS3 (yellow), Actin binding site ABS (red) and LD-motif (blue) at the C-terminal. The disorder prediction trace generated using DISOPRED3 (Jones and Cozzetto, 2015) is shown.

#### 7.4.9 Crystal Structure reveals TarP VBS1 mimics talin VBS

Due to the high sequence similarity TarP has to the talin VBS and the similar affinities they both have to Vd1, we hypothesised that TarP VBS1 would have a similar binding mechanism as the talin VBS. Previous VBS structures reveal a helix addition mechanism by which VBS bind to Vd1. They all bind into a hydrophobic groove sited between helices 1 and 2 on Vd1 (Izard et al., 2006; Papagrigoriou et al., 2004; Izard et al., 2004). To investigate whether the binding mechanism is the same between TarP we sought to gain an atomic structure using x-ray crystallography. Hanging drop vapour diffusion crystal trials were setup using a Vd1: TarP ratio of 1:1 in a Hampton crystal screen (HAMPTON), to screen multiple conditions with a high propensity for crystal formation. Following 24 hours of incubation at room temperature a suitably large crystal was identified in one of the wells (specific conditions are detailed in table 3.3), and was selected for data collection. The crystal diffracted to a resolution of 2.9 Å in the orthorhombic space group  $P2_12_12_1$ , containing one molecule of the complex within the asymmetric unit. The structure was solved by molecular replacement (fig. 7.17; statistics in table 7.1).

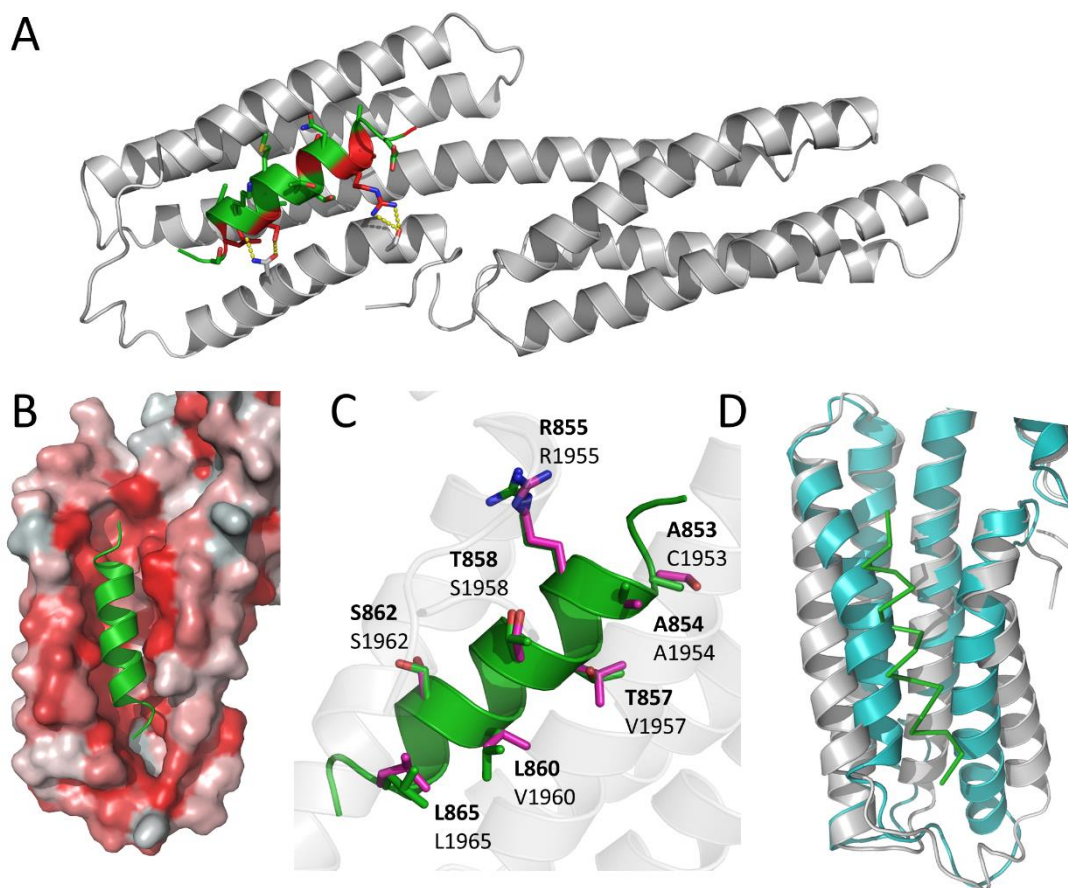


Figure 7.19: **Crystal structure of TarP in complex with Vd1.** (A) Cartoon representation of the complex of Vd1 (grey) bound to TarP VBS (green); the consensus VBS residues are shown in red. (B) TarP VBS (green) docks into a hydrophobic groove on Vd1. Vd1 is represented as surface coloured by hydrophobicity: hydrophobic = red, hydrophilic = white. (C) TarP VBS peptide (green) aligned with talin VBS46 peptide (purple, PDB:1RKC) with Vd1-interacting sidechains from both VBS shown as sticks and TarP residues (top bold) and corresponding vbs46 residues are shown. (D) VBS binding causes conformational change in the Vd1 domain. Comparison of apo Vd1 (cyan, PDB:1TR2) and TarP bound Vd1 (grey). The TarP peptide is shown as a ribbon (green).

Table 7.1: **X-ray data collection and refinement statistics for TarP-Vd1 complex.** Data collected from a single crystal. *A* Values in parentheses are for highest-resolution shell. *B* Values in parentheses indicate percentile scores as determined by Molprobity.

Data collection	
Synchrotron and BeamLine	Diamond Light Source; I03
Space group	$P2_12_12$
Molecule/a.s.u	1
Cell dimensions	
$\alpha, b, c$ (Å)	51.80, 66.87, 95.83
$\alpha, \beta, \gamma$ (°)	90, 90, 90
Resolution (Å)	95.83–2.9 (2.96–2.9) <sub>a</sub>
$R_{\text{merge}}$	0.156 (0.806)

$I/\sigma I$	8.1 (2.5)
$CC(1/2)$	0.994 (0.903)
Completeness (%)	99.8 (99.9)
Redundancy	6.1 (6.3)
Refinement	
Resolution (Å)	2.9
No. reflections	7455 (519)
$R_{\text{work}}/R_{\text{free}}$	0.28/0.34
No. atoms	
Protein	2082
Water	3
$B$ -factors (Å <sup>2</sup> )	
Protein/Peptide	94.24/95.73
Water	84.04
R.m.s. deviations	
Bond lengths (Å)	0.010
Bond angles (°)	1.430
Ramachandran plot	
Favoured/allowed/outlier (%)	93/6/1
Rotamer	
Favoured/poor (%)	59.2/21.01
Molprobit scores	
Protein geometry	3.42 (37th) <a href="#">b</a>
Clash score all atoms	29 (81st) <a href="#">b</a>
PDB accession no.	<a href="#">6FQ4</a>

The final structure showed good agreement with other Vd1 VBS complexes from talin (Izard et al., 2004; Papagrigoriou et al., 2004), Sca-4 (Lee et al., 2013b) and IpaA (Park et al., 2011c). The TarP VBS1 forms an  $\alpha$ -helix that embeds into the hydrophobic groove formed between  $\alpha$ -helices 1 and 2 of the Vd1 N-terminal 4-helix bundle, forming a structure that resembles a five-helix bundle (fig. 7.17 B). Analysis of the complex interface by PISA indicated that 54.1% of the VBS surface area, including the consensus residues, are buried in the complex interface (fig. 7.17 A). Additionally,

three hydrogen bonds were identified: TarP Arg-855 to Vd1 Ser-11, TarP Thr-858 to Vd1 Ile-12, and TarP Ser-862 to Vd1 Gln-19, stabilising the complex by holding the  $\alpha$ -helix of TarP in the correct orientation. Alignment of this structure with other VBS structures indicate these hydrogen bonds are a well conserved feature of the interaction. Upon complex formation, TarP significantly alters the positions of Vd1 helices 1 and 2, widening the groove between the two and exposing the hydrophobic core (fig. 7.17 D), mimicking the way talin activates vinculin, causing the release of the vinculin tail (Bois et al., 2006b; Izard et al., 2004). With sidechains almost identical in length and character to talin VBS, TarP VBS1 is able to pack tightly into the Vd1 hydrophobic groove accounting for the high affinity measured in the fluorescence polarisation assay. The strong resemblance of the TarP VBS1 to the VBS in talin demonstrates the molecular mimicry employed by TarP.

#### 7.4.10 The TarP VBS1 competes with talin, disrupting talin:vinculin complexes

Since TarP VBS1 binds to the same site on vinculin as the talin VBS, this raises the possibility that TarP binding might compete with talin for vinculin binding. A similar phenomenon was seen in *Drosophila*, where expression of a GFP-VBS construct was found to disrupt talin:vinculin interactions *in vivo* (Maartens et al., 2016). Using analytical gel filtration, we measured the interaction between Vd1 and a VBS-containing talin helical bundle. We selected talin rod domain R10, which contains a single VBS (VBS46) (Goult et al., 2010b). Equimolar amounts of Vd1 and talin R10 incubated together at 37°C formed a 1:1 complex (fig. 7.18 A-B). Adding a stoichiometric amount of TarP VBS1 peptide (fig. 7.18 A) resulted in a significant reduction in the talin:Vd1 peak and concomitant increases in the monomer peaks of the respective proteins. To confirm that disruption of the talin:Vd1 complex was due to competition by the TarP VBS1 peptide, we spiked the TarP VBS1 peptide with 30 nM of fluorescein-TarP VBS1 peptide. The fluorescein-coupled TarP VBS1 eluted in the same fractions as Vd1, confirming that the TarP peptide was bound to Vd1. To quantitate this competition we used the SEC-MALS OmniSEC software to determine the weight fraction (%) of each peak in (fig. 7.18 A-B) and this analysis is shown in (fig. 7.18 C). Together this

demonstrates the constitutively active TarP VBS can disrupt and out-compete talin. To demonstrate this is not a specific property of TarP VBS, and that any VBS that is constitutively active has the propensity to out compete talin domains, the experiment was repeated using the talin VBS36 peptide (fig. 7.18 B). In agreement with the TarP VBS1, the addition of the VBS36 peptide also led to a significant reduction in the Vd1:R10 complex peak, demonstrating that any constitutively active VBS can disrupt and out-compete folded talin.

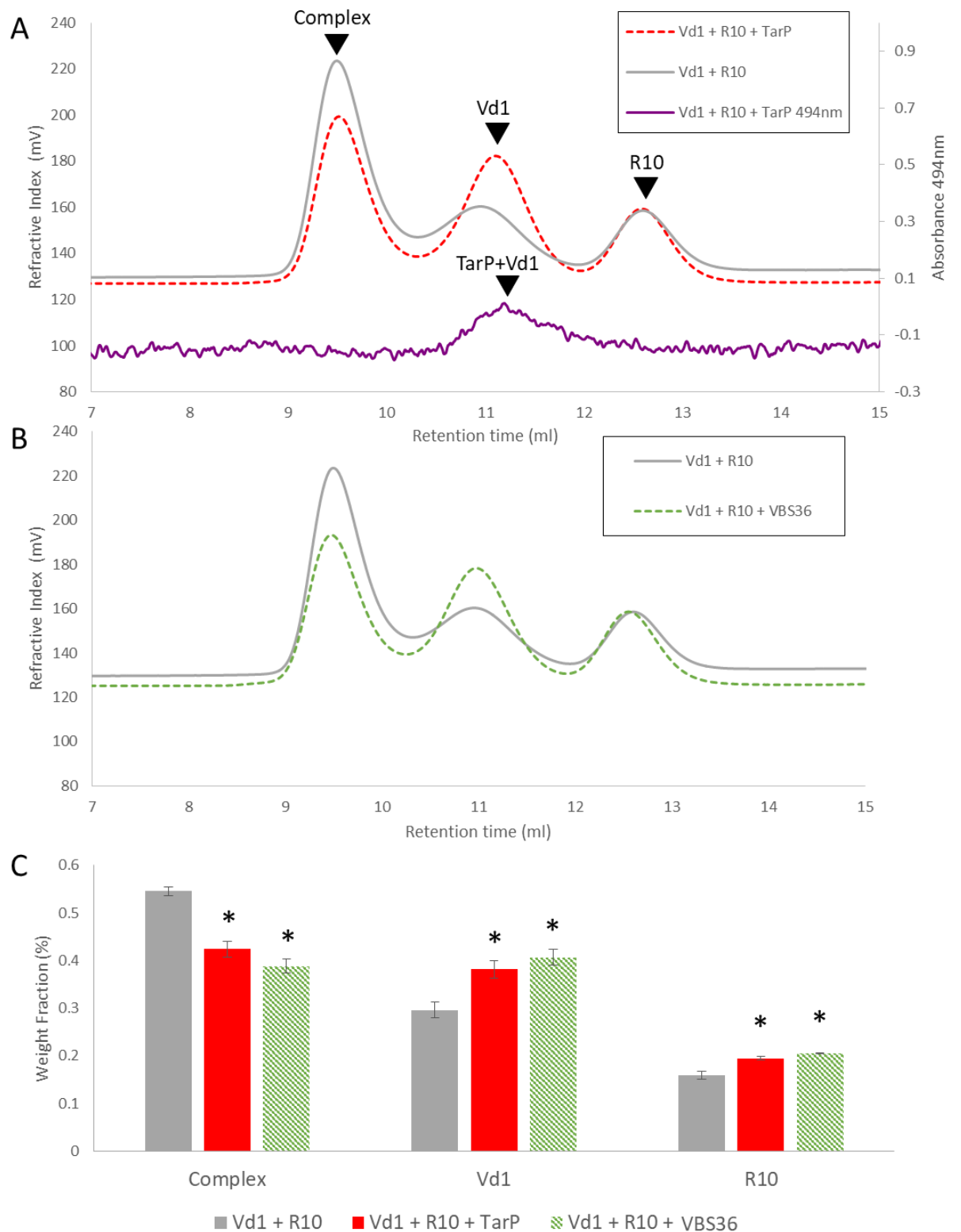


**Figure 7.20: TarP VBS disrupts the interaction between talin R10 and vinculin Vd1.** Vd1 was incubated with talin R10 at 37 °C for 30 min then analysed on a gel filtration column (grey). The experiment was repeated with the addition of a stoichiometric amount of TarP VBS peptide (A) and then with talin VBS36 (B). All experiments were done in triplicate. 1% fluorescein-labelled TarP VBS peptide was added to monitor TarP VBS elution at 494 nm which confirmed that TarP eluted bound to Vd1 (purple). (C) the relative 'Weight Fraction' percentage for talin:vinculin complex, talin, vinculin peaks in the absence and presence of both TarP VBS and VBS36 peptides. Data are means  $\pm$  SEM; \* $P < 0.05$  by T-test ( $n=3$ ). Both peptides reduced the R10-Vd1 complex.



#### 7.4.11 Investigating TarP VBS3

TarP VBS2 and VBS3 were reported not to be vital for the actin recruiting role of TarP, unlike VBS1. Additionally, some species of Chlamydia express a TarP that contains only one VBS (Thwaites et al., 2015), suggesting TarP VBS2 and VBS3 are redundant. However, multiple sequence alignment of them with other known VBS revealed both TarP VBS2 and VBS3 have a high sequence homology to the other VBS analysed and they both contain the VBS consensus sequence (fig. 7.10). To further understand the roles of TarP VBS2 and VBS3 we designed synthetic peptides of the two regions containing the consensus binding sequence.

To make use of the synthetic peptides we must first dissolve them in water or buffer.

Unfortunately, the TarP VBS2 peptide would not dissolve fully into solution after multiple attempts to try to dissolve it. We were therefore unable to make use of it.

In contrast, the TarP VBS3 peptide went straight into buffer. To investigate if the peptide bound to Vd1 we used a fluorescence polarisation assay, in which Vd1 was titrated against fluorescein labelled TarP VBS3 peptide. Strikingly, the TarP VBS3 peptide bound with a  $K_d < 100$  nM. As our FP assay uses a peptide concentration of 100 nM for good signal to noise, the affinity of the TarP VBS3 to Vd1 was too high to accurately measure using the fluorescent polarisation assay, and considerably greater than the affinity measured for the TarP VBS1 peptide (fig. 7.19).

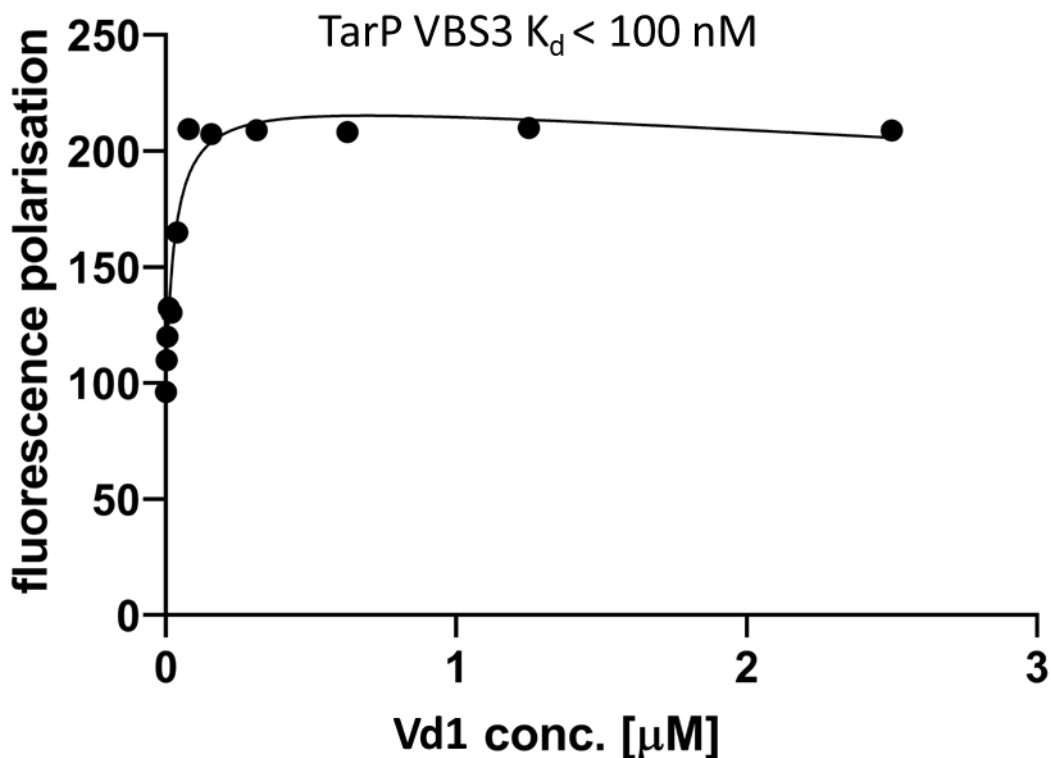
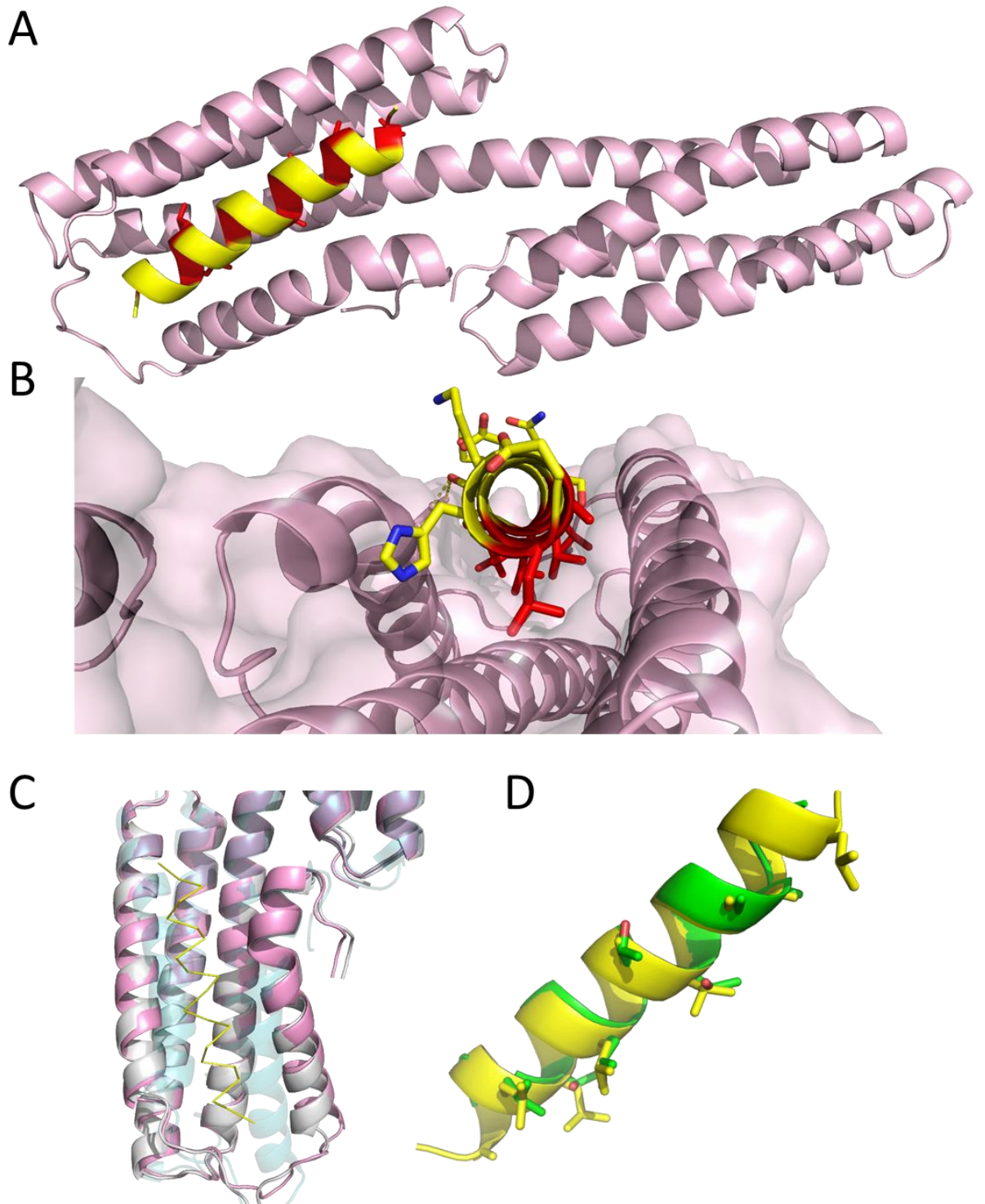


Figure 7.21: *TarP VBS3 binds Vd1 with extraordinarily high affinity*. Binding of fluorescein labelled TarP VBS3 to Vd1, measured using a fluorescence polarisation assay. Dissociation constant was not accurately attainable <100 nM (n=1).

#### 7.4.12 Crystal Structure of Vd1 bound to TarP VBS3 reveals strong hydrophobic interaction

To investigate why TarP VBS3 binds to Vd1 significantly tighter than the TarP VBS1 we sought a structural insight into the interaction. Therefore to gain the atomic structure of the VBS3-Vd1 complex we crystallised the complex. Using a Vd1: TarP ratio of 3:1 the complex was screened in a JCSGplus screen at 21°C. After 24hrs incubation multiple small crystals were observed, in well H3, 0.1 M Bis/Tris, pH 5.5 with 25% w/v PEG 3350. The crystals were optimised in 2 µL drops, in which very large crystals were formed. Multiple crystals from slightly differing conditions were selected and vitrified in motherliquor containing 20% glycerol, and used for data collection. The crystal diffracted to a high resolution of 1.5 Å in the same space group as the TarP VBS1 structure,  $P2_12_12_1$ , containing one molecule of the complex within the asymmetric unit. The structure was solved by molecular replacement using the TarP VBS1 structure as the template model (fig. 7.20, statistics in table 7.2).



**Figure 7.22: Crystal structure of TarP VBS3 in complex with Vd1.** (A) Cartoon representation of the complex of Vd1 (pink) bound to TarP VBS3 (yellow); the consensus VBS residues are shown in red. (B) TarP VBS (yellow) docks into a hydrophobic groove on Vd1, consensus hydrophobic residues (red) are all buried into the groove, enabling VBS3 to pack tightly into Vd1 (C) Comparison of apo Vd1 (cyan, PDB:1TR2), TarP VBS1 bound Vd1 (grey) and TarP VBS3 bound Vd1 (pink); the TarP VBS3 peptide is shown as a ribbon (yellow). (D) Alignment of Vd1 bound TarP VBS3 (yellow) and VBS1 (green) peptides, consensus residues shown as sticks.

Table 6.2: *X-ray data collection and refinement statistics for TarP VBS3-Vd1 complex*. Data collected from a single crystal. *A* Values in parentheses are for highest-resolution shell. *B* Values in parentheses indicate percentile scores as determined by Molprobit.

<b>Data collection</b>	
Synchrotron and BeamLine	Diamond light source; I04-1
Space group	P21 21 2
Molecule/a.s.u	1
<b>Cell dimensions</b>	
<i>a</i> , <i>b</i> , <i>c</i> (Å)	52.187, 63.895, 95.763
$\alpha$ , $\beta$ , $\gamma$ (°)	90, 90, 90
Resolution (Å)	1.49-95.76
<i>CC</i> (1/2)	0.999
Completeness (%)	99.4
<b>Refinement</b>	
Resolution (Å)	1.49
No. reflections	43804
<i>R</i> <sub>work</sub> / <i>R</i> <sub>free</sub>	0.24/0.29
<b>No. atoms</b>	
Protein	1963
Peptide	143
Water	154
<b>B-factors (Å<sup>2</sup>)</b>	
Protein	42.54
Peptide	36.43
Water	49.04
<b>R.m.s. deviations</b>	
Bond lengths (Å)	0.0215
Bond angles (°)	1.83
<b>Ramachandran plot</b>	
Favoured/allowed/outlier (%)	99.63/ 0.37/ 0
Rotamer outliers (%)	1.68
<b>Molprobit scores</b>	
Protein geometry	1.65
Clash score all atoms	8.87
PDB accession no.	Pending submission

As with other VBS the TarP VBS3 forms an amphipathic helix which embeds into the hydrophobic groove formed between Vd1 helices 1 and 2. Interface analysis using PISA indicated 57.9% of the VBS surface area was buried in the complex interface, slightly higher than the TarP VBS1-Vd1 complex. Conversely, only two hydrogen bonds were identified, both bonds were between TarP Ser-862 and Vd1 Gln-19. As expected, all the consensus residues are buried in the complex interface (fig. 7.20 B). Upon complex formation, TarP VBS3 considerably alters the positions of

Vd1 helices 1 and 2, as is apparent in most VBS:Vd1 interactions. Interestingly, the TarP VBS3 achieves an extra turn in the helix at the C-terminal region compared the TarP VBS1 despite similar length peptides being used. Furthermore, TarP VBS3 binding leads to a substantial kink in Vd1 helix-1, spreading it around 3Å wider than the equivalent position in the TarP VBS1 structure (fig. 7.20 C). Overall, the TarP VBS3 interaction with Vd1 is compliant with other known Vd1:VBS interactions, demonstrating the same molecular mimicry as described in section (TarP VBS1 crystal section).

Despite TarP VBS3 binding to Vd1 with a higher affinity than TarP VBS1, there are only subtle differences between the two structures. What is clear from the PISA analysis and the extra turn on the  $\alpha$ -helix is that the VBS3 peptide has a greater contact area with Vd1, most likely responsible for the higher affinity. TarP VBS3 is able to bury deeper into the Vd1 hydrophobic pocket than VBS1, due to the presence of more hydrophobic residues in the consensus sequence positions than in VBS1. An example of this is at positions 8 and 9 in the consensus sequence, VBS3 contains the hydrophobic residues valine and alanine, and in contrast VBS1 contains two polar threonines that would disrupt the hydrophobic interactions (fig. 7.20 D). The tighter binding is made most apparent by the greater separation between Vd1 helix-1 and -2 in the VBS3 structure compared to the VBS1 structure (fig. 7.20 C), as the Vd1 helices accommodate the more tightly bound VBS3 peptide.

## 7.5 Discussion: Chlamydial virulence factor TarP mimics talin to disrupt the talin-vinculin complex.

### 7.5.1 TarP hijacks the host adhesion machinery

Through this work, we have further refined our understanding of the molecular mechanisms employed by chlamydiae species to gain entry into host cells through actin cytoskeleton remodelling. Atomic models demonstrate that chlamydiae employ molecular mimicry through the

virulence factor TarP to recruit and activate vinculin at the site of invasion. This may cause significant actin cytoskeleton remodelling through the actin regulatory role of active vinculin, directly through its interactions with actin (Thievensen et al., 2013) and indirectly through the arp2/3 complex (DeMali et al., 2002) and vinexin (Kioka et al., 1999). Moreover, by combining the TarP VBS with the multiple actin binding sites located on the protein (Tolchard et al., 2018), TarP has the propensity to mimic the talin-vinculin axis; onto this mimicked axis TarP can hijack the full adhesion machinery to form pseudo-focal adhesion structures at the site of injection. Current work is now being done to investigate pseudo-adhesion formation complex using the whole vinculin and actin binding region of TarP *in vitro*, with the eventual aim to investigate these structures further *in vivo*.

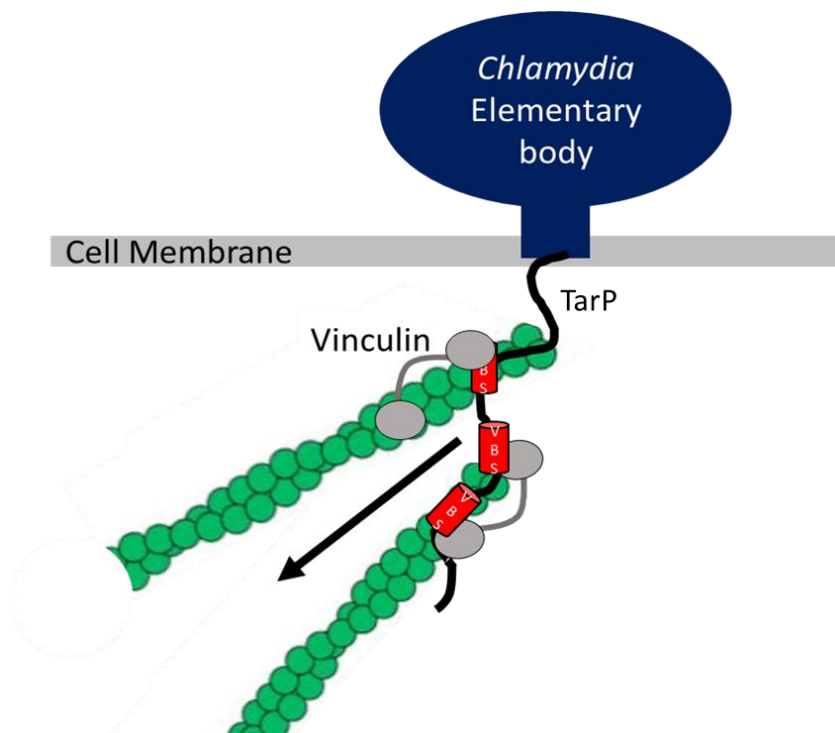


Figure 7.23: **TarP hijacks adhesion machinery.** Schematic showing TarP mimicking the talin-vinculin axis at the point of injection by combining the VBS and actin binding sites.

### 7.5.2 Disruption of talin-vinculin complexes by constitutively active VBS

Whilst being able to mimic talin to bind to vinculin we demonstrated the constitutively active TarP VBS out competes talin-vinculin complexes, leading to uncoupling of the complex. Vinculin is an important regulator of FA dynamics (Atherton et al., 2015) and cell:cell junctions (Yao et al.,

2014b); the capacity of TarP VBS1 to uncouple vinculin-mediated cytoskeletal connections during infection is therefore likely to have significant biological implications. Thus, it will be important to determine to what extent chlamydial infection alters the integrity and dynamics of cell:cell and cell:ECM junctions.

Moreover, the action of the constitutively active TarP VBS, decoupling adhesion complexes provides a model for a new class of adhesion turnover regulation. It raises the possibility that endogenous adhesion proteins might exist with constitutively active VBS. Indeed, it has been demonstrated that talin is subject to calpain mediated proteolysis, a process involved in adhesion turnover (Bate et al., 2012; Critchley, 2004; Zhang et al., 2012), which may expose or leave constitutively active VBS to assist in adhesion breakdown.

### 7.5.3 Lack of observable binding of TarP LD

The lack of observable binding of the TarP LD to FAK and talin was unexpected due the high sequence homology with other important LD motifs within adhesions. This, however, might be explained by the presence of a proline residue in the middle of the sequence, Pro-675. This proline likely destabilises and/or causes a kink in the  $\alpha$ -helix formed by the LD-motif. This would disrupt the helix-addition mechanism LD-motifs utilise to bind to their target sites. Furthermore, the TarP LD-motif might lack the binding ability due to substitution of the glutamate for aspartate in the "LD" region. Despite the similarity between these residues the length of the glutamate might sterically hinder the start of the LD-binding site. It is possible the TarP LD might bind to a different LD-binding domain protein, currently not recognised. It is possible the co-localisation of TarP and FAK was observed via a tripartite interaction between vinculin, paxillin and FAK putting the TarP and FAK in close proximity (Wood et al., 1994; Thomas et al., 1999). Altogether, our data suggests that the previous co-localisation of TarP to FAK reported *in cellulo* requires additional components to bring the two proteins together.

### 7.5.3 Future work

To further investigate the effects of TarP and the constitutively active VBS *in vivo*, it would be useful to apply a similar strategy to observe adhesions as that used in section 7.1 by our collaborators in the Danuser lab combining high resolution microscopy with traction force microscopy. In this case tracking the effects on the adhesions upon injection of TarP. The high resolution microscopy will provide vital information on the size and composition of pseudo-adhesion complexes formed at the site of injection and the traction force microscopy component will help determine the effects on adhesion breakdown by constitutively active VBS. It would be interesting to see if there is a loss of tension in adhesions around the point of TarP injection, correlating with adhesion breakdown. Altogether, this strategy would provide important information on the effects of TarP on adhesion dynamics, and give insight into the exact mechanisms used by TarP to aid host entry.

Details of this study can be read in: *Whitewood, A.J., A.K. Singh, D.G. Brown, and B.T. Goult. 2018. Chlamydial virulence factor TarP mimics talin to disrupt the talin-vinculin complex. FEBS Lett. 592:1751–1760. doi:10.1002/1873-3468.13074.*



## Chapter 8: Discussion

### 8.1 The not so simple core of cell-matrix adhesions

At the start of this thesis I mention that despite integrin-mediated adhesions being diverse complexes involving a large network of proteins and signaling molecules, they form upon a simple core of a few essential proteins involving integrin, talin, kindlin and vinculin. What is clear throughout my thesis is the way in which these proteins interact with themselves and each other adds another layer for complex regulation in the formation and fate of cell-matrix adhesions.

The complexity of core interactions was most apparent in the process of talin-mediated integrin activation. The current understanding of the topic suggests the main regulatory steps in integrin activation is first the recruitment of talin to sites of adhesion and then the activation of talin by various stimuli (Klapholz and Brown, 2017). Once relieved of the autoinhibited conformation the talin FERM domain F3 is then able to bind to and activate integrin (Banno et al., 2012; Goksoy et al., 2008; Goult et al., 2009a; Anthis et al., 2009; Calderwood et al., 1999). In collaboration with the Tanentzapf group we investigated the effects of constitutively active talin *in vivo* using an autoinhibition E1770A mutant. Whilst the mouse exhibited a phenotype of increased adhesion, there were no dramatic morphological defects one would expect with dysregulation of such an important process (Winograd-Katz et al., 2014; Haage et al., 2018). Thus, it is apparent there are more regulatory steps in talin-mediated integrin activation than previously thought. Indeed, we reported the possibility of three ways in which the talin FERM domain may be regulated in its ability to activate integrin. 1) Conformational regulation through discovery of a rotational axis between F1 and F2, enabling F0F1 to rotate 180° relative to F2F3. 2) The effect of the cell membrane lipid composition on the orientation of the talin head at the membrane. 3) A direct interaction between kindlin and the talin head which may support the talin head orientation and assist in binding to the  $\beta$ -integrin tail.

Moreover, we report an interaction between the talin head and the  $\alpha$ -tail. Integrin is activated through the separation of the  $\alpha$ - and  $\beta$ -tails, the current model suggests this is as a direct result of talin F3 binding to the  $\beta$ -tail, leading to tail separation by steric hindrance and disruption of intermolecular bonds (Ye et al., 2011). Our investigations suggest there are two  $\alpha$ -tail binding sites on the talin head. The first site we have identified is on F3 adjacent to the  $\beta$ -tail binding site. We suggest F3 is may be holding the two integrin tails together, maintaining integrin in an inactive state. The second site we have identified is on F1, which harbors a critical Rap1-binding site (Gingras et al., 2019); we have identified that the  $\alpha$ -tail binds both Rap1 and F1 weakly, thus, we hypothesized each component forms part of a high affinity tripartite interaction. We propose a model whereby the second alpha binding site on F1 holds the  $\alpha$ -tail separated from the  $\beta$ -tail bound to F3, fixing the distance between the two tails and maintaining integrin in the active conformation. Whilst this hypothesis still requires confirmation in cells, these results presented in this thesis add to the complexity of the current tail separation theory.

Finally, we report the talin rod domain R8 forms a pre-complex with vinculin prior to force transduction; this pre-complex formation is essential for nascent adhesion maturation as it enables more efficient and quicker force transmission across the adhesion complex (Han et al., 2019). The talin rod contains at least 11 cryptic vinculin binding sites that are revealed in a stepwise manner by mechanical force (Yao et al., 2014a, 2016). However, we have identified the VBS located in R8 can bind to vinculin independent of force, due to the presence of a threonine belt destabilising the domain. As to why the talin-vinculin pre-complex enables more efficient force transduction is yet to be fully elucidated. However, the pre-complex formation again adds another layer of complexity to cell-matrix adhesion formation.

## 8.2 Fine tuning of the talin domains

Talin is large mechanosensitive protein that links integrin to the actin cytoskeleton. Talin consists of 13 rod domains and 4 FERM domains, each with its own unique function (Gough and Goult,

2018). What is apparent throughout this thesis is how talin domains are finely tuned to adapt to their multiple functions. Indeed, it is a well-known property of talin, most evident in the mechanosensitive nature of the talin rod (Goult et al., 2018). However, what emerges from this thesis is that the talin domains are not just sensitive to force but other factors that alter domain conformation.

Force independent tuning is first apparent in the effect of lipid composition on the talin head and its ligands. We noticed that talin F0-F2 had a significant drop in affinity to the membrane when there was very large net negative charge, representative of substantial PIP2 enrichment, this was in contrast to the whole head and F2F3 constructs. Additionally, we report the F3 domain contains binding sites for both the  $\alpha$ - and  $\beta$ -tails and is capable of binding a plethora of ligands on the same face, demonstrating remarkable ligand plasticity (Gough and Goult, 2018). What controls the ability of talin F3 to switch between ligands is yet to be fully elucidated. However, we and others have demonstrated the affinity at which talin F3 binds both integrin tails is dependent on a PIP2 enriched membrane due to a series of basic residues which enable F3 orientation at the membrane (Moore et al., 2012). Together, these results indicate the talin head conformation and ligand binding are tuned to membrane composition, potentially leading to different strengths and compositions of the adhesions depending on the membrane composition.

Furthermore, we report talin R8 contains a “threonine-belt” that destabilizes the domain, enabling a force-independent interaction with vinculin. Talin R8 also forms part of ABS2 (Hemmings et al., 1996; Atherton et al., 2015) and behaves as an LD-motif binding domain (Zacharchenko et al., 2016b). What controls this ligand and conformational plasticity is not clear, nor are the cellular consequences, there is still much to learn about these mechanisms.

### 8.3 Potential limitations

The biochemical suite we have employed throughout this work has provided us with important details on the intricacies of integrin-mediated adhesion formation at the molecular and atomic scale. However, the observations and conclusions made are only true to the *in vitro* environment in which they were measured. Further *in vivo* studies to follow up our findings are required to fully understand the biological relevance of these newly determined interactions. Therefore, most mechanisms we have proposed are speculative models that provide a new perspective, which can be applied to future *in vivo* studies. As is apparent throughout the discussions, we have plans in place to confirm our observations *in vivo* once we have developed a strategy that enables us to do so.

## Chapter 9: References

- Abràmoff, M.D., P.J. Magalhães, and S.J. Ram. 2004. Image Processing with ImageJ Second Edition. *Biophotonics Int.* doi:10.1017/CBO9781107415324.004.
- Akbarzadeh, A., R. Rezaei-Sadabady, S. Davaran, S.W. Joo, N. Zarghami, Y. Hanifehpour, M. Samiei, M. Kouhi, and K. Nejati-Koshki. 2013. Liposome: classification, preparation, and applications. *Nanoscale Res. Lett.* 8:102. doi:10.1186/1556-276X-8-102.
- Alam, T., M. Alazmi, X. Gao, and S.T. Arold. 2014. How to find a leucine in a haystack? Structure, ligand recognition and regulation of leucine–aspartic acid (LD) motifs. *Biochem. J.* 460:317–329. doi:10.1042/BJ20140298.
- Albiges-Rizo, C., O. Destaing, B. Fourcade, E. Planus, and M.R. Block. 2009. Actin machinery and mechanosensitivity in invadopodia, podosomes and focal adhesions. *J. Cell Sci.* 122:3037–49. doi:10.1242/jcs.052704.
- An, Z., K. Dobra, J.G. Lock, S. Strömblad, A. Hjerpe, and H. Zhang. 2010. Kindlin-2 is expressed in malignant mesothelioma and is required for tumor cell adhesion and migration. *Int. J. Cancer.* 127:1999–2008. doi:10.1002/ijc.25223.
- Ananthanarayanan, B., R. V. Stahelin, M.A. Digman, and W. Cho. 2003. Activation Mechanisms of Conventional Protein Kinase C Isoforms Are Determined by the Ligand Affinity and Conformational Flexibility of Their C1 Domains. *J. Biol. Chem.* doi:10.1074/jbc.M307853200.
- Anthis, N.J., K.L. Wegener, F. Ye, C. Kim, B.T. Goult, E.D. Lowe, I. Vakonakis, N. Bate, D.R. Critchley, M.H. Ginsberg, and I.D. Campbell. 2009. The structure of an integrin/talin complex reveals the basis of inside-out signal transduction. *EMBO J.* 28:3623–32. doi:10.1038/emboj.2009.287.
- Atherton, P., B. Stutchbury, D.-Y. Wang, D. Jethwa, R. Tsang, E. Meiler-Rodriguez, P. Wang, N. Bate, R. Zent, I.L. Barsukov, B.T. Goult, D.R. Critchley, and C. Ballestrem. 2015. Vinculin

- controls talin engagement with the actomyosin machinery. *Nat. Commun.* 6:10038. doi:10.1038/ncomms10038.
- Bachir, A.I., J. Zareno, K. Moissoglu, E.F. Plow, E. Gratton, and A.R. Horwitz. 2014. Integrin-Associated Complexes Form Hierarchically with Variable Stoichiometry in Nascent Adhesions. *Curr. Biol.* 24:1845–1853. doi:10.1016/j.cub.2014.07.011.
- Bakolitsa, C., D.M. Cohen, L.A. Bankston, A.A. Bobkov, G.W. Dadwell, L. Jennings, D.R. Critchley, S.W. Craig, and R.C. Liddington. 2004. Structural basis for vinculin activation at sites of cell adhesion. *Nature*. doi:10.1038/nature02610.
- Banno, A., B.T. Goult, H. Lee, N. Bate, D.R. Critchley, and M.H. Ginsberg. 2012. Subcellular Localization of Talin Is Regulated by Inter-domain Interactions. *J. Biol. Chem.* 287:13799–13812. doi:10.1074/jbc.M112.341214.
- Bartoschik, T., S. Galinec, C. Kleusch, K. Walkiewicz, D. Breitsprecher, S. Weigert, Y.A. Muller, C. You, J. Piehler, T. Vercruyssen, D. Daelemans, and N. Tschammer. 2018. Near-native, site-specific and purification-free protein labeling for quantitative protein interaction analysis by MicroScale Thermophoresis. *Sci. Rep.* doi:10.1038/s41598-018-23154-3.
- Bate, N., A.R. Gingras, A. Bachir, R. Horwitz, F. Ye, B. Patel, B.T. Goult, and D.R. Critchley. 2012. Talin contains a C-terminal calpain2 cleavage site important in focal adhesion dynamics. *PLoS One.* 7:e34461. doi:10.1371/journal.pone.0034461.
- Beaty, B.T., Y. Wang, J.J. Bravo-Cordero, V.P. Sharma, V. Miskolci, L. Hodgson, and J. Condeelis. 2014. Talin regulates moesin-NHE-1 recruitment to invadopodia and promotes mammary tumor metastasis. *J. Cell Biol.* 205:737–751. doi:10.1083/jcb.201312046.
- Besenicar, M., P. Macek, J.H. Lakey, and G. Anderluh. 2006. Surface plasmon resonance in protein-membrane interactions. *Chem. Phys. Lipids.* 141:169–78. doi:10.1016/j.chemphyslip.2006.02.010.
- Bielez, B., Y. Sirin, H. Si, T. Niranjana, A. Gruenwald, S. Ahn, H. Kato, J. Pullman, M. Gessler, V.H. Haase, and K. Susztak. 2010. Epithelial Notch signaling regulates interstitial fibrosis development in the kidneys of mice and humans. *J. Clin. Invest.* 120:4040–4054. doi:10.1172/JCI43025.
- Bledzka, K., J. Liu, Z. Xu, H. Dhanuja Perera, S.P. Yadav, K. Bialkowska, J. Qin, Y.Q. Ma, and E.F. Plow. 2012. Spatial coordination of kindlin-2 with talin head domain in interaction with integrin  $\beta$  cytoplasmic tails. *J. Biol. Chem.* doi:10.1074/jbc.M111.336743.
- Blin, G., E. Margeat, K. Carvalho, C.A. Royer, C. Roy, and C. Picart. 2008. Quantitative analysis of the binding of ezrin to large unilamellar vesicles containing phosphatidylinositol 4,5 bisphosphate. *Biophys. J.* doi:10.1529/biophysj.107.110213.
- Boettner, B., and L. Van Aelst. 2009. Control of cell adhesion dynamics by Rap1 signaling. *Curr. Opin. Cell Biol.* 21:684–693. doi:10.1016/j.ceb.2009.06.004.
- Van Bogaart, G. Den, K. Meyenberg, U. Diederichsen, and R. Jahn. 2012. Phosphatidylinositol 4,5-bisphosphate increases Ca<sup>2+</sup> affinity of synaptotagmin-1 by 40-fold. *J. Biol. Chem.* 287:16447–16453. doi:10.1074/jbc.M112.343418.
- Bois, P.R.J., B.P. O’Hara, D. Nietlispach, J. Kirkpatrick, and T. Izard. 2006a. The Vinculin Binding Sites of Talin and  $\alpha$ -Actinin Are Sufficient to Activate Vinculin. *J. Biol. Chem.* 281:7228–7236. doi:10.1074/jbc.M510397200.
- Bois, P.R.J., B.P. O’Hara, D. Nietlispach, J. Kirkpatrick, and T. Izard. 2006b. The vinculin binding

- sites of talin and alpha-actinin are sufficient to activate vinculin. *J. Biol. Chem.* 281:7228–36. doi:10.1074/jbc.M510397200.
- Bond, P.J., and M.S.P. Sansom. 2006. Insertion and assembly of membrane proteins via simulation. *J. Am. Chem. Soc.* doi:10.1021/ja0569104.
- Böttcher, R.T., M. Veelders, P. Rombaut, J. Faix, M. Theodosiou, T.E. Stradal, K. Rottner, R. Zent, F. Herzog, and R. Fässler. 2017. Kindlin-2 recruits paxillin and Arp2/3 to promote membrane protrusions during initial cell spreading. *J. Cell Biol.* 216:3785–3798. doi:10.1083/jcb.201701176.
- Bouaouina, M., Y. Lad, and D.A. Calderwood. 2008. The N-terminal domains of talin cooperate with the phosphotyrosine binding-like domain to activate  $\beta$ 1 and  $\beta$ 3 integrins. *J. Biol. Chem.* doi:10.1074/jbc.M709527200.
- Bouchet, B.P., R.E. Gough, Y.-C. Ammon, D. van de Willige, H. Post, G. Jacquemet, A.M. Altelaar, A.J. Heck, B.T. Goult, and A. Akhmanova. 2016. Talin-KANK1 interaction controls the recruitment of cortical microtubule stabilizing complexes to focal adhesions. *Elife.* 5. doi:10.7554/eLife.18124.
- Bromberger, T., S. Klapproth, I. Rohwedder, L. Zhu, L. Mittmann, C.A. Reichel, M. Sperandio, J. Qin, and M. Moser. 2018. Direct Rap1/Talin1 interaction regulates platelet and neutrophil integrin activity in mice. *Blood.* 132:2754–2762. doi:10.1182/blood-2018-04-846766.
- Bromberger, T., L. Zhu, S. Klapproth, J. Qin, and M. Moser. 2019. Rap1 and membrane lipids cooperatively recruit talin to trigger integrin activation. *J. Cell Sci.* jcs.235531. doi:10.1242/jcs.235531.
- Brown, M.C., J.A. Perrotta, and C.E. Turner. 1996. Identification of LIM3 as the principal determinant of paxillin focal adhesion localization and characterization of a novel motif on paxillin directing vinculin and focal adhesion kinase binding. *J. Cell Biol.* 135:1109–23. doi:10.1083/jcb.135.4.1109.
- Burridge, K., and P. Mangeat. An interaction between vinculin and talin. *Nature.* 308:744–6. doi:10.1038/308744a0.
- Calderwood, D.A. 2004. Integrin activation. *J. Cell Sci.* 117:657–66. doi:10.1242/jcs.01014.
- Calderwood, D.A., I.D. Campbell, and D.R. Critchley. 2013. Talins and kindlins: partners in integrin-mediated adhesion. *Nat. Rev. Mol. Cell Biol.* 14:503–517. doi:10.1038/nrm3624.
- Calderwood, D.A., B. Yan, J.M. de Pereda, B.G. Alvarez, Y. Fujioka, R.C. Liddington, and M.H. Ginsberg. 2002. The Phosphotyrosine Binding-like Domain of Talin Activates Integrins. *J. Biol. Chem.* 277:21749–21758. doi:10.1074/jbc.M111996200.
- Calderwood, D.A., R. Zent, R. Grant, D.J.G. Rees, R.O. Hynes, and M.H. Ginsberg. 1999. The talin head domain binds to integrin  $\beta$  subunit cytoplasmic tails and regulates integrin activation. *J. Biol. Chem.* 274:28071–28074. doi:10.1074/jbc.274.40.28071.
- Camp, D., A. Haage, V. Solianova, W.M. Castle, Q.A. Xu, E. Lostchuck, B.T. Goult, and G. Tanentzapf. 2018. Direct binding of Talin to Rap1 is required for cell-ECM adhesion in *Drosophila*. *J. Cell Sci.* 131:jcs225144. doi:10.1242/jcs.225144.
- Campbell, I.D., and M.J. Humphries. 2011. Integrin structure, activation, and interactions. *Cold Spring Harb. Perspect. Biol.* 3. doi:10.1101/cshperspect.a004994.
- Carabeo, R.A., S.S. Grieshaber, E. Fischer, and T. Hackstadt. 2002. Chlamydia trachomatis induces remodeling of the actin cytoskeleton during attachment and entry into HeLa cells. *Infect.*

*Immun.* 70:3793–803.

- Carisey, A., and C. Ballestrem. 2011. Vinculin, an adapter protein in control of cell adhesion signalling. *Eur. J. Cell Biol.* 90:157–63. doi:10.1016/j.ejcb.2010.06.007.
- Carisey, A., R. Tsang, A.M. Greiner, N. Nijenhuis, N. Heath, A. Nazgiewicz, R. Kemkemer, B. Derby, J. Spatz, and C. Ballestrem. 2013. Vinculin Regulates the Recruitment and Release of Core Focal Adhesion Proteins in a Force-Dependent Manner. *Curr. Biol.* 23:271–281. doi:10.1016/j.cub.2013.01.009.
- Case, L.B., M.A. Baird, G. Shtengel, S.L. Campbell, H.F. Hess, M.W. Davidson, and C.M. Waterman. 2015. Molecular mechanism of vinculin activation and nanoscale spatial organization in focal adhesions. *Nat. Cell Biol.* 17:880–92. doi:10.1038/ncb3180.
- Case, L.B., and C.M. Waterman. 2015. Integration of actin dynamics and cell adhesion by a three-dimensional, mechanosensitive molecular clutch. *Nat. Cell Biol.* 17:955–63. doi:10.1038/ncb3191.
- Chang, Y.-C., H. Zhang, J. Franco-Barraza, M.L. Brennan, T. Patel, E. Cukierman, and J. Wu. 2014. Structural and mechanistic insights into the recruitment of talin by RIAM in integrin signaling. *Structure.* 22:1810–1820. doi:10.1016/j.str.2014.09.020.
- Chen, H., D.M. Choudhury, and S.W. Craig. 2006. Coincidence of Actin Filaments and Talin Is Required to Activate Vinculin. *J. Biol. Chem.* 281:40389–40398. doi:10.1074/jbc.M607324200.
- Chen, V.B., W.B. Arendall, J.J. Headd, D.A. Keedy, R.M. Immormino, G.J. Kapral, L.W. Murray, J.S. Richardson, and D.C. Richardson. 2010. *MolProbity* : all-atom structure validation for macromolecular crystallography. *Acta Crystallogr. Sect. D Biol. Crystallogr.* 66:12–21. doi:10.1107/S0907444909042073.
- Ciobanasu, C., H. Wang, V. Henriot, C. Mathieu, A. Fente, S. Csillag, C. Vigouroux, B. Faivre, and C. Le Clainche. 2018. Integrin-bound talin head inhibits actin filament barbed-end elongation. *J. Biol. Chem.* 293:2586–2596. doi:10.1074/JBC.M117.808204.
- Clifton, D.R., K.A. Fields, S.S. Grieshaber, C.A. Dooley, E.R. Fischer, D.J. Mead, R.A. Carabeo, and T. Hackstadt. 2004. From The Cover: A chlamydial type III translocated protein is tyrosine-phosphorylated at the site of entry and associated with recruitment of actin. *Proc. Natl. Acad. Sci.* 101:10166–10171. doi:10.1073/pnas.0402829101.
- Critchley, D.R. 2004. Cytoskeletal proteins talin and vinculin in integrin-mediated adhesion. *Biochem. Soc. Trans.* 32:831–836. doi:10.1042/BST0320831.
- D’Souza, M.-A.M.A., R.M. Kimble, and J.R. McMillan. 2010. Kindler Syndrome Pathogenesis and Fermitin Family Homologue 1 (Kindlin-1) Function. *Dermatol. Clin.* 28:115–118. doi:10.1016/j.det.2009.10.012.
- Debrand, E., Y. El Jai, L. Spence, N. Bate, U. Praekelt, C.A. Pritchard, S.J. Monkley, and D.R. Critchley. 2009. Talin 2 is a large and complex gene encoding multiple transcripts and protein isoforms. *FEBS J.* 276:1610–28. doi:10.1111/j.1742-4658.2009.06893.x.
- DeMali, K.A., C.A. Barlow, and K. Burridge. 2002. Recruitment of the Arp2/3 complex to vinculin: Coupling membrane protrusion to matrix adhesion. *J. Cell Biol.* doi:10.1083/jcb.200206043.
- Digman, M.A., P.W. Wiseman, C. Choi, A.R. Horwitz, and E. Gratton. 2009. Stoichiometry of molecular complexes at adhesions in living cells. *Proc. Natl. Acad. Sci. U. S. A.* 106:2170–5. doi:10.1073/pnas.0806036106.

- Dowling, J.J., E. Gibbs, M. Russell, D. Goldman, J. Minarcik, J.A. Golden, and E.L. Feldman. 2008. Kindlin-2 is an essential component of intercalated discs and is required for vertebrate cardiac structure and function. *Circ. Res.* 102:423–431. doi:10.1161/CIRCRESAHA.107.161489.
- Duhr, S., and D. Braun. 2006. Why molecules move along a temperature gradient. *Proc. Natl. Acad. Sci.* doi:10.1073/pnas.0603873103.
- Durbeej, M. 2010. Laminins. *Cell Tissue Res.* 339:259–268. doi:10.1007/s00441-009-0838-2.
- Elliott, P.R., B.T. Goult, P.M. Kopp, N. Bate, J.G. Grossmann, G.C.K. Roberts, D.R. Critchley, and I.L. Barsukov. 2010. The Structure of the Talin Head Reveals a Novel Extended Conformation of the FERM Domain. *Structure.* 18:1289–1299. doi:10.1016/j.str.2010.07.011.
- Ellis, S.J., E. Lostchuck, B.T. Goult, M. Bouaouina, M.J. Fairchild, P. López-Ceballos, D.A. Calderwood, and G. Tanentzapf. 2014. The Talin Head Domain Reinforces Integrin-Mediated Adhesion by Promoting Adhesion Complex Stability and Clustering. *PLoS Genet.* 10:e1004756. doi:10.1371/journal.pgen.1004756.
- Elosegui-Artola, A., R. Oria, Y. Chen, A. Kosmalska, C. Pérez-González, N. Castro, C. Zhu, X. Trepast, and P. Roca-Cusachs. 2016. Mechanical regulation of a molecular clutch defines force transmission and transduction in response to matrix rigidity. *Nat. Cell Biol.* doi:10.1038/ncb3336.
- Emsley, P., B. Lohkamp, W.G. Scott, K. Cowtan, and IUCr. 2010. Features and development of *Coot*. *Acta Crystallogr. Sect. D Biol. Crystallogr.* 66:486–501. doi:10.1107/S0907444910007493.
- Evans, P.R. 2011. An introduction to data reduction: space-group determination, scaling and intensity statistics. *Acta Crystallogr. Sect. D Biol. Crystallogr.* 67:282–292. doi:10.1107/S090744491003982X.
- Evans, P.R., and G.N. Murshudov. 2013. How good are my data and what is the resolution? *Acta Crystallogr. Sect. D Biol. Crystallogr.* 69:1204–1214. doi:10.1107/S0907444913000061.
- De Franceschi, N., M. Miihkinen, H. Hamidi, J. Alanko, A. Mai, L. Picas, C. Guzmán, D. Lévy, P. Mattjus, B.T. Goult, B. Goud, and J. Ivaska. 2019. ProLIF – Quantitative integrin protein–protein interactions and synergistic membrane effects on proteoliposomes. *J. Cell Sci.* 132. doi:10.1242/jcs.214270.
- Frantz, C., K.M. Stewart, and V.M. Weaver. 2010. The extracellular matrix at a glance. *J. Cell Sci.* 123:4195–4200. doi:10.1242/jcs.023820.
- Fukuda, K., K. Bledzka, J. Yang, H.D. Perera, E.F. Plow, and J. Qin. 2014. Molecular basis of kindlin-2 binding to integrin-linked kinase pseudokinase for regulating cell adhesion. *J. Biol. Chem.* 289:28363–28375. doi:10.1074/jbc.M114.596692.
- García-Alvarez, B., J.M. de Pereda, D.A. Calderwood, T.S. Ulmer, D. Critchley, I.D. Campbell, M.H. Ginsberg, and R.C. Liddington. 2003. Structural Determinants of Integrin Recognition by Talin. *Mol. Cell.* 11:49–58. doi:10.1016/S1097-2765(02)00823-7.
- Gardel, M.L., I.C. Schneider, Y. Aratyn-Schaus, and C.M. Waterman. 2010. Mechanical Integration of Actin and Adhesion Dynamics in Cell Migration. *Annu. Rev. Cell Dev. Biol.* doi:10.1146/annurev.cellbio.011209.122036.
- Gasteiger, E., C. Hoogland, A. Gattiker, S. Duvaud, M.R. Wilkins, R.D. Appel, and A. Bairoch. 2005. Protein Identification and Analysis Tools on the ExpASY Server. *In The Proteomics Protocols*



Handbook. Humana Press, Totowa, NJ. 571–607.

- Gingras, A.R., N. Bate, B.T. Goult, L. Hazelwood, I. Canestrelli, J.G. Grossmann, H. Liu, N.S.M. Putz, G.C.K. Roberts, N. Volkmann, D. Hanein, I.L. Barsukov, and D.R. Critchley. 2008. The structure of the C-terminal actin-binding domain of talin. *EMBO J.* 27:458–69. doi:10.1038/sj.emboj.7601965.
- Gingras, A.R., N. Bate, B.T. Goult, B. Patel, P.M. Kopp, J. Emsley, I.L. Barsukov, G.C.K. Roberts, and D.R. Critchley. 2010. Central Region of Talin Has a Unique Fold That Binds Vinculin and Actin. *J. Biol. Chem.* 285:29577–29587. doi:10.1074/jbc.M109.095455.
- Gingras, A.R., F. Lagarrigue, M.N. Cuevas, A.J. Valadez, M. Zorovich, W. McLaughlin, M.A. Lopez-Ramirez, N. Seban, K. Ley, W.B. Kiosses, and M.H. Ginsberg. 2019. Rap1 binding and a lipid-dependent helix in talin F1 domain promote integrin activation in tandem. *J. Cell Biol.* 218:1799–1809. doi:10.1083/jcb.201810061.
- Gingras, A.R., W.H. Ziegler, A.A. Bobkov, M.G. Joyce, D. Fasci, M. Himmel, S. Rothemund, A. Ritter, J.G. Grossmann, B. Patel, N. Bate, B.T. Goult, J. Emsley, I.L. Barsukov, G.C.K. Roberts, R.C. Liddington, M.H. Ginsberg, and D.R. Critchley. 2009. Structural determinants of integrin binding to the talin rod. *J. Biol. Chem.* doi:10.1074/jbc.M805937200.
- Gingras, A.R., W.H. Ziegler, R. Frank, I.L. Barsukov, G.C.K. Roberts, D.R. Critchley, and J. Emsley. 2005. Mapping and consensus sequence identification for multiple vinculin binding sites within the talin rod. *J. Biol. Chem.* doi:10.1074/jbc.M508060200.
- Ginsberg, M.H. 2014. Integrin activation. *BMB Rep.* 47:655–9. doi:10.5483/bmbrep.2014.47.12.241.
- Gkourogianni, A., M. Egot, V. Koloka, V. Moussis, V. Tsikaris, E. Panou-Pomonis, M. Sakarellos-Daitsiotis, C. Bachelot-Loza, and D.C. Tsoukatos. 2014. Palmitoylated peptide, being derived from the carboxyl-terminal sequence of the integrin  $\alpha_{IIb}$  cytoplasmic domain, inhibits talin binding to  $\alpha_{IIb}\beta_3$ . *Platelets.* 25:619–627. doi:10.3109/09537104.2013.850588.
- Goksoy, E., Y.Q. Ma, X. Wang, X. Kong, D. Perera, E.F. Plow, and J. Qin. 2008. Structural Basis for the Autoinhibition of Talin in Regulating Integrin Activation. *Mol. Cell.* doi:10.1016/j.molcel.2008.06.011.
- Goldmann, W.H., D. Hess, and G. Isenberg. 2001. The effect of intact talin and talin tail fragment on actin filament dynamics and structure depends on pH and ionic strength. *Eur. J. Biochem.* 260:439–445. doi:10.1046/j.1432-1327.1999.00177.x.
- Goodwin, K., S.J. Ellis, E. Lostchuck, T. Zulueta-Coarasa, R. Fernandez-Gonzalez, and G. Tanentzapf. 2016. Basal Cell-Extracellular Matrix Adhesion Regulates Force Transmission during Tissue Morphogenesis. *Dev. Cell.* 39:611–625. doi:10.1016/j.devcel.2016.11.003.
- Gough, R.E., and B.T. Goult. 2018. The tale of two talins - two isoforms to fine-tune integrin signalling. *FEBS Lett.* 592:2108–2125. doi:10.1002/1873-3468.13081.
- Goult, B.T., N. Bate, N.J. Anthis, K.L. Wegener, A.R. Gingras, B. Patel, I.L. Barsukov, I.D. Campbell, G.C.K. Roberts, and D.R. Critchley. 2009a. The structure of an interdomain complex that regulates Talin activity. *J. Biol. Chem.* doi:10.1074/jbc.M900078200.
- Goult, B.T., M. Bouaouina, P.R. Elliott, N. Bate, B. Patel, A.R. Gingras, J.G. Grossmann, G.C.K. Roberts, D.A. Calderwood, D.R. Critchley, and I.L. Barsukov. 2010a. Structure of a double ubiquitin-like domain in the talin head: A role in integrin activation. *EMBO J.* doi:10.1038/emboj.2010.4.

- Goult, B.T., M. Bouaouina, D.S. Harburger, N. Bate, B. Patel, N.J. Anthis, I.D. Campbell, D.A. Calderwood, I.L. Barsukov, G.C. Roberts, and D.R. Critchley. 2009b. The Structure of the N-Terminus of Kindlin-1: A Domain Important for  $\alpha$ IIb $\beta$ 3 Integrin Activation. *J. Mol. Biol.* 394:944–956. doi:10.1016/j.jmb.2009.09.061.
- Goult, B.T., A.R. Gingras, N. Bate, I.L. Barsukov, D.R. Critchley, and G.C.K. Roberts. 2010b. The domain structure of talin: Residues 1815–1973 form a five-helix bundle containing a cryptic vinculin-binding site. *FEBS Lett.* 584:2237–2241. doi:10.1016/J.FEBSLET.2010.04.028.
- Goult, B.T., X.P. Xu, A.R. Gingras, M. Swift, B. Patel, N. Bate, P.M. Kopp, I.L. Barsukov, D.R. Critchley, N. Volkman, and D. Hanein. 2013a. Structural studies on full-length talin1 reveal a compact auto-inhibited dimer: Implications for talin activation. *J. Struct. Biol.* doi:10.1016/j.jsb.2013.05.014.
- Goult, B.T., J. Yan, and M.A. Schwartz. 2018. Talin as a mechanosensitive signaling hub. *J. Cell Biol.* 217:3776–3784. doi:10.1083/jcb.201808061.
- Goult, B.T., T. Zacharchenko, N. Bate, R. Tsang, F. Hey, A.R. Gingras, P.R. Elliott, G.C.K. Roberts, C. Ballestrem, D.R. Critchley, and I.L. Barsukov. 2013b. RIAM and vinculin binding to talin are mutually exclusive and regulate adhesion assembly and turnover. *J. Biol. Chem.* 288:8238–49. doi:10.1074/jbc.M112.438119.
- Greenfield, N.J. 2007. Using circular dichroism spectra to estimate protein secondary structure. *Nat. Protoc.* doi:10.1038/nprot.2006.202.
- Grove, J., and M. Marsh. 2011. The cell biology of receptor-mediated virus entry. *J. Cell Biol.* 195:1071–82. doi:10.1083/jcb.201108131.
- Gureasko, J., W.J. Galush, H. Sondermann, J.T. Groves, and J. Kuriyan. 2010. Direct coupling of Ras to preformed maleimide-functionalized lipid membranes. *Protoc. Exch.* doi:10.1038/nprot.2010.155.
- Gutierrez, E., E. Tkachenko, A. Besser, P. Sundd, K. Ley, G. Danuser, M.H. Ginsberg, and A. Groisman. 2011. High Refractive Index Silicone Gels for Simultaneous Total Internal Reflection Fluorescence and Traction Force Microscopy of Adherent Cells. *PLoS One.* 6:e23807. doi:10.1371/JOURNAL.PONE.0023807.
- Haage, A., K. Goodwin, A. Whitewood, D. Camp, A. Bogutz, C.T. Turner, D.J. Granville, L. Lefebvre, S. Plotnikov, B.T. Goult, and G. Tanentzapf. 2018. Talin Autoinhibition Regulates Cell-ECM Adhesion Dynamics and Wound Healing In Vivo. *Cell Rep.* 25:2401-2416.e5. doi:10.1016/j.celrep.2018.10.098.
- Hacker, D.L., and S. Balasubramanian. 2016. Recombinant protein production from stable mammalian cell lines and pools. *Curr. Opin. Struct. Biol.* 38:129–136. doi:10.1016/J.SBI.2016.06.005.
- Han, J., C.J. Lim, N. Watanabe, A. Soriani, B. Ratnikov, D.A. Calderwood, W. Puzon-McLaughlin, E.M. Lafuente, V.A. Boussiotis, S.J. Shattil, and M.H. Ginsberg. 2006. Reconstructing and Deconstructing Agonist-Induced Activation of Integrin  $\alpha$ IIb $\beta$ 3. *Curr. Biol.* 16:1796–1806. doi:10.1016/J.CUB.2006.08.035.
- Han, S.J., K.M. Dean, A.J. Whitewood, A. Bachir, E. Gutierrez, A. Groisman, A.R. Horwitz, B.T. Goult, and G. Danuser. 2019. Formation of talin-vinculin pre-complexes dictates maturation of nascent adhesions by accelerated force transmission and vinculin recruitment. *bioRxiv.* 735183. doi:10.1101/735183.
- Han, S.J., Y. Oak, A. Groisman, and G. Danuser. 2015. Traction microscopy to identify force

- modulation in subresolution adhesions. *Nat. Methods*. 12:653–656. doi:10.1038/nmeth.3430.
- Harburger, D.S., M. Bouaouina, and D.A. Calderwood. 2009. Kindlin-1 and -2 Directly Bind the C-terminal Region of  $\beta$  Integrin Cytoplasmic Tails and Exert Integrin-specific Activation Effects. *J. Biol. Chem.* 284:11485–11497. doi:10.1074/jbc.M809233200.
- Harris, E.S., T.M. McIntyre, S.M. Prescott, and G.A. Zimmerman. 2000. The leukocyte integrins. *J. Biol. Chem.* 275:23409–23412. doi:10.1074/jbc.R000004200.
- Has, C., D. Castiglia, M. del Rio, M.G. Diez, E. Piccinni, D. Kiritsi, J. Kohlhase, P. Itin, L. Martin, J. Fischer, G. Zambruno, and L. Bruckner-Tuderman. 2011. Kindler syndrome: extension of FERMT1 mutational spectrum and natural history. *Hum. Mutat.* 32:1204–12. doi:10.1002/humu.21576.
- Hayes, S., B. Malacrida, M. Kiely, and P.A. Kiely. 2016. Studying protein-protein interactions: progress, pitfalls and solutions. *Biochem. Soc. Trans.* 44:994–1004. doi:10.1042/BST20160092.
- Hemmings, L., D.J. Rees, V. Ohanian, S.J. Bolton, A.P. Gilmore, B. Patel, H. Priddle, J.E. Trevithick, R.O. Hynes, and D.R. Critchley. 1996. Talin contains three actin-binding sites each of which is adjacent to a vinculin-binding site. *J. Cell Sci.*
- Hoellerer, M.K., M.E.M. Noble, G. Labesse, I.D. Campbell, J.M. Werner, and S.T. Arold. 2003. Molecular Recognition of Paxillin LD Motifs by the Focal Adhesion Targeting Domain. *Structure*. 11:1207–1217. doi:10.1016/J.STR.2003.08.010.
- Horton, E.R., A. Byron, J.A. Askari, D.H.J. Ng, A. Millon-Frémillon, J. Robertson, E.J. Koper, N.R. Paul, S. Warwood, D. Knight, J.D. Humphries, and M.J. Humphries. 2015. Definition of a consensus integrin adhesome and its dynamics during adhesion complex assembly and disassembly. *Nat. Cell Biol.* 17:1577–1587. doi:10.1038/ncb3257.
- Hughes, P.E., F. Diaz-Gonzalez, L. Leong, C. Wu, J.A. McDonald, S.J. Shattil, and M.H. Ginsberg. 1996. Breaking the integrin hinge. A defined structural constraint regulates integrin signaling. *J. Biol. Chem.* 271:6571–4. doi:10.1074/jbc.271.12.6571.
- Humphries, J.D., A. Byron, and M.J. Humphries. 2006. Integrin ligands at a glance. *J. Cell Sci.* 119:3901–3903. doi:10.1242/jcs.03098.
- Humphries, J.D., P. Wang, C. Streuli, B. Geiger, M.J. Humphries, and C. Ballestrem. 2007. Vinculin controls focal adhesion formation by direct interactions with talin and actin. *J. Cell Biol.* 179:1043–57. doi:10.1083/jcb.200703036.
- Hüttelmaier, S., P. Bubeck, M. Rudiger, and B.M. Jockusch. 1997. Characterization of Two F-Actin-Binding and Oligomerization Sites in the Cell-Contact Protein Vinculin. *Eur. J. Biochem.* 247:1136–1142. doi:10.1111/j.1432-1033.1997.01136.x.
- Hüttelmaier, S., S. Illenberger, I. Grosheva, M. Rüdiger, R.H. Singer, and B.M. Jockusch. 2001. Raver1, a dual compartment protein, is a ligand for PTB/hnRNPI and microfilament attachment proteins. *J. Cell Biol.* 155:775. doi:10.1083/JCB.200105044.
- Iwamoto, D. V, and D.A. Calderwood. 2015. Regulation of integrin-mediated adhesions. *Curr. Opin. Cell Biol.* 36:41–7. doi:10.1016/j.ceb.2015.06.009.
- Izard, T., G. Evans, R.A.R.A.R.A. Borgon, C.L.C.L. Rush, G. Bricogne, and P.R.J.P.R. Bois. 2004. Vinculin activation by talin through helical bundle conversion. *Nature*. 427:171–175. doi:10.2210/PDB1RKC/PDB.

- Izard, T., G. Tran Van Nhieu, and P.R.J. Bois. 2006. *Shigella* applies molecular mimicry to subvert vinculin and invade host cells. *J. Cell Biol.* 175:465–475. doi:10.1083/jcb.200605091.
- Jameson, D.M., and W.H. Sawyer. 1995. Fluorescence anisotropy applied to biomolecular interactions. *Methods Enzymol.* doi:10.1016/0076-6879(95)46014-4.
- Janssen, M.E.W., E. Kim, H. Liu, L.M. Fujimoto, A. Bobkov, N. Volkmann, and D. Hanein. 2006. Three-Dimensional Structure of Vinculin Bound to Actin Filaments. *Mol. Cell.* 21:271–281. doi:10.1016/j.molcel.2005.11.020.
- Jerabek-Willemsen, M., T. André, R. Wanner, H.M. Roth, S. Duhr, P. Baaske, and D. Breitsprecher. 2014. MicroScale Thermophoresis: Interaction analysis and beyond. *J. Mol. Struct.* 1077:101–113. doi:10.1016/j.molstruc.2014.03.009.
- Jiwani, S., S. Alvarado, R.J. Ohr, A. Romero, B. Nguyen, and T.J. Jewett. 2013. Chlamydia trachomatis Tarp harbors distinct G and F actin binding domains that bundle actin filaments. *J. Bacteriol.* 195:708–16. doi:10.1128/JB.01768-12.
- Jobard, F., B. Bouadjar, F. Caux, S. Hadj-Rabia, C. Has, F. Matsuda, J. Weissenbach, M. Lathrop, J.F. Prud'homme, and J. Fischer. 2003. Identification of mutations in a new gene encoding a FERM family protein with a pleckstrin homology domain in Kindler syndrome. *Hum. Mol. Genet.* 12:925–935. doi:10.1093/hmg/ddg097.
- Jones, D.T., and D. Cozzetto. 2015. DISOPRED3: precise disordered region predictions with annotated protein-binding activity. *Bioinformatics.* 31:857–863. doi:10.1093/bioinformatics/btu744.
- Kabsch, W. 2010. XDS. *Acta Crystallogr. D. Biol. Crystallogr.* 66:125–32. doi:10.1107/S0907444909047337.
- Kadler, K.E., A. Hill, and E.G. Canty-Laird. 2008. Collagen fibrillogenesis: fibronectin, integrins, and minor collagens as organizers and nucleators. *Curr. Opin. Cell Biol.* 20:495–501. doi:10.1016/j.ceb.2008.06.008.
- Kalli, A.C., I.D. Campbell, and M.S.P. Sansom. 2011. Multiscale simulations suggest a mechanism for integrin inside-out activation. *Proc. Natl. Acad. Sci. U. S. A.* 108:11890–5. doi:10.1073/pnas.1104505108.
- Kalli, A.C., K.L. Wegener, B.T. Goult, N.J. Anthis, I.D. Campbell, and M.S.P. Sansom. 2010. The Structure of the Talin/Integrin Complex at a Lipid Bilayer: An NMR and MD Simulation Study. *Structure.* doi:10.1016/j.str.2010.07.012.
- Kawabe, H., Y. Hata, M. Takeuchi, N. Ide, A. Mizoguchi, and Y. Takai. 1999. nArgBP2, a Novel Neural Member of Ponsin/ArgBP2/Vinexin Family That Interacts with Synapse-associated Protein 90/Postsynaptic Density-95-associated Protein (SAPAP). *J. Biol. Chem.* 274:30914–30918. doi:10.1074/jbc.274.43.30914.
- Kim, M., C. V Carman, and T.A. Springer. 2003. Bidirectional transmembrane signaling by cytoplasmic domain separation in integrins. *Science.* 301:1720–5. doi:10.1126/science.1084174.
- Kindler, T. 1954. Congenital Poikiloderma With Traumatic Bulla Formation and Progressive Cutaneous Atrophy. *Br. J. Dermatol.* 66:104–111. doi:10.1111/j.1365-2133.1954.tb12598.x.
- Kioka, N., S. Sakata, T. Kawauchi, T. Amachi, S.K. Akiyama, K. Okazaki, C. Yaen, K.M. Yamada, and S. Aota. 1999. Vinexin: a novel vinculin-binding protein with multiple SH3 domains enhances actin cytoskeletal organization. *J. Cell Biol.* 144:59–69. doi:10.1083/jcb.144.1.59.

- Klapholz, B., and N.H. Brown. 2017. Talin-the master of integrin adhesions. doi:10.1242/jcs.190991.
- Kloeker, S., M.B. Major, D.A. Calderwood, M.H. Ginsberg, D.A. Jones, and M.C. Beckerle. 2004. The Kindler Syndrome Protein Is Regulated by Transforming Growth Factor- $\beta$  and Involved in Integrin-mediated Adhesion. *J. Biol. Chem.* doi:10.1074/jbc.M307978200.
- Klotzsch, E., J. Stiegler, E. Ben-Ishay, and K. Gaus. 2015. Do mechanical forces contribute to nanoscale membrane organisation in T cells? *Biochim. Biophys. Acta - Mol. Cell Res.* 1853:822–829. doi:10.1016/J.BBAMCR.2014.10.025.
- Knezevic, I., T.M. Leisner, and S.C. Lam. 1996. Direct binding of the platelet integrin  $\alpha$ IIb $\beta$ 3 (GPIIb-IIIa) to talin. Evidence that interaction is mediated through the cytoplasmic domains of both  $\alpha$ IIb and  $\beta$ 3. *J. Biol. Chem.* 271:16416–21. doi:10.1074/jbc.271.27.16416.
- Kopp, P.M., N. Bate, T.M. Hansen, N.P.J. Brindle, U. Praekelt, E. Debrand, S. Coleman, D. Mazzeo, B.T. Goult, A.R. Gingras, C.A. Pritchard, D.R. Critchley, and S.J. Monkley. 2010. Studies on the morphology and spreading of human endothelial cells define key inter- and intramolecular interactions for talin1. *Eur. J. Cell Biol.* 89:661–673. doi:10.1016/j.ejcb.2010.05.003.
- Krissinel, E., and K. Henrick. 2007. Inference of Macromolecular Assemblies from Crystalline State. *J. Mol. Biol.* 372:774–797. doi:10.1016/j.jmb.2007.05.022.
- Kuijpers, T.W., E. Van De Vijver, M.A.J. Weterman, M. De Boer, A.T.J. Tool, T.K. Van Den Berg, M. Moser, M.E. Jakobs, K. Seeger, Ö. Sanal, S. Ünal, M. Çetin, D. Roos, A.J. Verhoeven, and F. Baas. 2009. LAD-1/variant syndrome is caused by mutations in FERMT3. *Blood.* 113:4740–4746. doi:10.1182/blood-2008-10-182154.
- Kumar, A., M. Ouyang, K. Van den Dries, E.J. McGhee, K. Tanaka, M.D. Anderson, A. Groisman, B.T. Goult, K.I. Anderson, and M.A. Schwartz. 2016. Talin tension sensor reveals novel features of focal adhesion force transmission and mechanosensitivity. 213:371–383. doi:10.1083/jcb.201510012.
- Lafuente, E.M., A.A.F.L. van Puijenbroek, M. Krause, C. V Carman, G.J. Freeman, A. Berezovskaya, E. Constantine, T.A. Springer, F.B. Gertler, and V.A. Boussiotis. 2004. RIAM, an Ena/VASP and Profilin ligand, interacts with Rap1-GTP and mediates Rap1-induced adhesion. *Dev. Cell.* 7:585–95. doi:10.1016/j.devcel.2004.07.021.
- Lagarrigue, F., A.R. Gingras, D.S. Paul, A.J. Valadez, M.N. Cuevas, H. Sun, M.A. Lopez-Ramirez, B.T. Goult, S.J. Shattil, W. Bergmeier, and M.H. Ginsberg. 2018. Rap1 binding to the talin 1 F0 domain makes a minimal contribution to murine platelet GPIIb-IIIa activation. *Blood Adv.* 2:2358–2368. doi:10.1182/BLOODADVANCES.2018020487.
- Lai-Cheong, J.E., A. Tanaka, G. Hawche, P. Emanuel, C. Maari, M. Taskesen, S. Akdeniz, L. Liu, and J.A. McGrath. 2009. Kindler syndrome: a focal adhesion genodermatosis. *Br. J. Dermatol.* 160:233–42. doi:10.1111/j.1365-2133.2008.08976.x.
- Lau, T.-L., C. Kim, M.H. Ginsberg, and T.S. Ulmer. 2009. The structure of the integrin  $\alpha$ IIb $\beta$ 3 transmembrane complex explains integrin transmembrane signalling. *EMBO J.* 28:1351–61. doi:10.1038/emboj.2009.63.
- Lawson, C., S.-T. Lim, S. Uryu, X.L. Chen, D.A. Calderwood, and D.D. Schlaepfer. 2012. FAK promotes recruitment of talin to nascent adhesions to control cell motility. *J. Cell Biol.* 196:223–32. doi:10.1083/jcb.201108078.
- Lee, H.-S., R.M. Bellin, D.L. Walker, B. Patel, P. Powers, H. Liu, B. Garcia-Alvarez, J.M. de Pereda, R.C. Liddington, N. Volkmann, D. Hanein, D.R. Critchley, and R.M. Robson. 2004.

- Characterization of an Actin-binding Site within the Talin FERM Domain. *J. Mol. Biol.* 343:771–784. doi:10.1016/J.JMB.2004.08.069.
- Lee, H.S., C.J. Lim, W. Puzon-McLaughlin, S.J. Shattil, and M.H. Ginsberg. 2009. RIAM activates integrins by linking talin to Ras GTPase membrane-targeting sequences. *J. Biol. Chem.* 284:5119–5122. doi:10.1074/jbc.M807117200.
- Lee, J.H., C. Vornrhein, G. Bricogne, and T. Izard. 2013a. Crystal structure of the N-terminal domains of the surface cell antigen 4 of *Rickettsia*. *Protein Sci.* 22:n/a-n/a. doi:10.1002/pro.2322.
- Lee, J.H., C. Vornrhein, G. Bricogne, and T. Izard. 2013b. Crystal structure of the N-terminal domains of the surface cell antigen 4 of *Rickettsia*. *Protein Sci.* 22:1425–31. doi:10.1002/pro.2322.
- Legate, K.R., S. Takahashi, N. Bonakdar, B. Fabry, D. Boettiger, R. Zent, and R. Fässler. 2011. Integrin adhesion and force coupling are independently regulated by localized PtdIns(4,5)2 synthesis. *EMBO J.* 30:4539–53. doi:10.1038/emboj.2011.332.
- Li, A., Q. Guo, C. Kim, W. Hu, and F. Ye. 2014. Integrin  $\alpha$ IIb tail distal of GFFKR participates in inside-out  $\alpha$ IIb $\beta$ 3 activation. *J. Thromb. Haemost.* 12:1145–1155. doi:10.1111/jth.12610.
- Li, H., Y. Deng, K. Sun, H. Yang, J. Liu, M. Wang, Z. Zhang, J. Lin, C. Wu, Z. Wei, and C. Yu. 2017a. Structural basis of kindlin-mediated integrin recognition and activation. *Proc. Natl. Acad. Sci.* doi:10.1073/pnas.1703064114.
- Li, J., and T.A. Springer. 2018. Energy landscape differences among integrins establish the framework for understanding activation. *J. Cell Biol.* 217:397–412. doi:10.1083/jcb.201701169.
- Li, J., Y. Su, W. Xia, Y. Qin, M.J. Humphries, D. Vestweber, C. Cabañas, C. Lu, and T.A. Springer. 2017b. Conformational equilibria and intrinsic affinities define integrin activation. *EMBO J.* 36:629–645. doi:10.15252/emj.201695803.
- Linder, S. 2007. The matrix corroded: podosomes and invadopodia in extracellular matrix degradation. *Trends Cell Biol.* 17:107–17. doi:10.1016/j.tcb.2007.01.002.
- Ling, K., R.L. Doughman, A.J. Firestone, M.W. Bunce, and R.A. Anderson. 2002. Type I $\gamma$  phosphatidylinositol phosphate kinase targets and regulates focal adhesions. *Nature.* 420:89–93. doi:10.1038/nature01082.
- Liu, J., K. Fukuda, Z. Xu, Y.Q. Ma, J. Hirbawi, X. Mao, C. Wu, E.F. Plow, and J. Qin. 2011. Structural basis of phosphoinositide binding to kindlin-2 protein pleckstrin homology domain in regulating integrin activation. *J. Biol. Chem.* 286:43334–43342. doi:10.1074/jbc.M111.295352.
- Liu, X., Y.-J. Pan, J.-N. Zheng, and D.-S. Pei. 2017. The Role of Tumor Suppressor DLC-1: Far From Clear. *Anticancer. Agents Med. Chem.* 17:896–901. doi:10.2174/1871520616666160907142754.
- López-Colomé, A.M., I. Lee-Rivera, R. Benavides-Hidalgo, and E. López. 2017. Paxillin: a crossroad in pathological cell migration. *J. Hematol. Oncol.* 10:50. doi:10.1186/s13045-017-0418-y.
- Lu, P., V.M. Weaver, and Z. Werb. 2012. The extracellular matrix: A dynamic niche in cancer progression. *J. Cell Biol.* 196:395–406. doi:10.1083/jcb.201102147.
- Ludwig, C. 1856. Diffusion zwischen ungleich erwärmten Orten gleich zusammengesetzter Lösung.

- Luo, B.-H., C. V Carman, and T.A. Springer. 2007. Structural basis of integrin regulation and signaling. *Annu. Rev. Immunol.* 25:619–47. doi:10.1146/annurev.immunol.25.022106.141618.
- Luxenburg, C., J.T. Parsons, L. Addadi, and B. Geiger. 2006. Involvement of the Src-cortactin pathway in podosome formation and turnover during polarization of cultured osteoclasts. *J. Cell Sci.* 119:4878–4888. doi:10.1242/jcs.03271.
- Maartens, A.P., J. Wellmann, E. Wictome, B. Klapholz, H. Green, and N.H. Brown. 2016. *Drosophila* vinculin is more harmful when hyperactive than absent, and can circumvent integrin to form adhesion complexes. *J. Cell Sci.* 129:4354–4365. doi:10.1242/jcs.189878.
- Madeira, F., Y.M. Park, J. Lee, N. Buso, T. Gur, N. Madhusoodanan, P. Basutkar, A.R.N. Tivey, S.C. Potter, R.D. Finn, and R. Lopez. 2019. The EMBL-EBI search and sequence analysis tools APIs in 2019. *Nucleic Acids Res.* 47:W636–W641. doi:10.1093/nar/gkz268.
- Mahawithitwong, P., K. Ohuchida, N. Ikenaga, H. Fujita, M. Zhao, S. Kozono, K. Shindo, T. Ohtsuka, K. Mizumoto, and M. Tanaka. 2013. Kindlin-2 expression in peritumoral stroma is associated with poor prognosis in pancreatic ductal adenocarcinoma. *Pancreas.* 42:663–669. doi:10.1097/MPA.0b013e318279bd66.
- Makrides, S.C. 1996. Strategies for achieving high-level expression of genes in *Escherichia coli*. *Microbiol. Rev.*
- Mandai, K., H. Nakanishi, A. Satoh, K. Takahashi, K. Satoh, H. Nishioka, A. Mizoguchi, and Y. Takai. 1999. Ponsin/SH3P12: an I-afadin- and vinculin-binding protein localized at cell-cell and cell-matrix adherens junctions. *J. Cell Biol.* 144:1001–17. doi:10.1083/jcb.144.5.1001.
- MBInfo. How do focal adhesions act as molecular clutches in lamellipodia?
- McCann, R.O., and S.W. Craig. 1997. The I/LWEQ module: a conserved sequence that signifies F-actin binding in functionally diverse proteins from yeast to mammals. *Proc. Natl. Acad. Sci. U. S. A.* 94:5679–84. doi:10.1073/pnas.94.11.5679.
- McCoy, A.J., R.W. Grosse-Kunstleve, P.D. Adams, M.D. Winn, L.C. Storoni, and R.J. Read. 2007. *Phaser* crystallographic software. *J. Appl. Crystallogr.* 40:658–674. doi:10.1107/S0021889807021206.
- Mehrbod, M., S. Trisno, and M.R.K. Mofrad. 2013. On the activation of integrin  $\alpha 5 \beta 3$ : outside-in and inside-out pathways. *Biophys. J.* 105:1304–15. doi:10.1016/j.bpj.2013.07.055.
- Meves, A., C. Stremmel, K. Gottschalk, and R. Fässler. 2009. The Kindlin protein family: new members to the club of focal adhesion proteins. *Trends Cell Biol.* 19:504–513. doi:10.1016/j.tcb.2009.07.006.
- Michael, M., R. Begum, G.K. Chan, A.J. Whitewood, D.R. Matthews, B.T. Goult, J.A. McGrath, and M. Parsons. 2019. Kindlin-1 Regulates Epidermal Growth Factor Receptor Signaling. *J. Invest. Dermatol.* 139:369–379. doi:10.1016/j.jid.2018.08.020.
- Moerke, N.J. 2009. Fluorescence Polarization (FP) Assays for Monitoring Peptide-Protein or Nucleic Acid-Protein Binding. *In* Current Protocols in Chemical Biology. John Wiley & Sons, Inc., Hoboken, NJ, USA. 1–15.
- Molony, L., D. Mccaslin, J. Abernethy, B. Paschal, and K. Burrige. 1987. THE JOURNAL OF BIOLOGICAL CHEMISTRY Properties of Talin from Chicken Gizzard Smooth Muscle &quot; 262. 7790–7795 pp.
- Monkley, S.J., C.A. Pritchard, and D.R. Critchley. 2001. Analysis of the mammalian talin2 gene

- TLN2. *Biochem. Biophys. Res. Commun.* 286:880–885. doi:10.1006/bbrc.2001.5497.
- Montanez, E., S. Ussar, M. Schifferer, M. Bösl, R. Zent, M. Moser, and R. Fässler. 2008. Kindlin-2 controls bidirectional signaling of integrins. *Genes Dev.* 22:1325–30. doi:10.1101/gad.469408.
- Moore, D.T., P. Nygren, H. Jo, K. Boesze-Battaglia, J.S. Bennett, and W.F. DeGrado. 2012. Affinity of talin-1 for the  $\beta$ 3-integrin cytosolic domain is modulated by its phospholipid bilayer environment. *Proc. Natl. Acad. Sci. U. S. A.* 109:793–798. doi:10.1073/pnas.1117220108.
- Mori, S., C. Abeygunawardana, M.O. Johnson, and P.C. van Zijl. 1995. Improved sensitivity of HSQC spectra of exchanging protons at short interscan delays using a new fast HSQC (FHSQC) detection scheme that avoids water saturation. *J. Magn. Reson. B.* 108:94–8. doi:10.1006/JMRB.1995.1109.
- Mory, A., S.W. Feigelson, N. Yarali, S.S. Kilic, G.I. Bayhan, R. Gershoni-Baruch, A. Etzioni, and R. Alon. 2008. Kindlin-3: A new gene involved in the pathogenesis of LAD-III. *Blood.* 112:2591. doi:10.1182/blood-2008-06-163162.
- Moser, M., B. Nieswandt, S. Ussar, M. Pozgajova, and R. Fässler. 2008. Kindlin-3 is essential for integrin activation and platelet aggregation. *Nat. Med.* 14:325–30. doi:10.1038/nm1722.
- Murshudov, G.N., P. Skubák, A.A. Lebedev, N.S. Pannu, R.A. Steiner, R.A. Nicholls, M.D. Winn, F. Long, and A.A. Vagin. 2011. REFMAC5 for the refinement of macromolecular crystal structures. *Acta Crystallogr. D. Biol. Crystallogr.* 67:355–67. doi:10.1107/S0907444911001314.
- Naik, U.P., P.M. Patel, and L. V Parise. 1997. Identification of a novel calcium-binding protein that interacts with the integrin  $\alpha$ IIb cytoplasmic domain. *J. Biol. Chem.* 272:4651–4. doi:10.1074/jbc.272.8.4651.
- Pankov, R., and K.M. Yamada. 2002. Fibronectin at a glance. *J. Cell Sci.* 115:3861–3863. doi:10.1242/jcs.00059.
- Di Paolo, G., L. Pellegrini, K. Letinic, G. Cestra, R. Zoncu, S. Voronov, S. Chang, J. Guo, M.R. Wenk, and P. De Camilli. 2002. Recruitment and regulation of phosphatidylinositol phosphate kinase type 1 $\gamma$  by the FERM domain of talin. *Nature.* 420:85–89. doi:10.1038/nature01147.
- Papagrigoriou, E., A.R. Gingras, I.L. Barsukov, N. Bate, I.J. Fillingham, B. Patel, R. Frank, W.H. Ziegler, G.C. Roberts, D.R. Critchley, and J. Emsley. 2004. Activation of a vinculin-binding site in the talin rod involves rearrangement of a five-helix bundle. *EMBO J.* 23:2942–2951. doi:10.1038/sj.emboj.7600285.
- Park, H., J.H. Lee, E. Gouin, P. Cossart, and T. Izard. 2011a. The rickettsia surface cell antigen 4 applies mimicry to bind to and activate vinculin. *J. Biol. Chem.* 286:35096–103. doi:10.1074/jbc.M111.263855.
- Park, H.J., J.H. Lee, E. Gouin, P. Cossart, and T. Izard. 2011b. The Rickettsia surface cell antigen 4 applies mimicry to bind to and activate vinculin. *J. Biol. Chem.* 286:35096–35103. doi:10.1074/jbc.M111.263855.
- Park, H.J., C. Valencia-Gallardo, A. Sharff, G.T. Van Nhieu, and T. Izard. 2011c. Novel vinculin binding site of the IpaA invasin of Shigella. *J. Biol. Chem.* 286:23214–23221. doi:10.1074/jbc.M110.184283.
- Parsons, J.T., A.R. Horwitz, and M.A. Schwartz. 2010. Cell adhesion: Integrating cytoskeletal dynamics and cellular tension. *Nat. Rev. Mol. Cell Biol.* doi:10.1038/nrm2957.



- Partridge, A.W., S. Liu, S. Kim, J.U. Bowie, and M.H. Ginsberg. 2005. Transmembrane domain helix packing stabilizes integrin  $\alpha$ IIb $\beta$ 3 in the low affinity state. *J. Biol. Chem.* 280:7294–300. doi:10.1074/jbc.M412701200.
- Pavalko, F.M., and C.A. Otey. 1994. Role of Adhesion Molecule Cytoplasmic Domains in Mediating Interactions with the Cytoskeleton. *Exp. Biol. Med.* 205:282–293. doi:10.3181/00379727-205-43709.
- Pereda, J.M. de, K.L. Wegener, E. Santelli, N. Bate, M.H. Ginsberg, D.R. Critchley, I.D. Campbell, and R.C. Liddington. 2005. Structural Basis for Phosphatidylinositol Phosphate Kinase Type I $\gamma$  Binding to Talin at Focal Adhesions. *J. Biol. Chem.* 280:8381–8386. doi:10.1074/JBC.M413180200.
- Plotnikov, S. V., A.M. Pasapera, B. Sabass, and C.M. Waterman. 2012. Force fluctuations within focal adhesions mediate ECM-rigidity sensing to guide directed cell migration. *Cell.* doi:10.1016/j.cell.2012.11.034.
- Qu, H., Y. Tu, X. Shi, H. Larjava, M.A. Saleem, S.J. Shattil, K. Fukuda, J. Qin, M. Kretzler, and C. Wu. 2011. Kindlin-2 regulates podocyte adhesion and fibronectin matrix deposition through interactions with phosphoinositides and integrins. *J. Cell Sci.* 124:879–891. doi:10.1242/jcs.076976.
- Rangarajan, E.S., and T. Izard. 2012. The Cytoskeletal Protein  $\alpha$ -Catenin Unfurls upon Binding to Vinculin. *J. Biol. Chem.* 287:18492–18499. doi:10.1074/jbc.M112.351023.
- Rantala, J.K., J. Pouwels, T. Pellinen, S. Veltel, P. Laasola, E. Mattila, C.S. Potter, T. Duffy, J.P. Sundberg, O. Kallioniemi, J.A. Askari, M.J. Humphries, M. Parsons, M. Salmi, and J. Ivaska. 2011. SHARPIN is an endogenous inhibitor of  $\beta$ 1-integrin activation. *Nat. Cell Biol.* 13:1315–24. doi:10.1038/ncb2340.
- Ratnikov, B., C. Ptak, J. Han, J. Shabanowitz, D.F. Hunt, and M.H. Ginsberg. 2005. Talin phosphorylation sites mapped by mass spectrometry. *J. Cell Sci.* 118:4921–3. doi:10.1242/jcs.02682.
- Raucher, D., T. Stauffer, W. Chen, K. Shen, S. Guo, J.D. York, M.P. Sheetz, and T. Meyer. 2000. Phosphatidylinositol 4,5-bisphosphate functions as a second messenger that regulates cytoskeleton-plasma membrane adhesion. *Cell.* 100:221–8. doi:10.1016/s0092-8674(00)81560-3.
- Reinhard, M., M. Halbrügge, U. Scheer, C. Wiegand, B.M. Jockusch, and U. Walter. 1992. The 46/50 kDa phosphoprotein VASP purified from human platelets is a novel protein associated with actin filaments and focal contacts. *EMBO J.* 11:2063–70.
- Reis, R.S. Dos, and F. Horn. 2010. Enteropathogenic Escherichia coli, Samonella, Shigella and Yersinia: cellular aspects of host-bacteria interactions in enteric diseases. *Gut Pathog.* 2:8. doi:10.1186/1757-4749-2-8.
- del Rio, A., R. Perez-Jimenez, R. Liu, P. Roca-Cusachs, J.M. Fernandez, and M.P. Sheetz. 2009. Stretching Single Talin Rod Molecules Activates Vinculin Binding. *Science (80- ).* 323:638–641. doi:10.1126/science.1162912.
- Rodius, S., O. Chaloin, M. Moes, E. Schaffner-Reckinger, I. Landrieu, G. Lippens, M. Lin, J. Zhang, and N. Kieffer. 2008. The talin rod IBS2  $\alpha$ -helix interacts with the  $\beta$ 3 integrin cytoplasmic tail membrane-proximal helix by establishing charge complementary salt bridges. *J. Biol. Chem.* 283:24212–23. doi:10.1074/jbc.M709704200.
- Rognoni, E., R. Ruppert, R. Fässler, and R. Fä. 2016. The kindlin family: functions, signaling

- properties and implications for human disease. *J. Cell Sci.* doi:10.1242/jcs.161190.
- Rosano, G.L., and E.A. Ceccarelli. 2014. Recombinant protein expression in *Escherichia coli*: Advances and challenges. *Front. Microbiol.* doi:10.3389/fmicb.2014.00172.
- Rowley, J., S. Vander Hoorn, E. Korenromp, N. Low, M. Unemo, L.J. Abu-Raddad, R.M. Chico, A. Smolak, L. Newman, S. Gottlieb, S. Thwin, N. Broutet, and M.M. Taylor. 2016. World Health Organization Global Health Sector Strategy on STIs.
- Ruppert, R., M. Moser, M. Sperandio, E. Rognoni, M. Orban, W.-H. Liu, A.S. Schulz, R.A.J. Oostendorp, S. Massberg, and R. Fässler. 2015. Kindlin-3-mediated integrin adhesion is dispensable for quiescent but essential for activated hematopoietic stem cells. *J. Exp. Med.* 212:1415–1432. doi:10.1084/jem.20150269.
- Saltel, F., E. Mortier, V.P. Hytönen, M.C. Jacquier, P. Zimmermann, V. Vogel, W. Liu, and B. Wehrle-Haller. 2009. New PI(4,5)P<sub>2</sub>- and membrane proximal integrin-binding motifs in the talin head control  $\beta$ 3-integrin clustering. *J. Cell Biol.* doi:10.1083/jcb.200908134.
- Schaefer, L., and R.M. Schaefer. 2010. Proteoglycans: From structural compounds to signaling molecules. *Cell Tissue Res.* 339:237–246. doi:10.1007/s00441-009-0821-y.
- Schaller, M.D. 2001. Paxillin: a focal adhesion-associated adaptor protein. *Oncogene.* 20:6459–6472. doi:10.1038/sj.onc.1204786.
- Schaller, M.D. 2010. Cellular functions of FAK kinases: insight into molecular mechanisms and novel functions. *J. Cell Sci.* 123:1007–13. doi:10.1242/jcs.045112.
- Schiemer, J., A. Bohm, L. Lin, G. Merrill-Skoloff, R. Flaumenhaft, J.S. Huang, G.C. Le Breton, and A.H. Chishti. 2016.  $\alpha$ 13 switch region 2 relieves talin autoinhibition to activate  $\alpha$ IIb $\beta$ 3 integrin. *J. Biol. Chem.* 291:26598–26612. doi:10.1074/jbc.M116.747279.
- Siegel, D.H., G.H.S. Ashton, H.G. Penagos, J. V Lee, H.S. Feiler, K.C. Wilhelmsen, A.P. South, F.J.D. Smith, A.R. Prescott, V. Wessagowit, N. Oyama, M. Akiyama, D. Al Aboud, K. Al Aboud, A. Al Githami, K. Al Hawsawi, A. Al Ismaily, R. Al-Suwaid, D.J. Atherton, R. Caputo, J.-D. Fine, I.J. Frieden, E. Fuchs, R.M. Haber, T. Harada, Y. Kitajima, S.B. Mallory, H. Ogawa, S. Sahin, H. Shimizu, Y. Suga, G. Tadini, K. Tsuchiya, C.B. Wiebe, F. Wojnarowska, A.B. Zaghloul, T. Hamada, R. Mallipeddi, R.A.J. Eady, W.H.I. McLean, J.A. McGrath, and E.H. Epstein. 2003. Loss of kindlin-1, a human homolog of the *Caenorhabditis elegans* actin-extracellular-matrix linker protein UNC-112, causes Kindler syndrome. *Am. J. Hum. Genet.* 73:174–87. doi:10.1086/376609.
- Sievers, F., and D.G. Higgins. 2014. Clustal Omega, Accurate Alignment of Very Large Numbers of Sequences. 105–116.
- Sin, S., F. Bonin, V. Petit, D. Meseure, F. Lallemand, I. Biche, A. Bellahcne, V. Castronovo, O. De Wever, C. Gespach, R. Lidereau, and K. Driouch. 2011. Role of the focal adhesion protein kindlin-1 in breast cancer growth and lung metastasis. *J. Natl. Cancer Inst.* 103:1323–1337. doi:10.1093/jnci/djr290.
- Skinner, S.P., B.T. Goult, R.H. Fogh, W. Boucher, T.J. Stevens, E.D. Laue, G.W. Vuister, and IUCr. 2015. Structure calculation, refinement and validation using *CcpNmr Analysis*. *Acta Crystallogr. Sect. D Biol. Crystallogr.* 71:154–161. doi:10.1107/S1399004714026662.
- Son, S., G.J. Moroney, and P.J. Butler. 2017.  $\beta$ 1-Integrin-Mediated Adhesion Is Lipid-Bilayer Dependent. *Biophys. J.* 113:1080–1092. doi:10.1016/j.bpj.2017.07.010.
- Srivastava, J., G. Barreiro, S. Groscurth, A.R. Gingras, B.T. Goult, D.R. Critchley, M.J.S. Kelly, M.P.

- Jacobson, and D.L. Barber. 2008. Structural model and functional significance of pH-dependent talin-actin binding for focal adhesion remodeling. *Proc. Natl. Acad. Sci. U. S. A.* 105:14436–41. doi:10.1073/pnas.0805163105.
- Stefanini, L., R.H. Lee, D.S. Paul, E.C. O’Shaughnessy, D. Ghalloussi, C.I. Jones, Y. Boulaftali, K.O. Poe, R. Piatt, D.O. Kechele, K.M. Caron, K.M. Hahn, J.M. Gibbins, and W. Bergmeier. 2018. Functional redundancy between RAP1 isoforms in murine platelet production and function. *Blood.* 132:1951–1962. doi:10.1182/blood-2018-03-838714.
- Subauste, M.C., O. Pertz, E.D. Adamson, C.E. Turner, S. Junger, and K.M. Hahn. 2004. Vinculin modulation of paxillin-FAK interactions regulates ERK to control survival and motility. *J. Cell Biol.* 165:371–81. doi:10.1083/jcb.200308011.
- Sun, N., D.R. Critchley, D. Paulin, Z. Li, and R.M. Robson. 2008. Identification of a repeated domain within mammalian  $\alpha$ -synemin that interacts directly with talin. *Exp. Cell Res.* 314:1839–1849. doi:10.1016/j.yexcr.2008.01.034.
- Sun, Z., M. Costell, and R. Fässler. 2019. Integrin activation by talin, kindlin and mechanical forces. *Nat. Cell Biol.* 21:25–31. doi:10.1038/s41556-018-0234-9.
- Sun, Z., H.-Y. Tseng, S. Tan, F. Senger, L. Kurzawa, D. Dedden, N. Mizuno, A.A. Wasik, M. They, A.R. Dunn, and R. Fässler. 2016. Kank2 activates talin, reduces force transduction across integrins and induces central adhesion formation. *Nat. Cell Biol.* 18:941–53. doi:10.1038/ncb3402.
- Svensson, L., K. Howarth, A. McDowall, I. Patzak, R. Evans, S. Ussar, M. Moser, A. Metin, M. Fried, I. Tomlinson, and N. Hogg. 2009. Leukocyte adhesion deficiency-III is caused by mutations in KINDLIN3 affecting integrin activation. *Nat. Med.* 15:306–312. doi:10.1038/nm.1931.
- Tadokoro, S., S.J. Shattil, K. Eto, V. Tai, R.C. Liddington, J.M. de Pereda, M.H. Ginsberg, and D.A. Calderwood. 2003. Talin binding to integrin beta tails: a final common step in integrin activation 10.1126/science.1086652 302/5642/103 [pii]. *Science (80- )*.
- Talaat, S., S. Somji, C. Toni, S.H. Garrett, X.D. Zhou, M.A. Sens, and D.A. Sens. 2011. Kindlin-2 expression in arsenite- and cadmium-transformed bladder cancer cell lines and in archival specimens of human bladder cancer. *Urology.* 77:1507.e1-1507.e7. doi:10.1016/j.urology.2011.02.040.
- Tamkun, J.W., D.W. DeSimone, D. Fonda, R.S. Patel, C. Buck, A.F. Horwitz, and R.O. Hynes. 1986. Structure of integrin, a glycoprotein involved in the transmembrane linkage between fibronectin and actin. *Cell.* 46:271–82. doi:10.1016/0092-8674(86)90744-0.
- Thapa, N., and R.A. Anderson. 2012. PIP2 signaling, an integrator of cell polarity and vesicle trafficking in directionally migrating cells. *Cell Adhes. Migr.* 6:409–412. doi:10.4161/cam.21192.
- Thapa, N., Y. Sun, M. Schramp, S. Choi, K. Ling, and R.A. Anderson. 2012. Phosphoinositide Signaling Regulates the Exocyst Complex and Polarized Integrin Trafficking in Directionally Migrating Cells. *Dev. Cell.* 22:116–130. doi:10.1016/j.devcel.2011.10.030.
- Theodosiou, M., M. Widmaier, R.T. Böttcher, E. Rognoni, M. Veelders, M. Bharadwaj, A. Lambacher, K. Austen, D.J. Müller, R. Zent, and R. Fässler. 2016. Kindlin-2 cooperates with talin to activate integrins and induces cell spreading by directly binding paxillin. *Elife.* 5. doi:10.7554/eLife.10130.
- Theriot, J.A., and T.J. Mitchison. 1991. Actin microfilament dynamics in locomoting cells. *Nature.* 352:126–31. doi:10.1038/352126a0.

- Thievesten, I., P.M. Thompson, S. Berlemont, K.M. Plevock, S. V. Plotnikov, A. Zemljic-Harpe, R.S. Ross, M.W. Davidson, G. Danuser, S.L. Campbell, and C.M. Waterman. 2013. Vinculin-actin interaction couples actin retrograde flow to focal adhesions, but is dispensable for focal adhesion growth. *J. Cell Biol.* doi:10.1083/jcb.201303129.
- Thomas, J.W., M.A. Cooley, J.M. Broome, R. Salgia, J.D. Griffin, C.R. Lombardo, and M.D. Schaller. 1999. The role of focal adhesion kinase binding in the regulation of tyrosine phosphorylation of paxillin. *J. Biol. Chem.* 274:36684–92. doi:10.1074/JBC.274.51.36684.
- Thwaites, T.R., A.T. Pedrosa, T.P. Peacock, and R.A. Carabeo. 2015. Vinculin Interacts with the Chlamydia Effector TarP Via a Tripartite Vinculin Binding Domain to Mediate Actin Recruitment and Assembly at the Plasma Membrane. *Front. Cell. Infect. Microbiol.* 5:88. doi:10.3389/fcimb.2015.00088.
- Tolchard, J., S.J. Walpole, A.J. Miles, R. Maytum, L.A. Eaglen, T. Hackstadt, B.A. Wallace, and T.M.A.A. Blumenschein. 2018. The intrinsically disordered Tarp protein from chlamydia binds actin with a partially preformed helix. *Sci. Rep.* 8:1960. doi:10.1038/s41598-018-20290-8.
- Unger, T., and Y. Peleg. 2012. Recombinant Protein Expression in the Baculovirus-Infected Insect Cell System. *In Methods in molecular biology* (Clifton, N.J.). 187–199.
- Ussar, S., H.V. Wang, S. Linder, R. Fässler, and M. Moser. 2006. The Kindlins: Subcellular localization and expression during murine development. *Exp. Cell Res.* 312:3142–3151. doi:10.1016/j.yexcr.2006.06.030.
- Vanarotti, M.S., D.B. Finkelstein, C.D. Guibao, A. Nourse, D.J. Miller, and J.J. Zheng. 2016. Structural Basis for the Interaction between Pyk2-FAT Domain and Leupaxin LD Repeats. *Biochemistry.* 55:1332–45. doi:10.1021/acs.biochem.5b01274.
- Vinogradova, O., A. Velyvis, A. Velyviene, B. Hu, T.A. Haas, E.F. Plow, and J. Qin. 2002. A Structural Mechanism of Integrin  $\alpha$ IIb $\beta$ 3 “Inside-Out” Activation as Regulated by Its Cytoplasmic Face. *Cell.* 110:587–597. doi:10.1016/S0092-8674(02)00906-6.
- Vogel, V., and M. Sheetz. 2006. Local force and geometry sensing regulate cell functions. *Nat. Rev. Mol. Cell Biol.* 7:265–75. doi:10.1038/nrm1890.
- Vonrhein, C., C. Flensburg, P. Keller, A. Sharff, O. Smart, W. Paciorek, T. Womack, and G. Bricogne. 2011. Data processing and analysis with the *autoPROC* toolbox. *Acta Crystallogr. Sect. D Biol. Crystallogr.* 67:293–302. doi:10.1107/S0907444911007773.
- Vranken, W.F., W. Boucher, T.J. Stevens, R.H. Fogh, A. Pajon, M. Llinas, E.L. Ulrich, J.L. Markley, J. Ionides, and E.D. Laue. 2005. The CCPN data model for NMR spectroscopy: Development of a software pipeline. *Proteins Struct. Funct. Bioinforma.* 59:687–696. doi:10.1002/prot.20449.
- Wang, Y., J. Yan, and B.T. Goult. 2019. Force-dependent binding constants. *Biochemistry.* doi:10.1021/acs.biochem.9b00453.
- Weaver, A.M. 2006. Invadopodia: Specialized cell structures for cancer invasion. *Clin. Exp. Metastasis.* 23:97–105. doi:10.1007/s10585-006-9014-1.
- Webb, D.J., M.J. Schroeder, C.J. Brame, L. Whitmore, J. Shabanowitz, D.F. Hunt, and A.R. Horwitz. 2005. Paxillin phosphorylation sites mapped by mass spectrometry. *J. Cell Sci.* 118:4925–4929. doi:10.1242/jcs.02563.
- Wee, P., and Z. Wang. 2017. Epidermal Growth Factor Receptor Cell Proliferation Signaling Pathways. *Cancers (Basel).* 9. doi:10.3390/cancers9050052.
- Wegener, K.L., J. Basran, C.R. Bagshaw, I.D. Campbell, G.C.K. Roberts, D.R. Critchley, and I.L.

- Barsukov. 2008. Structural Basis for the Interaction between the Cytoplasmic Domain of the Hyaluronate Receptor Layilin and the Talin F3 Subdomain. *J. Mol. Biol.* 382:112–126. doi:10.1016/J.JMB.2008.06.087.
- Wegener, K.L., and I.D. Campbell. 2008. Transmembrane and cytoplasmic domains in integrin activation and protein-protein interactions (review). *Mol. Membr. Biol.* 25:376–87. doi:10.1080/09687680802269886.
- Wegener, K.L., A.W. Partridge, J. Han, A.R. Pickford, R.C. Liddington, M.H. Ginsberg, and I.D. Campbell. 2007. Structural Basis of Integrin Activation by Talin. *Cell.* 128:171–182. doi:10.1016/j.cell.2006.10.048.
- Weljie, A.M., P.M. Hwang, and H.J. Vogel. 2002. Solution structures of the cytoplasmic tail complex from platelet integrin  $\alpha$ IIb- and  $\beta$ 3-subunits. *Proc. Natl. Acad. Sci.* 99:5878–5883. doi:10.1073/PNAS.092515799.
- Wen, J., T. Arakawa, and J.S. Philo. 1996. Size-Exclusion Chromatography with On-Line Light-Scattering, Absorbance, and Refractive Index Detectors for Studying Proteins and Their Interactions. *Anal. Biochem.* 240:155–166. doi:10.1006/abio.1996.0345.
- Whitewood, A.J., A.K. Singh, D.G. Brown, and B.T. Goult. 2018. Chlamydial virulence factor TarP mimics talin to disrupt the talin-vinculin complex. *FEBS Lett.* 592:1751–1760. doi:10.1002/1873-3468.13074.
- Wienken, C.J., P. Baaske, U. Rothbauer, D. Braun, and S. Duhr. 2010. Protein-binding assays in biological liquids using microscale thermophoresis. *Nat. Commun.* doi:10.1038/ncomms1093.
- Winograd-Katz, S.E., R. Fässler, B. Geiger, and K.R. Legate. 2014. The integrin adhesome: from genes and proteins to human disease. *Nat. Rev. Mol. Cell Biol.* 15:273–288. doi:10.1038/nrm3769.
- Wood, C.K., C.E. Turner, P. Jackson, and D.R. Critchley. 1994. Characterisation of the paxillin-binding site and the C-terminal focal adhesion targeting sequence in vinculin. *J. Cell Sci.* 107 (Pt 2):709–17.
- Xia, T., J. Takagi, B.S. Collier, J.H. Wang, and T.A. Springer. 2004. Structural basis for allostery in integrins and binding to fibrinogen-mimetic therapeutics. *Nature.* 432:59–67. doi:10.1038/nature02976.
- Yan, J., M. Yao, B.T. Goult, and M.P. Sheetz. 2015. Talin Dependent Mechanosensitivity of Cell Focal Adhesions. *Cell. Mol. Bioeng.* 8:151–159. doi:10.1007/s12195-014-0364-5.
- Yang, J., L. Zhu, H. Zhang, J. Hirbawi, K. Fukuda, P. Dwivedi, J. Liu, T. Byzova, E.F. Plow, J. Wu, and J. Qin. 2014. Conformational activation of talin by RIAM triggers integrin-mediated cell adhesion. *Nat. Commun.* 5:5880. doi:10.1038/ncomms6880.
- Yao, M., B.T. Goult, H. Chen, P. Cong, M.P. Sheetz, and J. Yan. 2014a. Mechanical activation of vinculin binding to talin locks talin in an unfolded conformation. *Sci. Rep.* 4:4610. doi:10.1038/srep04610.
- Yao, M., B.T. Goult, B. Klapholz, X. Hu, C.P. Toseland, Y. Guo, P. Cong, M.P. Sheetz, and J. Yan. 2016. The mechanical response of talin. *Nat. Commun.* 7:11966. doi:10.1038/ncomms11966.
- Yao, M., W. Qiu, R. Liu, A.K. Efremov, P. Cong, R. Seddiki, M. Payre, C.T. Lim, B. Ladoux, R.-M. Mège, and J. Yan. 2014b. Force-dependent conformational switch of  $\alpha$ -catenin controls vinculin binding. *Nat. Commun.* 5:4525. doi:10.1038/ncomms5525.

- Ye, F., G. Hu, D. Taylor, B. Ratnikov, A.A. Bobkov, M.A. McLean, S.G. Sligar, K.A. Taylor, and M.H. Ginsberg. 2010. Recreation of the terminal events in physiological integrin activation. *J. Cell Biol.* 188:157–173. doi:10.1083/jcb.200908045.
- Ye, F., C. Kim, and M.H. Ginsberg. 2011. Molecular mechanism of inside-out integrin regulation. *J. Thromb. Haemost.* 9:20–25. doi:10.1111/j.1538-7836.2011.04355.x.
- Ye, F., B.G. Petrich, P. Anekal, C.T. Lefort, A. Kasirer-Friede, S.J. Shattil, R. Ruppert, M. Moser, R. Fässler, and M.H. Ginsberg. 2013. The mechanism of kindlin-mediated activation of integrin  $\alpha$ IIb $\beta$ 3. *Curr. Biol.* 23:2288–2295. doi:10.1016/j.cub.2013.09.050.
- Yuan, W., T.M. Leisner, A.W. McFadden, Z. Wang, M.K. Larson, S. Clark, C. Boudignon-Proudhon, S.C.-T. Lam, and L. V. Parise. 2006. CIB1 is an endogenous inhibitor of agonist-induced integrin  $\alpha$ IIb $\beta$ 3 activation. *J. Cell Biol.* 172:169–175. doi:10.1083/jcb.200505131.
- Zacharchenko, T., X. Qian, B.T. Goult, D.R. Critchley, D.R. Lowy, I.L. Barsukov Correspondence, D. Jethwa, T.B. Almeida, C. Ballestrem, and I.L. Barsukov. 2016a. LD Motif Recognition by Talin: Structure of the Talin- DLC1 Complex LD Motif Recognition by Talin: Structure of the Talin-DLC1 Complex. *Struct. Des.* 24:1130–1141. doi:10.1016/j.str.2016.04.016.
- Zacharchenko, T., X. Qian, B.T. Goult, D. Jethwa, T.B. Almeida, C. Ballestrem, D.R. Critchley, D.R. Lowy, and I.L. Barsukov. 2016b. LD Motif Recognition by Talin: Structure of the Talin-DLC1 Complex. *Structure.* 24:1130–41. doi:10.1016/j.str.2016.04.016.
- Zaidel-Bar, R., M. Cohen, L. Addadi, and B. Geiger. 2004. Hierarchical assembly of cell–matrix adhesion complexes. *Biochem. Soc. Trans.* 32:416–420. doi:10.1042/BST0320416.
- Zhang, F., S. Saha, and A. Kashina. 2012. Arginylation-dependent regulation of a proteolytic product of talin is essential for cell-cell adhesion. *J. Cell Biol.* 197:819–36. doi:10.1083/jcb.201112129.
- Zhao, H., and P. Lappalainen. 2012. A simple guide to biochemical approaches for analyzing protein-lipid interactions. *Mol. Biol. Cell.* doi:10.1091/mbc.e11-07-0645.
- Zhu, L., J. Yang, T. Bromberger, A. Holly, F. Lu, H. Liu, K. Sun, S. Klapproth, J. Hirbawi, T. V. Byzova, E.F. Plow, M. Moser, and J. Qin. 2017. Structure of Rap1b bound to talin reveals a pathway for triggering integrin activation. *Nat. Commun.* 8:1744. doi:10.1038/s41467-017-01822-8.
- Ziegler, W.H., R.C. Liddington, and D.R. Critchley. 2006. The structure and regulation of vinculin. *Trends Cell Biol.* 16:453–460. doi:10.1016/J.TCB.2006.07.004.
- Zillner, K., M. Jerabek-Willemsen, S. Duhr, D. Braun, G. Längst, and P. Baaske. 2012. Microscale Thermophoresis as a Sensitive Method to Quantify Protein: Nucleic Acid Interactions in Solution. *Methods Mol. Biol.* doi:10.1007/978-1-61779-424-7\_18.
- Zimmerman, B., T. Volberg, and B. Geiger. 2004. Early molecular events in the assembly of the focal adhesion-stress fiber complex during fibroblast spreading. *Cell Motil. Cytoskeleton.* 58:143–59. doi:10.1002/cm.20005.

## Chapter 10: Appendix

bioRxiv preprint first posted online Aug. 14, 2019; doi: <http://dx.doi.org/10.1101/735183>. The copyright holder for this preprint (which was not peer-reviewed) is the author/funder, who has granted bioRxiv a license to display the preprint in perpetuity. It is made available under a [CC-BY-ND 4.0 International license](#).

### **Formation of talin-vinculin pre-complexes dictates maturation of nascent adhesions by accelerated force transmission and vinculin recruitment**

**Sangyoon J. Han<sup>1,2\*</sup>, Kevin M. Dean<sup>3</sup>, Austin J. Whitewood<sup>4</sup>, Alexia Bachir<sup>5</sup>, Edgar Gutierrez<sup>6</sup>, Alex Groisman<sup>6</sup>, Alan R. Horwitz<sup>5,7</sup>, Benjamin T. Goult<sup>4</sup> and Gaudenz Danuser<sup>1\*</sup>**

<sup>1</sup>Lyda Hill Department of Bioinformatics, University of Texas Southwestern Medical Center. Dallas, TX 75390. USA.

<sup>2</sup>Department of Biomedical Engineering, Michigan Technological University. Houghton, MI. 49931. USA.

<sup>3</sup>Department of Cell Biology, University of Texas Southwestern Medical Center. Dallas, TX. 75390. USA.

<sup>4</sup>School of Biosciences, University of Kent, Canterbury, Kent, CT2 7NJ, UK.

<sup>5</sup>Department of Cell Biology, University of Virginia. Charlottesville, VA. 22904. USA.

<sup>6</sup>Department of Physics, University of California San Diego. San Diego, CA. 92093. USA.

<sup>7</sup>current address: Allen Institute for Cell Science. Seattle, WA. 98109. USA.

\*Corresponding Author: [sjhan@mtu.edu](mailto:sjhan@mtu.edu), [gaudenz.danuser@utsouthwestern.edu](mailto:gaudenz.danuser@utsouthwestern.edu) (Lead Contact)

#### **Abstract**

Talin, vinculin, and paxillin are mechanosensitive proteins that are recruited early to nascent integrin-based adhesions (NAs). Using machine learning, high-resolution traction force microscopy, single-particle-tracking and fluorescence fluctuation time-series analysis, we find that, only in the NAs that eventually mature to focal adhesions, all three molecules are recruited concurrently and in synchrony with force onset. Thereafter, vinculin assembles at ~5 fold higher rates than in non-maturing NAs. We identify a domain in talin, R8, which exposes a vinculin-binding-site (VBS) without requiring tension. Stabilizing this domain via mutation lowers tension-free vinculin binding in conjunction with talin, impairs maturation of NAs, and reduces the rate of additional vinculin recruitment after force onset. Taken together, our data show that talin forms a complex with vinculin, before association with integrins, which is essential for NA maturation by talin's effective unfolding and exposure of additional VBSs that induce fast force growth and further vinculin binding.

## Introduction

Cell-matrix adhesions are multi-molecular complexes that link the extracellular matrix (ECM), typically via integrin transmembrane receptors, to the actin cytoskeleton. Being both a force-transmitter and a force-sensor, cell-matrix adhesions are critical to cell morphogenesis and mechanosensation (Discher et al., 2005; Parsons et al., 2010). Indeed, in response to ECM changes, adhesions undergo constant changes in morphology and motion that involve recruitment and recycling of a large number of adhesion molecules. For example, nascent adhesions (NAs) emerge within the actin-dense cell lamellipodia and then slide in the direction opposite to the protrusion as a result of polymerization-driven flow of the actin network (Parsons et al., 2010). Many of these NAs, which are less than 0.5  $\mu\text{m}$  long, and thus in a light microscope only resolved as diffraction-limited spots, turn over early; but some of them mature into longer focal complexes (FCs, >0.5  $\mu\text{m}$  in length) and focal adhesions (FAs, >2  $\mu\text{m}$  in length) at the lamellipodia-lamella interface (Gardel et al., 2010; Parsons et al., 2010). During this progression, NAs go through multiple decision processes regarding fate and morphology. Compared to the well-studied FAs, for which the interconnection between structure, signaling, and force transmission is largely understood (Balaban et al., 2001; Chrzanowska-Wodnicka and Burridge, 1996; Geiger et al., 2009; Han et al., 2012; Kanchanawong et al., 2010; Plotnikov et al., 2012; Riveline et al., 2001; Stricker et al., 2011; Thievessen et al., 2013), much less is known about the molecular and mechanical factors that determine NA assembly, turnover, and maturation. Until recently, it has also not been technically feasible to measure whether individual NAs bear traction forces. By applying high refractive-index soft substrates that are compatible with total internal reflection microscopy (Gutierrez et al., 2011) and numerical methods for the computational reconstruction of cell-substrate traction at the single micron length-scale, we recently postulated that, like FAs, force transmission is essential for the stabilization and maturation of NAs (Han et al., 2015). However, it remains unknown which factors determine whether a NA begins to bear forces and thus continues to assemble.

One possible factor is the stoichiometry among the earliest molecular components recruited to a NA (Digman et al., 2009; Zaidel-Bar et al., 2004). In particular, the recruitment of talin, vinculin, and paxillin could play a critical role as they all are known to be mechanosensitive (Austen et al., 2015; Carisey et al., 2013; del Rio et al., 2009; Humphrey et al., 2014; Humphries et al., 2007; Kumar et al., 2016; Pasapera et al., 2010; Schiller et al., 2011). Talin is an integrin activator (Moser et al., 2009; Tadokoro et al., 2003) that directly links integrins to the actin cytoskeleton (Calderwood et al., 2013). Under force, the helix bundle domains in talin's rod-like region unfold (del Rio et al., 2009), which both disrupts ligand binding and exposes cryptic binding sites for vinculin and other proteins (del Rio et al., 2009; Goult et al., 2018; Goult et al., 2013; Yan et al., 2015; Yao et al., 2016). Vinculin, when bound to talin's exposed binding sites, can indirectly strengthen the connection between actin and integrins by 1) forming a catch bond with F-actin (Case et al., 2015; Huang et al., 2017), 2) forming multiple linkages from a single talin to multiple F-actin filaments (Atherton et al., 2015; Yan et al., 2015; Yao et al., 2016), and 3) stabilizing talin's unfolded state (Yao et al., 2014). In this scenario, talin must bind to integrins and F-actin first, followed by unfolding and vinculin recruitment under initial tension. Indeed, at the level of FAs, direct evidence for catch-bonds (Bell, 1978; Thomas, 2008; Thomas et al., 2008), and the exposure of hidden binding sites under load (Vogel and Sheetz, 2006; Zhu et al., 2008), have established the idea of force-assisted adhesion growth. Further evidence for this model



indicates that downregulation of actomyosin contractility reduces the recruitment of vinculin (Pasapera et al., 2010) and other adhesion proteins (Kuo et al., 2011), as well as the association between talin and integrins (Bachir et al., 2014).

In contrast to the notion of FA growth and stabilization in a hierarchy talin-first-then-vinculin, fluorescence fluctuation analyses (Bachir et al., 2014) and co-immunoprecipitation experiments (Pasapera et al., 2010) suggest that in NAs talin and vinculin might form a complex before talin associates with integrin. While talin-vinculin pre-association implies vinculin's force-independent binding to talin, it is not clear whether this pre-association is required for NA assembly, and if so, whether the pre-association affects the decision processes for NA maturation. Moreover, paxillin, a scaffolding protein that works in close relationship with focal adhesion kinase (FAK) (Mitra and Schlaepfer, 2006; Parsons, 2003; Pasapera et al., 2010; Schlaepfer and Mitra, 2004), is thought to be recruited and stabilized by force at an early phase of NA assembly (Choi et al., 2008; Deakin and Turner, 2008; Plotnikov et al., 2012; Schiller et al., 2011); the relationship to vinculin recruitment remains to be established (Laukaitis et al., 2001; Webb et al., 2004; Wiseman et al., 2004).

Here, we investigate the role of molecular recruitment and mechanical forces in determining the fate of NAs. We combined high-resolution traction force microscopy for measuring the force levels in every NA with those of the sensitive and particle tracking of the recruitment of fluorescently labeled molecules to NAs to acquire time courses of force transmission and molecular composition at individual adhesions. A comprehensive inventory of these traces revealed broad heterogeneity in NA behaviors. We applied machine learning approaches to divide NAs into subgroups with distinct characteristics, determining that five subgroups are necessary to account for the different kinematic, kinetic and mechanical properties of NAs. Focusing on the NA subgroup maturing into stable FAs, we found that the formation of a talin-vinculin pre-complex was mediated by talin's R8 domain. These pre-complexes enforce the link between talin and actin, likely to allow the unfolding of talin and exposure of additional vinculin binding sites, which ultimately supports the transition of spontaneous molecular assemblies of in nascent adhesions into stable macromolecular focal adhesions.

## Results

### *Nine adhesion classes can be distinguished based on different kinetic, kinematic and mechanical behaviors*

To investigate time courses of traction and adhesion protein recruitment, we performed two-channel time-lapse, total internal reflection fluorescence (TIRF) imaging of Chinese Hamster Ovary epithelial cells (ChoK1, Fig 1a-f). For each experiment, images of beads, with the reference bead image of undeformed gel configuration, were processed for traction reconstruction using high-resolution TFM software, as described before (Han et al., 2015). As expected for a contractile cell, all traction vectors pointed from the cell periphery to the center, regardless of which adhesion protein was co-imaged (Fig 1a-c). Fluorescently tagged adhesion proteins (Fig 1d-f) were detected and tracked, and their intensity time courses extracted from the trajectories (Fig. 1g). Accounting for the heterogeneity of adhesions, we collected 22 features from each trajectory (Fig. 1h, Table S1). Based on these features, we classified the adhesion trajectories into nine groups (see Table S2 for a summary of each group). To this end, we implemented a supervised machine learning pipeline, where a human operator labeled, with the support of a dedicated graphical user

interface, ~120 adhesion tracks (at least 10 tracks per group) out of ~10,000 tracks per movie. These data were then used to train a support vector machine (SVM) classifier (validation accuracy: 70 – 80 %, Fig. S1a). All features were inspected for redundancy and similarity (Fig. S1b-c), and each group was distinct in terms of its Euclidian distance to the closest group in the feature space (Fig. S1d). SVM-based classification of all trajectories that were excluded from the training data assigned each adhesion to one of nine different classes, G1, G2, ..., G9 (Fig. 1i). Five of the nine classes (G1-G5) identified NAs, three (G6-G8) identified FAs, and one group (G9) contained insignificant, noise-like trajectories (Movie S1). The five NA classes significantly differed in terms of features such as “edge protrusion speed” (Fig. 1j), “adhesion movement speed” (Fig. 1k), “average fluorescence intensity” (Fig. 1l), and “lifetime” (Fig. 1m). For example, NAs classified into G3 form at the tip of the protruding edge and move forward with the protrusion. Of all NA classes, their fluorescence amplitude is lowest (Fig 1j-m). NAs classified into G2 form at the protruding edge but slide rearward relative to the substrate and mature to form larger FCs or FAs. They have the highest intensity and longest lifetime (Fig 1m-n). NAs classified into G1 also form at the protruding edge, but they stay relatively stationary (Fig. 1k) with a weak fluorescence intensity and a short lifetime (Fig. 1m-n).

Next, we tested the hypothesis that these spatially and kinetically distinguished groups generate distinct traction. Indeed, we found that the subgroup of maturing NAs, G2, shows highest traction magnitude shortly after initial assembly. This is consistent with previous findings about tension-mediated maturation of FAs (Choi et al., 2008; Schiller et al., 2011; Schiller et al., 2013). Interestingly, NAs in G3 exhibited an insignificant amount of traction without ever significantly increasing (Fig. S2), suggesting this population consists of assemblies of adhesion proteins that do not engage with the substrate. NAs in G1 had higher traction than those in G3, implicating that short-living, non-maturing NAs can transmit significant amount of traction, consistent with our previous finding (Han et al., 2015). These trends in traction as well as trends in feature variables after classification were consistent regardless of which adhesion protein was used for tracking (talín, vinculin or paxillin; Fig. S3). Altogether, these results confirm the reliability of the classifier and suggest that kinetically unique NAs also show mechanical differences.

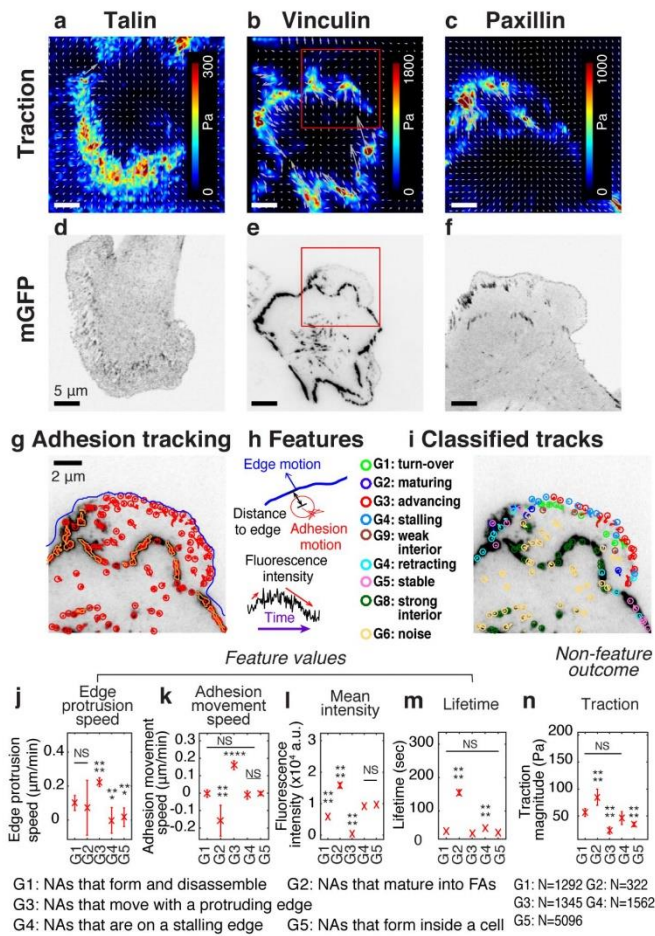


**Figure 1** Experimental/computational framework to analyze heterogeneous adhesion dynamics in ChoK1 cells. (a – c) high-resolution traction maps co-imaged with mGFP-tagged adhesion protein, talin (d), vinculin (e), and paxillin (f). 5 kPa silicone gel coated with high density beads was used as a TFM substrate. (g) Trajectories of individual nascent and focal adhesions overlaid on a region of interest cropped from (e). Tracking is based on all detected point sources, (red circles). Big segmented focal contacts/adhesions (orange, closed freeform overlays) were used as additional information for feature selection. (h) Some of the key features used for supervised classification, tabulated in Table 1. (i) Classification of adhesion trajectories into nine different groups, overlaid on the adhesion image. Five different NA groups, three FA groups and one noise group were distinguished using the error-correcting output codes classifier, multiclass model for support vector machines (L. Allwein et al., 2001). (j-m) Comparison of feature values among the five NA groups, G1, G2, G3, G4 and G5: edge protrusion speed (j), adhesion movement speed, positive when sliding toward protruding edge (k), mean intensity (l), and lifetime (m), extracted from six vinculin-tagged cells. All features show a significant shift in value for at least one subgroup. (n) Average traction magnitude, read from traction map, at individual NA trajectories per each group. The number of samples per each group is shown in the lower right corner of the figure.

*Talin, vinculin and paxillin are recruited sequentially in non-maturing NAs, but concurrently in maturing NAs with traction development*

To evaluate the relationship between molecular recruitment and traction force in NAs, we performed high-resolution traction force microscopy on cells labeled with talin, vinculin, or paxillin, and processed these data using the aforementioned classifier (Movies S1-S9). We focused our analysis on the differences between NAs in G1 (non-maturing) and G2 (maturing, Fig. 2). For all proteins evaluated, fluorescence intensity traces in G1 had a lifetime of ~6-7 min, with clear rising and decaying phases (Fig. 2a-f, top). The associated traction traces exhibited intermittent rises and falls with an overall magnitude much smaller than the traction traces in G2 (Fig. 2a-f, bottom). As expected, NAs in G2 showed a steady increase in both fluorescence intensity and traction traces with a lifetime greater than 15 minutes (Fig. 2g-l). The fluorescence intensity and traction of individual G1 and G2 NAs reflected this stereotypical behavior, and so did the average behavior, i.e. a slight increase and fall for G1 and more steady increase for G2 (Fig. S4a-i). A further analysis with cohort plots, where traces of similar lifetime are grouped and separately displayed, revealed that average traces of many cohorts follow the stereotypical behavior (Fig. S4j-o).

Next, we developed an event-based time-series analysis method that identifies the first time point of significant fluorescence and force increase, respectively, and then measures the time shift between the two (Fig. 2m). The blue and red arrows in Fig. 2d-f, j-l show, in two example traces, the time points identified statistically as the first intensity increase and the first traction increase, respectively. Using this approach, we first determined the fraction of NAs per group with a significant traction increase at any point throughout their lifetime (Fig. S5). Interestingly, both G1 and G2 NAs showed such a force increase, i.e. they were engaging at one point with the substrate. NAs in groups G3-5 exhibited lower fractions of force increases, suggesting that a very large number of adhesion protein aggregates, detectable through either talin, vinculin, or paxillin recruitment, never engage with the substrate.

Focusing then on the NAs in group G1 and G2, we analyzed the protein recruitment sequences using the initial force increase as a fiduciary. In non-maturing NAs (G1), talin and vinculin were recruited ~18 sec and ~8 sec before the onset of force transmission, respectively, whereas paxillin recruitment coincided with the onset of force transmission (Fig. 2n). In maturing NAs (G2), talin, vinculin and paxillin were recruited concurrently with the onset of force transmission (Fig. 2o). We also noted that the temporal distributions of protein recruitments were significantly wider in G1 adhesions than in G2 adhesions, and that of the three measured proteins, talin had by far the widest temporal recruitment window. These findings suggested that in G2 adhesions talin might form a pre-complex with vinculin prior to its association with integrin, which leads to force transmission and progression into maturation. In contrast, although G1 adhesions eventually also support some lower level of force transmission (Fig. 1n), talin and vinculin assemble sequentially in a long waiting period under force-free conditions.

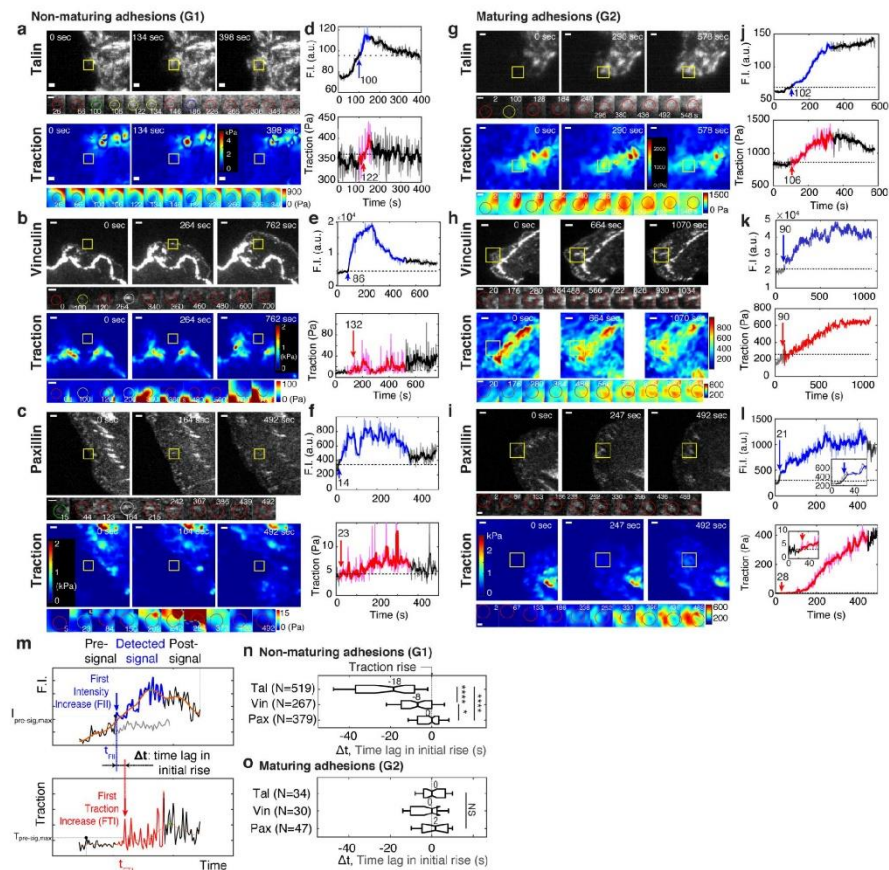


Figure 2 *Talin* and *vinculin* in non-maturing NAs are recruited in a sequential manner before traction development whereas they are recruited at the same time, along with *paxillin*, concurrent with the initial traction rise in maturing NAs. (a-l) Representative traces of talin, vinculin, and paxillin for non-maturing (a,b,c), or maturing (g,h,i) NAs. Yellow boxes show position of the example adhesions in time lapse image sequences of mGFP-tagged talin (a,g, top), vinculin (b,h, top), and paxillin (c,i, top) and associated traction maps (a-c, g-i, bottom). Scale bar: 1  $\mu$ m. (d-l) Traces of fluorescence intensity (top) and traction (bottom). Periods of significant fluorescence intensity of the tagged proteins are indicated in blue for fluorescence intensity and red for traction. An inset in (l) indicates that also in this trace the traction is gradually increasing. Blue and red arrows mark the time points of the first intensity increase (FII) and the first traction increase (FTI), respectively, which are defined in (m). (m-o) Analysis of time-shifts between protein recruitment and FTI. (m) Traces of fluorescence intensity (top) and traction (bottom). Illustrated is the detection of the first significant value in both series. Distinct distributions of time lags between FII and FTI in non-maturing (n) and maturing (o) NAs. Sample numbers, extracted from 6 cells for talin, 5 cells for vinculin and 4 cells for paxillin, are shown in each y-axis label. \*:  $p < 1 \times 10^{-2}$ , \*\*\*\*:  $p < 1 \times 10^{-30}$  by Mann-Whitney U test

*In maturing NAs, vinculin assembles faster than in non-maturing NAs, but talin and paxillin show no difference*

The rod domain of talin contains 13 helical bundles, 9 of which include cryptic vinculin binding sites (VBSs) that are exposed after mechanical unfolding under tension (del Rio et al., 2009; Geiger et al., 2009; Goult et al., 2013). Thus, we hypothesized that the simultaneous talin-vinculin recruitment in maturing NAs could result in accelerated further vinculin binding compared to non-maturing NAs. To test this, we quantified the assembly rate of each protein by obtaining the slope of the fluorescence intensity over the first 10 sec after initial appearance (Fig. 3a). Interestingly, only vinculin showed a significant difference in the assembly rate between non-maturing vs. maturing vinculin complexes, while talin and paxillin showed no such differences (Fig. 3a). Thus, with a talin-vinculin pre-complex involved in G2 NA formation, talin could be more amenable to unfolding additional VBS-containing domains, which in turn would reinforce further vinculin recruitment and adhesion maturation. We also quantified the traction force growth in those NAs with an expectation that there would be an immediate rise in force with faster vinculin binding. However, the traction force growth rate for the first 10 seconds showed no significant difference between non-maturing vs. maturing NAs (Fig. 3b). Nevertheless, a difference was observed when the force growth rate was quantified over a longer period, i.e., two minutes (Fig. 3c), consistent with our previous finding (Han et al., 2015). These findings imply that increased vinculin recruitment in maturing NAs – because of the effective tension development across the talin/vinculin mediated linkage between integrin and F-actin – supports the rise of traction force by connecting the protein complex to more F-actin, with some time delay.

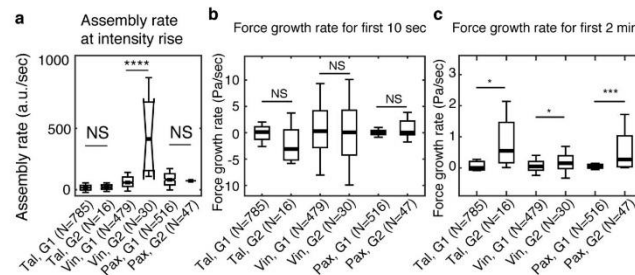


Figure 3 Vinculin, but not talin and paxillin, is recruited significantly faster in maturing NAs than in non-maturing NAs. (a) Assembly rate of talin, vinculin and paxillin, to G1 (non-maturing) or to G2 (maturing) NAs, quantified as the slope of fluorescence intensity over the initial 10 seconds after detection. (b) Traction force growth rate of the NAs in (a) for the initial 10 seconds after detection. (c) Force growth rate quantified over the first two minutes after detection. \*:  $p < 1 \times 10^{-2}$ , \*\*\*:  $p < 1 \times 10^{-10}$ , \*\*\*\*:  $p < 1 \times 10^{-30}$  by Mann-Whitney U test

#### Vinculin can bind to talin without force through a 'threonine belt' in talin R8 domain

Previous work established that under tension the talin R3 domain unfolds first, as it contains a destabilized hydrophobic core due to the presence of a 'threonine belt' of four threonine residues. By mutating the threonine residues to isoleucines and valines (the so called "IVVI mutant") it was possible to stabilize the core and prevent talin from unfolding, which significantly reduces the exposure of the two VBS (Elosegui-Artola et al., 2016; Goult et al., 2013; Yao et al., 2014). Moreover, we had shown that the VBS in R8 was able to bind vinculin readily in the absence of force (Gingras et al., 2010). Like R3, R8 also contains a threonine belt, consisting of T1502, T1542 and T1562 (Fig. 4a) (Yan et al., 2015). Thus, we hypothesized that a similar strategy, using a

T1502V, T1542V, T1562V “R8vzv mutant”, could stabilize the R8 domain and reduce the VBS activity. To test this hypothesis, we made a “R7R8vzv” construct and compared its unfolding characteristics to wild-type R7R8 fragment (R7R8wt) using circular dichroism (CD; Fig. 4b). We included the R7 domain to make the fragment more stable and better behaved than R8 alone and to maintain R8 in its native conformation. In the R7R8wt the two domains unfolded cooperatively with a single unfolding step at a melting temperature ( $T_m$ ) of 55°C. In contrast, stabilization of the R8 domain in the R7R8vzv mutant resulted in the domains unfolding independently, with R7 unfolding at a similar temperature to the wt ( $T_m$  56°C), but the temperature of R8 domain increased from 56°C to 82°C. Strikingly, the two unfolding steps indicate that in the R7R8vzv mutant the R7 and R8 behave independently with regard to thermal stability. Together, these results show that the R7R8vzv mutant stabilizes R8.

To test whether stabilization of R8 would affect its interaction with vinculin, we used analytical gel filtration to look at complex formation. Preincubation of both R7R8wt and R7R8vzv with vinculin Vd1 showed both constructs were able to form complexes with vinculin, however the R7R8vzv:Vd1 complex peak was substantially smaller than the wildtype:Vd1 peak, confirming that the R7R8vzv was less able to bind to Vd1 (Fig. 4c). This finding suggested that accessibility of the VBS was reduced with stabilization of the threonine belt by valine replacement. To further quantitate the interaction, we used microscale thermophoresis (MST), titrating the talin proteins against RED-tris-NTA labeled Vd1. R7R8wt bound with a relatively high affinity of 2.07  $\mu$ M whereas, under the same conditions, we were not able to detect any binding to R7R8vzv (Fig. 4d). The R8 domain is also an LD-motif binding site, i.e. it binds to multiple LD proteins including RIAM and DLC1 (Goult et al., 2018; Goult et al., 2013; Zacharchenko et al., 2016). Using a fluorescence polarization assay described previously (Whitewood et al., 2018), we measured the binding affinities of R8 ligands RIAM TBS1 and DLC1 peptides with R7R8wt and R7R8vzv (Fig. S6). Both peptides bound to the R7R8vzv with comparable affinities to the wildtype R7R8, confirming the R7R8vzv was still able to bind LD-motif proteins. Altogether, these biochemical characterizations of the R7R8vzv mutant suggested that the threonine belt in talin R8 is responsible for vinculin binding without force. The mutant also provided a tool for us to probe the functional implications of talin-vinculin pre-complex formation on NA assembly and maturation *in vivo* without interfering with binding of other binding partners.

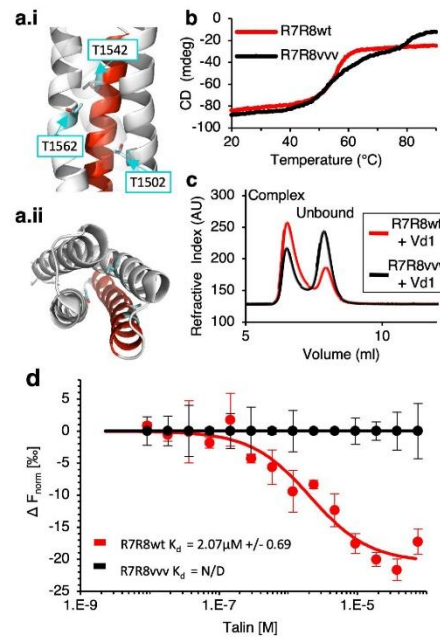


Figure 4 *Stabilizing the “threonine belt” in the R8 domain of talin inhibits talin-vinculin interactions under tension-free conditions.* (a) Cartoon representation of talin R7R8 (pdb id 2X0C) showing the ‘threonine belt’, comprised of residues T1502, T1542, and T1562, labeled and shown as sticks (cyan), the VBS helix is colored red. (a.i) side on view (N.B. helix 31 transparent), (a.ii) top down view. (b) Denaturation profiles for wildtype R7R8wt (red) and R7R8vzv (black) measured by monitoring the change in circular dichroism at 208 nm with increasing temperature. R7R8wt has a melting temperature of 55°C, whereas R7R8vzv unfolds in two steps, one (R7) with a melting temperature of 56°C and R8 unfolding at 82°C. (c) Chromatograms showing binding of talin R7R8 to the vinculin head (Vd1). R7R8wt (red) and R7R8vzv (black) binding to Vd1. Complex peaks and unbound peaks are indicated. (d) MST analysis of R7R8wt (red) and R7R8vzv (black) interaction with Vd1. Experiments were done in triplicate and analysed using the  $K_d$  fit model on NanoTemper analysis software. Dissociation constants  $\pm$  SE ( $\mu$ M) for the interactions are indicated in the legend. ND not determined.

#### *Cells with R8vzv mutant talin show less maturing NAs and sparser and smaller FAs*

To investigate whether the ability of talin to form a pre-complex with vinculin promotes adhesion maturation, we introduced the R8vzv mutation into full-length talin1, in addition to tagging the protein with the mNeonGreen fluorescent protein. We named this construct “tal1n1 R8vzv-mNG”. To express this talin mutant, we prepared talin1 KD ChoK1 cells using shRNA and rescued with sh-resistant forms of talin1 R8vzv-mNG, or WT talin1-mNG as a control. The expression of talin1 R8vzv-mNG was slightly less than that of WT ChoK1 cells but more than talin1 KD ChoK1 cells (Fig. S7). We imaged the mNeonGreen signal of talin1 R8vzv mutant or WT talin1 of each cell on 5 kPa gel along with high-resolution traction force analysis. Cells with talin1 R8vzv-mNG contained many more NAs (Fig. 5a,b,f,g,k) and less and smaller FCs and FAs (Fig. 5a,b,f,g,l,m) than control cells with WT talin1-mNG. Cells expressing the talin1 R8vzv-mNG also showed less traction compared to WT the talin1-mNG rescue condition (Fig. 5c,h,n). With less traction and



more NAs, edge protrusion and retraction of cells with talin1 R8vvv-mNG were faster than cells with WT talin1-mNG (Fig. 5d,i). Moreover, a lower fraction of NAs and FCs in R8vvv mutant cells grew in size to FAs than NAs in cells with WT talin1 rescue (Fig. 5e,j,o,p). Together, these results demonstrate that talin R8vvv mutation restricts NAs from maturing into focal adhesions.

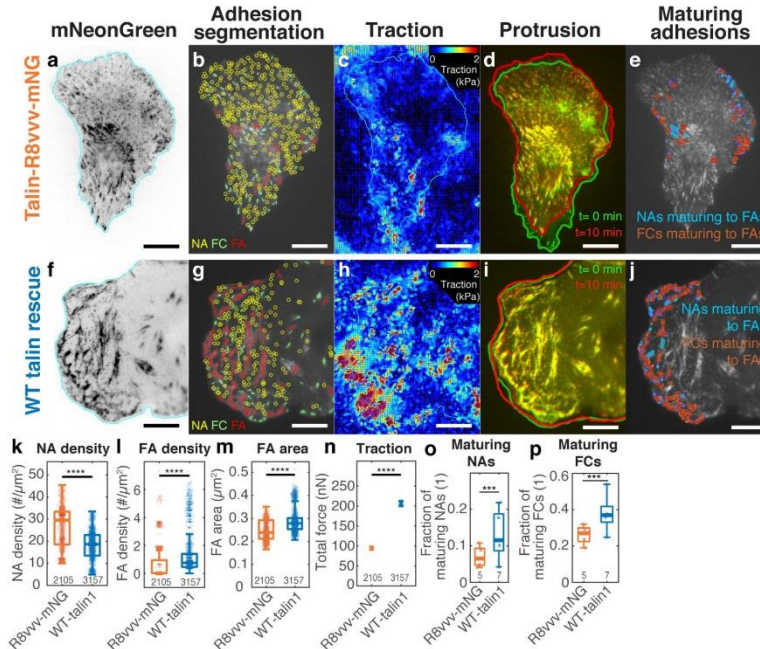
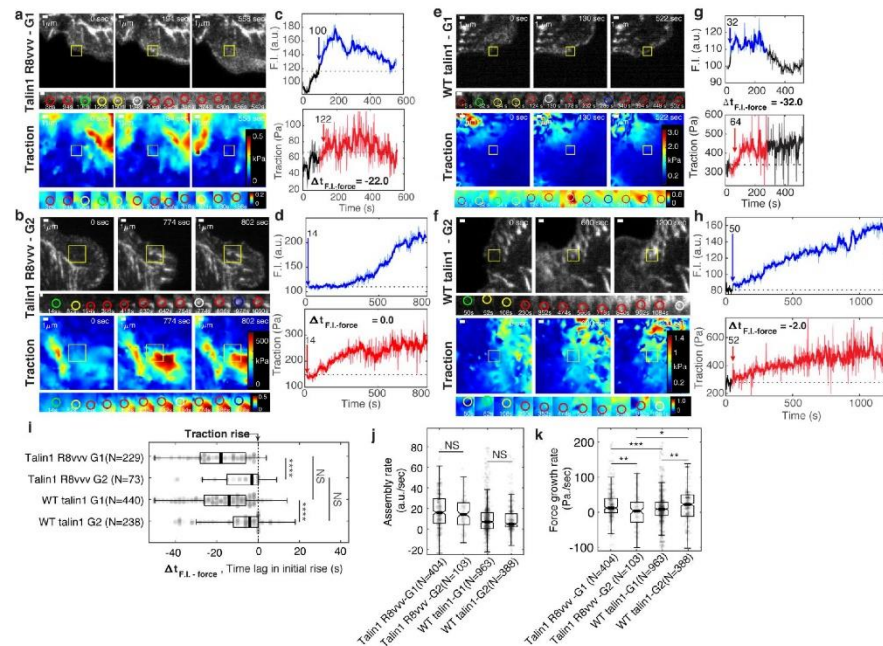


Figure 5 Expression of the talin1 R8vvv mutant results in formation of denser NAs, but lesser and smaller FAs, lower traction, more active protrusion and less maturing adhesions compared to expression of the talin wildtype. (a-j) Adhesion, traction and protrusion phenotype of a representative ChoK1 cell on 5 kPa gel substrates expressing talin R7R8vvv mutant (a-e) vs a representative ChoK1 cell expressing WT talin (f-j). (a,f) inverted talin-mNeonGreen images. (b,g) detection of NAs, FCs and FAs. (c,h) traction maps. (d,i) snapshots of computer vision-extracted cell boundaries at 0 and 10 min of a movie. (e,j) overlay of NAs and FCs that mature to FAs. (k-m) Box plots of NA density (k), FA density (l), and FA area (m). (n) Total traction integrated over cell area. Numbers of adhesions collected from M=5 and M=7 independently imaged cells for talin1 R8vvv-mNG and WT talin1-mNG rescue, respectively, are indicated under each box plot. (o, p) Box plots of the fraction of NAs maturing to FAs relative to all NAs (o) and of the fraction of FCs maturing to FAs (relative to all FCs) (p). Here, N=5 and 7 are the number of independently imaged cells. Scale bar: 10  $\mu\text{m}$ . \*\*\*\*:  $p < 1 \times 10^{-30}$  by Mann-Whitney U test

#### R8vvv mutation does not affect talin recruitment but impedes traction growth rate

To investigate whether talin pre-complex formation with vinculin affects talin recruitment itself, we compared the time of talin recruitment in talin1 R8vvv mutant cells vs. WT talin1 rescue cells for non-maturing (G1) and maturing (G2) NAs. Consistent with the data in Fig. 3, in both cell types G1 adhesions showed talin recruitment, on average,  $\sim 14$  sec prior to the initial rise in traction (Fig. 6a,c,e,g,i), while G2 adhesions showed a near coincidental talin recruitment (Fig. 6b,d,f,h,i). This indicates that the ability of talin to bind vinculin does not affect talin recruitment. For both WT and R7R8vvv mutant talin, the assembly rates were statistically indistinguishable between non-

maturing and maturing NAs (Fig. 6j). The rate of traction development in NAs, however, was significantly affected in talin1 R8vvv-mNG mutant cells. Overall, the traction increase was reduced in mutant cells, both for G1 and G2 (Fig. 6k). Moreover, while in WT talin1 rescue cells G2 NAs showed faster traction growth than G1 NAs, consistent with the data in Fig. 3c, in talin1 R8vvv-mNG mutant cells G2 adhesions exhibited an even slower force growth than G1 NAs. These results suggest that the talin-vinculin pre-complex is essential for the development of force across NAs, which is required for further adhesion maturation.



**Figure 6** Expression of talin1 R8vvv-mNG mutant does not change the recruitment timing of talin to NAs, but reduces the force growth rate in NAs. (a-h) Representative talin and traction force images of talin1 R8vvv-mNG expressing cells (a-d) and WT talin-mNG rescue cells (e-h) within non-maturing (a,c,e,g) and maturing (b,d,f,h) NAs. (a,b,e,f) talin-mNeonGreen images (top) and traction images (bottom) of three different time points, i.e. at initial nucleation, at maximum fluorescence intensity, and at the end of the NA portion of the track. Yellow boxes on both images and traction maps indicate the position of a representative NA, for which a time lapse sequence is assembled in the bottom row. Scale bar: 1  $\mu$ m. (c-d, g-h) Traces of talin-mNeonGreen fluorescence intensity (top) and traction (bottom). Phases of the traces with significant fluorescence above background are indicated in blue and red, respectively. Blue and red arrows mark the time points of the first intensity increase and the first traction increase, respectively (i-k) Distributions of time lags of fluorescence intensity onset relative to traction onset (i), talin assembly rates (j), and traction growth rates (k) of non-maturing (G1) and maturing (G2) NAs in talin1 R8vvv-mNG mutant and WT talin1-mNG rescue cells. \*:  $p < 1 \times 10^{-2}$ , \*\*:  $p < 1 \times 10^{-3}$ , \*\*\*:  $p < 1 \times 10^{-10}$ , \*\*\*\*:  $p < 1 \times 10^{-30}$  by Mann-Whitney U test

*Differential vinculin recruitment between non-maturing vs. maturing NAs vanishes with talin1 R8vvv mutation*

Vinculin recruitment to the NA is critical for both force growth and adhesion maturation (Fig. 3) (Thievessen et al., 2013). To examine whether the assembly rate of vinculin is affected by talin's ability to form a pre-complex with vinculin, we performed two-channel imaging of vinculin-SnapTag-TMR-Star and WT talin1 or talin1 R8vvv mutated talin-mNeonGreen (see Methods). As for prior analyses, we captured and analyzed time-series of each pair of talin-vinculin signals in non-maturing vs. maturing NAs (Fig. 7a-h) and quantified the vinculin assembly rate within 30 seconds after first detection (Fig. 7i). In talin1 R8vvv-mNG mutant cells, vinculin assembly rates were statistically indistinguishable between non-maturing (G1) and maturing (G2) NAs, whereas in WT talin1-rescue cells vinculin rates were significantly higher in G2, consistent with the data acquired in control cells (Fig. 3a). This result suggests that early vinculin binding to talin R8 domain indeed contributes to faster recruitment of additional vinculins. The insignificant difference in vinculin recruitment in R7R8vvv mutant cells for G1 vs. G2 NAs might be related to the reverted traction growth rates between the two NA groups observed in these mutant cells (Fig. 6k). It is also worth noting that the vinculin signal in G2 NAs of cells with WT talin-rescue tended to keep increasing while talin intensity was relatively flat ( $t=200-600$  sec in Fig. 7h,d), suggesting that the number of exposed talin VBSs is increasing over time under tension. The same trend was observed in talin1 R8vvv mutant cells (Fig. 7b,f), but the vinculin recruitment rate was again much less than those found in WT talin1-rescue. Altogether, this data strongly suggest that vinculin recruitment is significantly reduced when no vinculin-talin pre-complex can form.

*Simultaneous talin-vinculin imaging confirms vinculin's recruitment after talin for non-maturing NAs and concurrent recruitment for maturing NAs*

To confirm the recruitment order of talin and vinculin with respect to traction force development (Fig. 2), we quantified the time difference between the first significant increase in talin fluorescence intensity and the first significant increase in vinculin fluorescence intensity (blue and magenta arrows in Fig. 7a-h, j). At non-maturing NAs, both in talin1 R8vvv mutant and WT talin1-rescue cells, vinculin was delayed to talin on average by ~10 seconds (Fig. 7j), consistent with the delay we inferred indirectly based on alignment of the fluorescent intensity increases with the first significant traction force increase (Fig. 2n). At maturing NAs, vinculin and talin recruitment coincided (Fig. 7j), also consistent with the indirect inference presented in Fig. 2n. This shows directly that the formation of a talin-vinculin pre-complex indeed enhances the probability of NA maturation. In more detail, vinculin recruitment in maturing NAs of talin1 R8vvv mutant cells was ~4 seconds after talin recruitment, whereas vinculin recruitment in WT talin rescue condition preceded the talin recruitment by ~2 seconds (Fig. 7j). We interpret this difference as the result of the mutation in talin's R8 domain, which reduces the ability of vinculin to bind talin prior to mechanical unfolding. Moreover, even though some maturing NAs eventually grow also in talin1 R8vvv mutant cells, the absence of efficient vinculin binding to the VBS in R8 propagates into an overall less efficient vinculin recruitment. In agreement with this interpretation, we found that the lifetimes of maturing G2 NAs in the mutant cells were much shorter than those in cells with WT-talin1 rescue (Fig. 7k). Altogether, our data establishes that talin's pre-association with vinculin via the talin R8 domain is critical for accelerated vinculin binding, which in turn contributes to the development of the level of force transmission required for NA maturation.

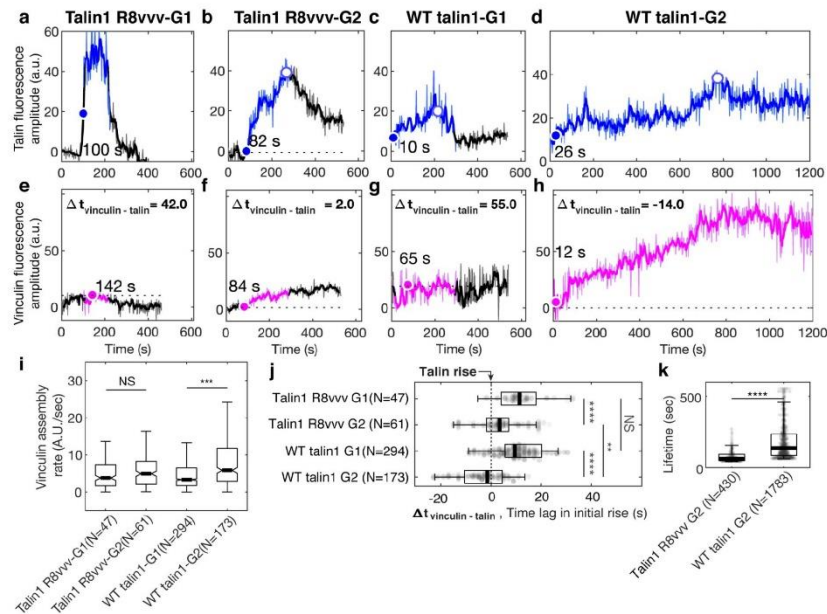


**Figure 7 Vinculin recruitment is reduced in talin1 R8vvv mutant cells.** (a-h) Representative traces of talin-mNeonGreen (a-d) and vinculin-SnapTag-TMR-Star (e-h) fluorescence intensity at G1 non-maturing (a,c,e,g) and G2 maturing (b,d,f,h) NAs in cells expressing the talin1 R8vvv mutant (a-b, e-f) and WT talin (c-d, g-h) constructs. Phase of the traces with significant intensity above background are shown in color (blue for talin, magenta for vinculin). Blue and magenta arrows indicate the time of talin and vinculin recruitment onset, respectively. (i) Vinculin assembly rates at non-maturing and maturing NAs in R8vvv mutant and WT talin rescue cells, quantified by the slope of vinculin-SnapTag-TMR-Star fluorescence intensity over the initial 30 seconds after the first detection in the talin-mNeonGreen channel. (j) Time delays of vinculin recruitment onset relative to talin recruitment onset of non-maturing vs. maturing NAs in talin1 R8vvv-mNG mutant and WT talin1 mNG cells. Vinculin recruitment onsets in non-maturing NAs are positive, i.e. vinculin recruitment starts after talin. In contrast, vinculin recruitment onsets in maturing NAs are nearly coincidental with talin. See the text for further description. (k) Lifetimes of maturing NAs classified in talin1 R8vvv mutant and WT talin1 mNG rescue cells. \*\*\*\*:  $p < 1 \times 10^{-30}$  by Mann-Whitney U test. The numbers of adhesions (N), extracted from 7 cells each for cells with talin1 R8vvv-mNG and WT talin1-mNG, are shown per each condition name at each panel.

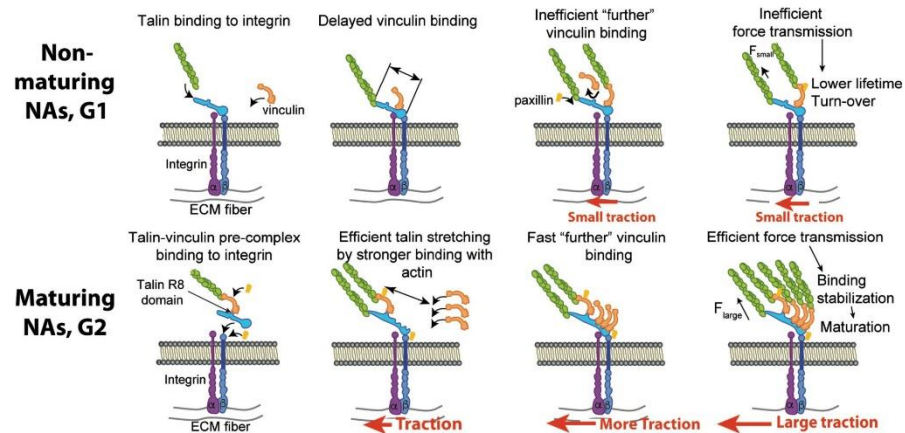


Figure 8 A suggested mechanism of differential recruitment of talin and vinculin determining maturation of nascent adhesions. (Top) For non-maturing NAs, talin binds to integrin before vinculin recruitment. Talin stretching is limited to a shorter level, which limits the exposure of vinculin-binding-sites. Inefficient vinculin binding, in turn, limits the number of F-actin that can connect to the adhesion complex, allowing for only a low amount of tension across the complex. Insufficient loading level reduces the lifetime of catch-bond like associations between molecules, resulting in turnover of the NA complex. (Bottom) For maturing NAs, talin and vinculin form a pre-complex before association with integrin. Upon pre-complex recruitment to the NA traction force builds immediately. Talin is stretched in a faster manner by pre-associated vinculin and talin's own binding to F-actin accommodate faster, efficient recruitment of additional vinculin. High loading levels across the complex stabilizes molecular bonds, which facilitates the maturation of the NA.

## Discussion

Our experiments show that the maturation of NAs depends on the formation and recruitment of a talin-vinculin pre-complex. Previous models have inferred that tension across talin, which can establish direct bridges between integrins and actin filaments, is sufficient to unfold the molecule and expose several vinculin binding sites. These binding sites were thought to promote the recruitment of vinculin to further strengthen the link between the integrin-talin complex and actin (Goult et al., 2018; Sun et al., 2016). However, these models were derived primarily from observations in focal adhesions, i.e. at a late stage of the maturation process (Atherton et al., 2015; Thievensen et al., 2013). Here, we exploit our ability to concurrently measure traction and molecular associations at the scale of individual NAs using total internal reflection microscopy on high-refractive index soft substrates (Gutierrez et al., 2011; Han et al., 2015). Our data suggests that the tension borne by an individual talin bridge between integrin and actin filaments is insufficient to fully unfold the talin rod domain and expose the number of VBSs necessary for talin to form a stable link to F-actin. This further lowers the lifetimes of catch-bond-like molecular associations (Hakonardottir et al., 2015; Huang et al., 2017; Sun et al., 2016) between talin and vinculin, vinculin and actin, and talin and actin, resulting in turnover of the NAs (Fig. 8, top). In contrast, pre-assembled talin-vinculin complexes immediately establish a strong link between integrin and F-actin, as indicated by the concurrent recruitment of talin and vinculin and traction force onset. The fast loading rate promotes a fast and efficient unfolding of the talin rod domain, which exposes several additional VBSs for further recruitment of vinculin and strengthening of the talin/F-actin interaction. This results in robust increase of traction force transmission and

stabilization of catch-bond-like molecular associations that contribute to the maturation of the NA (Fig. 8, bottom).

Our data show that the formation of a talin-vinculin pre-complex is promoted by talin's R8 domain, which contains a VBS that is exposed for vinculin recruitment without tension-mediated unfolding of talin. We generated a talin mutant with a more stable R8 domain that prevents spontaneous association with vinculin. Cells expressing this mutant have a large fraction of NAs that cannot mature into FAs and transmit only low-level forces. This identification is different from previous findings, including ours, where talin's R3 domain has been described as the weakest domain that can unfold under tension (Atherton et al., 2015; Yao et al., 2016). Thus, we speculate that in maturing NAs, vinculin's R8 binding leads to unfolding of R3, followed by exposure of additional VBSs in R1-R2. Our data suggest that the fraction of maturing NAs must be initiated with this R8-mediated talin-vinculin pre-complex. Intriguingly, pre-complex formation prior to incorporation into adhesion requires spontaneous encounters of mobile talin and vinculin at the plasma membrane or even in the cytosol. These are likely rare events, which may explain the surprising finding that the number of maturing (G2) NAs ( $3.5 \pm 1.6$  %, Mean  $\pm$  Standard Error of the Mean, N=20 movies) is so low compared to G1 NAs ( $28.8 \pm 3.5$  %, Mean  $\pm$  S.E.M., N=20 movies) among all NAs.

Our data also indicates that paxillin is recruited concurrently with the onset of traction force regardless of the fate of a NA (Fig. 2). This means that, especially in non-maturing NAs, paxillin is recruited after vinculin. Tension dependency of paxillin recruitment is well-established (Schiller et al., 2011). Our data suggests that tension-dependent recruitment of paxillin is through vinculin, which is consistent with a previous finding that paxillin recruitment can be induced by vinculin (Humphries et al., 2007) as it binds to the tail-domain of vinculin (Tumer et al., 1990). Alternatively, paxillin has been reported to be recruited after focal adhesion kinase (FAK) in endothelial cells (Hu et al., 2014). Given evidence that talin can also be recruited by FAK (Lawson et al., 2012), paxillin's recruitment after talin and vinculin might be coincident with vinculin-paxillin binding mediated by FAK. In line with our measurements, a FRET-based tension sensor study has shown that of the three molecules paxillin, talin and vinculin, paxillin levels correlate strongest with traction force levels (Morimatsu et al., 2015). Altogether, our findings agree with previous evidence that paxillin levels are an accurate reporter of traction levels but is not an early protein to indicate the nucleation of NAs.

In the case of non-maturing NAs, talin and vinculin were recruited significantly before our measurements could detect a significant traction onset. This finding implies that there are sub-populations of talin and vinculin that carry only little force. Additionally, talin is present for a longer time than vinculin before traction onset in non-maturing adhesions. While this is conceptually consistent with a previous finding that vinculin binding to talin requires talin's actin binding for tension development (Austen et al., 2015), the time lag between talin and vinculin recruitment suggests that talin's sole engagement with F-actin without vinculin potentially impedes talin's own role as an integrin activator (Shattil et al., 2010) and promoter of integrin clustering (Saltel et al., 2009). Additionally, before vinculin binding, talin may be bound to the Rap1-interacting adaptor molecule (RIAM) (Lee et al., 2009), which is replaced by vinculin once talin's R2R3 domain unfolds (Goult et al., 2013).

How the talin-vinculin pre-complex can promote faster tension development and talin unfolding in maturing adhesions remains to be determined. Potential mechanisms imply: 1) that

the complex is also pre-bound to F-actin through the vinculin tail as vinculin bound to talin is almost certainly in an open conformation (Golji and Mofrad, 2013; Humphries et al., 2007); and 2) that the talin-vinculin interactions via talin's R8-domain do not interfere with talin's direct binding to F-actin, thus accelerating talin's actin-binding rate. Additionally, in maturing adhesions paxillin is recruited concurrently with the talin-vinculin pre-complexes. A paxillin-binding-site in vinculin's tail domain has not been co-localized with paxillin when studied with a vinculin-tail fragment (Humphries et al., 2007). Our data suggests a possibility that a full-length vinculin in a living cell might be immediately associated with paxillin upon its pre-complex formation with talin (Carisey and Ballestrem, 2011).

In summary, our work establishes an unexpected role for a talin-vinculin pre-complex as a mechanical prerequisite to the further recruitment of vinculin to talin, which is the foundation of adhesion maturation. While the possibility of talin-vinculin pre-complexes has been discussed in previous studies (Bachir et al., 2014; Pasapera et al., 2010), their function has remained obscure. Here, we now show that this complex formation is an essential step in adhesion assembly. Where this complex forms and whether the formation is regulated by cellular signals are two of the critical questions to be addressed in future studies.

## **Materials and Methods**

### **Cell Culture**

ChoK1 cells were cultured in Dulbecco's Modified Eagle Medium (DMEM) with 4.5 g/L D-Glucose, L-Glutamine, and Sodium Pyruvate (Gibco, 11995-065) supplemented with 10% Fetal Bovine Serum (Equitech-Bio, Inc, SFBU30), 1% Anti-Anti (Gibco, 15240112), and 1% Non-Essential Amino Acids (Gibco, 11140076). For transfection, cells were plated in a 6-well plate at ~30% confluency and transfected the next day with 350 ng of fluorescent protein-, or SNAP-tagged adhesion marker, 1 µg of pBluescript (Stratagene) as non-specific DNA, 10 µL of Lipofectamine LTX (Gibco, 15338030), and 2 mL of reduced serum Opti-MEM (Gibco, 31985088) according to the manufacturer's directions. Four hours after adding the DNA-lipid mixture to the cells, the media was replaced with full DMEM media. 24 hours later, cells were trypsinized, and enriched with flow cytometry for low-level GFP-positive cells. Of this pool, 50,000 cells were seeded on fibronectin-coated (see below) traction-force microscopy substrates in pH 7.4 HyQ-CCM1 media (GE Lifesciences, SH30058.03), supplemented with 1.2 g/L of sodium bicarbonate and 25 mM HEPES. mGFP-talin1 (provided by N. Bate and D. Critchley), paxillin-eGFP (provided by I. Schneider), and mGFP-vinculin (provided by M. Humphries) were used for adhesion-TFM two-channel experiments.

For knock-down experiments, a previously validated shRNA hairpin against talin (GGAAAGCTTTGGACTACTA) was stably introduced into ChoK1 cells with a pLVX-shRNA1 lentiviral system and selected for with 5 µg/mL of puromycin. Western blot analysis indicated decreased levels of talin expression (Figure S7). For rescue experiments, talin was subcloned into the pCDNA3.1(+) mammalian expression vector (ThermoFisher Scientific, V79020), and silent mutations were introduced into the corresponding shRNA target sequence for both the WT talin1-mNG and the talin1 R8vvv-mNG constructs. The R8 mutations (T1502V, T1542V, and T1562V, according to mouse numbering), alter the stability of the talin R8 domain. For vinculin imaging, mNeonGreen (Allele Biotechnology) was replaced with SNAP-Tag using seamless cloning, and labeled with SNAP-Cell TMR-Star (New England Biolabs, S9105S) or SNAP-Cell

647-SiR (New England Biolabs, S9102S) according to manufacturer's recommendations. All protein-coding regions of expression constructs were verified with traditional primer walking and Sanger sequencing.

#### ***Expression of recombinant polypeptides.***

For in vitro analyses, murine vinculin Vd1 (residues 1–258), murine talin R7R8wt (residues 1357–1653) and R7R8vvv (residues 1357–1653; T1502V, T1542V and T1562V) were cloned into a pET151 vector (Invitrogen) and expressed in E.coli BL21(DE3) cells cultured in LB. Standard nickel-affinity chromatography was used to purify the His-tagged recombinant proteins as described previously (Whitewood et al., 2018). The proteins were further purified using anion exchange chromatography following cleavage of the 6xHis-tag with TEV protease. Protein concentrations were determined using their respective extinction coefficients at 280 nm.

#### ***Circular Dichroism (CD)***

Spectroscopy was performed using a JASCO J-715 spectropolarimeter equipped with a PTC-423S temperature control unit. Denaturation profiles were measured from 20–80°C at 0.2°C intervals by monitoring the unfolding of  $\alpha$ -helices at 208 nm. 0.1 mg/mL of protein was dissolved in phosphate buffered saline (PBS). Measurements were made in a quartz cell of 0.1 cm path length.

#### ***Fluorescence polarization assays***

To determine if other binding partners of talin R8 domain except for vinculin can still bind to R7R8vvv fragment, the relative binding affinities were measured using an in vitro fluorescence polarization assay. The R8 interacting, LD-motif containing peptides from DLC1 and RIAM, i.e., DLC1\_465-489-C (IFPELDDILYHVKGMQRIVNQWSEK-C) and RIAM\_6-30-C (DIDQMFSTL LGEMDLLTQSLGVDVDT-C), were coupled to a thiol-reactive fluorescein dye via the terminal cysteine. Peptides with a C-terminal cysteine were synthesized by GLBiochem (China). Stock solutions (i.e., peptide + fluorescein) were made in phosphate-buffered saline (PBS; 137 mM NaCl, 27 mM KCl, 100 mM Na<sub>2</sub>HPO<sub>4</sub>, 18 mM KH<sub>2</sub>PO<sub>4</sub>, pH 7.4), 1 mM TCEP and 0.05% Triton X-100. Excess dye was removed using a PD-10 desalting column (GE Healthcare, Chicago, IL, USA). Titrations were performed in PBS using a constant 1  $\mu$ M concentration of fluorescein-coupled peptide with increasing concentration of R7R8 fragment (either wild type or vvv mutant); final volume 100  $\mu$ M in a black 96-well plate. Fluorescence polarization (FP) measurements, in which the binding between the two polypeptides results in an increase in the fluorescence polarization signal, were recorded on a BMGLabTech CLARIOstar plate reader at room temperature and analyzed using GraphPad Prism.  $K_d$  values were calculated with nonlinear curve fitting using a one-site total binding model.

#### ***Microscale Thermophoresis (MST) assay***

Recombinantly expressed vinculin head domain (Vd1) was coupled to an equimolar amount of NT-647 dye (RED-tris-NTA NanoTemper) via its N-terminal 6xHis-Tag in a one-step coupling reaction (Tscharmer et al., 2016). Titrations were performed in phosphate buffered saline (PBS; 137 mM NaCl, 27 mM KCl, 100 mM Na<sub>2</sub>HPO<sub>4</sub>, 18 mM KH<sub>2</sub>PO<sub>4</sub>) using a constant 50 nM concentration of RED-tris-NTA coupled Vd1, with increasing concentration of recombinantly



expressed talin R7R8wt and R7R8vvv; final volume 20  $\mu$ L. Prepared samples were filled into Monolith NT.115 Capillaries (NanoTemper). Measurements were recorded on a Monolith NT.115 at 25°C, excited under red light, medium MST power and 40% excitation power. The data was analyzed using MO. Affinity Analysis software (v2.3) and fitted using the Kd fit model.

#### **Analytical gel filtration**

Gel filtration was performed using a Superdex-75 size exclusion chromatography column (GE Healthcare) at a flow rate of 0.7 mL/min at room temperature in 50 mM Tris pH 7.5, 150 mM NaCl, 2 mM DTT. A sample of 100  $\mu$ L consisting of 100  $\mu$ M of each protein was incubated at a 1:1 ratio at 25°C for 10 minutes. The elution was monitored by a Malvern Viscotek SEC-MALS-9 (Malvern Panalytical, Malvern, UK).

#### **Western blot**

Cells were transfected under identical conditions as they were for imaging experiments but with a 10 cm dish and sorted with a flow cytometer (FACS Aria II SORP) for low expression. Cells were lysed by adding 2x laemmli + 10% b-ME, vortexing, and heating at 95°C for 10 minutes. Protein concentration was measured, and the same amount was loaded for each lane. The gel was semi-dry transferred with a turbo blot, and then incubated overnight in 5% milk in tris-buffered saline with 0.1% Tween 20 (TBST) at 4 degrees. Protein was visualized with an anti-talin antibody at 1:1000 and the loading control was visualized with anti-b-actin at 1:5000, each in 0.5% milk/TBST overnight at 4°C. Gels were then rinsed with TBST, and probed with IgG:horseradish peroxidase in 0.5% milk/TBST at 4°C for 1 hour and then at room temperature for another 30 minutes. Gels were rinsed three times for 20 minutes in TBST and then detected with enhanced chemiluminescence.

#### **TFM Substrate Preparation**

All silicone substrates had a diameter of 35 mm, a stiffness of 5 kPa, were embedded with 580/605 or 640/647 ( $\lambda_{EX}/\lambda_{EM}$ ) 40 nm-diameter beads, and were compatible with total internal reflection fluorescence illumination. Substrates were coated with fibronectin (Sigma Aldridge, F1141) the same day as imaging experiments were conducted by mixing 20  $\mu$ L of a 10 mg/mL 1-ethyl-3-(3-dimethylaminopropyl) carbodiimide hydrochloride (EDC) solution, 30  $\mu$ L of a 5 mg/mL fibronectin solution, and 2 mL of  $Ca^{2+}$  and  $Mg^{2+}$  containing Dulbecco's Phosphate Buffered Saline (DPBS, Gibco, 14040117) for 30 minutes at room temperature. Thereafter, the substrate was rinsed 2 times with DPBS, and incubated with 2 mL of 0.1% (w/v) bovine serum albumin in DPBS for another 30 minutes at room temperature, and rinsed several times with PBS prior to seeding with 50,000 transiently transfected cells.

#### **TIRF Imaging for TFM and adhesion proteins**

Cells were imaged with a DeltaVision OMX SR (General Electric) equipped with ring-TIRF, which mitigates laser coherence effects and provides a more homogeneous illumination field. This microscope is equipped with a 60x, NA=1.49, objective, and 3 sCMOS cameras, configured at a 95 MHz readout speed to further decrease readout noise. The acquired images were in 1024x1024 pixel format with an effective pixel size of 80 nm. Imaging was performed at 37°C, 5% carbon dioxide, and 70% humidity. Laser-based identification of the bottom of the substrate was

performed prior to image acquisition, with a maximum number of iterations set to 10. Laser powers were decreased as much as possible, and the integration time set at 200 milliseconds, to avoid phototoxicity. At the back pupil of the illumination objective, the laser power for both 488 and 568 nm lasers was ~22 mW. Imaging was performed at a frequency of 1 Hz for 5-10 minutes, and deviations between the alignment for each camera were corrected in a post-processing step that provides sub-pixel accuracy. After imaging, cells were removed from the substrate with a 30% bleach solution, and the beads on the relaxed gel substrate were imaged for each cell position. Rapid imaging was necessary to mitigate swelling effects in the silicone substrate and to resolve traction forces in nascent adhesions.

### **TFM Force Reconstruction**

Bead images of the deformed gel – acquired when a cell was on the substrate – and a ‘reference bead image’ of the relaxed gel acquired after cell removal – were processed for traction reconstruction as described previously (Han et al., 2015). Briefly, the bead images of the deformed gel were compared with the reference image using particle image velocimetry. A template size of 17 to 21 pixels, and a maximum displacement of 10 to 80 pixels, depending on the bead density and overall deformation, were used for cross-correlation-based tracking of the individual beads. The displacement field, after outlier removal, was used for traction field estimation over an area of interest. The area of interest on the reference bead image was meshed with square grids of the same width, which depends on the average area per bead. The forward map, which defines the expected deformation of the gel at all bead locations given a unit force at a particular mesh of the force grid, was created by solving Boussinesq Eq. under the assumption of infinite gel depth. This forward map was then used to solve the inverse problem, i.e. given the measured field of bead displacements, the underlying traction field is determined. The solution to this inverse problem is ill-conditioned in that small perturbations in the measured displacement field can yield strong variation in the reconstructed traction field. To circumvent this problem, the traction field was estimated subject to L1-norm regularization. As discussed in detail in (Han et al., 2015), L1-norm regularization preserved the sparsity and magnitude of the estimated traction field. Also as discussed and validated in (Han et al., 2015), the application of L1-norm regularization over the L2-norm regularization most traction force microscopy studies employ is essential to resolve force variation at the length scale of the distances between individual nascent adhesions. The level of regularization is determined by a control parameter. We chose the parameter based on L-curve analysis, which guaranteed a fully automated and unbiased estimate of the traction field (Han et al., 2015). Strain energy, which represents the mechanical work a cell has put into the gel, was quantified as  $1/2 \times \text{displacement} \times \text{traction}$ , integrated over a segmented cell area. The unit of this integral is femto-Joule.

### **Adhesion segmentation, detection and tracking**

Focal adhesions (FAs) and diffraction-limited nascent adhesions (NAs) were detected and segmented as previously described (Han et al., 2015). Briefly, FAs from images of either labelled paxillin, talin, or vinculin were segmented with a threshold determined by a combination of Otsu’s and Rosin’s algorithms after image pre-processing with noise removal and background subtraction. Segmented areas larger than  $0.2 \mu\text{m}^2$  were considered for focal contacts (FCs) or FAs, based on the criteria described by Gardel et al. (Gardel et al., 2010). Individual

segmentations were assessed for the area and the length, which is estimated by the length of major axis in an ellipse that fit in each FA segmentation. FA density was calculated as the number of all segmentations divided by the cell area. Nascent adhesions were detected using the point source detection described in (Aguet et al., 2013). Briefly, fluorescence images were filtered using the Laplacian of Gaussian filter and then local maxima were detected. Each local maximum was then fitted with an isotropic Gaussian function (standard deviation: 2.1 pixels, i.e. ~180 nm) and outliers were removed using a goodness of fit test ( $p = 0.05$ ). NA density was defined as the number of NAs divided by the entire cell area.

#### **Adhesion classification**

From the adhesion tracks, features 1-9 in Table 1 were captured from the individual fluorescence intensity traces, and features 10-21 in Table 1 from the corresponding spatial properties, some in reference to the position and movement of the proximal cell edge and to the overlap with segmentations of focal adhesions and focal complexes. The classification was accomplished using a cubic support vector machine (SVM). The classifier was evolved in a human-in-the-loop fashion, i.e. the user iteratively adjusted machine-generated classifications. The initial training data was labeled with qualitative criteria described in Table 2. To facilitate the labeling process, an automatic, filtering-based, labeling was also employed (see Table 3).

Both manual labeling and automatic labeling have advantages and drawbacks in terms of classification accuracy: while the manual labeling is less consistent due to subjectivity and human error, the automatic labeling has deficiencies in terms of incompleteness of the filtering criteria in capturing all essential properties of different adhesion classes. To overcome these drawbacks, both methods were employed in a way that the automatic labeling was performed first, and then manual labeling was added for insufficiently-labeled classes. During the manual labeling, adhesion classifications were immediately updated and presented to the user to allow class reassignments of selected adhesions. The labeling process was regarded to be completed once at least 10 adhesions were labeled for each class. To remove classification bias due to potential imbalance in the number of labels across the classes, the minority classes were oversampled, and the majority classes were undersampled, based on the mean number of labels (Krawczyk, 2016). After training a classifier on one movie, for a new movie, another iteration of automatic-and-manual labeling was executed to update the classifier, which was applied to predict the classes of adhesions in the movie. Separate classifiers were built for talin-, vinculin-, and paxillin-tagged adhesions.

#### **Acknowledgement**

We would like to thank Joseph Chi and Dana Reed for preparing DNA constructs and assisting western blot. We also acknowledge Assaf Zaritsky for providing helpful comments about machine learning. This work was funded by the following grants: NIH F32GM117793 (K.M.D.), NIH P01GM098412 (A.G., A.R.H., and G.D.), NIH R01GM067230 (G.D.), Biotechnology and Biological Sciences Research Council grant BB/N007336/1 (B.T.G.) and a Human Frontier Science Program grant RGP00001/2016 (B.T.G.).

#### **Author contribution**

S.J.H., A.R.H and G.D. conceived the project. K.M.D performed imaging experiments with talin constructs and its variations (e.g. R8vvv mutant). K.M.D. created ChoK1 cells with talin1 shRNA and talin1 R8vvv expression. A.B. performed imaging experiments for WT GFP-tagged vinculin and paxillin. S.J.H designed the experiments and performed TFM reconstruction, nascent adhesion analysis and machine learning from the images. S.J.H. and G.D. wrote the manuscript and S.J.H. made the figures. B.T.G. provided suggestions for talin structure and mutation. A.J.W. and B.T.G. performed biochemical experiments and analyses. Silicone substrates were provided by A.G. and E.G. All authors reviewed and provided feedback on the manuscript.

#### Competing Interests

The authors declare no competing interests.

#### References

- Aguet, F., Antonescu, C.N., Mettlen, M., Schmid, S.L., and Danuser, G. (2013). Advances in analysis of low signal-to-noise images link dynamin and AP2 to the functions of an endocytic checkpoint. *Dev Cell* 26, 279-291.
- Atherton, P., Stutchbury, B., Wang, D.Y., Jethwa, D., Tsang, R., Meiler-Rodriguez, E., Wang, P., Bate, N., Zent, R., Barsukov, I.L., *et al.* (2015). Vinculin controls talin engagement with the actomyosin machinery. *Nature communications* 6, 10038.
- Austen, K., Ringer, P., Mehlich, A., Chrostek-Grashoff, A., Kluger, C., Klingner, C., Sabass, B., Zent, R., Rief, M., and Grashoff, C. (2015). Extracellular rigidity sensing by talin isoform-specific mechanical linkages. *Nat Cell Biol* 17, 1597-1606.
- Bachir, A.I., Zareno, J., Moissoglu, K., Plow, E.F., Gratton, E., and Horwitz, A.R. (2014). Integrin-associated complexes form hierarchically with variable stoichiometry in nascent adhesions. *Curr Biol* 24, 1845-1853.
- Balaban, N.Q., Schwarz, U.S., Riveline, D., Goichberg, P., Tzur, G., Sabanay, I., Mahalu, D., Safran, S., Bershadsky, A., Addadi, L., *et al.* (2001). Force and focal adhesion assembly: a close relationship studied using elastic micropatterned substrates. *Nat Cell Biol* 3, 466-472.
- Bell, G.I. (1978). Models for the specific adhesion of cells to cells. *Science* 200, 618-627.
- Calderwood, D.A., Campbell, I.D., and Critchley, D.R. (2013). Talins and kindlins: partners in integrin-mediated adhesion. *Nat Rev Mol Cell Biol* 14, 503-517.
- Carisey, A., and Ballestrem, C. (2011). Vinculin, an adapter protein in control of cell adhesion signalling. *Eur J Cell Biol* 90, 157-163.
- Carisey, A., Tsang, R., Greiner, A.M., Nijenhuis, N., Heath, N., Nazgiewicz, A., Kemkemer, R., Derby, B., Spatz, J., and Ballestrem, C. (2013). Vinculin regulates the recruitment and release of core focal adhesion proteins in a force-dependent manner. *Curr Biol* 23, 271-281.
- Case, L.B., Baird, M.A., Shtengel, G., Campbell, S.L., Hess, H.F., Davidson, M.W., and Waterman, C.M. (2015). Molecular mechanism of vinculin activation and nanoscale spatial organization in focal adhesions. *Nat Cell Biol* 17, 880-892.
- Choi, C.K., Vicente-Manzanares, M., Zareno, J., Whitmore, L.A., Mogilner, A., and Horwitz, A.R. (2008). Actin and alpha-actinin orchestrate the assembly and maturation of nascent adhesions in a myosin II motor-independent manner. *Nat Cell Biol*.
- Chrzanowska-Wodnicka, M., and Burridge, K. (1996). Rho-stimulated contractility drives the formation of stress fibers and focal adhesions. *J Cell Biol* 133, 1403-1415.
- Deakin, N.O., and Turner, C.E. (2008). Paxillin comes of age. *J Cell Sci* 121, 2435-2444.
- del Rio, A., Perez-Jimenez, R., Liu, R., Roca-Cusachs, P., Fernandez, J.M., and Sheetz, M.P. (2009). Stretching single talin rod molecules activates vinculin binding. *Science* 323, 638-641.

- Digman, M.A., Wiseman, P.W., Choi, C., Horwitz, A.R., and Gratton, E. (2009). Stoichiometry of molecular complexes at adhesions in living cells. *Proc Natl Acad Sci U S A* 106, 2170-2175.
- Discher, D.E., Janmey, P., and Wang, Y.L. (2005). Tissue cells feel and respond to the stiffness of their substrate. *Science* 310, 1139-1143.
- Elosegui-Artola, A., Oria, R., Chen, Y., Kosmalska, A., Perez-Gonzalez, C., Castro, N., Zhu, C., Trepac, X., and Roca-Cusachs, P. (2016). Mechanical regulation of a molecular clutch defines force transmission and transduction in response to matrix rigidity. *Nat Cell Biol* 18, 540-548.
- Gardel, M.L., Schneider, I.C., Aratyn-Schaus, Y., and Waterman, C.M. (2010). Mechanical integration of actin and adhesion dynamics in cell migration. *Annu Rev Cell Dev Biol* 26, 315-333.
- Geiger, B., Spatz, J.P., and Bershadsky, A.D. (2009). Environmental sensing through focal adhesions. *Nat Rev Mol Cell Biol* 10, 21-33.
- Gingras, A.R., Bate, N., Goult, B.T., Patel, B., Kopp, P.M., Emsley, J., Barsukov, I.L., Roberts, G.C., and Critchley, D.R. (2010). Central region of talin has a unique fold that binds vinculin and actin. *J Biol Chem* 285, 29577-29587.
- Golji, J., and Mofrad, M.R. (2013). The interaction of vinculin with actin. *PLoS Comput Biol* 9, e1002995.
- Goult, B.T., Yan, J., and Schwartz, M.A. (2018). Talin as a mechanosensitive signaling hub. *J Cell Biol* 217, 3776-3784.
- Goult, B.T., Zacharchenko, T., Bate, N., Tsang, R., Hey, F., Gingras, A.R., Elliott, P.R., Roberts, G.C., Ballestrem, C., Critchley, D.R., *et al.* (2013). RIAM and vinculin binding to talin are mutually exclusive and regulate adhesion assembly and turnover. *J Biol Chem* 288, 8238-8249.
- Gutierrez, E., Tkachenko, E., Besser, A., Sundd, P., Ley, K., Danuser, G., Ginsberg, M.H., and Groisman, A. (2011). High refractive index silicone gels for simultaneous total internal reflection fluorescence and traction force microscopy of adherent cells. *PLoS One* 6, e23807.
- Hakonardottir, G.K., Lopez-Ceballos, P., Herrera-Reyes, A.D., Das, R., Coombs, D., and Tanentzapf, G. (2015). In vivo quantitative analysis of Talin turnover in response to force. *Mol Biol Cell* 26, 4149-4162.
- Han, S.J., Bielawski, K.S., Ting, L.H., Rodriguez, M.L., and Sniadecki, N.J. (2012). Decoupling substrate stiffness, spread area, and micropost density: a close spatial relationship between traction forces and focal adhesions. *Biophys J* 103, 640-648.
- Han, S.J., Oak, Y., Groisman, A., and Danuser, G. (2015). Traction microscopy to identify force modulation in subresolution adhesions. *Nat Methods* 12, 653-656.
- Hu, Y.L., Lu, S., Szeto, K.W., Sun, J., Wang, Y., Lasheras, J.C., and Chien, S. (2014). FAK and paxillin dynamics at focal adhesions in the protrusions of migrating cells. *Scientific reports* 4, 6024.
- Huang, D.L., Bax, N.A., Buckley, C.D., Weis, W.I., and Dunn, A.R. (2017). Vinculin forms a directionally asymmetric catch bond with F-actin. *Science* 357, 703-706.
- Humphrey, J.D., Dufresne, E.R., and Schwartz, M.A. (2014). Mechanotransduction and extracellular matrix homeostasis. *Nat Rev Mol Cell Biol* 15, 802-812.
- Humphries, J.D., Wang, P., Streuli, C., Geiger, B., Humphries, M.J., and Ballestrem, C. (2007). Vinculin controls focal adhesion formation by direct interactions with talin and actin. *J Cell Biol* 179, 1043-1057.
- Kanchanawong, P., Shtengel, G., Pasapera, A.M., Ramko, E.B., Davidson, M.W., Hess, H.F., and Waterman, C.M. (2010). Nanoscale architecture of integrin-based cell adhesions. *Nature* 468, 580-584.
- Krawczyk, B. (2016). Learning from imbalanced data: open challenges and future directions. *Progress in Artificial Intelligence* 5, 221-232.
- Kumar, A., Ouyang, M., Van den Dries, K., McGhee, E.J., Tanaka, K., Anderson, M.D., Groisman, A., Goult, B.T., Anderson, K.I., and Schwartz, M.A. (2016). Talin tension sensor

- reveals novel features of focal adhesion force transmission and mechanosensitivity. *J Cell Biol* **213**, 371-383.
- Kuo, J.C., Han, X., Hsiao, C.T., Yates, J.R., 3rd, and Waterman, C.M. (2011). Analysis of the myosin-II-responsive focal adhesion proteome reveals a role for beta-Pix in negative regulation of focal adhesion maturation. *Nat Cell Biol* **13**, 383-393.
- L. Allwein, E., E. Schapire, R., and Singer, Y. (2001). Reducing Multiclass to Binary: A Unifying Approach for Margin Classifiers, Vol 1.
- Laukaitis, C.M., Webb, D.J., Donais, K., and Horwitz, A.F. (2001). Differential dynamics of alpha 5 integrin, paxillin, and alpha-actinin during formation and disassembly of adhesions in migrating cells. *J Cell Biol* **153**, 1427-1440.
- Lawson, C., Lim, S.T., Uryu, S., Chen, X.L., Calderwood, D.A., and Schlaepfer, D.D. (2012). FAK promotes recruitment of talin to nascent adhesions to control cell motility. *J Cell Biol* **196**, 223-232.
- Lee, H.S., Lim, C.J., Puzon-McLaughlin, W., Shattil, S.J., and Ginsberg, M.H. (2009). RIAM activates integrins by linking talin to ras GTPase membrane-targeting sequences. *J Biol Chem* **284**, 5119-5127.
- Mitra, S.K., and Schlaepfer, D.D. (2006). Integrin-regulated FAK-Src signaling in normal and cancer cells. *Curr Opin Cell Biol* **18**, 516-523.
- Morimatsu, M., Mekhdjian, A.H., Chang, A.C., Tan, S.J., and Dunn, A.R. (2015). Visualizing the interior architecture of focal adhesions with high-resolution traction maps. *Nano Lett* **15**, 2220-2228.
- Moser, M., Legate, K.R., Zent, R., and Fassler, R. (2009). The tail of integrins, talin, and kindlins. *Science* **324**, 895-899.
- Parsons, J.T. (2003). Focal adhesion kinase: the first ten years. *J Cell Sci* **116**, 1409-1416.
- Parsons, J.T., Horwitz, A.R., and Schwartz, M.A. (2010). Cell adhesion: integrating cytoskeletal dynamics and cellular tension. *Nat Rev Mol Cell Biol* **11**, 633-643.
- Pasapera, A.M., Schneider, I.C., Rericha, E., Schlaepfer, D.D., and Waterman, C.M. (2010). Myosin II activity regulates vinculin recruitment to focal adhesions through FAK-mediated paxillin phosphorylation. *J Cell Biol* **188**, 877-890.
- Plotnikov, S.V., Pasapera, A.M., Sabass, B., and Waterman, C.M. (2012). Force fluctuations within focal adhesions mediate ECM-rigidity sensing to guide directed cell migration. *Cell* **151**, 1513-1527.
- Riveline, D., Zamir, E., Balaban, N.Q., Schwarz, U.S., Ishizaki, T., Narumiya, S., Kam, Z., Geiger, B., and Bershadsky, A.D. (2001). Focal contacts as mechanosensors: externally applied local mechanical force induces growth of focal contacts by an mDia1-dependent and ROCK-independent mechanism. *J Cell Biol* **153**, 1175-1186.
- Saltel, F., Mortier, E., Hytonen, V.P., Jacquier, M.C., Zimmermann, P., Vogel, V., Liu, W., and Wehrle-Haller, B. (2009). New PI(4,5)P2- and membrane proximal integrin-binding motifs in the talin head control beta3-integrin clustering. *J Cell Biol* **187**, 715-731.
- Schiller, H.B., Friedel, C.C., Boulegue, C., and Fassler, R. (2011). Quantitative proteomics of the integrin adhesome show a myosin II-dependent recruitment of LIM domain proteins. *EMBO Rep* **12**, 259-266.
- Schiller, H.B., Hermann, M.R., Polleux, J., Vignaud, T., Zanivan, S., Friedel, C.C., Sun, Z., Raducanu, A., Gottschalk, K.E., Thery, M., *et al.* (2013). beta1- and alpha-v-class integrins cooperate to regulate myosin II during rigidity sensing of fibronectin-based microenvironments. *Nat Cell Biol* **15**, 625-636.
- Schlaepfer, D.D., and Mitra, S.K. (2004). Multiple connections link FAK to cell motility and invasion. *Curr Opin Genet Dev* **14**, 92-101.
- Shattil, S.J., Kim, C., and Ginsberg, M.H. (2010). The final steps of integrin activation: the end game. *Nat Rev Mol Cell Biol* **11**, 288-300.

- Stricker, J., Aratyn-Schaus, Y., Oakes, P.W., and Gardel, M.L. (2011). Spatiotemporal constraints on the force-dependent growth of focal adhesions. *Biophys J* *100*, 2883-2893.
- Sun, Z., Guo, S.S., and Fassler, R. (2016). Integrin-mediated mechanotransduction. *J Cell Biol* *215*, 445-456.
- Tadokoro, S., Shattil, S.J., Eto, K., Tai, V., Liddington, R.C., de Pereda, J.M., Ginsberg, M.H., and Calderwood, D.A. (2003). Talin binding to integrin beta tails: a final common step in integrin activation. *Science* *302*, 103-106.
- Thievessen, I., Thompson, P.M., Berlemont, S., Plevock, K.M., Plotnikov, S.V., Zemljic-Harpf, A., Ross, R.S., Davidson, M.W., Danuser, G., Campbell, S.L., *et al.* (2013). Vinculin-actin interaction couples actin retrograde flow to focal adhesions, but is dispensable for focal adhesion growth. *J Cell Biol* *202*, 163-177.
- Thomas, W. (2008). Catch bonds in adhesion. *Annu Rev Biomed Eng* *10*, 39-57.
- Thomas, W.E., Vogel, V., and Sokurenko, E. (2008). Biophysics of catch bonds. *Annu Rev Biophys* *37*, 399-416.
- Tschammer, N., Galinec, S., Weigert, S., Muller, Y., You, C., Piehler, J., and Breitsprecher, D. (2016). One-step, purification-free and site-specific labeling of polyhistidine-tagged proteins for MST. *Protein Labeling*.
- Turner, C.E., Glenney, J.R., Jr., and Burridge, K. (1990). Paxillin: a new vinculin-binding protein present in focal adhesions. *J Cell Biol* *111*, 1059-1068.
- Vogel, V., and Sheetz, M. (2006). Local force and geometry sensing regulate cell functions. *Nat Rev Mol Cell Biol* *7*, 265-275.
- Webb, D.J., Donais, K., Whitmore, L.A., Thomas, S.M., Turner, C.E., Parsons, J.T., and Horwitz, A.F. (2004). FAK-Src signalling through paxillin, ERK and MLCK regulates adhesion disassembly. *Nat Cell Biol* *6*, 154-161.
- Whitwood, A.J., Singh, A.K., Brown, D.G., and Goult, B.T. (2018). Chlamydial virulence factor TarP mimics talin to disrupt the talin-vinculin complex. *FEBS letters* *592*, 1751-1760.
- Wiseman, P.W., Brown, C.M., Webb, D.J., Hebert, B., Johnson, N.L., Squier, J.A., Ellisman, M.H., and Horwitz, A.F. (2004). Spatial mapping of integrin interactions and dynamics during cell migration by image correlation microscopy. *J Cell Sci* *117*, 5521-5534.
- Yan, J., Yao, M., Goult, B.T., and Sheetz, M.P. (2015). Talin Dependent Mechanosensitivity of Cell Focal Adhesions. *Cell Mol Bioeng* *8*, 151-159.
- Yao, M., Goult, B.T., Chen, H., Cong, P., Sheetz, M.P., and Yan, J. (2014). Mechanical activation of vinculin binding to talin locks talin in an unfolded conformation. *Scientific reports* *4*, 4610.
- Yao, M., Goult, B.T., Klapholz, B., Hu, X., Toseland, C.P., Guo, Y., Cong, P., Sheetz, M.P., and Yan, J. (2016). The mechanical response of talin. *Nature communications* *7*, 11966.
- Zacharchenko, T., Qian, X., Goult, B.T., Jethwa, D., Almeida, T.B., Ballestrem, C., Critchley, D.R., Lowy, D.R., and Barsukov, I.L. (2016). LD Motif Recognition by Talin: Structure of the Talin-DLC1 Complex. *Structure* *24*, 1130-1141.
- Zaidel-Bar, R., Cohen, M., Addadi, L., and Geiger, B. (2004). Hierarchical assembly of cell-matrix adhesion complexes. *Biochem Soc Trans* *32*, 416-420.
- Zhu, J., Luo, B.H., Xiao, T., Zhang, C., Nishida, N., and Springer, T.A. (2008). Structure of a complete integrin ectodomain in a physiologic resting state and activation and deactivation by applied forces. *Mol Cell* *32*, 849-861.

# Kindlin-1 Regulates Epidermal Growth Factor Receptor Signaling

Magdalene Michael<sup>1</sup>, Rumena Begum<sup>1,2</sup>, Grace K. Chan<sup>1</sup>, Austin J. Whitewood<sup>3</sup>, Daniel R. Matthews<sup>4</sup>, Benjamin T. Goult<sup>3</sup>, John A. McGrath<sup>1</sup> and Maddy Parsons<sup>2,4</sup>



JID Open

Kindler syndrome is an autosomal recessive genodermatosis that results from mutations in the *FERMT1* gene encoding t kindlin-1. Kindlin-1 localizes to focal adhesion and is known to contribute to the activation of integrin receptors. Most cases of Kindler syndrome show a reduction or complete absence of kindlin-1 in keratinocytes, resulting in defective integrin activation, cell adhesion, and migration. However, roles for kindlin-1 beyond integrin activation remain poorly defined. In this study we show that skin and keratinocytes from Kindler syndrome patients have significantly reduced expression levels of the EGFR, resulting in defective EGF-dependent signaling and cell migration. Mechanistically, we show that kindlin-1 can associate directly with EGFR in vitro and in keratinocytes in an EGF-dependent, integrin-independent manner and that formation of this complex is required for EGF-dependent migration. We further show that kindlin-1 acts to protect EGFR from lysosomal-mediated degradation. This shows a new role for kindlin-1 that has implications for understanding Kindler syndrome disease pathology.

*Journal of Investigative Dermatology* (2019) 139, 369–379; doi:10.1016/j.jid.2018.08.020

## INTRODUCTION

Kindler syndrome (KS) (OMIM 173650) is a rare autosomal recessive skin disorder for which there is currently no cure. Genome-wide linkage analysis showed that KS is caused by an abnormality in the actin cytoskeleton and its association with the extracellular matrix due to a deficiency or defect in the focal adhesion protein kindlin-1 (also known as fermitin family homologue 1) (Jobard et al., 2003; Siegel et al., 2003). Clinical features of KS range from trauma-induced blistering, progressive poikiloderma and skin atrophy, photosensitivity, destructive periodontal disease, severe colitis, and squamous cell carcinoma (Ashton, 2004; Lai-Cheong et al., 2007). Since identifying the *FERMT1* gene, at least 170 patients and 60 mutations have been reported. These mutations include nonsense, frameshift splice site, and internal deletion changes all resulting in loss of expression (Has et al., 2011; Techanukul et al., 2011). The human *FERMT1* gene encodes the protein kindlin-1, and other members of this protein family include kindlin-2 and kindlin-3 (Siegel et al., 2003). Although related, these proteins exhibit differential expression patterns: kindlin-1 expression is predominantly

restricted to epithelial cells, kindlin-2 is widely expressed, and kindlin-3 is present in hematopoietic and endothelial cells (Bialkowska et al., 2010; Lai-Cheong et al., 2009; Siegel et al., 2003; Wiebe et al., 2008). Both kindlin-1 and kindlin-2 localize to focal adhesions, and kindlin-2 is also recruited to cell-cell junctions (Brahme et al., 2013; Lai-Cheong et al., 2008), whereas kindlin-3 localizes to podosomes (Meves et al., 2009). All kindlins have a bipartite FERM (i.e., 4.1 protein, ezrin, radixin, moesin) domain consisting of four subdomains (F0, F1, F2, and F3) that are present in many proteins involved in cytoskeletal organization (Baines et al., 2014; Goult et al., 2009). The kindlin F2 subdomain differs from other FERM domain proteins by an insertion of a pleckstrin homology (i.e., PH) domain that binds phosphoinositide phosphates (Meves et al., 2009).

Kindlins have all been shown to bind directly to the cytoplasmic domain of  $\beta$ -integrin subunits and contribute to integrin activation (Rognoni et al., 2016). In normal skin, kindlin-1 localizes in basal keratinocytes at the dermal-epidermal junction and accumulates at cell-matrix adhesion sites. In isolated keratinocytes, kindlin-1 localizes to the cell leading edge and focal adhesions (Larjava et al., 2008). Depletion of kindlin-1 leads to reduced proliferation, adhesion, and spreading and to reduced directed migration, with the cells displaying multiple leading edges and multipolar shapes (Has et al., 2008; Herz et al., 2006; Zhang et al., 2016). The role of kindlin-1 in integrin-mediated processes provides explanation for some of the clinical features observed in patients with KS. Potential non-integrin-related roles for kindlin-1 in controlling cell behavior remain unclear.

In this study we performed mass spectrometry analysis of keratinocytes from KS patients and identified significantly reduced levels of the epidermal growth factor receptor (EGFR) in KS samples. Further analysis showed defective downstream signaling of EGFR and attenuated cell responses to EGF stimulation. The expression of kindlin-1 in KS cells was able to restore EGFR expression levels and responses to EGF. Our

<sup>1</sup>Randall Division of Cell and Molecular Biophysics, King's College London, Guy's Campus, London, UK; <sup>2</sup>St. Johns Institute of Dermatology, King's College London, Guy's Campus, London, UK; <sup>3</sup>School of Biosciences, University of Kent, Canterbury, Kent, UK; and <sup>4</sup>Nikon Imaging Centre, King's College London, Guy's Campus, London, UK

Correspondence: Maddy Parsons, Randall Division of Cell and Molecular Biophysics, New Hunts House, King's College London, Guy's Campus, London, UK, SE1 1UL. E-mail: maddy.parsons@kcl.ac.uk

Abbreviations: EGFR, epidermal growth factor receptor; FRET, fluorescence resonance energy transfer; IP, immunoprecipitation; KS, Kindler syndrome; MST, microscale thermophoresis; PBS, phosphate buffered saline; WT, wild type

Received 7 May 2018; revised 9 August 2018; accepted 10 August 2018; accepted manuscript published online 21 September 2018; corrected proof published online 31 October 2018

© 2018 The Authors. Published by Elsevier, Inc. on behalf of the Society for Investigative Dermatology. This is an open access article under the CC BY license (<http://creativecommons.org/licenses/by/4.0>).

[www.jidonline.org](http://www.jidonline.org) 369



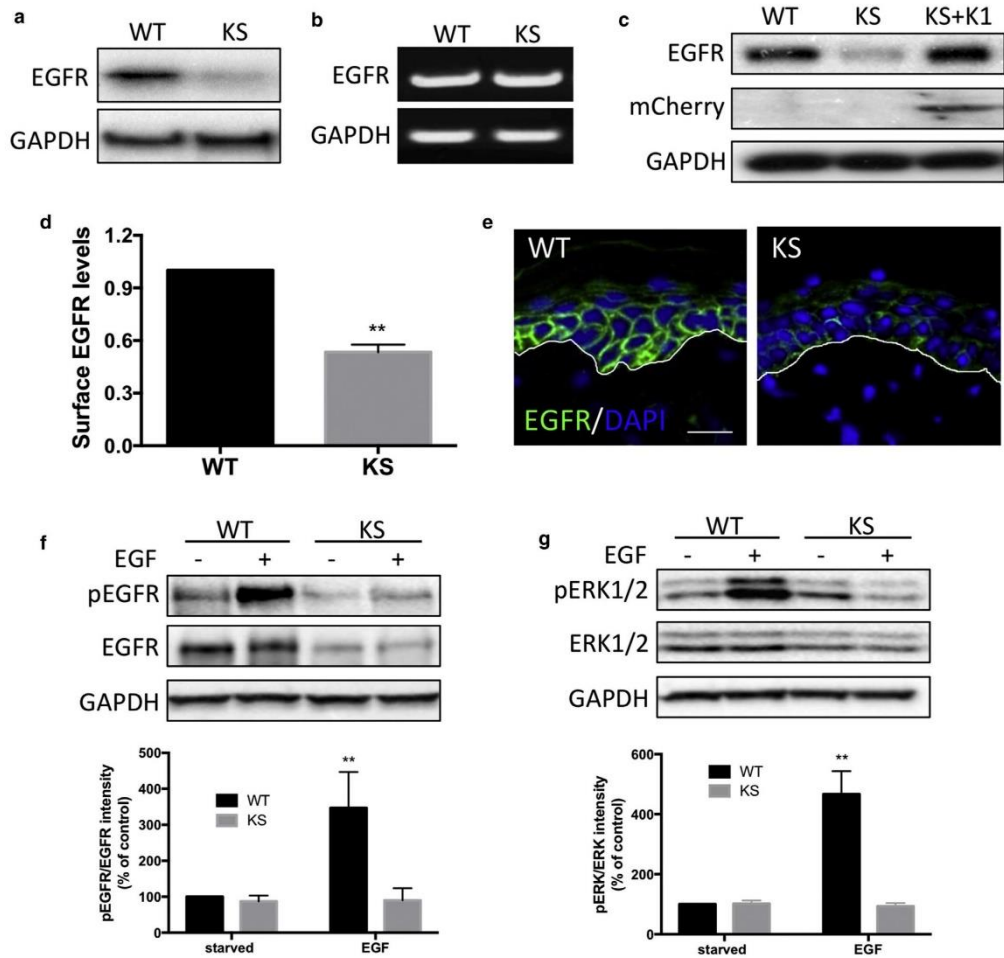


**Figure 1. EGFR levels are reduced in keratinocytes lacking kindlin-1.** (a, b) Levels of (a) EGFR protein and (b) mRNA in WT and KS keratinocytes. (c) Western blot of EGFR levels in WT, KS, KS re-expressing mCherry–kindlin-1 cells. (d) Quantification of EGFR surface levels in WT and KS cells by FACS. (e) Immunostaining of WT and KS skin for EGFR (green) and DAPI (blue). White line indicates dermal-epidermal junction. (f, g) Analysis of (f) EGFR and (g) ERK1/2 phosphorylation in WT and KS cells after 10 minutes of EGF stimulation. GAPDH was used as a loading control for Western blots. Scale bar = 20  $\mu$ m. Data are means  $\pm$  standard error of the mean. \*\* $P < 0.01$  by  $t$  test. EGFR, epidermal growth factor receptor; KS, Kindler syndrome; WT, wild type.

investigations showed a direct interaction between kindlin-1 and EGFR at the plasma membrane that acts to protect EGFR from lysosomal degradation, independent of kindlin-1 binding to integrins. These data provide new insight into kindlin-1 function in keratinocytes and may provide new avenues for pursuit of therapeutic strategies to treat KS patients.

#### RESULTS AND DISCUSSION

##### KS keratinocytes have reduced levels of EGFR and attenuated response to EGF stimulation

To identify new pathways downstream of kindlin-1, we profiled lysates of keratinocytes from healthy donors (wild type

[WT]) and two different KS patients using mass spectrometry. This analysis showed a reduction in protein levels of EGFR in KS keratinocytes, which was verified using Western blotting (Figure 1a). However, no change in mRNA levels of EGFR was detected in KS cells by semiquantitative reverse transcriptase–PCR (Figure 1b). Analysis of normal human lung (16HBE) and breast (MCF10A) epithelial cell lines also showed a reduction of EGFR levels upon small interfering RNA depletion of kindlin-1 (see Supplementary Figure S1a and b online), suggesting a common role for kindlin-1 in regulating EGFR levels in human epithelial cells. Exogenous expression of kindlin-1 in keratinocytes restored EGFR levels

(Figure 1c), thereby specifically attributing this phenotype to kindlin-1 expression. Taken together, these findings show a global reduction in EGFR levels when kindlin-1 is absent or depleted. Further analysis by FACS analysis confirmed a reduction in EGFR surface levels in KS keratinocytes (Figure 1d). Moreover, immunostaining of healthy donor and KS patient skin sections showed a striking reduction of EGFR in the basal keratinocytes in KS skin compared with WT skin (Figure 1e).

EGFR regulates a number of signaling pathways, which act to regulate keratinocyte survival, growth, adhesion, and migration (Bakker et al., 2017). To examine the effect of loss of kindlin-1 on EGFR signaling, cells were starved overnight and stimulated with EGF for 10 minutes, and the phosphorylations of EGFR (Figure 1f) and its downstream effector ERK1/2 (Figure 1g) were assessed. As expected, EGFR phosphorylation in response to EGF was significantly reduced in KS keratinocytes, in line with the constitutively lower levels of EGFR in these cells (Figure 1f), with a resulting loss of EGF-dependent ERK1/2 phosphorylation (Figure 1g). To determine whether this loss of EGF responsiveness had an impact on functional cell behavior, we assessed migratory responses to EGF by time lapse microscopy. Data showed that KS cells exhibited higher migration speeds compared with WT cells under starved conditions, as we have shown previously (see Supplementary Figure 1c and d) (Maiuri et al., 2012). Addition of EGF led to increased WT keratinocyte migration rates but had no effect on KS cell speed, confirming a failure to respond to EGF in the absence of kindlin-1. Migration speeds were rescued in KS cells re-expressing mCherry-kindlin-1, confirming that the observed phenotypes were due to loss of kindlin-1 expression (see Supplementary Figure 1d and e). Together, these findings show that kindlin-1-deficient human keratinocytes have reduced EGFR levels, resulting in impaired responses to EGF.

#### Kindlin-1 regulates subcellular distribution and dynamics of EGFR

To determine whether the reduced levels of EGFR in KS cells coincided with altered subcellular distribution, we analyzed the localization of EGFR in sparsely plated WT and KS keratinocytes after EGF stimulation. Total and surface levels of EGFR were quantified by measuring the mean fluorescence intensities of either the whole cell area or plasma membrane. Consistent with the Western blot analyses (Figure 1a and f), EGF stimulation did not alter the relative intensity of EGFR in either cell type, but there was a marked reduction in total EGFR levels in KS cells (Figure 2a–c). In starved WT cells, EGFR was localized at the plasma membrane and cytoplasmic compartments, whereas KS cells showed very weak EGFR staining at the plasma membrane with increased accumulation in perinuclear compartments (Figure 2a–c). After EGF treatment, EGFR redistributed from the plasma membrane into perinuclear compartments in WT cells, coincident with reduced EGFR at the plasma membrane (Figure 2c). In contrast, EGFR remained in the perinuclear compartments of KS cells after EGF stimulation (Figure 2c). Kindlin-2 has been shown previously to be expressed at normal levels in KS patients (Lai-Cheong et al., 2008), suggesting that it is not disrupted upon loss of kindlin-1 but also

cannot functionally replace kindlin-1 in these cells. However, to determine whether loss of kindlin-1 and resulting EGFR mislocalization could be compensated for overexpression of kindlin-2, WT and KS cells were transfected with GFP–kindlin-2, and total and surface EGFR levels were analyzed by confocal microscopy. Data showed that kindlin-2 overexpression had no effect on EGFR levels or localization in either WT or KS keratinocytes (see Supplementary Figure 1e and f), suggesting that kindlin-2 cannot compensate for loss of kindlin-1 in these cells. Indeed, functional, nonredundant roles for kindlin-1 and -2 have also been suggested in the context of integrin binding in keratinocytes (Bandyopadhyay et al., 2012), further supporting the notion that these proteins have different roles in epithelial cell function.

EGFR is known to undergo endocytosis and, depending on the cell type and EGF concentration, can be recycled back to the plasma membrane or routed for degradation (Bakker et al., 2017). To determine whether kindlin-1 may play a role in regulating EGFR dynamics at the plasma membrane, we analyzed WT and KS cells stably expressing EGFR–GFP after fluorescence recovery after photobleaching at the plasma membrane under growth conditions. Despite expressing lower levels of EGFR, KS cells showed enhanced early recovery profiles compared with WT and reduced T1/2 speed without changing the mobile fraction (see Supplementary Figure S2a online). We confirmed that this effect of kindlin-1 was not due to global changes in clathrin-mediated endocytosis, because transferrin-Texas Red uptake assays showed no differences between WT and KS cells (see Supplementary Figure S2b), indicating that global receptor internalization was unperturbed by the loss of kindlin-1. Inhibition of dynamin activity, but not recycling (through dynasore and primaquine treatment, respectively), resulted in a slower fluorescence recovery T1/2 and reduced EGFR mobile fraction (see Supplementary Figure 2c and d). These data show that loss of kindlin-1 destabilizes EGFR under steady state conditions and that inhibition of EGFR internalization, but not receptor recycling, reduces EGFR dynamics at the plasma membrane.

To determine potential kindlin-1-dependent changes in EGFR subcellular compartmentalization, we used colocalization analysis to study EGFR localization with key endocytic markers at time points after EGFR stimulation: early endosomes (EEA1, 10 minutes), lysosomes (LAMP1, 30 minutes), and recycling endosomes (Rab11a, 1 hour). Pearson correlation analysis showed significantly reduced co-localization between EGFR/EEA1 and EGFR/Rab11 in KS compared with WT cells (Figure 2d and f). In contrast, a significant increase in colocalization between EGFR and LAMP1 was observed in KS cells compared with WT (Figure 2e). To further explore the real-time dynamics of the EGFR-positive compartments after EGF stimulation, we performed live cell imaging on WT and KS cells expressing EGFR–GFP and cherry-Rab11a and labeled with LysoTracker Far Red (Molecular Probes, Eugene, OR), for 30 minutes after EGF stimulation. Upon addition of EGF, EGFR-positive vesicles moved in a retrograde fashion from the plasma membrane into the cell interior, increasing in number and size over time (Figure 2g and h and see Supplementary Movie S1 online). In contrast, EGFR-labeled

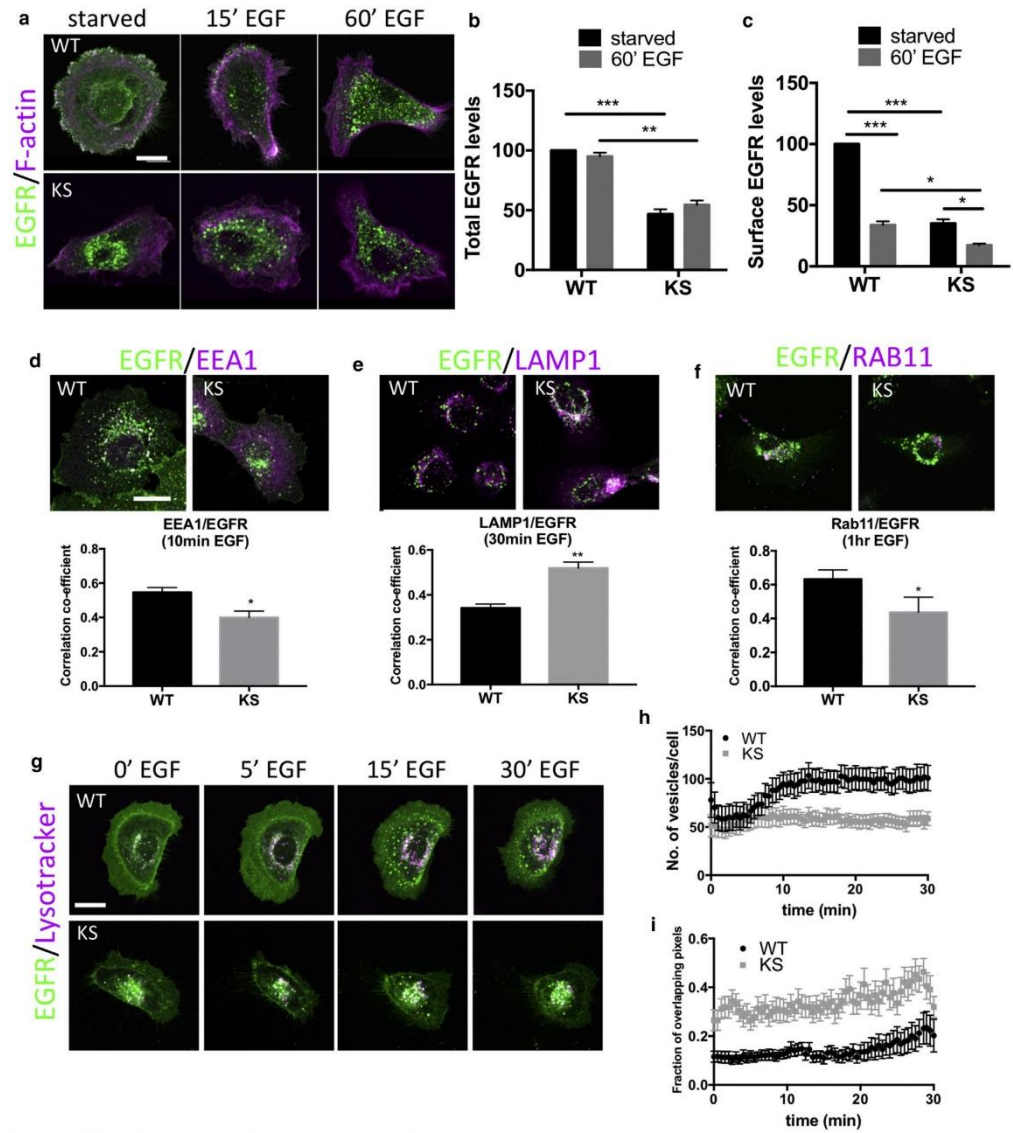


**Figure 2. EGFR localizes to lysosomal compartments in KS cells.** (a) Immunostaining of EGFR (green) and F-actin (magenta) and (b) quantification of EGFR surface and (c) total levels from images in WT and KS cells after EGF stimulation. (d–f) Immunostaining and quantification of EGFR (green) localization with (d) EEA1, (e) LAMP1, or (f) Rab11a vesicles (all shown in magenta) after EGF stimulation (10 ng/ml). Graphs beneath images show Pearson correlation coefficient analysis of EGFR and specified compartments. N = 30 cells for each. (g) Still images from movies of WT and KS cells expressing EGFR-GFP labeled with LysoTracker Deep Red (Molecular Probes, Eugene, OR) (magenta) after EGF stimulation. (h) Quantification of the number of EGFR-positive vesicles and (i) EGFR/LysoTracker co-localization from WT and KS movies. N = 25 cells over three independent experiments. Data are all means  $\pm$  standard error of the mean. \*\*\* $P$  < 0.001, \*\* $P$  < 0.01, \*\*\* $P$  < 0.001 using two-way analysis of variance (b and c) and  $t$  test (d–f). Scale bars = 10  $\mu$ m throughout. EGFR, epidermal growth factor receptor; hr, hour; KS, Kindler syndrome; min, minute; WT, wild type.

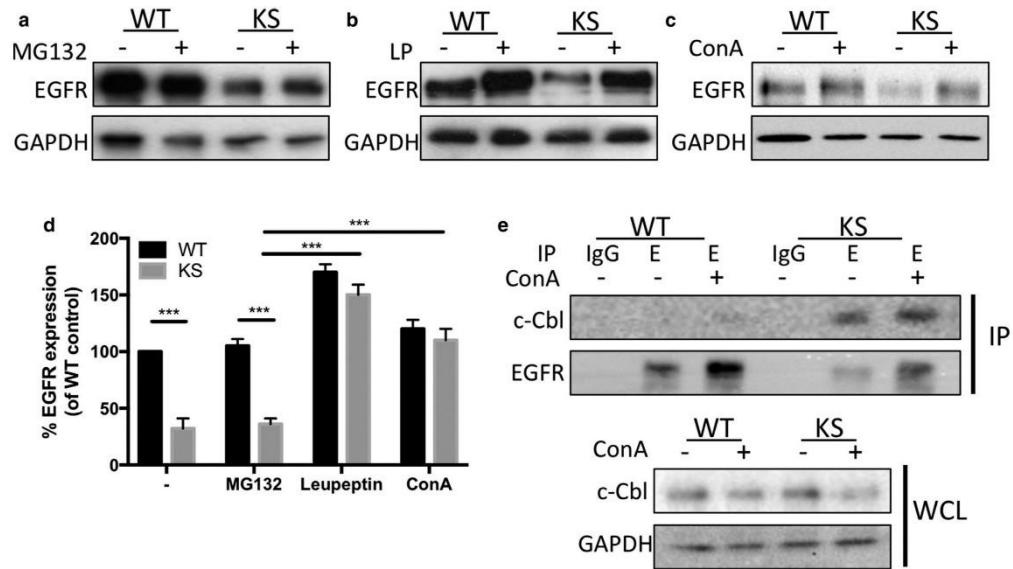


**Figure 3.** EGFR is degraded in the lysosome in KS cells through increased Cbl interactions. (a–c) Treatment of WT and KS cells with (a) proteasome inhibitor (MG132; 10  $\mu$ mol/L, 24 hours) or lysosome inhibitors (b) leupeptin (100 nmol/L, 24 hours) (c) or concanamycin A (100 nmol/L, 24 hours) and analysis of EGFR levels by Western blotting. (d) Quantification of Western blots in a–c from four independent experiments. (e) Immunoprecipitation of EGFR from WT and KS cells after DMSO (–) or ConA treatment (100 nmol/L, 24 hours; +) and immunoblotting for c-Cbl. Blots beneath show c-Cbl levels in whole cell lysates. ConA, concanamycin A; EGFR, epidermal growth factor receptor; IP, immunoprecipitation; KS, Kindler syndrome; LP, leupeptin; WT, wild type.

vesicles in KS cells displayed random movement in the perinuclear region throughout the 30 minutes of observation, with the size and vesicle number remaining largely unaltered (Figure 2g and h, and see [Supplementary Movie S2](#) online). Analysis of overlapping pixels in the EGFR-GFP– and lysotracker-labeled vesicles confirmed the LAMP1 data in fixed cells (Figure 2e), showing a constitutively higher colocalization between EGFR-positive vesicles and lysosomal compartments in KS cells compared with WT cells throughout the period of EGF stimulation (Figure 2i).

#### Kindlin-1 regulates cellular EGFR levels by restricting lysosomal degradation of EGFR

EGFR is subject to ligand-induced degradation via the lysosomal or proteasomal pathways (Singh and Coffey, 2014). Given the increased EGFR within lysosomal compartments in KS cells, we next analyzed whether EGFR was reduced in KS cells because of enhanced protein degradation. Treatment of WT and KS cells with the proteasome inhibitor MG132 did not change EGFR levels in KS cells (Figure 3a and d). However, treatment with lysosomal inhibitors leupeptin or concanamycin A restored EGFR expression in KS cells up to WT levels (Figure 3b–d), suggesting that loss of kindlin-1 leads to increased lysosomal-dependent EGFR degradation. EGFR binds to the E3 ubiquitin ligase c-Cbl in response to EGF, either at the plasma membrane or on early endosomes, which in turn promotes polyubiquitination of EGFR, resulting in degradation (Duan et al., 2003). To determine whether kindlin-1–dependent changes to EGFR altered c-Cbl

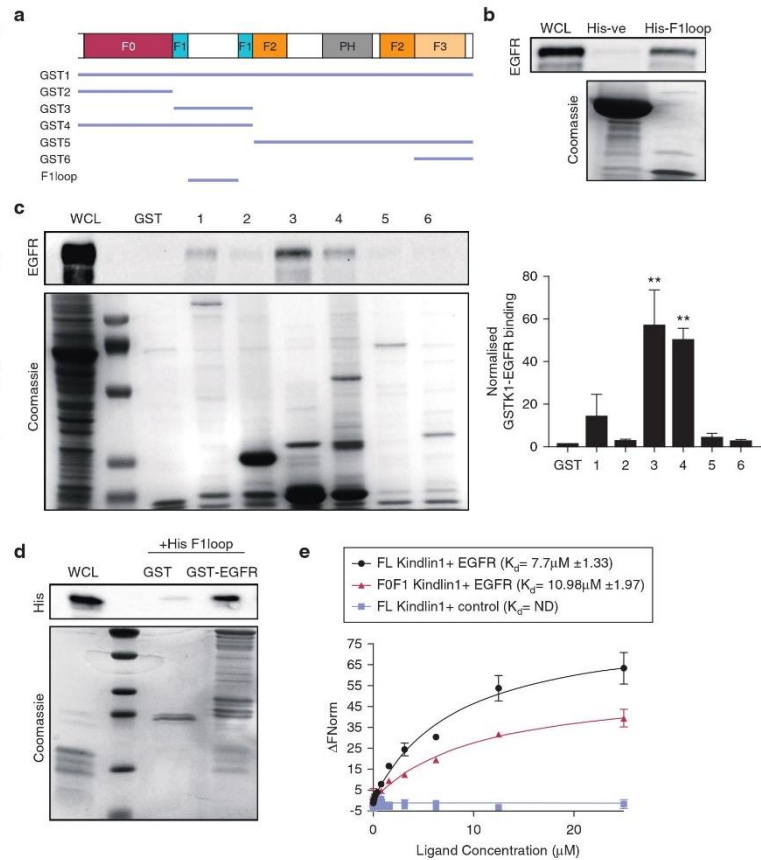
association with the receptor, we analyzed c-Cbl-EGFR binding by co-immunoprecipitation (IP) in WT and KS cells treated with DMSO or concanamycin A under growth conditions. A dramatic increase in c-Cbl binding to EGFR in KS cell lysates was observed, with or without treatment with concanamycin A (Figure 3e), suggesting that increased constitutive c-Cbl binding in the absence of kindlin-1 may result in increased targeting of EGFR for lysosomal degradation.

#### Kindlin-1 directly interacts with EGFR

Kindlin-2 has previously been suggested to directly interact with EGFR through an association with the EGFR kinase domain (Guo et al., 2015). To determine whether kindlin-1 could interact with EGFR, individual domains of kindlin-1 were generated as GST fusion proteins and used to pull out endogenous EGFR from cell lysates (Figure 4a). Full-length GST–kindlin-1 (GST1) bound to EGFR and a consistently strong binding with the F1 domain of kindlin-1 was also observed (GST3) (Figure 4b). The F1 domain contains an unstructured loop that we postulated could be a potential binding region for EGFR (Bouaouina et al., 2012). We tested this hypothesis by expressing a His-tagged F1 loop to capture EGFR from cell lysates. As predicted, the F1 loop bound strongly to EGFR in cell lysates in contrast to the His-kinesin light chain domain that served as a negative control (Figure 4c). To test whether association between kindlin-1 and EGFR was direct, a GST fusion of the EGFR cytoplasmic domain was incubated with His-F1 loop of kindlin-1

**Figure 4. EGFR directly interacts with kindlin-1 via the F1 loop region.**

(a) Diagram of GST- and His-tagged kindlin protein domains were used. (b) GST pull-down of kindlin-1 domains and immunoblotting for EGFR in WT keratinocytes. Quantification of GST-K1 domains and EGFR interaction are shown in the graph. (c) His kinesin light chain (-ve control) or kindlin-1 F1 loop incubated with purified GST-EGFR cytoplasmic domain. (d) In vitro binding of GST-EGFR cytoplasmic tail and His-kindlin F1 loop (His1) using GST pull-down. (e) MST analysis of full-length (black) or F0F1 (red) kindlin-1 and EGFR cytoplasmic tail interaction. R7–R9 of Talin (blue) was used as a control. All data are means  $\pm$  standard error of the mean from three independent experiments.  $**P < 0.01$  using one-way analysis of variance. EGFR, epidermal growth factor receptor; M, mol/L; MST, microscale thermophoresis; ND, not done; WCL, whole cell lysate.



in solution. Pull-down of the GST-EGFR cytoplasmic tail showed a strong interaction with the His-kindlin-1 F1 loop (Figure 4d), indicating a direct interaction between the two proteins. Moreover, assessment of binding kinetics between these proteins by microscale thermophoresis (MST) showed a robust interaction between the EGFR cytoplasmic tail membrane proximal region and both full-length and F0F1 domains of kindlin-1 (Figure 4e). Taken together, these data show that kindlin-1 binds directly to the EGFR cytoplasmic domain via the kindlin-1 F1 loop. Moreover, the fact that c-Cbl binding is significantly and constitutively enhanced in cells lacking kindlin-1 (Figure 3e) suggests that binding of kindlin-1 to the EGFR cytoplasmic tail restricts binding of c-Cbl, leading to retention of EGFR at the plasma membrane, enhanced signaling, and reduced degradation.

To further define when and where kindlin-1 may associate with EGFR in cells, we analyzed their relative subcellular distributions using live-cell structure illumination microscopy superresolution imaging of KS cells expressing mCherry-kindlin-1 and EGFR-GFP. Images and subsequent analysis

showed that co-localization between the two proteins occurred within the first 15 minutes of EGF stimulation at the plasma membrane (Figure 5a, and see Supplementary Figure S3a online). We were also unable to detect any kindlin-1 co-localizing with EGFR within endosomes. IP of endogenous EGFR from KS cells re-expressing mCherry-kindlin-1 also showed that kindlin-1 forms a complex with EGFR in a time-dependent manner, with strongest interactions occurring 5 minutes after EGF stimulation and resuming to basal levels by 60 minutes (Figure 5b). However, we were unable to detect kindlin-2 in these immunoprecipitated complexes (see Supplementary Figure S3b), suggesting that the binding of kindlin-1 may be specific in keratinocytes.

Analysis of direct binding between the two proteins using fluorescence lifetime imaging microscopy to analyze fluorescence resonance energy transfer (FRET) also showed a direct interaction between EGFR-GFP and mCherry-kindlin-1 in cells that was increased after 10 minutes of EGF stimulation (Figure 5c). Moreover, kindlin-1-to-EGFR binding was independent of kindlin-1-to-integrin binding, because

FRET-fluorescence lifetime imaging microscopy analysis showed strong, constitutive interaction between EGFR-GFP and mCherry-W612Akindlin-1, which is defective in integrin binding (see Supplementary Figure S3c) (Bouaouina et al., 2012; Huet-Calderwood et al., 2014). Further analysis of these cells showed that expression of mCherry-W612Akindlin-1 in KS cells was also able to partially restore the migration response to EGF (see Supplementary Figure S3d), further indicating that kindlin-1-to-EGFR binding plays an important role in control of EGF responses and that this can act at least in part independently of kindlin-1-to-integrin complex formation.

To explore whether EGFR kinase activity regulates kindlin-1-EGFR binding, we assessed the co-localization between endogenous EGFR and GFP-kindlin-1 expressed in KS cells in the presence of either DMSO or AG1478, an EGFR-specific tyrosine kinase inhibitor. Inhibition of EGFR activity resulted in an increase in co-localization between EGFR and GFP-kindlin-1 (Figure 5d), potentially through enrichment of EGFR at the plasma membrane. Finally, because kindlin-2 has previously been suggested to be tyrosine phosphorylated (Liu et al., 2015; Qu et al., 2014), we sought to determine whether the same modification on kindlin-1 could occur through EGFR-mediated signaling. IP analysis showed that GFP-kindlin-1 was tyrosine phosphorylated under basal conditions (Figure 5e). However, treatment with AG1478 had no effect on kindlin-1 tyrosine phosphorylation levels, suggesting that kindlin-1 is constitutively tyrosine phosphorylated in growth conditions and that this does not depend on signals downstream of active EGFR.

In summary, our data show a direct interaction between kindlin-1 and EGFR that acts to restrict c-Cbl-EGFR association and thus protect EGFR from lysosomal degradation. Although our data do not allow us to conclusively state that EGFR-Cbl binding in KS cells is constitutive, our data support the notion that the presence of kindlin-1 is required to ensure correct regulation of the EGFR-Cbl complex. Our proposed model is that binding of kindlin-1 to the EGFR cytoplasmic tail can displace Cbl binding and potentially act to stabilize EGFR at the membrane and subsequently control modulation of EGFR routing to the endo-lysosomal system. Loss of kindlin-1 expression in patients with KS results in lower EGFR levels in the skin and isolated keratinocytes, resulting in loss of EGF-induced signaling and migratory behavior. This newly described function for kindlin-1 is very likely to contribute to the clinical features observed in KS patients in agreement with our recent discovery of an EGFR loss-of-function mutation in patients with skin fragility (Campbell et al., 2014). Based on our data, investigations of strategies to modulate EGFR stability may represent a valid therapeutic avenue for treating skin fragility patients in future.

## MATERIALS AND METHODS

### Plasmids and small interfering RNAs

GFP-kindlin-1, GFP-kindlin-1W612A, and GFP-kindlin-2 constructs were generously provided by David Calderwood (Yale University, New Haven, CT [Bouaouina et al., 2012; Huet-Calderwood et al., 2014]). EGFR-GFP was provided by Andy Reynolds (AstraZeneca, Cambridge, UK [Reynolds et al., 2003]). EGFR cytoplasmic domain GST fusion constructs were generously provided by Bob

Adelstein (National Institutes of Health, Bethesda, MD [Kim et al., 2012]). Murine full-length kindlin-1 and kindlin-1 FOF1 (1-275) were cloned into a pET151 vector (Invitrogen, Waltham, MA). Cherry-kindlin1 and cherry-kindlin1W612A lentiviral constructs have been previously described (Zhang et al., 2016). mCherry-Rab11a was a gift from Patrick Caswell (University of Manchester, Manchester, UK [Caswell et al., 2007]).

### Reverse Transcriptase PCR

RNA extraction from cells was performed using RNeasy Mini Kit (Qiagen, Hilden, Germany) and reverse transcription of RNA was carried out using RevertAid Reverse Transcriptase (Thermo Fisher Scientific, Waltham, MA), according to the manufacturer's instructions. Reverse transcriptase-PCR primer sequences are as follows: GAPDH (forward 5'-AGAAGGCTGGGGCTCATTTG-3', reverse 5'-AGGGCCATCCACAGTCTTC-3'); kindlin-1 (forward 5'-TCAACAGTGGAAATGAACTGG-3', reverse 5'-TACATGCTGGCACGTTAGG-3').

### Cell culture and transfections

Immortalized WT keratinocytes and those from a KS patient (harboring the mutation c.676insC/c.676insC) have both been previously described (Lai-Cheong et al., 2007; Zhang et al., 2016). The original study in which the cells were isolated was conducted according to the principles of the Declaration of Helsinki. All cells were obtained under the St. Thomas Hospital Ethics Committee-approved project "Molecular Basis of Inherited Skin Disease" (07/H0802/104) after participating individuals gave written, informed consent. Both cell lines were grown in serum-free keratinocyte growth medium containing EGF and bovine pituitary extract (Gibco, Waltham, MA) and supplemented with penicillin and streptomycin. HEK293T cells were cultured in DMEM supplemented with penicillin and streptomycin, L-glutamine, and 10% fetal bovine serum. 16HBE cells were grown in minimum essential media supplemented with penicillin and streptomycin, L-glutamine, and 10% FBS. MCF10A cells were cultured in DMEM supplemented with penicillin and streptomycin, L-glutamine, 5% horse serum, EGF (20 ng/ml), hydrocortisone (0.5 µg/ml), cholera toxin (100 ng/ml) and insulin (10 µg/ml). HEK 293T transfections were performed using polyethylenimine transfection reagent at a 1:7 ratio of DNA to polyethylenimine reagent. Keratinocyte transfection of plasmids was carried out using Attractene transfection reagent (Qiagen), and all small interfering RNA transfections were performed using Dharmofect transfection reagent (Dharmacon, Lafayette, CO), in accordance with the manufacturer's instructions. Inhibitors were all purchased from Sigma and used at the following concentrations: leupeptin (100 nmol/L, 4 hours), MG132 (20 µmol/L, 4 hours), concanamycin A (100 nmol/L, 16 hours), dynasore (80 µmol/L, 1 hour), primaquine (100 µmol/L, 1 hour), and AG1478 (5 nmol/L, 1 hour).

### Antibodies

Primary antibodies used were EGFR (for Western blot: Cell Signaling Technologies, Danvers, MA; for IP: Cell Signaling Technology; and for immunofluorescence: Santa Cruz Biotechnology, Dallas, TX), kindlin-2 (Abcam, Cambridge, UK), phospho-EGFR Y1173 (Cell Signaling Technology), phospho-tyrosine (4G10; Millipore, Billerica, MA), GFP (Roche, Basel, Switzerland), HA (Cell Signaling Technology), c-Cbl (Cell Signaling Technology), GAPDH (Genetex, Taiwan, China), HSC70 (Santa Cruz Biotechnology), EEA1 (Cell Signaling Technology), LAMP1 (Cell Signaling Technology), phospho-ERK1/2 (Cell Signaling Technology), ERK1/2 (Cell Signaling Technology),

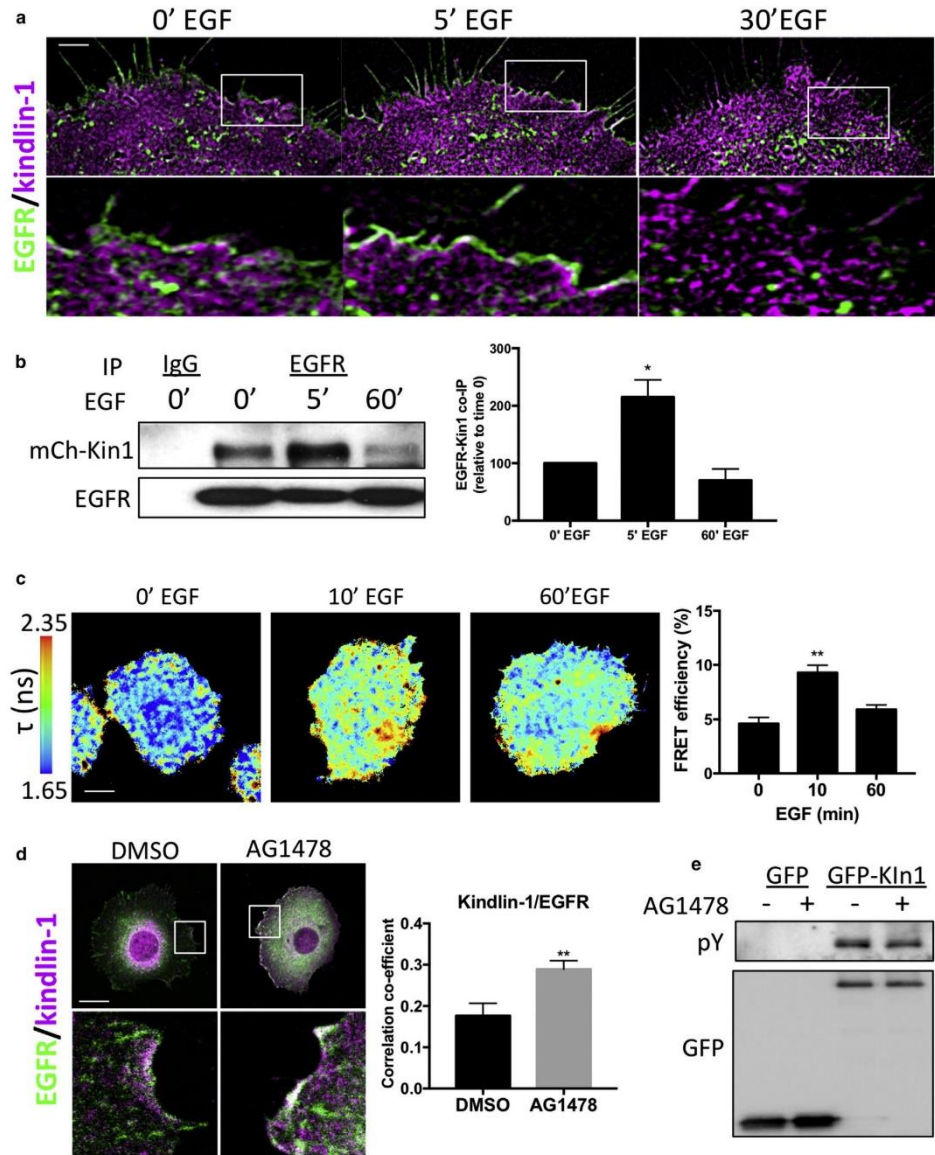


**Figure 5.** EGFR-kindlin-1 binding in human keratinocytes is EGF regulated. (a) SIM imaging of EGFR-GFP (green) and mCherry-kindlin-1 (magenta) after EGF stimulation. Inset boxes shown below each time point. (b) Immunoprecipitation of EGFR from KS cells re-expressing mCherry-kindlin-1 under starved conditions or after EGF stimulation (10 ng/ml). Graph on right shows quantification of five independent experiments. (c) Example lifetime images of KS cells expressing kindlin-GFP and mCherry-kindlin-1 after EGF stimulation. Graph on right shows quantification of 25 cells per condition over three experiments. (d) Example images of KS cells re-expressing mCherry-kindlin-1 (magenta) under growth conditions with DMSO or AG1478 treatment, fixed and stained for EGFR (green). Inset boxes shown below. Graph on right shows quantification of co-localization from 30 cells. (e) Immunoprecipitation of GFP or GFP-kindlin-1 under same conditions as in d, probed for phosphotyrosine (pY) and GFP. \* $P < 0.05$ , \*\* $P < 0.01$  using two-way analysis of variance. Scale bars = 1  $\mu\text{m}$  in a and 10  $\mu\text{m}$  in c and d. EGFR, epidermal growth factor receptor; min, minute; SIM, structure illumination microscopy.

GST (Sigma-Aldrich, St. Louis MO), His (horseradish peroxidase conjugate; Millipore). All anti-species horseradish peroxidase-conjugated secondary antibodies were from Dako (Carpinteria, CA), and all AlexaFluor conjugated antibodies were from Molecular Probes. Other reagents and suppliers were Phalloidin AlexaFluor (Molecular Probes), Hoechst (Sigma-Aldrich), lysotracker deep red (Molecular Probes), transferrin Texas Red (Thermo Fisher Scientific).

#### GST- and His-tagged protein purification

Protein production was induced in *Escherichia coli* BL21 bacterial strains with IPTG (100  $\mu$ mol/L) overnight at 18°C. For GST-tagged proteins, bacterial pellets were resuspended in 50 mmol/L Tris, 300 mmol/L NaCl, pH 8.0 in the presence of protease inhibitors; sonicated; and cleared by centrifugation. The protein solution was then incubated with glutathione Sepharose beads (GE Healthcare, Little Chalfont, UK) for 2 hours at 40°C followed by three washes in 50 mmol/L Tris, 300 mmol/L NaCl, pH 8.0 with 2 mmol/L  $\beta$ -mercaptoethanol. The GST-tagged proteins were either left bound to the beads (for GST pulldown experiments) or eluted with glutathione solution (50 mmol/L Tris, 300 mmol/L NaCl, 40 mmol/L glutathione, pH 8.0) and dialyzed overnight. For His-tagged proteins, bacterial pellets were resuspended in His lysis buffer (25 mmol/L HEPES pH 8.0, 500 mmol/L NaCl, 10 mmol/L imidazole) containing protease inhibitors, sonicated, and cleared by centrifugation. Nickel NTA beads (Qiagen) were incubated with the protein solution for 2 hours at 4°C, followed by three washes in lysis buffer containing 50 mmol/L imidazole. The His-tagged proteins were eluted from the beads with lysis buffer containing 250 mmol/L imidazole, followed by overnight dialysis. For MST analysis, standard nickel-affinity chromatography was used to purify the His-tagged recombinant proteins, as described previously (Banno et al., 2012). Purified samples were analyzed by SDS-PAGE on a 10% gel and stained with Coomassie blue. Protein concentrations were determined using the respective extinction coefficients at 280 nm calculated using ProtParam (<https://web.expasy.org/protparam/>).

#### GFP traps, IP, and Western blotting

Cells were lysed in cold lysis buffer (50 mmol/L Tris-HCl, pH 7.4; 200 mmol/L NaCl, 1% NP-40, 2 mmol/L MgCl<sub>2</sub>, 10% glycerol) containing protease inhibitors and phosphatase inhibitors, and lysates were cleared by centrifugation. For GFP traps, the cleared lysates were incubated with GFP trap beads for 2 hours at 4°C, followed by three washes in lysis buffer. For other IPs, cleared lysates were incubated with either antibody- or species-matched IgG overnight and then incubated for 2 hours with protein A/G beads (pre-blocked with 0.2% bovine serum albumin). Beads were washed three times in lysis buffer and resuspended in sample buffer, boiled for 10 minutes, and resolved on a 12% SDS-PAGE gel. For mass spectrometry analysis, WT and KS lysates were resolved on 10% SDS-PAGE gels and silver stained, and identified bands were excised and sent for processing and analysis to Aberdeen Proteomics (University of Aberdeen, School Medical Sciences, Aberdeen, MD).

#### Flow cytometry

FACS analysis was performed as previously described (Worth et al., 2010). Briefly, cells were scraped with phosphate buffered saline (PBS) and fixed with 4% paraformaldehyde for 20 minutes. Cells were then blocked in PBS containing 2% bovine serum albumin, incubated with primary antibody for 90 minutes, washed three times, and then incubated with secondary antibody for 45 minutes,

followed by three washes and final resuspension in PBS. As a negative control, a secondary antibody-only sample was used, and fluorescence reading from this was used to indicate background fluorescence values. Data were analyzed using FlowJo software (FlowJo, Ashland, OR).

#### Immunofluorescence and microscopy

Cells were plated onto coverslips or optical plastic-bottom dishes coated with human fibronectin (10 ng/ml, Millipore). After respective treatments, cells were either used for live cell imaging or fixed using 4% paraformaldehyde (paraformaldehyde/PBS) for 10 minutes, washed with PBS, and then permeabilized with either methanol at -20°C (for endocytic markers) or 0.2% Triton-X/PBS for 5 minutes. Coverslips were then washed with PBS and blocked with 5% bovine serum albumin/PBS for 30 minutes. The primary and secondary antibodies were diluted in 5% bovine serum albumin/PBS and incubated for 1 hour each at room temperature, with PBS washes between the antibody incubations. Coverslips were mounted onto slides using FluorSave reagent (Calbiochem, San Diego, CA). Cell images, fixed and live, were acquired on the Nikon A1R confocal microscope (Nikon Instruments, Kingston, UK) at excitation wavelengths of 405 nm, 488 nm, 543 nm, and 633 nm using a PlanApo VC 60 $\times$  Oil NA 1.4 objective.

#### Random migration assay

Cells were seeded onto 12-well plates, starved overnight in Opti-MEM (Gibco), and then stimulated with EGF (10 ng/ml) before imaging, which was performed on an Olympus (Tokyo, Japan) IX71 microscope using an automated x,y,z scanning stage (Ludl, Hawthorne, NY). Phase contrast images were acquired using a 10 $\times$  N-Achroplan NA 0.25 objective, and images were taken every 10 minutes for 16 hours using a Sensicam (PCO Cook, Kelheim, Germany) charge-coupled device camera and AQM acquisition software (Andor Bioimaging, Belfast, UK). Single, nondividing cells from the time-lapse movies were then tracked using IQ Tracking Software (Andor Bioimaging). The generated position coordinates for each cell per frame were subject to motion analysis using Wolfram Mathematica 6 notebooks (Wolfram, Champaign, IL) to obtain speed measurements.

#### Fluorescence recovery after photobleaching analysis

Fluorescence recovery after photobleaching experiments were performed on cells stably expressing EGFR-GFP. Live cell images were acquired at 5 seconds per frame for three frames, followed by photobleaching of a circular region of interest of 25 pixels in diameter near the cell leading edge using a 488-nm laser at 100% power. Images were acquired for a further 3 minutes at 5 seconds per frame. The rate of fluorescence recovery was calculated by measuring the fluorescence intensity of the region of interest over time. The fluorescence recovery values were corrected for overall fading across the entire image during the imaging period and were represented as a percentage of the pre-bleached values (the average values of the first three frames), which represented the 100% fluorescence signal. Values were fitted to a mono-exponential equation from which the T<sub>1/2</sub> and the percentage mobile fraction (plateau) values were determined.

#### FRET analysis

FRET efficiency was quantified from KS keratinocytes expressing donor and acceptor fluorophores by measuring time domain fluorescence lifetime with a multiphoton microscope system (TE2000, Nikon). Briefly, cells were fixed in 3.6% formaldehyde for 15 minutes, permeabilized with 0.1% Triton, and quenched with 1 mg/ml sodium borohydride for 10 minutes at room temperature. Cells were



**M Michael et al.**  
Kindlin-1 Stabilizes EGFR

mounted or immunostained for flag detection. Fluorescence lifetime was measured as described previously (Zanet et al., 2012), and histogram data show mean FRET efficiency from denoted numbers of cells per condition in three independent experiments using TRI2 analysis software (Paul Barber, University of Oxford, Oxford, UK).

**Image analysis**

All images were analyzed using Fiji (<https://imagej.net/Fiji>) unless otherwise stated. For quantification of surface levels and total levels of EGFR, images were manually thresholded, and intensity values were calculated per cell area and normalized to the control cells in that sample set. Co-localization analysis was performed on the fixed confocal images using the Coloc2 plugin in Fiji, by either drawing a region of interest around the cells to measure total co-localization within the cell or drawing a 10 pixels wide line along the leading edge to measure co-localization at the leading edge. A Python script was created in-house for the analysis of vesicle size, number, and EGFR-LAMP1 co-localization. Vesicles were identified by wavelet-filtering the images, followed by thresholding and watershed segmentation, using a similar process to that described by Izeddin et al. (2012). After segmentation, vesicle analysis proceeded using a similar methodology as previously published (Rizk et al., 2014).

**Microscale thermophoresis**

Recombinantly expressed kindlin-1 constructs were coupled to an equimolar amount of RED-tris-NTA NT-647 dye (NanoTemper Technologies, München, Germany) via its N-terminal 6×His-Tag in a one-step coupling reaction (Bartoschik et al., 2018). Titrations were performed in PBS (137 mmol/L NaCl, 27 mmol/L KCl, 100 mmol/L Na<sub>2</sub>HPO<sub>4</sub>, 18 mmol/L KH<sub>2</sub>PO<sub>4</sub>) using a constant 50-nmol/L concentration of RED-tris-NTA-coupled kindlin, with increasing concentration of synthetic EGFR peptide (residues 668-711: CMRRRHIVKRTLRLQLQER-ELVEPLTPSGEAPNQALLRILKETE) and final volume of 20 μL. Prepared samples were filled into Monolith NT.115 Capillaries (NanoTemper). Measurements were recorded on a Monolith NT.115 at 25°C, excited under red light, medium MST power, and 40% excitation power. The data were analyzed using MO Affinity Analysis software (NanoTemper) and fitted using the K<sub>d</sub> fit model.

**Statistical analysis**

All statistical tests were performed using either t tests or analysis of variance in GraphPad Prism (GraphPad, La Jolla, CA). All data represent at least three independent experiments. Statistically significant results were taken as *P* < 0.05, and significance values were assigned in specific figures/experiments as shown.

**CONFLICT OF INTEREST**

The authors state no conflict of interest.

**ACKNOWLEDGMENTS**

The authors thank David Calderwood, Andy Reynolds, Bob Adelstein, and Patrick Caswell for providing plasmids for this study. We also thank the Nikon Imaging Centre@King's for assistance with microscopy and Nick Brown and Silvia Aldaz Casonava for helpful discussions. This work was funded by the Medical Research Council (MR/M018512/1) and the British Skin Foundation. BTG is funded by Biotechnology and Biological Sciences Research Council grant (BB/N007336/1), and BTG and AW are funded by Human Frontier Science Program grant (RGP00001/2016).

**AUTHOR CONTRIBUTIONS**

MM and RB performed all the experiments, with the exception of MST analysis, which was performed by BTG and AW, and FRET/fluorescence lifetime imaging microscopy analysis, which was performed by MP. GKC performed the analysis of kindlin-2-overexpressing cells. DRM wrote the algorithm and analyzed the lysosomal tracking data. WT and KS cells were

isolated from patients by JAM. MP, JAM, and MM conceived the study and cowrote the manuscript.

**SUPPLEMENTARY MATERIAL**

Supplementary material is linked to the online version of the paper at [www.jidonline.org](http://www.jidonline.org), and at <https://doi.org/10.1016/j.jid.2018.08.020>.

**REFERENCES**

Ashton GH. Kindler syndrome. *Clin Exp Dermatol* 2004;29:116–21.

Baines AJ, Lu HC, Bennett PM. The protein 4.1 family: hub proteins in animals for organizing membrane proteins. *Biochim Biophys Acta* 2014;1838:605–19.

Bakker J, Spits M, Neefjes J, Berlin I. The EGFR odyssey—from activation to destruction in space and time. *J Cell Sci* 2017;130:4087–96.

Bandyopadhyay A, Rothschild G, Kim S, Calderwood DA, Raghavan S. Functional differences between kindlin-1 and kindlin-2 in keratinocytes. *J Cell Sci* 2012;125:2172–84.

Banno A, Goult BT, Lee H, Bate N, Critchley DR, Ginsberg MH. Subcellular localization of talin is regulated by inter-domain interactions. *J Biol Chem* 2012;287:13799–812.

Bartoschik T, Galinec S, Kleusch C, Walkiewicz K, Breitsprecher D, Weigert S, et al. Near-native, site-specific and purification-free protein labeling for quantitative protein interaction analysis by microscale thermophoresis. *Sci Rep* 2018;8:4977.

Bialkowska K, Ma YQ, Bledzka K, Sossey-Alaoui K, Izem L, Zhang X, et al. The integrin co-activator kindlin-3 is expressed and functional in a non-hematopoietic cell, the endothelial cell. *J Biol Chem* 2010;285:18640–9.

Bouaouina M, Goult BT, Huet-Calderwood C, Bate N, Brahme NN, Barsukov IL, et al. A conserved lipid-binding loop in the kindlin FERM F1 domain is required for kindlin-mediated αIIbβ3 integrin coactivation. *J Biol Chem* 2012;287:6979–90.

Brahme NN, Harburger DS, Kemp-O'Brien K, Stewart R, Raghavan S, Parsons M, et al. Kindlin binds migfilin tandem LIM domains and regulates migfilin focal adhesion localization and recruitment dynamics. *J Biol Chem* 2013;288:35604–16.

Campbell P, Morton PE, Takeichi T, Salam A, Roberts N, Proudfoot LE, et al. Epithelial inflammation resulting from an inherited loss-of-function mutation in EGFR. *J Invest Dermatol* 2014;134:2570–8.

Caswell PT, Spence HJ, Parsons M, White DP, Clark K, Cheng KW, et al. Rab25 associates with α5β1 integrin to promote invasive migration in 3D microenvironments. *Dev Cell* 2007;13:496–510.

Duan L, Miura Y, Dimri M, Majumder B, Dodge IL, Reddi AL, et al. Cbl-mediated ubiquitylation is required for lysosomal sorting of epidermal growth factor receptor but is dispensable for endocytosis. *J Biol Chem* 2003;278:28950–60.

Goult BT, Bouaouina M, Harburger DS, Bate N, Patel B, Anthis NJ, et al. The structure of the N-terminus of kindlin-1: a domain important for αIIbβ3 integrin activation. *J Mol Biol* 2009;394:944–56.

Guo B, Gao J, Zhan J, Zhang H. Kindlin-2 interacts with and stabilizes EGFR and is required for EGF-induced breast cancer cell migration. *Cancer Lett* 2015;361:271–81.

Has C, Castiglia D, del Rio M, Diez MG, Piccinni E, Kiritis D, et al. Kindler syndrome: extension of FERMT1 mutational spectrum and natural history. *Hum Mutat* 2011;32:1204–12.

Has C, Ludwig RJ, Herz C, Kern JS, Ussar S, Ochsendorf FR, et al. C-terminally truncated kindlin-1 leads to abnormal adhesion and migration of keratinocytes. *Br J Dermatol* 2008;159:1192–6.

Herz C, Aumailley M, Schulte C, Schlotzer-Schrehardt U, Bruckner-Tuderman L, Has C. Kindlin-1 is a phosphoprotein involved in regulation of polarity, proliferation, and motility of epidermal keratinocytes. *J Biol Chem* 2006;281:36082–90.


Huet-Calderwood C, Brahme NN, Kumar N, Stiegler AL, Raghavan S, Boggan TJ, et al. Differences in binding to the ILK complex determines kindlin isoform adhesion localization and integrin activation. *J Cell Sci* 2014;127:4308–21.

Izeddin I, El Beheiry M, Andilla J, Ciepielewski D, Darzacq X, Dahan M. PSF shaping using adaptive optics for three-dimensional single-molecule super-resolution imaging and tracking. *Opt Express* 2012;20:4957–67.

- Jobard F, Bouadjar B, Caux F, Hadj-Rabia S, Has C, Matsuda F, et al. Identification of mutations in a new gene encoding a FERM family protein with a pleckstrin homology domain in Kindler syndrome. *Hum Mol Genet* 2003;12:925–35.
- Kim JH, Wang A, Conti MA, Adelstein RS. Nonmuscle myosin II is required for internalization of the epidermal growth factor receptor and modulation of downstream signaling. *J Biol Chem* 2012;287:27345–58.
- Lai-Cheong JE, Liu L, Sethuraman G, Kumar R, Sharma VK, Reddy SR, et al. Five new homozygous mutations in the KIND1 gene in Kindler syndrome. *J Invest Dermatol* 2007;127:2268–70.
- Lai-Cheong JE, Tanaka A, Hawche G, Emanuel P, Maari C, Taskesen M, et al. Kindler syndrome: a focal adhesion genodermatosis. *Br J Dermatol* 2009;160:233–42.
- Lai-Cheong JE, Ussar S, Arita K, Hart IR, McGrath JA. Colocalization of kindlin-1, kindlin-2, and migfilin at keratinocyte focal adhesion and relevance to the pathophysiology of Kindler syndrome. *J Invest Dermatol* 2008;128:2156–65.
- Larjava H, Plow EF, Wu C. Kindlins: essential regulators of integrin signalling and cell-matrix adhesion. *EMBO Rep* 2008;9:1203–8.
- Liu Z, Lu D, Wang X, Wan J, Liu C, Zhang H. Kindlin-2 phosphorylation by Src at Y193 enhances Src activity and is involved in migfilin recruitment to the focal adhesions. *FEBS Lett* 2015;589:2001–10.
- Maiuri P, Terriac E, Paul-Gilloteaux P, Vignaud T, McNally K, Onuffer J, et al. The first World Cell Race. *Curr Biol* 2012;22(17):R673–5.
- Meves A, Stremmel C, Gottschalk K, Fassler R. The kindlin protein family: new members to the club of focal adhesion proteins. *Trends Cell Biol* 2009;19:504–13.
- Qu H, Tu Y, Guan JL, Xiao G, Wu C. Kindlin-2 tyrosine phosphorylation and interaction with Src serve as a regulatable switch in the integrin outside-in signaling circuit. *J Biol Chem* 2014;289:31001–13.
- Reynolds AR, Tischler C, Verwee PJ, Rocks O, Bastiaens PI. EGFR activation coupled to inhibition of tyrosine phosphatases causes lateral signal propagation. *Nat Cell Biol* 2003;5:447–53.
- Rizk A, Paul G, Incardona P, Bugarski M, Mansouri M, Niemann A, et al. Segmentation and quantification of subcellular structures in fluorescence microscopy images using Squassh. *Nat Protoc* 2014;9:586–96.
- Rognoni E, Ruppert R, Fassler R. The kindlin family: functions, signaling properties and implications for human disease. *J Cell Sci* 2016;129:17–27.
- Siegel DH, Ashton GH, Penagos HG, Lee JV, Feiler HS, Wilhelmsen KC, et al. Loss of kindlin-1, a human homolog of the *Caenorhabditis elegans* actin-extracellular-matrix linker protein UNC-112, causes Kindler syndrome. *Am J Hum Genet* 2003;73:174–87.
- Singh B, Coffey RJ. Trafficking of epidermal growth factor receptor ligands in polarized epithelial cells. *Annu Rev Physiol* 2014;76:275–300.
- Techanukul T, Sethuraman G, Zlotogorski A, Horev L, Macarov M, Trainer A, et al. Novel and recurrent FERMT1 gene mutations in Kindler syndrome. *Acta Derm Venereol* 2011;91:267–70.
- Wiebe CB, Petricca G, Hakkinen L, Jiang G, Wu C, Larjava HS. Kindler syndrome and periodontal disease: review of the literature and a 12-year follow-up case. *J Periodontol* 2008;79:961–6.
- Worth DC, Hodivala-Dilke K, Robinson SD, King SJ, Morton PE, Gertler FB, et al.  $\alpha v \beta 3$  integrin spatially regulates VASP and RIAM to control adhesion dynamics and migration. *J Cell Biol* 2010;189:369–83.
- Zanet J, Jayo A, Plaza S, Millard T, Parsons M, Stramer B. Fascin promotes filopodia formation independent of its role in actin bundling. *J Cell Biol* 2012;197:477–86.
- Zhang G, Gu Y, Begum R, Chen H, Gao X, McGrath JA, et al. Kindlin-1 regulates keratinocyte electrotaxis. *J Invest Dermatol* 2016;136:2229–39.

 This work is licensed under a Creative Commons Attribution 4.0 International License. To view a copy of this license, visit <http://creativecommons.org/licenses/by/4.0/>

## Chlamydial virulence factor TarP mimics talin to disrupt the talin-vinculin complex

Austin J. Whitewood, Abhimanyu K. Singh, David G. Brown and Benjamin T. Goult 

School of Biosciences, University of Kent, Canterbury, UK

### Correspondence

B. T. Goult, School of Biosciences,  
University of Kent, Canterbury, Kent, CT2  
7NJ, UK  
E-mail: b.t.goult@kent.ac.uk

(Received 8 March 2018, revised 12 April  
2018, accepted 21 April 2018, available  
online 15 May 2018)

doi:10.1002/1873-3468.13074

Edited by Stuart Ferguson

**Vinculin is a central component of mechanosensitive adhesive complexes that form between cells and the extracellular matrix. A myriad of infectious agents mimic vinculin binding sites (VBS), enabling them to hijack the adhesion machinery and facilitate cellular entry. Here, we report the structural and biochemical characterisation of VBS from the chlamydial virulence factor TarP. Whilst the affinities of isolated VBS peptides from TarP and talin for vinculin are similar, their behaviour in larger fragments is markedly different. In talin, VBS are cryptic and require mechanical activation to bind vinculin, whereas the TarP VBS are located in disordered regions, and so are constitutively active. We demonstrate that the TarP VBS can uncouple talin:vinculin complexes, which may lead to adhesion destabilisation.**

**Keywords:** adhesion; chlamydia; crystallography; molecular mimicry; talin; vinculin

Interactions between cells and the surrounding extracellular matrix (ECM), mediated *via* the integrin family of cell adhesion molecules, are fundamental to the development of multicellular life. These adhesions serve not just as attachment points but also as mechanosensitive signalling hubs, enabling cells to sense and respond to the external environment. Integrin receptors bound to ECM are coupled to the actin cytoskeleton *via* the mechanosensitive protein talin [1]. Under force, helical bundles in the talin rod domain unfold, exposing multiple cryptic vinculin binding sites (VBS) [2,3] that bind to the vinculin head (Vd1), activating autoinhibited vinculin by displacing the vinculin tail [4] (Fig. 1A). Activation of talin and vinculin also exposes numerous other cryptic binding sites for ligands that affect the assembly and regulation of both cell:ECM focal adhesions (FAs) and cell:cell junctions [5,6].

These highly conserved attachment points linking the cell to the outside world have also become

recognition sites for numerous infectious agents [7,8] with some bacteria specifically targeting adhesion proteins for cellular entry. It has previously been shown that the *Shigella flexneri* effector protein IpaA [9] and the *Rickettsia* cell surface antigen Sca4 interact with vinculin [10]. The atomic structures of these virulence factors reveal mimicry of the talin VBS. Thus, by forming amphipathic  $\alpha$ -helices that bind to Vd1, these virulence factors activate autoinhibited vinculin and hijack cell adhesion to aid pathogenesis.

Chlamydia invasion has been shown to require the effector protein translocated actin recruiting protein (TarP) which is thought to play an important role in actin recruitment [11,12]. TarP is translocated into the host cell by a chlamydial type 3 secretory system upon early elementary body (EB) attachment to the host cell. TarP injection by the bacteria leads to the recruitment and bundling of actin filaments at the point of invasion [12]. Recently, Thwaites *et al.* reported the presence of a vinculin binding region in TarP,

### Abbreviations

FP, fluorescence polarisation; HSQC, heteronuclear single quantum coherence; LD-motif, leucine-aspartic acid motif; TarP, translocated actin recruitment protein; VBS, vinculin-binding site.

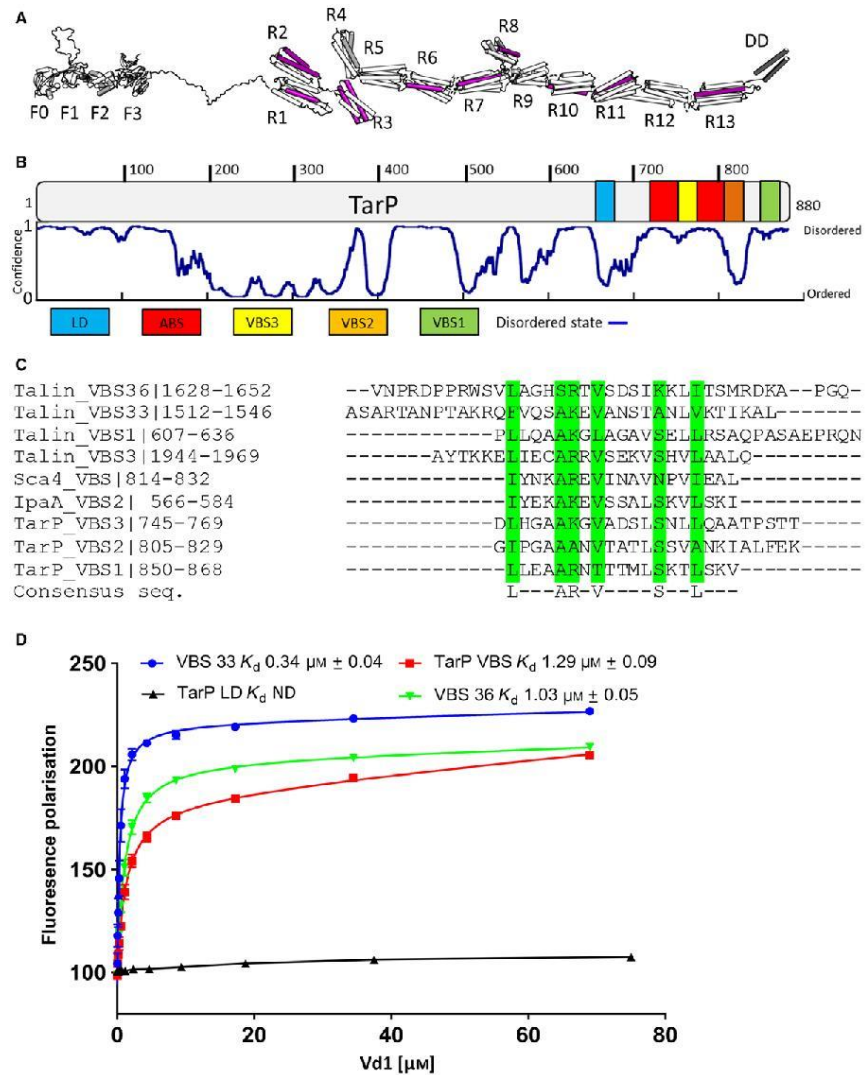


**Fig. 1.** Biochemical characterisation of the TarP interaction with the vinculin head (Vd1). (A) Schematic of talin structure, with the location of the 11 talin VBS indicated (purple). (B) Schematic of TarP, indicating locations of VBS1 (green), VBS2 (orange), VBS3 (yellow), Actin binding site ABS (red) and LD-motif (blue) at the C-terminal. The disorder prediction trace generated using DISOPRED3 [44] is shown. (C) Multiple sequence alignment of vinculin binding sites, aligned using Clustal Omega. The consensus residues are highlighted in green. (D) Comparison of the Vd1:TarP and Vd1:talin interactions. Binding of fluorescein labelled talin VBS33, VBS36, TarP VBS (850-868)C and LD (655-680)C peptides to Vd1, measured using a fluorescence polarisation assay. Dissociation constants  $\pm$  SE ( $\mu\text{M}$ ) for the interactions are indicated in the legend. All measurements were performed in triplicate. ND, not determined.

containing three vinculin binding sites (VBS) with 'VBS1' being essential for vinculin recruitment [13]. Additionally, TarP was reported to contain a Leucine-Aspartic acid motif (LD-motif) with a similar consensus sequence to the second paxillin LD-motif (LD2) which interacts with focal adhesion kinase (FAK) [14], and thus may provide TarP with a means of engaging FAK and altering cell adhesion signalling.

Here, we report the structure of the TarP:vinculin Vd1 complex and biochemically characterise and compare the interaction of the TarP VBS and talin VBS with vinculin. Whilst the affinities of the isolated VBS from TarP and talin are similar, their behaviour in larger polypeptide fragments is very different. Thus, the TarP VBS are positioned in unstructured regions, and TarP VBS1 is constitutively active whilst the talin VBS are buried inside folded rod domains and are cryptic. Furthermore, we demonstrate TarP VBS1 disrupts talin:vinculin complexes *in vitro*. This ability to uncouple vinculin from talin suggests that TarP and other virulence factors may have the capacity to trigger FA disassembly during invasion.

## Materials and methods

### Expression of recombinant polypeptides

Chicken vinculin Vd1 (residues 1–259), murine talin R10 (residues 1815–1973), and the FAK-FAT domain (residues 941–1090) were cloned into a pET151 vector (Invitrogen) and expressed in *E. coli* BL21 (DE3) cells cultured in LB. Standard nickel-affinity chromatography was used to purify the His-tagged recombinant proteins as described previously [15]. The proteins were further purified using anion-exchange chromatography following cleavage of the 6xHis-tag with TEV protease. Protein concentrations were determined using the respective extinction coefficients at 280 nm.

### Fluorescence polarisation assays

Peptides with either a C- or N-terminal cysteine were synthesised by GLBiochem (China).

TarP\_VBS1 (LLEAARNNTTMLSRTLKVC;  
*C. caviae* residues 850–868)

TarP\_LD (EGAEGLEHLLPQLRSHLDDAFDQQGN-  
*C. caviae* residues 655–680)

Pax\_LD2 (C-NLSELDRLLELN; paxillin residues 141–  
153)

Pax\_LD4 (C-ATREDELMSALS; paxillin residues  
262–274)

mTalin\_VBS33 (C-ASARTANPTAKRQFVQSAKE-  
VANSTANLVKTIKAL; talin residues 1512–1546)

mTalin\_VBS36 (C-VNPRDPPRWSVLGHSRTVSD-  
SIKKLITSMRDKAP; talin residues 1622–1656)

Peptides were coupled to a thiol-reactive fluorescein dye *via* the terminal cysteine. Stock solutions were made in phosphate-buffered saline (PBS; 137 mM NaCl, 27 mM KCl, 100 mM Na<sub>2</sub>HPO<sub>4</sub>, 18 mM KH<sub>2</sub>PO<sub>4</sub>, pH 7.4), 1 mM TCEP and 0.05% Triton X-100. Excess dye was removed using a PD-10 desalting column (GE Healthcare, Chicago, IL, USA). Titrations were performed in PBS using a constant 1 μM concentration of fluorescein-coupled peptide with increasing concentration of protein; final volume 100 μL in a black 96-well plate. Fluorescent polarisation (FP) measurements were recorded on a BMGLabTech CLARIOstar plate reader at room temperature and analysed using GraphPad Prism. *K<sub>d</sub>* values were calculated with nonlinear curve fitting using a one-site total binding model.

### Analytical gel filtration

Gel filtration was performed using a Superdex-75 size-exclusion chromatography column (GE healthcare) at a flow rate of 1 mL·min<sup>-1</sup> at 4 °C in 50 mM Tris pH 7.5, 150 mM NaCl, 2 mM DTT. A sample of 100 μL was run consisting of 100 μM of each protein/peptide, incubated at a 1 : 1 (talin:Vd1) or 1 : 1 : 1 (talin:Vd1:TarP VBS1/talin VBS36) ratio, at 37 °C for 30 min. In the competition experiment, an additional 30 nM of fluorescein-coupled TarP peptide was added to visualise the TarP elution *via* absorbance at 494 nm. The elution absorbance was measured at three wavelengths: 220 nm, 280 nm and 494 nm (fluorescein absorbance). Elution was monitored by a Malvern Viscotek SEC-MALS-9 (Malvern Panalytical, Malvern, UK). Molar mass, refractive index and weight fraction (%) were determined using the OmniSEC software (Malvern Panalytical) and statistical significance assessed using a *T*-test.

### X-ray crystallography

Crystallisation trials for Vd1 in the presence of TarP VBS peptide were conducted at 21 °C by hanging drop vapour diffusion while maintaining a 1 : 1 protein to peptide ratio. Crystals were obtained in a condition containing 0.1 M sodium citrate tribasic dehydrate pH 5.6 and 20% v/v 2-propanol. Crystals were cryoprotected in the same solution supplemented with 20% v/v glycerol prior to vitrification in liquid nitrogen. Diffraction dataset was collected at 100 K on beamline I03 at Diamond Light Source (Didcot, UK) using a Pilatus3 6M detector (Dectris, Baden, Switzerland). Crystallographic data were processed by autoPROC [16], which incorporates XDS [17], AIMLESS [18] and TRUNCATE [19] for data integration, scaling and merging. Structure of the Vd1/TarP complex was determined using chicken vinculin head as template (PDB: 3ZDL [20]) for

molecular replacement search carried out with PHASER [21]. Manual model adjustment and refinement were performed with COOT [22] and REFMAC [23] respectively. Model was validated with MOLPROBITY [24] and interaction properties were determined by PISA [25]. Figure preparation was carried out with PYMOL (Schrödinger LLC, Cambridge MA, USA). For data collection, phasing and refinement statistics, Table 1. The structure has been deposited to RCSB Protein Data Bank with accession code 6FQ4.

### NMR Spectroscopy

NMR spectra were obtained using a Bruker AVANCE III 600 MHz spectrometer equipped with CryoProbe. Experiments were performed at 298 K in 20 mM sodium phosphate pH 6.5, 50 mM NaCl, 2 mM DTT with 5% (v/v)

**Table 1.** X-ray data collection and refinement statistics for TarP-Vd1 complex. Data collected from a single crystal.

Data collection	
Synchrotron and Beamline	Diamond Light Source; I03
Space group	$P2_12_12$
Molecule/a.s.u	1
Cell dimensions	
<i>a</i> , <i>b</i> , <i>c</i> (Å)	51.80, 66.87, 95.83
$\alpha$ , $\beta$ , $\gamma$ (°)	90, 90, 90
Resolution (Å)	95.83–2.9 (2.96–2.9) <sup>a</sup>
$R_{merge}$	0.156 (0.806)
$I/\sigma I$	8.1 (2.5)
$CC(1/2)$	0.994 (0.903)
Completeness (%)	99.8 (99.9)
Redundancy	6.1 (6.3)
Refinement	
Resolution (Å)	2.9
No. reflections	7455 (519)
$R_{work}/R_{free}$	0.28/0.34
No. atoms	
Protein	2082
Water	3
B-factors (Å <sup>2</sup> )	
Protein/Peptide	94.24/95.73
Water	84.04
R.m.s. deviations	
Bond lengths (Å)	0.010
Bond angles (°)	1.430
Ramachandran plot	
Favoured/allowed/outlier (%)	93/6/1
Rotamer	
Favoured/poor (%)	59.2/21.01
Molprobrity scores	
Protein geometry	3.42 (37th) <sup>b</sup>
Clash score all atoms	29 (81st) <sup>b</sup>
PDB accession no.	6FQ4

<sup>a</sup>Values in parentheses are for highest-resolution shell.

<sup>b</sup>Values in parentheses indicate percentile scores as determined by Molprobrity.

<sup>2</sup>H<sub>2</sub>O. Ligand binding was evaluated from <sup>1</sup>H,<sup>15</sup>N-HSQC chemical shift changes using 130 μM <sup>15</sup>N-labelled FAK-FAT domain. Peptides were added at a 3 : 1 peptide:protein ratio.

## Results

### Chlamydial VBS interacts with vinculin

It has previously been shown that the interaction between TarP and vinculin is required for Chlamydia infection [13]. TarP was shown to contain three VBS with only the C-terminal VBS, VBS1, being critical for TarP function (Fig. 1B). Multiple sequence alignment with the VBS of talin (Fig. 1C) confirmed the region that contains the vinculin head domain (Vd1) consensus binding motif LxxAAxxVxVxxLxxA [26] as reported previously [13].

To evaluate how the interaction of Vd1 with the TarP VBS1 compares to its interaction with talin VBS, we measured the relative binding affinities using an *in vitro* fluorescence polarisation (FP) assay. In this assay, synthetic VBS peptides (Materials and methods) were fluorescently labelled with fluorescein and titrated against an increasing concentration of Vd1. Binding of the VBS peptide to Vd1 results in an increase in fluorescence polarisation (Fig. 1D), which can be used to determine the binding constant,  $K_d$ . The TarP VBS1 peptide bound to Vd1 with an affinity of 1.29 μM. The talin VBS located on talin helices, 33 and 36 (VBS33 and VBS36), bound with comparable affinities of 0.34 μM and 1.03 μM respectively (Fig. 1D). The TarP LD region (residues 655–680), which does not interact with Vd1, was used as a negative control.

Although the affinity of the TarP VBS1 for vinculin is comparable to the VBS in talin, the location of the VBS are markedly different between the two proteins. Talin VBS are maintained in a cryptic conformation, buried inside the hydrophobic core of the talin rod domain bundles [27], and require exposure by mechanical force across talin to unfold the bundles [3,28]. In contrast, the VBS in TarP are situated in disordered regions of the molecule and are therefore likely to be constitutively active (Fig. 1B). The affinity of talin VBS in folded rod domains for Vd1 is significantly lower due to the energy required to unfold the domain to expose the VBS [29]. However, this reduced affinity of talin for vinculin is rapidly overcome by force exerted on talin, an effect that is readily reversible when force is removed, meaning that the talin:vinculin interactions are exquisitely force-dependent [28]. Therefore, in the absence of mechanical force, TarP has the potential to outcompete folded talin to bind vinculin.

### The structure of TarP VBS1 in complex with the vinculin head

To further characterise the interaction between TarP VBS1 and vinculin, we crystallised a complex of TarP (850–868) with vinculin Vd1. The crystals containing one molecule of the complex in the asymmetric unit were in orthorhombic space group  $P2_12_12$  and diffracted to a useful resolution of 2.9 Å.

The structure of the complex was determined by molecular replacement (Fig. 2A; statistics in Table 1) and shows good agreement with the complexes of Vd1 with other VBS from talin [4,30], sca-4 [31] and IpaA [32]. The TarP VBS1 forms an  $\alpha$ -helix that embeds into the hydrophobic groove formed between  $\alpha$ -helices 1 and 2 of the Vd1 N-terminal 4-helix bundle, forming a structure that resembles a five-helix bundle (Fig. 2B). Analysis of the complex interface by PISA indicated that 54.1% of the VBS surface area, including the consensus residues, is buried in the complex interface (Fig. 2A). Furthermore, two hydrogen bonds were identified: TarP Arg-855 to Vd1 Ser-11, and TarP Ser-862 to Vd1 Gln-18. Structural alignment of known VBS structures indicates that these hydrogen bonds are well conserved. Upon complex formation, TarP significantly alters the positions of Vd1 helices 1 and 2, widening the groove between the two and exposing the hydrophobic core (Fig. 2C), mimicking the way talin activates vinculin, causing the release of the vinculin tail [4,33]. With sidechains almost identical in length and character to talin VBS, TarP VBS1 is able to pack tightly into the Vd1 hydrophobic groove accounting for the high affinity we measured (Fig. 1C). The strong resemblance of the TarP VBS1 to the VBS in talin demonstrates the molecular mimicry employed by TarP to hijack the host cell adhesion machinery.

### The TarP peptide competes with talin for binding to vinculin

Since TarP VBS1 binds to the same site on vinculin as the talin VBS, this raises the possibility that TarP binding might compete with talin for vinculin binding. A similar phenomenon was seen in *Drosophila* recently, where expression of a GFP-VBS construct was found to disrupt talin:vinculin interactions *in vivo* [34]. Using analytical gel filtration, we measured the interaction between Vd1 and a VBS-containing talin helical bundle. We selected talin rod domain R10, which contains a single VBS (VBS46) [35]. Equimolar amounts of Vd1 and talin R10 incubated together at 37 °C formed a 1 : 1 complex (Fig. 3A-B). Adding a stoichiometric amount of TarP VBS1 peptide

(Fig. 3A), or a peptide of an isolated talin VBS (VBS36; Fig. 3B) resulted in a significant reduction in the talin:Vd1 peak and concomitant increases in the monomer peaks of the respective proteins. To confirm that disruption of the talin:Vd1 complex was due to competition by the TarP VBS1 peptide, we spiked the TarP VBS1 peptide with 30 nM of fluorescein-TarP VBS1 peptide (as used in the FP assay). The fluorescein-coupled TarP VBS1 eluted in the same fractions as Vd1, confirming that the TarP peptide was bound to Vd1. To quantitate this competition, we used the SEC-MALS OmniSEC software to determine the weight fraction (%) of each peak in Fig. 3A-B and this analysis is shown in Fig. 3C. This demonstrates that TarP, and exposed VBS in general, can out-compete talin for binding to Vd1 *in vitro* even when the vinculin:talin complex is already formed. Whilst the isolated talin VBS and TarP VBS1 peptides have similar affinities, the affinity of Vd1 for the intact talin rod domain is reduced significantly due to the cryptic nature of talin VBS in the folded talin helical bundles [29]. As a consequence, the constitutively active nature of the TarP VBS allows it to disrupt vinculin:talin complexes. Vinculin binding to talin inhibits talin refolding [28] and is important for FA stabilisation. TarP disruption of this complex could lead to the loosening of adhesion by disrupting the talin:vinculin:actin cytoskeletal connection. This may mean that, as well as providing a means of entry and a mechanism to hijack the actin machinery, infection might also destabilise FAs at the point of entry.

### The TarP leucine-aspartic acid motif

Leucine-Aspartic acid motifs (LD-motifs) are well-recognised protein:protein interaction motifs [36], first identified in the FA protein paxillin, and shown to be required for paxillin to interact with focal adhesion kinase (FAK) [37]. The FAK–paxillin interaction was subsequently mapped to the focal adhesion targeting (FAT) domain of FAK [38]. It was reported previously that TarP contains an LD-motif (residues 655–680; TarP LD-motif) with sequence homology to paxillin LD2 [14], and that this LD-motif interacts with the FAK-FAT domain and plays a role in actin recruitment. The alignment of the TarP LD-motif with the LD domains in KANK1 [39], RIAM [40], DLC1 [20] and the paxillin LD1 and LD2 motifs are shown in Fig. 4A. To investigate the interaction of TarP LD-motif with FAK, we used the FP assay utilising fluorescein-labelled LD-motif peptides, and measured their binding to the FAK-FAT domain. As expected, paxillin LD2 bound well to the FAK-FAT domain

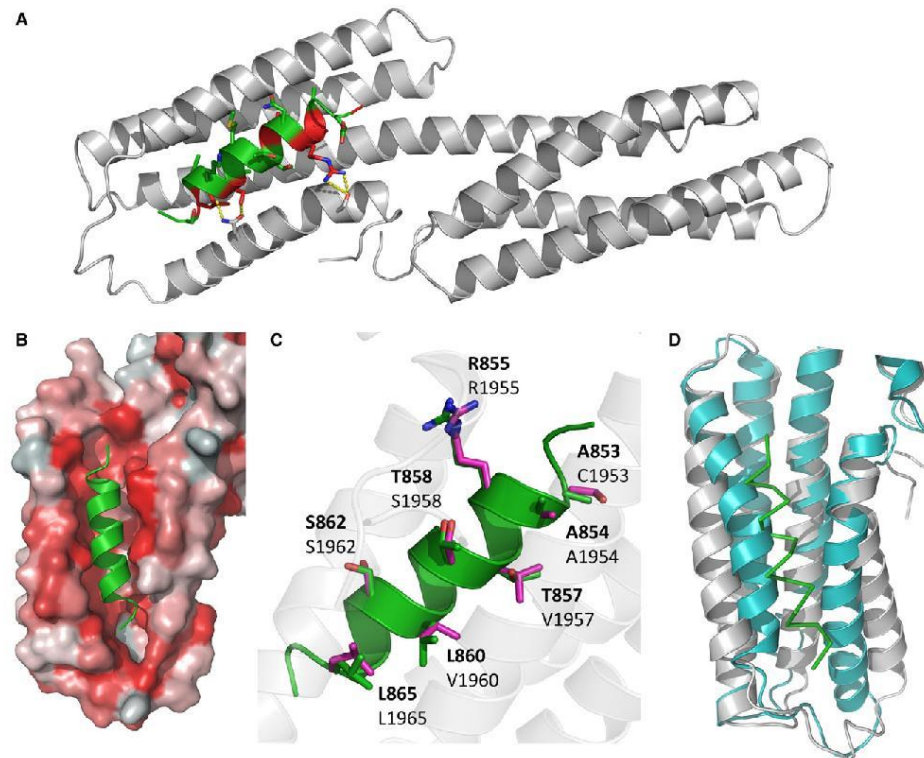


**Fig. 2.** Crystal structure of TarP in complex with Vd1. (A) Cartoon representation of the complex of Vd1 (grey) bound to TarP VBS (green); the consensus VBS residues are shown in red. (B) TarP VBS (green) docks into a hydrophobic groove on Vd1. Vd1 is represented as surface coloured by hydrophobicity: hydrophobic = red, hydrophilic = white. (C) TarP VBS peptide (green) aligned with talin VBS46 peptide (purple, PDB:1RKC [4]) with Vd1-interacting sidechains from both VBS shown as sticks and TarP residues (top bold) and corresponding vbs46 residues are shown. (D) VBS binding causes conformational change in the Vd1 domain. Comparison of apo Vd1 (cyan, PDB:1TR2 [45]) and TarP bound Vd1 (grey). The TarP peptide is shown as a ribbon (green).

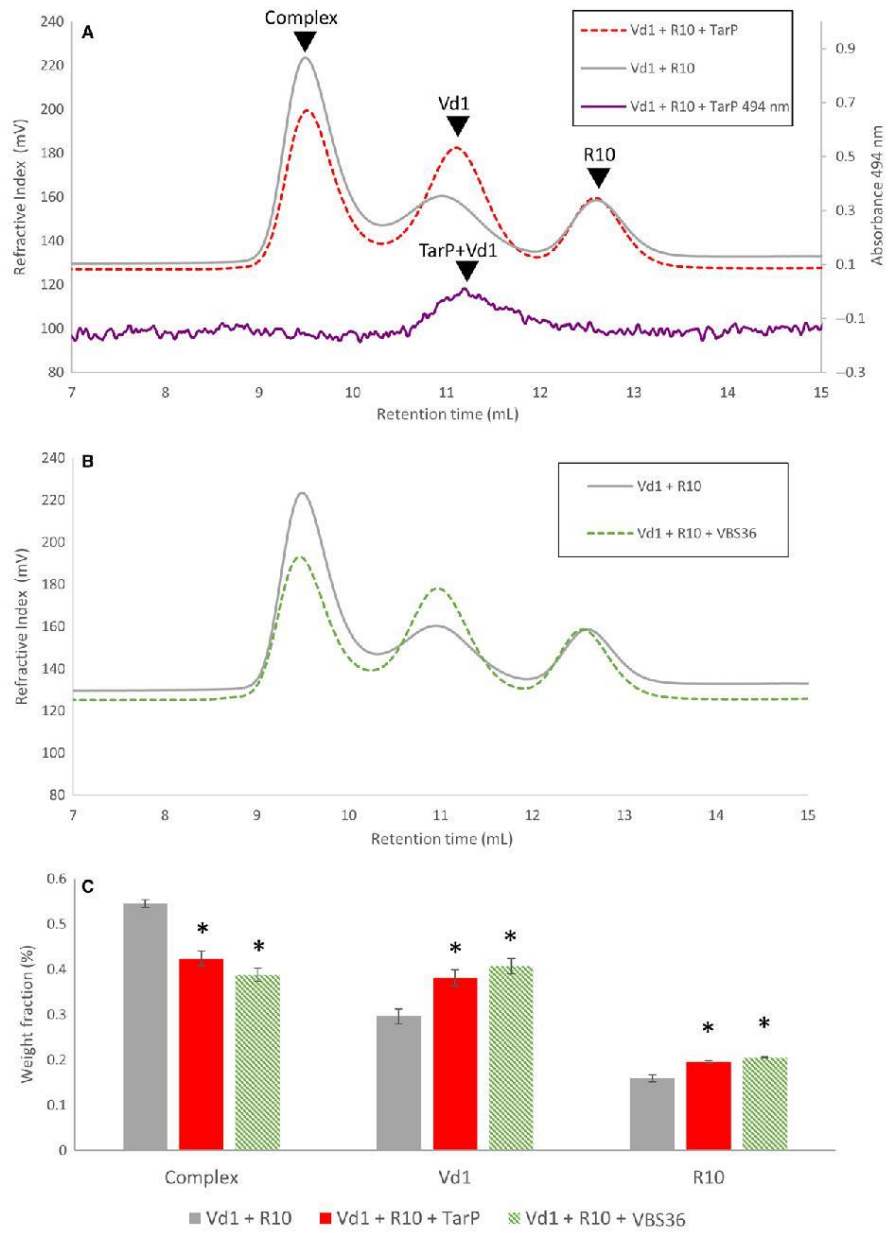
( $K_d \sim 9 \mu\text{M}$ ) in line with previous reports [38]. However, we observed no increase in polarisation with the TarP LD-motif, suggesting that any interaction between TarP and FAK is too weak to be detected by the FP assay.

NMR is a powerful technique for studying interactions, even very weak (millimolar  $K_d$ ) interactions.

Addition of paxillin LD2 peptide to  $^{15}\text{N}$ -labelled FAK-FAT resulted in large chemical shift changes indicative of a robust interaction (Fig. 4C). In contrast, addition of a threefold excess of TarP LD-motif resulted in only very small shift changes, suggesting the peptide interacts only very weakly with FAK-FAT ( $K_d > \text{mM}$ ). This weak interaction explains the lack of

**Fig. 3.** TarP VBS disrupts the interaction between talin R10 and vinculin Vd1. Vd1 was incubated with talin R10 at 37 °C for 30 min then analysed on a gel filtration column (grey). The experiment was repeated with the addition of a stoichiometric amount of TarP VBS peptide (A) and then with talin VBS36 (B). All experiments were done in triplicate. 1% fluorescein-labelled TarP VBS peptide was added to monitor TarP VBS elution at 494 nm which confirmed that TarP eluted bound to Vd1 (purple). (C) the relative 'Weight Fraction' percentage for talin: vinculin complex, talin, vinculin peaks in the absence and presence of both TarP VBS and VBS36 peptides. Data are means  $\pm$  SEM; \* $P < 0.05$  by *T*-test. Both peptides reduced the R10-Vd1 complex.





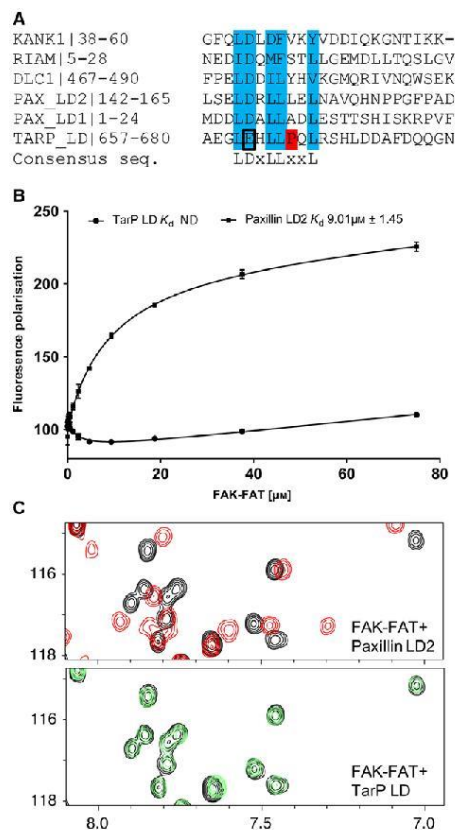


**Fig. 4.** The TarP LD-motif does not bind to FAK. (A) Multiple sequence alignment of known LD-motifs and TarP, generated using Clustal Omega; the consensus binding residues are highlighted in blue. (B) Binding of fluorescein-labelled TarP LD (655–680)C and Paxillin LD2 (141–153)C peptides to FAK-FAT, measured using a fluorescence polarisation assay. Dissociation constants  $\pm$  SE ( $\mu\text{M}$ ) for the interactions are indicated in the legend. ND, not determined. (C)  $^1\text{H}$ ,  $^{15}\text{N}$ -HSQC spectra of  $130 \mu\text{M}$   $^{15}\text{N}$ -labelled FAK-FAT in the absence (black) or presence of paxillin LD2 peptide (red; top panel) or TarP LD (green; bottom panel) at a ratio of 1 : 3.

binding in the FP experiment. The difference in binding affinity between the TarP LD-motif and paxillin LD2 to FAK-FAT may be explained by the presence of a proline residue, Pro675, in the middle of the TarP LD-motif (Fig. 4A). It is likely the proline destabilises and/or causes a kink in the  $\alpha$ -helix formed by the TarP LD-motif, but lack of binding might also be due to

the substitution of glutamate for aspartate in the 'LD' region of the TarP LD-motif. Therefore, despite the sequence homology, the TarP LD-motif binds much weaker than paxillin-LD2 to FAK-FAT, further refining the specificity determinants of LD-motifs and highlighting the fact that subtle changes in the sequence can significantly alter binding specificity.

It is possible that the TarP LD-motif may bind to another, currently unrecognised LD-binding domain protein, but it does not bind to FAK. Therefore, it seems likely that the TarP:FAK colocalisation reported previously *in cellulo* requires additional components that bring FAK and TarP together.

## Conclusions

In this study, we have further refined understanding of the molecular mechanisms underlying chlamydial infection *via* remodelling of the actin cytoskeleton; the ability of TarP to bind vinculin characterised here, and the recently characterised TarP WH2 motif that binds actin [41], look to be major components. Our data show that the constitutively active TarP VBS1 can out-compete the mechanosensitive interaction between talin and vinculin. Vinculin is a key player in the regulation of FA dynamics [42] and cell:cell junctions [43], and the capacity of TarP VBS1 to uncouple vinculin-mediated cytoskeletal connections during infection is therefore likely to have significant biological implications. Thus, it will be important to determine to what extent chlamydial infection alters the integrity and dynamics of cell:cell and cell:ECM junctions. Moreover, it raises the possibility that endogenous mammalian proteins might exist with constitutively active VBS, and that these could represent a new class of protein with the ability to regulate cell adhesion and migration.

## Acknowledgements

We thank Marie Anderson for help with the initial crystallography screen and David Critchley for critical reading of the manuscript. We also thank Diamond Light Source beamline I03 staff for their help in crystallographic data collection. B.T.G. is funded by BBSRC grant (BB/N007336/1) and HFSP grant (RGP00001/2016).

## Author contributions

BTG conceived and supervised the study; AJW and BTG designed experiments; AJW and AKS performed experiments; BTG, AJW, AKS and DGB analysed data; BTG and AJW wrote the manuscript.

## References

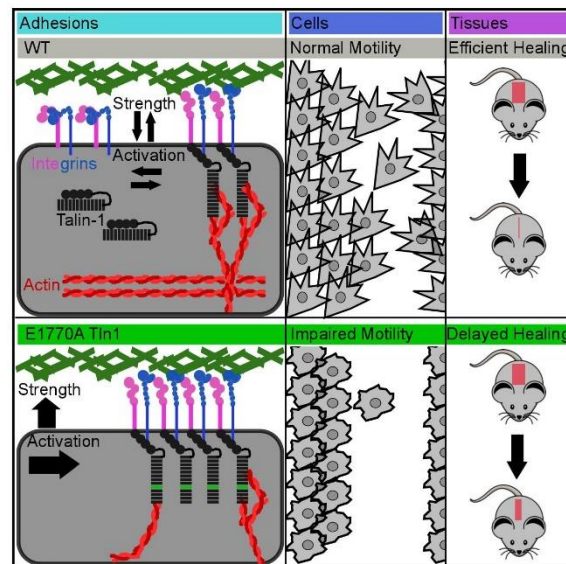
- 1 Calderwood DA, Campbell ID and Critchley DR (2013) Talins and kindlins: partners in integrin-mediated adhesion. *Nat Rev Mol Cell Biol* **14**, 503–517.
- 2 del Rio A, Perez-Jimenez R, Liu R, Roca-Cusachs P, Fernandez JM and Sheetz MP (2009) Stretching single talin rod molecules activates vinculin binding. *Science* (80-.) **323**, 638–641.
- 3 Yao M, Goult BT, Klapholz B, Hu X, Toseland CP, Guo Y, Cong P, Sheetz MP and Yan J (2016) The mechanical response of talin. *Nat Commun* **7**, 11966.
- 4 Izard T, Evans G, Borgon RA, Rush CL, Bricogne G and Bois PR (2004) Vinculin activation by talin through helical bundle conversion. *Nature* **427**, 171–175.
- 5 Carisey A, Tsang R, Greiner AM, Nijenhuis N, Heath N, Nazgiewicz A, Kemkemer R, Derby B, Spatz J and Ballestrem C (2013) Vinculin regulates the recruitment and release of core focal adhesion proteins in a force-dependent manner. *Curr Biol* **23**, 271–281.
- 6 le Duc Q, Shi Q, Blonk I, Sonnenberg A, Wang N, Leckband D and de Rooij J (2010) Vinculin potentiates E-cadherin mechanosensing and is recruited to actin-anchored sites within adherens junctions in a myosin II-dependent manner. *J Cell Biol* **189**, 1107–1115.
- 7 Dos Reis RS and Horn F (2010) Enteropathogenic *Escherichia coli*, *Salmonella*, *Shigella* and *Yersinia*: cellular aspects of host-bacteria interactions in enteric diseases. *Gut Pathog* **2**, 8.
- 8 Grove J and Marsh M (2011) The cell biology of receptor-mediated virus entry. *J Cell Biol* **195**, 1071–1082.
- 9 Izard T, Tran Van Nhiu G and Bois PR (2006) *Shigella* applies molecular mimicry to subvert vinculin and invade host cells. *J Cell Biol* **175**, 465–475.
- 10 Park H, Lee JH, Gouin E, Cossart P and Izard T (2011) The rickettsia surface cell antigen 4 applies mimicry to bind to and activate vinculin. *J Biol Chem* **286**, 35096–35103.
- 11 Carabeo RA, Grieshaber SS, Fischer E and Hackstadt T (2002) Chlamydia trachomatis induces remodeling of the actin cytoskeleton during attachment and entry into HeLa cells. *Infect Immun* **70**, 3793–3803.
- 12 Clifton DR, Fields KA, Grieshaber SS, Dooley CA, Fischer ER, Mead DJ, Carabeo RA and Hackstadt T (2004) From the cover: a chlamydial type III translocated protein is tyrosine-phosphorylated at the site of entry and associated with recruitment of actin. *Proc Natl Acad Sci* **101**, 10166–10171.
- 13 Thwaites TR, Pedrosa AT, Peacock TP and Carabeo RA (2015) Vinculin interacts with the chlamydia effector TarP via a tripartite vinculin binding domain to mediate actin recruitment and assembly at the plasma membrane. *Front Cell Infect Microbiol* **5**, 88.
- 14 Thwaites T, Nogueira AT, Campeotto I, Silva AP, Grieshaber SS and Carabeo RA (2014) The Chlamydia effector TarP mimics the mammalian leucine-aspartic acid motif of paxillin to subvert the focal adhesion kinase during invasion. *J Biol Chem* **289**, 30426–30442.
- 15 Banno A, Goult BT, Lee H, Bate N, Critchley DR and Ginsberg MH (2012) Subcellular localization of talin is regulated by inter-domain interactions. *J Biol Chem* **287**, 13799–13812.
- 16 Vonrhein C, Flensburg C, Keller P, Sharff A, Smart O, Paciorek W, Womack T and Bricogne G (2011) Data processing and analysis with the *autoPROC* toolbox. *Acta Crystallogr D Biol Crystallogr* **67**, 293–302.
- 17 Kabsch W (2010) XDS. *Acta Crystallogr D Biol Crystallogr* **66**, 125–132.
- 18 Evans PR and Murshudov GN (2013) How good are my data and what is the resolution? *Acta Crystallogr D Biol Crystallogr* **69**, 1204–1214.
- 19 Evans PR (2011) An introduction to data reduction: space-group determination, scaling and intensity statistics. *Acta Crystallogr D Biol Crystallogr* **67**, 282–292.
- 20 Zacharchenko T, Qian X, Goult BT, Jethwa D, Almeida TB, Ballestrem C, Critchley DR, Lowy DR and Barsukov IL (2016) LD motif recognition by talin: structure of the Talin-DLC1 complex. *Structure* **24**, 1130–1141.
- 21 McCoy AJ, Grosse-Kunstleve RW, Adams PD, Winn MD, Storoni LC and Read RJ (2007) *Phaser* crystallographic software. *J Appl Crystallogr* **40**, 658–674.
- 22 Emsley P, Lohkamp B, Scott WG and Cowtan K (2010) Features and development of *Coot*. *Acta Crystallogr D Biol Crystallogr* **66**, 486–501.
- 23 Murshudov GN, Skubák P, Lebedev AA, Pannu NS, Steiner RA, Nicholls RA, Winn MD, Long F and Vagin AA (2011) REFMAC5 for the refinement of macromolecular crystal structures. *Acta Crystallogr D Biol Crystallogr* **67**, 355–367.
- 24 Chen VB, Arendall WB, Headd JJ, Keedy DA, Immormino RM, Kapral GJ, Murray LW, Richardson JS and Richardson DC (2010) MolProbity: all-atom structure validation for macromolecular crystallography. *Acta Crystallogr D Biol Crystallogr* **66**, 12–21.
- 25 Krissinel E and Henrick K (2007) Inference of macromolecular assemblies from crystalline state. *J Mol Biol* **372**, 774–797.
- 26 Gingras AR, Ziegler WH, Frank R, Barsukov IL, Roberts GCK, Critchley DR and Emsley J (2005) Mapping and consensus sequence identification for multiple vinculin binding sites within the talin rod. *J Biol Chem* **280**, 37217–37224.
- 27 Hytönen VP and Vogel V (2008) How force might activate talin's vinculin binding sites: SMD reveals a structural mechanism. *PLoS Comput Biol* **4**, e24.

- 28 Yao M, Goult BT, Chen H, Cong P, Sheetz MP and Yan J (2015) Mechanical activation of vinculin binding to talin locks talin in an unfolded conformation. *Sci Rep* **4**, 4610.
- 29 Yan J, Yao M, Goult BT and Sheetz MP (2015) Talin dependent mechanosensitivity of cell focal adhesions. *Cell Mol Bioeng* **8**, 151–159.
- 30 Papagrigoiriou E, Gingras AR, Barsukov IL, Bate N, Fillingham IJ, Patel B, Frank R, Ziegler WH, Roberts GC, Critchley DR *et al.* (2004) Activation of a vinculin-binding site in the talin rod involves rearrangement of a five-helix bundle. *EMBO J* **23**, 2942–2951.
- 31 Lee JH, Vonrhein C, Bricogne G and Izard T (2013) Crystal structure of the N-terminal domains of the surface cell antigen 4 of Rickettsia. *Protein Sci* **22**, 1425–1431.
- 32 Park H, Valencia-Gallardo C, Sharff A, Van Nhieu GT and Izard T (2011) Novel vinculin binding site of the IpaA invasin of shigella. *J Biol Chem* **286**, 23214–23221.
- 33 Bois PRJ, O'Hara BP, Nietlispach D, Kirkpatrick J and Izard T (2006) The vinculin binding sites of talin and  $\alpha$ -actinin are sufficient to activate vinculin. *J Biol Chem* **281**, 7228–7236.
- 34 Maartens AP, Wellmann J, Wictome E, Klapholz B, Green H and Brown NH (2016) *Drosophila* vinculin is more harmful when hyperactive than absent, and can circumvent integrin to form adhesion complexes. *J Cell Sci* **129**, 4354–4365.
- 35 Goult BT, Gingras AR, Bate N, Barsukov IL, Critchley DR and Roberts GCK (2010) The domain structure of talin: residues 1815–1973 form a five-helix bundle containing a cryptic vinculin-binding site. *FEBS Lett* **584**, 2237–2241.
- 36 Alam T, Alazmi M, Gao X and Arold ST (2014) How to find a leucine in a haystack? Structure, ligand recognition and regulation of leucine-aspartic acid (LD) motifs. *Biochem J* **460**, 317–329.
- 37 Thomas JW, Cooley MA, Broome JM, Salgia R, Griffin JD, Lombardo CR and Schaller MD (1999) The role of focal adhesion kinase binding in the regulation of tyrosine phosphorylation of paxillin. *J Biol Chem* **274**, 36684–36692.
- 38 Hoellerer MK, Noble MEM, Labesse G, Campbell ID, Werner JM and Arold ST (2003) Molecular recognition of paxillin LD motifs by the focal adhesion targeting domain. *Structure* **11**, 1207–1217.
- 39 Bouchet BP, Gough RE, Ammon Y-C, van de Willige D, Post H, Jacquemet G, Altelaar AM, Heck AJ, Goult BT and Akhmanova A (2016) Talin-KANK1 interaction controls the recruitment of cortical microtubule stabilizing complexes to focal adhesions. *Elife* **5**, e18124.
- 40 Goult BT, Zacharchenko T, Bate N, Tsang R, Hey F, Gingras AR, Elliott PR, Roberts GCK, Ballestrem C, Critchley DR *et al.* (2013) RIAM and vinculin binding to talin are mutually exclusive and regulate adhesion assembly and turnover. *J Biol Chem* **288**, 8238–8249.
- 41 Tolchard J, Walpole SJ, Miles AJ, Maytum R, Eaglen LA, Hackstadt T, Wallace BA and Blumenschein TMA (2018) The intrinsically disordered Tarp protein from chlamydia binds actin with a partially preformed helix. *Sci Rep* **8**, 1960.
- 42 Atherton P, Stutchbury B, Wang D-Y, Jethwa D, Tsang R, Meiler-Rodriguez E, Wang P, Bate N, Zent R, Barsukov IL *et al.* (2015) Vinculin controls talin engagement with the actomyosin machinery. *Nat Commun* **6**, 10038.
- 43 Yao M, Qiu W, Liu R, Efremov AK, Cong P, Seddiki R, Payre M, Lim CT, Ladoux B, Mège R-M *et al.* (2014) Force-dependent conformational switch of  $\alpha$ -catenin controls vinculin binding. *Nat Commun* **5**, 4525.
- 44 Jones DT and Cozzetto D (2015) DISOPRED3: precise disordered region predictions with annotated protein-binding activity. *Bioinformatics* **31**, 857–863.
- 45 Borgon RA, Vonrhein C, Bricogne G, Bois PR and Izard T (2004) Crystal structure of human vinculin. *Structure* **12**, 1189–1197.

# Cell Reports

## Talin Autoinhibition Regulates Cell-ECM Adhesion Dynamics and Wound Healing *In Vivo*

### Graphical Abstract



### Authors

Amanda Haage, Katharine Goodwin, Austin Whitewood, ..., Sergey Plotnikov, Benjamin T. Goult, Guy Tanentzapf

### Correspondence

tanentz@mail.ubc.ca

### In Brief

Using a new transgenic mouse model that disrupts talin autoinhibition, Haage et al. characterize in quantitative detail the results of a wholesale increase in cell-ECM adhesion. Increasing adhesion delays wound healing due to a shift to more mature and stable adhesions, which inhibit dynamic cell movements.

### Highlights

- Disrupting talin autoinhibition via E1770A mutation results in viable mice
- Disrupting talin autoinhibition delays wound healing *in vitro* and *in vivo*
- E1770A Talin increases focal adhesion maturity, stability, and strength
- E1770A Talin disrupts actin organization and traction force generation



Haage et al., 2018, Cell Reports 25, 2401–2416  
November 27, 2018 © 2018 The Authors.  
<https://doi.org/10.1016/j.celrep.2018.10.098>

CellPress

# Talin Autoinhibition Regulates Cell-ECM Adhesion Dynamics and Wound Healing *In Vivo*

Amanda Haage,<sup>1</sup> Katharine Goodwin,<sup>1</sup> Austin Whitewood,<sup>2</sup> Darius Camp,<sup>1</sup> Aaron Bogutz,<sup>3</sup> Christopher T. Turner,<sup>4</sup> David J. Granville,<sup>4</sup> Louis Lefebvre,<sup>3</sup> Sergey Plotnikov,<sup>5</sup> Benjamin T. Goult,<sup>2</sup> and Guy Tanentzap<sup>1,6,\*</sup>

<sup>1</sup>Department of Cellular and Physiological Sciences, 2350 Health Sciences Mall, University of British Columbia, Vancouver, BC V6T 1Z3, Canada

<sup>2</sup>School of Biosciences, Giles Ln, University of Kent, Canterbury CT2 7NZ, UK

<sup>3</sup>Department of Medical Genetics, 2350 Health Sciences Mall, University of British Columbia, Vancouver, BC V6T 1Z3, Canada

<sup>4</sup>Department of Pathology and Laboratory Medicine, 2211 Wesbrook Mall, University of British Columbia, Vancouver, BC V6T 2B5, Canada

<sup>5</sup>Department of Cell and Systems Biology, 25 Harbord Street, University of Toronto, Toronto, ON M5S 3H7, Canada

<sup>6</sup>Lead Contact

\*Correspondence: [tanentz@mail.ubc.ca](mailto:tanentz@mail.ubc.ca)

<https://doi.org/10.1016/j.celrep.2018.10.098>

## SUMMARY

Cells in multicellular organisms are arranged in complex three-dimensional patterns. This requires both transient and stable adhesions with the extracellular matrix (ECM). Integrin adhesion receptors bind ECM ligands outside the cell and then, by binding the protein talin inside the cell, assemble an adhesion complex connecting to the cytoskeleton. The activity of talin is controlled by several mechanisms, but these have not been well studied *in vivo*. By generating mice containing the activating point mutation E1770A in talin (*Tln1*), which disrupts autoinhibition, we show that talin autoinhibition controls cell-ECM adhesion, cell migration, and wound healing *in vivo*. In particular, blocking autoinhibition gives rise to more mature, stable focal adhesions that exhibit increased integrin activation. Mutant cells also show stronger attachment to ECM and decreased traction force. Overall, these results demonstrate that modulating talin function via autoinhibition is an important mechanism for regulating multiple aspects of integrin-mediated cell-ECM adhesion *in vivo*.

## INTRODUCTION

Integrin-mediated adhesion to the extracellular matrix (ECM) contributes to multiple processes during animal development and tissue homeostasis. To allow integrins to perform diverse roles with a high degree of spatial and temporal specificity, integrin-mediated adhesion must be modulated rapidly and precisely (Iwamoto and Calderwood, 2015; Wolfenson et al., 2013). One of the best-characterized methods of regulation is integrin activation. During integrin activation, the integrin extracellular domain extends, which substantially increases its binding affinity for ECM ligands (Shattil et al., 1995). Integrin activation can be induced by interactions between the integrin cytoplasmic domain and various cytoplasmic factors (inside-out activation)

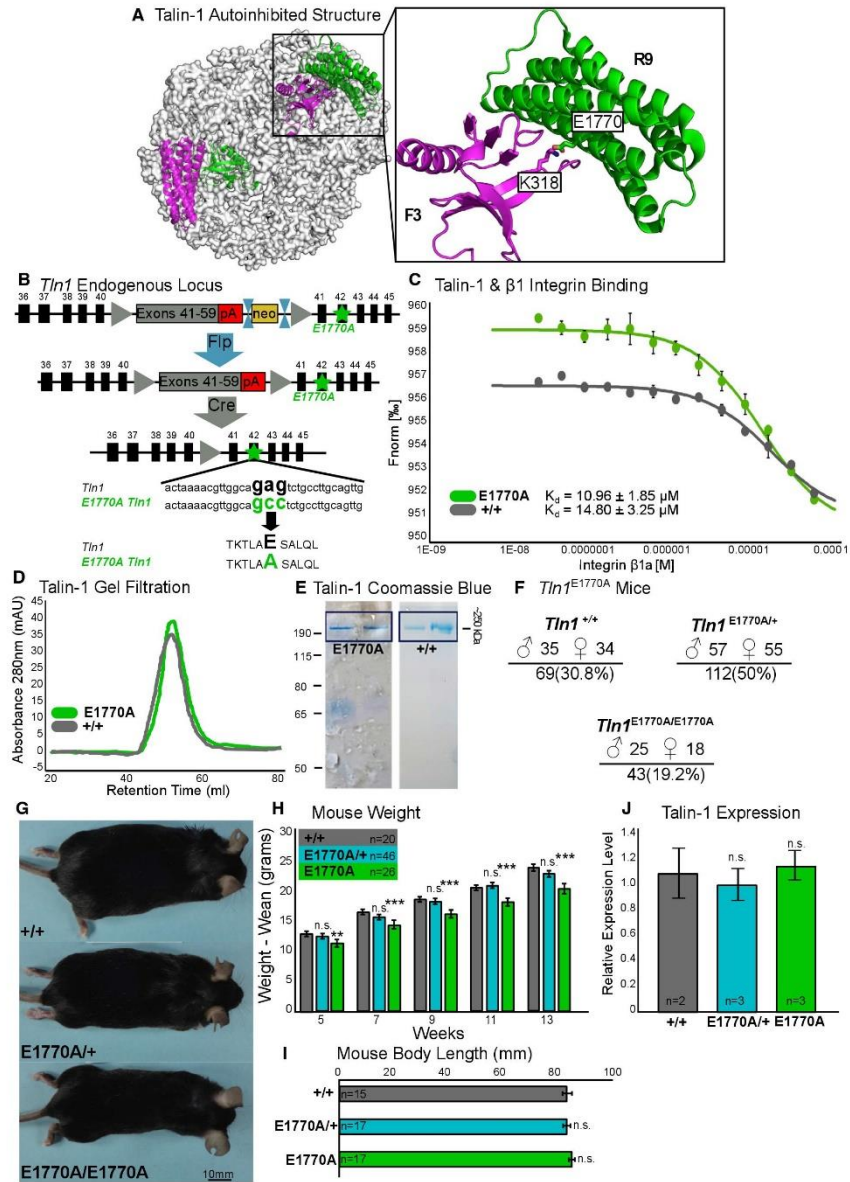
or by interactions with insoluble extracellular ligands (outside-in activation) (Calderwood, 2004a; Ginsberg, 2014). In particular, the large cytoplasmic adaptor protein talin is known as a key player in inside-out activation, and the regulation of talin recruitment to the membrane modulates integrin activity (Calderwood, 2004b; Ginsberg, 2014).

Talin connects integrins to the rest of the adhesion complex by binding directly to the cytoplasmic tail of  $\beta$ -integrins and then connecting either directly, through its actin binding domains, or indirectly, via other adaptor proteins, to the cytoskeleton (Horwitz et al., 1986; Kanchanawong et al., 2010). Talin function is essential for cell-ECM adhesion, and it is required for assembly and maintenance of the integrin adhesion complex (Klapholz and Brown, 2017). Talin is a large cytoplasmic protein composed of a globular N-terminal head region, containing a FERM (protein 4.1, ezrin, radixin, and moesin) domain, and a flexible rod region. There are two known integrin binding sites (IBSs) in talin: IBS-1, located within the FERM domain, and IBS-2, at the C terminus (Critchley, 2009). The IBS-1 site in the FERM domain mediates inside-out activation by binding to the  $\beta$ -integrin cytoplasmic tail. This initiates a cascade of events resulting in conformational changes of the integrin extracellular domain that increase its affinity for ECM ligands (Tadokoro et al., 2003). Loss of talin in cells and in animal models largely phenocopies the loss of integrin function (Brown et al., 2002; Monkley et al., 2000; Priddle et al., 1998). Conversely, overexpression of the talin head domain is sufficient to induce inside-out integrin activation (Calderwood et al., 1999; Kim et al., 2003). Due to its central role in integrin-based adhesions, elucidating how talin function is regulated is important for a mechanistic understanding of how integrin-mediated cell-ECM adhesion is regulated.

Previously, talin function has been shown to be regulated by several mechanisms (Klapholz and Brown, 2017). Similar to other FERM domain-containing proteins, talin can form intramolecular autoinhibitory interactions between the FERM domain and other parts of the molecule (Goult et al., 2009). Previous biochemical experiments have shown that the talin head can interact with the talin rod. Cell culture experiments have further shown that mutations that block this interaction result in increased integrin activation (Goksoy et al., 2008; Kopp et al.,



Cell Reports 25, 2401–2416, November 27, 2018 © 2018 The Authors. 2401  
This is an open access article under the CC BY-NC-ND license (<http://creativecommons.org/licenses/by-nc-nd/4.0/>).



(legend on next page)

2010). Moreover, biochemical experiments have shown that the talin rod binds the same region in the talin head as  $\beta$ -integrin cytoplasmic tails. This suggests that these two interactions are mutually exclusive, which is consistent with autoinhibition (Goult et al., 2009). Cryoelectron microscopy (cryo-EM) analysis of full-length talin suggests that it forms a compact donut-shaped autoinhibited structure by dimerizing with another talin molecule (Goult et al., 2013). This allows many intra- and intermolecular interactions to form and stabilize the globular structure of talin in its autoinhibited, dimerized conformation (Zhang et al., 2016). Some evidence from cell culture experiments supports an important functional role for autoinhibition in regulating talin function. Cell fractionation experiments suggest that forcing talin into a non-autoinhibited or open conformation increases its localization to the membrane (Banno et al., 2012). In cultured human umbilical vein endothelial cell (HUVEC) cells transfected with *TLN1* small interfering RNA (siRNA) and an autoinhibition mutant rescue transgene, cell spreading was defective and there was an increased number of focal adhesions (FAs) (Kopp et al., 2010).

To date, the only characterization of the requirement for autoinhibition *in vivo* comes from experiments in *Drosophila*, in which endogenous Talin was replaced with mutant, autoinhibition-defective Talin (Ellis et al., 2013). This Talin autoinhibition mutant behaved in the manner expected from a gain-of-function allele, and morphogenetic defects were observed because of too much, rather than too little, adhesion (Ellis et al., 2013; Goodwin et al., 2016). These phenotypes were hypothesized to be due to enhanced recruitment and binding of Talin and integrins, as well as reduced Talin turnover at sites of adhesion. Consequently, morphogenetic processes that require cyclic adhesion assembly and disassembly were disrupted. In contrast, integrin-based adhesion at myotendinous junctions, a non-morphogenetic context involving adhesive structures that are more stable and persistent, is largely normal in Talin autoinhibition-defective flies (Ellis et al., 2013). Furthermore, detailed analysis of morphogenetic events in Talin autoinhibition-defective flies showed that autoinhibition could regulate the large-scale biomechanical properties of cells and tissues. This defect was manifested in Talin autoinhibition-defective embryos as a failure to regulate cell migration and force transmission, leading to disrupted and delayed tissue development (Goodwin et al., 2016).

Here, we describe the phenotypic characterization of mice containing a mutation in talin (*Tln1*) that abrogates its ability to undergo autoinhibition (*Tln1*<sup>E1770A</sup>). We confirm earlier cell culture observations that autoinhibition regulates the recruitment of Tln1 to sites of adhesion, including regulating FA size. Using comprehensive phenotypic analysis of mouse embryonic fibroblasts (MEFs) derived from *Tln1*<sup>E1770A</sup> embryos and a range of techniques including quantitative imaging, total internal reflection fluorescence (TIRF), and traction force microscopy, we were able to uncover diverse functional phenotypes. Phenotypes observed include effects at the level of single FAs, such as changes in composition and stability, as well as effects at the level of the entire cell, such as abnormal shape, behavior, and migration. Finally, we extend our analysis to tissue-level effects *in vivo* and show that Tln1 autoinhibition-defective mice exhibit impaired tissue repair following injury. Our results demonstrate the importance and versatility of Tln1 autoinhibition as a regulatory tool for controlling integrin-mediated cell-ECM adhesion *in vivo*.

## RESULTS

### Generation of a *Tln1* Autoinhibition-Defective Mouse Mutant

Previous structural and biochemical studies have mapped the autoinhibitory regions in Tln1 to the F3 lobe of the FERM domain (residues 306–400 in mouse Tln1) and R9 (rod domain 9), which forms an amphipathic helical bundle (residues 1,655–1,822). Point mutations have been identified in both the R9 and the FERM domains that block their interaction *in vitro* (Goult et al., 2009). However, the region of the FERM domain that is involved is known to have multiple roles, including binding to  $\beta$ -integrin cytoplasmic tails and PIP2. We therefore decided to mutate a residue from the R9 domain that *in vitro* abrogates binding with the FERM domain and thus blocks autoinhibition. The mutation selected changes a conserved glutamate residue in R9 (E1770 in mouse Tln1), which forms a buried salt bridge with the K318 residue in the FERM domain, to an alanine (E1770A) (Figures 1A and 1B). We confirmed that the overall stability and function of Tln1 was not compromised by the E1770A mutation using microscale thermophoresis and analytical gel filtration experiments. In particular, we observed that in 150 mM NaCl, both wild-type and E1770A mutant full-length Tln1 were able to bind to the cytoplasmic tail of  $\beta$ 1-integrin

#### Figure 1. Talin Autoinhibition Is Not Essential for Viability in Mice

- (A) Structure of the autoinhibited talin dimer. The gray envelope represents the autoinhibited dimer as visualized by electron microscopy (Goult et al., 2013). The two monomers are shown in green and purple. Inset: the structure of the F3:R9 complex (PDB: 4F7G) (Song et al., 2012) with the key buried salt bridge between R9 E1770 and F3 K318 highlighted.
- (B) Schematic of the mutagenesis of the E1770 site in *Tln1*.
- (C) Microscale thermophoresis assay demonstrating binding of RED-Tris-NTA-labeled full-length Tln1 wild-type (gray) and E1770A (green) to the  $\beta$ 1a-integrin peptide.
- (D) Gel filtration (Superdex 200) elution profiles of purified recombinant wild-type (gray) and E1770A Tln1 (green).
- (E) Coomassie-stained SDS-PAGE gel of purified recombinant wild-type and E1770A Tln1.
- (F) Genotyping results of 40 *Tln1*<sup>E1770A/+</sup> intercrosses (224 mice total). The observed segregation ratio is statistically significant with a chi-square test,  $p < 0.05$ .
- (G) Male mice at 21 weeks of age.
- (H) Male mouse weight over time minus weight at weaning.
- (I) Mouse body length measured from nose tip to base of tail of male mice 18–22 weeks of age.
- (J) Relative Tln1 expression levels determined via qRT-PCR from MEFs.
- All error bars denote SEM, with \*\*\* $p \leq 0.0001$ , \*\* $p \leq 0.001$ , and \* $p \leq 0.01$ .



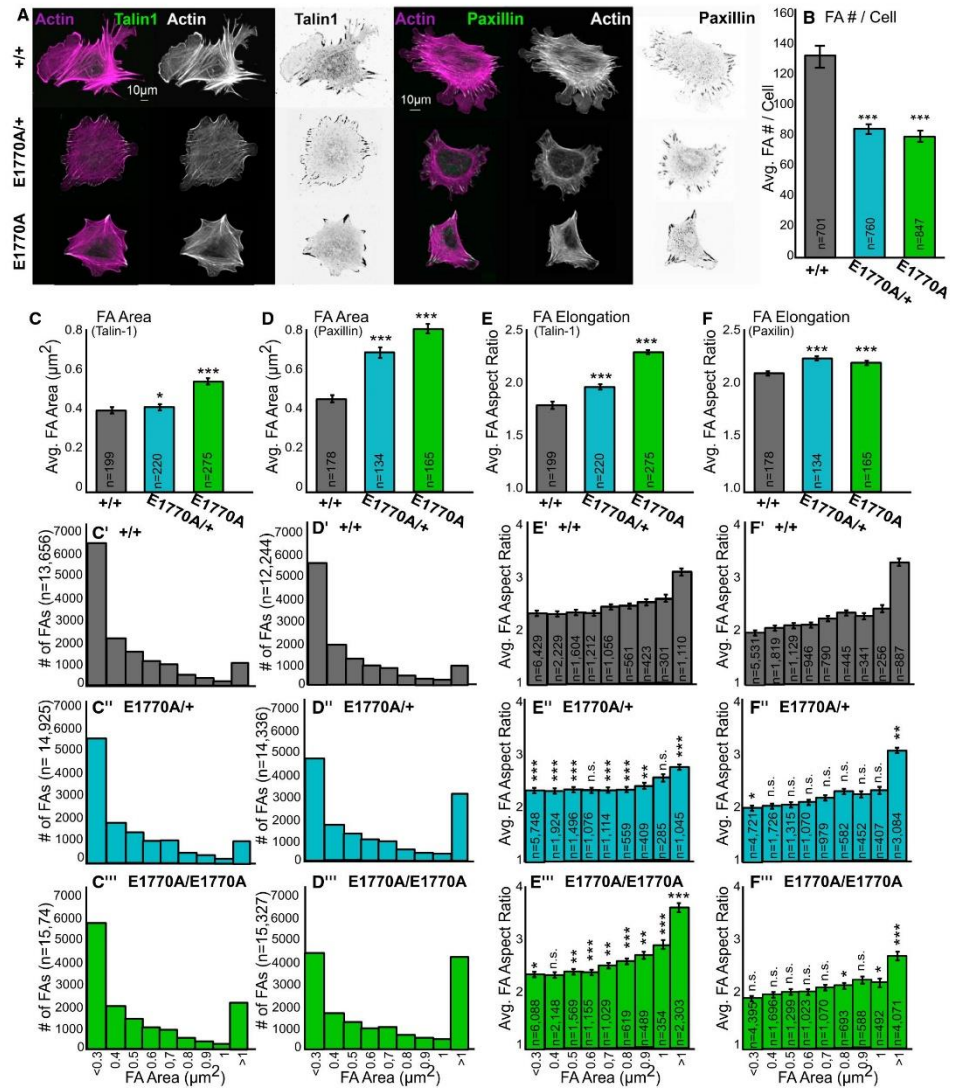


**Figure 2. Talin Autoinhibition Regulates FA Maturation**

(A) Representative images of MEFs derived from *Tln1*<sup>E1770A</sup> mutant embryos plated on fibronectin and stained with a TLN1-specific antibody or a Paxillin-specific antibody (green is black in inverted images; actin is magenta or white).

(B) *Tln1*<sup>E1770A</sup> mutant MEFs have a significantly reduced average number of FAs per cell.

(C) The average FA area per cell marked by Tln1 staining. n values in (C) represent cells. Data are binned in groups ranging from less than 0.3  $\mu\text{m}^2$  to more than 1  $\mu\text{m}^2$  for each genotype, with (C) *Tln1*<sup>+/+</sup>, (C') *Tln1*<sup>E1770A/+</sup>, and (C'') *Tln1*<sup>E1770A/E1770A</sup>. n values for data in (C)-(C'') represent FAs.

(legend continued on next page)

with similar affinity (Figure 1C) and that both proteins have the same gel filtration elution profile (Figures 1D and 1E). We then generated mice containing the *Tln1*<sup>E1770A</sup> mutation (see STAR Methods). These mice were viable and fertile (Figure 1F) and did not exhibit gross morphological defects (Figure 1G). However, the number of live *Tln1*<sup>E1770A/E1770A</sup> homozygotes recovered at weaning from intercrosses between heterozygous mice was slightly below the expected Mendelian ratio: 19.2% instead of 25% (n = 224, p = 0.0489) (Figure 1F). This could suggest a slight survival disadvantage in the homozygous mutants. In addition, *Tln1*<sup>E1770A/E1770A</sup> mice exhibited a small but statistically significant reduction in weight gain compared to *Tln1*<sup>+/+</sup> controls or *Tln1*<sup>E1770A/+</sup> mice (Figures 1G and 1H). Despite this, their overall body length was normal (Figure 1I). To ensure that the phenotypes observed were specifically due to the E1770A mutation, we confirmed that Tln1 was expressed at normal levels in primary MEF cultures derived from *Tln1*<sup>+/+</sup>, *Tln1*<sup>E1770A/+</sup>, and *Tln1*<sup>E1770A/E1770A</sup> mutant embryos (Figure 1J).

#### Talin Autoinhibition Regulates FA Maturation in MEFs

To investigate the effect of the E1770A mutation on FAs, we isolated primary cultures of MEFs from *Tln1*<sup>+/+</sup>, *Tln1*<sup>E1770A/+</sup>, and *Tln1*<sup>E1770A/E1770A</sup> mutant embryos at embryonic day 13.5 (E13.5). We comprehensively analyzed the FA number, composition, and shape in these fibroblasts using multiple markers and high-resolution, quantitative, automated image analysis (Figure 2). In MEFs from all three genotypes analyzed, characteristic FAs and stress fibers were present that contained typical markers (Figure 2A). The average number of FAs per cell was lower by about a third in *Tln1*<sup>E1770A/+</sup> and *Tln1*<sup>E1770A/E1770A</sup> mutant MEFs (Figure 2B). Though there were fewer total FAs, the FAs observed in *Tln1*<sup>E1770A/+</sup> and *Tln1*<sup>E1770A/E1770A</sup> mutant MEFs were on average larger in area (Figures 2C and 2D), and plotting histograms showing the distribution of areas across the genotypes revealed a large increase in the number of FAs more than 1  $\mu\text{m}^2$  in size (Figures 2C and 2D). The increased size of FAs in the presence of *Tln1*<sup>E1770A</sup> is consistent with the presence of more mature adhesions. A characteristic of maturing adhesions is that as they increase in area, they also elongate (Geiger and Yamada, 2011; Wolfenson et al., 2009). We determined that the average aspect ratio of FAs in MEFs from *Tln1*<sup>E1770A/+</sup> and *Tln1*<sup>E1770A/E1770A</sup> embryos was also larger compared to *Tln1*<sup>+/+</sup> MEFs. This increase in aspect ratio was consistent across the spectrum of the FA area, plotted in relation to the FA area (Figures 2E and 2F). These measurements revealed that the *Tln1*<sup>E1770A</sup> mutation increased the number of larger, more elongated adhesions, consistent with an overall increase in FA maturation.

#### Talin Autoinhibition Regulates Integrin Activation and Integrin Signaling

Increased FA maturation is associated with higher integrin activation (Lee et al., 2013), which might be one predicted outcome of lower Tln1 autoinhibition. To test whether the *Tln1*<sup>E1770A</sup> mutation promoted integrin activation, we used the active  $\beta 1$ -integrin-specific antibody 9EG7 (Bazzoni et al., 1995). MEFs from *Tln1*<sup>+/+</sup>, *Tln1*<sup>E1770A/+</sup>, and *Tln1*<sup>E1770A/E1770A</sup> embryos were co-stained using a general  $\beta 1$ -integrin antibody and 9EG7. The ratio of the staining intensity of these two antibodies within FAs was used to measure activation. These data showed a significant increase in integrin activation in *Tln1*<sup>E1770A</sup> mutant MEFs (Figures 3A and 3B). In addition, *Tln1*<sup>E1770A</sup> mutants had increased co-localization of both Tln1 and paxillin with either general  $\beta 1$ -integrin or active  $\beta 1$ -integrin, though this effect was more striking with activated  $\beta 1$ -integrin (Figure 3E; Figures S1 and S2). All of these data are consistent with higher integrin activation in *Tln1*<sup>E1770A</sup> mutants. Integrin activation is closely linked with modulation of integrin signaling (Clark and Brugge, 1995). The phosphorylation of focal adhesion kinase (FAK) at Y397 is a useful marker for activation of integrin signaling. FAK phosphorylation was similarly assessed by co-staining MEFs from *Tln1*<sup>+/+</sup>, *Tln1*<sup>E1770A/+</sup>, and *Tln1*<sup>E1770A/E1770A</sup> embryos with antibodies that detect either all FAK protein or phosphorylated FAK(Y397) specifically. The ratio of intensity between these two antibodies was measured within FAs and showed increased phosphorylation of FAK at Y397 in *Tln1*<sup>E1770A</sup> mutant MEFs (Figures 3C and 3D). Altogether, these results suggest an increase in both integrin activation and signaling in the presence of the *Tln1*<sup>E1770A</sup> mutation.

#### Talin Autoinhibition Regulates FAs Stability

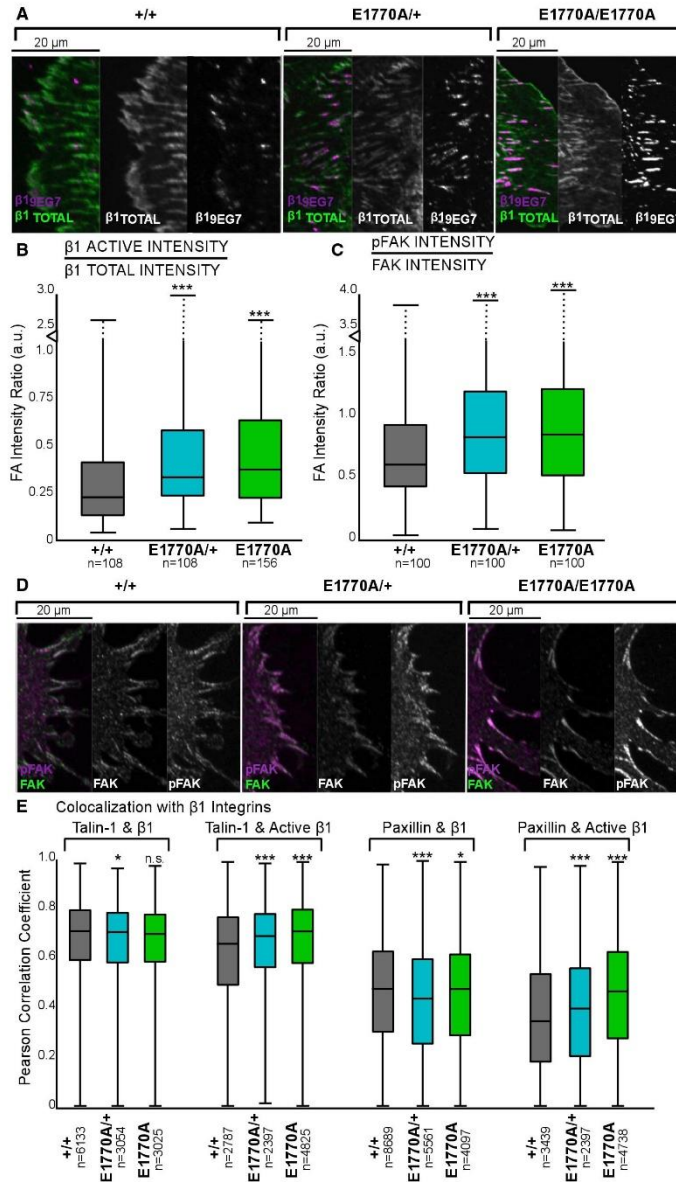
Because an increase in either FA maturation or integrin activation would be consistent with increased FA stability, we analyzed FA dynamics in MEFs from *Tln1*<sup>+/+</sup>, *Tln1*<sup>E1770A/+</sup>, and *Tln1*<sup>E1770A/E1770A</sup> embryos. FA dynamics were analyzed in two ways. First, FRAP (fluorescence recovery after photobleaching) was used to determine the mobile fraction of three FA markers: paxillin-GFP (Figures 4A and 4B; Figures S3A–S3C), Tln1-GFP (Figures 4C and 4D), and Tln1-GFP containing the E1770A point mutation (Figures 4E and 4F). This analysis showed that the mobile fraction of paxillin-GFP and Tln1-GFP in FAs in *Tln1*<sup>E1770A/E1770A</sup> MEFs was  $\sim 28\%$  and  $\sim 40\%$  lower, respectively, compared to controls (Figures 4A–4D). The mobile fraction of paxillin-GFP in FAs in *Tln1*<sup>E1770A/+</sup> MEFs was not significantly different (Figures S4A and S4B). Introducing the E1770A point mutation into Tln1-GFP resulted in a 66% reduction in the mobile fraction compared to the wild-type construct in *Tln1*<sup>+/+</sup> MEFs (Figures 4E and 4F). Furthermore, for the Tln1-GFP containing

(D) The average FA area per cell marked by paxillin staining. n values in (D) represent cells. Data are binned in groups ranging from less than 0.3  $\mu\text{m}^2$  to more than 1  $\mu\text{m}^2$  for each genotype, with (D') *Tln1*<sup>+/+</sup>, (D'') *Tln1*<sup>E1770A/+</sup>, and (D''') *Tln1*<sup>E1770A/E1770A</sup>. n values in (D)–(D''') represent FAs.

(E) The average FA aspect ratio (length/width) per cell marked by Tln1 staining. n values in (E) represent cells. Data are binned in groups ranging from a less than 0.3  $\mu\text{m}^2$  area to a more than 1  $\mu\text{m}^2$  area for each genotype, showing the average aspect ratio for each group, with (E') *Tln1*<sup>+/+</sup>, (E'') *Tln1*<sup>E1770A/+</sup>, and (E''') *Tln1*<sup>E1770A/E1770A</sup>. n values for data in (E)–(E''') represent FAs.

(F) The average FA aspect ratio (length/width) per cell marked by paxillin staining. n values in (F) represent cells. Data are binned in groups ranging from a less than 0.3  $\mu\text{m}^2$  area to a more than 1  $\mu\text{m}^2$  area for each genotype, showing the average aspect ratio for each group, with (F') *Tln1*<sup>+/+</sup>, (F'') *Tln1*<sup>E1770A/+</sup>, and (F''') *Tln1*<sup>E1770A/E1770A</sup>. n values for data in (F)–(F''') represent FAs.

All error bars denote SEM, with \*\*\*p  $\leq$  0.0001, \*\*p  $\leq$  0.001, and \*p  $\leq$  0.01.



(legend on next page)

the E1770A point mutation, similar mobile fractions were observed in either  $Tln1^{+/+}$  or  $Tln1^{E1770A/E1770A}$  MEFs, consistent with the autoinhibition-defective Talin already being present in  $Tln1^{E1770A/E1770A}$  MEFs (Figures 4E and 4F). Second, TIRF microscopy was employed, using paxillin-GFP as a marker to analyze FA dynamics. To study their dynamics, FAs in  $Tln1^{+/+}$ ,  $Tln1^{E1770A/+}$ , and  $Tln1^{E1770A/E1770A}$  MEFs were imaged over the course of 1 hr (Figure 4G). Analysis of the TIRF data revealed a small but significant increase in the average longevity of FAs (Figure 4H). To relate FA stability and maturation, we looked at the percentage of FAs per cell that were either small and short lived (Figure 4I, nascent FAs) or large and stable (Figure 4J, mature FAs) across the genotypes. Both  $Tln1^{E1770A/+}$  and  $Tln1^{E1770A/E1770A}$  MEFs had a significant decrease in the percentage of nascent FAs per cell and a significant increase in the percentage of mature FAs per cell (Figures 4I and 4J). In addition, we looked at the lifetime of tracked FAs using a previously established modeling method in which the duration and slopes of the assembly, stability, and disassembly phases of FAs are shown to scale (Berginski et al., 2011). Both  $Tln1^{E1770A/+}$  and  $Tln1^{E1770A/E1770A}$  MEFs showed greater assembly and a longer duration of the stability phase compared to control MEFs (Figure 4K, homozygous example only). Altogether, our data show that FAs in MEFs derived from  $Tln1^{E1770A}$  mutants are longer lasting and more stable than FAs in controls.

#### The $Tln1^{E1770A}$ Phenotype Is Independent of $Tln2$

It is known that in some instances, loss of  $Tln1$  is compensated by increased expression of the talin 2 ( $Tln2$ ) gene (Zhang et al., 2008). We wanted to determine whether, similarly, the  $Tln1^{E1770A}$  phenotype was modified by changes in expression of  $Tln2$ . Relative levels of  $Tln2$  protein expression were analyzed in MEFs from  $Tln1^{+/+}$ ,  $Tln1^{E1770A/+}$ , and  $Tln1^{E1770A/E1770A}$  embryos. This analysis showed that overall levels of  $Tln2$  were not significantly changed (Figure S3A). We then performed a siRNA knockdown of  $Tln2$  in  $Tln1^{+/+}$  and  $Tln1^{E1770A/E1770A}$  MEFs (Figures S3B–S3J). Western blot analysis confirmed that the siRNA produced a robust knockdown of the  $Tln2$  protein (Figure S3B). Loss of  $Tln2$  did not have the dramatic effect on FA formation seen in MEFs that lack  $Tln1$  (Zhang et al., 2008), although FAs were slightly smaller (Figures S3C and S3D). When  $Tln2$  knockdown was performed in the background of the  $Tln1^{E1770A}$  mutation, there was no substantial or consistent enhancement or suppression of the E1770A phenotype beyond the reduction of FA size seen in  $Tln1^{+/+}$  MEFs (Figures S3E and S3F). Knockdown of  $Tln2$  did not alter the relative difference in FA dynamics between  $Tln1^{+/+}$  and  $Tln1^{E1770A/E1770A}$  mutants (Figures S3G–S3J). Alto-

gether, these results argue that the  $Tln1^{E1770A}$  phenotype is independent of  $Tln2$ .

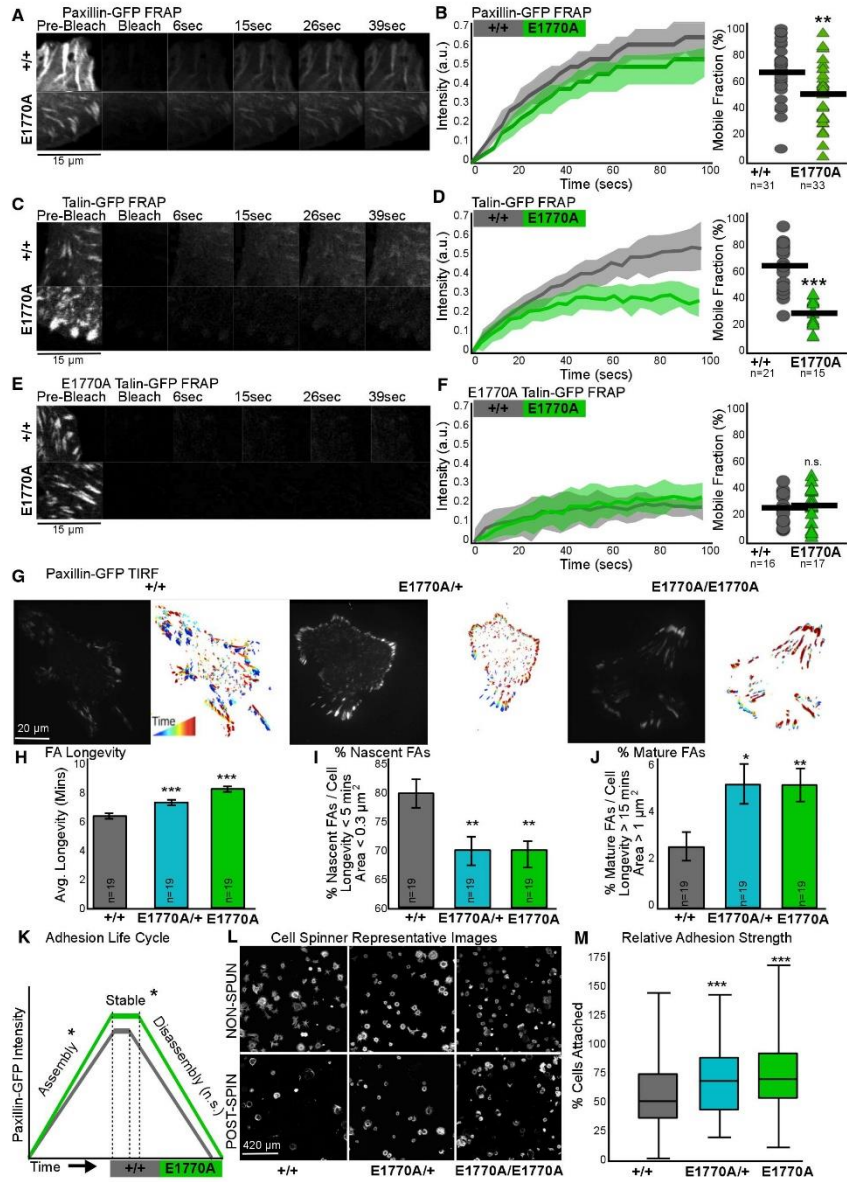
#### Talin Autoinhibition Regulates Adhesion Strength and Cell Spreading in MEFs

The changes in FAs observed in  $Tln1^{E1770A}$  mutants would be expected to affect aspects of cell-ECM adhesion and cell morphology. To assess the strength of cell-ECM adhesions, we adapted an assay that uses a cell-spinning device (García et al., 1997) to determine the relative attachment strength of cells to an underlying ECM. In this assay, cells are incubated on fibronectin-coated coverslips and allowed to attach. Following attachment, they are spun, exposing them to centrifugal force and detaching more loosely affixed cells. Relative adhesion strength is then calculated by determining the ratio of cells attached after spinning compared to a same-day non-spun control. This technique revealed that  $Tln1^{E1770A}$  mutant MEFs showed stronger attachment to the ECM relative to  $Tln1^{+/+}$  MEFs (Figures 4L and 4M). Moreover, MEFs from either  $Tln1^{E1770A/+}$  or  $Tln1^{E1770A/E1770A}$  mutant embryos exhibited a spreading defect. When plated on fibronectin, they exhibited reduced growth in cell area over 90 min compared to controls (Figures 5A and 5B). This spreading phenotype was not due to a defect in the initial attachment of cells, because both mutant and control cells adhered to the ECM-coated coverslips equally well (Figure 5C). The morphology of  $Tln1^{E1770A/+}$  or  $Tln1^{E1770A/E1770A}$  MEFs was also different from that of  $Tln1^{+/+}$  MEFs (Figure 5A). Calculating the cell aspect ratio and circularity of MEFs from  $Tln1^{E1770A/E1770A}$  embryos showed that they were rounder than  $Tln1^{+/+}$  controls (Figures 5D and 5E). In line with this, there was a reduction in the number of actin-based cell protrusions in  $Tln1^{E1770A}$  mutant MEFs, and these protrusions were shorter and thicker compared to  $Tln1^{+/+}$  (Figures 5F and 5H). This defect did not improve with time (Figure 5G). The cell-spreading defects that we observed could result from defects in the formation of nascent adhesions. We analyzed nascent adhesion formation by using Paxillin-GFP and TIRF microscopy to track adhesion formation and assembly rate during cell spreading (Figures S4D–S4H). We found that  $Tln1^{E1770A/E1770A}$  mutant MEFs exhibit longer-lasting FAs and that there is a decrease in the rate of formation of nascent adhesions and a corresponding increase in the rate of formation of mature adhesions (Figures S4E–S4G). Altogether, these results show that  $Tln1^{E1770A}$  mutant MEFs not only show increased adhesion strength to their ECM ligands, but also exhibit persistent defects in cell spreading and actin-based cell protrusions. These defects, which possibly occur due to reduced ability to form

**Figure 3. Talin Autoinhibition Regulates Integrin Activation and Signaling**

(A) Representative images of the leading edge of MEFs plated on fibronectin and stained with the active  $\beta1$ -integrin-specific monoclonal antibody 9EG7 (magenta) and a polyclonal  $\beta1$ -integrin antibody (green).  
(B) Ratio of FA intensities of the stainings represented in (A) of active  $\beta1$ -integrin to total  $\beta1$ -integrin. n values represent numbers of cells.  
(C) Ratio of FA intensities of the stainings represented in (A) of phosphorylated FAK (phosphoFAK) to total FAK. n values represent numbers of cells.  
(D) Representative confocal images of the leading edge of MEFs plated on fibronectin and stained with a phosphoFAK-specific monoclonal antibody (Y397, magenta) and a polyclonal FAK antibody (green).  
(E) Pearson correlation coefficients of FA markers. See also Figures S1 and S2. n values represent numbers of FAs, and only FAs with positive correlation were included.

All error bars denote SEM, with \*\*\* $p \leq 0.0001$ , \*\* $p \leq 0.001$ , and \* $p \leq 0.01$ .



(legend on next page)

nascent FAs, result in a rounder appearance of the cells compared to wild-type controls.

#### Talin Autoinhibition Regulates Wound Healing Both *In Vitro* and *In Vivo*

Although several phenotypes were observed in *Tln1*<sup>E1770A</sup> mutant MEFs, including abnormal integrin activation and signaling, increased adhesion, reduced cell protrusions, and defective cell spreading, it was unclear whether these would result in a functional defect. One possible effect of such phenotypes is a defect in cell migration. Therefore, cell migration was assessed in the background of the *Tln1*<sup>E1770A</sup> mutation using a scratch assay, a well-established *in vitro* assay for cell migration (Liang et al., 2007). This analysis showed that both *Tln1*<sup>E1770A/+</sup> and *Tln1*<sup>E1770A/E1770A</sup> MEFs exhibited delayed wound closure compared to *Tln1*<sup>+/+</sup> controls (Figures 6A and 6B). Because fibroblasts also migrate to close wounds *in vivo*, the effects of the *Tln1*<sup>E1770A</sup> mutation were analyzed in a biopsy punch wound healing assay in mice (Ganguli-Indra, 2014) (Figures 6C and 6D). Statistically significant delays in wound closure were observed in both *Tln1*<sup>E1770A/+</sup> and *Tln1*<sup>E1770A/E1770A</sup> mutant mice, though the wounds eventually closed. Overall, these data suggest that regulation of Tln1 function by autoinhibition is important for cell migration in MEFs and, more generally, for wound healing in mice.

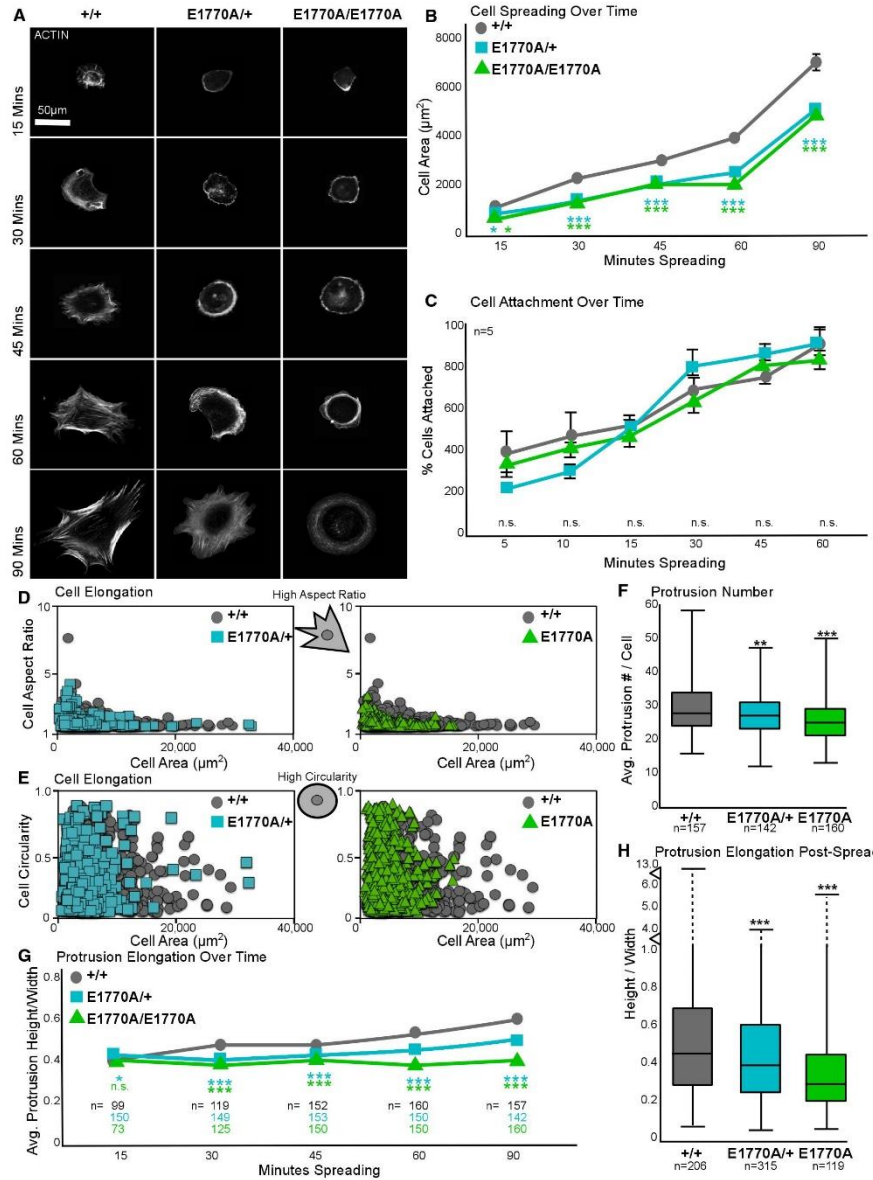
#### Talin Autoinhibition Regulates Actin Organization and Traction Force in MEFs

We hypothesized that the wound healing phenotypes seen in *Tln1*<sup>E1770A</sup> mutants were in part due to abnormal traction force, because the ability of fibroblasts to generate traction forces is thought to be essential for multiple stages of wound closure (Li and Wang, 2011; Tomasek et al., 2002). To investigate this, we measured the total traction force generated by MEFs derived from *Tln1*<sup>+/+</sup>, *Tln1*<sup>E1770A/+</sup>, and *Tln1*<sup>E1770A/E1770A</sup> embryos using traction force microscopy (Figure 7A). Surprisingly, we found that both total traction force (Figure 7B) and traction force per cell area (Figure 7C) were markedly reduced in *Tln1*<sup>E1770A</sup> mutant MEFs compared to *Tln1*<sup>+/+</sup>. This result was unexpected,

because larger and/or more stable FAs, such as those seen in *Tln1*<sup>E1770A</sup> mutant MEFs, are typically associated with higher traction forces (Ballestrem et al., 2001; Munevar et al., 2001). However, because lower traction forces can be associated with altered actin dynamics (Gardel et al., 2008; Thievsen et al., 2013; Tojkander et al., 2015), we used live imaging and various quantitative approaches to analyze the actin cytoskeleton. First, to quantitatively describe actin fibers within these cells, we adapted a previously described method (Cetera et al., 2014) to provide a measurement of the overall level of actin alignment. In *Tln1*<sup>E1770A</sup> mutant MEFs, there is an overall decrease in the alignment of actin (Figure 7D). Specifically, the percentage of the cell that contains aligned bundles, termed cell fibrousness, is smaller in both *Tln1*<sup>E1770A/+</sup> and *Tln1*<sup>E1770A/E1770A</sup> mutant MEFs (Figure 7E). Moreover, the defects in actin alignment persist over time as cells spread (Figure 7F). Second, to directly study actin dynamics, the live cell actin marker F-tractin-GFP (Belin et al., 2014) was used to track actin behavior in MEFs. Using kymograph analysis over time within active cell protrusions (Figure 7G), the flow rate of actin in *Tln1*<sup>E1770A</sup> mutant MEF protrusions was shown to be higher than controls (Figure 7H). When we controlled for cell shape by limiting our analysis to cells with a similar aspect ratio, actin flow rate was still higher in *Tln1*<sup>E1770A</sup> mutant MEFs compared to *Tln1*<sup>+/+</sup> (Figure 7I). In addition, to directly study actin dynamics, a previously described modified FRAP technique (Tojkander et al., 2015) was used in cells in which the FAs were labeled with a live mCherry-paxillin marker (Figures 7K–7M). Here, areas of dorsal stress fibers directly adjacent to FAs were bleached, and kymograph analysis of the recovery was used to determine actin polymerization rate. *Tln1*<sup>E1770A/E1770A</sup> mutant MEFs exhibited a small but significant shift to a slower actin polymerization rate in dorsal stress fibers (Figure 7M). These results indicate that, consistent with lower traction force, *Tln1*<sup>E1770A/E1770A</sup> MEFs have a more dynamic actin cytoskeleton. Global FA organization has previously been shown to be important for the formation of an organized and efficient contractile actin network. This was measured using a previously established method (Wu et al., 2012) that assigns a value to the degree of distribution of FA angles in a cell, termed the FA

**Figure 4. Talin Autoinhibition Regulates FA Stability and Adhesion Strength in MEFs**

- (A) Representative images of the leading edge of MEFs plated on fibronectin and transfected with paxillin-GFP (white). Region of interests (ROIs) were bleached, and recovery was imaged over time.
- (B) Average recovery intensity over time (solid) with 95% confidence intervals (shaded) and mobile fractions, with a black line representing the mean. See also Figures S4A–S4C.
- (C) Representative images of the leading edge of MEFs plated on fibronectin and transfected with Talin-1-GFP (white). ROIs were bleached, and recovery was imaged over time.
- (D) Average recovery intensity over time (solid) with 95% confidence intervals (shaded) and mobile fractions, with a black line representing the mean.
- (E) Representative images of the leading edge of MEFs plated on fibronectin and transfected with E1770A Talin-1-GFP (white). ROIs were bleached, and recovery was imaged over time.
- (F and G) Average percentage of total FAs per cell meeting each criterion is presented per genotype. (F) Average recovery intensity over time (solid) with 95% confidence intervals (shaded) and mobile fractions, with a black line representing the mean. (G) Representative TIRF images stacked over 60 min of MEFs plated on fibronectin and transfected with paxillin-GFP (white). Maximum intensity images were colored based on time point and overlaid.
- (H) Average minutes persisted throughout TIRF imaging.
- (I) Nascent FAs, defined as lasting <5 min and area < 0.3  $\mu\text{m}^2$ , were counted per cell.
- (J) Mature FAs, defined as lasting >15 min and area > 1  $\mu\text{m}^2$ , were counted per cell.
- (K) Summary of FA life cycle, with the duration of each phase (length) and rates (slope) presented to scale.
- (L) Representative images of MEFs plated on fibronectin and spun at 4,000 rpm compared to non-spun controls.
- (M) Cell counts for cell-spinning assay per genotype. All n values represent numbers of cells.
- All error bars denote SEM, with \*\*\* $p \leq 0.0001$ , \*\* $p \leq 0.001$ , and \* $p \leq 0.01$ .



(legend on next page)

alignment index (FAAI). Surprisingly, despite the loss of actin fiber alignment and the increase in flow rate (Figures 7A–7I, 7L, and 7M), the average FAAI increased in *Tln1*<sup>E1770A</sup> mutant MEFs (Figure 7J). Altogether, our data show that *Tln1*<sup>E1770A</sup> mutant MEFs exhibit a reduction in traction force consistent with a less organized and more dynamic actin cytoskeleton. However, these changes in actin architecture appear to be decoupled from the organization of FAs. This loss of interdependence between actin and FA organization could contribute to the reduction in traction force generation.

## DISCUSSION

Here we report the characterization of a mouse mutant that disrupts talin autoinhibition. Although these mice are viable, analysis of MEFs revealed several defects consistent with increased FA maturation and stability, as well as increased activation of integrins. Furthermore, MEFs from talin autoinhibition-defective mice exhibit stronger adhesion to the substrate, defective cell spreading, abnormal morphology, and cell migration defects. These defects have functional consequences in adult mice as revealed by *in vivo* wound healing assays. Finally, MEFs from talin autoinhibition-defective mice produce lower traction force but show increased actin dynamics. Our results reveal the importance of the regulatory mechanisms that fine-tune integrin-mediated cell-ECM adhesion *in vivo*. Moreover, they establish *Tln1*<sup>E1770A</sup> mice as a useful tool to explore the range of phenotypes caused by increased talin activity in diverse cellular contexts.

*Tln1*<sup>E1770A/E1770A</sup> mice are viable and do not exhibit any of the dramatic morphological defects that are known to occur when integrin-mediated cell-ECM adhesion is disrupted. However, MEFs derived from these mice displayed a range of defects. How can we reconcile these somewhat contradictory observations? Many cellular phenotypes identified in *Tln1*<sup>E1770A</sup> mutant MEFs were subtle and only became apparent after detailed quantitative analysis. This may be because many functionally overlapping regulatory mechanisms act on integrin-mediated adhesion (Iwamoto and Calderwood, 2015). However, it is also likely that regulatory mechanisms such as talin autoinhibition exhibit a tissue- and process-specific requirement. Thus, while we observe noticeable defects on the cellular or subcellular FA level in *Tln1*<sup>E1770A</sup> MEFs, these defects only become apparent on the gross scale in specific contexts, such as wound healing. We believe that as we explore other cellular and tissue-specific

contexts in greater detail, we will uncover additional phenotypes associated with defective talin autoinhibition.

Gain-of-function approaches provide the possibility of identifying novel functional requirements for genes in tissues and cells that are too disrupted in a simple loss-of-function mutant. Our goal in making the *Tln1*<sup>E1770A</sup> mice was to produce a mutant that modulates talin function in a positive direction, because no such tool was available previously. Several lines of evidence presented here support the conclusion that disrupting talin autoinhibition gives rise to a gain-of-function allele. One risk of a gain-of-function approach is the possibility that it will affect processes that are not regulated by the wild-type form of the protein. However, the phenotypes observed in *Tln1*<sup>E1770A</sup> mutants are in line with what would be expected from hyperactivated talin: increased integrin activity and signaling, stronger adhesion, and more recruitment of adhesion complex components. Nonetheless, in a few contexts, for example, in cell spreading, the *Tln1*<sup>E1770A</sup> phenotype resembles a loss of function. These results are reminiscent of previous observations in similarly mutated flies. In the case of the Talin autoinhibition-defective mutant fly, it was proposed that phenotypes that resemble those seen in loss-of-function mutants occur when cellular function requires precise regulation of the level of adhesion and too much or too little adhesion disrupts the process to similar extents (Ellis et al., 2013; Goodwin et al., 2016). The *Tln1*<sup>E1770A</sup> mutant behaves like a dominant mutation, because we observed phenotypes in both heterozygous and homozygous contexts. Here, the dosage of the *Tln1*<sup>E1770A</sup> allele corresponded to the strength of the effect, with homozygous giving rise to stronger phenotypes than heterozygous. Overall, *Tln1*<sup>E1770A</sup> mutant mice represent a versatile tool for manipulating the level of integrin-mediated cell-ECM adhesion *in vivo*. Given the ubiquity of talin and its central role in many types of integrin-based adhesions, we expect the *Tln1*<sup>E1770A</sup> to be useful in future studies.

Using our gain-of-function approach, we identify a requirement for modulation of integrin-based adhesion during wound healing. Wound closure requires coordination of tissue-scale deformations, matrix assembly, and cell migration (Sakar et al., 2016). During wound healing, fibroblasts migrate to sites of injury and are one of the cell types that differentiate into myofibroblasts. These cells then assist wound closure by synthesizing ECM and by generating contractile forces that bring together the edges of the wound (Li and Wang, 2011). The wound healing phenotype we observe in *Tln1*<sup>E1770A</sup> mutants could represent a defect in fibroblast recruitment and/or myofibroblast

### Figure 5. Talin Autoinhibition Regulates Cell Spreading in MEFs

- (A) Representative images of MEFs plated on fibronectin with actin stained by phalloidin (white).  
 (B) Average cell area was calculated at 15 min intervals over the course of 90 min. n values represent numbers of cells and are the same as in (G). Error bars are small enough that they are contained within the data marker.  
 (C) The average number of cells attached, calculated at 15 min intervals over the course of 60 min and shown as the percentage of attached cells at the final time point (90 min).  
 (D) Cell elongation, defined as the aspect ratio of the cell, plotted against cell area.  
 (E) Cell circularity, defined as  $4\pi \text{ area}/\text{perimeter}^2$ , is plotted against cell area. n values are same as in (G) at 90 min.  
 (F) Average number of actin-based protrusions per cell at 90 min. Protrusions were determined from phalloidin stains, counting instances in which there is a minimal distance between the cell contour and the convex hull (see STAR Methods).  
 (G) Average protrusion shape, measured as protrusion height (length from cell center) divided by width, calculated at 15 min intervals over the course of 90 min.  
 (H) Average protrusion elongation per cell at 90 min. n values represent numbers of cells and are the same as in (F). See also Figures S4D–S4H.  
 All error bars denote the SEM, with \*\*\*p ≤ 0.0001, \*\*p ≤ 0.001, and \*p ≤ 0.01.



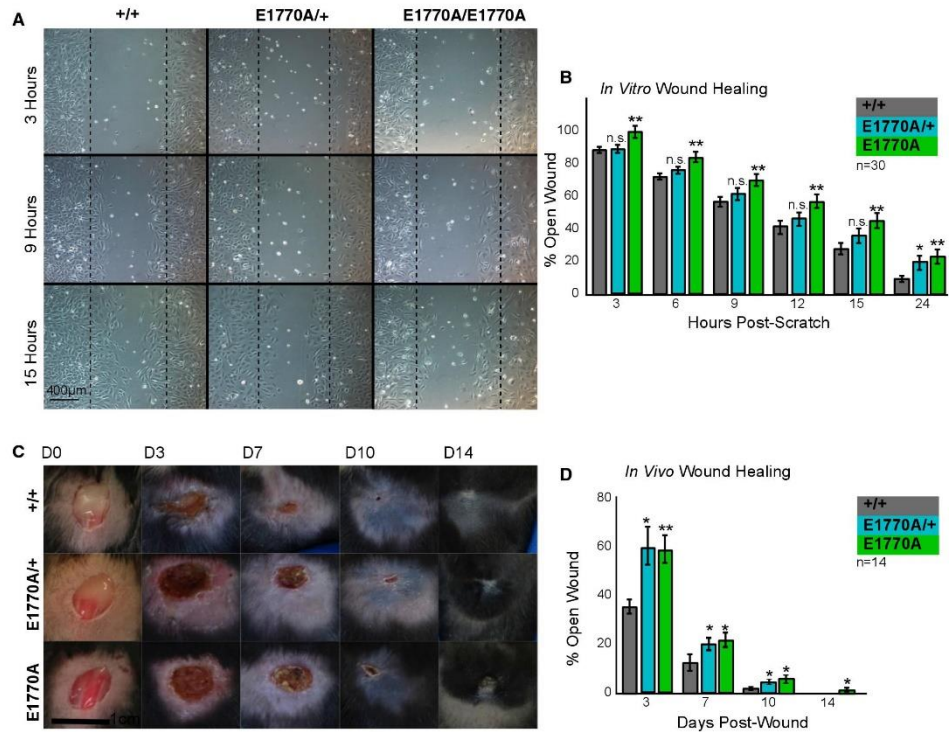


**Figure 6. Talin Autoinhibition Regulates Wound Healing Both *In Vitro* and *In Vivo***

(A) Representative images of MEFs plated on fibronectin 3, 9, and 15 hr after a scratch is introduced in the monolayer with a pipette tip. The dotted line represents the wound edge at time 0.

(B) Average area of open wound per genotype, shown as the percentage of wound area at time 0, calculated at 3 hr intervals over the course of 24 hr.

(C) Representative images of biopsy punch wounds induced on the dorsal side of mice over 14 days.

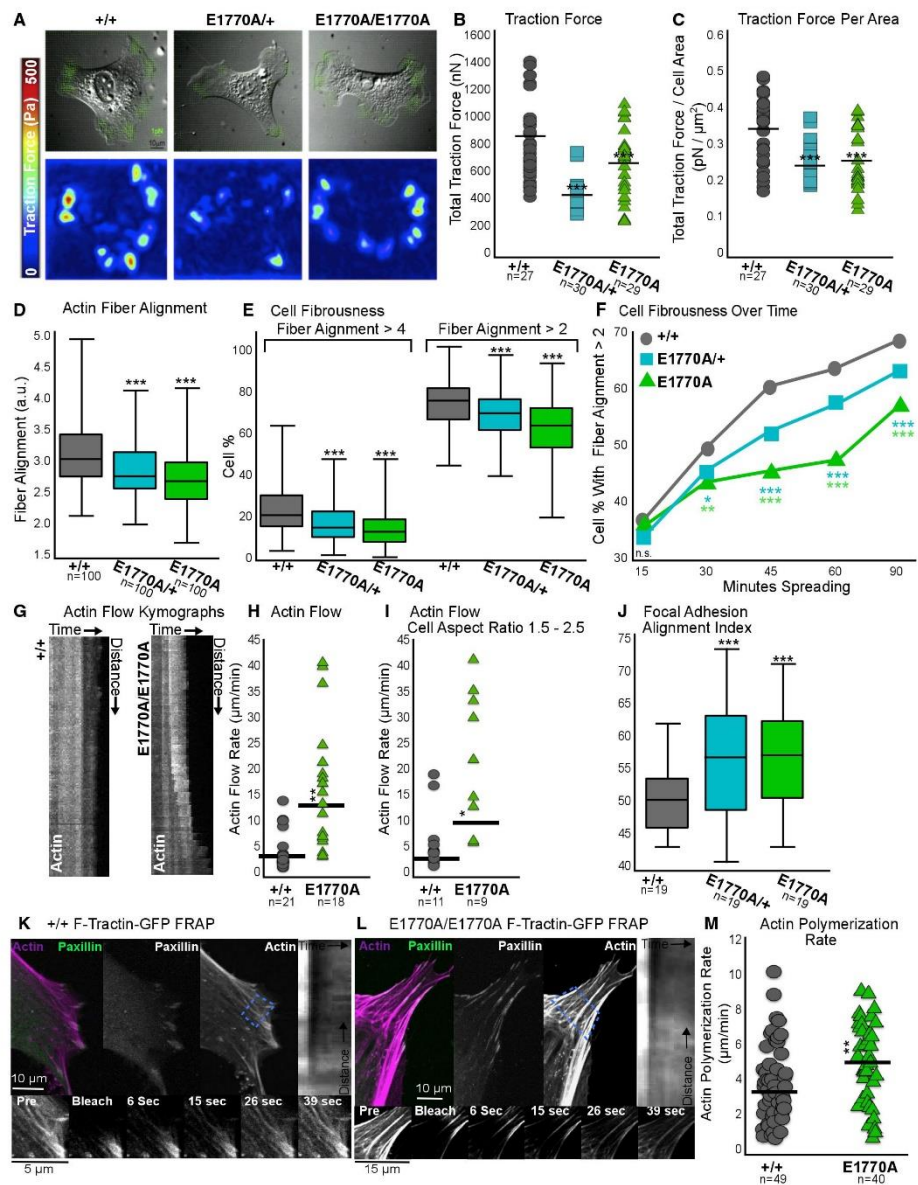
(D) Average area of open wound per genotype for biopsy punches, shown as the percentage of area at initial wounding.

All error bars denote SEM, with \*\*\* $p \leq 0.0001$ , \*\* $p \leq 0.001$ , and \* $p \leq 0.01$ .

contractility. Our data show that the *Tln1*<sup>E1770A</sup> mutation disrupts actin dynamics and gives rise to lower traction force in fibroblasts. Additional insight into how increased adhesion could give rise to a wound healing delay comes from our previous work on dorsal closure during fly embryogenesis (Ellis et al., 2013; Goodwin et al., 2016). Dorsal closure involves the sealing of a gap between two lateral sheets of epidermis and is an important model for animal morphogenesis and wound healing. There are strong parallels between wound healing in vertebrates and mechanisms of dorsal closure (Martin and Parkhurst, 2004). Integrin and Talin are essential for this process, and their absence results in defective closure, which leaves a dorsal hole in the embryo and causes embryonic lethality (Brown et al., 2002; Narasimha and Brown, 2004). Our work in flies has shown that Talin autoinhibition-defective mutants also have de-

fects in dorsal closure and that these are due to the disruption of the biomechanical properties of the tissue (Ellis et al., 2013; Goodwin et al., 2016). In particular, we find that Talin autoinhibition mutants exhibit features consistent with increased cell-ECM adhesion, as well as problems in the regulation of the transmission of mechanical forces generated by actomyosin-based contractility. It is striking that in the context of wound closure in mice, we again encounter similar defects involving changes in adhesion, cell morphology, and mechanical force. This suggests conservation in the requirement for mechanisms that regulate cell-ECM adhesion during morphogenetic processes that mediate wound closure.

Our work shows that autoinhibition regulates multiple aspects of FA structure and function, because *Tln1*<sup>E1770A</sup> mutants exhibit changes in the shape, size, composition, actin dynamics, and



(legend on next page)

stability of FAs. Not all of these changes are congruous. For example, in *Tln1*<sup>E1770A</sup> mutant MEFs, we observed not only that Talin was stabilized at adhesions compared to wild-type but also that there were fewer total adhesions, fewer nascent adhesions, and increased actin dynamics. These results suggest that in the wild-type, autoinhibition negatively regulates the stability of Talin at the membrane but promotes the formation of nascent adhesions and actin dynamics. How can we reconcile these disparate observations? One possibility is that the increased residence of E1770A in FAs relative to the wild-type is sequestering Talin in such a way that it is then unavailable to form nascent adhesions and support cell spreading. This scenario illustrates how even a potentially minor change in the regulation of Talin can alter the precisely regulated steady state that is required for proper adhesion and lead to diverse phenotypes in cell-ECM adhesion.

The relationships among cell-ECM adhesion, actin cytoskeleton dynamics, and traction force are well established (Parsons et al., 2010). Talin, which links ECM-bound integrins to the actin cytoskeleton, is needed to slow actin retrograde flow, produce traction forces, and stiffen cells in response to tension (Case and Waterman, 2015; Zhang et al., 2008). Integrin activation, which is increased *Tln1*<sup>E1770A</sup> mutants, has been shown to increase cell traction forces (Lin et al., 2013). It is therefore surprising that we find increased actin dynamics and lower traction force in *Tln1*<sup>E1770A</sup> mutants. There are several possible explanations. First, it has been proposed that cell geometry and spread area, rather than factors like substrate stiffness or adhesion density, are key determinants of traction force (Oakes et al., 2014). Specifically, increased cell aspect ratio correlates with increased traction force. We show that *Tln1*<sup>E1770A</sup> mutant MEFs are more circular than *Tln1*<sup>+/+</sup> MEFs. This is consistent with lower traction force if geometry is the key regulator of traction stress. Second, the correlation between FA size and traction force is not a simple linear relationship. For example, strongly reducing myosin contractility does not significantly affect FA composition during maturation, knocking down  $\alpha$ -actinin increases traction force

but decreases FA size (Oakes et al., 2014), and depletion of vinculin decreases traction force but increases FA size. In particular, using vinculin mutants with defects in actin binding, it was demonstrated that FA growth is directly proportional to actin flow rate (Thievsen et al., 2013). These phenotypes bear a striking resemblance to those we describe in the *Tln1*<sup>E1770A</sup> mutants. Third, the interaction between Kank2 and Talin has been shown to modulate Talin-actin binding and traction force generation (Sun et al., 2016; Bouchet et al., 2016). It is possible that the *Tln1*<sup>E1770A</sup> mutation affects Kank2-Talin interactions, thus altering actin dynamics. We conclude that while at this point the precise mechanisms underlying the biomechanical phenotypes resulting from compromised talin autoinhibition are unknown, these likely involve changes in cell geometry and/or the ability of actin to associate with the adhesion complex. Overall, our data show that regulating integrin-mediated adhesion via talin autoinhibition can be used to modulate actin dynamics and the biomechanical properties of tissues.

#### STAR★METHODS

Detailed methods are provided in the online version of this paper and include the following:

- KEY RESOURCES TABLE
- CONTACT FOR REAGENT AND RESOURCE SHARING
- EXPERIMENTAL MODEL AND SUBJECT DETAILS
- METHOD DETAILS
  - Biochemistry
  - qRT-PCR
  - Primary Cell Culture
  - siRNA Knockdown & Western Blotting
  - Antibodies & Immunofluorescence
  - Live Cell Imaging
  - Relative Adhesive Strength
  - Scratch Assays
  - Biopsy Wound Assay

#### Figure 7. Talin Autoinhibition Regulates Actin Organization and Traction Force in MEFs

- (A) Representative traction force microscopy (TFM) images. Top: overlaid with traction vectors. Bottom: traction heatmaps.
- (B) Total traction force per cell, with the black line as the mean.
- (C) Total traction force per square micrometer of cell area, with the black line as the mean.
- (D) Actin fiber alignment of phalloidin-stained MEFs plated on fibronectin. n values represent numbers of cells and are the same for (E).
- (E) Cell fibrousness, defined as the percentage of the cell with an actin fiber alignment above a strict (>4) or relaxed (>2) cutoff.
- (F) Average cell fibrousness over time with a relaxed (>2) cutoff. n values are the same as in Figure 5B.
- (G) Representative kymographs generated from F-tractin-GFP-labeled cells imaged for 15 min at 1 s/frame. Kymographs were generated from lines drawn through active protrusions.
- (H) Actin flow rate determined from kymographs, with the black line as the mean. n values represent numbers of cells.
- (I) Actin flow rate determined from kymographs from cells with aspect ratios ranging from 1.5 to 2.5. The black line represents the mean, and n values represent numbers of cells.
- (J) FA alignment index per cell, defined as 90° minus the difference between individual FA angles from the reference FA angle, so high FAAl equates to high global alignment (Wu et al., 2012).
- (K) Representative images of the leading edge of *Tln1*<sup>+/+</sup> MEFs plated on fibronectin and transfected with paxillin-mCherry (green and white) and F-tractin-GFP (magenta and white). ROIs encompassing dorsal stress fibers were bleached, and recovery was imaged over time. Kymographs of the recovery were made, and the angle of the contrast boundary was used to determine the actin flow rate.
- (L) Representative images of the leading edge of *Tln1*<sup>E1770A/E1770A</sup> MEFs plated on fibronectin and transfected with paxillin-mCherry (green and white) and F-tractin-GFP (magenta and white). ROIs encompassing dorsal stress fibers were bleached, and recovery was imaged over time. Kymographs of the recovery were made, and the angle of the contrast boundary was used to determine the actin flow rate.
- (M) Actin polymerization rate determined from kymographs, with the black line as the mean. n values represent numbers of cells.
- All error bars denote SEM, with \*\*\*p ≤ 0.0001, \*\*p ≤ 0.001, and \*p ≤ 0.01.

● **QUANTIFICATION AND STATISTICAL ANALYSIS**

- Live Cell Imaging
- Fixed Cell Imaging
- Scratch Assays & Wound Healing

● **DATA AND SOFTWARE AVAILABILITY**

**SUPPLEMENTAL INFORMATION**

Supplemental Information includes four figures and can be found with this article online at <https://doi.org/10.1016/j.celrep.2018.10.098>.

**ACKNOWLEDGMENTS**

This study was supported by CIHR Operating Grants to G.T. (MOP-285391) and L.L. (MOP-119357), a CIHR grant-in-aid to D.J.G., a CIHR post-doctoral fellowship to C.T.T., a Canada Foundation for Innovation Grant to S.P. (#34473), and NSERC Discovery Grants to L.L. (386979-12) and S.P. (RGPIN-2015-05114). In addition, B.T.G. is funded by Biotechnology and Biological Sciences Research Council grant (BB/N007336/1) and B.T.G. and A.W. are funded by a Human Frontier Science Program grant (RGP0001/2016).

**AUTHOR CONTRIBUTIONS**

A.H. and G.T. conceived this study. A.H. performed all cell and mouse experiments, with the exception of traction force microscopy performed by S.P. A.W. and B.T.G. performed all biochemistry experiments. D.C. performed qRT-PCR experiments. K.G. developed MATLAB scripts for automated image analysis of fixed FA morphology, cell morphology, and actin fibers. A.B. and L.L. provided reagents and expertise in training for primary cell culture and mouse husbandry. C.T.T. and D.J.G. provided expertise and guidance on *in vivo* wound healing assays. A.H. and G.T. wrote this manuscript, with contributions from all other co-authors.

**DECLARATION OF INTERESTS**

The authors declare no competing interests.

Received: April 18, 2018  
Revised: September 7, 2018  
Accepted: October 25, 2018  
Published: November 27, 2018

**REFERENCES**

Ballestrem, C., Hinz, B., Imhof, B.A., and Wehrle-Haller, B. (2001). Marching at the front and dragging behind: differential alphaVbeta3-integrin turnover regulates focal adhesion behavior. *J. Cell Biol.* *155*, 1319–1332.

Banno, A., Goult, B.T., Lee, H., Bate, N., Critchley, D.R., and Ginsberg, M.H. (2012). Subcellular localization of talin is regulated by inter-domain interactions. *J. Biol. Chem.* *287*, 13799–13812.

Bazzoni, G., Shih, D.T., Buck, C.A., and Hemler, M.E. (1995). Monoclonal antibody 9EG7 defines a novel beta 1 integrin epitope induced by soluble ligand and manganese, but inhibited by calcium. *J. Biol. Chem.* *270*, 25570–25577.

Belin, B.J., Goins, L.M., and Mullins, R.D. (2014). Comparative analysis of tools for live cell imaging of actin network architecture. *Bioarchitecture* *4*, 189–202.

Berginski, M.E., Vitriol, E.A., Hahn, K.M., and Gomez, S.M. (2011). High-resolution quantification of focal adhesion spatiotemporal dynamics in living cells. *PLoS ONE* *6*, e22025.

Bouchet, B.P., Gough, R.E., Ammon, Y.C., van de Willige, D., Post, H., Jacquemet, G., Altelaar, A.M., Heck, A.J.R., Goult, B.T., and Akhmanova, A. (2016). Talin-KANK1 interaction controls the recruitment of cortical microtubule stabilizing complexes to focal adhesions. *eLife* *5*, e18124.

Brown, N.H., Gregory, S.L., Rickoll, W.L., Fessler, L.I., Prout, M., White, R.A., and Fristrom, J.W. (2002). Talin is essential for integrin function in *Drosophila*. *Dev. Cell* *3*, 569–579.

Calderwood, D.A. (2004a). Integrin activation. *J. Cell Sci.* *117*, 657–666.

Calderwood, D.A. (2004b). Talin controls integrin activation. *Biochem. Soc. Trans.* *32*, 434–437.

Calderwood, D.A., Zent, R., Grant, R., Rees, D.J., Hynes, R.O., and Ginsberg, M.H. (1999). The Talin head domain binds to integrin beta subunit cytoplasmic tails and regulates integrin activation. *J. Biol. Chem.* *274*, 28071–28074.

Case, L.B., and Waterman, C.M. (2015). Integration of actin dynamics and cell adhesion by a three-dimensional, mechanosensitive molecular clutch. *Nat. Cell Biol.* *17*, 955–963.

Cetera, M., Ramirez-San Juan, G.R., Oakes, P.W., Lewellyn, L., Fairchild, M.J., Tanentzapf, G., Gardel, M.L., and Horne-Badovinac, S. (2014). Epithelial rotation promotes the global alignment of contractile actin bundles during *Drosophila* egg chamber elongation. *Nat. Commun.* *5*, 5511.

Clark, E.A., and Brugge, J.S. (1995). Integrins and signal transduction pathways: the road taken. *Science* *268*, 233–239.

Critchley, D.R. (2009). Biochemical and structural properties of the integrin-associated cytoskeletal protein talin. *Annu. Rev. Biophys.* *38*, 235–254.

Debrand, E., Jai, Y.E., Spence, L., Bate, N., Praekelt, U., Pritchard, C.A., Monkley, S.A., and Critchley, D.R. (2009). Talin 2 is a large and complex gene encoding multiple transcripts and protein isoforms. *FEBS J.* *6*, 1610–1628.

Ellis, S.J., Goult, B.T., Fairchild, M.J., Harris, N.J., Long, J., Lobo, P., Czerniecki, S., Van Petegem, F., Schöck, F., Peifer, M., and Tanentzapf, G. (2013). Talin autoinhibition is required for morphogenesis. *Curr. Biol.* *23*, 1825–1833.

Ganguli-Indra, G. (2014). Protocol for cutaneous wound healing assay in a murine model. *Methods Mol. Biol.* *1210*, 151–159.

Garcia, A.J., Ducheyne, P., and Boettiger, D. (1997). Quantification of cell adhesion using a spinning disc device and application to surface-reactive materials. *Biomaterials* *18*, 1091–1098.

Gardel, M.L., Sabass, B., Ji, L., Danuser, G., Schwarz, U.S., and Waterman, C.M. (2008). Traction stress in focal adhesions correlates biphasically with actin retrograde flow speed. *J. Cell Biol.* *183*, 999–1005.

Geiger, B., and Yamada, K.M. (2011). Molecular architecture and function of matrix adhesions. *Cold Spring Harb. Perspect. Biol.* *3*, a005033.

Ginsberg, M.H. (2014). Integrin activation. *BMB Rep.* *47*, 655–659.

Goksoy, E., Ma, Y.-Q.Q., Wang, X., Kong, X., Perera, D., Plow, E.F., and Qin, J. (2008). Structural basis for the autoinhibition of talin in regulating integrin activation. *Mol. Cell* *31*, 124–133.

Goodwin, K., Ellis, S.J., Lostchuck, E., Zulueta-Coarasa, T., Fernandez-Gonzalez, R., and Tanentzapf, G. (2016). Basal cell-extracellular matrix adhesion regulates force transmission during tissue morphogenesis. *Dev. Cell* *39*, 611–625.

Goult, B.T., Bate, N., Anthis, N.J., Wegener, K.L., Gingras, A.R., Patel, B., Barsukov, I.L., Campbell, I.D., Roberts, G.C., and Critchley, D.R. (2009). The structure of an interdomain complex that regulates talin activity. *J. Biol. Chem.* *284*, 15097–15106.

Goult, B.T., Xu, X.-P.P., Gingras, A.R., Swift, M., Patel, B., Bate, N., Kopp, P.M., Barsukov, I.L., Critchley, D.R., Volkman, N., and Hanein, D. (2013). Structural studies on full-length talin1 reveal a compact auto-inhibited dimer: implications for talin activation. *J. Struct. Biol.* *184*, 21–32.

Horwitz, A., Duggan, K., Buck, C., Beckerle, M.C., and Burridge, K. (1986). Interaction of plasma membrane fibronectin receptor with talin—a transmembrane linkage. *Nature* *320*, 531–533.

Iwamoto, D.V., and Calderwood, D.A. (2015). Regulation of integrin-mediated adhesions. *Curr. Opin. Cell Biol.* *36*, 41–47.

Kanchanawong, P., Shtengel, G., Pasapera, A.M., Ramko, E.B., Davidson, M.W., Hess, H.F., and Waterman, C.M. (2010). Nanoscale architecture of integrin-based cell adhesions. *Nature* *468*, 580–584.

Kim, M., Carman, C.V., and Springer, T.A. (2003). Bidirectional transmembrane signaling by cytoplasmic domain separation in integrins. *Science* *301*, 1720–1725.

- Klapholz, B., and Brown, N.H. (2017). Talin—the master of integrin adhesions. *J. Cell Sci.* **130**, 2435–2446.
- Kopp, P.M., Bate, N., Hansen, T.M., Brindle, N.P., Prækelt, U., Debrand, E., Coleman, S., Mazzeo, D., Goult, B.T., Gingras, A.R., et al. (2010). Studies on the morphology and spreading of human endothelial cells define key inter- and intramolecular interactions for talin1. *Eur. J. Cell Biol.* **89**, 661–673.
- Lee, H.-S.S., Anekal, P., Lim, C.J., Liu, C.-C.C., and Ginsberg, M.H. (2013). Two modes of integrin activation form a binary molecular switch in adhesion maturation. *Mol. Biol. Cell* **24**, 1354–1362.
- Li, B., and Wang, J.H. (2011). Fibroblasts and myofibroblasts in wound healing: force generation and measurement. *J. Tissue Viability* **20**, 108–120.
- Liang, C.-C.C., Park, A.Y., and Guan, J.-L.L. (2007). *In vitro* scratch assay: a convenient and inexpensive method for analysis of cell migration *in vitro*. *Nat. Protoc.* **2**, 329–333.
- Lin, G.L., Cohen, D.M., Desai, R.A., Breckenridge, M.T., Gao, L., Humphries, M.J., and Chen, C.S. (2013). Activation of beta 1 but not beta 3 integrin increases cell traction forces. *FEBS Lett.* **587**, 763–769.
- Martin, P., and Parkhurst, S.M. (2004). Parallels between tissue repair and embryo morphogenesis. *Development* **131**, 3021–3034.
- Maruthamuthu, V., Sabass, B., Schwarz, U.S., and Gardel, M.L. (2011). Cell-ECM traction force modulates endogenous tension and cell-cell contacts. *Proc. Natl. Acad. Sci. USA* **108**, 4708–4713.
- Monkley, S.J., Zhou, X.H., Kinston, S.J., Giblett, S.M., Hemmings, L., Priddle, H., Brown, J.E., Pritchard, C.A., Critchley, D.R., and Fässler, R. (2000). Disruption of the talin gene arrests mouse development at the gastrulation stage. *Dev. Dyn.* **219**, 560–574.
- Munevar, S., Wang, Y.L., and Dembo, M. (2001). Distinct roles of frontal and rear cell-substrate adhesions in fibroblast migration. *Mol. Biol. Cell* **12**, 3947–3954.
- Narasimha, M., and Brown, N.H. (2004). Novel functions for integrins in epithelial morphogenesis. *Curr. Biol.* **14**, 381–385.
- Oakes, P.W., Banerjee, S., Marchetti, M.C., and Gardel, M.L. (2014). Geometry regulates traction stresses in adherent cells. *Biophys. J.* **107**, 825–833.
- Oh-McGinnis, R., Bogutz, A.B., Kang, Y.L., Higgins, M.J., and Lefebvre, L. (2010). Rescue of placental phenotype in a mechanistic model of Beckwith-Wiedemann syndrome. *BMC. Dev. Biol.* **10**, 50.
- Parsons, J.T., Horwitz, A.R., and Schwartz, M.A. (2010). Cell adhesion: integrating cytoskeletal dynamics and cellular tension. *Nat. Rev. Mol. Cell Biol.* **11**, 633–643.
- Priddle, H., Hemmings, L., Monkley, S., Woods, A., Patel, B., Sutton, D., Dunn, G.A., Zicha, D., and Critchley, D.R. (1998). Disruption of the talin gene compromises focal adhesion assembly in undifferentiated but not differentiated embryonic stem cells. *J. Cell Biol.* **142**, 1121–1133.
- Romsey, N.R., Hou, Y., Lara Rodriguez, L., and Schneider, I.C. (2014). The number of lines a cell contacts and cell contractility drive the efficiency of contact guidance. *Cell. Mol. Bioeng.* **7**, 122–135.
- Sabass, B., Gardel, M.L., Waterman, C.M., and Schwarz, U.S. (2008). High resolution traction force microscopy based on experimental and computational advances. *Biophys. J.* **94**, 207–220.
- Sakar, M.S., Eyckmans, J., Pieters, R., Eberli, D., Nelson, B.J., and Chen, C.S. (2016). Cellular forces and matrix assembly coordinate fibrous tissue repair. *Nat. Comm.* **7**, 11036.
- Schindelin, J., Arganda-Carreras, I., Frise, E., Kaynig, V., Longair, M., Pietzsch, T., Preibisch, S., Rueden, C., Saalfeld, S., Schmid, B., et al. (2012). Fiji: an open-source platform for biological-image analysis. *Nat. Methods.* **7**, 676–682.
- Shattil, S.J., O'Toole, T., Eigenthaler, M., Thon, V., Williams, M., Babior, B.M., and Ginsberg, M.H. (1995).  $\beta_3$ -endonexin, a novel polypeptide that interacts specifically with the cytoplasmic tail of the integrin  $\beta_3$  subunit. *J. Cell Biol.* **131**, 807–816.
- Song, X., Yang, J., Hirbawi, J., Ye, S., Perera, H.D., Goksoy, E., Dwivedi, P., Plow, E.F., Zhang, R., and Qin, J. (2012). A novel membrane-dependent on/off switch mechanism of talin FERM domain at sites of cell adhesion. *Cell Res.* **22**, 1533–1545.
- Sun, Z., Tseng, H.Y., Tan, S., Senger, F., Kurzawa, L., Dedden, D., Mizuno, N., Wasik, A.A., They, M., Dunn, A.R., and Fässler, R. (2016). Kank2 activates talin, reduces force transduction across integrins and induces central adhesion formation. *Nat. Cell Biol.* **18**, 941–953.
- Tadokoro, S., Shattil, S.J., Eto, K., Tai, V., Liddington, R.C., de Pereda, J.M., Ginsberg, M.H., and Calderwood, D.A. (2003). Talin binding to integrin beta tails: a final common step in integrin activation. *Science* **302**, 103–106.
- Thievensen, I., Thompson, P.M., Berlemont, S., Plevocek, K.M., Plotnikov, S.V., Zemljic-Harpf, A., Ross, R.S., Davidson, M.W., Danuser, G., Campbell, S.L., and Waterman, C.M. (2013). Vinculin-actin interaction couples actin retrograde flow to focal adhesions, but is dispensable for focal adhesion growth. *J. Cell Biol.* **202**, 163–177.
- Tojkander, S., Gateva, G., Husain, A., Krishnan, R., and Lappalainen, P. (2015). Generation of contractile actomyosin bundles depends on mechanosensitive actin filament assembly and disassembly. *eLife* **10**, e06126.
- Tomasek, J.J., Gabbiani, G., Hinz, B., Chaponnier, C., and Brown, R.A. (2002). Myofibroblasts and mechano-regulation of connective tissue remodelling. *Nat. Rev. Mol. Cell Biol.* **3**, 349–363.
- Tschammer, N., Galinec, S., Weigert, S., Muller, Y., You, C., Piehler, J., and Breitsprecher, D. (2016). Protein labeling one-step, purification-free and site-specific labeling of polyhistidine-tagged proteins for MST. *Protein Labeling Application Note NT-MO-29*. [https://www.researchgate.net/publication/311582381\\_Protein\\_Labeling\\_One-step\\_purification-free\\_and\\_site-specific\\_labeling\\_of\\_polyhistidine-tagged\\_proteins\\_for\\_MST](https://www.researchgate.net/publication/311582381_Protein_Labeling_One-step_purification-free_and_site-specific_labeling_of_polyhistidine-tagged_proteins_for_MST).
- Wingate, A.D., Martin, K.J., Hunter, C., Carr, J.M., Clacher, C., and Arthur, J.S. (2009). Generation of a conditional CREB Ser133Ala knockin mouse. *Genesis* **47**, 688–696.
- Wolfenson, H., Henis, Y.I., Geiger, B., and Bershadsky, A.D. (2009). The heel and toe of the cell's foot: a multifaceted approach for understanding the structure and dynamics of focal adhesions. *Cell Motil. Cytoskeleton* **66**, 1017–1029.
- Wolfenson, H., Lavelin, I., and Geiger, B. (2013). Dynamic regulation of the structure and functions of integrin adhesions. *Dev. Cell* **24**, 447–458.
- Wu, C., Asokan, S.B., Berginski, M.E., Haynes, E.M., Sharpless, N.E., Griffith, J.D., Gomez, S.M., and Bear, J.E. (2012). Arp2/3 is critical for lamellipodia and response to extracellular matrix cues but is dispensable for chemotaxis. *Cell* **148**, 973–987.
- Zhang, X., Jiang, G., Cai, Y., Monkley, S.J., Critchley, D.R., and Sheetz, M.P. (2008). Talin depletion reveals independence of initial cell spreading from integrin activation and traction. *Nat. Cell Biol.* **10**, 1062–1068.
- Zhang, H., Chang, Y.-C.C., Huang, Q., Brennan, M.L., and Wu, J. (2016). Structural and functional analysis of a talin triple-domain module suggests an alternative talin autoinhibitory configuration. *Structure* **24**, 721–729.

## STAR★METHODS

### KEY RESOURCES TABLE

REAGENT or RESOURCE	SOURCE	IDENTIFIER
<b>Antibodies</b>		
Talin-1	Santa Cruz	YQ-16; RRID:AB_2303406
Paxillin	BD	349/Paxillin; RRID:AB_397464
β1-integrin total	R&D	Gln21-Ala738; RRID:AB_416591
β1-integrin active	BD	9EG7; RRID:AB_393729
FAK	BD	77/FAK; RRID:AB_397494
pTyr397FAK	Thermo-Fisher	31H5L17; RRID:AB_2533701
Talin-2	Abcam	68E7
β-tubulin	DHSB	E7; RRID:AB_528499
<b>Chemicals, Peptides, and Recombinant Proteins</b>		
β1a-integrin (752-798)	Ben Goult	N/A
Tln1 WT	Ben Goult	N/A
Tln1 E1770A	Ben Goult	N/A
<b>Critical Commercial Assays</b>		
Tln2 ON-TARGET plus SMARTpool	Dharmacon	L-065877-00-0005
ON-TARGET plus Non-targeting Pool	Dharmacon	D-001810-10-05
<b>Deposited Data</b>		
F3:R9 talin interaction complex	<a href="#">Song et al., 2012</a>	PDB: 4F7G
<b>Experimental Models: Organisms/Strains</b>		
<i>Tln1</i> <sup>E1770A</sup> Mice	Genoway	<i>Tln1</i> <sup>E1770A</sup>
<b>Oligonucleotides</b>		
Primer: <i>Tln1</i> <sup>E1770A</sup> Mice Genotyping Forward: 5'ACTAAGACATCGAAGGCTGGGATATGCTG3'	Genoway / This paper	N/A
Primer: <i>Tln1</i> <sup>E1770A</sup> Mice Genotyping Reverse: 5'GTCAGGTAAGTCTTAACTATCTCCTCAGCTCC3'	Genoway / This paper	N/A
Primer: Tln1 qRT Forward: 5'AGCTTTCCAAGAAGTGG3'	This Paper	N/A
Primer: Tln1 qRT Reverse: 5'TTCTGAAGGGTCAGCAGCAC3'	This Paper	N/A
Primer: Tln2 qRT Forward: 5'GGATAGGGCCACCATTTC3'	<a href="#">Debrand et al., 2009</a>	a
Primer: Tln2 qRT Reverse: 5'GCTCCGCAATGAGCAGTAGCT3'	<a href="#">Debrand et al., 2009</a>	b
Primer: Ppia qRT Forward: 5'CGCGTCTCCTTCGAGCTGTTG3'	<a href="#">Oh-McGinnis et al., 2010</a>	N/A
Primer: Ppia qRT Reverse: 5'TGTAAAGTCACCACCCTGGCACAT3'	<a href="#">Oh-McGinnis et al., 2010</a>	N/A
<b>Recombinant DNA</b>		
Tln1-GFP	Chinten James Lim	N/A
E1770A Tln1-GFP	Ben Goult	N/A
F-tractin-GFP	Sergey Plotnikov	N/A
mCherry-paxillin	Mike Gold	N/A
paxillin-GFP	Addgene	#15233
<b>Software and Algorithms</b>		
MATLAB	Commercial	<a href="https://www.mathworks.com/products/matlab.html">https://www.mathworks.com/products/matlab.html</a>
Focal Adhesion Analysis Server	<a href="#">Berginski et al., 2011</a>	<a href="http://faas.bme.unc.edu/">http://faas.bme.unc.edu/</a>
Fiji	<a href="#">Schindelin et al., 2012</a>	<a href="https://fiji.sc/">https://fiji.sc/</a>

## CONTACT FOR REAGENT AND RESOURCE SHARING

Further information and requests for resources and reagents should be directed to and will be fulfilled by the Lead Contact, Guy Tanentzapf ([tanentz@mail.ubc.ca](mailto:tanentz@mail.ubc.ca)).

## EXPERIMENTAL MODEL AND SUBJECT DETAILS

*Tln1*<sup>E1770A</sup> mice were generated by Genoway S.A. (France) on the C57BL/6J genetic background. A Cre-activated mini gene approach was used (Wingate et al., 2009). Briefly, a targeting construct was used containing a hybrid of genomic DNA and cDNA containing the entire wild-type *Tln1* sequence from exons 41 to the terminal coding exon 59, followed by a polyadenylation cDNA sequence. Prior to Cre-mediated recombination, wild-type *Tln1* is transcribed through the endogenous promoter using this mini gene. After Cre-mediated recombination, the mini gene is excised and mutant *Tln1*<sup>E1770A</sup> is transcribed using the endogenous promoter. To create the conventional point mutated (*Tln1*<sup>E1770A</sup>) allele we used a ubiquitous Cre-deleter (pCMV-Cre) line that expresses Cre in the germ cells to make a permanently recombined line. This conventional, point-mutated allele, *Tln1*<sup>E1770A</sup>, was used for all subsequent experiments. Mice were genotyped at weaning using the following primers at 65°C annealing temperature: 5'ACTAAGACATCGAAGGCTGGGATATGCTG3' and 5'GTCAGGTACTGTTAACCTATCTCCTCAGTCC3'. These produced a 451bp mutant band and a 381bp wild-type band. All animals were housed at the Centre for Disease Modeling at the University of British Columbia using standard husbandry. The University of British Columbia Animal Care and Use Program approved all procedures. *Tln1*<sup>E1770A/+</sup> intercrosses were set up at 7 weeks of age, only the first three litters of each breeding pair was included in progeny counts. Images of male mice were taken between 18 and 22 weeks of age post-euthanasia for presentation and body length measurements. Littermate males were weighed weekly on the same day at approximately the same time.

## METHOD DETAILS

### Biochemistry

#### Purification of Recombinant Polypeptides

Full length mouse *Tln1*, wild-type and E1770A mutants, were cloned into a pET21a vector, and the cytoplasmic tail of  $\beta$ 1a-integrin (752-798) was cloned into a pET151 vector (Invitrogen) and expressed in E.coli BL21(DE3) cells cultured in LB. Standard nickel-affinity chromatography was used to purify the His-tagged recombinant proteins as described previously (Banno et al., 2012).  $\beta$ 1a-Integrin was further purified using anion-exchange chromatography following cleavage of the 6xHis-tag with TEV protease. The talin constructs were further purified and analyzed using a HiLoad 16/600 Superdex 200 size exclusion chromatography column (GE healthcare). 5 mL of sample was loaded and run at 0.5 ml/min flow rate at 4°C in 50 mM Tris, 150 mM NaCl, 2mM DTT. Purified samples were further analyzed by SDS-PAGE on a 10% gel and stained using Coomassie blue. Protein concentrations were determined using the respective extinction coefficients at 280nm calculated using ProtParam.

#### Microscale Thermophoresis

*Tln1* was coupled to an equimolar amount of NT-647 dye (RED-tris-NTA, NanoTemper) via its C-terminal 6xHis-Tag in a one-step coupling reaction (Tschammer et al., 2016). Titrations were performed in phosphate buffered saline (PBS; 137 mM NaCl, 27 mM KCl, 100 mM Na<sub>2</sub>HPO<sub>4</sub>, 18 mM KH<sub>2</sub>PO<sub>4</sub>) using a constant 50 nM concentration of RED-tris-NTA coupled *Tln1*, with an increasing concentration of recombinant  $\beta$ 1a-integrin peptide; final volume 20  $\mu$ l. Prepared samples were loaded into Monolith NT.115 Capillaries (NanoTemper) and measurements were recorded on a Monolith NT.115 at 25°C, excited under red light with medium MST power and 40% excitation power. The data was analyzed using MO Affinity Analysis software and fitted using the K<sub>d</sub> fit model.

#### qRT-PCR

Total RNA was isolated from MEFs in culture using TRIzol. A total of 0.5  $\mu$ g total RNA was converted into cDNA using a qScript cDNA Synthesis Kit (Quanta Biosciences). Subsequently, qPCR was performed using iQ SYBR Green Supermix (BIORAD). *Tln1* & *Tln2* mRNA levels was averaged between three independent experiments performed four times and normalized to Ppia (Peptidyl Prolyl Isomerase A) expression. Primers used for Ppia are as follows: 5'CGCGTCTCCTTCGAGCTGTTTG3' and 5'TGTAAGTCACC ACCTGGCACAT3' Primers used for *Tln1* are as follows: 5'AGCTTTCCAAGAAGTGG3' and 5'TTCTGAAGGGTCAGCAGCAC3'. Primers used for *Tln2* are as follows: 5'GGATAGGGCCACCATTTTCA3' and 5'GCTCCGAATGAGACAGTAGCT3'.

#### Primary Cell Culture

Primary MEFs were isolated from E13.5 embryos. MEFs were plated on 0.1% gelatin in Dulbecco's Modified Eagle's Medium (DMEM) supplemented with 10% Fetal Bovine Serum, 1% penicillin-streptomycin (15140122 Thermo-Fisher), 2mM L-Glutamine, and 1mM Sodium Pyruvate. Cells were used for experiments up to passage 5.

#### siRNA Knockdown & Western Blotting

For siRNA mediated knockdown of *Tln2*, a ON-TARGET plus SMARTpool (L-065877-00-0005) was used. A ON-TARGET plus Non-targeting Pool (D-001810-10-05) was used for controls. MEFs were plated on either 0.1mg/ml fibronectin coated coverslips

or in gelatin coated 6-well plates for 90 minutes before transfection with siRNA. Cells were then incubated overnight before being stained (see below for immunofluorescence) or collected for western blotting. Protein samples were isolated via TRIzol combining 3 wells of a 6-well plate per sample and were resolved using a 7% gel. Primary antibody used: 1:500 Tin2 (68E7, Abcam) and 1:500  $\beta$ -tubulin (E7, DSHB). Secondary antibody used: 1:3000 anti-mouse-HRP (Biorad). Chemiluminescent substrate (Clarity Western ECL Biorad) was applied via manufacturer instruction and blots were exposed to X-ray film.

#### Antibodies & Immunofluorescence

For immunofluorescence stains, MEFs were plated on 0.1 mg/ml fibronectin-coated coverslips for 90 minutes (unless otherwise indicated). Cells were fixed with 4% paraformaldehyde for 15 minutes at room temperature. Cells were then permeabilized with 0.3% Triton-X for 5 minutes at room temperature, blocked with 1% BSA with 1:200 Rhodamine-Phalloidin or Alexafluor 633-Phalloidin for 60 minutes at room temperature, incubated with primary antibody (with or without 1% BSA) for 180 minutes at room temperature, and finally incubated with secondary antibody diluted in PBS for 60 minutes at room temperature. Between each step slides were washed 3 times for 5 minutes at room temperature with PBS. Slides were then mounted with vectashield containing a DAPI stain. Primary antibody dilutions used: 1:100 Talin-1 (with BSA, YQ-16 Santa Cruz), Paxillin (349/Paxillin BD),  $\beta$ 1-integrin total (Gln21-Ala738, R&D),  $\beta$ 1-integrin active (9EG7 BD), 1:200 FAK (77/FAK BD), 1:200 pTyr397FAK (31H5L17 Thermo-Fisher). Z stack images were taken with an Olympus Fluoview (FV1000) inverted confocal microscope at 0.5  $\mu$ m slice thickness and 2048 resolution.

#### Live Cell Imaging

##### Fluorescence Recovery After Photobleaching (FRAP)

MEFs were plated on 0.1 mg/ml fibronectin coated coverslips. After spreading for 90 minutes cells were transfected with paxillin-GFP (Addgene #15233), Tin1-GFP (from Chinten James Lim), E1770A Tin1-GFP (from B.T.G), mCherry-paxillin (from Mike Gold), and/or F-tractin-GFP (from S.P.). Cells were incubated overnight before imaging at 37°C on an Olympus Fluoview (FV1000) inverted confocal microscope. Small portions of the cell edge were bleached using the Tornado scanning tool (Olympus) with a 405nm laser at 100% power.

##### Total Internal Reflection Fluorescence (TIRF)

MEFs were plated on 0.1 mg/ml fibronectin coated coverslips. After spreading for 90 minutes cells were transfected with paxillin-GFP (Addgene #15233). For post-spread analysis, cells were incubated overnight before being imaged using an Olympus IX83 automated inverted microscopy with an Olympus CellTIRF system. For during spreading analysis, cells were incubated overnight, then trypsinized and plated onto a 0.1 mg/ml fibronectin coated coverslip for 15 minutes before imaging. Cells were imaged at 37°C every 1 minute for 60 minutes at 100X using a penetration depth of 60nm.

##### Traction Force Microscopy (TFM)

Traction force microscopy was performed as described previously (Sabass et al., 2008). Briefly, elastic polyacrylamide substrates (8.6kPa shear modulus,  $\approx$ 20  $\mu$ m gel thickness) with embedded 40nm red and far-red fluorescent beads (Invitrogen) were prepared on glass coverslips and the top surface of the substrates was functionalized with 1mg/mL human plasma fibronectin (Millipore) to facilitate cell attachment. Cells were plated on fibronectin-coupled polyacrylamide substrates. After spreading for 120 minutes, the coverslips were mounted in a perfusion chamber (RC30, Warner Instruments), and a series of DIC images of the cells and fluorescent images of the beads within the substrate were acquired by a spinning disk confocal microscope (Nikon Ti2 equipped with CSUX10 confocal head and Photometrics Myo CCD camera). The cells were removed from the substrate by perfusing 5 mL of 0.5% phenol red-free trypsin-EDTA (Thermo) into the chamber, and an image of beads in the unstrained substrate was captured.

#### Relative Adhesive Strength

We used a method adapted from Garcia et al. (1997) that has been previously published by Romsey et al. (2014). MEFs were plated on 0.1 mg/ml fibronectin-coated coverslips for 90 minutes. Non-spun control coverslips were then fixed with 4% paraformaldehyde for 15 minutes at room temperature. Experimental coverslips were spun at 4000RPM while 1 mL of DMEM media was applied for approximately 15 s and then fixed. After fixing cells were permeabilized as described above and incubated with 1:200 AlexaFluor 488 Phalloidin overnight. 20 fields of view of 5 different coverslips were imaged for each spun and non-spun condition at 20X using an Olympus Fluoview (FV1000) inverted confocal microscope.

#### Scratch Assays

MEFs were cultured in 6-well plates on 0.1% gelatin. When the cells formed a confluent monolayer a wound was introduced with a pipette tip (VWR 53508-810). Scratches were imaged over time under phase contrast with a Leica DMIL inverted microscope equipped with a QImaging MicroPublisher 5.0 RTV camera.

#### Biopsy Wound Assay

Littermate female mice were subjected to wounding at 8 weeks of age. Mice were anesthetized with isoflurane and then shaved and cleaned on the dorsal side. A single full thickness wound was then created on the dorsal side with a sterile 6mm biopsy punch. Prior to wounding mice received sub-cutaneous fluids, a Meloxicam sub-cutaneous injection at 5mg/kg, and a sub-cutaneous injection of Bupivacaine at 8mg/kg near the wound site. After wounding mice received sub-cutaneous injections of Meloxicam for at least



two days or longer depending on monitoring. Wounded mice were monitored daily for 14 days and imaged throughout with a digital Sony Cyber-shot camera.

## QUANTIFICATION AND STATISTICAL ANALYSIS

### Live Cell Imaging

#### Fluorescence Recovery After Photobleaching (FRAP)

Movies for FRAP of FAs were then analyzed with ImageJ using a previously developed Jython script available at [https://imagej.net/Analyze\\_FRAP\\_movies\\_with\\_a\\_Jython\\_script](https://imagej.net/Analyze_FRAP_movies_with_a_Jython_script). Here, ROIs for analysis are chosen specifically drawn over FAs labeled in the pre-bleach time frames. Movies for FRAP of F-tractin-GFP were then analyzed with ImageJ using the Kymographbuilder plugin on lines drawn over dorsal stress fibers specifically.

#### Total Internal Reflection Fluorescence (TIRF)

Live FAs (Figures 4 and 7) were analyzed from TIRF movies (see above). Movies were submitted to the Focal Adhesion Analysis Server (Berginski et al., 2011) for analysis with standard settings used. Briefly, FAs are tracked throughout the movie and longevity refers to the number of minutes the FA persists. Static FA properties are also measured at each frame, including area. We defined nascent FAs as having longevity < 5 minutes and an area < 0.3  $\mu\text{m}^2$ . We defined mature FAs as having a longevity > 15 minutes and an area > 1  $\mu\text{m}^2$ . FA assembly and disassembly rates were determined by paxillin-GFP intensity values fit overtime to a log-linear model. The results only include FAs with positive rates and with model p values  $\leq 0.05$ . These are presented as the slopes in Figure 4H. The length in minutes that each individual FA spent undergoing assembly or disassembly are presented as the length of the lines in Figure 4H. Stability phase length was determined as the amount of time between assembly and disassembly for each FA. The Focal Adhesion Alignment Index (FAAI) measure presented in Figure 7H was previously described by Wu et al., 2012. This is also determined from TIRF movies as analyzed by the Focal Adhesion Analysis Server. Briefly, the FAAI is a measure of the global alignment of FAs across the whole cell. FA angles are determined at each time point throughout imaging and the reference angle is determined as the angle that minimizes the deviation of FA angles across the whole cell.  $\text{FAAI} = 90 - \text{standard deviation of adhesion angles at a particular reference angle}$ . High FAAI = low standard deviation = high global alignment. Low FAAI = high standard deviation = low global alignment.

#### Traction Force Microscopy (TFM)

Correlation-based particle tracking velocimetry code in MATLAB was used to quantify the cell-induced deformation of the polyacrylamide gel. Deformations were interpolated onto a 0.47  $\mu\text{m}$  displacement grid, and the stress field was reconstructed by Fourier-amidde traction cytometry and interpolated on a 0.47  $\mu\text{m}$  grid (Sabass et al., 2008). To analyze total force exerted by a cell on the ECM, a binary cell mask was created by outlining cell boundaries manually and dilated by 50 pixels to include traction vectors that enter the region of interest (ROI), but whose origins lay just outside the ROI. Traction vectors outside the cell were defined as background forces and only vectors whose magnitudes greater than or equal to 2x above background were included in the analysis. The sum of traction stresses per square micrometer was calculated and multiplied by the area of the entire cell (Maruthamuthu et al., 2011).

### Fixed Cell Imaging

#### Focal Adhesions (FAs)

Fixed FAs (Figures 2 and 3) were segmented using MATLAB. Briefly, confocal z-projections of single cells stained for FA markers were subject to difference of gaussians filtering in which background is reduced and smaller objects are enhanced. Filtered images were thresholded to generate a binary image in which individual bright objects containing more than 6 pixels were identified as FAs. From these images, we quantified FA number, area, and aspect ratio. To quantify intensity, the mask was applied to the original image and average pixel intensity was measured within each FA detected. For co-localization analysis, the mask obtained using one marker was then applied to the original image for another marker. We then extracted the list of individual pixel intensities within each FA for both markers, and computed the correlation coefficient between the two sets.

#### Cell Morphology

Cell contours were obtained automatically by processing confocal z-projections of cells stained for F-actin (Phalloidin) in MATLAB. Images were first blurred with a Gaussian filter, then an edge detection algorithm was applied to identify cell borders. The resultant binary image was refined through successive dilations and erosions to yield the final cell contour. These contours were used to measure cell area, aspect ratio (long axis/short axis), and circularity ( $4\pi \times \text{area} / \text{perimeter}^2$ ). Morphology of cell protrusions was quantified automatically in MATLAB. First, cell contours were identified as outlined above. Next, we obtained the contour coordinates of the convex hull of the binary image representing cell area. At each point along the cell contour, we computed the minimum distance between the convex hull and the actual cell contour. Based on these distances, minima corresponding to protrusions could be identified. To be counted as protrusions, minima had to be at least 10 pixels apart along the contour and of height greater than 5 pixels. Based on the coordinates of adjacent peaks, the width, height, and aspect ratio of protrusions could be computed.

#### Actin Fibers

To quantitatively described actin fibers within cells, we adapted previously used methods (Cetera et al., 2014). First, we identified cell contours as described above. Next, the cell was subdivided into 32x32 pixel windows overlapping by 50%. We then computed the

two-dimensional Fourier transform of each window. If a window contains no fibers, the fourier transform will be a central, diffuse point of bright pixels. However, if a window contains aligned fibers, the fourier transform will consist of an elongated accumulation of bright pixels at a 90 degree angle to the original fibers. Based on the aspect ratio and orientation of the fourier transform, we determined fibrousness and fiber orientation in a given window. The data for individual windows could then be compared across the entire cell to estimate the cell fibrousness, defined here as the percentage of cell area (% of windows) with aspect ratio greater than a cut-off value.

#### **Relative Adhesive Strength**

Corresponding fields of view between non-spun control and spun experiments were compared. Cells were counted and relative adhesive strength is expressed as the percent of cells left in the spun experiment compared to the total number of cells in the relative same field of view in the non-spun control.

#### **Scratch Assays & Wound Healing**

ImageJ was then used to measure open wound area at each time point.

#### **DATA AND SOFTWARE AVAILABILITY**

The accession number for the structure of the F3:R9 talin interaction complex reported in this paper is PDB: 4F7G (Song et al., 2012). Other data are available from the Lead Contact upon reasonable request.